NASA Conference Publication 3248
Part 2

Orbiter Experiments (OEX) Aerothermodynamics Symposium

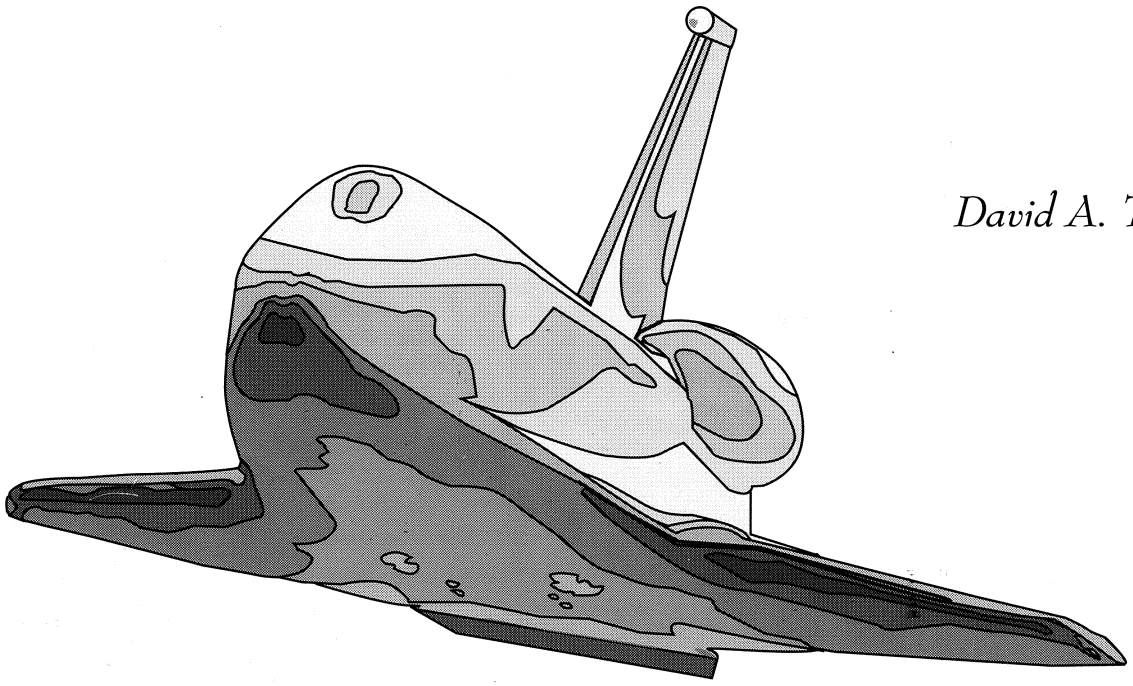

Edited by
David A. Throckmorton

Proceedings of a symposium sponsored by the National Aeronautics and Space Administration Washington, DC, and held in Williamsburg, Virginia April 27-30, 1993

April 1995

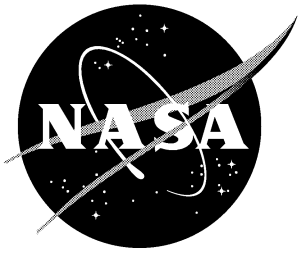

NASA Conference Publication 3248
Part 2

Orbiter Experiments (OEX) Aerothermodynamics Symposium

Edited by
David A. Throckmorton
Langley Research Center • Hampton, Virginia

Proceedings of a symposium sponsored by the
National Aeronautics and Space Administration,
Washington, D.C., and held in
Williamsburg, Virginia
April 27–30, 1993

National Aeronautics and Space Administration
Langley Research Center • Hampton, Virginia 23681-0001

April 1995

The use of trade names of manufacturers in this report does not constitute an official endorsement of such products or manufacturers, either expressed or implied, by the National Aeronautics and Space Administration.

This publication is available from the following source:

NASA Center for AeroSpace Information
800 Elkridge Landing Road
Linthicum Heights, MD 21090-2934
(301) 621-0390

PREFACE

Operations of the Nation's Space Transportation System (STS) have provided recurring opportunities for the aerothermodynamicist to study entry aerothermal phenomena unique to lifting vehicles in hypersonic flight. Initiated in the mid-1970s, the NASA Orbiter Experiments (OEX) Program provided a mechanism for utilization of the Shuttle Orbiter as an entry aerothermodynamic flight-research vehicle, as an adjunct to its normal operational missions.

Under the auspices of the OEX Program, various elements of aerothermodynamic research instrumentation flew aboard the Orbiters *Columbia* and *Challenger*. These OEX experiment instrumentation packages obtained in-flight measurements of the requisite parameters for (1) determination of Orbiter aerodynamic characteristics (both static and dynamic) over the entire entry flight regime, and (2) determination of the aerodynamic heating rates imposed upon the vehicle's thermal protection system during the hypersonic portion of atmospheric entry.

The data derived from the OEX complement of experiments represent benchmark hypersonic flight data heretofore unavailable for a lifting entry vehicle. These data are being used in a continual process of validation of state-of-the-art methods, both experimental and computational, for simulating/predicting the aerothermodynamic characteristics of advanced space transportation vehicles.

The ***Orbiter Experiments (OEX) Aerothermodynamics Symposium*** provided a forum for dissemination of OEX experiment flight data and for demonstration of the manner in which these data are being used for validation of advanced vehicle aerothermodynamic design tools. The Symposium's invited speakers included both OEX experiment Principal Investigators and other researchers who have been active users and analysts of the Orbiter entry flight data. This NASA Conference Publication comprises a compendium of the papers presented at the Symposium.

CONTENTS

*Part 1 is presented under separate cover.

Part 2

*Retired.

*Retired.

Part 2

SHUTTLE ENTRY AIR DATA SYSTEM (SEADS): AN EVALUATION OF FLIGHT PRESSURE DATA WITH COMPARISONS TO WIND TUNNEL AND COMPUTATIONAL PREDICTIONS

M. W. Henry*, S. M. Deshpande†, and J. B. Eades‡, Jr.
Analytical Mechanics Associates, Inc.
Hampton, VA

Paul M. Siemers III §
NASA Langley Research Center
Hampton, VA

ABSTRACT

The Shuttle Entry Air Data System (SEADS) flight pressure data is utilized to verify the simulation capabilities/performance of ground test facilities and theoretical computational techniques. SEADS is an implementation of the flush pressure orifice air data system concept conceived at the NASA Langley Research Center. The system uses an array of flush pressure orifices and associated measurement hardware located in the nosecap and forward fuselage of the Space Shuttle Orbiter to provide stagnation region pressure profiles during entry. These data were analyzed to provide the desired air data parameters. Implementation of the SEADS required the design and development of system hardware as well as the computational methodology needed for data reduction and analysis. The development of the computational techniques and the data reduction algorithm used in producing the SEADS across-the-speed-range air data was aided by an extensive series of wind tunnel tests and computer simulations.

---

* Senior Programmer/Analyst
† Project Engineer
‡ Senior Scientist
§ Aerospace Technologist

Support for this research was provided by NASA Langley Research Center, Hampton, VA. under Contract No. NAS1-17990.

Additionally, the more recent development of advanced computational techniques has provided new tools with the capability to predict flowfield parameters and thus the potential to support the design of flush air data systems. A verification of these data sources, wind tunnels and computational, is accomplished through the comparison of results acquired from the SEADS developmental wind tunnel tests and computational predictions to the pressure data acquired from the five flights of the SEADS on the Orbiter *Columbia*.

NOMENCLATURE

P	Pressure
P_{t_2}	Total Pressure
P_∞	Freestream static pressure
R	Ratio of freestream static to total pressure, $\frac{P_\infty}{P_{t_2}}$
α	Angle of attack
β	Angle of sideslip
ζ	Orifice normal clock angle measured clockwise looking forward
θ	Orifice flow incidence angle
η	Orifice normal cone angle
Φ	Orifice latitude
λ	Orifice longitude

Subscripts

∞	Freestream value
i	References orifice i
T	Wind Tunnel Data
F	Flight Data

Acronyms

SEADS	Shuttle Entry Air Data System
OEX	Orbiter Experiment Program
BET	Best Estimated Trajectory

INTRODUCTION

The five successful flights of the Shuttle Entry Air Data System (SEADS) provide an opportunity to verify the performance of ground test facilities and theoretical computational techniques. The repeatability of data obtained on these flights permits this verification through a comparison of flight data with the preflight data base.

Between January 1986 and June 1991, the Space Shuttle Orbiter *Columbia* flew five missions: STS-61C, STS-28, STS-32, STS35, STS-40. SEADS was included in the orbiter during these missions as part of the Orbiter Experiment Program (OEX). SEADS is an implementation of the flush pressure orifice air data system concept which was developed at the NASA Langley Research Center. SEADS employs an array of flush mounted pressure orifices located in the Shuttle orbiter's nosecap and forward fuselage to obtain aerodynamic pressure data. It is from these pressure measurements that the desired air data parameters are determined. The analysis of SEADS data and the determination of the required air data parameters necessitated the development of new analytical methods in air data parameter estimation. The pressure model/digital-filter-method proposed for the SEADS experiment required an extensive series of wind tunnel tests to provide the data base needed for algorithm development and verification. The various wind tunnel tests (Table 1) used three different scale models (Fig. 1) to obtain data over the range of Mach numbers (subsonic to hypersonic) and angles of attack and sideslip expected to be encountered during the Space Shuttle Orbiter's atmospheric entry and descent. The final preflight data reduction and the analysis system demonstration and verification were accomplished through computational simulations and flight tests.[1,2,3,4]

This paper demonstrates first, based on representative wind tunnel data, the sensitivity of the Shuttle Orbiter's stagnation region pressure distribution to angle of attack and Mach number (and, thereby, the premise of the flush pressure orifice air data system). The wind tunnel measured pressure distributions are presented for several angles of attack and for a range of Mach numbers.

The paper then shows a verification of the preflight wind tunnel data base and a demonstration of the capabilities of the computational techniques. This is accomplished

with representative comparisons made using pressures obtained from the Newtonian theory model, from wind tunnel data measurements, from the Computational Fluid Dynamics (CFD) High Alpha Inviscid Solution (HALIS) code, and from the SEADS flights. The flight measured pressures were taken at discrete trajectory points, chosen to provide a close match with wind tunnel tests, i.e., at corresponding angles of attack, sideslip, and Mach numbers. The agreement verifies the use of the Newtonian theoretical model as a tool for system definition studies. In addition, at selected trajectory points, a comparison of measured pressures from all five flights is made to demonstrate the repeatability of the SEADS data and the reliability of the hardware.

The flight verification of the wind tunnel and computational predictions is demonstrated through several data comparisons for which flight data and computational data were selected to correspond to wind tunnel Mach numbers. Wind tunnel and computational data were chosen for angles of attack and sideslip which corresponded to the flight conditions. The resulting comparisons provide verification of the wind tunnel and computational methodologies.

SEADS SYSTEM

SEADS consists of both hardware and data reduction software. The hardware is comprised of a reinforced carbon-carbon Orbiter nosecap drilled to accommodate fourteen (14) flush pressure orifices in a cruciform array. This array is supplemented by six (6) static pressure orifices located on the orbiter forward fuselage. Tubing leads to 20 pairs of pressure transducers, each pair consisting of one 0-1 psia and one 0-20 psia transducer.[5] The Orbiter nosecap is shown in Fig. 2. Measured flight orifice locations on the flight nosecap are listed in Table 2 in terms of the cone and clock angles necessary to describe the local surface unit normal vector (these angles are defined in Ref. 6). Also listed in Table 2 are orifice latitude, longitude and S/S_{ref}, as defined below. A schematic of the Orbiter nosecap and forward fuselage orifice locations is shown in Fig. 3. The relationship of the cone and clock angles to the body axes of the Orbiter is demonstrated in Fig. 4.

The SEADS experiment was designed so that the measured orifice pressures needed for the derivation of air data parameters could be mathematically analyzed to yield stagnation pressure, the freestream dynamic pressure, and the associated angles of attack and sideslip.[7] This

information was acquired through the use of the SEADS data reduction software. The software consists of several computer programs which are designed to reformat data recorder information, merge it with reference sources, apply data reduction methodologies and compare the results with reference data. The selected data reduction methodology employs a pressure prediction model which is based on Newtonian theory.[8] The air data were extracted from the pressures by means of a weighted least square digital filter, based on this theoretical model. Digital filter theory allows refinement of an a priori estimate using an iterative procedure which is equivalent to an application of the 4-dimensional analog of the Newton-Raphson method. Convergence is achieved in relatively few iterations (2 to 4) when using a good initial state estimate, which is typically available during SEADS data reduction (for example, from a previous converged solution).

ALGORITHM DEVELOPMENT

Wind Tunnel Tests

At the beginning of the SEADS development, various aerodynamic flow theories were examined as possible candidates for the pressure model. Although Newtonian theory only provided an approximate pressure model, the theory was selected because of its relative simplicity and ease of use. This model proved to be a good tool for verifying the SEADS system design and was used to support decisions concerning orifice locations and transducer sizing.

Since the Newtonian pressure model is only an approximation, corrections had to be applied prior to its use with flight data. In order to obtain these corrections, numerous wind tunnel pressure measurement tests were performed on 0.02-scale, 0.04-scale and .10-scale models of the Orbiter forebody. These model scales were dictated by the wind tunnel dimensions. Each orbiter wind tunnel model was instrumented with orifices which matched the proposed locations of the SEADS orifices at the time of the test, supplemented by additional orifices intended to provide comprehensive pressure profiles over the forebody. The data obtained in early tests were used to finalize the SEADS orifice locations.

Because of the nature of the SEADS algorithm, which uses overall pressure distributions rather than particular pressure differences and/or ratios, slight errors in orifice locations do not devalue the preflight data base nor impair the accuracy of the SEADS derived air data

parameters. It was important to duplicate the overall Orbiter's nosecap geometry on the wind tunnel models, since this geometry affects the flowfield and, consequently, the pressure distributions. The relationship of the wind tunnel models to the Orbiter is shown in Fig. 1. The tests were conducted for a speed range from Mach number 0.25 to Mach number 21.57, with angles of attack ranging from -10° to 50°, and angles of sideslip ranging from -6° to 6°. Each wind tunnel's test conditions, and the scale of the models used for the tests, are listed in Table 1. This table also details the Mach numbers and the ranges of angles of attack and sideslip.

The pressure data from these tests form the data base from which the algorithm corrections were derived. These corrections were subsequently applied to the derived air data parameters obtained by the SEADS filter algorithm which is based on Newtonian theory. These correction factors, together with the filter algorithm, are the basis for the SEADS flight data reduction program.

WIND TUNNEL PRESSURE DISTRIBUTION

The sensitivity of the SEADS measured pressure distributions to the flow incidence angle and to the angle of attack is shown in Figures 5 through 11.

This sensitivity is the fundamental premise upon which the flush pressure orifice air data system concept is based. Only representative graphs from the full data base are presented. Each figure represents a specific wind tunnel/Mach number/sideslip angle combination. Three widely separated angles of attack are used to prepare the normalized pressure distributions (ordinate values are $\frac{P_i}{P_{t_2}}$ where P_i is the local measured pressure and P_{t_2} is the total pressure behind the shock). The pressure distributions are plotted for the orifices located in the plane-of-symmetry (vertical plane) and are numbered 1-8 (see Fig. 3). These data are presented as a function of Φ_i, the orifice "latitude", a quantity obtained from the cone and clock angles[6] for each orifice as follows:

$$\sin\Phi_i = \sin\eta_i \ \sin\zeta_i \qquad (1)$$

Similarly, λ_i, the "longitude" for the horizontal plane orifices, is obtained from:

$$\sin\lambda_i = \sin\eta_i \cos\zeta_i \qquad (2)$$

From information shown in Figures 5-11, it can be seen that the peak pressure value is generally found at the orifice with a Φ_i value nearest to the angle of attack, α; thus, the angle of attack may be inferred from the location of the maximum. It is further noted that the curves become progressively more shallow as the test Mach number decreases, since the dynamic pressure decreases, compared to the static pressure. Consequently, the determination of pressures becomes more uncertain for Mach numbers less than 0.3. The figures and results are consistent across the speed range corresponding to the Mach number range ($0.25 < M_\infty < 21.57$).

FLIGHT PRESSURE DISTRIBUTION

The full trajectory pressure profile at orifice 5 for each SEADS flight is shown in Fig. 12. The altitude scale in this figure is altitude above mean sea level. Figures 13 through 16 demonstrate the close agreement and repeatability of SEADS flight measured data across the speed range from subsonic through hypersonic speeds. The plane-of-symmetry pressure distribution for the five SEADS flights at Mach 0.80, shown in Fig. 13, demonstrates the close agreement and repeatability of flight data throughout the life of the experiment. An enlarged representation of the normalized pressures at each of three orifices (2, 5 and 8), for the five flights, is also shown in the figure. In this figure, as well as Figs. 14-16, there is no flight measured pressure for orifice 7. This is a consequence of an inoperative high range (0-20 psia) transducer. Similar pressure distributions and relative pressures at Mach 2.46, Mach 4.63 and Mach 10.02 are illustrated in Figs. 14-16. As can be seen from viewing these figures, flight conditions vary from flight to flight for the same Mach number. The various differences in angle of attack, angle of sideslip and total pressure account for the minor differences in the pressure readings from one flight to another at the same orifice location. The repeatability of the pressure from flight to flight is dramatically demonstrated by the individual relative pressure plots shown in Figs. 13-16. The relative pressure differences are less than three percent before the variations in total pressure and angles of attack and sideslip are taken into account. This repeatability is important since it provides a flight data base with which the preflight data can be verified and evaluated with great confidence.

COMPARISONS OF WIND TUNNEL MEASURED PRESSURES AND FLIGHT MEASURED PRESSURES WITH NEWTONIAN AND HALIS COMPUTED PROFILES

It is of interest to compare the flight measured pressures with those obtained from the wind tunnel tests, and to compare these results with those predicted from the underlying Newtonian theory and those obtained from the HALIS code. These comparisons are best accomplished by normalizing the measured and predicted pressures (P_i) using total pressure (P_{t_2}).

Briefly, in Newtonian theory, the pressure ratios $\frac{P_i}{P_{t_2}}$ are calculated from the following equations:

$$\frac{P_i}{P_{t_2}} = [(1 - R) \cos^2 \theta_i + R] \tag{3}$$

where

$$\cos\theta_i = \cos\alpha \cos\beta \cos\eta_i + \sin\beta \sin\eta_i \cos\zeta_i + \sin\alpha \cos\beta \sin\eta_i \sin\zeta_i \tag{4}$$

and

$$R \equiv \frac{P_\infty}{P_{t_2}} \ . \tag{5}$$

In the preceding expressions, P_∞ is the freestream static pressure. For mathematical and developmental details, see Ref. 6.

The High Alpha Inviscid Solution (HALIS) flowfield code was initially developed to handle high angle of attack flowfields, such as sensed by the Space Shuttle Orbiter, which are characterized by large regions of embedded subsonic flow on the windward surface of the body. The HALIS code is a time-asymptotic solution of the Euler equations which utilizes an unsplit MacCormack differencing scheme. The code is designed to allow grid points in any of the three coordinate directions to be clustered in a region of high gradients. The HALIS code is set up to handle arbitrary gases, behaving as a perfect gas, or as a real gas in thermodynamic equilibrium. For details of the HALIS predictions, see Ref. 9.

Since wind tunnel test data are available only at discrete Mach numbers and discrete angles of attack and sideslip, points from the flight data base were selected which most closely matched data available from the wind tunnel tests. The points selected are those shown for the five SEADS flights in Tables 3 through 7, respectively. The altitudes shown in these tables are altitudes above mean sea level. Points in these tables which have a Mach number value denoted by a "+" character are the points which are shown in the various figures in this paper. The HALIS predictions were made at the indicated Mach numbers in the hypersonic speed range.

Both Newtonian and HALIS derived pressure points were made at selected points along the surface geometry model in both the vertical and horizontal planes. The resulting profiles are displayed as curves of "predicted" normalized pressures with which wind tunnel data and flight measured data can be compared. Representative comparisons are shown in Figs. 17-23. The predicted and measured pressures are plotted as functions of S/S_{ref}, where S is a distance measured along the nosecap surface from a reference point (in this case, orifice 4) and S_{ref} is a normalizing value. The predicted profiles and measured pressures are shown for orifices in both the vertical and horizontal planes. Data obtained in the AEDC 16' Wind Tunnel are shown in Figs. 17 and 18, those from the LaRC Unitary Plan Wind Tunnel in Figs. 19, 20 and 21, those from the LaRC Mach 6 Air Tunnel in Fig. 22, and those from the LaRC Mach 10 Tunnel in Fig. 23. Flight pressure data are shown for the same Mach number in Figs. 17-23. In each case, wind tunnel values of P_{t_2}, R, α and ß were used in the Newtonian and HALIS computations. Related wind tunnel pressure distributions are shown in Figs. 5, 6, 8, 9, 10 and 11.

CONCLUSIONS

The SEADS pressure data obtained from the five SEADS flights have been analyzed and compared to the preflight data base and computational predictions. The results of this analysis demonstrate that:

1. Repeatable pressure data have been obtained for all flights, permitting verification and evaluation of the preflight data base.

2. Newtonian theory provides a useful tool for the design of a flush air data system.

3. Ground based wind tunnel tests provide a preflight data base which demonstrates the feasibility and accuracy of a flush orifice air data system and enables the derivation of corrections to appoximate theoretical models.

4. HALIS accurately predicted pressures in high supersonic and hypersonic flight.

REFERENCES

1. Larson, T. J. and Siemers, P. M. III, "Subsonic Tests of an All-Flush-Pressure-Orifice Air Data System," NASA TP 1871, June 1981.

2. Larson, T. J., Whitmore, S. A., Ehernberger, L. J., Johnson, J. B. and Siemers, P.M. III, "Qualitative Evaluation of a Flush Air Data System at Transonic Speeds and High Angles of Attack," NASA TP 2716, April 1987.

3. Bradley, P. F., Siemers, P. M. III, and Weilmunster, K. J., "An Evaluation of Space Shuttle Orbiter Forward Fuselage Surface Pressures: Comparison with Wind Tunnel and Theoretical Predictions," AIAA Paper No. 83-0119, January 1983.

4. Siemers, P. M. III, Wolf, H. and Flanagan, P. F., "Shuttle Entry Air Data System Concepts Applied to Space Shuttle Orbiter Flight Pressure Data to Determine Air Data - STS 1-4," AIAA Paper No. 83-0118, January 1983.

5. Siemers, P.M. III, Wolf, H. and Henry, M. W., "Shuttle Entry Air Data System (SEADS): Flight Verification of an Advanced Air Data System Concept," AIAA Paper No. 88-2103, May 1988.

6. Henry, M. W., Wolf, H. and Siemers, P. M. III, "An Evaluation of Shuttle Air Data System (SEADS) Flight Pressures: Comparisons With Wind Tunnel and Theoretical Predictions," AIAA Paper No. 88-2054, May 1988.

7. Pruett, C. D., Wolf, H., Siemers, P. M. III, and Heck, M. L., "An Innovative Air Data System for the Space Shuttle Orbiter: Data Analysis Techniques," AIAA Paper No. 81-2455, Nov. 1981.

8. Zuckrow, Maurice J. and Hoffman, Joe D., "Gas Dynamics, Volume I," John Wiley & Sons, New York, 1976, pp. 549, 132.

9. Weilmunster, K. J. and Hamilton, H. H. II, "A Comparison of Computed Space Shuttle Orbiter Surface Pressures with Flight Measurements," AIAA Paper 83-1798, July 1983.

TABLE 1. Wind Tunnel Tests

Tunnel	Model(s)	Mach No.	Angle of attack (α)	Angle of sideslip (β)
LaRC Hypersonic He	0.02	21.57	-10° to 50°	-5° to 5°
LaRC M10 Air	0.02, 0.04	10.02	-10° to 45°	-5° to 5°
LaRC CF_4	0.02	6.2	-10° to 45°	0° to 4°
LaRC M6Air	0.02, 0.04	6.0	-10° to 45°	-4° to 0°
LaRC Unitary	0.04	1.5-4.63	-5° to 30°	-6° to 4.5°
AEDC 16T	0.10	0.25-1.5	-2° to 18°	-6° to 6°
AMES 8x7	0.10	2.46-3.48	-2° to 24°	-6° to 6°
AMES 9x7	0.10	1.6-2.46	-2° to 24°	-6° to 6°

TABLE 2. Orifice Cone (η) and Clock (ζ) Angles, Latitude (Φ), Longitude (λ) and Surface Location (S/S_{ref}) for the Space Shuttle Orbiter

Orifice ID	Cone $\eta°$	Clock $\zeta°$	Latitude Φ	Longitude λ	Surface Location S/S_{ref}
1	24.8813	-90.0000	-24.8813	.0000	-14.1878
2	13.5133	-90.0000	-13.5133	.0000	-9.4039
3	0.0018	-90.0000	-.0018	.0000	-4.6602
4	12.2970	90.0000	12.2970	.0000	.0000
5	24.5105	90.0000	24.5105	.0000	4.8260
6	34.9106	90.0000	34.9106	.0000	9.6240
7	43.3277	90.0000	43.3277	.0000	14.5003
8	49.8664	90.0000	49.8664	.0000	19.3946
9	32.2780	172.0119	4.2560	-31.9275	-14.2890
10	24.0011	160.5255	7.7937	-22.5496	-9.5058
11	15.6884	135.2101	10.9821	-11.0640	-4.7824
12	15.6884	44.7899	10.9821	11.0640	4.7824
13	24.0021	19.4745	7.7940	22.5506	9.5058
14	32.2780	7.9881	4.2560	31.9275	14.2890
15	59.3468	-93.4826	-59.1687	-2.9955	
16	59.8427	170.9744	7.8044	-58.7472	
17	59.9518	9.0713	7.8352	58.6313	
18	67.3264	93.6815	67.0450	-3.3966	45.5299
19	75.2314	-179.6382	-.3498	-75.2271	
20	75.3511	-.4938	-.4777	75.3430	

TABLE 3. Flight Conditions at Wind Tunnel Test Points
STS-61C

Tunnel Mach No.	Flight Values α°	β°	P_{t_2} (PSF)	Altitude (ft)
21.570	39.2	-.1	73.1	224656
10.020+	39.5	.3	196.4	164348
6.220	30.2	-.1	257.5	134075
6.000+	28.5	-.2	283.6	130062
4.630+	23.6	.4	338.0	114237
3.500+	17.9	-.3	417.9	97342
3.480	17.8	-.4	418.9	97052
3.020	16.1	.2	440.5	90032
2.960+	15.9	-.1	443.4	89017
2.660	14.7	-.1	437.4	84877
2.460+	14.3	-.2	429.0	82109
2.300	14.5	-.3	416.6	80124
2.280	14.5	-.3	414.4	79911
2.000	12.4	.3	372.2	77108
1.980	12.1	.3	368.8	76849
1.770	10.6	-.7	361.5	73161
1.595	10.2	-.5	375.8	68632
1.500+	10.2	.2	380.9	66209
1.400	9.4	1.0	388.6	63579
1.300	8.7	1.0	411.7	60215
1.200	8.2	-.1	445.3	56348
1.150	7.7	-1.8	455.9	54656
1.100+	7.8	-2.1	458.7	53335
.950	7.3	-.8	505.7	47786
.800+	5.4	.3	795.9	35195
.600+	8.4	.8	1192.7	21917

TABLE 4. Flight Conditions at Wind Tunnel Test Points
STS-28

Tunnel Mach No.	Flight Values α°	β°	P_{t_2} (PSF)*	Altitude (ft)
21.570	39.9	.0	.0	225590
10.020+	39.1	-.3	.0	169856
6.220	31.0	-.2	.0	141345
6.000+	30.2	.2	.0	138738
4.630+	24.0	.2	.0	117810
3.500+	18.1	-.1	.0	100438
3.480	18.1	.0	.0	100121
3.020	15.4	-.1	.0	92082
2.960+	15.3	-.2	.0	91188
2.660	14.1	.0	.0	86117
2.460+	13.9	.1	.0	82721
2.300	15.2	.1	.0	80973
2.280	14.8	.0	.0	80794
2.000	11.9	-.1	.0	78673
1.980	11.7	-.2	.0	78534
1.770	10.2	.1	.0	75484
1.595	9.9	.0	.0	70878
1.500+	9.6	.0	.0	67875
1.400	8.9	-.6	.0	64771
1.300	8.2	.1	.0	60871
1.200	7.9	-.7	.0	57243
1.150	7.7	-.7	.0	55500
1.100+	7.5	-.3	.0	53992
.950	7.2	-.5	.0	49856
.800+	7.0	.0	.0	32714
.600+	7.3	-.3	.0	21543

*P_{t_2} reference source not available

TABLE 5. Flight Conditions at Wind Tunnel Test Points
STS-32

Tunnel Mach No.	Flight Values			
	$\alpha°$	$\beta°$	P_{t_2} (PSF)*	Altitude (ft)
21.570	40.3	-.3	.0	222666
10.020+	38.8	-.1	.0	161659
6.220	29.8	-.4	.0	133321
6.000+	28.8	.0	.0	130080
4.630+	23.0	-.2	.0	111226
3.500+	18.2	-.1	.0	94874
3.480	18.1	-.2	.0	94579
3.020	15.8	.0	.0	87152
2.960+	15.2	.1	.0	85943
2.660	13.7	.1	.0	80986
2.460+	14.6	-.3	.0	78069
2.300	14.9	-.2	.0	76720
2.280	14.6	-.1	.0	76579
2.000	10.4	.3	.0	74680
1.980	10.4	.3	.0	74515
1.770	10.2	.2	.0	70432
1.595	9.7	-.6	.0	65334
1.500+	9.7	-.4	.0	62476
1.400	8.6	-.4	.0	59059
1.300	8.3	.0	.0	55893
1.200	8.2	-.1	.0	52677
1.150	8.0	-.3	.0	51326
1.100+	8.2	.6	.0	50191
.950	7.4	-.3	.0	44853
.800+	5.7	.0	.0	32473
.600+	8.2	.3	.0	19500

*P_{t_2} reference source not available

TABLE 6. Flight Conditions at Wind Tunnel Test Points
STS-35

Tunnel Mach No.	Flight Values			
	$\alpha°$	$\beta°$	P_{t_2} (PSF)	Altitude (ft)
21.570	40.0	.0	89.7	221440
10.020+	39.2	.1	214.3	161503
6.220	30.1	.2	284.4	132292
6.000+	28.5	.2	296.7	129722
4.630+	22.9	.1	378.7	112376
3.500+	18.2	.1	433.1	96890
3.480	18.2	.0	432.9	96674
3.020	16.9	.3	447.1	89910
2.960+	16.1	.3	451.6	88902
2.660	14.5	.3	492.3	82821
2.460+	15.0	.0	501.2	78980
2.300	14.5	-.1	482.6	77143
2.280	14.5	-.1	480.9	77047
2.000	10.8	.0	427.6	74538
1.980	10.5	.0	424.9	74264
1.770	9.9	-.1	426.4	70219
1.595	9.4	-.1	456.9	65229
1.500+	9.0	-.4	475.9	62267
1.400	8.1	-.5	498.3	59134
1.300	7.7	.7	514.3	56210
1.200	7.5	.3	524.4	53364
1.150	7.7	.5	529.0	51991
1.100+	7.6	-.1	530.6	50838
.950	7.3	.3	551.7	46444
.800+	6.1	.2	833.7	34126
.600+	7.8	-.2	1384.0	17837

TABLE 7. Flight Conditions at Wind Tunnel Test Points
STS-40

Tunnel Mach No.	BET Values			
	α°(BET)	β°(BET)	P_{t_2} (PSF)	Altitude (ft)
21.570	40.0	.0	91.0	225029
10.020+	39.2	.1	214.5	166516
6.220	30.7	.2	262.2	136843
6.000+	29.6	-.1	275.2	133858
4.630+	23.1	.0	380.5	113427
3.500+	17.8	-.1	455.3	96776
3.480	17.7	-.1	455.9	96621
3.020	15.7	.1	483.9	89106
2.960+	15.5	-.5	485.3	88230
2.660	14.6	.0	487.7	83663
2.460+	14.2	-.2	486.6	80521
2.300	14.8	.1	471.0	78430
2.280	14.7	.2	467.9	78218
2.000	12.6	-.2	414.5	75630
1.980	12.1	.0	409.8	75383
1.770	9.9	-.3	392.9	71809
1.595	9.8	-.4	417.3	66776
1.500+	9.6	.7	438.5	63589
1.400	8.6	.2	457.8	60396
1.300	8.1	-.2	476.6	57221
1.200	7.8	-.3	500.0	53776
1.150	7.7	-.1	504.4	52383
1.100+	7.5	-.3	507.7	51033
.950	7.1	-.3	551.3	45834
.800+	6.0	-.1	829.9	34057
.600+	9.4	.5	1179.7	21764

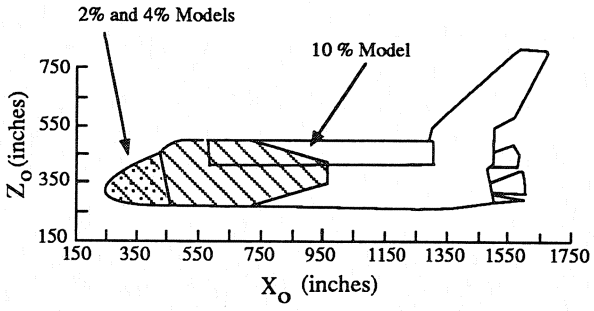

Fig. 1 Wind Tunnel Models

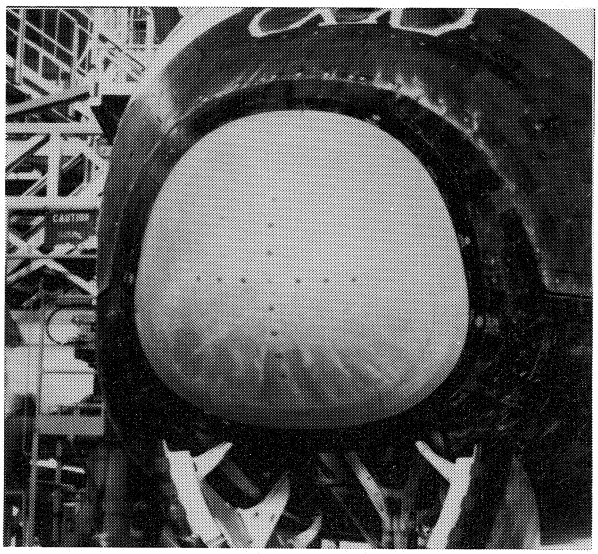

Fig. 2 SEADS Preflight

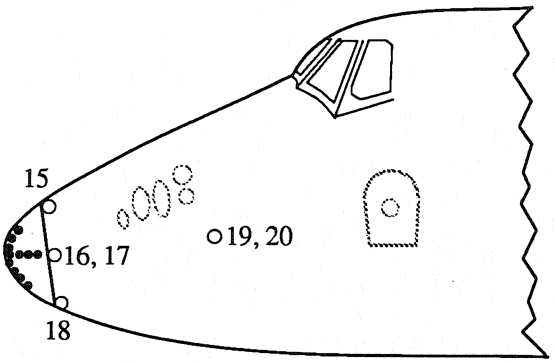

Orbiter Forebody (Side View)

● Nosecap Orifices (14)

○ Forebody Orifices (6)

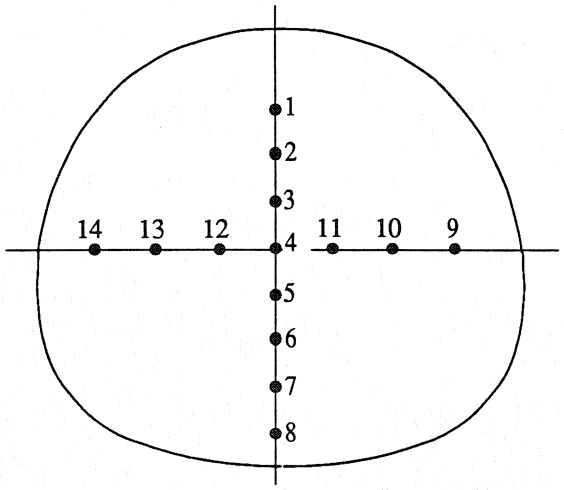

Nosecap (Front View)

Fig. 3 SEADS Flush Orifices

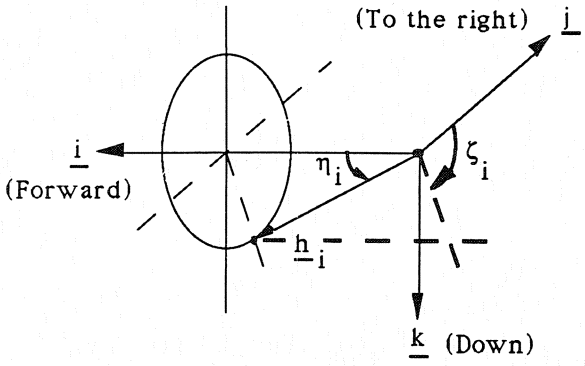

Fig. 4 Description of cone (η_i) and clock (ζ_i) angles

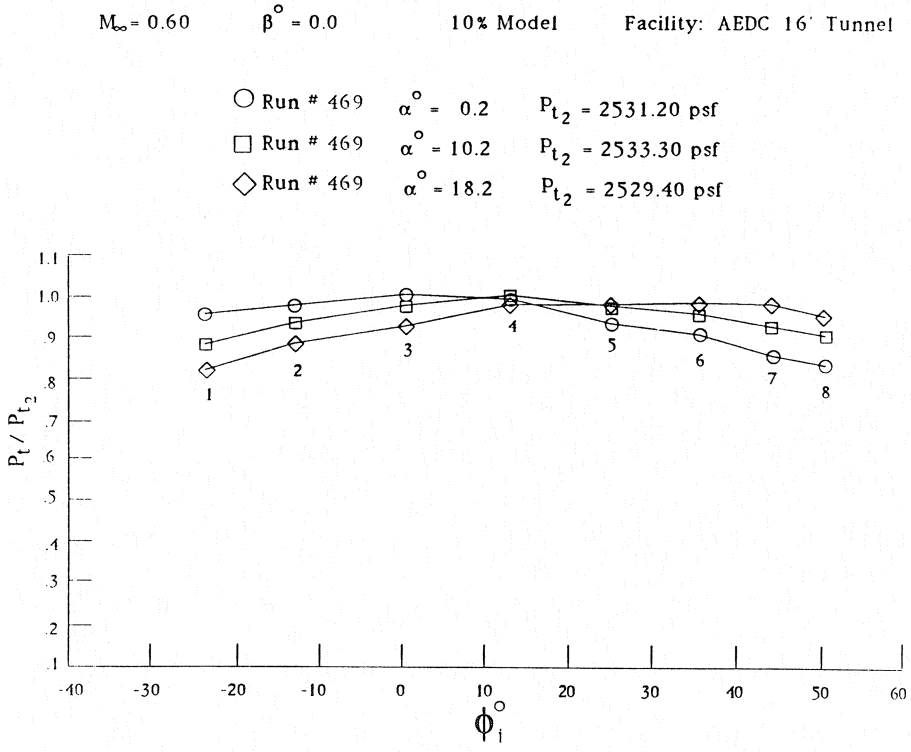

Fig. 5 Wind Tunnel Measured Pressure Distribution

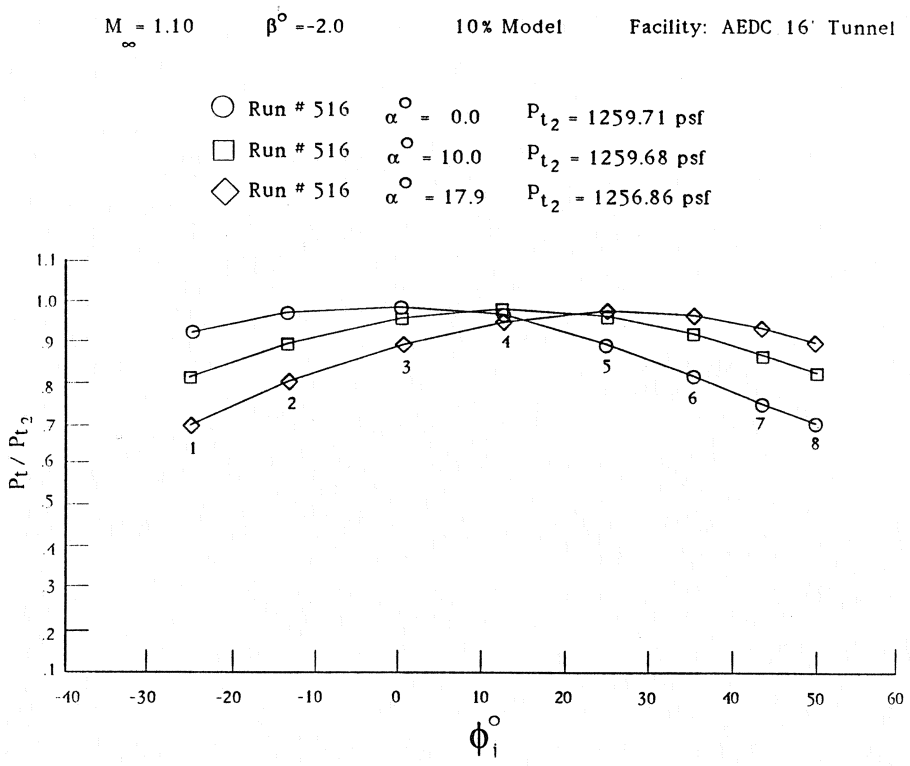

Fig. 6 Wind Tunnel Measured Pressure Distribution

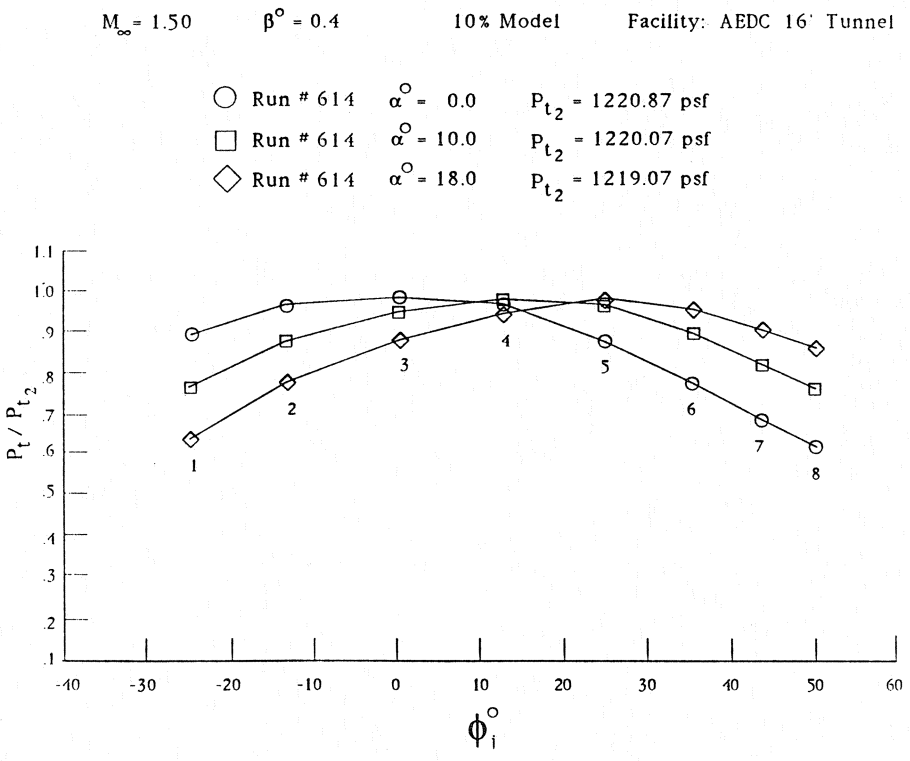

Fig. 7 Wind Tunnel Measured Pressure Distribution

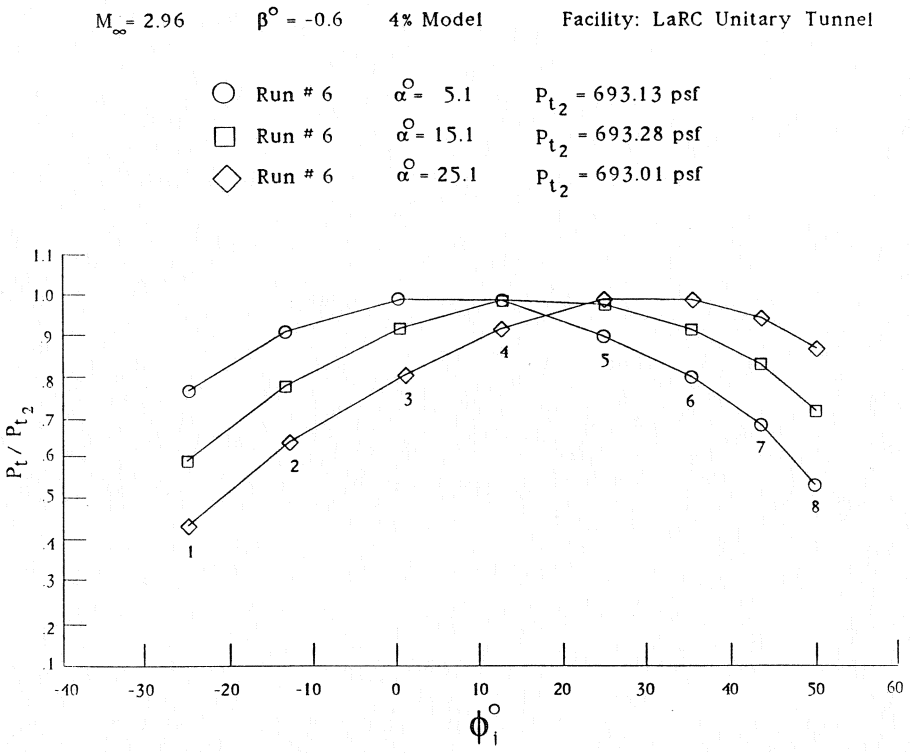

Fig. 8 Wind Tunnel Measured Pressure Distribution

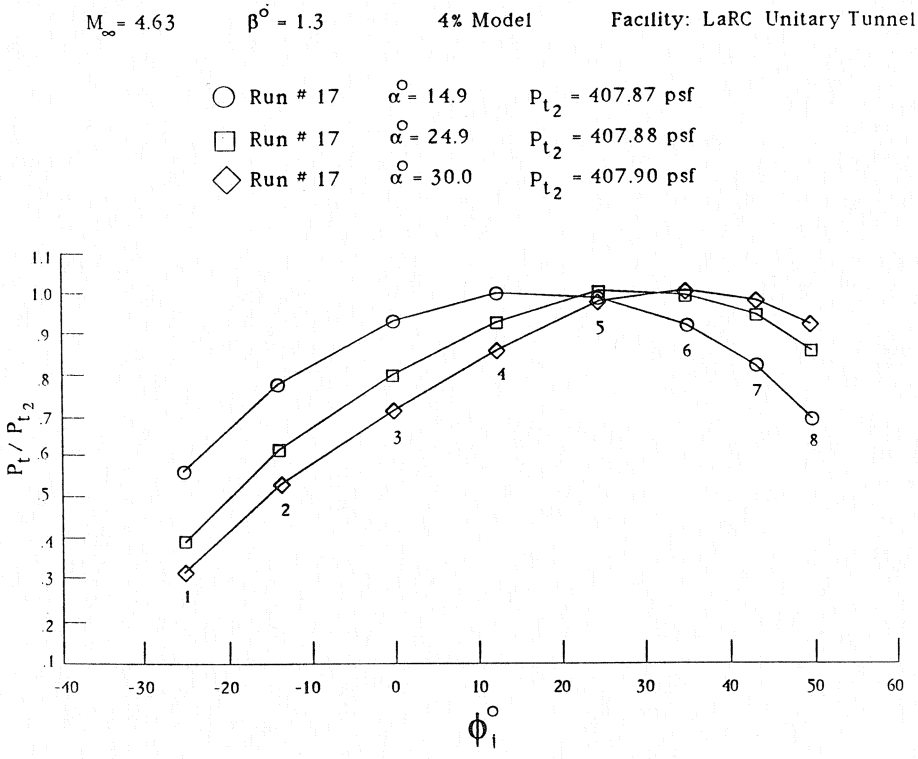

Fig. 9 Wind Tunnel Measured Pressure Distribution

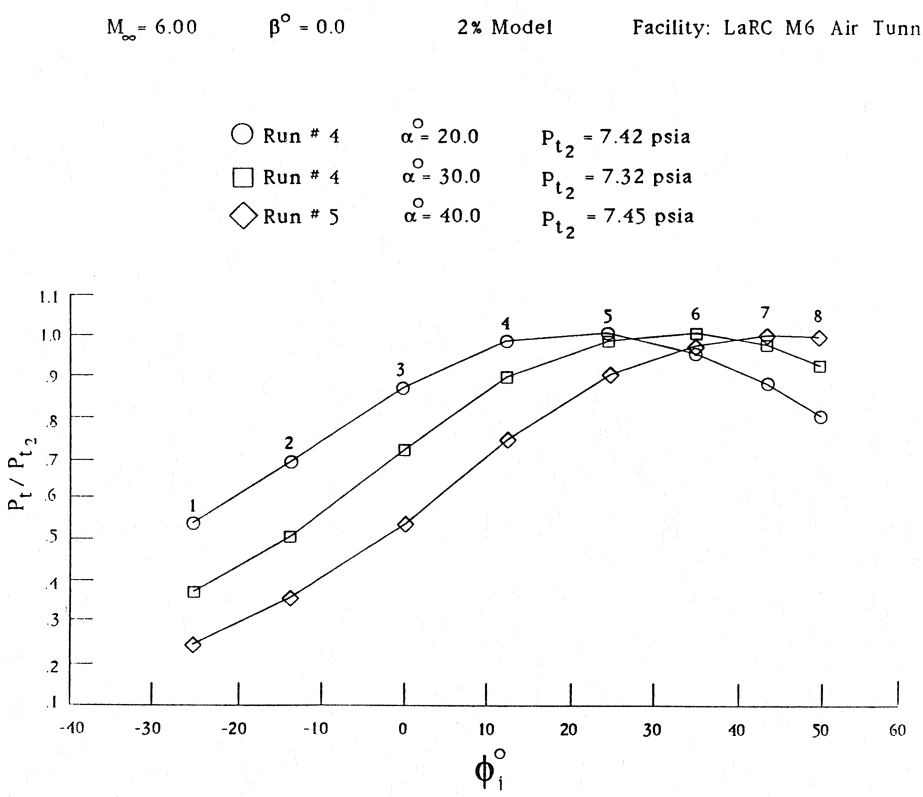

Fig. 10 Wind Tunnel Measured Pressure Distribution

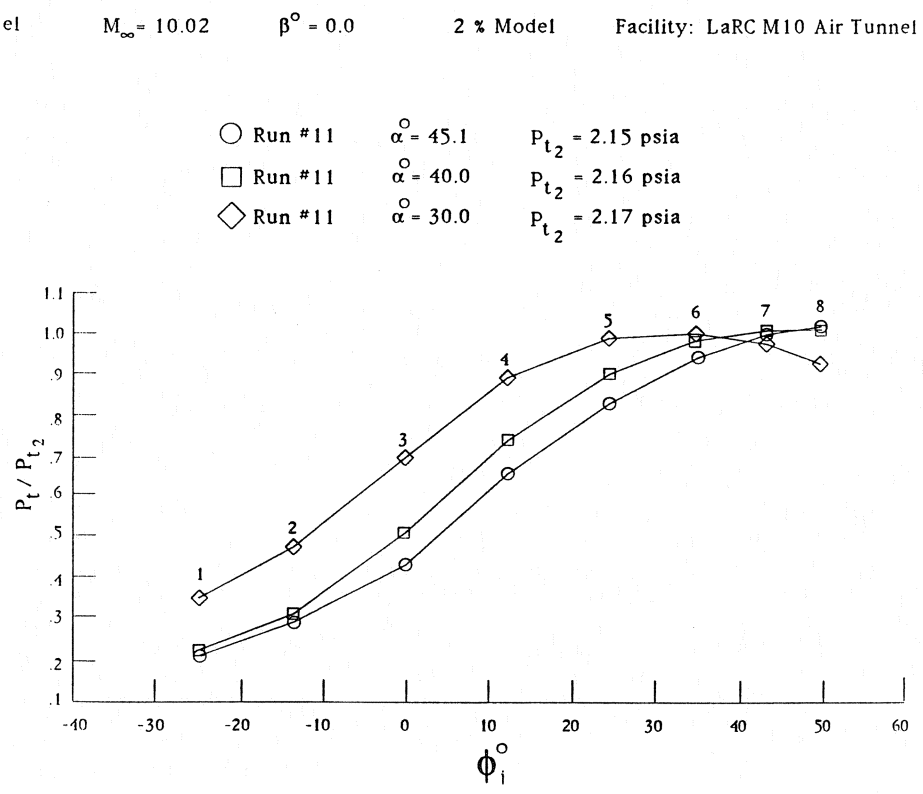

Fig. 11 Wind Tunnel Measured Pressure Distribution

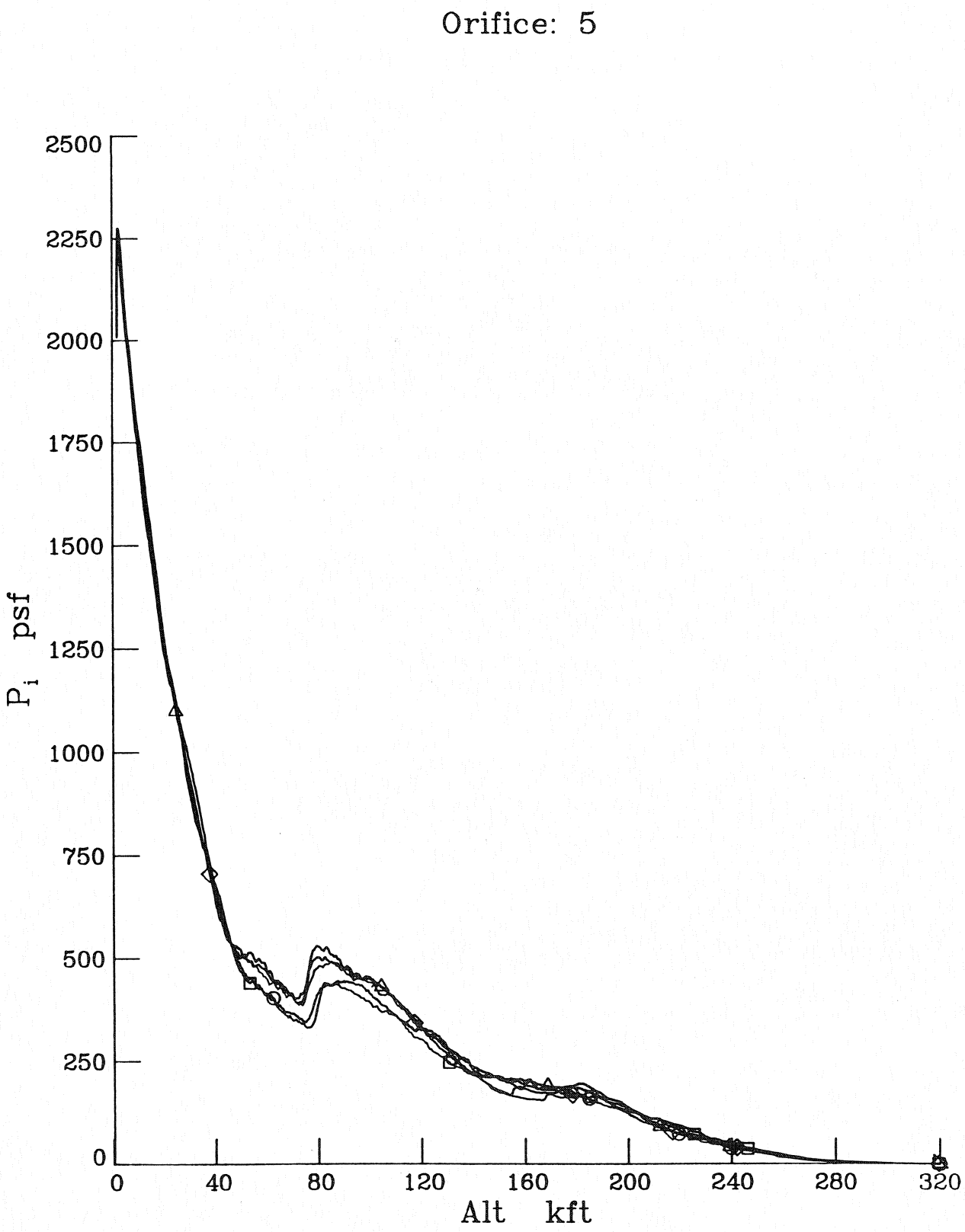

Fig. 12 Trajectory Pressure Profile for Orifice #5

M_∞ = .80	α° = 6.0	β° =-.14	P_{t_2} = 829.90	q_∞ = 245.29 psf
M_∞ = .80	α° = 6.1	β° = .22	P_{t_2} = 833.70	q_∞ = 246.77 psf
M_∞ = .80	α° = 5.7	β° = -.01	P_{t_2} = 854.50	q_∞ = 249.47 psf
M_∞ = .80	α° = 7.0	β° = -.03	P_{t_2} = 927.10	q_∞ = 268.84 psf
M_∞ = .80	α° = 5.4	β° = .29	P_{t_2} = 795.90	q_∞ = 235.23 psf

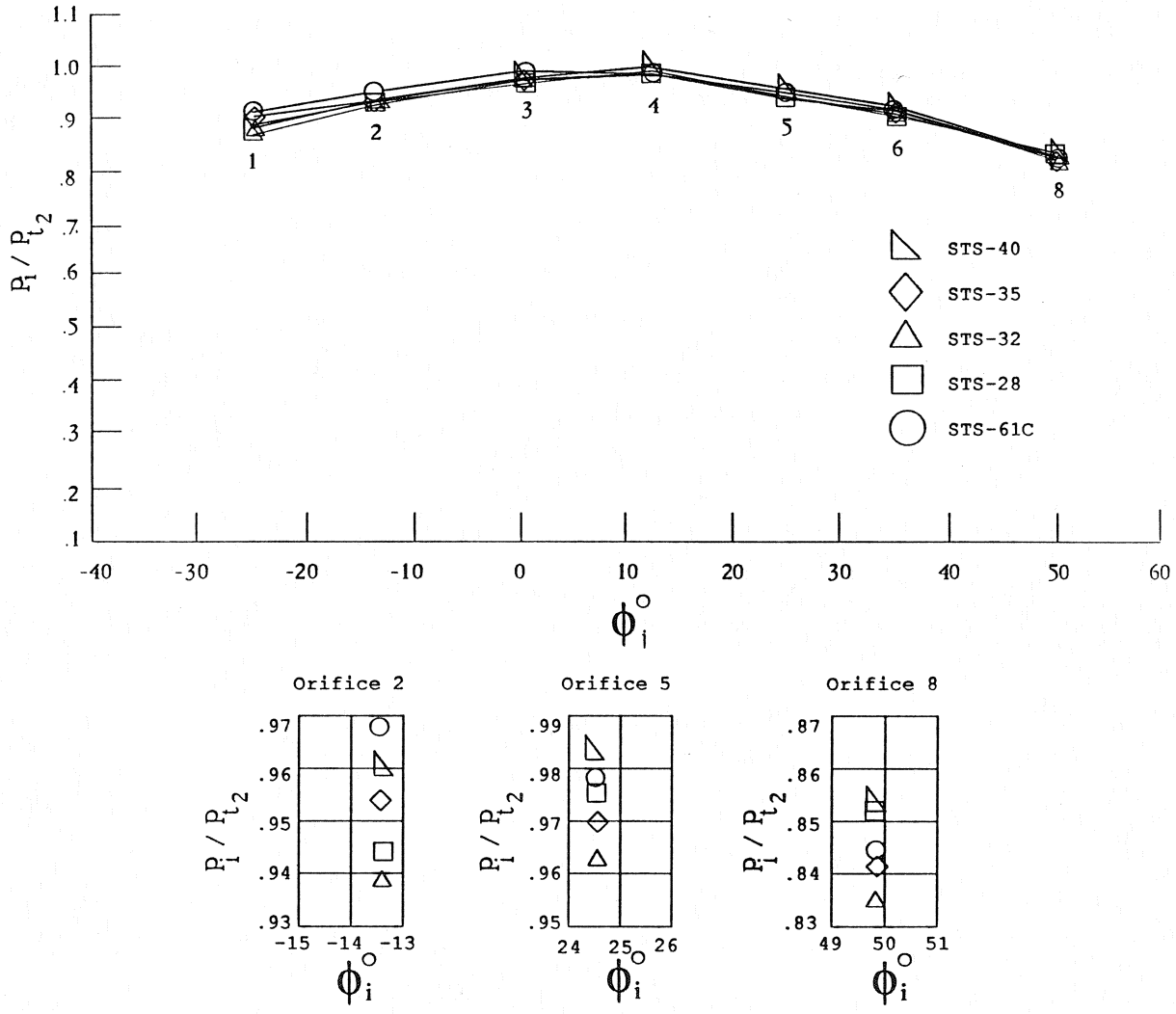

Fig. 13 Flight Data Repeatability at Selected Points

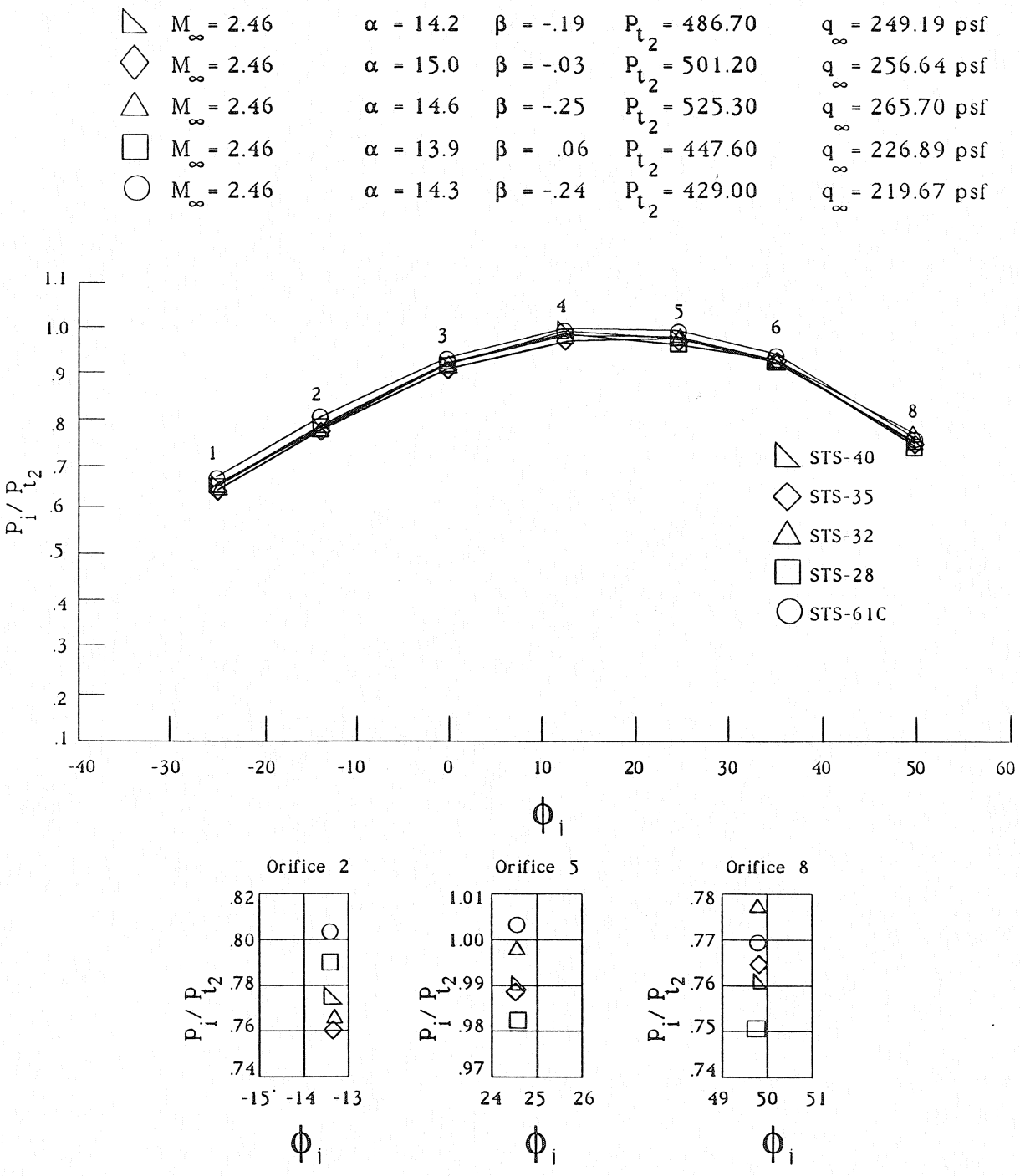

Fig. 14 Flight Data Repeatability at Selected Points

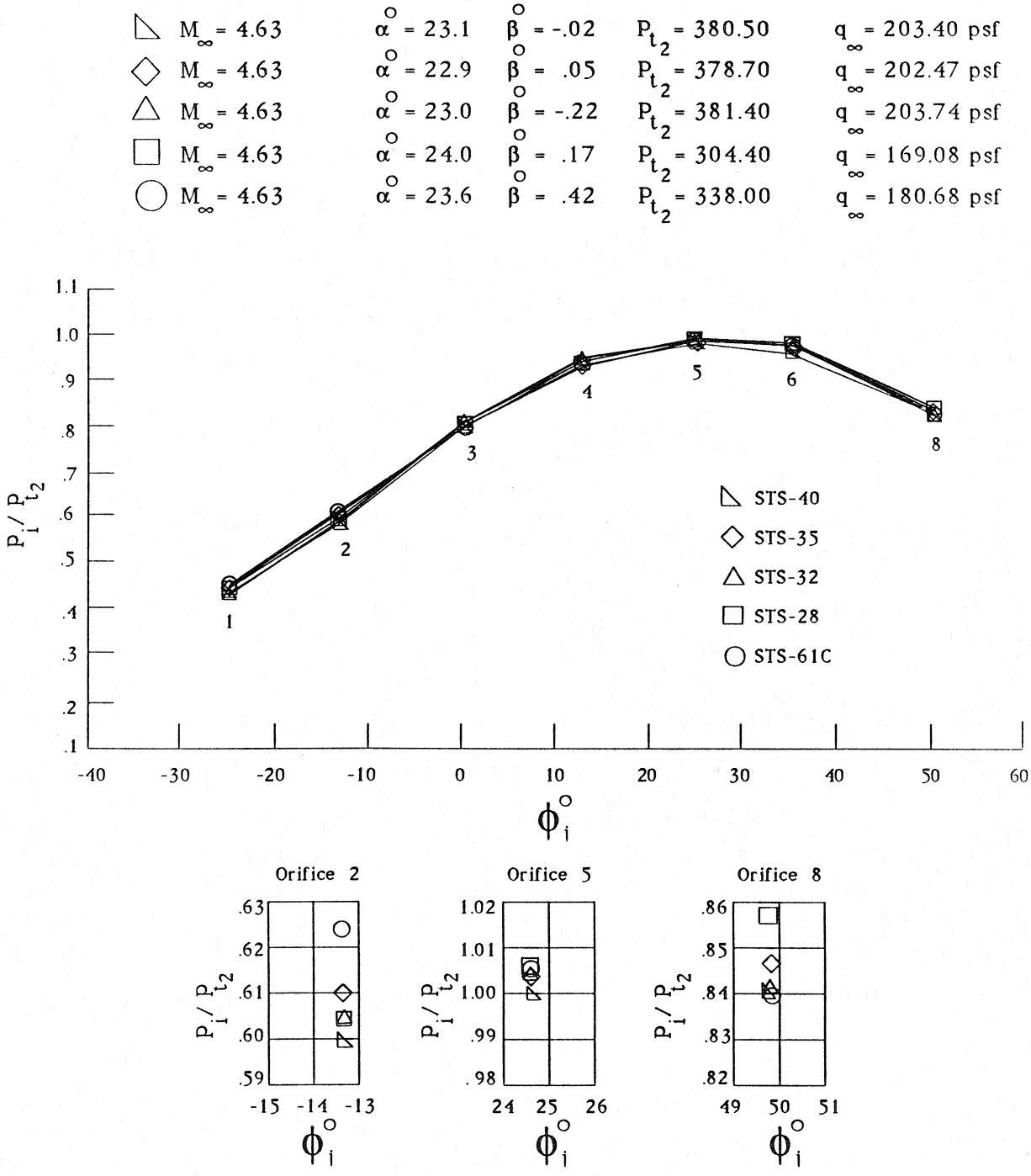

Fig. 15 Flight Data Repeatability at Selected Points

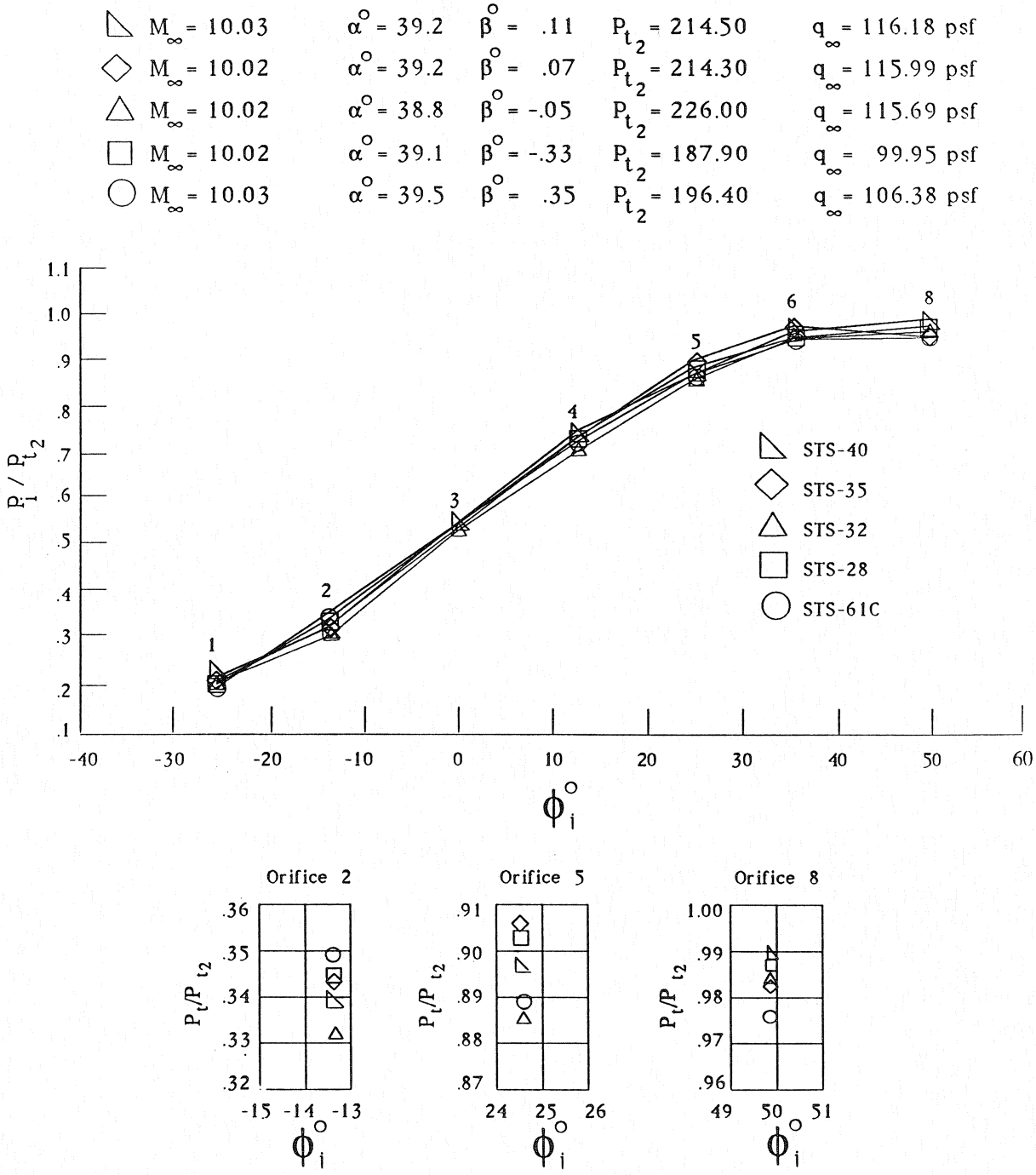

Fig. 16 Flight Data Repeatability at Selected Points

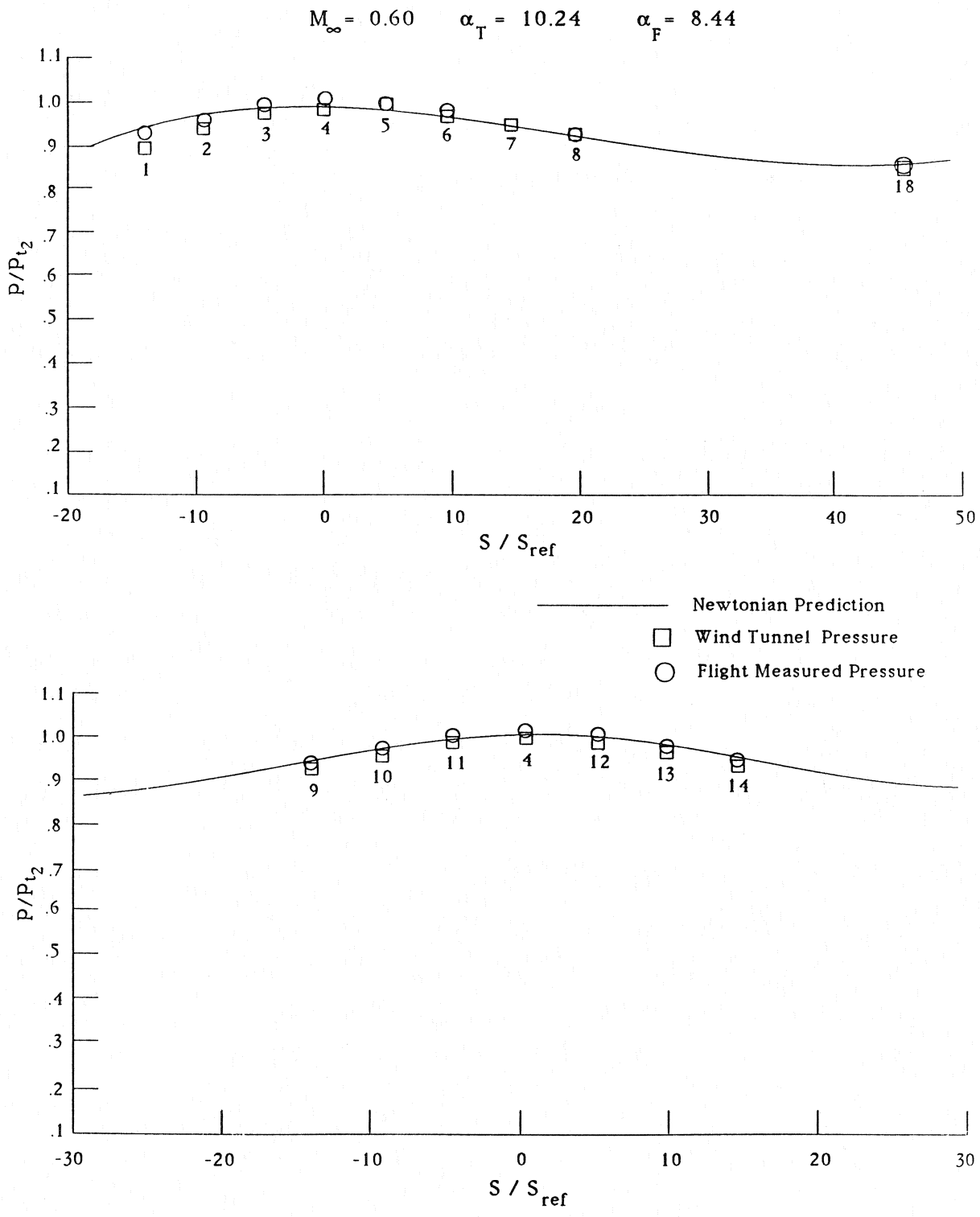

Fig. 17 Measured and Computed Pressure Comparison

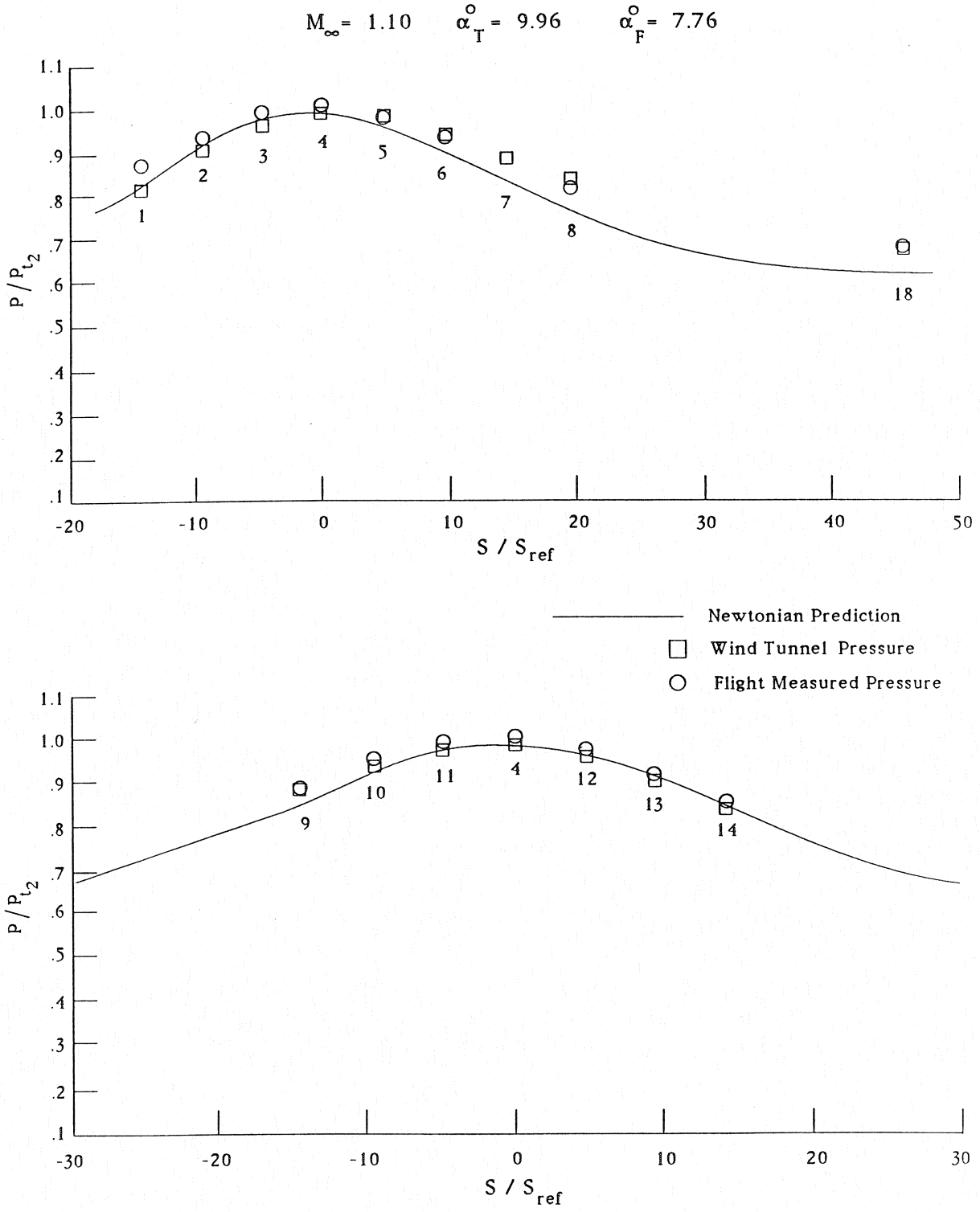

Fig. 18 Measured and Computed Pressure Comparison

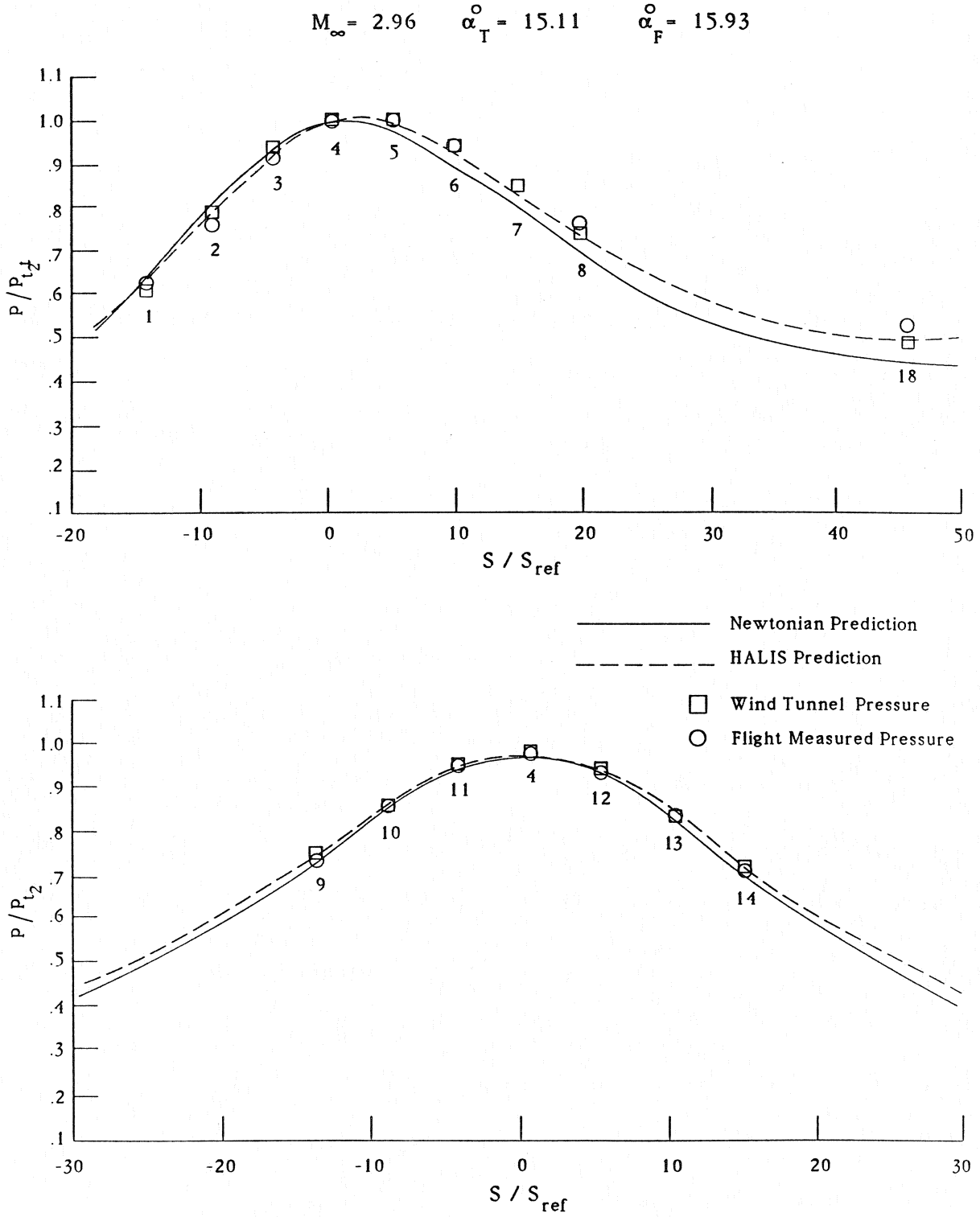

Fig. 19 Measured and Computed Pressure Comparison

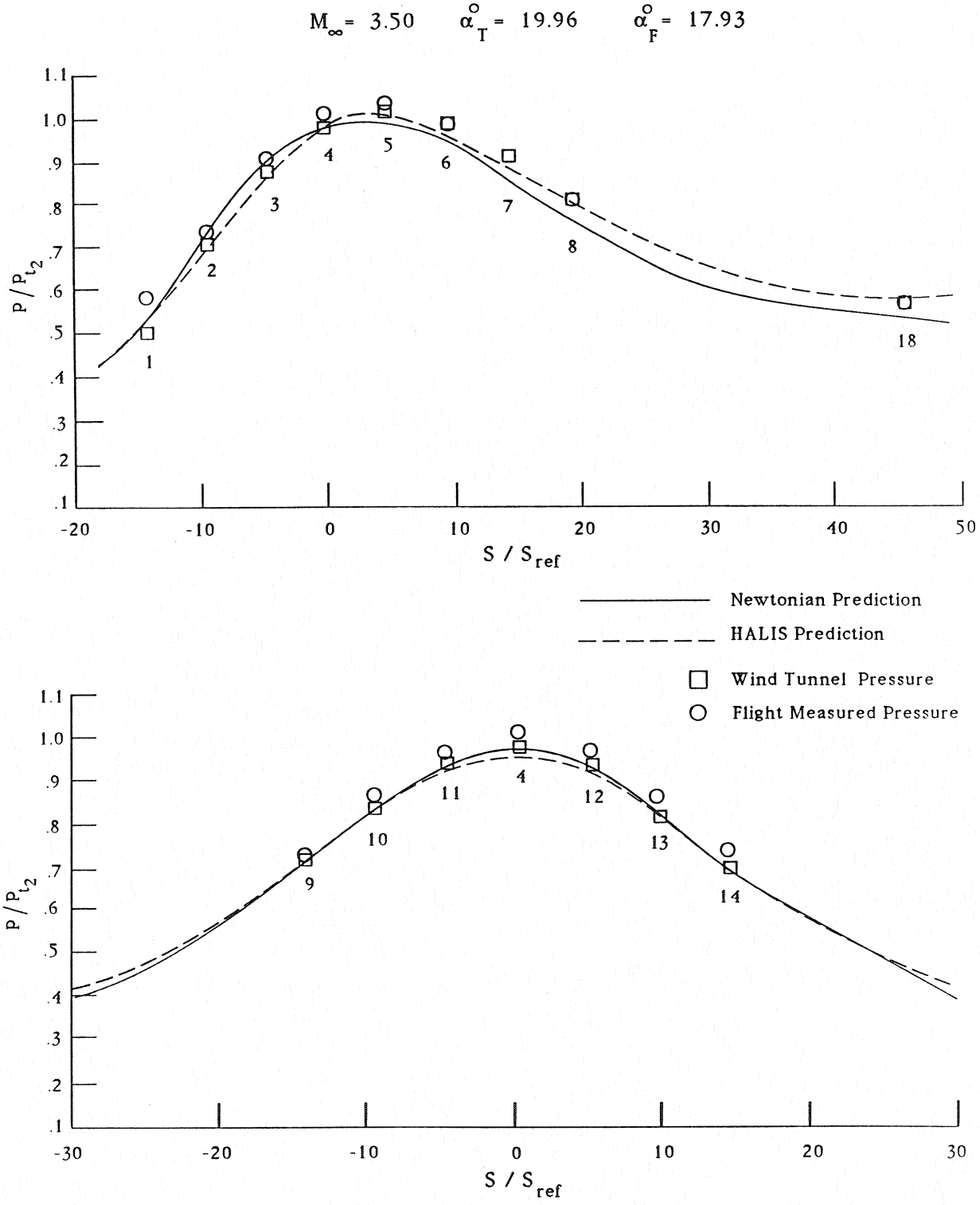

Fig. 20 Measured and Computed Pressure Comparison

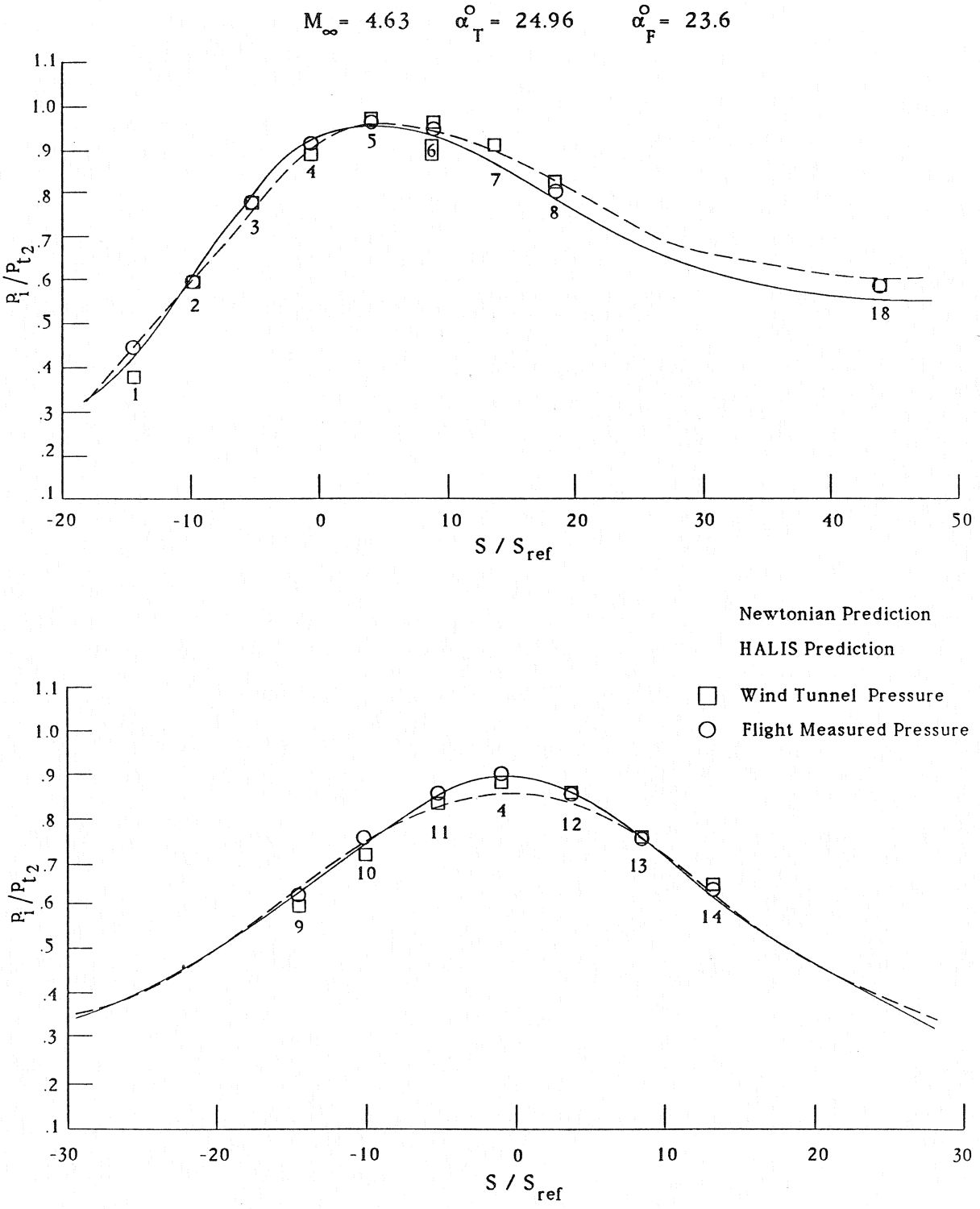

Fig. 21 Measured and Computed Pressure Comparison

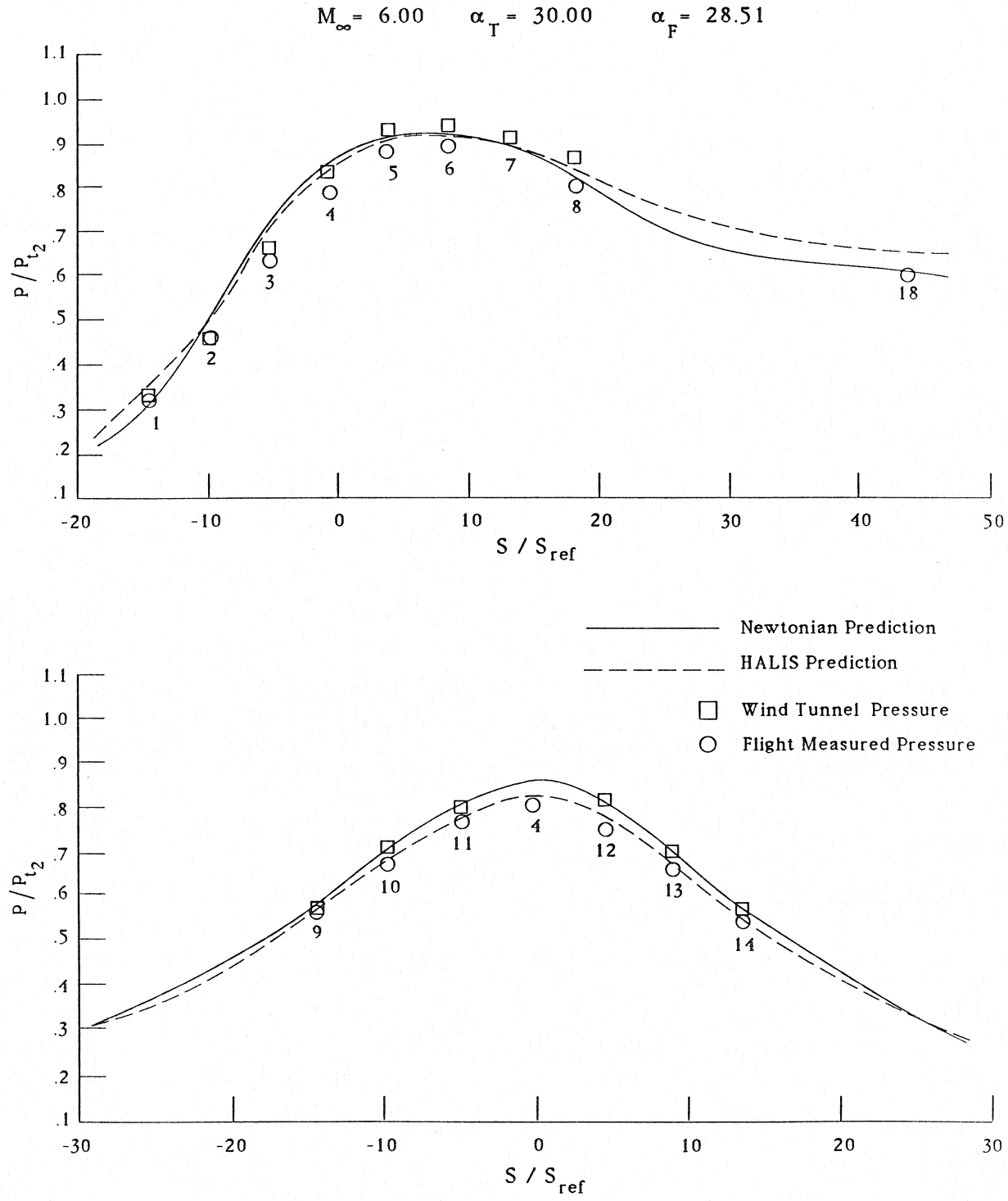

Fig. 22 Measured and Computed Pressure Comparison

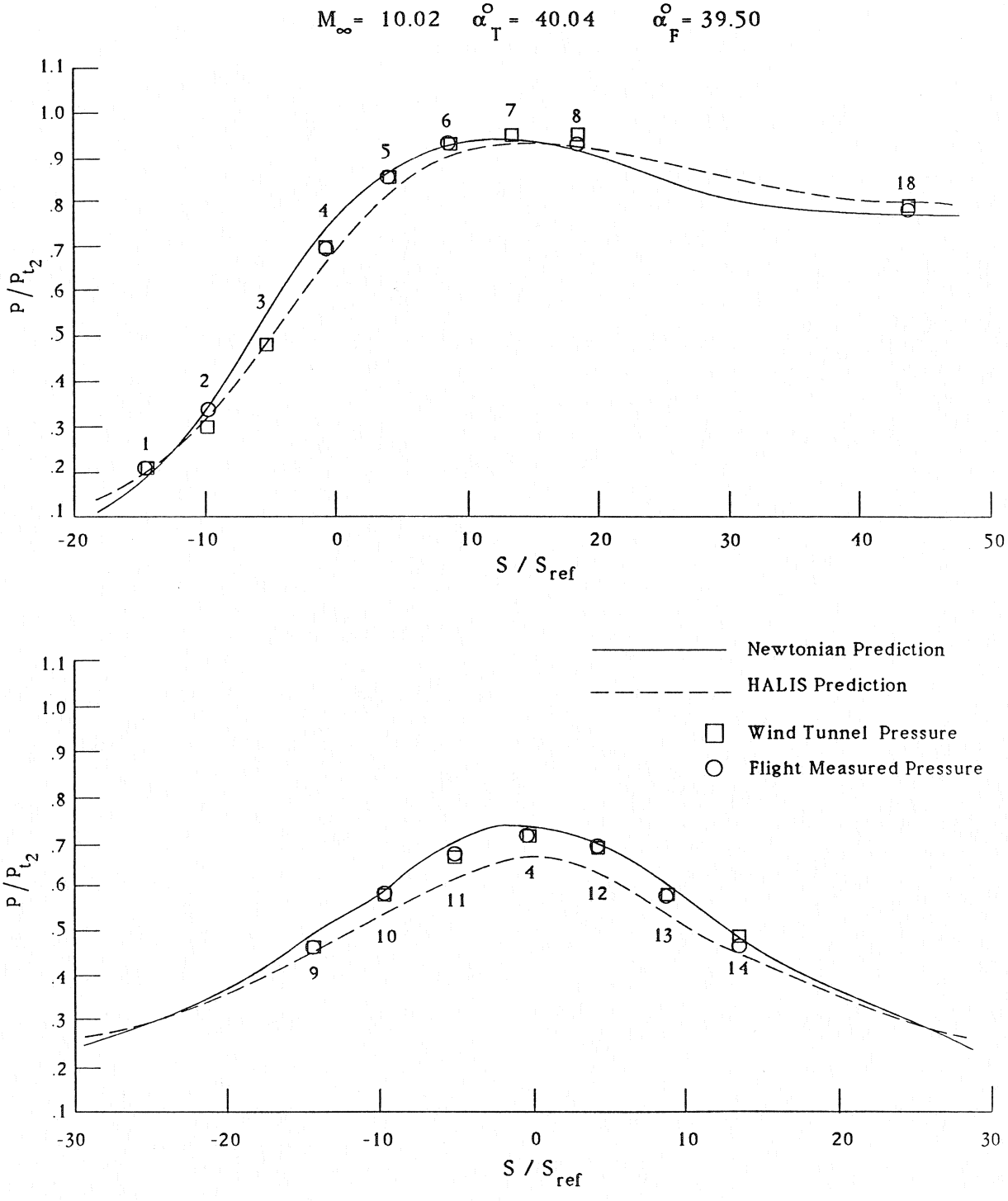

Fig. 23 Measured and Computed Pressure Comparison

SHUTTLE ENTRY AIR DATA SYSTEM PREFLIGHT ALGORITHM DEVELOPMENT BASED ON COMPUTATIONAL RESULTS

Samir M. Deshpande* and Martin W. Henry**
Analytical Mechanics Associates, Inc.
Hampton, VA

Paul M. Siemers III#, and K. James Weilmuenster†
NASA Langley Research Center
Hampton, VA

ABSTRACT

The Shuttle Entry Air Data System (SEADS) preflight air data extraction algorithm is based on stagnation-region pressure distributions predicted by Newtonian theory. To enhance the accuracy of the algorithm, an empirically derived correction factor based on experimental pressure distribution data was applied. These experimental pressure distributions were obtained from models tested in various wind tunnels at operational speeds ranging from subsonic to hypersonic. The present work addresses the potential for utilizing Computational Fluid Dynamics techniques, instead of wind tunnels, as a source of the pressure distribution data necessary for the definition of preflight algorithm correction factors. The use of these techniques can enhance the accuracy of the corrections, and reduce the level of effort required to obtain the required correction factors. The pressure distributions used to calculate the correction coefficients were obtained by the High Alpha Inviscid Solution code for selected flight conditions.

The corrected angle of attack obtained from the present work is compared to similar data obtained from wind tunnel test based corrections and Best Estimate

---

* Project Engineer

** Senior Analyst / Programmer

\# Aero-Space Technologist

† Senior Research Engineer

Support for this research was provided by NASA Langley Research Center, Hampton, Virginia, under contract no. NAS1-17990.

Trajectory. This comparison was used to ascertain compatibility between the two procedures, and to assess the applicability of computational methods for the determination of algorithm correction factors.

NOMENCLATURE

h = enthalpy
M_∞ = freestream Mach number
n = number of orifices
P = pressure
P_N = Newtonian theory predicted pressure
$\bar{q}_\infty$ = freestream dynamic pressure
R = freestream static to stagnation pressure ratio
$\overline{V}_\infty$ = freestream velocity
α = angle of attack
β = sideslip angle
ρ = density
γ = ratio of specific heats
η = cone angle
ζ = clock angle
θ = flow incidence angle

Subscripts

i = ith orifice location
m = measured value
r = reference value
t = stagnation value
∞ = freestream condition

INTRODUCTION

Conventional pitot static tube air data systems have traditionally been used in aircraft to determine the angle of attack, sideslip angle and the freestream dynamic pressure. For hypersonic re-entry vehicles these air data parameters are of utmost

importance, but the conventional air data system approach can not be used in this flight regime due to the high energy nature of the flow-field. The Shuttle Entry Air Data System (SEADS) [1-3], an experimental system based on the flush-orifice air data system concept developed at the NASA Langley Research Center, was designed to solve this problem and to provide air data from atmospheric re-entry to touchdown. Incorporated as a part of the Orbiter Experiments Program (OEX) on the Space Shuttle Columbia, SEADS used the pressure data obtained from flush orifices on the blunt nose region of the shuttle orbiter to determine the required air data parameters.

The SEADS orifice array was designed to consist of 20 flush orifices located on the nosecap and forward fuselage of the orbiter (Figure 1). Flight-measured pressure data obtained during orbiter re-entry flights 61-C, 28, 32, 35 and 40 was used to estimate the air data parameters--angle of attack α, sideslip angle β and freestream dynamic pressure $\bar{q}_\infty$. Data reduction was accomplished through the use of a "filter" algorithm [1], which incorporates a Newtonian theory [4] based mathematical model of the pressure field on the orbiter's forebody. The "filter" algorithm extracts the aerodynamic state vector (Eq. 5) from the flight-measured pressures. The freestream dynamic pressure is calculated from the predicted stagnation pressure. However, it was expected that the differences between the flight-measured pressure distributions and the Newtonian theory based predictions would result in filter-derived air data parameters which would be inaccurate. A reduction of these errors, during the extraction of the air data parameters, was achieved by applying corrections to the preflight algorithm. These correction factors were derived from the pressure data obtained from extensive wind tunnel tests on various models in a variety of wind tunnels (Mach-6 air, Mach-10 air, Mach-6 CF4, Langley and Ames Unitary, AEDC propulsion, and Mach-20 Helium) [11-15]. It is significant that these wind tunnel tests required a large effort in terms of resources - facilities, time and manpower. In the present work, the correction coefficients were derived with a comparatively small computational and manpower effort through the use of CFD techniques.

The present work addresses the possibility of obtaining surface pressure distributions, similar to those acquired through conventional wind tunnel testing, through the use of CFD techniques. This approach would reduce both the

time and effort required to develop and obtain the preflight algorithm corrections, and to increase the accuracy of the air data predictions.

The first step in this process was the development of an accurate SEADS nosecap geometry model. This geometry model was constructed through the use of photogrammetric data. A computational grid was formed by numerical interpolation and smoothing of the model (Figure 2). Next, the flowfield solutions were obtained by using the HALIS code [5] for various flight conditions, and these solutions were used in the calculation of preflight algorithm corrections. Since the HALIS code provides accurate results for flowfields with freestream conditions ranging from hypersonic down to high supersonic, the present work was restricted to correction coefficients obtained for Mach numbers exceeding 3. A second set of preflight corrections was obtained from the wind tunnel data. Each of these two sets of corrections was used in the extraction algorithm to estimate the air data parameters from the flight pressure data obtained from the shuttle orbiter flights 61-C and STS-35. Finally, these estimates were compared to the Best Estimate Trajectory (BET) predicted values to define the relative errors in the predictions, and to verify the accuracy of the corrections derived by the two methods.

SEADS "FILTER" ALGORITHM

The air data calculations were performed using a "filter" algorithm which is based on the Newtonian theory. The Newtonian predicted pressures are determined from the following equation:

$$P_{N_i} = P_t \left[(1 - R) \cos^2 \theta_i + R\right] \tag{1}$$

where the freestream static to stagnation pressure ratio R is related to the freestream Mach number M_∞ by the perfect gas relationship (for $M_\infty > 1$)

$$R = \left[\frac{2}{(\gamma + 1) M_\infty^2}\right]^{\frac{\gamma}{(\gamma-1)}} \left[\frac{2\gamma M_\infty^2 - \gamma + 1}{\gamma + 1}\right]^{\frac{\gamma}{\gamma-1}} \tag{2}$$

and the flow incidence angle θ is related to the surface normal parameters (cone and clock angles) and air relative spacecraft attitude by the following equation:

$$\cos\theta_1 = \cos\alpha\cos\beta\cos\eta_i + \sin\beta\sin\eta_i\cos\zeta_i + \sin\alpha\cos\beta\sin\eta_i\cos\zeta_i \qquad (3)$$

The air data parameters are obtained by solving a system with M equations in N unknowns (M > N) such that the solution is the best possible fit in the least-squares sense. The governing system of equations for the calculations is

$$\begin{Bmatrix} P_{m_1} \\ P_{m_2} \\ \vdots \\ P_{m_n} \end{Bmatrix} \approx \begin{Bmatrix} P_{t_m}\,[(1 - R_m)\cos^2\theta_{m_1} + R_m] \\ P_{t_m}\,[(1 - R_m)\cos^2\theta_{m_2} + R_m] \\ \vdots \\ P_{t_m}\,[(1 - R_m)\cos^2\theta_{m_n} + R_m] \end{Bmatrix} \qquad (4)$$

This system of equations can be solved in the least-squares sense by solving the following problem:

$$\min_{X \in R^4} \left\| \left\{ P_{m_i} - f(X, \eta_i, \zeta_i) \right\} \right\|_2 \qquad (5)$$

where $\|\cdot\|_2$ denotes the Euclidian norm, R^4 denotes a real four dimensional search space, and X is the aerodynamic state vector given by

$$X = \begin{Bmatrix} P_{t_m} \\ R_m \\ \alpha_m \\ \beta_m \end{Bmatrix} \qquad (6)$$

The system of equation (4) is solved by linearizing the right-hand side of that system. The linearized system is given by

$$\{P_{m_i} - f(X, \eta_i, \zeta_i)\} = \left[\frac{\partial f(X, \eta_i, \zeta_i)}{\partial X}\right]\{\Delta X\} \qquad (7)$$

where the partial derivatives are found to be

$$\frac{\partial f}{\partial P_{t_m}} = R_m + (1 - R_m)\cos^2\theta_{m_i} \tag{7a}$$

$$\frac{\partial f}{\partial R_m} = P_{t_m}(1 - \cos^2\theta_{m_i}) \tag{7b}$$

$$\frac{\partial f}{\partial \alpha_m} = -2P_{t_m}(1 - R_m)\cos\theta_i(\sin\alpha_m\cos\beta_m\cos\eta_i - \cos\alpha_m\cos\beta_m\sin\eta_i\sin\zeta_1) \tag{7c}$$

$$\frac{\partial f}{\partial \beta_m} = -2P_{t_m}(1 - R_m)\cos\theta_i(\cos\alpha_m\sin\beta_m\cos\eta_i + \sin\alpha_m\sin\beta_m\sin\eta_i\sin\zeta_i - \cos\beta_m\sin\eta_i\cos\zeta_1) \tag{7d}$$

The linearized system is solved by using an iteration scheme. Starting guess values for the freestream static to stagnation pressure ratio, angle of attack, sideslip angle, and the stagnation pressure are used to calculate the left hand side of equation (7) and the matrix of partial derivatives on the right side of the equation. The ΔX vector is calculated by the best fit solution to equation (7), and then used to update the "guess" values of X, $f(X, \eta_i, \zeta_i)$ and $\partial f(X, \eta_i, \zeta_i)/\partial X$. The iteration step is repeated until a converged solution for the aerodynamic state vector is obtained.

HALIS FLOWFIELD CODE

The High Alpha Inviscid Solution (HALIS) [5-8] flowfield code was initially developed to handle high angle of attack flowfields. These flowfields are characterized by large regions of embedded subsonic flow on the windward surface of flight vehicles such as the Space Shuttle Orbiter. Briefly, the HALIS code obtains a time-asymptotic solution of the Euler equations utilizing an unsplit MacCormack differencing scheme. The solution space is the volume between the body surface and the bow-shock wave, which is treated as a time-dependent boundary. This leads to a coordinate system defined by the position of the

bow-shock and the body, as well as the spatial derivatives along those surfaces. The code is designed to allow grid points in any of the three coordinate directions to be clustered in a region of high gradients.

The HALIS code is designed to handle arbitrary gases behaving as a perfect gas (constant γ), or as a real gas in thermodynamic equilibrium. In the case of a real gas, the thermodynamic properties (of the gas in question) must be quantified in a functional form relating pressure, enthalpy, temperature, density and internal energy, e.g., P = Ph(h, ρ) etc., for use in the code. For equilibrium air properties, the curve fits of Tannehill [9] are used, while Sutton's functional relations [10] are used for CF4 equilibrium properties.

CALCULATION OF CORRECTION COEFFICIENTS

The preflight correction coefficients for the air data extraction algorithm are calculated by utilizing wind-tunnel measured, or CFD computed, pressure distributions on the orbiter's nosecap. The pressure at each orifice location is obtained for various flight conditions (α and M_∞), and the air data is extracted from these pressures using the "filter" algorithm. The computed angle of attack is then compared to the reference angle of attack at various freestream Mach number conditions to obtain the offset and linear angle of attack correction coefficients as a function of the freestream static to stagnation pressure ratio R.

The relation between "measured" (computed) and reference (input to the HALIS flowfield code) angles of attack is given as

$$\alpha_m = C_0 + C_1\alpha_r \tag{8}$$

where C_0 and C_1 are the offset and linear correction coefficients, respectively. First, the offset correction is obtained from the computed angle of attack for a zero reference angle of attack (i.e., α_m when $\alpha_r = 0$). Next, the linear correction is obtained from the remaining data points by choosing a value for which minimizes the root mean square (R.M.S.) of error between the data points and the line defined

by the right-hand side of equation (8). The linear coefficient value obtained by this approach is determined by

$$C_1 = \frac{\sum_{i=1}^{n} \alpha_{r_i} \alpha_{m_i} - C_0 \sum_{i=1}^{n} \alpha_{r_i}}{\sum_{i=1}^{n} \alpha_{r_i}^2} \qquad (9)$$

where n is the total number of points used for obtaining the curve-fit.

RESULTS

The HALIS code was used to obtain the orbiter nose region flowfield solutions corresponding to various freestream re-entry flight conditions selected from flights 61-C and STS-35. A perfect gas version of the code was used to obtain the results. The pressure at each SEADS orifice location was extracted from the computed surface pressure distribution by utilizing a two dimensional interpolation algorithm. A sample pressure distribution corresponding to $M_\infty = 5.97$ and $\alpha = 35.00^o$ is shown in figure 3. The orifice pressures extracted by utilizing the interpolation algorithm are denoted on the pressure distribution curve by the numbered solid symbols.

As explained earlier, the CFD computed orifice pressures were used to extract the air data using the "filter" algorithm. The various air data results obtained for a given Mach number were used to obtain the offset (C_0) and linear (C_1) correction coefficients. The algorithm extracted angle of attack, as a function of the reference (input) angle of attack, for $M_\infty = 2.96$, is shown in figure 4.

These extracted angles of attack were used in the computation of the offset and linear correction coefficients as given in equations (8, 9). The correction coefficients were obtained for various freestream conditions, and are shown in figures 5 and 6 with solid symbols as a function of the square-root of freestream static to stagnation pressure ratio ($\sqrt{R}$). Regression curve-fits for the correction coefficients were obtained in order to use these coefficients for correcting the algorithm extracted angle of attack. These curve fits were second order polynomials which provided least-squares fits to the data points, with the restriction that the slope of these

curves be zero at R = 0 (this heuristic restriction was applied to the curve-fits since it was expected that the correction coefficients would approach a constant value as freestream Mach number tended to infinity). The curve-fits are shown in figures 5 and 6 with dashed lines, and are described by the following relations:

$$C_0 = 26.1346^* R - 0.2042 \quad (10)$$

$$C1 = - 0.9808^* R + 1.0928 \quad (11)$$

Correction coefficients based on the CFD generated pressure distributions were used to correct the "filter" derived air data. The "corrected" angle of attack was compared to the BET derived air data [16,17] to ascertain the accuracy of the CFD derived correction coefficients. These comparisons for orbiter flights 61-C and STS-35 are shown in figures 7 and 8, respectively. It can be seen that the SEADS derived (uncorrected) angle of attack differs from the BET derived results by about 3 to 4 degrees. However, the corrected SEADS results are virtually indistinguishable from the BET derived results.

The corrected results obtained by using the wind-tunnel derived corrections and the present method are presented for comparison in figures 9 and 10 for orbiter flights 61-C and STS-35, respectively. As can be seen, the results from the present method compare very well to those obtained from the BET. For the results shown in figures 7 and 8, the root mean square (R.M.S.) error between the results obtained by the present method and those from the BET is 0.4645 compared to an R.M.S. error of 0.5515 for the wind-tunnel corrected results.

CONCLUSION

A method for the calculation of correction coefficients needed to optimize the SEADS preflight algorithm has been demonstrated. This method provides accurate preflight corrections using CFD techniques, at a cost of relatively small computational and manpower effort. On the other hand, wind tunnel tests, which were previously used to calculate correction coefficients, required a large effort in terms of resources - facilities, time and manpower.

The present work has focused on the computation of correction coefficients for the angle of attack. Future work should address similar computations for the sideslip angle and the freestream static to stagnation pressure ratio.

REFERENCES

1. Pruett, C.D.; Wolf, H.; Heck, M.L; and Siemers, P.M. III: An Innovative Air Data System for the Space Shuttle Orbiter : Data Analysis Techniques. AIAA Paper 81-2455, AIAA 1st Flight Testing Conference, November 1981.

2. Henry, M.W.; Wolf, H.; and Siemers, P.M. III: An Evaluation of Shuttle Entry Air Data System (SEADS) Flight Pressures : Comparison with Wind Tunnel and Theoretical Predictions. AIAA Paper 88-2052, May 1988.

3. Siemers, P.M. III; Wolf, H.; and Henry, M.W.: Shuttle Entry Air Data System (SEADS) - Flight Verification of an Advanced Air Data System Concept. AIAA Paper 88-2104, May 1988.

4. "Ballistic Missile & Space Vehicle Systems," (edited by Seifert, H. and Brown, K.) John Wiley, 1961, pp. 453-455.

5. Weilmuenster, K.J. and Hamilton, H.H. II: A Method for Computation of Inviscid Three-Dimensional Flow Over Blunt Bodies Having Large Embedded Subsonic Regions. AIAA Paper 81-1203, June 1981.

6. Weilmuenster, K.J. and Hamilton, H.H. II: A Comparison of Computed Space Shuttle Orbiter Surface Pressures with Flight Measurements. AIAA Paper 82-0937, June 1982.

7. Weilmuenster, K.J. and Hamilton, H.H. II: Calculations of Inviscid Flow Over Shuttle-Like Vehicles at High Angles of Attack and Comparisons with Experimental Data. NASA TP-2103, May 1983.

8. Weilmuenster, K.J.: High Angle-of-Attack Inviscid Flow Calculations Over a Shuttle-Like Vehicle with Comparisons to Flight Data. AIAA Paper 83-1798, July 1983.

9. Tannehill, J.C.; and Mugge, P.H.: Improved Curve Fits for the Thermodynamic Properties of Equilibrium Air Suitable for Numerical Computation Using Time-Dependent or Shock Capturing Methods, Part I - Final Report. NASA CR-2470, October 1974.

10. Sutton, K.: Relations for the Thermodynamics and Transport Properties in the Testing Environment of the Langley Hypersonic CF4 Tunnel. NASA TM-83220, October 1981.

11. Bradley, P.F.; Siemers, P.M. III; Flanagan, P.F.; and Henry, M.W.: Pressure Distributions Obtained on a 0.04-Scale Model of the Space Shuttle Orbiter's Forward Fuselage in the Langley Unitary Plan Wind Tunnel. NASA TM-84628, March 1983.

12. Bradley, P.F.; Siemers, P.M. III; Flanagan, P.F.; and Henry, M.W.: Pressure Distributions Obtained on a 0.04-Scale and 0.02-Scale Model of the Space Shuttle Orbiter's Forward Fuselage in the Langley 20-Inch Mach 6 Air Tunnel. NASA TM-84629, March 1983.

13. Bradley, P.F.; Siemers, P.M. III; Flanagan, P.F.; and Henry, M.W.: Pressure Distributions Obtained on a 0.04-Scale and 0.02-Scale Model of the Space Shuttle Orbiter's Forward Fuselage in the Langley Continuous Flow Hypersonic Tunnel. NASA TM-84630, March 1983.

14. Siemers, P.M. III; and Henry, M.W.: Pressure Distributions Obtained on a 0.10-Scale Model of the Space Shuttle Orbiter's Forebody in the AEDC 16T Propulsion Tunnel. NASA TM-87653, January 1986.

15. Siemers, P.M. III; and Henry, M.W.: Pressure Distributions Obtained on a 0.10-Scale Model of the Space Shuttle Orbiter's Forebody in the Ames Unitary Plan Wind Tunnel. NASA TM-87654, January 1986.

16. Findlay, J.T.; and Kelly, G.M.: STS-32 (61-C) Columbia Entry BET Products and Summary Results. NASA CR-178262, June 1987.

17. Oakes, K.F.; Findlay, J.T.; Jasinski, R.A.; and Wood, J.S.: STS-35 Columbia Descent BET Products and Results for LaRC OEX Investigation. NASA CR-189569, November 1991.

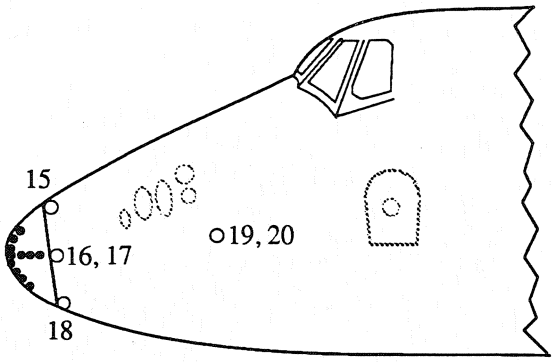

Orbiter Forebody (Side View)

● Nosecap Orifices (14)

○ Forebody Orifices (6)

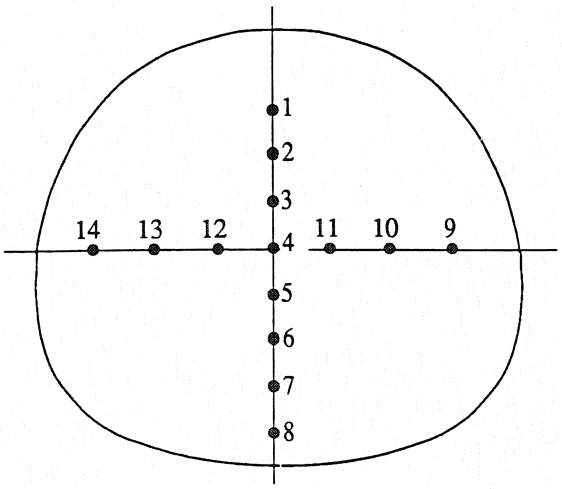

Nosecap (Front View)

Figure 1. SEADS nosecap orifice configuration

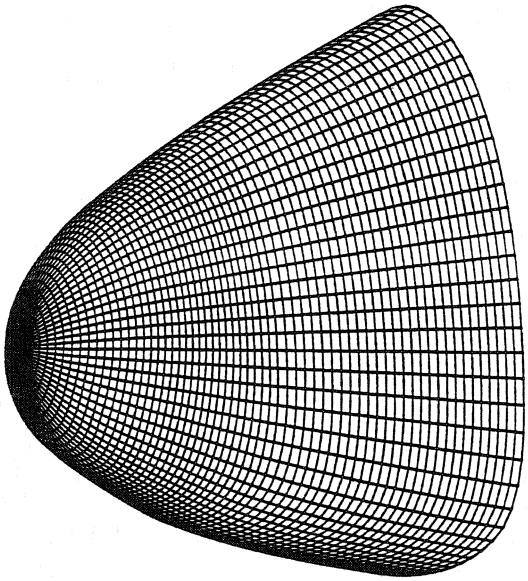

Figure 2. Computational grid for the SEADS nosecap

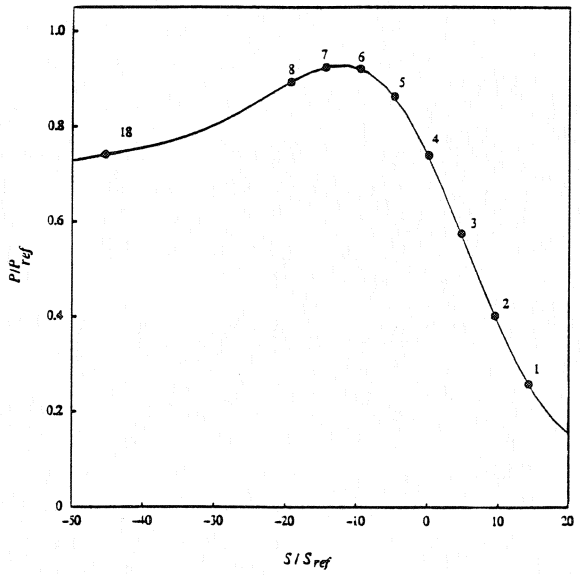

Figure 3. Vertical ray pressure distribution
($M_\infty = 5.97, \alpha = 35.00°$)

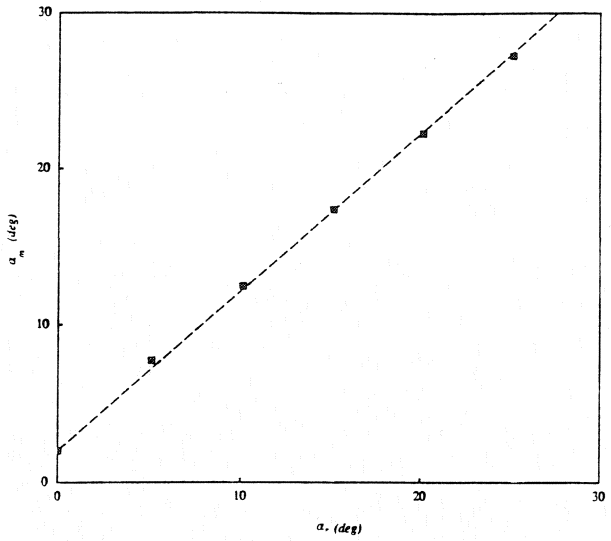

Figure 4. Extracted angle of attack ($M_\infty = 2.96$)

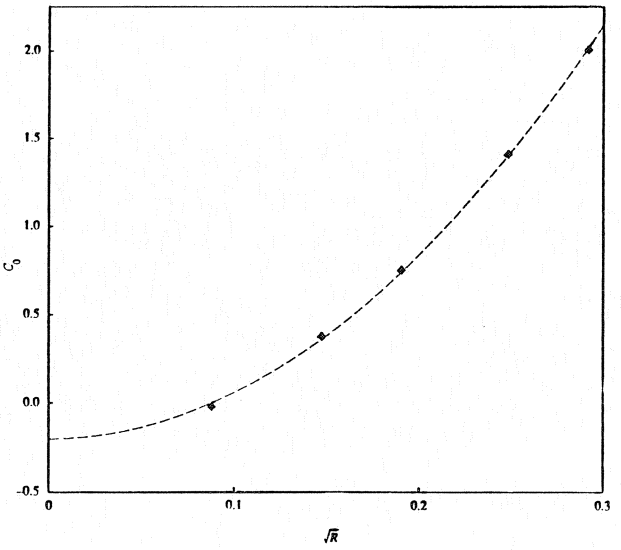

Figure 5. Offset correction coefficient

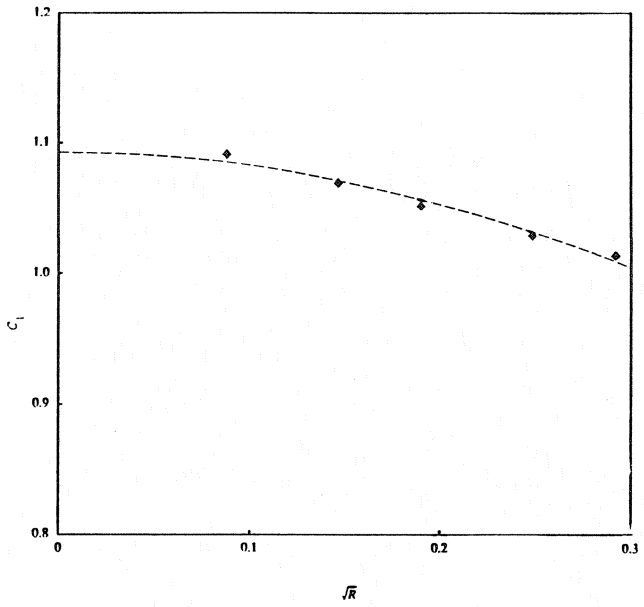

Figure 6. Linear correction coefficient

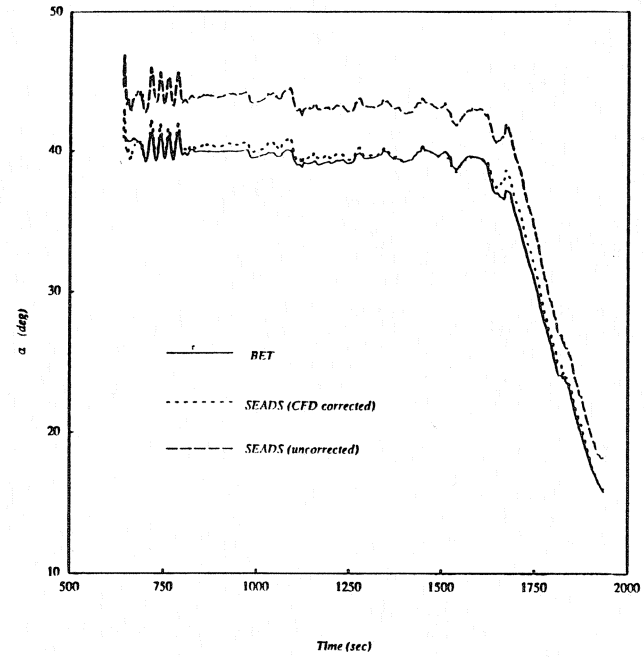

Figure 7. Comparison of BET and SEADS derived angle of attack for flight 61-C

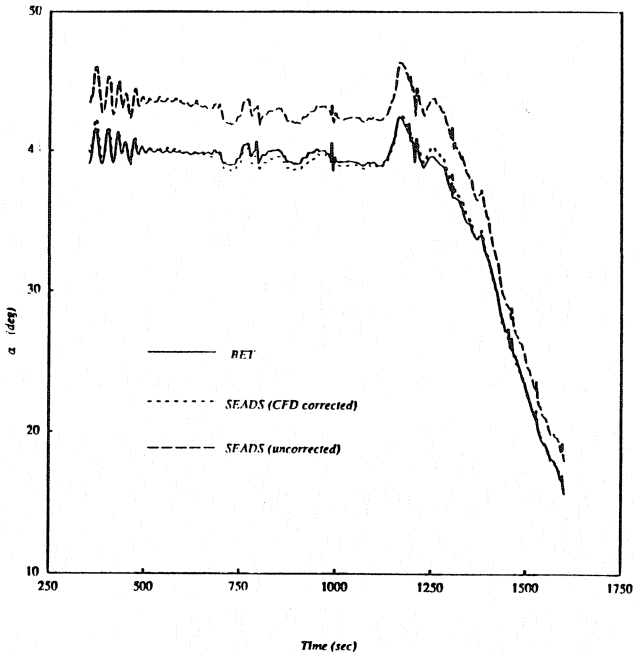

Figure 8. Comparison of BET and SEADS derived angle of attack for flight STS-35

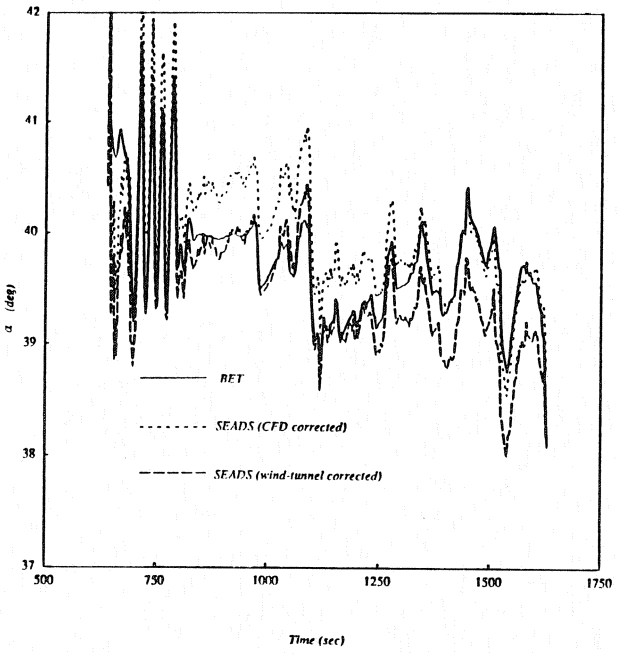

Figure 9. Comparison of CFD and wind-tunnel derived angle of attack for flight 61-C

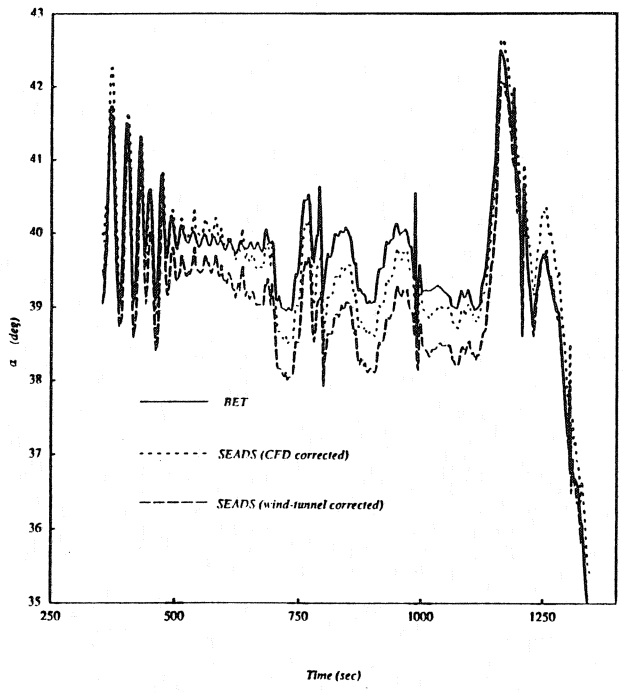

Figure 10. Comparison of CFD and wind-tunnel derived angle of attack for flight STS-35

Orbiter Rarefied-Flow Aerodynamics and Upper Atmosphere Density Flight Measurements

Robert C. Blanchard
NASA Langley Research Center
Hampton, Virginia 23681-0001

John Y. Nicholson
ViGYAN, Inc.
Hampton, Virginia 23666-1325

Kevin T. Larman
Lockheed Engineering & Sciences Company
Hampton, Virginia 23666-1339

Thomas A. Ozoroski
ViGYAN, Inc.
Hampton, Virginia 23666-1325

Abstract

A model of the Shuttle Orbiter rarefied-flow aerodynamic force coefficients has been derived from the ratio of flight acceleration measurements. The in-situ, low frequency (<1 Hz), low level acceleration (~ 1 x 10^{-6} g) measurements are made during atmospheric reentry. The experiment equipment designed and used for this task is the High Resolution Accelerometer Package (HiRAP), one of the suite of sensor packages in the Orbiter Experiments (OEX) Program. To date, 12 HiRAP reentry mission data sets have been processed, spanning a period of about 10 years. A HiRAP derived aerodynamics model has been developed which compares well with flight data and appropriate wind tunnel data. The flight accelerometer data and the derived aerodynamic coefficients are subsequently used to infer upper atmospheric density characteristics along the trajectory path of the Orbiter. The inferred upper atmosphere density calculations are presented as a function of altitude and normalized to the 1976 U.S. standard atmosphere model. The HiRAP atmosphere density data base includes measurements made during most of a solar cycle and during various local solar

times and solar zenith angles, including morning and evening terminator crossings. All flight densities exhibit a wave-like structure between 80 and 140 km altitude and the corresponding normalized density amplitudes indicate an annual variation, with larger amplitudes occurring during the summer months.

Nomenclature

a	acceleration
A	axial or X-axis force
C	aerodynamic coefficient
g	acceleration due to gravity, 9.81 m/s^2
micro-g	$1x10^{-6}$ g
m	mass
N	normal or Z-axis force
S	reference surface area, 249.9 m^2
V	velocity
X,Y,Z	Orbiter body axis system coordinates
ρ	atmospheric density

Acronyms

APU	auxiliary power unit
BET	best estimated trajectory
CFD	computational fluid dynamics
HiRAP	High Resolution Accelerometer Package
OADDB	Operational Aerodynamic Design Data Book
OEX	Orbiter experiments program
STS	Space Transportation System
SUMS	Shuttle Upper Atmosphere Mass Spectrometer

Subscripts

i	The ith direction, ie. X,Y,Z axes or normal or axial axis

Introduction

The development of a reusable space vehicle which delivers payloads to orbit in the vertical rocket configuration, and returns from orbit in a horizontal aircraft configuration provided an unprecedented opportunity to the flight research community. One of the unique flight research areas which can be assessed regularly is the aerodynamic performance of a winged reentry vehicle traversing the rarefied-flow transition regime from free-molecule to hypersonic continuum, roughly 160 to 60 km altitude. The altitude range of this flight regime is too low for satellite measurements and too high for sounding rocket measurements, as depicted in Fig 1.

Computational fluid dynamics (CFD) techniques research[1] was being conducted during the early Orbiter development flight tests, but was not mature enough for aerodynamic design predictions. Extensive wind tunnel testing went into the design of the Shuttle Orbiter[2], but under conditions which were not in the rarefied-flow regime (except for one set of data which is shown in this report). Therefore, prior to the initial Orbiter development flights, no applicable rarefied-flow reentry aerodynamics test data were available. The solution to this limitation was to adapt empirical expressions resulting from earlier flight tests of Apollo-like blunt bodies to a winged reentry vehicle.

Decisions were made early in the Orbiter development program to use the Orbiter as a flight test vehicle to make in-situ measurements of this largely unexplored flight regime. Making full scale, repeated measurements during atmospheric reentry would permit a better understanding of both the reentry aerodynamics and the reentry environment. This, in turn, would provide an improved data base for future development of winged reentry vehicles. One of the experiments developed to make these aerodynamic measurements was the High Resolution Accelerometer Package (HiRAP). The HiRAP experiment was one of a number of flight experiments designed and flown on the Orbiter as part of the Orbiter Experiments Program (OEX). The OEX Program was initiated to provide aerothermodynamic and aerodynamic flight data for application to reusable winged reentry vehicle designs.

Experiment Description

HiRAP is a package of three orthogonal, pendulous, gas-damped, micro-g resolution accelerometers mounted on the Orbiter in the wing box. The axes of the accelerometer sensors are co-aligned with the Orbiter body axes. The HiRAP is designed to measure the Orbiter aerodynamic acceleration signal during reentry. In particular, HiRAP measures the low frequency (< 1 Hz), low level acceleration (i.e micro-g sensitivity) signals during the reentry from free molecule flow to hypersonic continuum transition. During the un-powered gliding reentry of the Orbiter, the aerodynamic acceleration signal is directly related to the aerodynamic force coefficients (Fig. 3). The signals measured by the HiRAP are converted into calibrated aerodynamic acceleration data sets and merged with mission-specific trajectory state vector data. These merged aerodynamic data sets are then further processed to determine Orbiter aerodynamic coefficients and to infer atmospheric density. HiRAP accelerometer measurements have been made on Space Shuttle Orbiter missions since STS-6 in April of 1983[3]. The measurement data base includes ascent, orbit, and reentry data.

A variety of spatial and temporal assessments of the inferred density measurements can be made due to the time span of instrument operation and the attributes of the Orbiter reentry trajectory over many missions. For example, data have been collected for nearly a decade, which allows a correlation of inferred density with solar intensity over one complete 11 year solar cycle. The reentry trajectory provides a descent of approximately 100 km in altitude with a ground-track distance of about 8000 km. This permits the study of horizontal slices of the atmosphere in a regime not regularly assessed by satellites or by ground LIDAR, which samples vertical profiles.

Flight Data Results

Extraction Technique

The principle behind making aerodynamic acceleration measurements during reentry is to remove the non-aerodynamic acceleration inputs. In un-powered gliding flight the predominant non-aerodynamic forces on the Orbiter are thrust firings, APUs, and rotationally induced linear accelerations (the sensors are not

at the center-of-gravity). The flight data is transformed into aerodynamic acceleration data using a rigorous, detailed process to remove these effects. [4,5,6,7]

Force Ratio Data

A common measure of aerodynamic performance is the ratio of the normal to axial acceleration measurement. This ratio corresponds to force coefficient ratios, C_N/C_A. Fig. 4 presents the force coefficient ratio data during reentry for all 12 currently available missions. The reentry data set consists of about 11.6 hours of flight measurements. It is from this compendium of data that the aerodynamic model has been determined and the atmospheric density inferred. The ascent data base consists of approximately 4 hours of measurements and the orbital data base contains about 10 hours of measurements. For the purposes of the various HiRAP project analyses, the acceleration data sets consist of time, X- and Z-axis acceleration measurements. The HiRAP instrument does measure and record the Y-axis sensor output but it is not used for the purposes of this paper.

Rarefied-Flow Aerodynamics Model

Beginning with early analytic models[3,4] the HiRAP data were used to derive an aerodynamics model. This aerodynamics model is composed of curve fits to data described by the Operation Orbiter Aerodynamic Data Book (OADDB)[8] combined with a transition bridging formula developed during the HiRAP program[9]. The rarefied flow aerodynamics model is composed of three sections: the free-molecule flow coefficients, transition formulae, and the hypersonic continuum coefficients. Fig. 5 shows the set of aerodynamic coefficient equations in the form of C_N and C_A functional relationships. The exact equation details are in the literature[10].

The reentry aerodynamic data sets are the basis for the determination of the Orbiter rarefied aerodynamics model. The equation for this process is a particular arrangement of the classical aerodynamic force equation, namely

$$C_i = \frac{a_i}{(\frac{1}{2}\rho V^2)\frac{S}{m}} \quad , \quad (1)$$

where C_i is the aerodynamic force coefficient in the ith direction, a_i is the corresponding acceleration, and S/m is the vehicle area to mass ratio. In general, the dynamic pressure, $(\frac{1}{2}\rho V^2)$ can be obtained from pressure transducers, mass spectrometer measurements[11], or atmospheric models.

In order to calculate the coefficient C_i in equation (1), all of the terms on the right of the equation must be known. The HiRAP instrument measures acceleration (a_i) along each Orbiter axis. The mass m and the reference surface area S (249.9 m^2) are known and velocity V is determined as a function of flight time from a BET process[12-23]. Since no measurements of the density were available for most of the earlier flights, a statistical approach was developed to determine the aerodynamic coefficients. This technique is described in the literature along with the results for several of the earlier flights [9,24-29].

Reentry Trajectory Data

Reentry trajectory data from each mission are required for the development and the calculation of the rarefied-flow aerodynamics model[12-23]. These data are also required to present the analytical results in spatial and temporal perspectives for density correlations. The sign conventions used in the aerodynamic analyses are presented in Fig. 6. Angle of attack and control surface data for all missions are presented in Fig. 7a-7c. The Orbiter average angle of attack is seen to be 41° until an altitude of about 110 km is reached when it decreases to about 40°. During the early Orbiter flights, the initial body-flap and elevon settings were varied, until an apparent optimum setting was realized. Currently, all flights use -4.5° and -2.7° as the settings for the body-flap and elevons, repectively. The mass of the Orbiter at entry interface (121 km) and the velocity profile of each mission were used to complete the analyses.

Aerodynamics Model Comparisons

The HiRAP derived Orbiter rarefied-flow aerodynamics model is presented in the form of a force ratio, C_N/C_A as a function of Knudsen Number (Kn) in Fig. 8. The ratio measurement vs. model residuals are also presented for all missions. The average residual for $Kn < 10^{-3}$ is not completely random, suggesting that further model adjustments are possible. The Kn in this figure is derived from the 1976 Standard Atmosphere[30] and uses the mean aerodynamic chord of the Orbiter as a reference length (12.058 m). The model is compared to the same force ratio from wind tunnel data in Fig. 9. The HiRAP aerodynamics model agrees well with the wind tunnel data in the rarefied flow flight regime.

Upper Atmosphere Density Variability

The HiRAP flight aerodynamics model provides a means to calculate upper atmospheric density for each flight[29,31]. Equation (1) can be rearranged to obtain the following:

$$\rho = \frac{a_i}{\frac{1}{2}V^2 C_i \frac{S}{m}} \qquad (2)$$

The above calculation produces two sets of inferred density from the X- and Z-axis aerodynamic acceleration measurements. A much greater noise level exists in the Z-axis measurement due to Auxiliary Power Unit (APU) exhaust disturbances[6] than in the X-axis measurement. This noise is transferred to the inferred density. As a result of the noise, a composite density is formed using X-axis derived density at high altitude and Z-axis derived density at low altitude. This composite of inferred density is normalized to the 1976 Standard Atmosphere density and presented in Figs. 10a and 10b. Examination of these plots shows a wavelike density structure with peak amplitudes deviating from the measured average by more than 20%. Typical waves span

horizontal distances of approximately 1800 km in the altitude range from 115-80 km. These waves appear to be somewhat random, since maxima and minima occur at different altitudes and since the wave amplitudes vary from flight to flight.

The cause of the wave structure seen during the individual flights has not been definitely determined. Horizontal or vertical gusts cannot produce the required accelerations because unreasonably high wind speeds would be required. If the variations are temporal, their fluctuations are too rapid to be caused directly by slowly varying influences such as $F_{10.7}$, time of year, or even local solar time or solar zenith angle. However, these variables could influence the mechanisms which produce the waves and thereby indirectly influence both their temporal and spatial dependence, as well as their amplitude.

A twelve flight density envelope showing the separate components of the composite density is presented in Fig. 11. The effect of the APU in the Z-Axis component derived density shows an increased spread in the envelope at high altitudes. A twelve flight average of the separate density components is presented in Fig. 12. Included in Fig. 12 is a one standard deviation envelope around the 12 flight average. The APU effect is also evident in the magnitude of the Z-axis standard deviation at high altitudes.

Density Correlations

The HiRAP experiment has been in operation for a decade and to date 12 missions have been analyzed. As a result of this long time span and the variety of reentry parameters, several spatial and temporal comparisons can be made. These include polar and equatorial reentry ground tracks, reentry solar zenith angles, local solar times, annual atmospheric density amplitude variations and density measurements relative to solar cycle. The reentry ground tracks for the 12 missions analyzed to date are limited between 40 S and 60 N latitude over the Pacific Ocean and are presented in Fig. 13. The reentry paths are grouped into high and low inclination sets as a function of the primary mission orbital mechanics parameters. The solar zenith angles for each of the 12 missions is presented in Fig. 14. All missions except STS-08 and STS-35 flew into the morning terminator and landed during daylight hours. The solar cycle itself has a direct effect on the atmospheric density, particularly in the rarefied flow region. The 10.7 cm flux is a standard index of solar intensity[32] and is presented in Fig. 15. Superimposed on this cycle are the times that

HiRAP aerodynamic accelerations were measured. These measurements, and therefore the inferred densities, span the complete cycle.

The amplitude of the density ratio (ρ/ρ_{76}) wave between 80 and 115 km altitude was calculated for each flight. Each amplitude was then divided by the corresponding average density ratio to give a normalized amplitude. In turn, the normalized amplitudes were correlated with time of year, $F_{10.7}$, local solar time, and solar zenith angle by the method of least squares. Only the correlation with time of year was statistically significant (the others were marginal). The normalized amplitudes were next corrected by removing the effects of the $F_{10.7}$, local solar time, and solar zenith angle. This corrected data set was then correlated with time of year. The results are shown in Fig. 16. This fit to the amplitude variation shows a roughly 20% change during the year with the maximum amplitude occurring in the summer.

Summary

The Orbiter Experiments (OEX) program provides a unique opportunity to use the repeated Shuttle Orbiter reentries to make in-situ aerothermodynamic and aerodynamic measurements. One of these experiments, the High Resolution Accelerometer Package (HiRAP) experiment was devised to make low frequency, low acceleration aerodynamic acceleration measurements in the rarefied flow flight transition regime. These measurements in the transition flight regime during the Shuttle Orbiter reentry are in a flight region difficult to simulate. With the twelve HiRAP missions spanning about 10 years, a unique flight aerodynamic acceleration data base has been built. From this data base a rarefied flow aerodynamics model has been developed. This model compares well with flight data and wind tunnel data. These flight aerodynamic acceleration measurements and the subsequent development of the aerodynamics model are currently being used to evaluate CFD techniques.

The verified aerodynamics model and the calibrated aerodynamic acceleration measurements have been used to infer upper atmospheric density. The inference of atmospheric density from the 12 sets of flight data permits a variety of statistical analyses and comparisons with the conditions associated with the collection of the data. Due to unique characteristics of the Orbiter reentry, the inferred density characteristics are unlike any previous measurements at this altitude. The data are measured

along a nearly horizontal slice of the atmosphere, while traveling into both the morning and evening terminator, during a nearly complete solar cycle, and between latitude ranges of 40S to 60N over the Pacific Ocean. The ratio of the inferred density to the 1976 Standard Atmosphere density for each of the 12 missions displays a random wave structure. A seasonal component of this wave structure has been detected.

References

1. Moss, J.N. and Bird, G.A., "Direct Simulation of Transitional Flow for Hypersonic Reentry Conditions," AIAA Paper 84-0406, Jan 1984.

2. "Aerodynamics Design Substantiation Report-Vol. I: Orbiter Vehicle", Rockwell International, Space Division, Downy, CA SD74-SH0206-1H, Jan 1986

3. Blanchard, R.C.; and Rutherford, J.F.: Shuttle Orbiter High Resolution Accelerometer Package Experiment: Preliminary Flight Results. Journal of Spacecraft and Rockets, vol. 22, no 4, July-August 1985, pp. 474-480.

4. Blanchard, R.C., and Buck, G.M.: Determination of Rarefied-flow Aerodynamics of the Shuttle Orbiter from Flight Measurements on STS-6 and STS-7. AIAA Paper 85-0347, January 1985.

5. Thompson, J.M.; Russel, J.W.; and Blanchard, R.C.: Methods for Extracting Aerodynamic Accelerations from Orbiter High Resolution Accelerometer Package Flight Data. AIAA paper 87-2365, August 1987.

6. Blanchard, R.C.: Larman, K.T.: and Barrett, M.: The High Resolution Accelerometer Package (HiRAP) Flight Experiment Summary for the First Ten flights, NASA RP-1267, March 1992.

7. Blanchard, R.C.; Larman, K.T. ; and Moats, C.D.: Flight Calibration Assessment of HiRAP Accelerometer Data. AIAA Paper 93-0836, January 1993

8. Operational Aerodynamic Design Data Book, STS-85-0118 Chg 3, September 1991.

9. Blanchard, R.C.; and Hinson, E.W.: Hypersonic Rarefied-Flow Aerodynamics Inferred from Shuttle Orbiter Acceleration Measurements. Paper No. 7 presented at the International Congress on Hypersonic Aerodynamics, Manchester, England, September 4-6 1989.

10. Blanchard, R.C.; Larman, K.T.; and Moats, C.D.: Rarefied-flow Shuttle Aerodynamics Flight Model. AIAA Paper 93-3441, August 1993.

11. Blanchard, R.C.; Duckett, R.J.; and Hinson, E.W.:The Shuttle Upper Atmosphere Mass Spectrometer Experiment. Journal of Spacecraft and Rockets, vol 21, no.2 March-April 1984, pp. 202-208.

12. Findlay, J.T., Kelly, G.M., Heck, M.L., McConnell, J.G.; Results of the First Entry Flight of the NASA Space Shuttle Challenger, STS-6, NASA CR-176666, June 1983.

13. Findlay, J.T., Kelly, G.M., Heck, M.L., McConnell, J.G.; STS-07 Post Flight Best Estimate Trajectory Products, AMA Report 83-17, September 1983.

14. Findlay, J.T., Kelly, G.M., Heck, M.L., McConnell, J.G.; STS-8 BET Results, NASA CR-172257, November 1983.

15. Findlay, J.T., Kelly, G.M., Heck, M.L., McConnell, J.G., Henry, M.W.; STS-9 BET Products, NASA CR-172314, February, 1984.

16. Kelly, G.M., McConnell, J.G., Findlay, J.T., Heck, M.L.; Final STS-11(41B) Best Estimate Trajectory Products, Development and Results from the First Cape Landing, NASA CR-172349, April 1984.

17. Findlay, J.T., Kelly, G.M., McConnell, J.G. Heck, M.L.; STS-13(41-C) BET Products, NASA CR-172350, July 1984.

18. Kelly, G.M., Heck, M.L McConnell, J.G.,Findlay, J.T.; Post Flight Results from Challenger Mission 51B(STS-24), NASA CR-178039, February,1986.

19. Findlay, J.T., Kelly, G.M.; STS-26(51F) Challenger Post -Flight Best Estimate Trajectory Results, NASA CR-178234, June 1987.

20. Findlay, J.T., Kelly, G.M.; Best Estimate Trajectory Results for the Challenger STS-30(61A) Entry Flight, NASA CR-178253, June, 1987.

21. Findlay, J.T., Kelly, G.M.; STS-32(61C) Columbia Entry BET Products and Summary Results, NASA CR-178262, June 1987.

22. Oakes, K.F., Findlay, J.T. Jasinski, R.A., Wood, J.S.; Final STS-35 Columbia Descent BET Products and Results for LaRC OEX Investigations, NASA CR-189569, November 1991.

23. Oaks, Kevin, F. Wood, James, S.,and Findlay, John, T.: Final Report: STS-40 Descent BET Products- Development and Results: Flight Mechanics & Control, Inc.; NASA Contractor Report 189570: November 1991.

24. Blanchard, R.C.; Overview of Shuttle Data on Density. Proceedings of workshop, Nov 19-21, 1985; Upper and Middle Atmosphere Density Modeling Requirements for Spacecraft Design and Operations, NASA CP-2460.

25. Buck, G.M.; and Blanchard, R.C.: Rarefied Aerodynamics and Upper Atmosphere Density from Multiple Orbiter flight Measurements. AIAA Paper 86-0269.

26. Blanchard, R.C.: Rarefied Flow Lift-to-Drag Measurements of the Shuttle Orbiter. ICAS Paper 86-2.10.2, London, United Kingdom, September 1986.

27. Blanchard, R.C.; and Larman, K.T. Rarefied Aerodynamics and Upper Atmosphere Flight Results from the Orbiter High Resolution Accelerometer Package Experiment. AIAA Paper 87-2366, August 1987.

28. Blanchard, R.C.; and Buck, G.M.: Rarefied Flow Aerodynamics and Thermosphere Structure from Shuttle Flight Measurements. Journal of Spacecraft and Rockets, vol 24, no 6, November-December 1987.

29. Blanchard, R.C.; Hinson, E.W.; and Nicholson, J.Y.: Shuttle High Resolution Accelerometer Package Experiment Results: Atmospheric Density Measurements Between 60-160 km., Journal of Spacecraft and Rockets, vol 26, no 3, May-June 1989, pp.173-180.

30. U.S. Standard Atmosphere, 1976. NOAA, NASA and U.S. Air Force, Oct 1976.

31. Blanchard, R.C.; Shuttle Reentry Density Measurements (Between 60 and 160 km). Proceedings of Workshop held at AFGL, October 20-21, 1987, Environmental Research papers, No. 1053 GL-TR-90-0033 I&II, Editor, Frank A. Marcos, February, 1990.

32. "Solar-Geophysical Data Reports", Published quarterly by the National Geophysical Data Center.

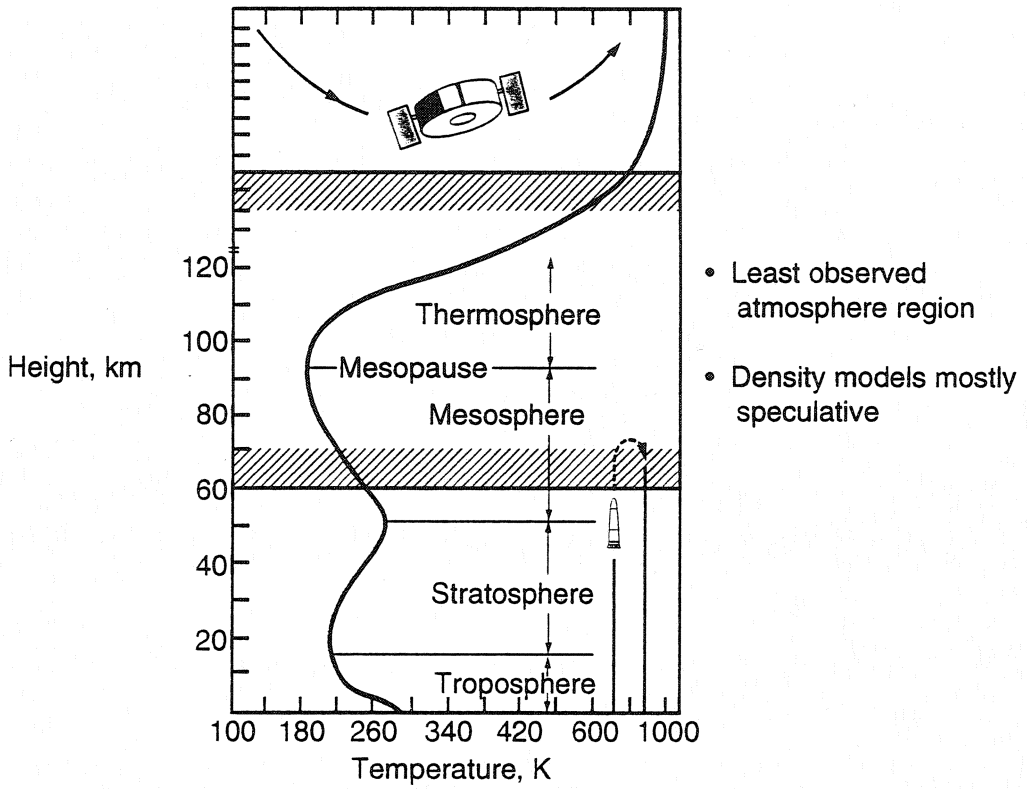

Figure 1. Density measurements status.

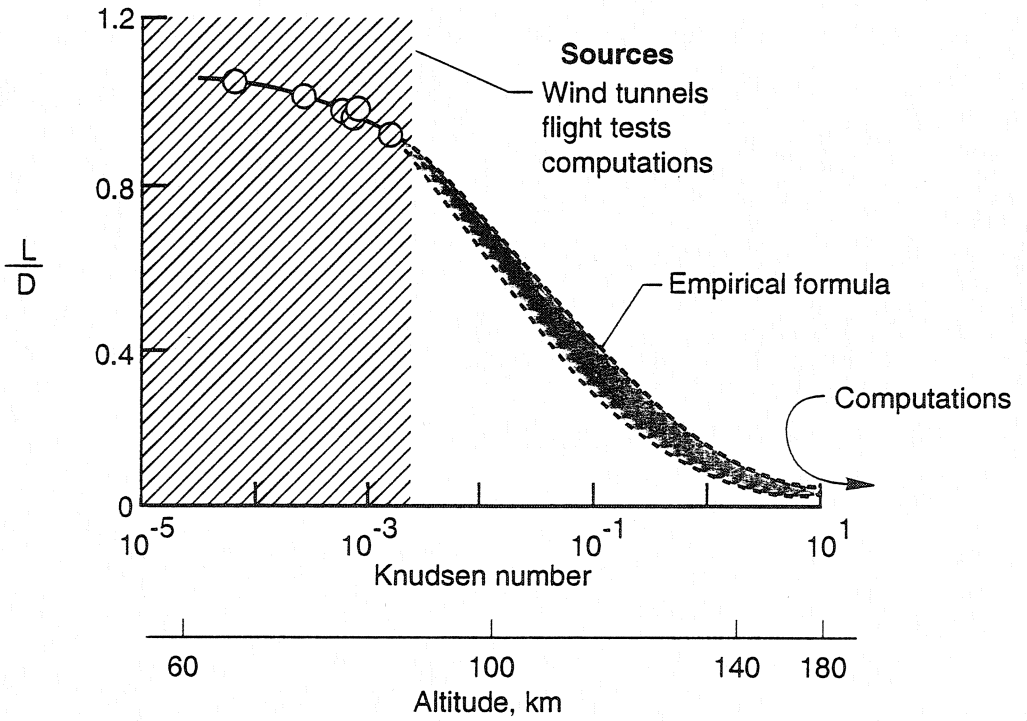

Figure 2. Orbiter rarefied-flow aerodynamics status during early 1908's.

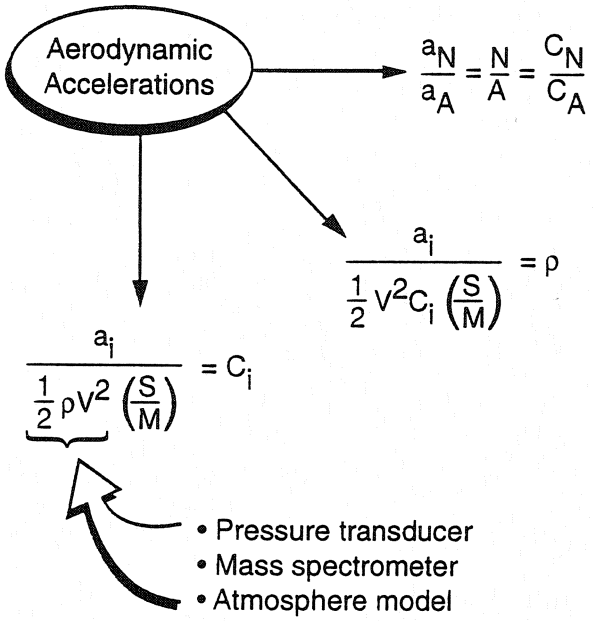

Figure 3. Accelerometer experiment concepts.

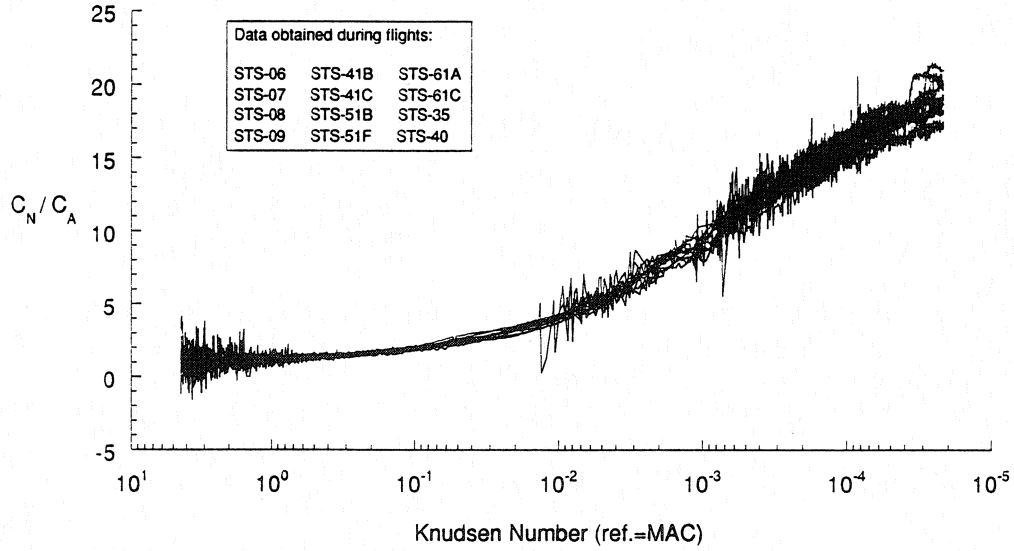

Figure 4. HiRAP C_N / C_A flight measurements.

$$C_N = C_{Nc} + (C_{Nf} - C_{Nc}) * \bar{C}_N$$

$$C_A = C_{Ac} + (C_{Af} - C_{Ac}) * \bar{C}_A$$

where, for i = N,A

Free molecule flow coefficients $C_{if} = C_{if}(\alpha) + [C_{if}(\delta_{bf}) + C_{if}(\delta_{el})]$

Hypersonic continuum coefficients $C_{ic} = C_{ic}(\alpha) + C_{ic}(\delta_{bf}) + C_{ic}(\delta_{el})$

and, for j= 1 to 3

"Bridging" coefficients $\bar{C}_N = \exp[a_j, \log_{10}(Kn)]$, $\bar{C}_A = \exp[b_j, \log_{10}(Kn)]$

Figure 5. Rarefied-flow aerodynamics model outline.

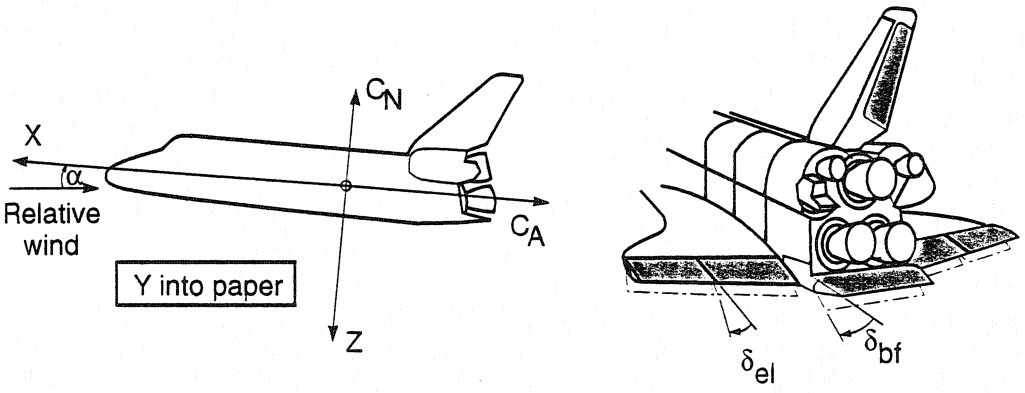

Figure 6. Sign conventions.

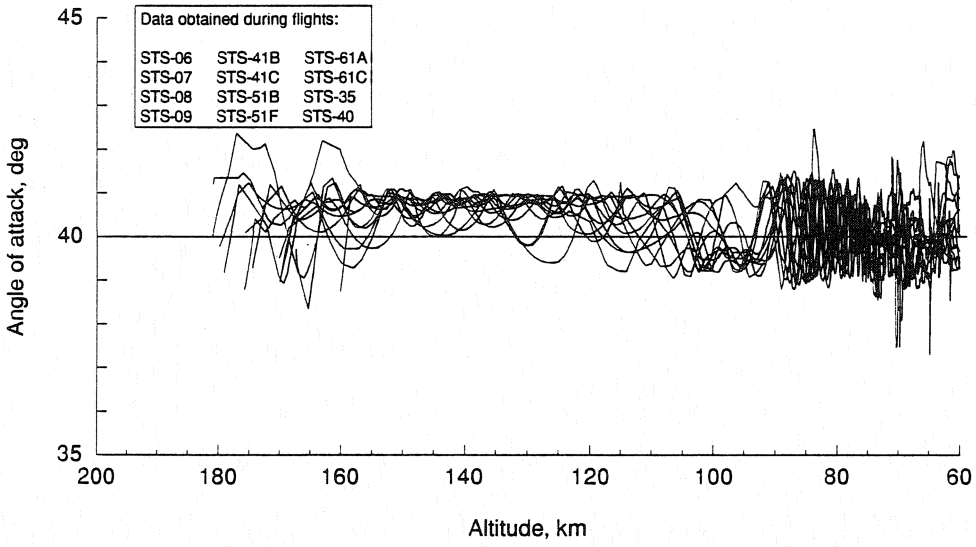

Figure 7a. Orbiter angle of attack during re-entry.

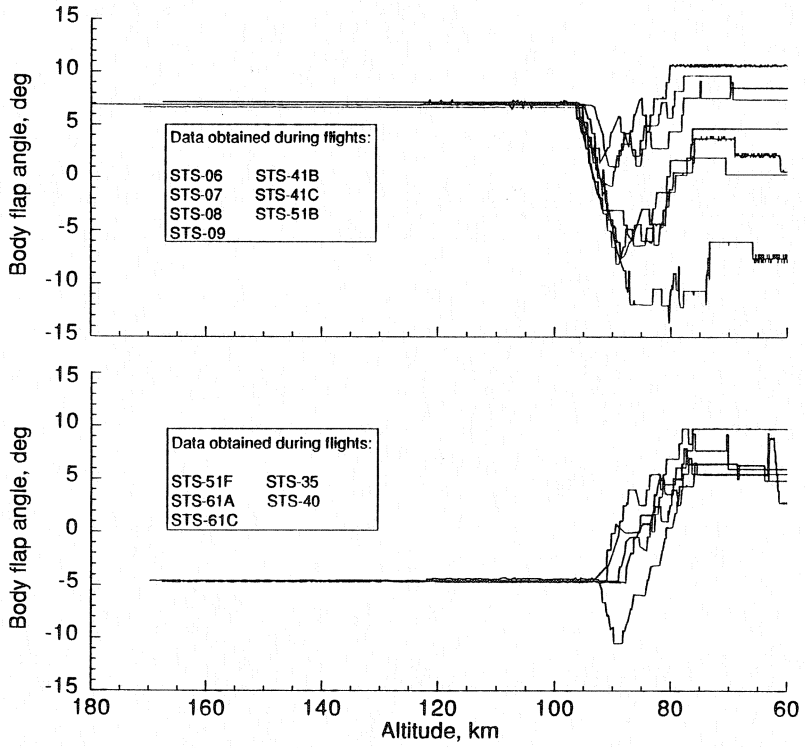

Figure 7b. Body flap deflection during re-entry.

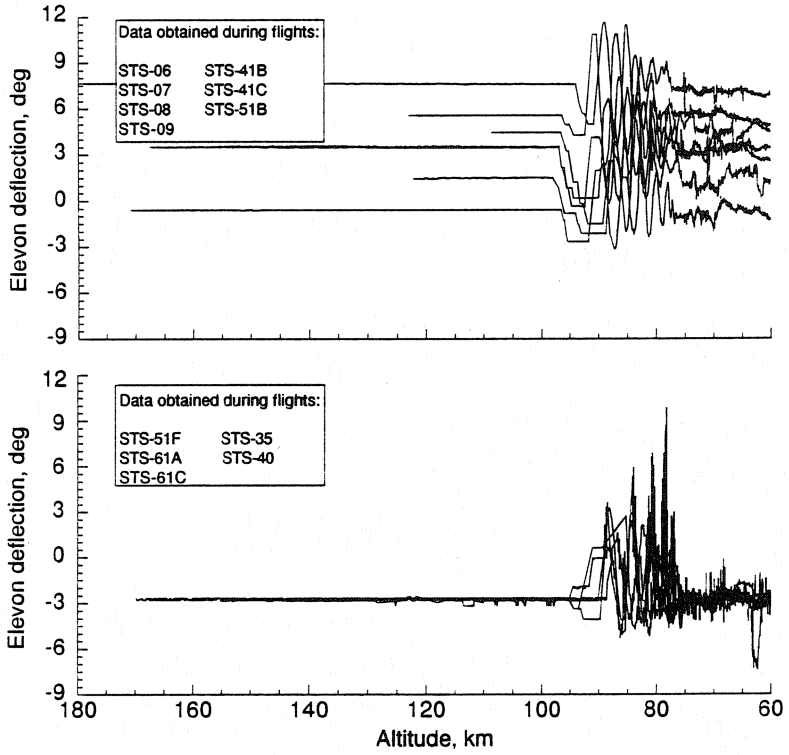

Figure 7c. Elevon deflection during re-entry.

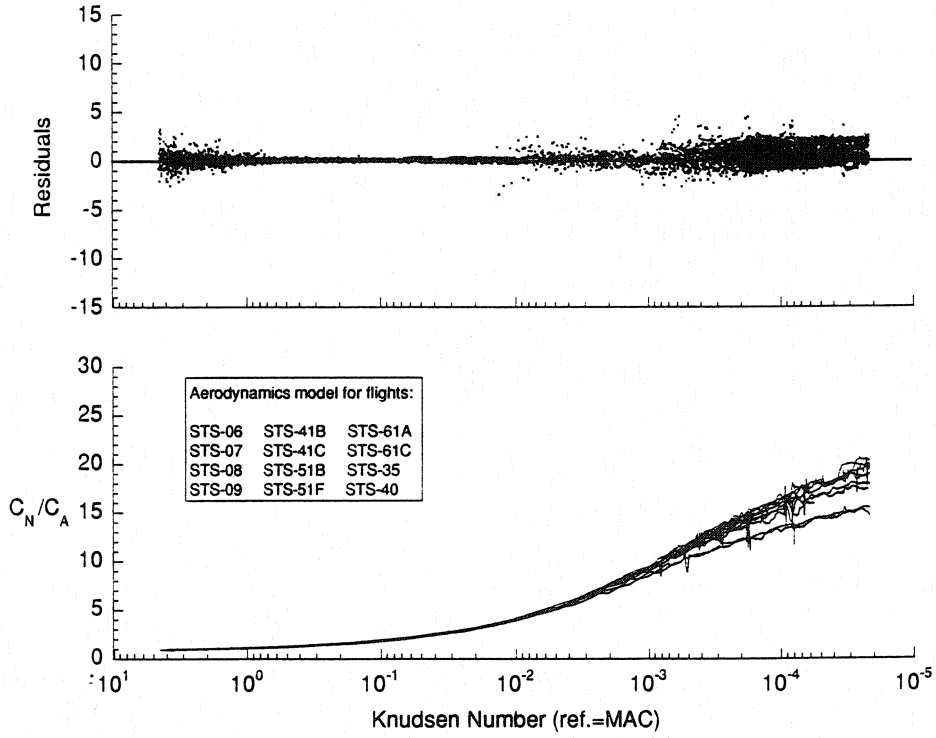

Figure 8. C_N/C_A Model and HiRAP flight measurement comparisons.

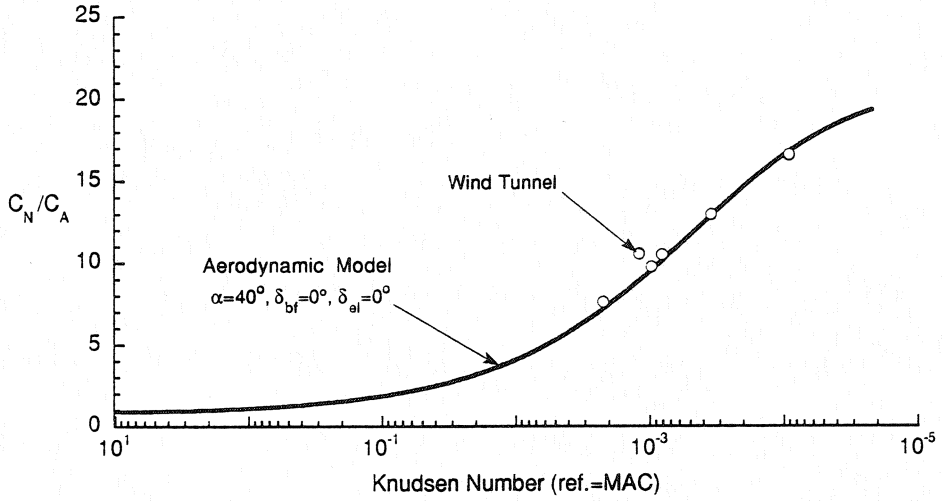

Figure 9. Model and wind tunnel data comparison.

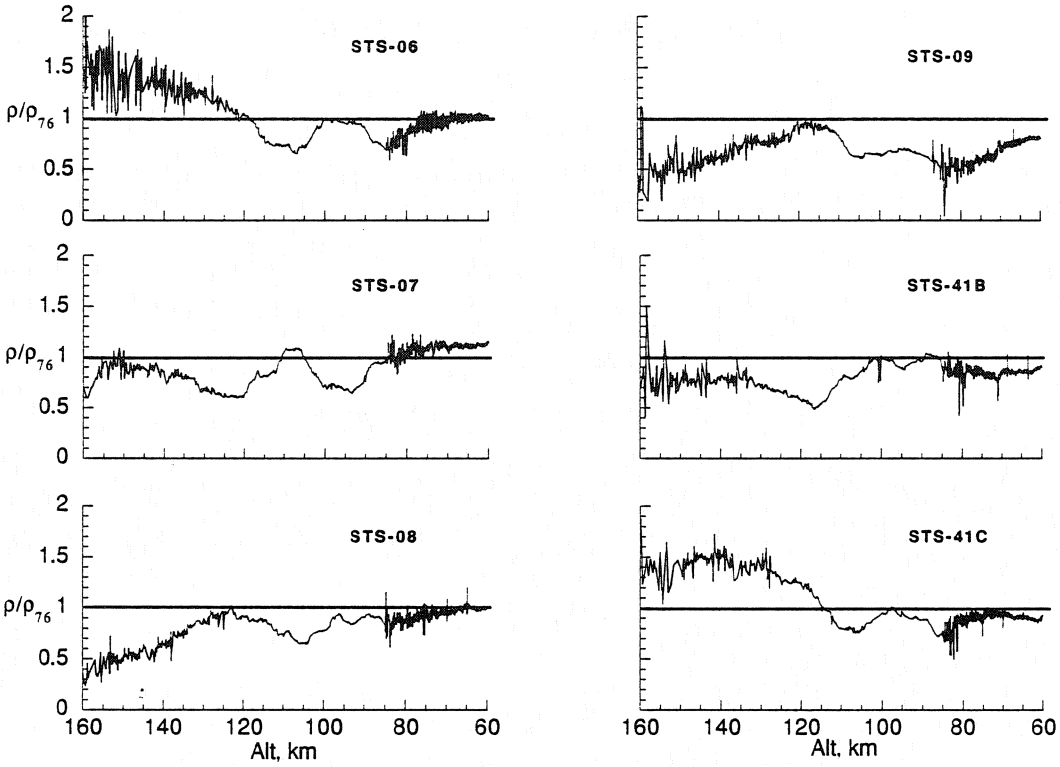

Figure 10a. HiRAP density ratio altitude profiles.

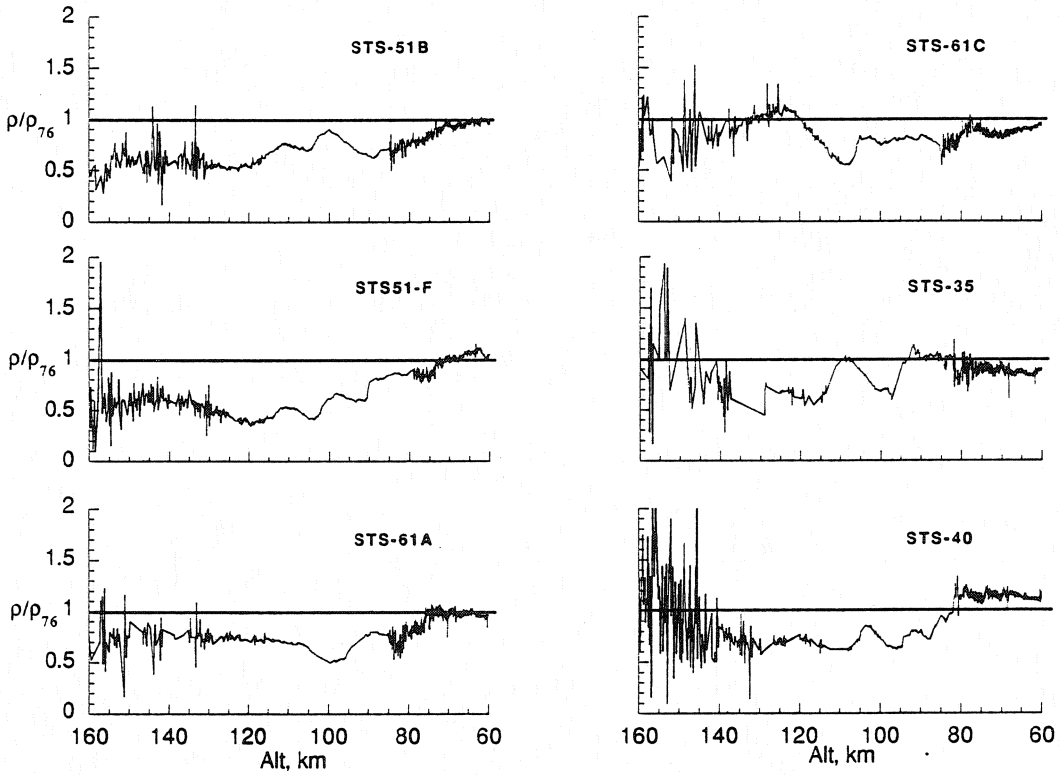

Figure 10b. HiRAP density ratio altitude profiles.

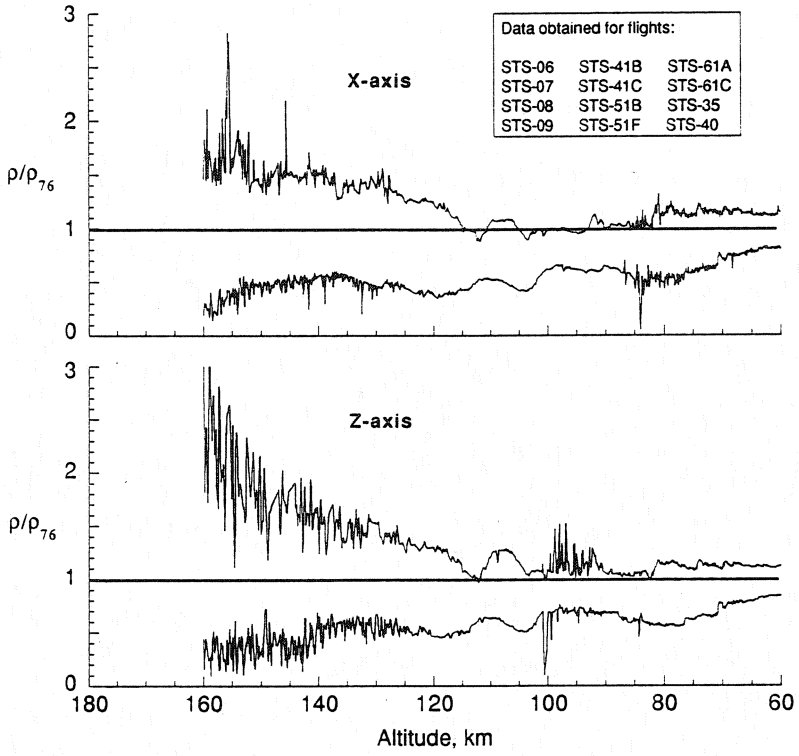

Figure 11. HiRAP 12 flight density envelope.

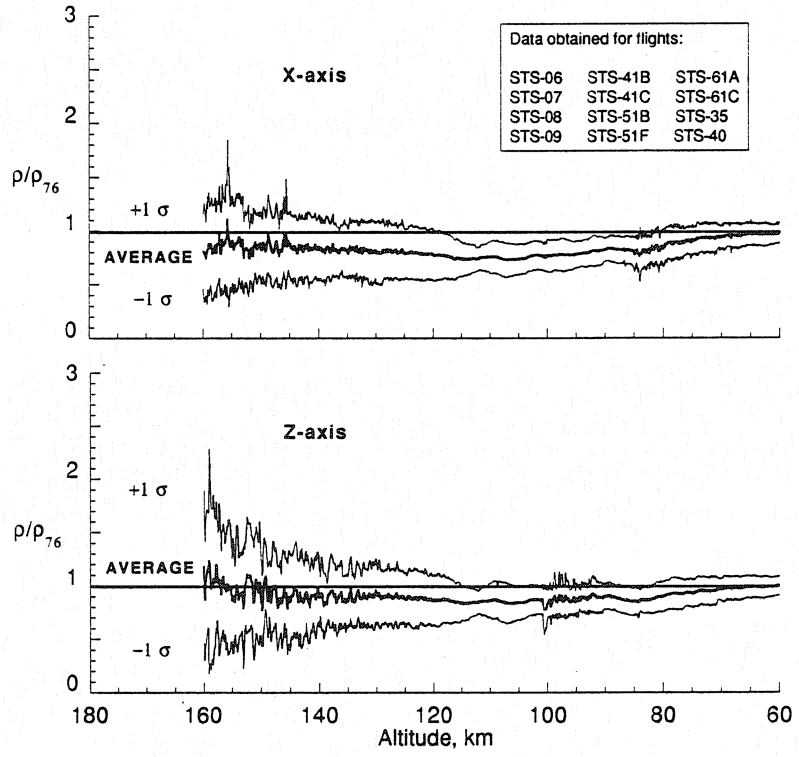

Figure 12. HiRAP 12 flight average density ratio.

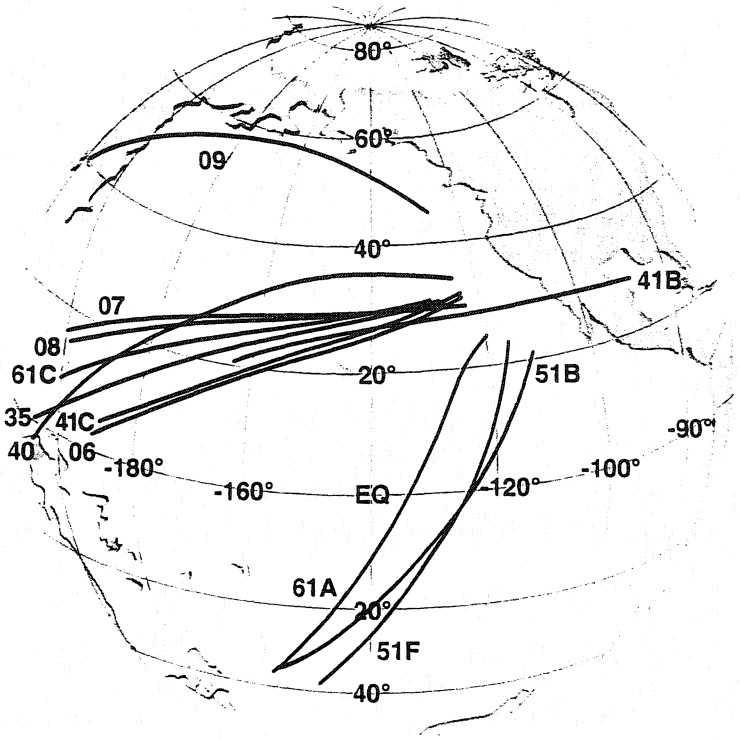

Figure 13. Reentry ground tracks during HiRAP measurements.

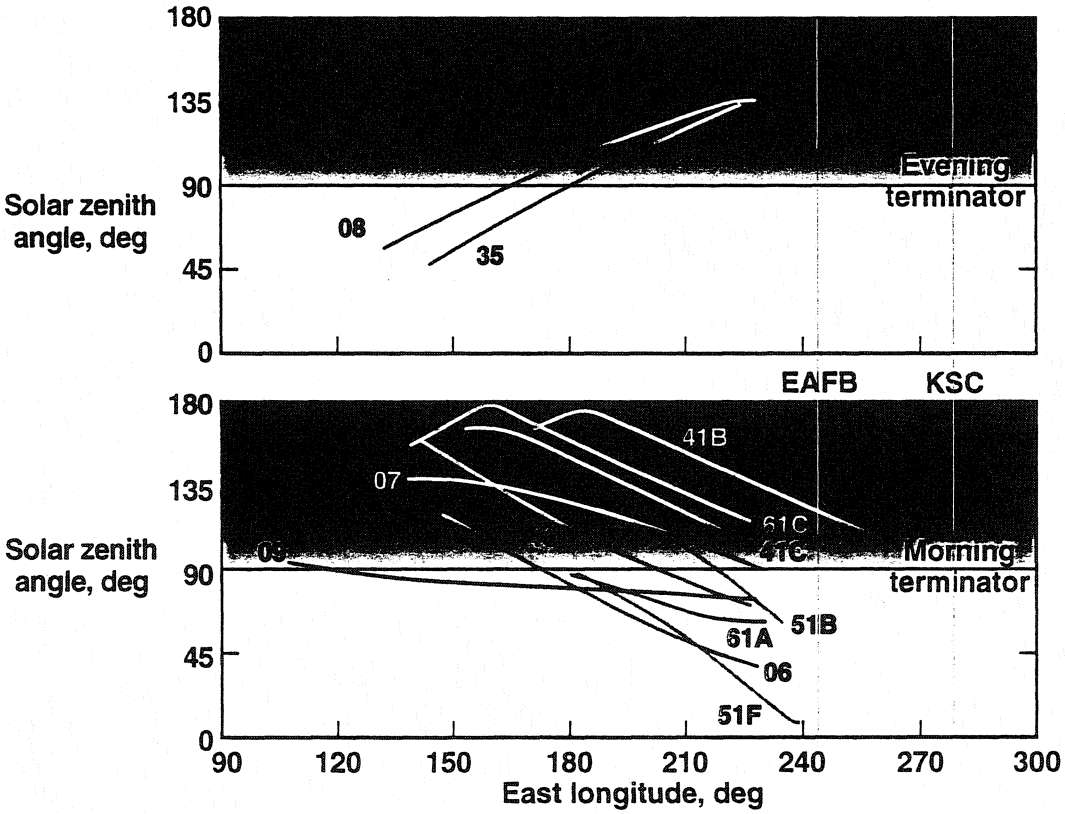

Figure 14. Solar zenith angle during HiRAP measurements.

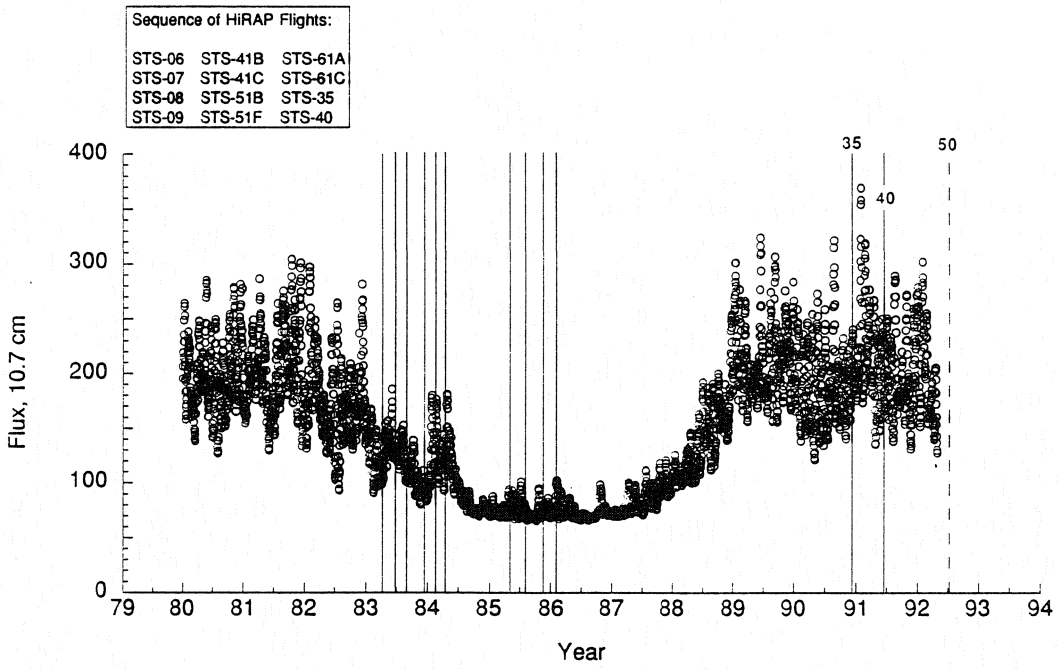

Figure 15. Solar cycle activity during HiRAP flights.

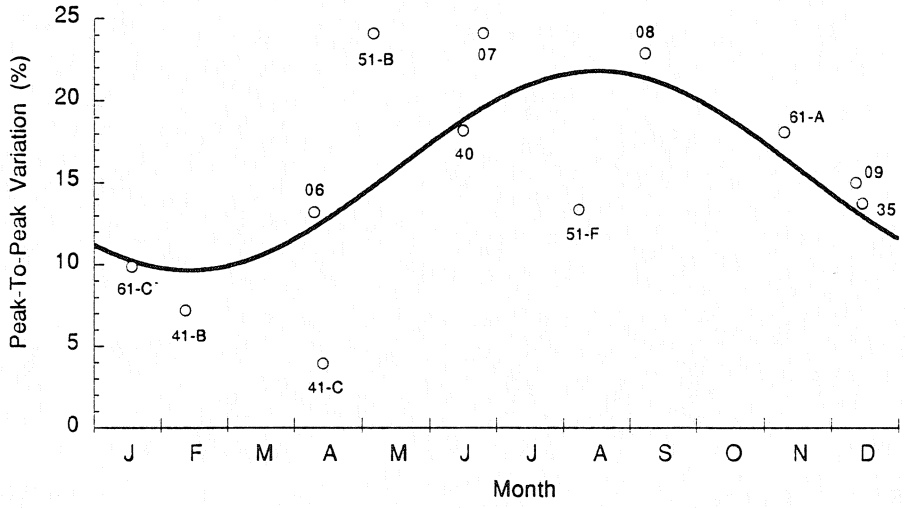

Figure 16. Annual variation of density ratio amplitude between 85 and 115 km.

DIRECT SIMULATION MONTE CARLO (DSMC) MODELLING OF ORBITER REENTRY AND ON-ORBIT AERODYNAMICS

Didier F. G. Rault
NASA Langley Research Center
Hampton, VA

ABSTRACT

A three-dimensional direct simulation Monte Carlo method is used to evaluate the aerodynamics of the Shuttle Orbiter in the early phase of atmospheric reentry from low-Earth Orbit down to 100 km altitude. Simulation results are compared with Blanchard's Shuttle aerodynamic model, which is based on a series of in-flight high sensitivity accelerometer measurements. Good agreement is shown except for the normal force and pitching moment coefficient.

INTRODUCTION

Flight data recorded during the reentry of the Space Shuttle Orbiter offer the possibility of studying the aerodynamics of flight vehicles over all flow regimes, from the free molecule regime at orbit altitudes, through the transition regime in the 100-200 km range and the continuum hypersonic, supersonic and subsonic flow regimes at lower altitudes. These data are of special interest in the low-density, high Knudsen number domain in which very few flight data are available to validate simulation codes and methods. The present paper is concerned with the three-dimensional computer simulation of the flow field around a reentering Shuttle Orbiter from orbit altitude down to 100 km and the comparison of the computed values of the aerodynamic forces and moments with the values derived from flight data. Special codes and methods have been developed to perform this simulation. In the high Knudsen number flow regime, the conventional computational fluid dynamic (CFD) methods, which are based on solving the Navier-Stokes equations, cannot be used. Instead, we have used a particle simulation approach, namely the direct simulation Monte Carlo method, as shown in Section 2. The flow conditions and atmospheric properties which are considered in this work are described in Section 3. The Shuttle aerodynamic characteristics were computed at 5 nominal altitudes along the reentry trajectory, namely 100 km, 110 km, 120 km, 145 km, and 170 km. Results are presented in Sections 4-5. It is shown that, as the Shuttle altitude decreases, the structure of the flowfield gradually changes from a shockless thick compression layer, typical of the free molecule flow regime, to a viscous shock layer and finally to a more continuum like shock-boundary layer structure characterized by a strong leading edge shock. The computed aerodynamics compare fairly well with flight data derived values, except for two instances, namely the normal force coefficient and the pitching moment coefficient. The normal force coefficient appears to remain close to or above its free molecule limit value over most of the transition flow regime. This peculiarity is discussed and analyzed in Section 6. The pitching moment increases significantly

*Aero-Space Technologist, Aerothermodynamics Branch, Space Systems Division.

with rarefaction, and the Center of Pressure is found to move forward about 2.5 meters from orbit altitude to 100 km. These observations are attributed to a redistribution of the shear and pressure forces on the Shuttle surface as illustrated in Section 7. Finally, in the last section, the aerodynamics of the Shuttle in Low-Earth Orbit (LEO) with open cargo bay doors are presented.

SIMULATION METHOD: DIRECT SIMULATION MONTE CARLO

In the low density-high Knudsen number flow regime, the computer simulation of flowfield around vehicles can be extremely complex due to nonequilibrium in all energy levels. Collisionality among gas molecules may be very low and the gas is typically non Maxwellian. Simulation methods relying on Navier-Stokes equations fail because of the breakdown of the Chapman-Enskog relationships for transport properties and the inability to uniquely define a translational temperature. An alternative method, devised by Bird (Ref. 1), consists of simulating the gas no longer as a continuum fluid but as a large ensemble of discrete molecules. This method is called the direct simulation Monte Carlo (DSMC) and has been highly documented in the literature (Refs. 2 and 3) and used by several authors in the past 30 years over a wide range of geometrical shapes. Our present implementation of the DSMC method uses the variable hard sphere (VHS) model to simulate intermolecular collisions, the Larsen-Borgnakke model to evaluate the internal energy transfer among colliding molecules, and Bird's chemistry model. The molecule-wall interactions are modelled as completely diffuse for both momentum and energy.

Recent effort has been aimed at extending the method to allow for the simulation of flowfield around bodies of arbitrarily complex geometry in three dimensions. The code that was used for the present work was developed in the course of recent studies on the aerodynamics of slender and blunt reentry vehicles (Refs. 4-6) and satellites (Ref. 7) and the self contamination of satellites (Ref. 8). A special feature has been included in the code for the present study to accurately account for and simulate the thin-body layer that typically develops on the windside of flight vehicles due to the characteristically large stagnation-to-wall temperature ratio on these vehicles (Ref. 9). This body layer is characterized by high densities and large density gradients. In a computer simulation, adequate spatial resolution of the computational grid within this thin layer is crucial to accurately predict the shear forces on the body surface. As will be shown below, the shear forces which, in the continuum flow regime are relatively small with respect to pressure forces, may become predominant as the free molecular flow regime is approached. Special grid adaption and solution tuning techniques were developed and used, which made it possible to perform the simulation down to the relatively low altitude of 100 km.

FLOW CONDITIONS, ATMOSPHERIC PROPERTIES AND VEHICLE GEOMETRY

As the Shuttle Orbiter reenters the atmosphere from orbit down to 100 km, it traverses a flight domain where the Knudsen and Reynolds numbers vary by several orders of magnitude as illustrated in Fig. 1, which shows the reentry trajectory of the Shuttle in a Mach-Reynolds-Knudsen number domain. The Reynolds and Knudsen numbers are based on the vehicle length and the vehicle orbital velocity of 7500 m/s. For Knudsen numbers larger than 10, the flow regime is free molecular, i.e., the aerodynamics of the vehicle depend little on collisions among gas molecules, and for a convex body shape such as the Shuttle Orbiter, the forces and moments can be evaluated semi-analytically (Ref. 1). In the transition domain, which extends from

Knudsen numbers of 10 to at least 0.01 (Shuttle altitudes of 200 km down to 100 km, approximately), a particle tracing code, such as DSMC, must be used, as explained below. Such code, however, becomes extremely difficult to use and requires large amounts of computer time and memory when the Knudsen numbers are less than 0.01.

Table 1 shows the atmospheric conditions that were assumed at the five nominal altitudes considered in this study. Atmospheric densities can be seen to vary nearly 3 orders of magnitude over the 100 to 170 km altitude range.

The Shuttle Orbiter geometry was obtained from NASA Johnson Space Flight Center as a file of discrete data points, each being defined by three coordinates. The original geometry corresponded to a body flap deflection of 0 degrees, an inboard elevon deflection of 10 degrees, an outboard elevon deflection of 5 degrees and a closed cargo bay door configuration. Using data on the hinge line of the control surfaces and cargo bay doors, it was possible to generate files corresponding to arbitrary control surface deflection and cargo bay door configuration. The results presented herein were obtained with 0 degree deflection for all control surfaces. The cargo bay doors are closed in the reentry phase and open in orbit.

SIMULATED FLOWFIELD AROUND THE SHUTTLE ORBITER

The structure of the flowfield around a reentering Shuttle Orbiter is illustrated in Figs. 2-6, which show the total gas densities around the vehicle as altitudes decrease from 170 km to 100 km. Densities are shown normalized to the undisturbed freestream density. At 170 km, the flow disturbance expands relatively far away from the Shuttle surface and the computational domain is consequently large. The collisionality among gas molecules is low and the Shuttle actually "snowplows" into the ambient atmosphere. The molecules which reach the vehicle surface lose most of their energy and momentum as they diffusely reflect on the surface, and then slowly travel to the boundary of the computational domain, with little chance of colliding with incoming molecules. No shock is formed since gas molecules interact little with each other. As altitude is decreased, the extent of the flow disturbance upstream of the Shuttle decreases, which allows for a reduction of the size of the computational domain. Collisionality among the gas molecules is gradually increasing and density gradients steepen. At 100 km, a shock front can clearly be seen to have formed. It is characterized by a rapid density increase from 1 to 4 times the freestream density. The density also increases very sharply near the vehicle surface. Figures 7 and 8 show the density profile along the stagnation streamline at 110 km and 100 km, respectively. At 100 km, the density can be seen to increase 5-fold within one centimeter of the surface, reaching a value of 220 times the freestream value near the vehicle surface. It must be noted here, however, that his latter value is an overestimate of actual gas density near the vehicle surface. All the computations presented herein assume that the Shuttle surface is still cold and isothermal at 300°K, whereas the thermocouple measurements on the windward surface indicate that, at 100 km, the temperature near the stagnation point may be in the range of 600°K to 800° K (Ref. 10). Figures 7-8, however, do show the capability of our present code to adequately spatially resolve the thin sub-centimeter body layer over the 32 meter long Shuttle Orbiter.

AERODYNAMIC CHARACTERISTICS. COMPARISON WITH FLIGHT DATA

Normal-to-Axial Force Ratio

Blanchard (Refs. 11-13) has used high sensitivity micro-g accelerometers to measure forces on the Shuttle Orbiter during reentry in the altitude range of 60 km to 160 km. The aerodynamic forces F_A and F_N in the axial and normal directions are derived from the measured data upon removal of the effects of thrust, rotational acceleration, auxiliary power unit (APU) exhaust plumes, and control surface deflection. The force ratio F_N/F_A is of special interest since it is independent of the dynamic pressure, i.e., atmospheric density and Orbiter reentry velocity. Figure 9 compares Blanchard's reduced data with the results of our DSMC computation. All the results refer to a zero deflection for the elevons and body flap. A good agreement can be observed over the whole altitude range considered in this study. Also shown in Fig. 9 are the results obtained with the DSMC code run in a collisionless mode. In this mode, free molecular conditions are simulated, which, by comparison, allows one to quantify the transitional effects, i.e., the effects of intermolecular collisions on the aerodynamics. It can be observed that these effects seem to disappear at 170 km where the DSMC transitional and free molecular results converge. The preflight estimates for the normal to axial force ratio are also shown in Fig. 9 (Aerodynamic data book, Ref. 14). These early estimates appear to be somewhat low. Finally, results obtained using Potter's bridging formula (Ref. 15) are shown. The bridging formula is based on wind tunnel and Blanchard's early Shuttle data. A good agreement is therefore expected with Blanchard's reduced data.

Lift to Drag Ratio

The lift to drag ratio L/D can be derived from the F_N/F_A ratio if the incidence angle α is known:

$$\frac{L}{D} = \frac{F_N/F_A - \tan\alpha}{1 + F_N/F_A} \qquad (1)$$

This ratio is also independent of the dynamic pressure. Figure 10 shows the L/D ratio computed with the DSMC code run in the transitional and collisionless modes. The results are compared with wind tunnel data (corresponding to altitudes lower than 90 km) and flight data. The grey band shown in the figure corresponds to a series of Shuttle flights, each one occurring at different elevon and body flap deflection angles and different atmospheric conditions (Ref. 12). The grey band data was not corrected for control surface deflection angle, i.e., this data was not reduced to a zero deflection angle. Agreement between computed results and flight data can be observed to be quite good over the whole range of altitudes considered in the present work. A future study will be done to investigate the effects of elevon and body flap deflections on the aerodynamics of the vehicle in the transition flow regime. The results obtained by Bird (Ref. 19) using an early version of our present code are also shown for comparison. The modified Newtonian limit, corresponding to a hypersonic inviscid flow, is shown to be L/D = 1.10, which is very close to the value L/D = 1.06, computed by Weilmuenster and Gnoffo (Ref. 16) using the continuum fluid LAURA code. Figure 11 shows that the preflight estimates for L/D ratio are somewhat smaller than the measured values. Also shown are Blanchard's proposed aerodynamic model, which is based on flight data (Ref. 13) and Potter's bridging formula.

Axial Coefficient

To unambiguously determine the axial and normal coefficients C_A and C_N from the axial and normal accelerometer measurements would require the simultaneous measurement of the freestream dynamic pressure or, alternatively, the atmospheric density and vehicle velocity. However, in situ measurements of atmospheric density cannot readily be done between 90 km and Low-Earth orbit altitude. To estimate C_A and C_N from flight data, Blanchard had to devise an iterative procedure as described in Ref. 11. Figure 12 compares the DSMC computed values of the axial coefficient with the values obtained by Blanchard and by using Potter's bridging formula. Good agreement can be observed at all altitudes. The preflight estimates, however, can be seen to overestimate C_A. When comparing the transition and collisionless DSMC results, it can be observed that, for the axial force, transition flow effects are still significant at 170 km.

Normal Coefficient

Figure 13 compares the computed values of the normal coefficient with Blanchard's proposed model and Potter's bridging formula. A fairly large discrepancy of up to 20 percent can be observed between the DSMC computation and Blanchard's model results. Moreover, when comparing the transitional and collisionless DSMC results, it can be seen that C_N does not monotonously increase from the low continuum flow regime values to the higher free molecular values. Instead, C_N reaches a maximum within the transitional domain at about 120 km, and then decreases afterwards towards the free molecular limit. This singular behavior of the normal coefficient is discussed in the next section. Neither Blanchard's proposed model nor Potter's bridging formula reproduces this behavior. The preflight estimates of C_N appear to be closer to our present results, but do not predict the "overshoot" observed with DSMC.

Drag Coefficient

As shown in Fig. 14, the drag coefficient on the Shuttle Orbiter increases by a factor of more than two within the transition flow domain. The DSMC results appear to be about 10 percent larger than the ones predicted with Blanchard's proposed model or Potter's bridging formula.

Lift Coefficient

Figure 15 shows that the lift coefficient decreases rapidly between 100 km and 170 km from the near Newtonian inviscid continuum limit of 0.85 to the free molecular value of less than 0.1. Similarly to the drag coefficient, the DSMC values for the lift coefficient appear to be about 10 percent larger than the values obtained with Blanchard's proposed model.

Pitching Moment

Figure 16 shows the pitching moment around the Shuttle Orbiter nominal center of gravity located at Shuttle coordinates x = 1076.7", z = 375.0". Rarefaction effects can be seen to significantly increase the magnitude of the pitching moment from the modified Newtonian value, which is close to wind tunnel measured data, to the free molecular limit value. This pitching

moment increase is due to a redistribution of the pressure and shear forces acting on the Shuttle surface, as will be seen below. Our present results are compared with the ones obtained by Blanchard (Ref. 17). Blanchard used the rate of change of the Orbiter effective incidence angle between two control thruster firings to evaluate the overall pitching moment acting on the Shuttle body. The contribution of aerodynamics to the overall pitching moment was deduced upon removal of the effects of APU exhaust and gravity gradients. Blanchard's reduced data shown in Fig. 16 corresponds to a zero deflection angle for the elevons and body flap. Figure 16 shows our present results to markedly differ from the ones derived by Blanchard.

Center of Pressure

Figure 17 shows that the rarefaction effects shift the center of pressure in the forward direction by about 2.5 meters as the Shuttle descends from LEO to 100 km. The DSMC results are shown to be close to the preflight estimates, but differ markedly from the estimates derived from flight data by Blanchard.

ANALYSIS OF THE NORMAL FORCE COEFFICIENT

The singularity on C_N observed in our present DSMC computation, namely, the overshoot of C_N over both continuum and free molecular values, had been observed earlier by Dogra and Moss (Ref. 3) in their study of flat plates at 40 degrees incidence. Their results, which are reproduced in Fig. 18, were obtained with the two -dimensional DSMC code devised by Bird (Ref. 1). A thorough analysis of this overshoot will be conducted later, but a few remarks can already be made at this point. Figure 19 shows that the aerodynamic force on the Shuttle in the normal direction is mostly due to pressure forces. The shear, or friction, forces contribute little to C_N and mainly affect the axial forces, as shown in Fig. 20. For a flat plate, C_N is entirely due to pressure forces. The overshoot in C_N is therefore due to an overhoot of the pressure forces on the vehicle, that is, an overshoot of the momentum transfer from the gas molecules to the surface. Koppenwallner and Legge (Ref. 18) have identified and explained a similar overshoot on the drag coefficient of simple geometrical shapes. They have argued that, at high Mach numbers, freestream molecules which, in free molecular regime would not reach the body surface, are scattered within the high density gas cloud developing on the windside and redirected towards the vehicle surface. Figure 21 schematically illustrates this flux and pressure enhancing effect.

SURFACE FORCES

The magnitude and distribution of the pressure and shear forces on the Shuttle windside surface vary with altitudes as illustrated in Figs. 22 through 31. These figures show the pressure and shear coefficients Cp and Cs, which are defined as follows:

$$Cp = (P - P_O)/q$$
$$Cs = S/q \qquad (2)$$

where, P, S, q are, respectively, the pressure (i.e., normal momentum flux) and shear (i.e., tangential momentum flux) and the dynamic pressure. P_O is the freestream pressure. At high

altitudes (above 120 km), the pressure forces appear to be fairly uniform over the whole windside of the Shuttle, with maxima near the stagnation point and the wing leading edges. As discussed above, it can be observed that the pressure coefficients slightly increase as the Shuttle altitude decreases from 170 km to 120 km. At the lower altitudes, the pressure is mostly acting on the stagnation region and the wing leading edges. Wide bands of relatively high pressure appear to develop near the centerline of the vehicle at 100 km, with lower pressure on the centerline itself. The origin of these bands is presently not well understood. The thin streaks appearing on the wing at 100 km, however, are not real and known to be due to the median filter used in the graphical postprocessor, and therefore, not to any flow instability. This point is further illustrated in Fig. 32 which shows shearlines at 110 km. These shearlines, which are everywhere tangent to the local shear vectors on the vehicle surface, suggest a smooth, laminar flow over the whole surface windside.

The shear forces uniformly decrease in magnitude from 170 km to 100 km, as was shown in Fig. 20. Moreover, they appear to be fairly uniform over the windside at the higher altitudes with minima in the stagnation region and near the wing leading edges. At the lower altitudes, high shear forces can be seen to develop near the wing leading edges.

ORBIT AERODYNAMICS. FREE MOLECULAR SIMULATION

In orbit, the atmospheric density is very low and intermolecular collisions have little effect on the aerodynamics of the vehicle. The aerodynamic forces and moments on an orbital vehicle can be independently computed with either a DSMC code run in a collisionless mode or semi-analytical free molecule code. The free molecule code developed by Rault (Ref. 7) was used to evaluate the aerodynamic characteristics of an orbiting Shuttle at 40 deg incidence in an open cargo bay door configuration. Results are shown in Figs. 33 and 34 in the form of pressure and shear coefficients on the vehicle surface. These results can be observed to be very similar to the ones obtained with the DSMC code at 170 km. Table 3 provides a further comparison between the DSMC and free molecule codes. This table shows the aerodynamic force and moment coefficients computed for a closed cargo bay configuration using the collisionless DSMC and the free molecule codes for altitudes ranging from 100 km to 170 km. Good agreement can be observed between the particle tracing DSMC code and the semi-analytical free molecule code.

CONCLUSION

The simulation of the flowfield around the Shuttle Orbiter during the early phase of its reentry into the Earth atmosphere has been conducted. Computations have been performed for altitudes ranging from LEO down to 100 km. The present work was primarily done using a three-dimensional direct simulation Monte Carlo code which allowed us to simulate and analyze the highly nonequilibrium flow field over a wide range of Knudsen numbers. For this task, the code was specially enhanced to allow for the spatial resolution of the high density gradients which typically develop near the windside surface of reentry vehicles. The aerodynamic force and moment coefficients were evaluated. Fairly good agreement has been found with Blanchard's proposed aerodynamic model, which is based on highly sensitive accelerometer data measured in flight. Major discrepancies, however, have been observed regarding the normal coefficient C_N and the pitching moment. Our computations show that the C_N coefficient is characterized by an overshoot in the transition domain, similar to the one observed in an earlier

two-dimensional DSMC simulation over flat plates at incidence. If confirmed, such an overshoot should be taken into account in future reduction of flight data. Our values for the pitching moment seem to indicate that the center of pressure is further aft than predicted by Blanchard.

REFERENCES

1. Bird, G. A.: Molecular Gas Dynamics, Clarendon Press, Oxford, 1976.

2. Bird, G. A.: Monte Carlo Simulation in an Engineering Context. AIAA Progress in Astronautics and Aeronautics: Rarefied Gas Dynamics, Vol. 74, Part 1, edited by Sam S. Fisher, 1981, pp. 235-239.

3. Dogra, V. K.; and Moss, J. N.: Hypersonic Rarefied Flow About Plates at Incidence. AIAA Paper 89-1712, 1989.

4. Rault, D. F.; Wilmoth, R. G.; and Bird, G. A.: An Efficient DSMC Algorithm Applied to a Delta Wing. AIAA Paper 91-1316, June 1991.

5. Rault, D. F.: Aerodynamic Characteristics of a Hypersonic Viscous Optimized Waverider at High Altitudes. AIAA Paper 92-0306, January 1992.

6. Rault, D. F.: Towards an Efficient Three Dimensional DSMC Code for Complex Geometry Problems, 18th Rarefied Gas Dynamics Symposium, July 1992.

7. Rault, D. F.: Aerodynamic Characteristics of Magellan Spacecraft in Venus Upper Atmosphere. AIAA Paper 93-0723, January 1993.

8. Rault, D. F.; and Woronowicz, M. S.: Spacecraft Contamination Investigation by Direct Simulation Monte Carlo. Contamination on UARS/HALOE, AIAA Paper 93-0724, January 1993.

9. Rault, D. F.: Aerodynamics of Shuttle Orbiter at High Altitudes, AIAA Paper 93-2815, July 1993.

10. Hartung, L. C.; and Throckmorton, D. A.: Space Shuttle Entry Heating Data Book, Volume I-STS 2, NASA Reference Publication 1991, May 1988.

11. Blanchard, R. C.; Larman, K. T.; and Barrett, M..: The High Resolution Accelerometer Package (HiRAP) Flight Experiment Summary for the First 10 Flights, NASA Reference Publication 1267, April 1992.

12. Blanchard, R. C.: Rarefied Flow Lift-to-Drag Measurements of the Shuttle Orbiter, 15th Congress of International Council of Aeronautical Sciences (ICAS), Paper ICAS-86-2.10.2, London, England, Sept. 1986.

13. Blanchard, R. C.; Larman, K. T.; and Moats, C. D.: Rarefied-Flow Shuttle Aerodynamics Flight Model. NASA TM-107698, February 1993.

14. Aerodynamics Design Data Book. Volume 1: Orbiter Vehicle. NASA CR-160386, 1978.

15. Potter, J. L.: Procedure for Estimating Aerodynamics of Three-Dimensional Bodies in Transitional Flow. AIAA Progress in Astronautics and Aeronautics: Rarefied Gas Dynamics, Vol. 118, edited by E. P. Muntz, D. P. Weaver, and D. H. Campbell.

16. Weilmuenster, K, J.; and Gnoffo, P. A.: Navier Stokes Simulations of Orbiter Aerodynamic Characteristics, Orbiter Experiments Aerothermodynamics Symposium, Williamsburg, Virginia, April 1993. NASA CP-3248, 1994.

17. Blanchard, R. C.; and Hinson, E. W.: Flight Measurements of Shuttle Orbiter Pitching Moment Coefficient and Elevon Effectiveness in the Rarefied Flow Regime, NASA Technical Paper 2889, March 1989.

18. Koppenwallner, G.; and Legge, H.: Drag of Bodies in Rarefied Hypersonic Flow, AIAA Progress in Astronautics and Aeronautics: Rarefied Gas Dynamics, Vol. 103, edited by J. N. Moss and C. D. Scott.

19. Bird, G. A.: Application of the Direct Simulation Monte Carlo Method of the Full Shuttle Geometry. AIAA Paper 90-1962, June 1990.

Table 1. Nominal Atmospheric Properties

Nominal Altitude (km)	100	110	120	145	170
Number density ($mols/m^3$)	$1.20\ E^{+19}$	$2.20E^{+18}$	$5.77\ E^{+17}$	$6.56\ E^{+16}$	$2.06\ E^{+16}$
Temperature	193.7	250.0	335.0	628.0	790.4
Molar composition					
02	0.18	0.12	0.08	0.055	0.040
N2	0.78	0.77	0.74	0.622	0.523
0	0.04	0.11	0.18	0.323	0.437

Table 2. DSMC Numerical Results. Aerodynamic Coefficients

Altitude (km)	Drag C_D	Lift C_L	Axial C_A	Normal C_N	Pitching Moment C_m around CG	Center of Pressure wrt CG (m)	L/D ratio
100.	1.15	0.824	0.354	1.37	$-9.80\ E^{-02}$	-0.861	0.714
110.	1.38	0.696	0.606	1.42	-0.145	-1.24	0.506
120.	1.65	0.564	0.901	1.49	-0.207	-1.68	0.342
145	1.97	0.297	1.32	1.49	-0.286	-2.31	0.151
170.	2.07	0.193	1.46	1.48	-0.293	-2.39	$9.31\ E^{-02}$

Table 3 Comparison of Collisionless DSMC and Free Molecular (FM) Results

Altitude (km)	Code	Drag C_D	Lift C_L	Axial C_A	Normal C_N
100.	DSMC	2.15	$6.21E^{-02}$	1.61	1.43
	FM	2.12	$7.35E^{-02}$	1.58	1.42
110.	DSMC	2.15	$7.08E^{-02}$	1.60	1.44
	FM	2.13	$7.59E^{-02}$	1.58	1.43
120.	DSMC	2.16	$7.46E^{-02}$	1.61	1.45
	FM	2.14	$7.85E^{-02}$	1.59	1.44
145.	DSMC	2.19	$7.87E^{-02}$	1.63	1.47
	FM	2.22	$8.70E^{-02}$	1.64	1.49
170.	DSMC	2.19	$8.45E^{-02}$	1.63	1.48
	FM	2.22	$9.23E^{-02}$	1.64	1.50

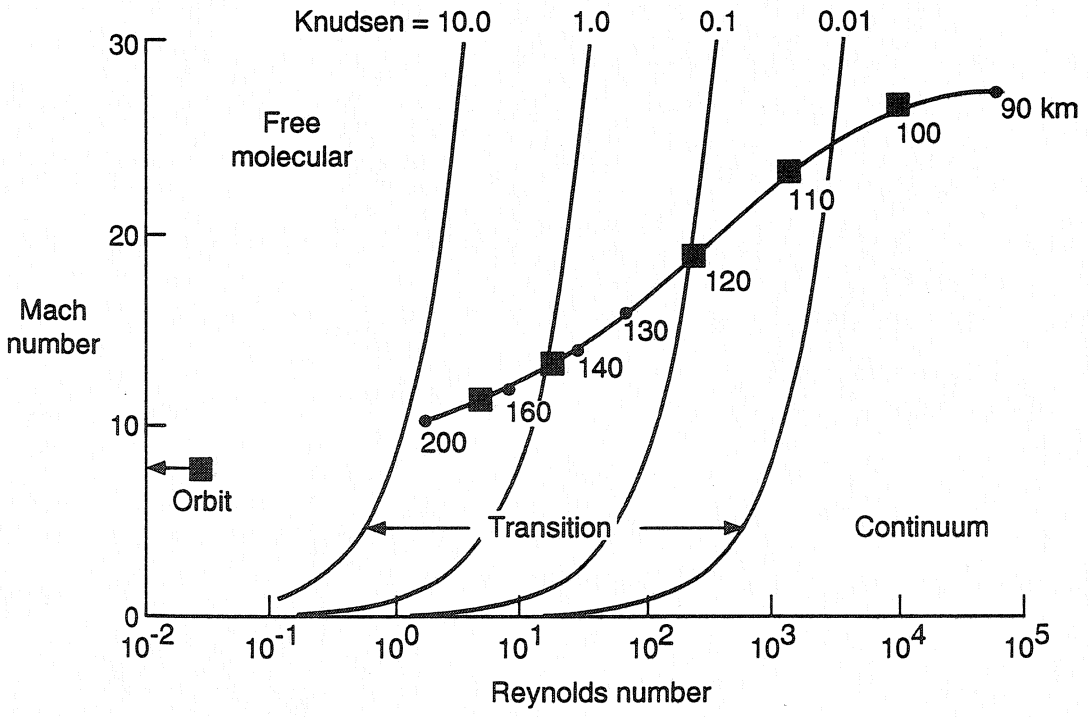

Figure 1. Shuttle trajectory in Reynolds-Mach-Knudsen number domain.

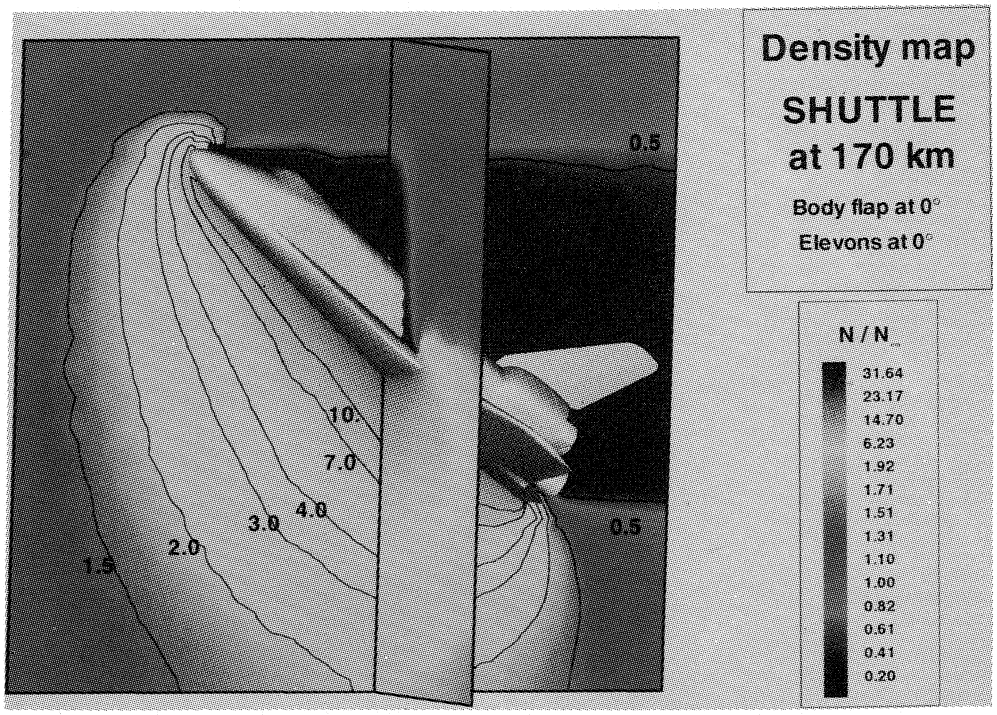

Figure 2. Total density map around Shuttle Orbiter at 170 km altitude.

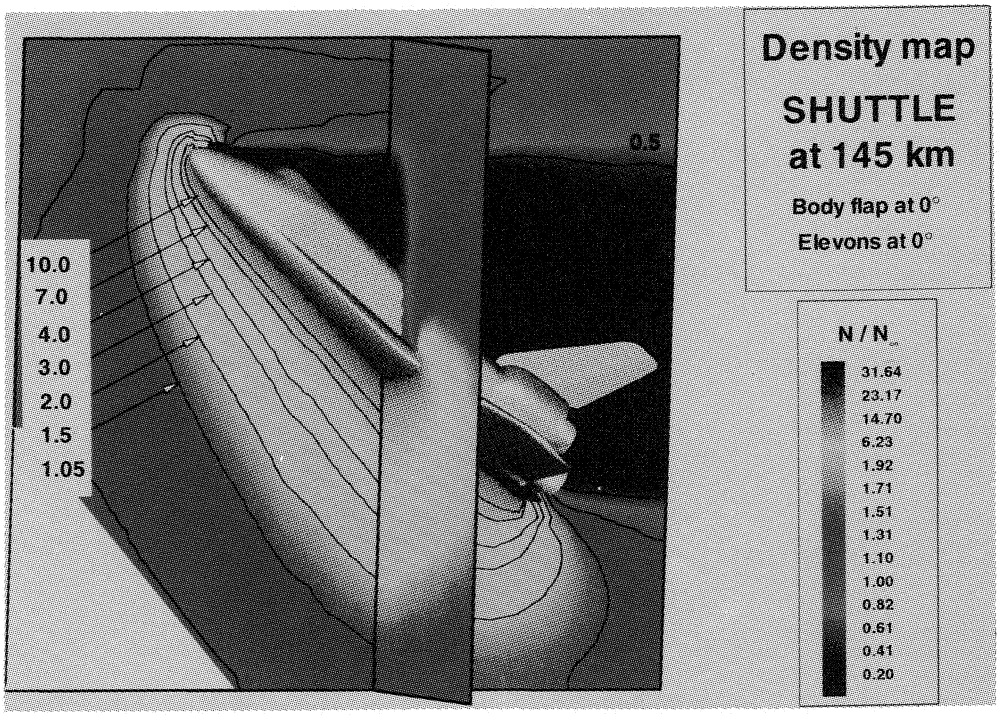

Figure 3. Total density map around Shuttle Orbiter at 145 km altitude.

(Color versions of figures 2 and 3 are shown on page 937.)

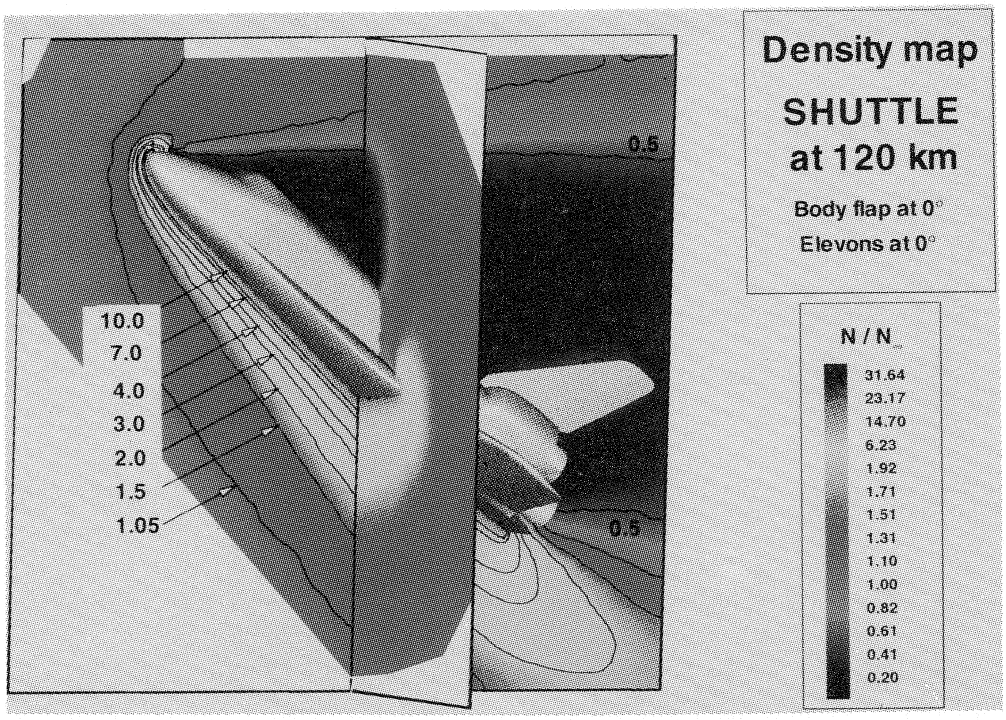

Figure 4. Total density map around Shuttle Orbiter at 120 km altitude.

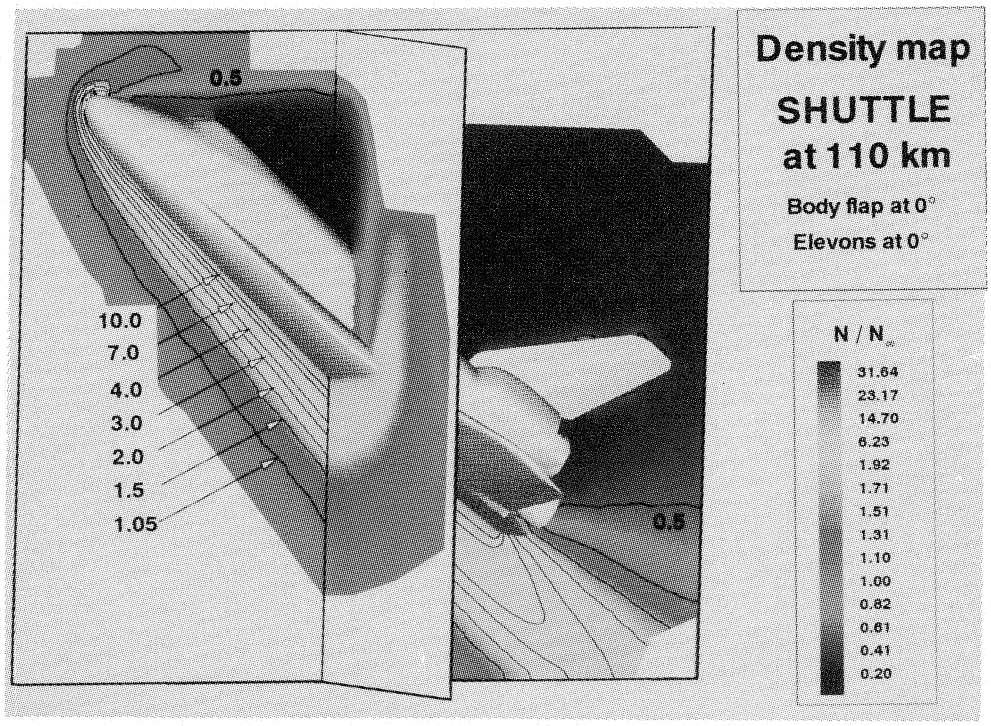

Figure 5. Total density map around Shuttle Orbiter at 110 km altitude.

(Color versions of figures 4 and 5 are shown on page 938.)

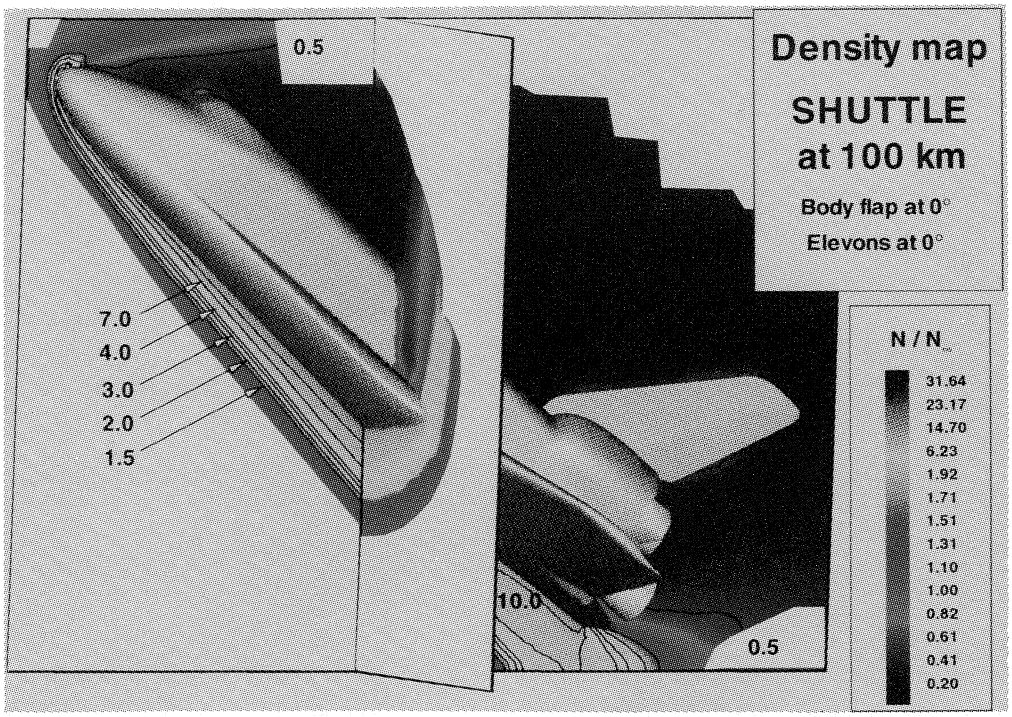

Figure 6. Total density map around Shuttle Orbiter at 100 km altitude.

(Color version of figure 6 is shown on page 939.)

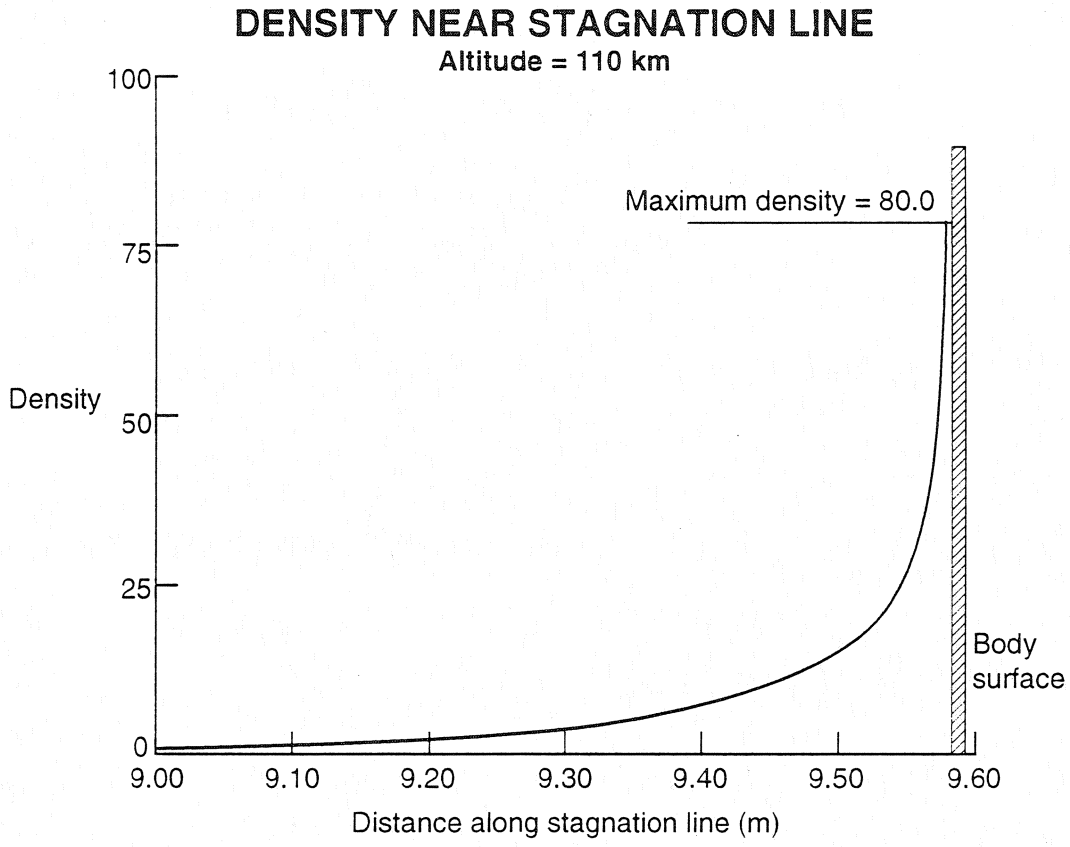

Figure 7. Density profile along stagnation streamline on Shuttle Orbiter at 110 km altitude.

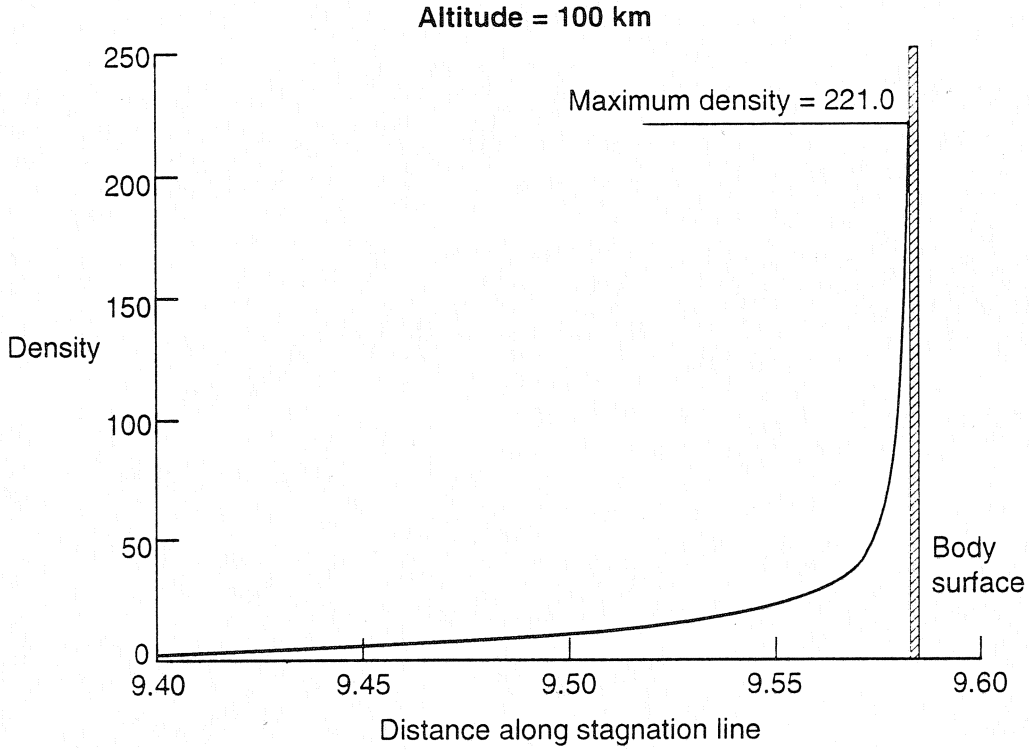

Figure 8. Density profile along stagnation streamline on Shuttle Orbiter at 100 km altitude.

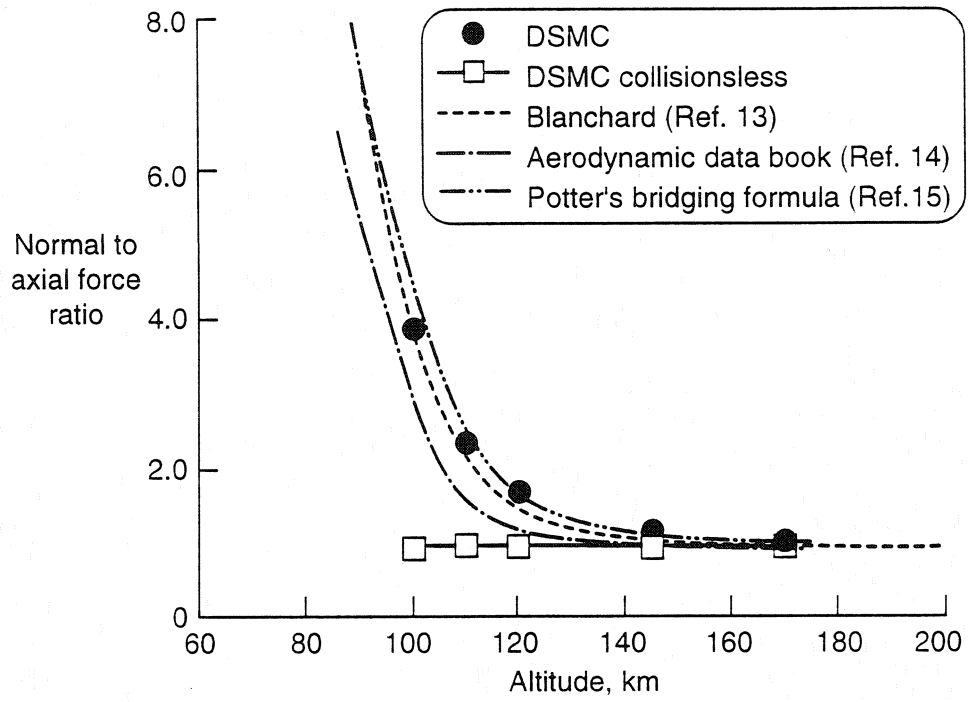

Figure 9. Normal-to-axial force ratio on Shuttle Orbiter.

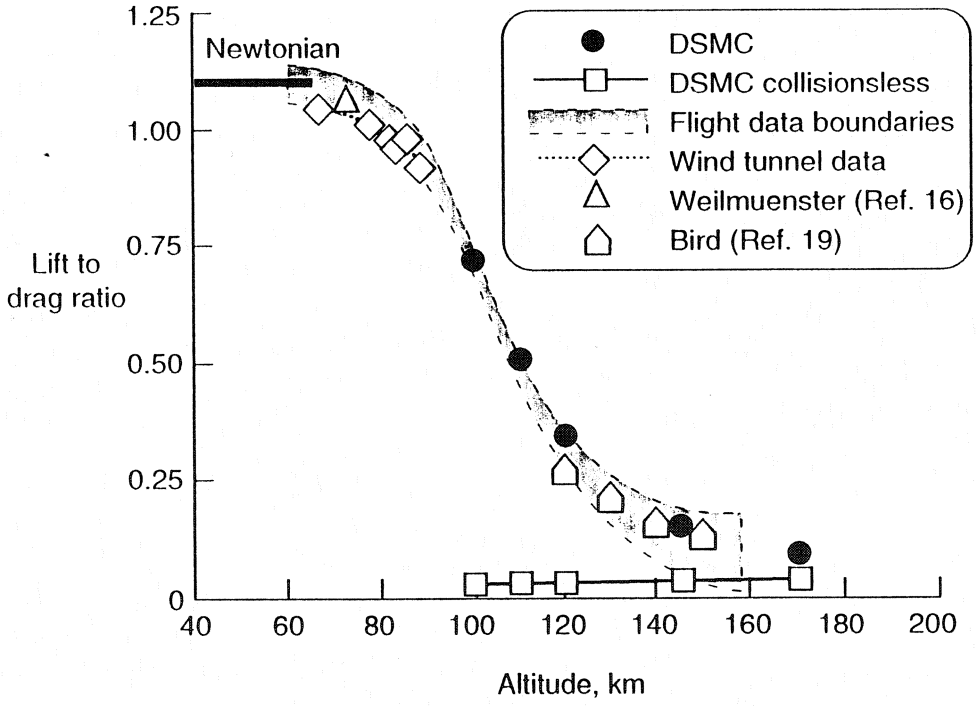

Figure 10. Lift-to-drag ratio on Shuttle Orbiter.

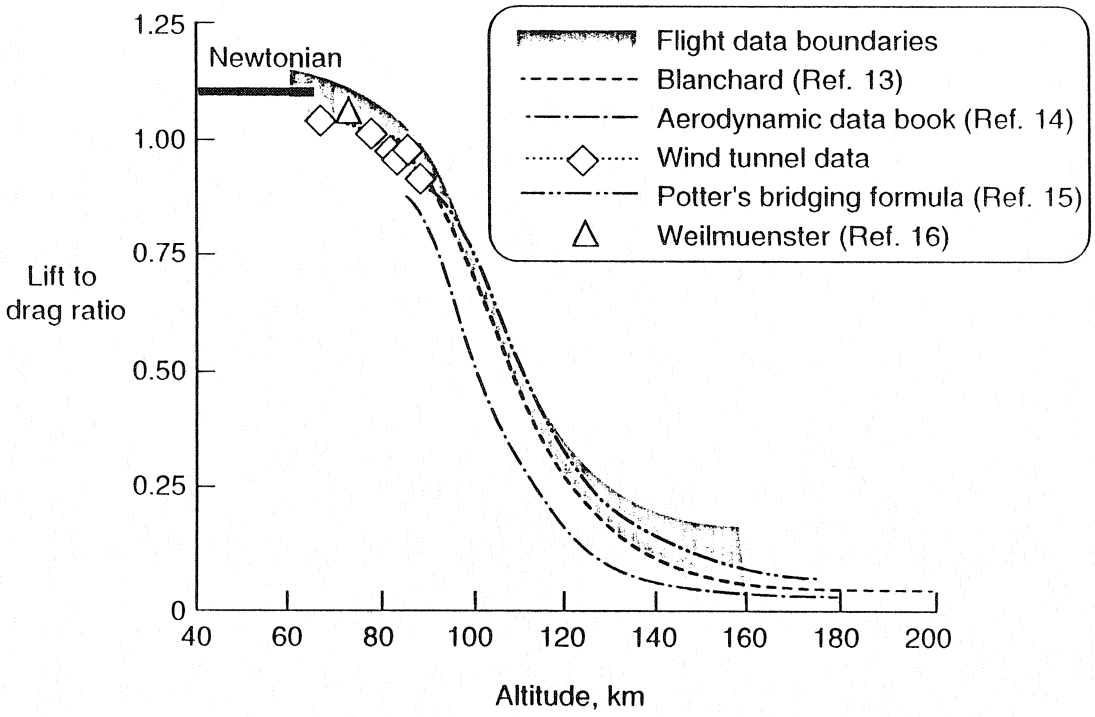

Figure 11. Lift-to-drag ratio on Shuttle Orbiter.

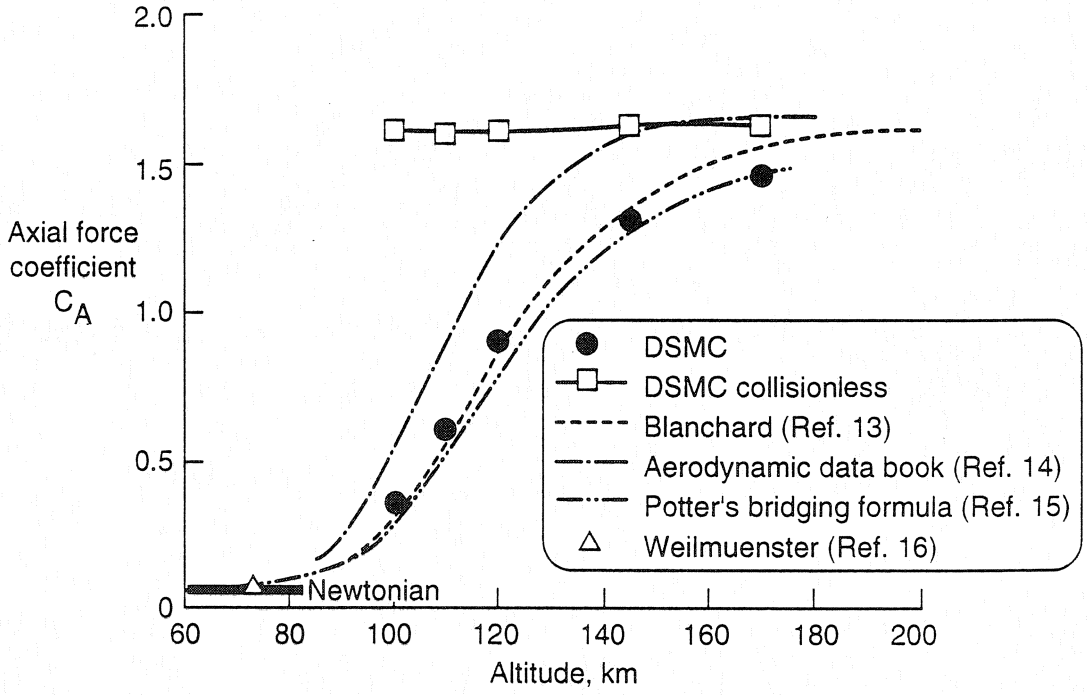

Figure 12. Axial force coefficient on Shuttle Orbiter.

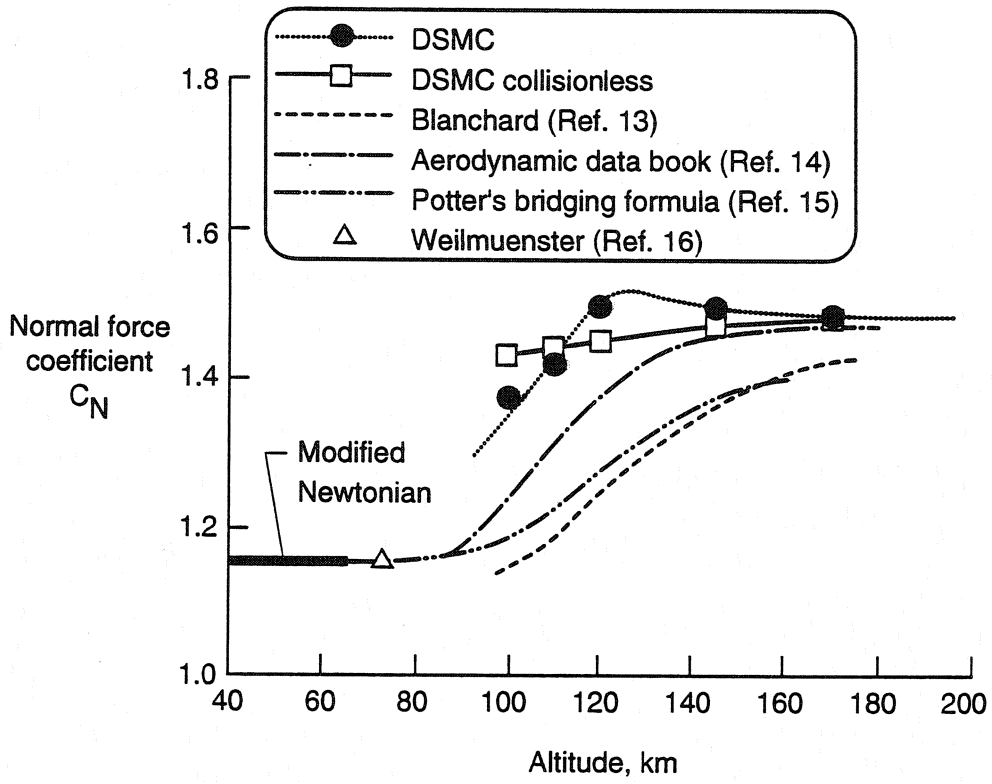

Figure 13. Normal force coefficient on Shuttle Orbiter.

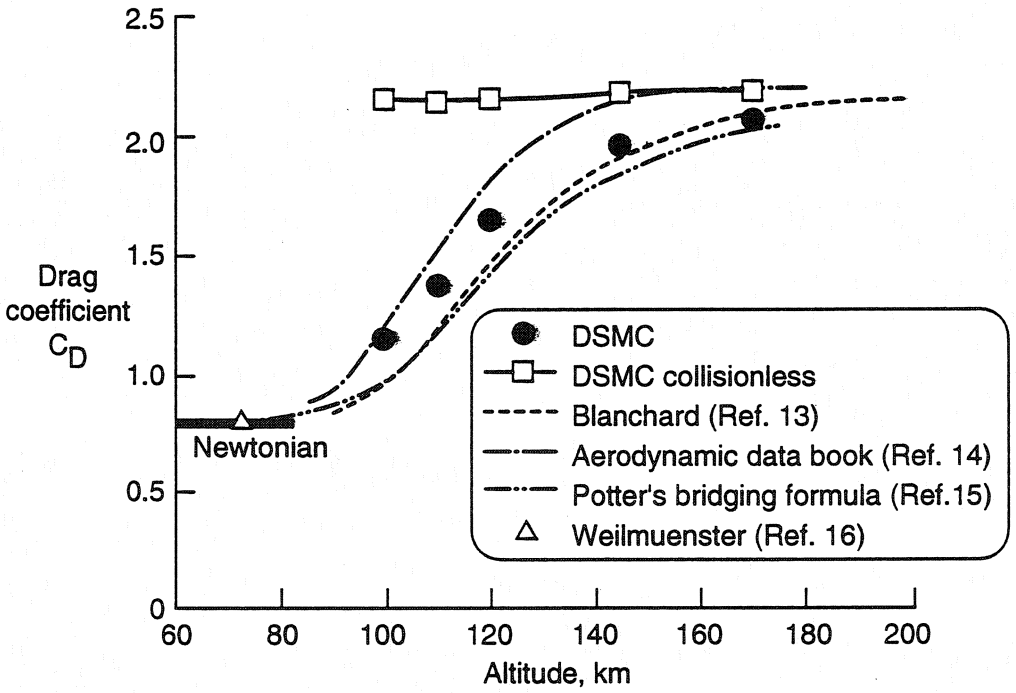

Figure 14. Drag coefficient on Shuttle Orbiter.

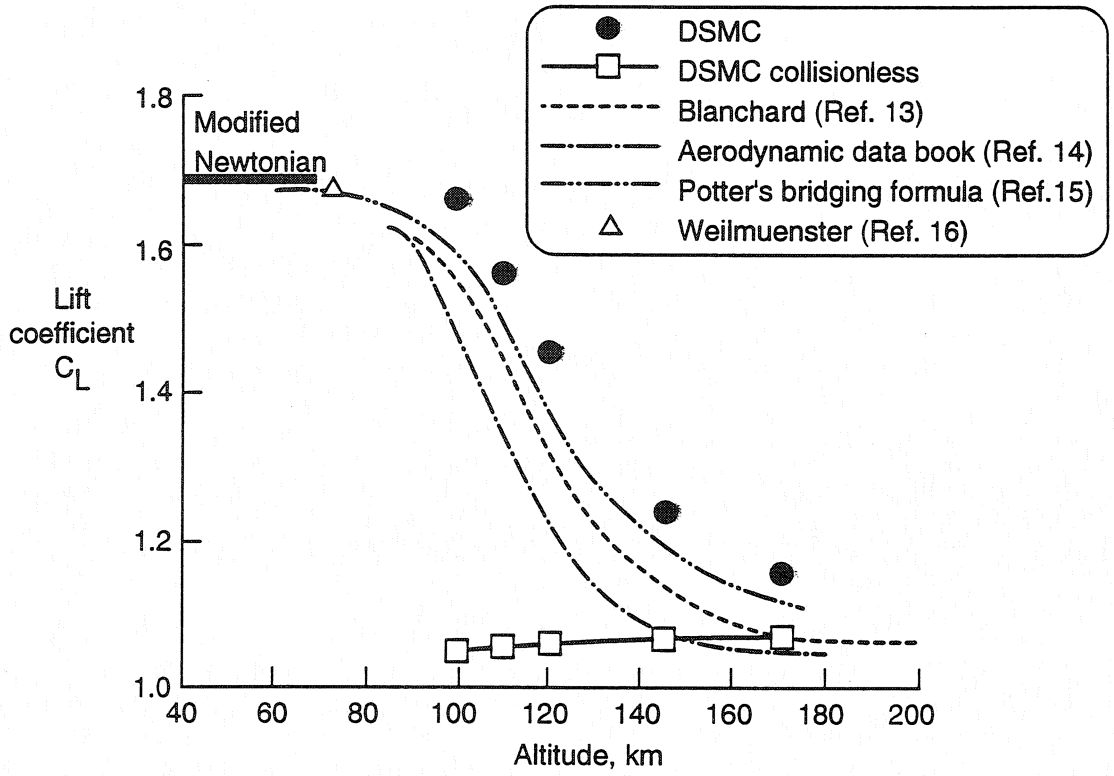

Figure 15. Lift coefficient on Shuttle Orbiter.

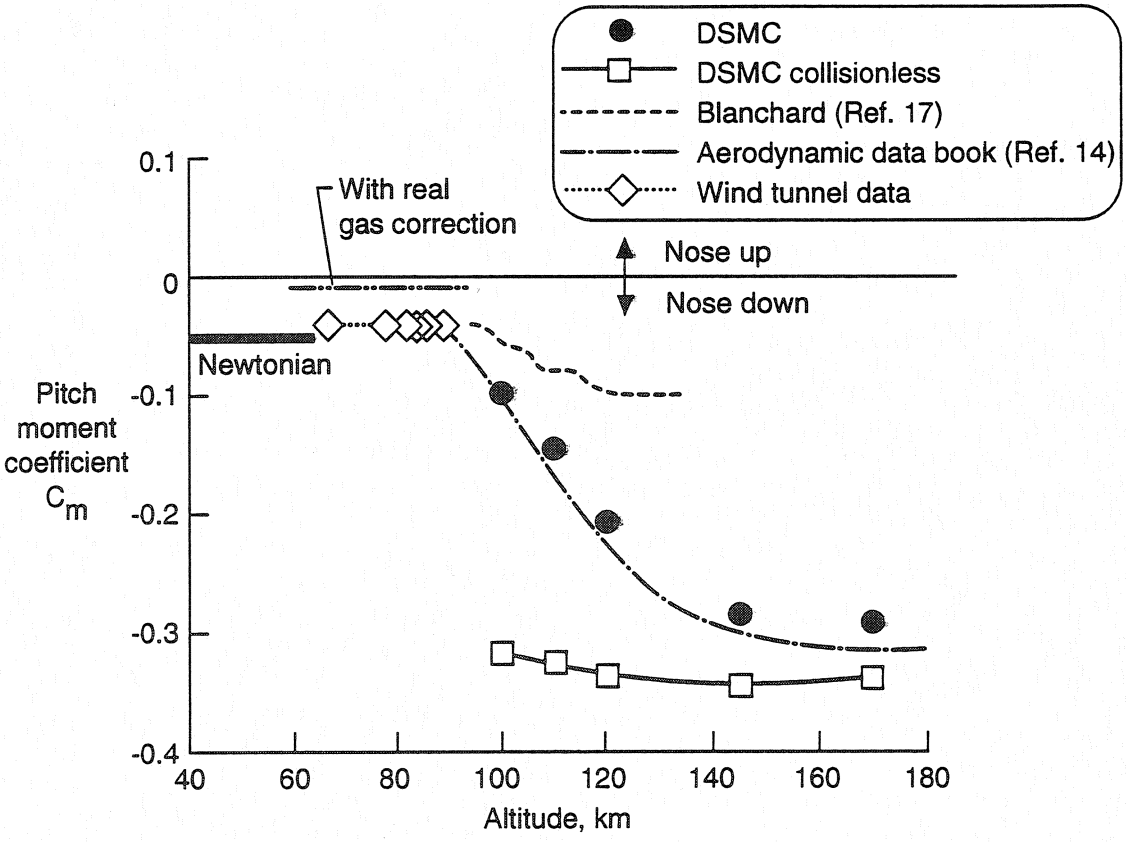

Figure 16. Pitching Moment coefficient on Shuttle Orbiter.

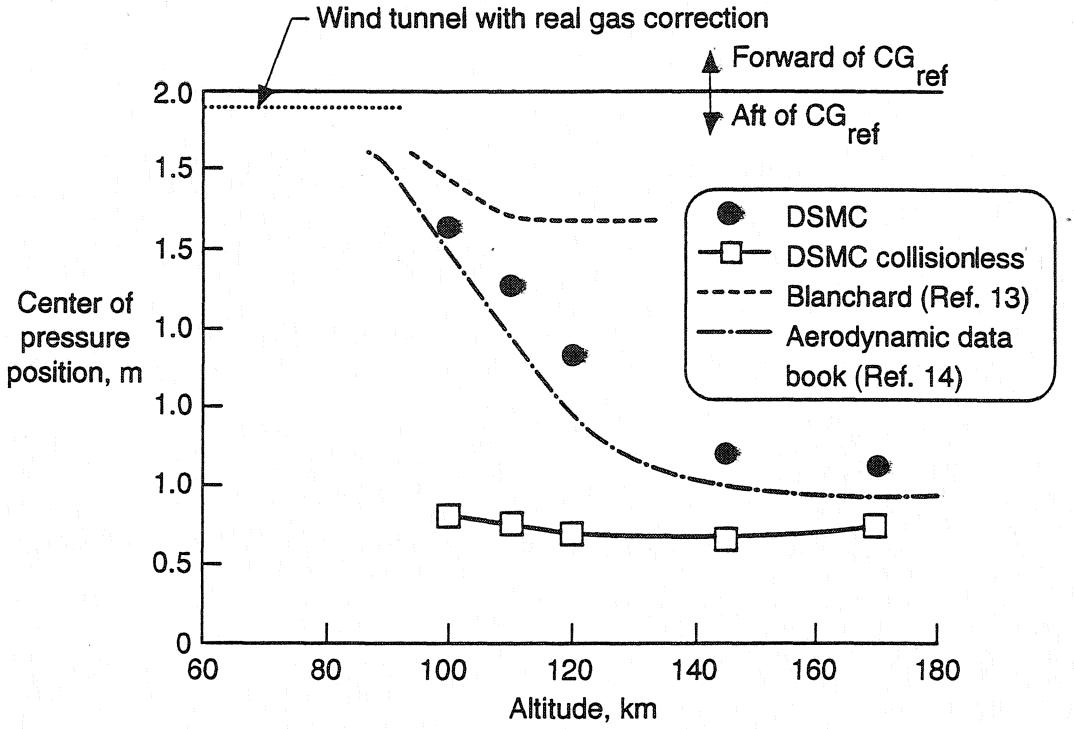

Figure 17. Location of Center of Pressure relative to Shuttle Orbiter nominal Center of gravity.

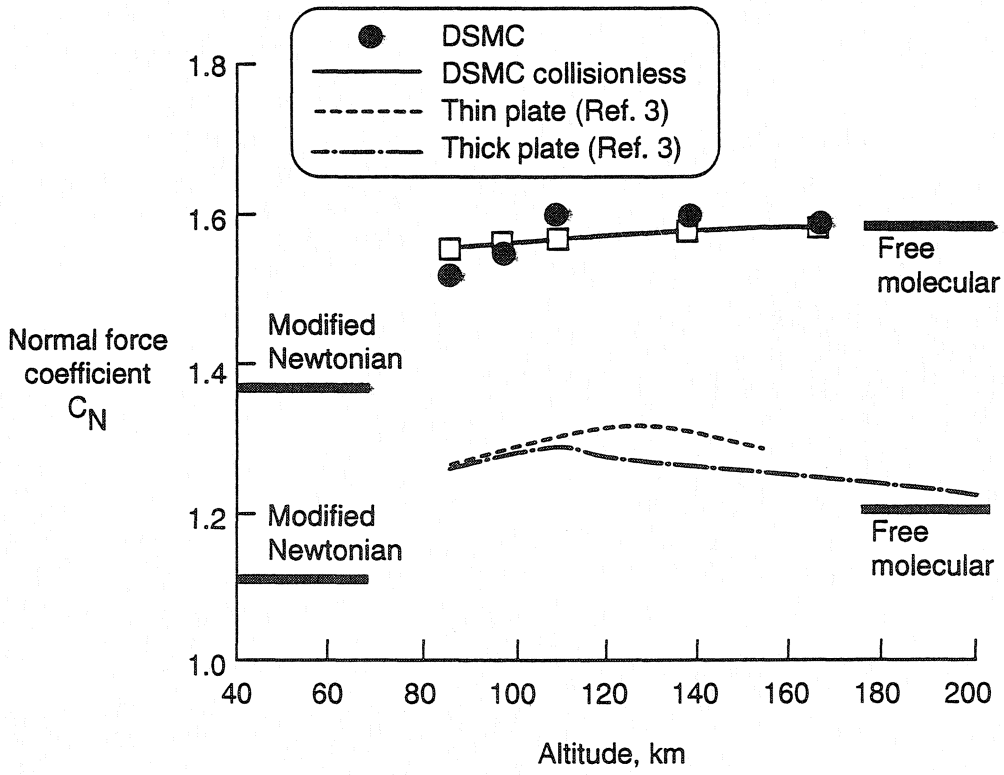

Figure 18. Normal force coefficient on Shuttle Orbiter and flat plates.

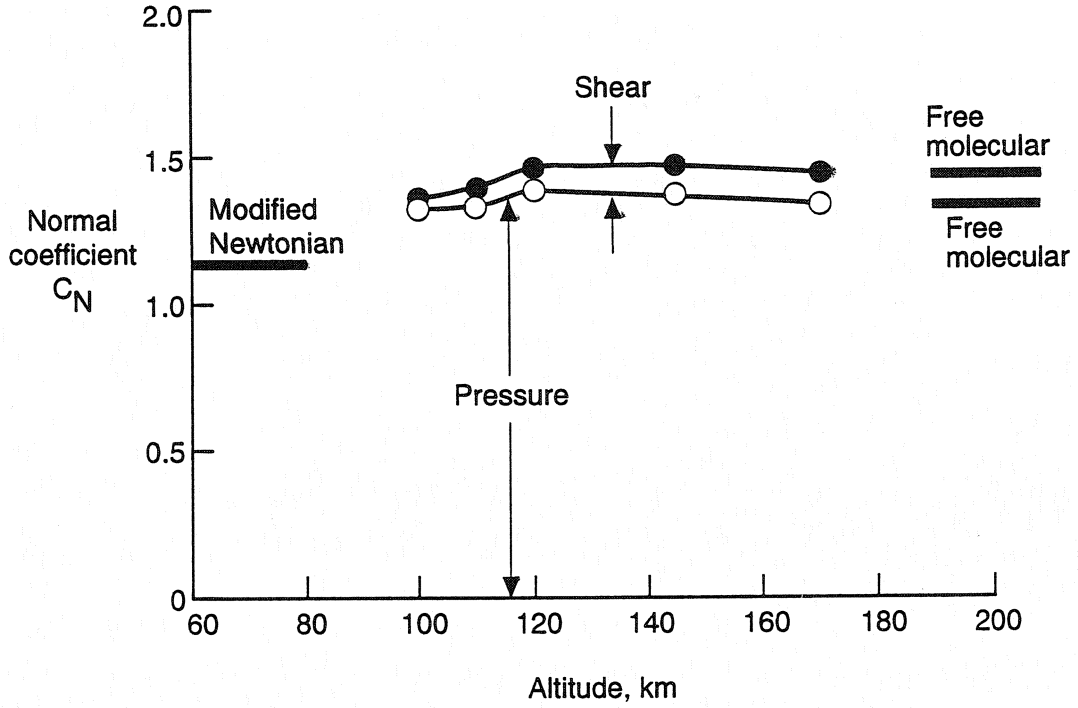

Figure 19. Pressure and shear contribution to normal force coefficient.

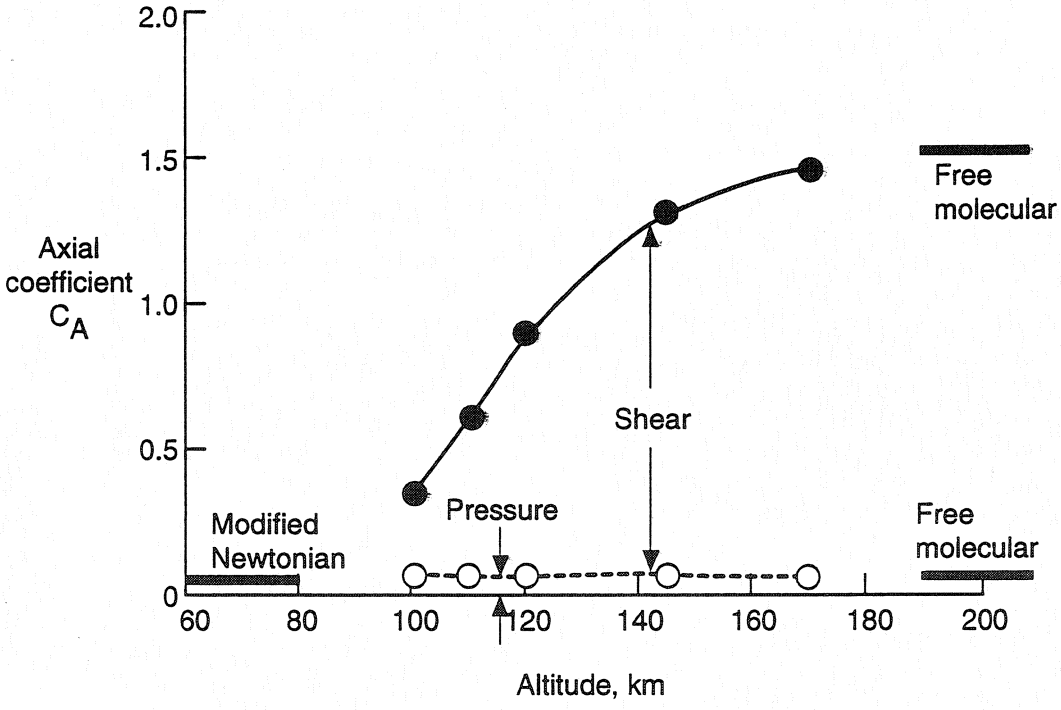

Figure 20. Pressure and shear contribution to axial force coefficient.

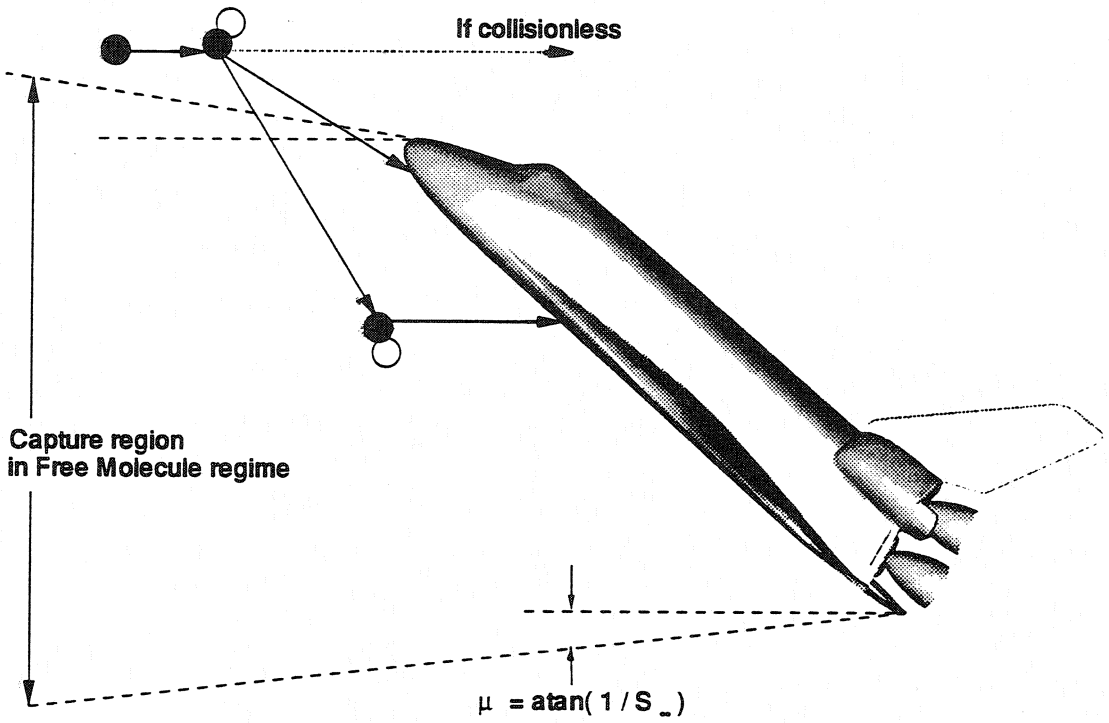

Figure 21. Particle flux and momentum transfer enhancing mechanism.

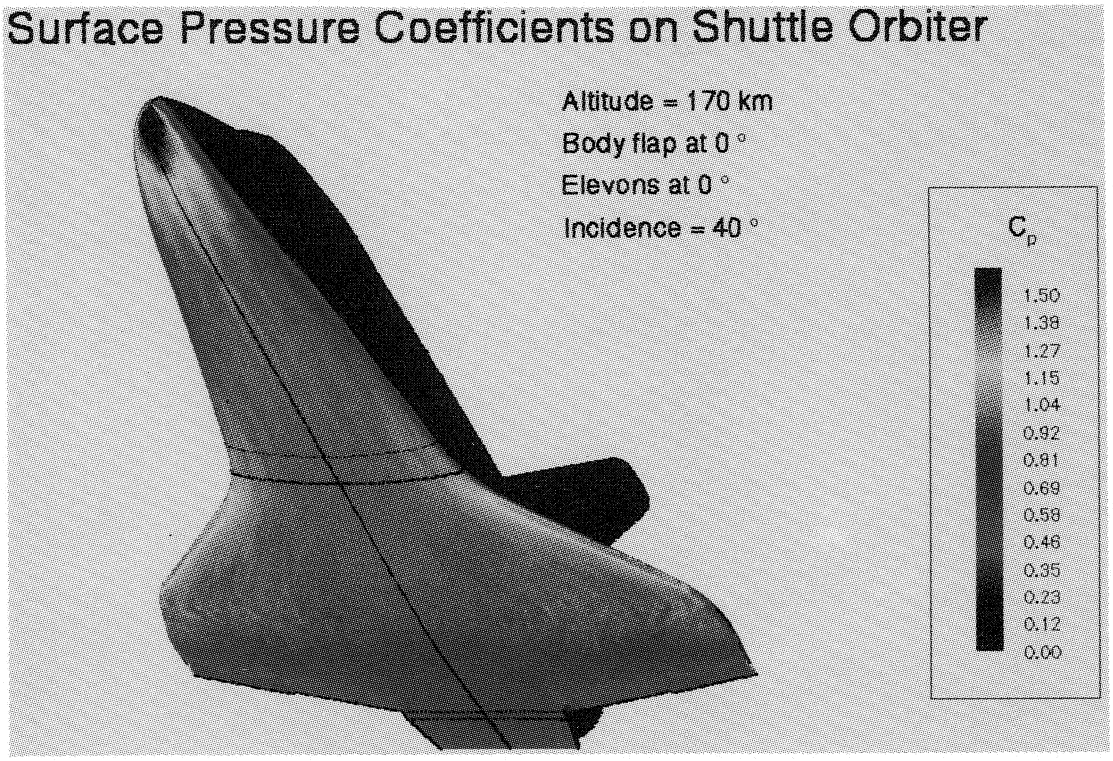

Figure 22. Pressure force distribution on Shuttle Orbiter at 170 km.

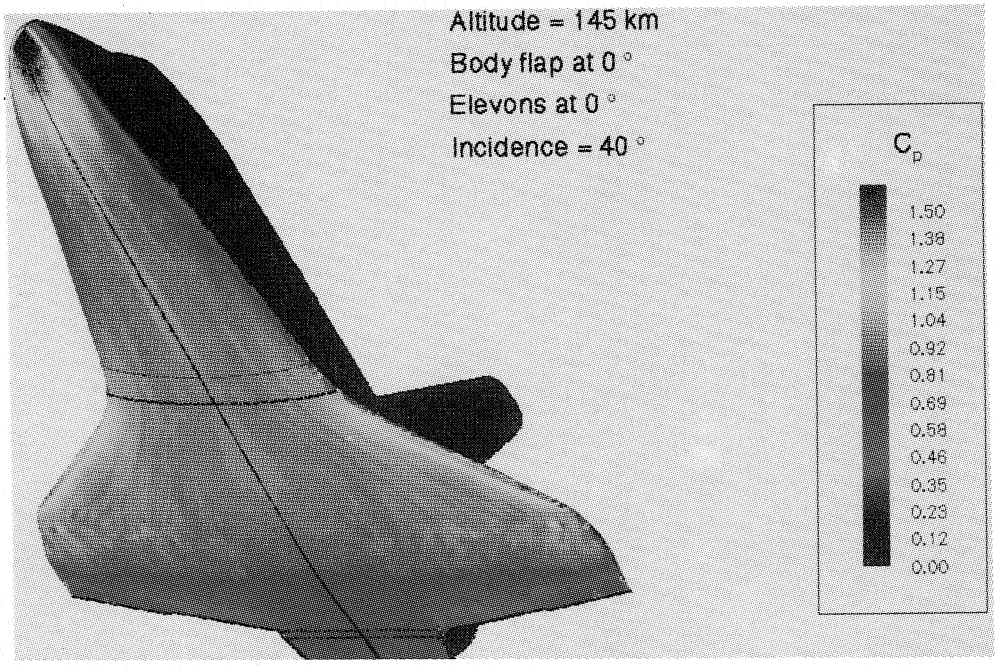

Figure 23. Pressure force distribution on Shuttle Orbiter at 145 km.

(Color versions of figures 22 and 23 are shown on page 940.)

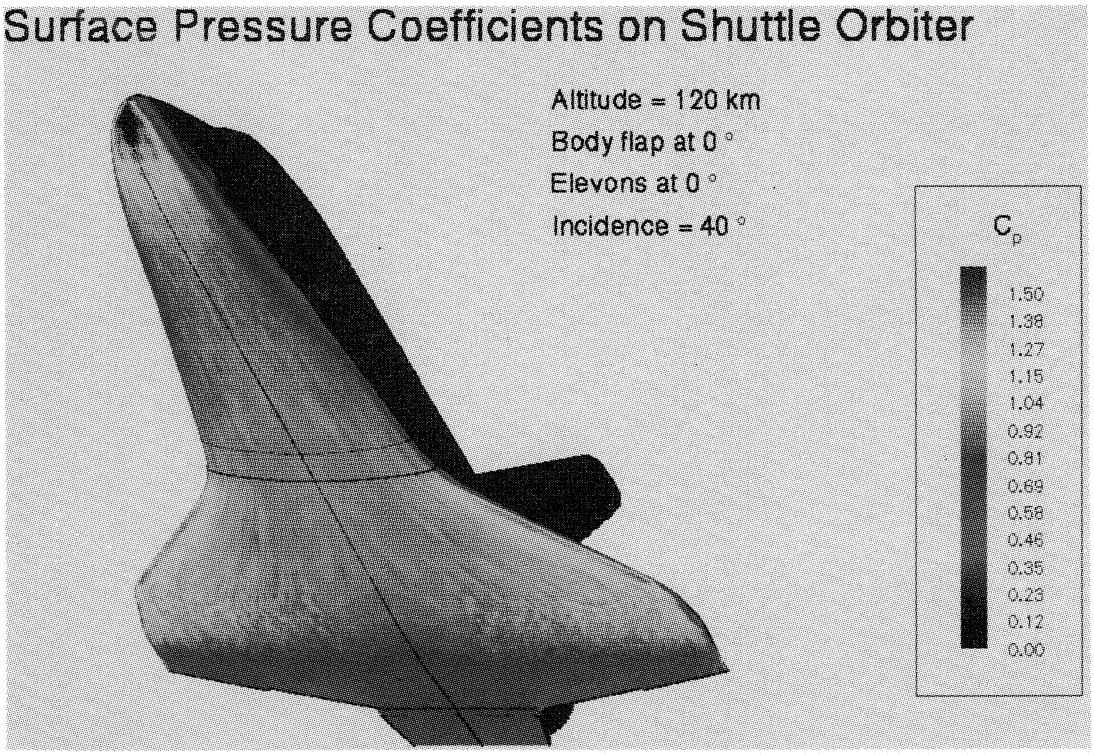

Figure 24. Pressure force distribution on Shuttle Orbiter at 120 km.

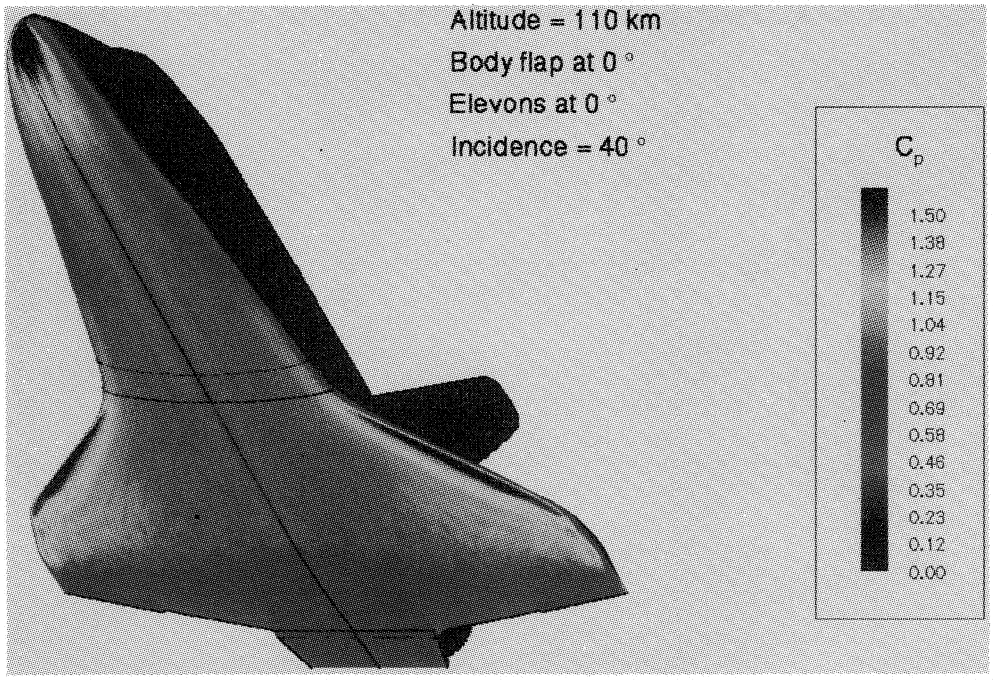

Figure 25. Pressure force distribution on Shuttle Orbiter at 110 km.

(Color versions of figures 24 and 25 are shown on page 941.)

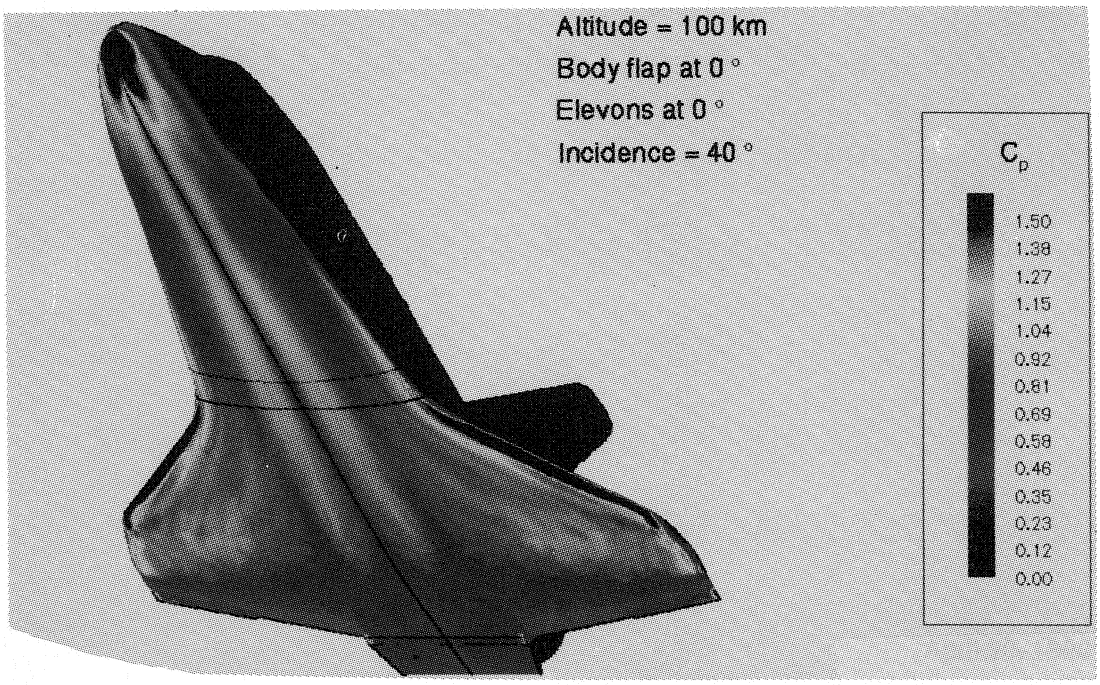

Figure 26. Pressure force distribution on Shuttle Orbiter at 100 km.

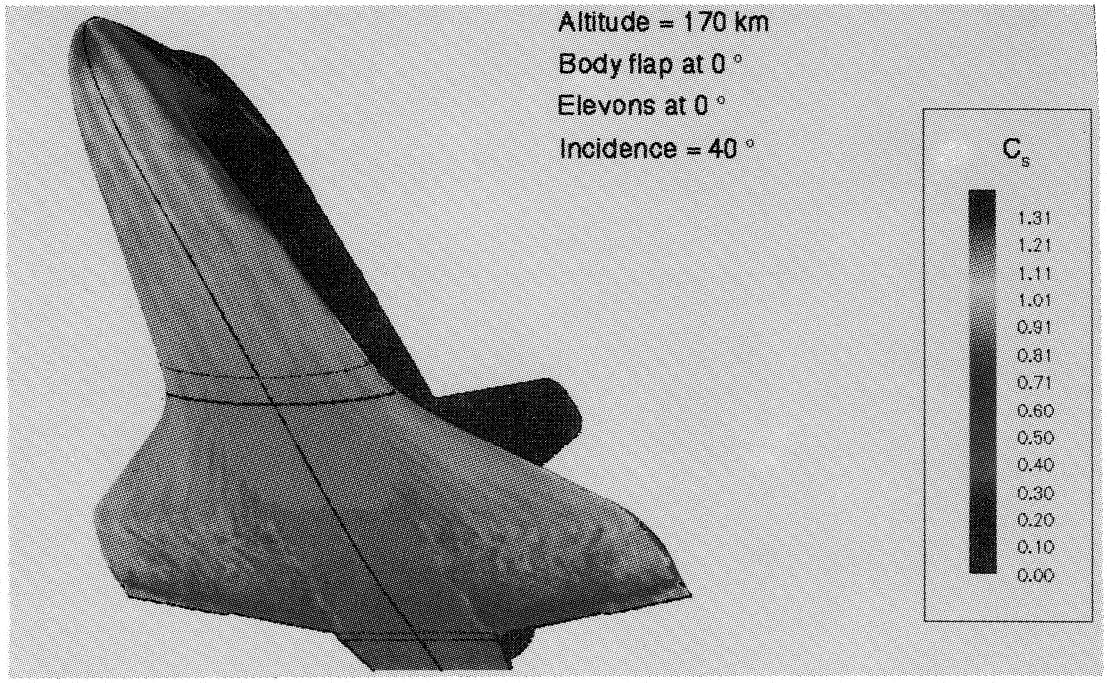

Figure 27. Shear force distribution on Shuttle Orbiter at 170 km.
(Color versions of figures 26 and 27 are shown on page 942.)

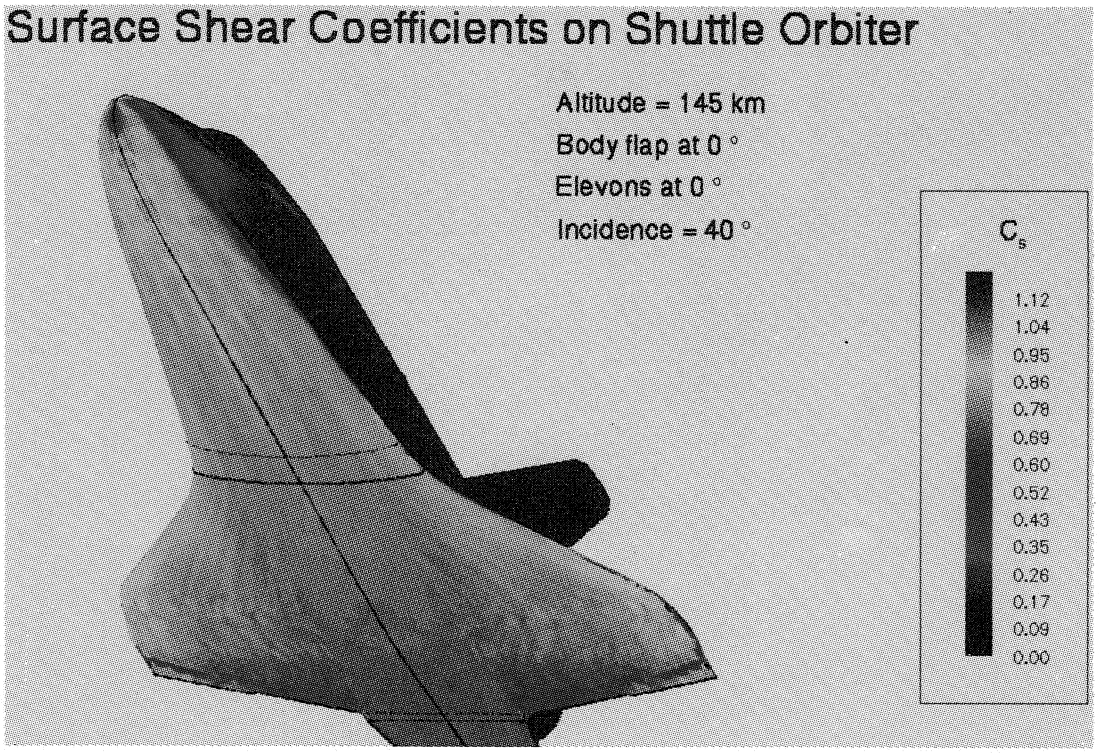

Figure 28. Shear force distribution on Shuttle Orbiter at 145 km.

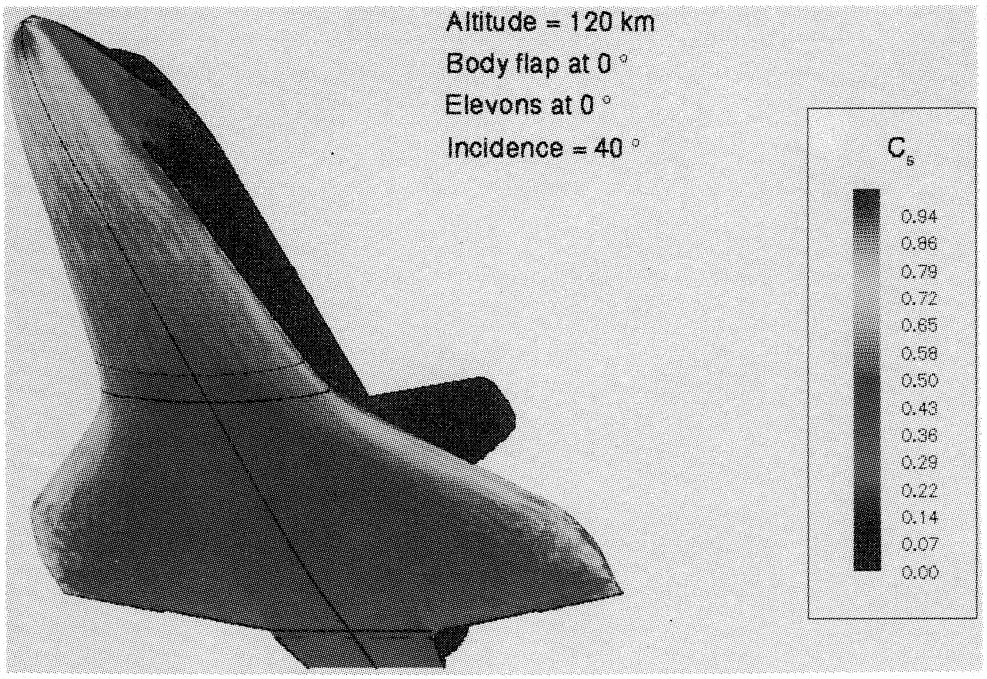

Figure 29. Shear force distribution on Shuttle Orbiter at 120 km.

(Color versions of figures 28 and 29 are shown on page 943.)

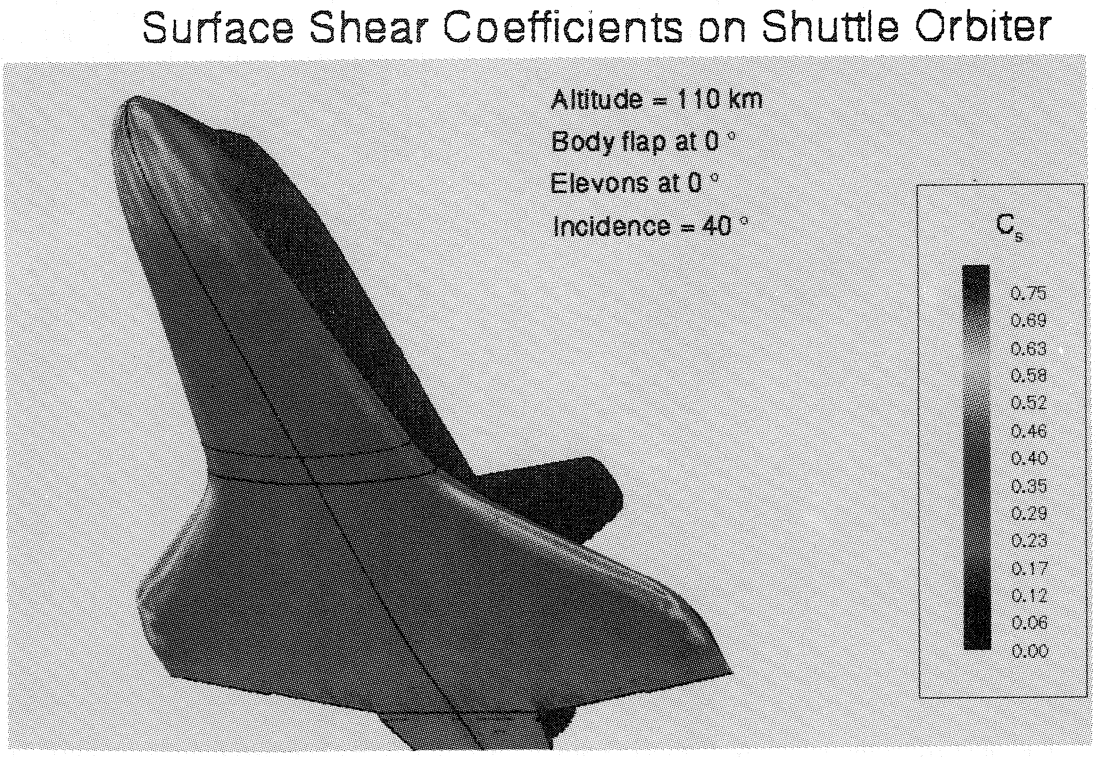

Figure 30. Shear force distribution on Shuttle Orbiter at 110 km.

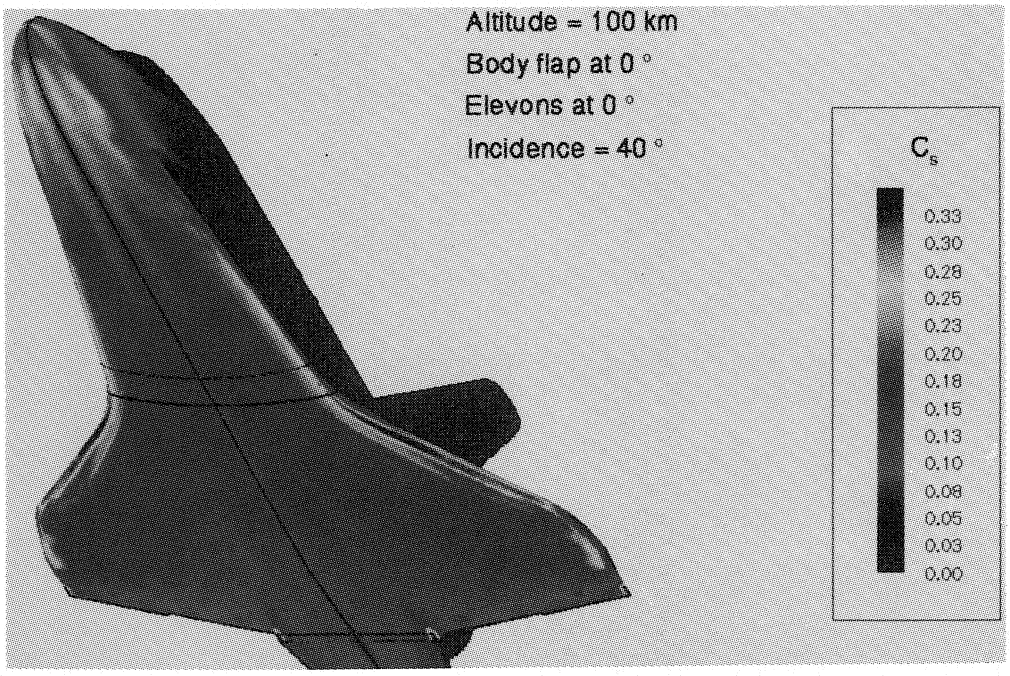

Figure 31. Shear force distribution on Shuttle Orbiter at 100 km.
(Color versions of figures 30 and 31 are shown on page 944.)

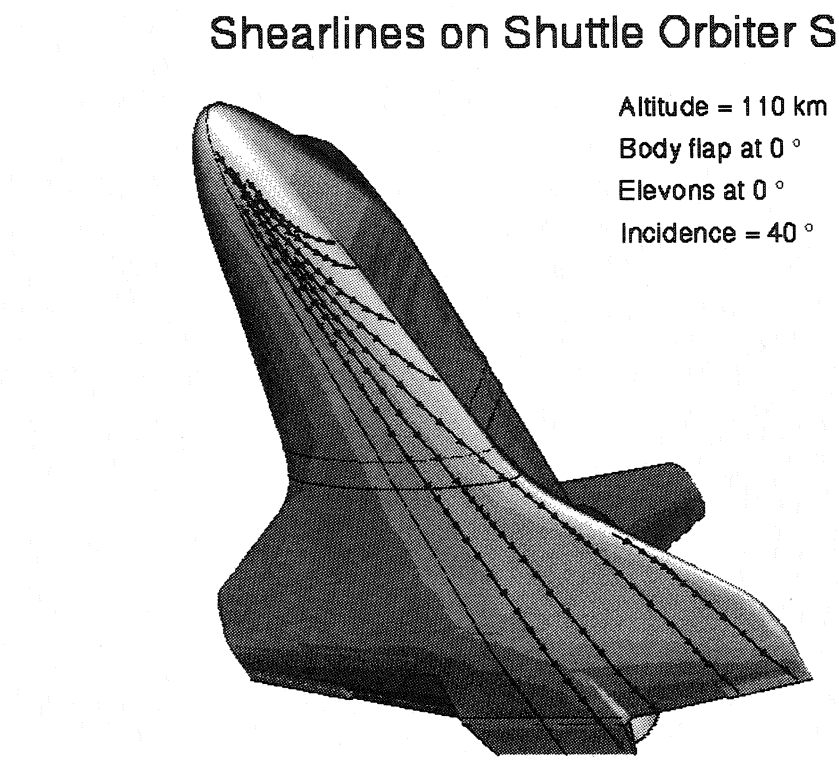

Figure 32. Shearlines on Shuttle Orbiter at 110 km.

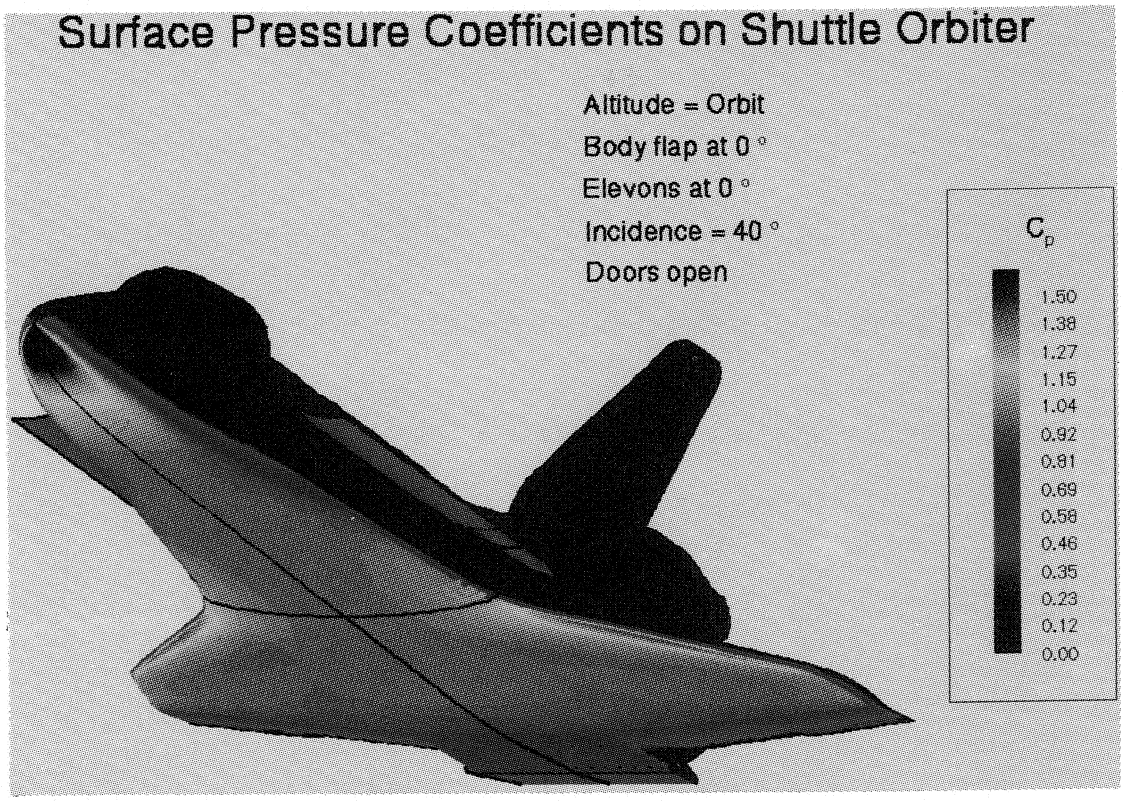

Figure 33. Pressure force distribution on Shuttle Orbiter in orbit at 40 degrees incidence.

(A color version of figure 33 is shown on page 945.)

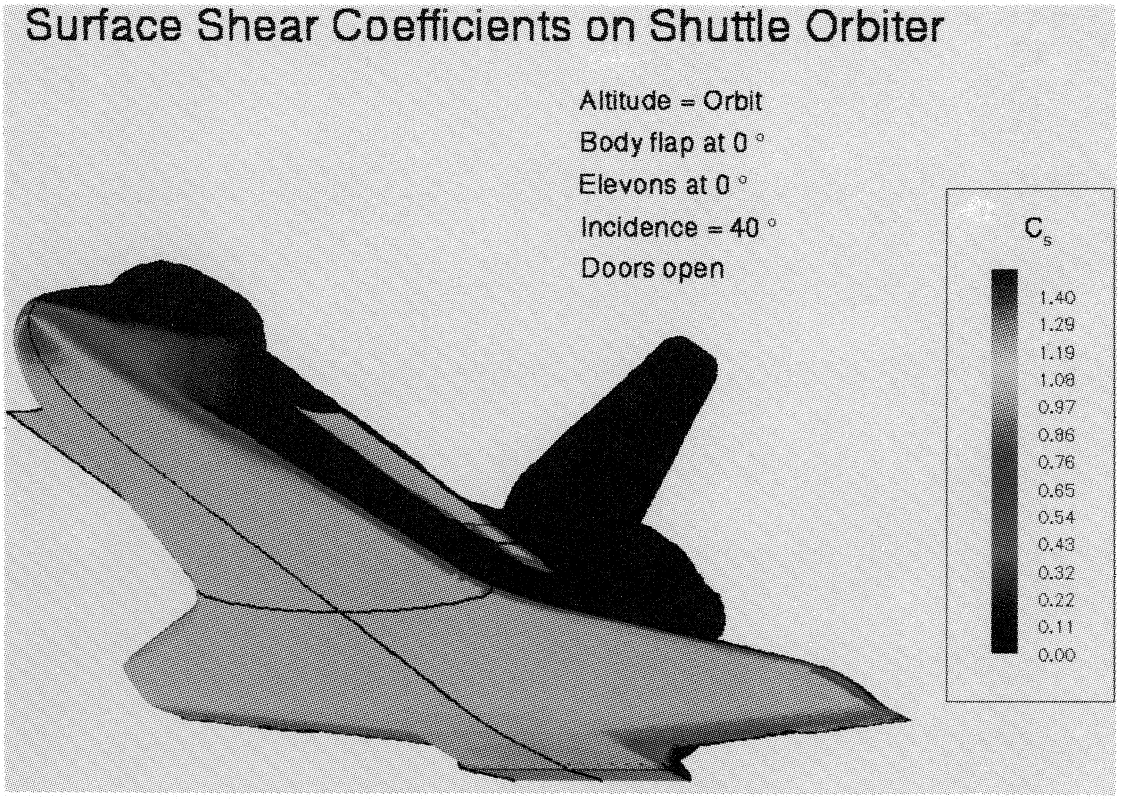

Figure 34. Shear force distribution on Shuttle Orbiter in orbit at 40 degrees incidence.

(Color version of figure 34 is shown on page 946.)

Orbiter (Pre STS-1) Aeroheating Design Data Base Development Methodology: Comparison of Wind Tunnel and Flight Test Data*

Joseph W. Haney
Rockwell International
Downey, California

ABSTRACT

The aerothermodynamic methodology utilized in the design process to prescribe the aeroheating environment of the Space Shuttle Orbiter during atmospheric entry is evaluated. This evaluation addresses both the development of the wind tunnel derived aerothermodynamic data base, and the methods used to extrapolate these ground bases experimental results to the entry flight environment. The evaluation addresses the predictive methods used to estimate the influence of all relevant flow field phenomena, including but not limited to: nonequilibrium flow field chemistry, finite rate catalytic efficiency of the thermal protection system surface materials, windward surface boundary layer transition, and bow shock wave / wind shock interactions. Ground test data correlation techniques, data uncertainty assessments, and the philosophy for inclusion of flight safety margins in aerothermodynamic design environments are also addressed. Methodology is addressed as it affects acreage areas as well as localized flow interaction regions on the orbiter.

Typical flight test data is compared with both appropriate wind tunnel results and predictions derived from application of the pre-flight aerothermodynamic design methodology. The adequacy of the predictive techniques used to define the Orbiter's aerothermodynamic flight environment, and their applicability to the design of future hypersonic vehicles is assessed.

* Work performed on contract at Rockwell International, NAS1-19243

INTRODUCTION

In developing the aeroheating methods for the Space Shuttle Orbiter there wasn't a large data base of hypersonic knowledge to draw upon. The Apollo program covered the entire Mach number range but the ablative heat shield made reduction of aeroheating data difficult and sometimes uncertain. The estimates of heating for the Apollo were perceived to be conservative, not because they were necessary, but because the thermal protection system (TPS) was designed for relative velocities associated with lunar entry. Therefore, for earth orbital entries the ablator charring was not as significant as it could have been. This perception carried forward to the shuttle, and required a lot of effort in the early stage of the program to correct this perception. The other hypersonic source to draw upon was the X15 program. The X15 was at the low end of hypersonics, Mach less than 6.7, and therefore didn't provide extensive Mach number experience. Even with those caveats, both of these programs did advance the development of theoretical approaches to aeroheating and did develop a series of experimental data bases and flight test data.

There were several aeroheating challenges associated with the shuttle orbiter: the basic heating distribution, scaling of wind tunnel derived methods to flight conditions, how to model localized interference regions and shock impingement, a criteria for boundary layer transition, and basic understanding of surface catalytic effects.

In the area of basic heating distributions, the computational fluid dynamics (CFD) codes of today weren't available. For the basic distributions of heating, wind tunnel test data was relied upon heavily. Engineering codes were utilized to predict heating to basic geometric shapes: spheres, cones, wedges, and cylinders. These codes were accurate for the basic shapes, but had to be adjusted to account for three dimensional effects. This was accomplished by correlating the basic shape heating with wind tunnel data on the actual configuration, Figure 1.

On the windward surface this approach was relatively straightforward. However, on the orbiter leeside, using attached boundary layer theories with separate flows didn't make much sense. In these regions heating was correlated with angle of attack and freestream Reynolds number.

Once the basic heating distribution was developed the next question was on how to scale wind tunnel developed correlations to flight conditions. The wind tunnel data was correlated with simple geometric theories and used to develop adjustment factors, Lamfac and Turbfac, depending on whether the flow was laminar or turbulent. In scaling to flight conditions, these factors were held constant. The variables in scaling to flight were the local properties that went into the basic equations; perfect gas conditions were used for the wind tunnel while real gas conditions were used for flight. Though this approach sounds relatively simple it agreed quite well with flight test data. For the leeside regions or regions where wind tunnel data wasn't correlated with theory, extrapolation was accomplished by matching the flight freestream Reynolds number with the Reynolds number correlated data.

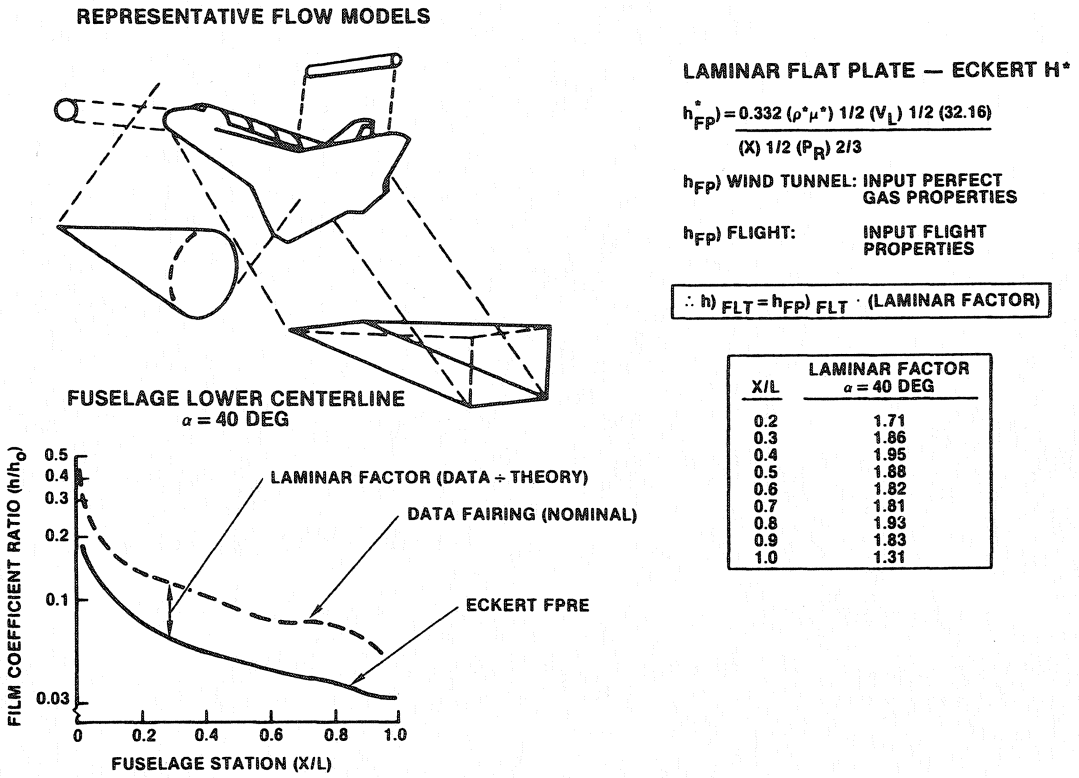

Figure 1. Simple geometric modeling used for aeroheating methods.

Certain localized regions on the orbiter were treated differently in terms of methods than the basic acreage approaches just discussed. These areas were identified by protuberances or penetrations to the basic orbiter surface or regions of rapid change in surface slope. Some of these areas such as small penetrations or protuberances didn't have wind tunnel data as part of the overall shuttle test program. They had to be modeled by using test data on generic shapes and then applying that to the shuttle reference heating. This was accomplished by first developing multipliers factors to account for the protuberance on the generic model allowing for boundary layer state or thickness and then applying these factors to the undisturbed heating predictions where the protuberances occurred on the shuttle.

However there were certain areas where specific tests were performed to obtain the localized effects. These areas included: the aft OMS pod side, elevon-elevon gap, aft fuselage side, canopy, and the SILTS pod. These regions either had specific tests to obtain data or the orbiter models were instrumented to investigate these areas. These are discussed in more detail later in the paper.

SYMBOLS

AFRSI	Advanced flexible reusable surface insulation
Cp	Pressure coefficient
Cp_f	Frozen specific heat
ETR	Eastern Test Range
fp	Flat plate
FRSI	Flexible reusable surface insulation
g	Gravitational constant
h	local heat transfer coefficient
H	Enthalpy
k	roughness element
M	Mach number
OML	Outer mold line
OMS	Orbital maneuvering system
OV	Orbiter vehicle
P	Local pressure
Pr	Prandtl number
q	Heat flux
R	Radius
RCC	Reinforced carbon-carbon
RCS	Reaction control system
Re	Reynolds number
Re_k	Trip Reynolds number
Re_{xk}	Trip position Reynolds number
Re_{δ^*}	Displacement thickness Reynolds number at trip location for effective tripping
Re_θ	Momentum thickness Reynolds number
R_o	Universal gas constant
S	Distance from nose in feet
STS	Space transportation system
T	Temperature
TPS	Thermal protection system
V	Velocity

WTR	Western test range
x	Axial coordinate
x_k	Trip position measured from stagnation point
x_t	Transition position measured from stagnation point
X/L	Nondimensional axial location
X/C	Nondimensional wing chord location
Z	Compressibility
α	Angle of attack
β	Angle of side slip
δ	Control surface deflection
δ^*	Displacement thickness of boundary layer
θ	Momentum thickness of boundary layer or local flow angle
ρ	Density
μ	Viscosity
η	Defined in equation 11
γ_R	Defined in equation 12
Λ	Sweep

Subscripts

aw	Adiabatic wall
D	Dissociation
EFF	Effective
El	Left elevon
Er	Right elevon
eq	Equilibrium, or equivalent roughness
f	Frozen
Flt	Flight condition
G	Gap
o	Reference conditions, one foot radius sphere
pc	Partially catalytic
TEST	Test conditions
w	Wall condition
δ,e,L	boundary layer edge conditions
∞	Freestream condition

APPROACH TO AEROHEATING METHODS DEVELOPMENT

In developing the aeroheating methods for the Space Shuttle orbiter a specific philosophy was developed, Figure 2. That philosophy was to base the methods largely on wind tunnel tests using a nominal fit of the wind tunnel data considering several test facilities. This nominal fit of the ground test data would be correlated and extrapolated to flight conditions. Based on uncertainties in test data and in analytical tools an uncertainty band would be utilized for the various regions of the orbiter. Design of the orbiter TPS would use the nominal heating methods. The decision to use nominal methods was based on the idea that other design disciplines were either conservative in their analysis or had accounted for factors of safety that would cover the aeroheating uncertainties. In addition, the TPS would be designed for a Western Test Range, WTR, mission with high cross range. Initial flights were planned for the Eastern Test Range, ETR, which provided a less severe thermal environment. This margin also would help cover heating uncertainties. The main thrust in this approach was to save TPS weight. However, prior to the first flight, all of the uncertainties would be accounted for to verify there were no safety of flight issues. With the exceptions of a few areas that sustained localized damage, this approach was very successful.

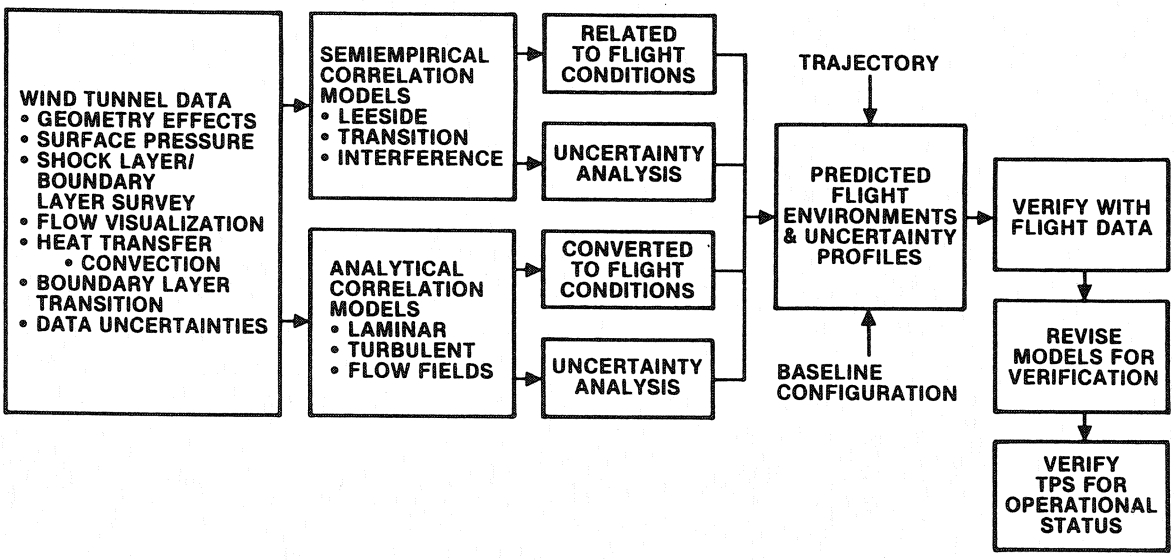

Figure 2. Aeroheating design and verification logic

Wind Tunnel Data Base

Because the development of aeroheating methods was so dependent on wind tunnel data, wind tunnel testing covered a period of twelve years, from the start of Phase A studies to the first orbital flight of Columbia (OV102). Over this time period 50 wind tunnel tests were conducted resulting in approximately 5200 hours of facility testing. During this time period the basic shape evolved resulting in 9 different configurations being tested: 07D-ATD, 089, 089B-Mod, 130Mod, 139, 139Mod, 140B, 147B, 140C STS-1. These models were tested from .006 to .0175 scales for complete configurations from 0.025 to full scale partial models of specific components. Several types of instrumentation were used to obtain the data necessary for aeroheating modeling. Instrumentation included thermocouples, calorimeters, thin film gages, temperature sensitive paint, pressure taps, oil flow, and infrared measurements. These instruments provided temperature, heating, pressure, and boundary layer data. With the enormity of testing and the desire to obtain data at a wide variety of test conditions, testing was conducted in seven facilities: NASA Langley VDT, NASA Langley CF4, NASA Langley CFHT, NASA Ames 3.5', CALSPAN, AEDC Tunnel B, and AEDC Tunnel F as shown in Figure 3. Unfortunately a lot of the entry trajectory was not a one for one match with ground test data. This required the test data to be correlated and extrapolated to flight conditions.

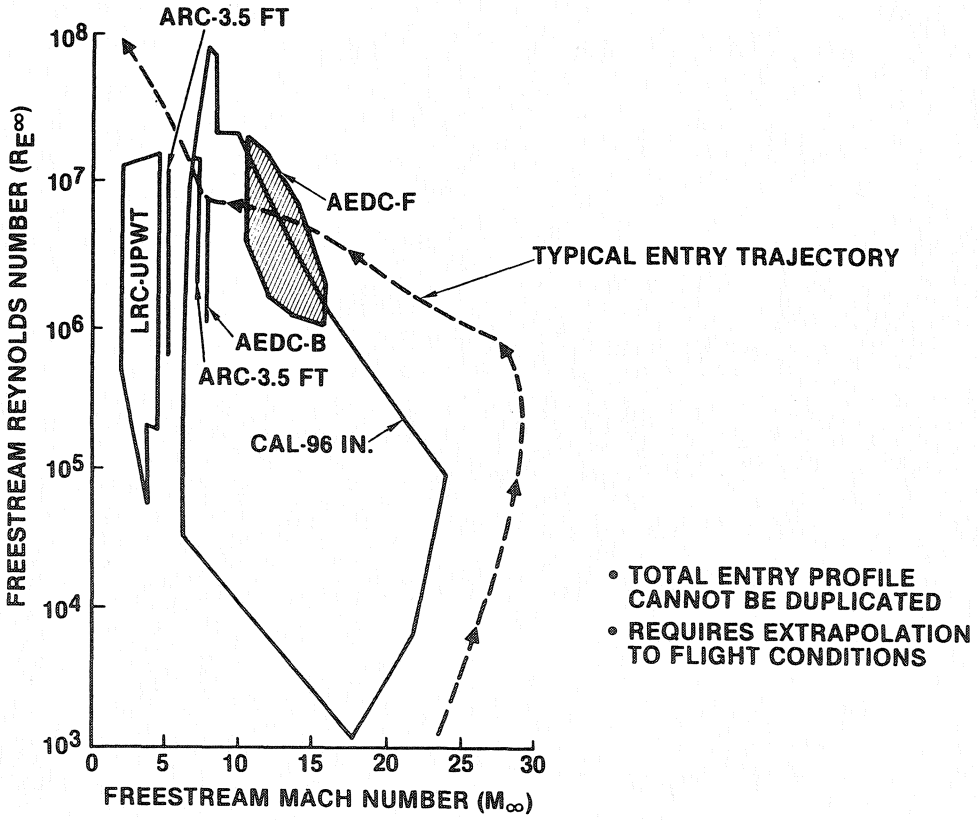

Figure 3 . Wind tunnel test simulation of orbiter mission .

Testing to gather data to build aeroheating methods for the shuttle encompassed a Mach Number range from 5.3 to 19. Because of the nature of the orbiter re-entry trajectory, angle of attack data had to be obtained up to 40° angle of attack. To account for or cover potential uncertainties, data was obtained up to 50° angle of attack. To account for possible sideslip during the orbiter's re-entry, yaw data was obtained up to 10° sideslip. However, most of the side slip data was obtained between zero and ±2°.

The effects of control surfaces (elevon, body flap, and speed brake) were also investigated. The elevon deflections were varied from -30° to +10° while the body flap was tested at 0, 5, 10, 15, and 22°.

Of all the test techniques used to obtain aeroheating methods, paint test data was used early in the program to screen configurations changes and to get first order effects on heating. However, reduction of paint data was labor intensive requiring hours on hours in front of a projection screen tracing paint melt patterns. However, this low cost technique was able to provide remarkable agreement with thermocouple data using low paint melt temperatures if semi-infinite assumptions weren't violated in model geometry as on wings and tails.

Figure 4. 0.0175 scale thermocouple model installed at AEDC.

Most of the final aeroheating methods were derived from thin skin thermocouple models as shown in Figure 4. This figure shows the 0.0175 scale orbiter model installed in the Arnold Engineering Development Center, AEDC, Tunnel B in Tennessee. From this type of model aeroheating methods were developed for all the major vehicle areas such as fuselage, wings, vertical, and OMS pod.

To obtain more detailed data to account for various penetrations such as the canopy, partial models were fabricated and tested, Figure 5. This forebody model was a 0.04 scale model of the orbiter configuration designated -139. This model provided aeroheating data on the orbiter forebody accounting for the canopy window geometry; penetrations such as reaction control system, RCS, nozzles; and protuberances such as the payload bay door hinges.

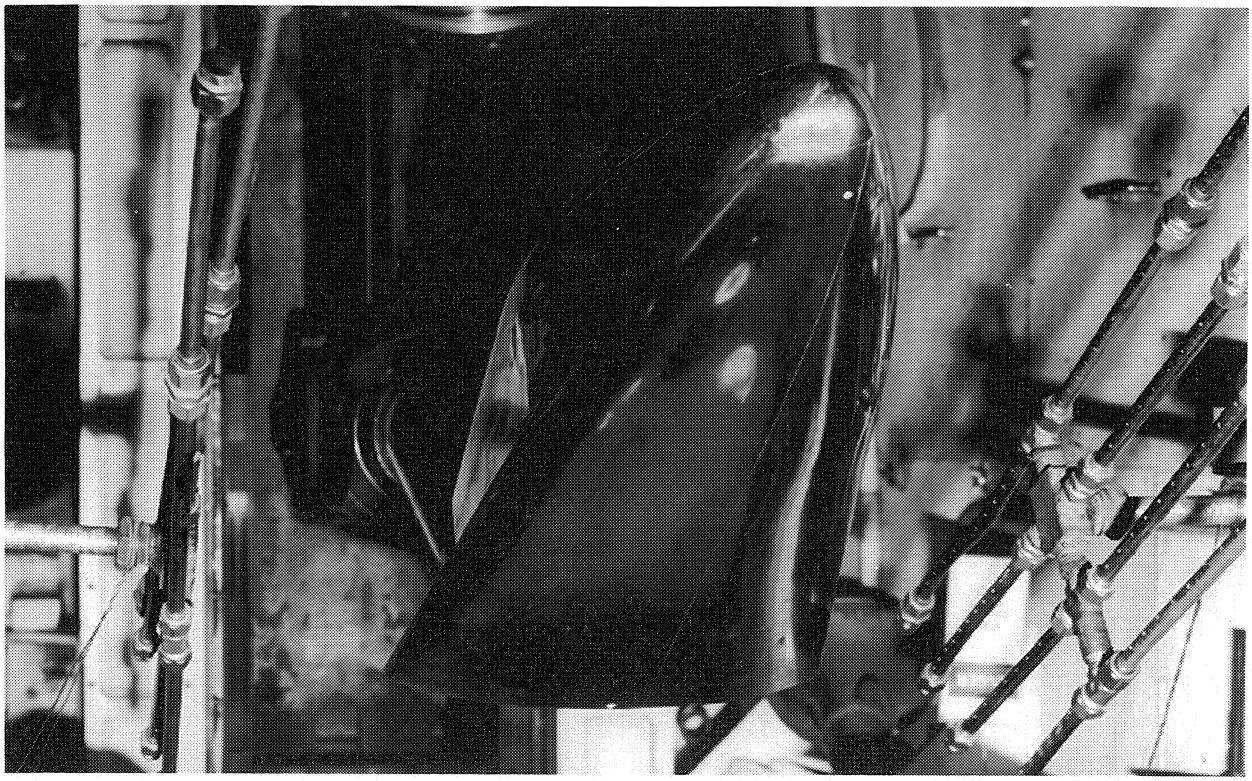

Figure 5. Partial model of the orbiter forebody.

Another type of data that proved very useful in the wind tunnel test program was that of oil flow data. This test technique used an epoxy model that was coated or sprayed with oil. The oil had particles suspended in it so that it would be visible on the model. The movement of the oil due to surface shear conditions was photographed. From these photographs insight was gathered as to the origin of various flows, the regions of impact of shock and vortex structures, and a general idea of where the complex flow phenomena occurred. Figure 6 is an example of this type of test technique. This figure shows regions of oil streaking and accumulation due to attached

flow, vortex flow, and separated flow. From partial and complete oil flow models the understanding of the heat transfer test data was enhanced and the overall orbiter flow fields modeled.

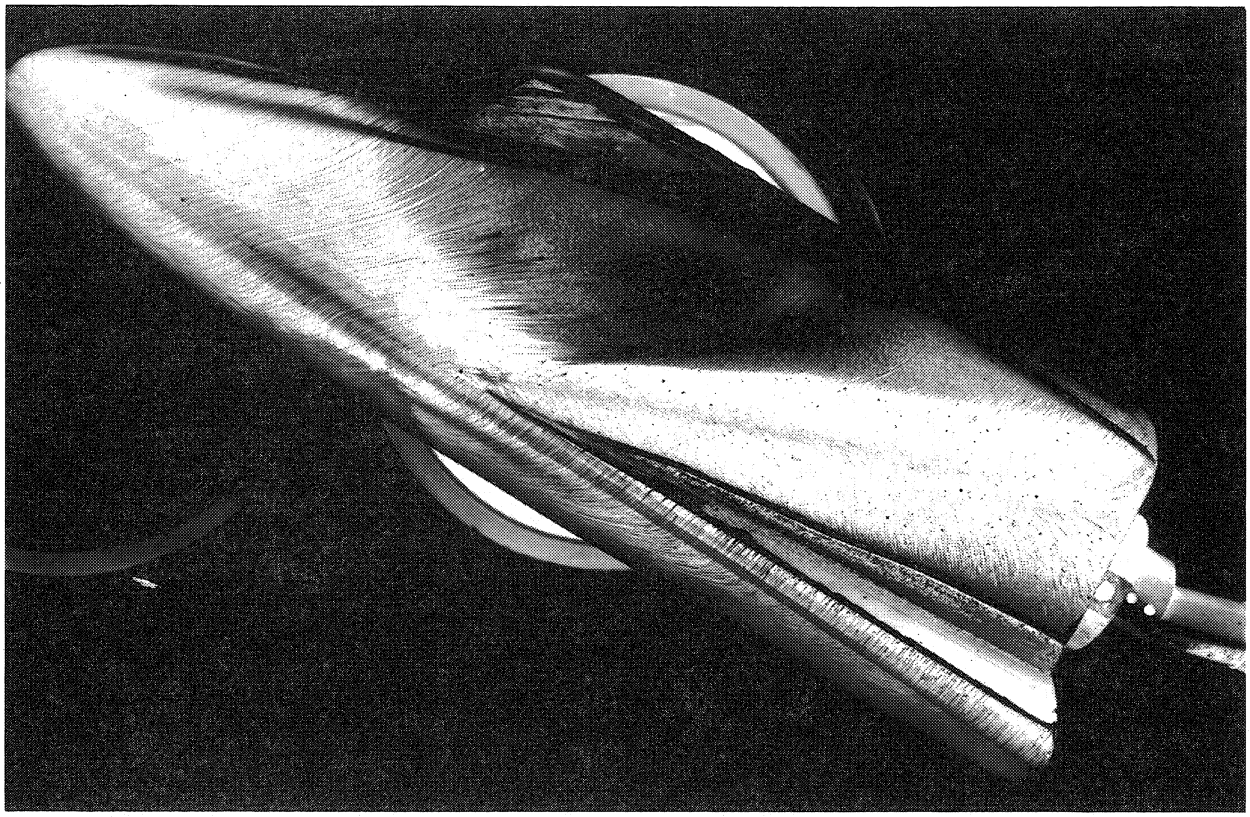

Figure 6 . Oil flow patterns on the fuselage forebody side

In Figure 6 the origin of the fuselage side vortex is clearly visible. Some of the separated regions on the top of the wing glove is evident. Flow interactions around the canopy are not very clear but will be presented later in the paper. Also the downstream effects of penetrations and protuberances are presented later with other oil flow pictures.

DEVELOPMENT OF AEROHEATING DATA BASE METHODS

Orbiter Acreage

Two basic approaches were taken to develop methods for the acreage area of the shuttle orbiter. Acreage areas are those where there aren't large discontinuities in the orbiter mold line, OML, or regions influenced by shock or vortex interactions. The first approach as mentioned earlier is the simple geometric theory approach, used mainly for the lower surfaces. The second approach correlated wind tunnel test data with specific flight parameters and then applied those correlations to flight conditions. This approach was used for the upper areas of the orbiter.

Fuselage Lower Surface

The simple geometric theory approach subdivides the orbiter into simple or basic shapes such as spheres, cylinders, wedges, and cones for which standard analytical solutions existed. This was illustrated in Figure 1. These simple geometric theories (mainly wedges) were adjusted to match wind tunnel heat transfer test data. Because these simple geometric assumptions couldn't entirely match the orbiter 3D geometries they had to be adjusted to match the heating distribution obtained in wind tunnel testing. These adjustments were made from the standard Eckert reference enthalpy flat place solutions, Reference 1. These adjustment factors, developed for both laminar and turbulent boundary layers in the wind tunnel, were held constant when extrapolating to flight conditions. These factors, referred to as Lamfacs (laminar flow) and Turbfac (turbulent flow), varied with vehicle location and angle of attack. For attached regions such as the lower surface of the orbiter these factors did not vary as a function of Reynolds number except when the flow transitioned from laminar to turbulent flow. Heating was usually nondimensionalized to a reference heating or film coefficient based on Fay and Riddell correlations, Reference 2.

The fuselage lower surface was divided into regions of both blunt body and slender body flow. Generally slender body flows were used when the change in slope of local velocity went to zero. In the blunt flow dominated regions heating rates were impacted due to entropy swallowing as the free stream flow passed through the blunt bow shock. In these regions heating test data correlated well with Cohen & Beckwith theory, Reference 3, as shown in Figure 7. As illustrated, there is an excellent match between theory and heat transfer test data on the lower centerline for an angle of attack of 30°. To improve the correlation approach, local pressures and velocities from test data were substituted into the Cohen and Beckwith theory. Peak heating occurred slightly downstream of the zero angle of attack stagnation point.

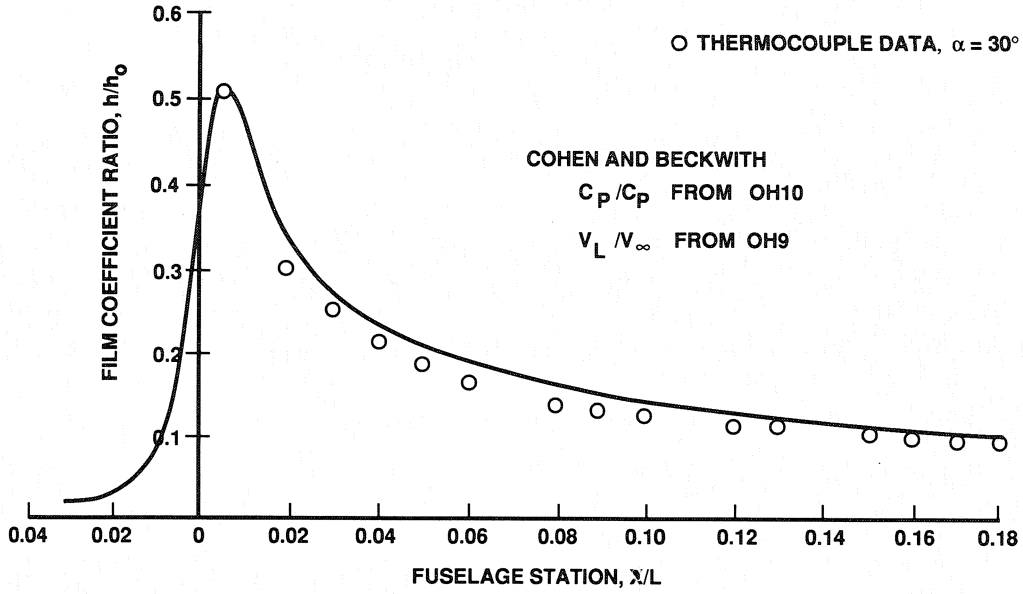

Figure 7. Cohen and Beckwith modeling of the fuselage forebody.

Down stream of the blunt region, slender body approaches were used. Eckert's flat plate reference enthalpy method was used as the basic theory to compare heat transfer data against. To compute the reference heating certain assumptions needed to be made on both pressure and velocity. Generally the conic pressure relationship matched wind tunnel pressure values; however, velocity relationship didn't work due to the entropy swallowing effects. To account for entropy swallowing a simple relationship was developed based on wind tunnel test data, Equation 1. This relation provided an excellent match with test data. Reference 4 provides a more detail discussion on this velocity correlation approach.

$$\frac{V_L}{V_\infty} = \left[.8189 \left(\frac{\theta + 30}{S} \right)^{-.0774} \right] \cos(\theta + \alpha) \qquad (1)$$

where: θ is the local body angle,

α is the angle of attack, and

S is the distance from the nose in feet

With pressure and velocity inputs based on wind tunnel verified approaches flat plate heating was calculated and compared with test data at various stations on the fuselage and at different

angles of attack. Figure 8 presents the heat transfer data on the orbiter lower centerline at an angle of attack of 30°. The heat transfer data presents many pieces of data needed to develop methods. First by looking at the low Reynolds number data, Re/Ft=0.5 & $1.0x10^6$, the relationship of laminar heating to flat plate and cone heating was determined. From this data the Lamfacs were determined. Laminar factors varied with angle of attack leaving the values near flat plate and increasing towards cone as the angle of attack increased. The centerline is affected by the wing impact on the bow shock. The expansion due to the fuselage wasn't modeled in the local properties case. When a Prandtl Meyer expansion was used, a better match of the data was obtained. The test data also showed a good relationship with the Spalding & Chi turbulent theory, Reference 5. The high Reynolds number data, Re/Ft=$3.7x10^6$, also provided data on the onset of boundary layer transition.

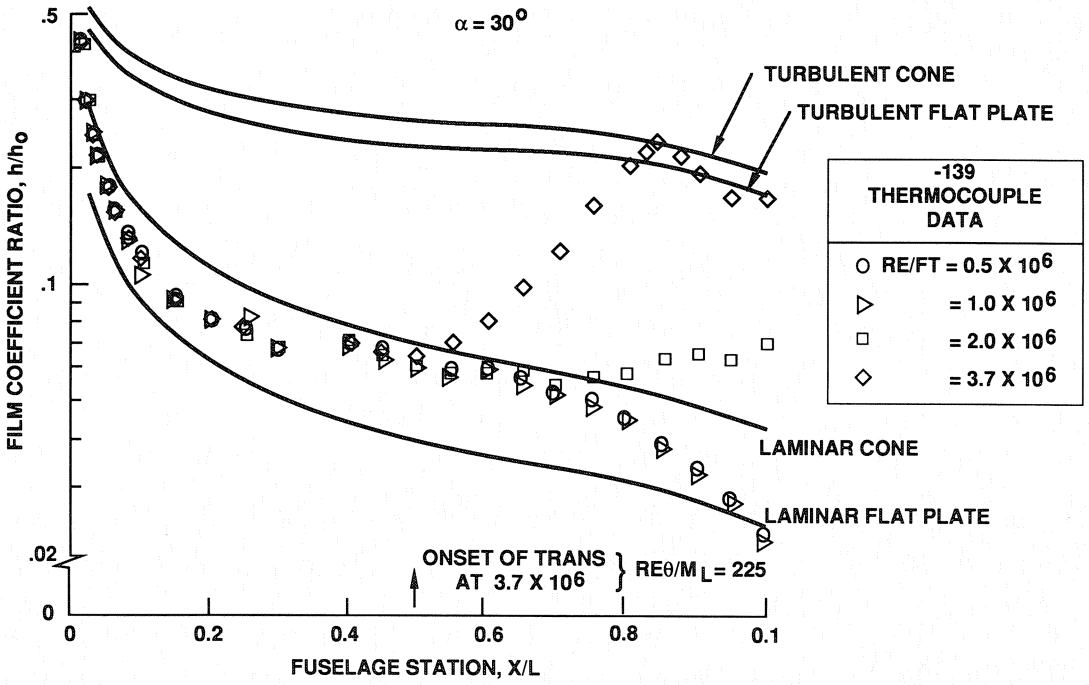

Figure 8. Fuselage lower centerline heating distribution.

By using this type of data the variation in Lamfac was determined at every location where heating was defined for the entry trajectory, i.e., body points. For those body points, Lamfacs were correlated with three linear segments as a function of angle of attack. Figure 9 shows the variation in Lamfac as a function of angle of attack for body point 1600. Body point 1600 corresponded to a station at sixty percent of the fuselage body length on the lower centerline. As indicated, at low angles of attack, ie. 20°, the heating level was twenty percent above that of a flat plate. However, by the time the vehicle was at an angle of attack of 35° the heating level had reached that of a cone.

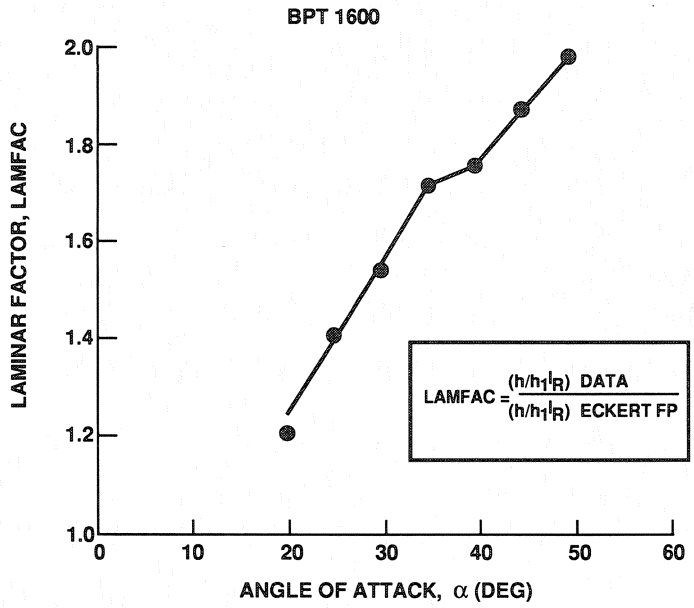

Figure 9. Variation in lamfac with angle of attack on the fuselage lower centerline.

Away from the vehicle centerline heating methods were handled in a similar manner except cross sectional heating data was used. Cross sectional pressure levels varied by a $\sin^2$ relationship from vehicle centerline pressures while cross sectional heating varied with surface slope and distance from the stagnation point. Figure 10 presents one of the approaches investigated to correlate forebody heating into a single correlation. Data was correlated for fuselage cross sections from X/L=0.025 (25% vehicle length) to X/L=0.5 (50% vehicle length). This correlation did not provide a tight grouping of the cross sectional heat transfer data. However, it did indicate that the variation could be roughly correlated in geometric terms as shown in equation (2).

$$\left(\frac{h}{h_{CL}}\right)\Big/\left(\cos\theta^{.55}\right) = f\left(S \bullet \sin^2\theta\right) \qquad (2)$$

where: h = film coefficient

θ= local inclination angle in the cross section

S=distance from nose

cl=centerline

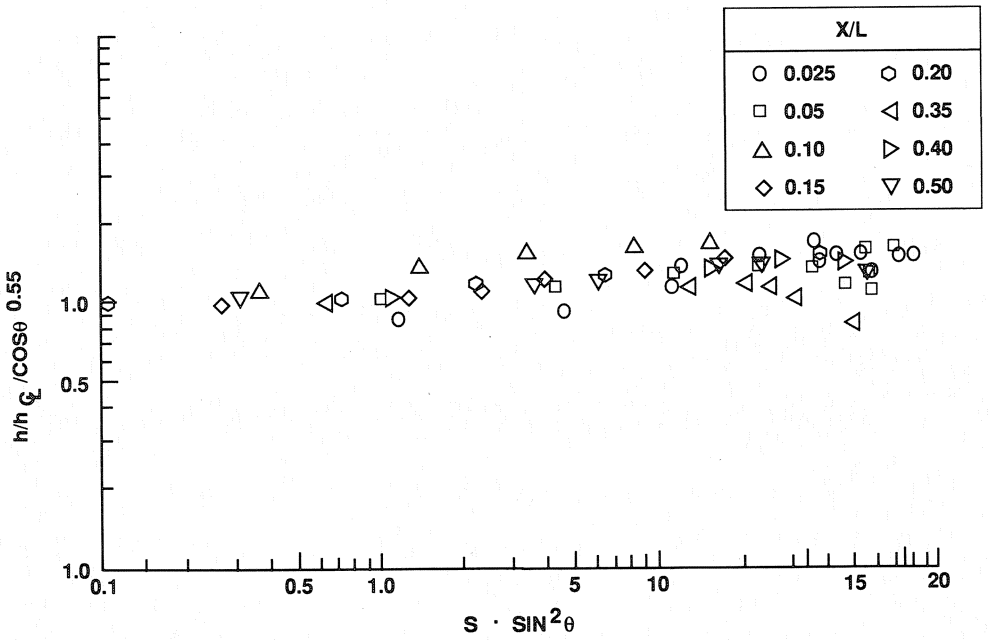

Figure 10. Correlation of fuselage cross sectional heating.

Wing Lower Surface

Aeroheating methods for the wing lower surface utilized the same approach as the fuselage lower surface even though the wing possessed a much more complex flow system. The wing lower surface experienced several flow phenomena. The inboard spans (30% and 40%) were influenced by the fuselage flow attempting to diverge from the fuselage. This flow was contained by the wing flow and turned back . The outboard spans were influenced by downstream effects of the bow - leading edge shock interactions. The wing was treated in a similar manner to that of the fuselage. It was divided into blunt and slender body flow regions with the leading edge making up the blunt region and the wing proper the slender body region.

These flows impacted both heating levels and transition. Figure 11 shows a comparison of wind tunnel data versus theory for 60% wing span. Usually the laminar factors were close to one indicating wedge flow as would be expected for a wing. In regions impacted by the wing-fuselage body shock interaction factors deviated from this level. This interaction created a vortex or jet which impinged on the outbound region of the wing causing earlier transition and higher heating levels. As shown in this figure Eckert's Reference Enthalpy flat plate solution was a good approach for the wing and the Spalding and Chi turbulent flat plate approach represented the turbulent flow heating levels.

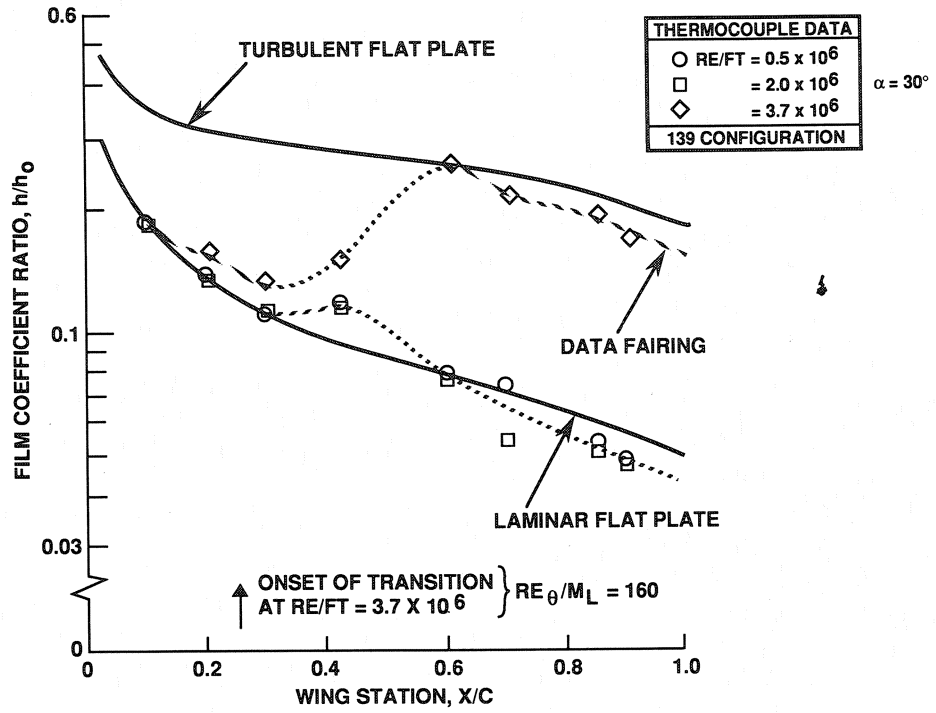

Figure 11. Wing lower surface heating distribution at 60% semispan.

Wing Leading Edge Methods

The orbiter wing leading edge was modeled as a swept cylinder. This basic approach was used to predict the maximum stagnation line heating but was adjusted to account for the effects of the wing surface on the leading edge shock shape (captured as an effective radius), leading edge sweep angle, and the effects of shock impingement on increased heating.

The basic swept cylinder approach used a simple formula as shown in equation (3).

$$\frac{q_{LE}}{q_{1'R}} = \frac{1}{\sqrt{2}}\sqrt{\frac{12}{R_{EFF}}}\cos^{1.2}\Lambda_{EFF} \qquad (3)$$

In this equation: q_{LE} is the leading edge stagnation line heating,
$q_{1'R}$ is the reference heating on a one foot radius sphere,
R_{EFF} is the effective leading edge radius, and
Λ_{EFF} is the effective sweep

The effective sweep was defined as $\Lambda_{EFF} = Sin^{-1}(Cos\ \alpha Sin\Lambda)$ and the effective leading edge radius was determined by comparing leading edge predictions with wind tunnel data. The effect of the wing was to have no impact at zero degrees angle of attack but to be almost a factor of four at $\alpha=50°$.

The effect of shock impingement was also considered. Based on wind tunnel testing, the interaction of the fuselage bow shock and wing leading edge shock strikes the leading edge at 55% half span. This position was influenced as expected to some extent with angle of attack. Review of Schlerien photographs of the wing interaction indicated this was a type V interaction, not as severe as a Type IV, Figure 12. These types of interactions were discussed in References 6 and 7.

Scaling of wind tunnel derived shock impingement effects was the subject of many decisions and several technical papers at the time. This was due to what was called a "double shock" phenomena where the flow had to pass through two shocks before reaching the leading edge. The presumption was that the real gas effects would result in a change in shock angles leading to larger pressures and thereby heating would rise over that experienced in the wind tunnel. An increase by as much as a factor of two over wind tunnel derived shock impingement effects was postulated. For nominal heating wind tunnel data was scaled directly as a ratio of reference heating, but the double shock effects were accounted for as an uncertainty.

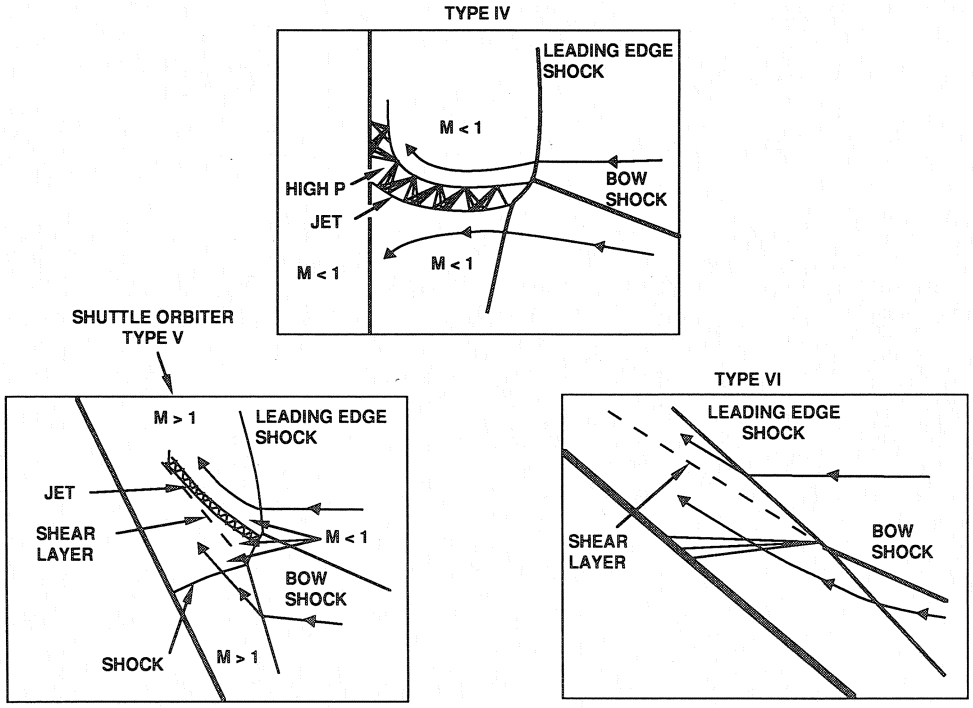

Figure 12. Potential shock impingement patterns.

Basic pressure levels on the wing leading edge correlated well with pressure coefficient ratio Cp/Cps based on $Cos^2 \Lambda eff$. Distribution away from that maximum pressure level was represented by a $Sin^2 \theta$ distribution where q was the leading edge cross sectional angle.

Control Surface Methods

Aerodynamic control of the orbiter during reentry was accomplished with three control surfaces: the fuselage body flap, the wing elevons, and the vertical speed brakes. The body flap and elevon heating methods are discussed here.

Consistent with the overall shuttle philosophy simple approaches were taken in predicting heating to the body flap and elevons. The basic phenomena resulting from a deflected control surface are described below.

The boundary layer grows undisturbed from the nose (or the leading edge) up to the point where the separation interaction begins. The first shock comes from a rapid thickening of the boundary layer due to a buildup of pressure as the control surface is approached. This causes the boundary layer to separate from the fuselage due to the adverse pressure gradient that is strong enough to reduce the normal velocity gradient at the wall to zero before the end of the pressure rise. When the flow separates, the dividing streamline leaves the wall and is accelerated by the outer inviscid flow acting in shear across the separated boundary layer. This acceleration takes place at an almost constant plateau pressure and continues until the streamline acquires sufficient energy to overcome the adverse reattachment pressure gradient, which is a function of inviscid flap pressure.

The two factors that determine the separation length are the pressure rise that causes the separation and the effective viscosity of the boundary layer that accelerates the dividing streamline. The adverse pressure gradient at separation acts as a boundary layer trip to induce early transition. The dividing (separating) streamline makes an almost constant angle with the fuselage (or wing). After separation the pressure reaches a plateau pressure value determined by the separation angle. The flow reattaches, resulting in a reattachment shock. After reattachment, the pressure rises to a peak value and then decays to the value for the inviscid flow, Figure 13. When the boundary layer becomes fully turbulent upstream of the control surface, the region of separated flow reduces drastically and thereby produces a sharper pressure and heating rise.

In modeling this phenomenon a similar approach was used for the body flap or elevon. Wind tunnel data were correlated with Eckert's reference enthalpy flat plate equation using undeflected flow properties. The local pressure levels based on surface geometric angles were adjusted for Prandtl Meyer expansion (justified by using wind tunnel data at zero body flap deflection). Based on a large wind tunnel base of thermocouple data plus paint data, a deflection equation was developed that covered the average effect of surface deflection under both laminar and turbulent flow conditions.

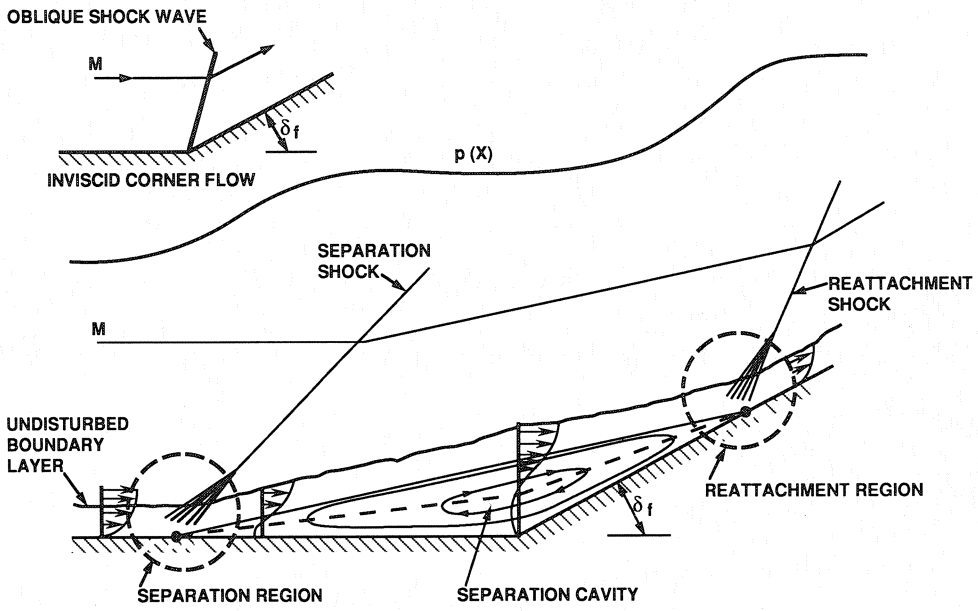

Figure 13. Flow separation phenomena associated with control surfaces.

As the body flap deflection angle increased, the 3D nature of the separation region increased and influenced the heating to the body flap. However, the basic approach remained in that both laminar and turbulent factors compared to the undeflected reference were obtained for different control surface positions and different vehicle angles of attack based on wind tunnel data. The same approach was used for the wing elevon.

Figure 14 presents the wind tunnel heating data on the aft fuselage and body flap at an angle of attack of 30° from M=8 test data. Examining each of the sets of Reynolds number data provides important insights into this phenomenon. For the low Reynolds number case of Re/Ft=0.5x10^6 the on coming flow to the body flap was laminar. As can be seen the heating data matched conical flow but decreased to wedge flow on the body flap. With the body flap deflected, the flow separated and reattached probably in a transitional mode. Even though it was above the turbulent level, the added effect of the compression wasn't fully realized in the heating level.

However, in considering the mid Reynolds number range of Re/Ft=2.0x10^6 the oncoming flow to the body flap was transitional. This flow didn't separate. The heating level on the body flap was greater than the turbulent theory consistent with a value expected for a deflection of ten degrees. For this case, the deflected surface caused the flow to become fully turbulent.

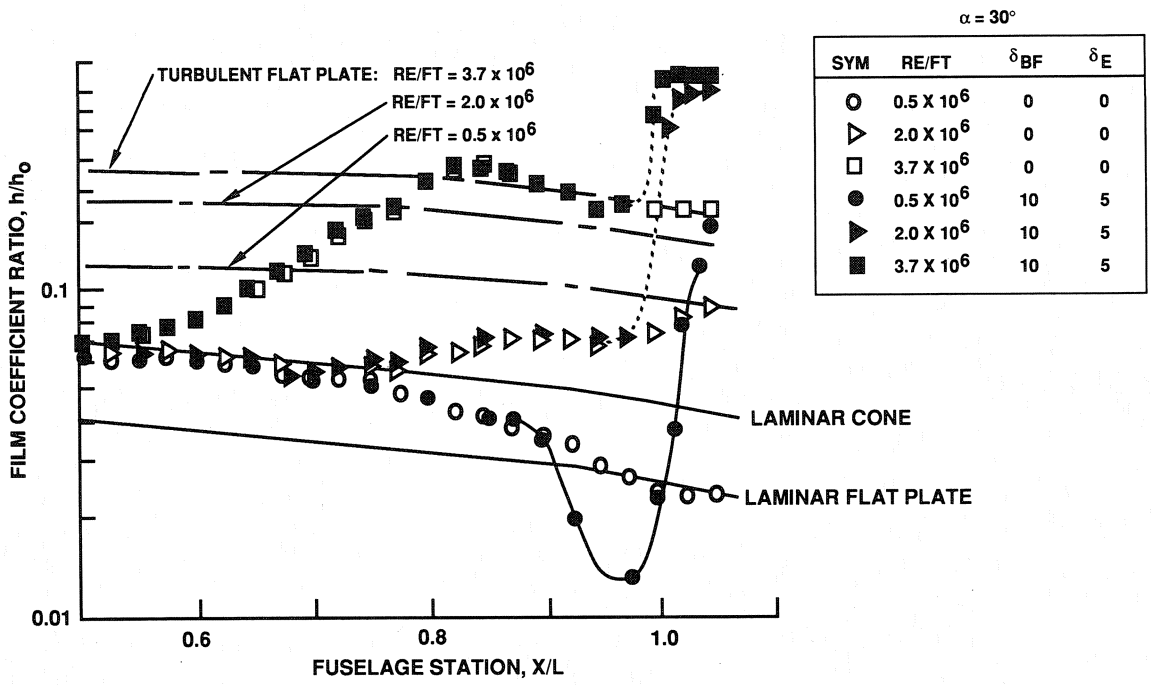

Figure 14. Impact of deflected body flap on heating levels.

For the high Reynolds number case of Re/Ft=3.7x10^6 the oncoming flow was turbulent. Heating on the body flap reflected the added effect of the added compression only. This type of data was used to develop a set of correlations to account for the effects of control surface deflections as a function of deflection angle and vehicle angle of attack.

Leeside Flow Methods

As mentioned earlier, the leeside of the orbiter was modeled differently than the lower surface. The direct application of wind tunnel data for the upper surfaces of the orbiter was obtained by correlations of wind tunnel data (in terms of a nondimensional local film coefficient to that of a one foot radius sphere) as a function of angle of attack, angle of sideslip (yaw), free-stream Reynolds number, and free-stream Mach number . This essentially correlated the orbiter leeside into blunt body relationships. Regions of vortex scrubbing and flow impingement were allowed to vary somewhat beyond the wind tunnel values based on local pressure levels.

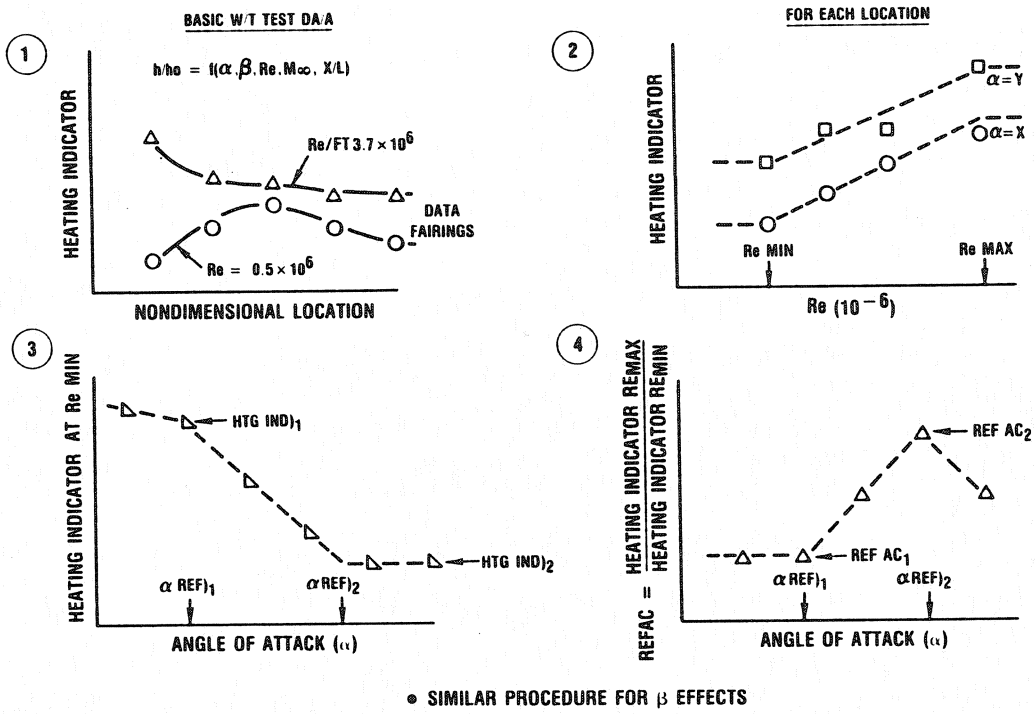

Figure 15. Orbiter leeside heating methodology.

The approach to the side and upper surfaces of the orbiter was to develop nominal fairings of the test data along vehicle axial tracings, usually at constant Y or Z locations for each body point on the leeside as shown in section 1 of Figure 15. Then at a selected non-dimensional location, i.e., percent fuselage length, the data was correlated with Reynolds number for discrete angles of attack. Linear fits of the data were used. A minimum and maximum Reynolds number was selected for a group of points, section 2. This data was then correlated again in two steps. First the minimum Reynolds number was selected where there was a break in the heat transfer data or an artificial value of 0.5 X 10^6 was selected. These minimum Reynolds number heating values were correlated with three linear segments as a function of angle of attack, section 3. The ratio of the heating at the maximum Reynolds number to the value at the minimum Reynolds number from section 2 was correlated with three linear segments as a function of angle of attack, section 4. With these sets of linear correlations, heating data on the orbiter leeside were correlated. This approach worked remarkably well considering the variation in flow fields on the leeside of the shuttle orbiter.

Fuselage Side and Upper Surface

The leeside flow field of the Space Shuttle orbiter differed from that of what might be considered conventional separated flow. In conventional separated flow the flow field analyzed

consists of a thin, constant pressure, viscous mixing layer separated from a solid surface by an enclosed region of low-velocity "dead" air. However the shuttle experienced a highly complex flow developed with the presence of vortices.

Early Shuttle concepts and simplified Shuttle geometries all exhibited the presence of vortices on the leeward surface. Because vortices were affected by chine radius, forebody half angle, planform area, cross-sectional area, nose bluntness, and canopy presence and location, the correlations and results could not be directly applied to different Shuttle configurations. However, these studies were very useful in understanding the fluid mechanics of complex leeside flow fields.

The surface discontinuity involving the forebody sidewall, and the windward flow separation over the glove leading edge created another vortex. This vortex interacted with the fuselage side, affecting regions in Figure 16. The viscous flow attached briefly, then separated. This vortex (shear layer) influenced not only the fuselage side, but also the OMS pod and vertical tail.

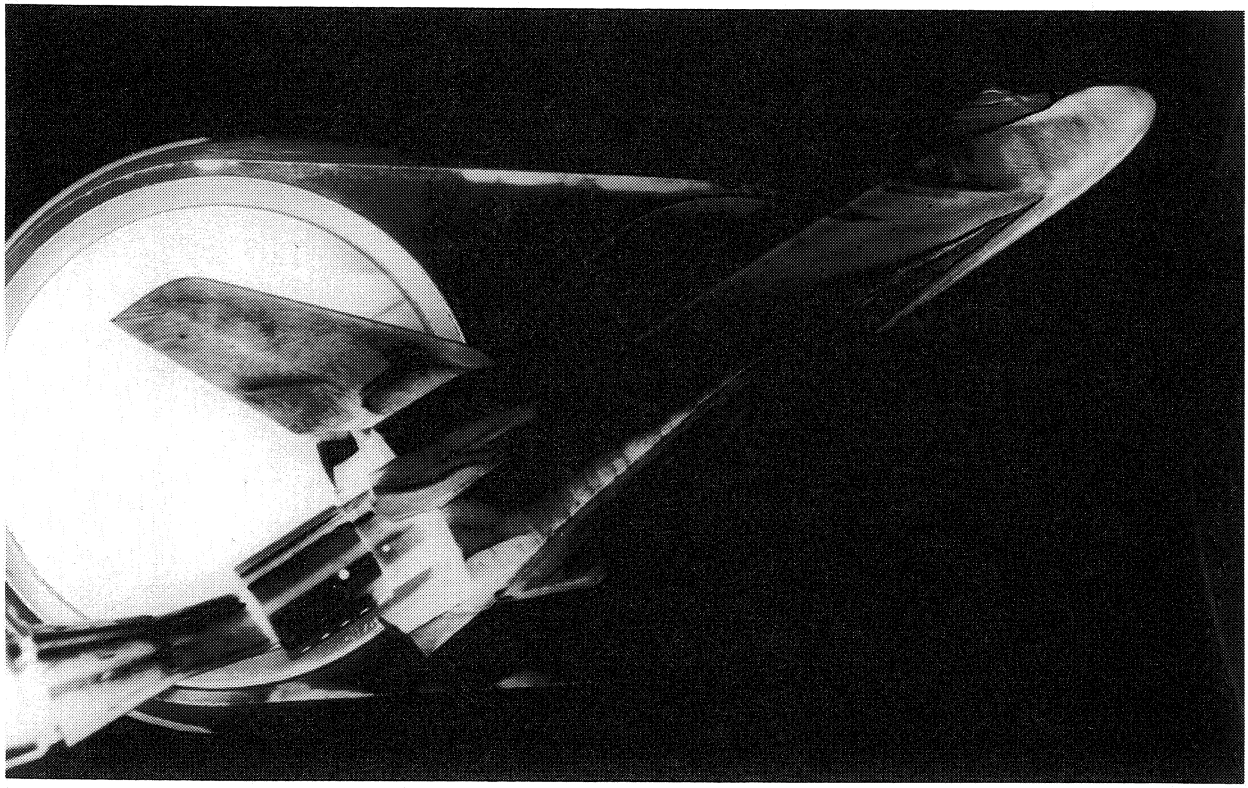

Figure 16. Oil flow patterns indicate vortex impingement.

Figure 16 shows oil flow patterns on the side of the fuselage at 40° angle of attack. Where the wing meets the fuselage a vortex was formed which scrubs the side of the vehicle and continued aft striking the OMS pod and vertical tail. One of the scaling to flight issues experienced during the flight test program was how the heating scaled to flight with vortex interaction. On the fuselage the vortex formed on the forebody wrapped around and attached on the upper centerline in

front of and on the canopy. This was very similar in structure to a cone at angle of attack. The results of primary and secondary vortices were scrubbing of the upper surface of the pay load bay doors. These vortices were not as intense as those on the forebody or fuselage side.

Because of the circular downward motion of the vortices, the viscous layer on the surface was thinned to a minimum. Thus, the region between the high energy inviscid flow and the surface was reduced, while the circular motion also tended to bring the high energy flow close to the surface, resulting in increased heating.

The vortex-induced heating was highly sensitive to the changes in Reynolds number, while angle of attack affected the location of the peak value and generates secondary vortices. Reynolds number seemed to have little influence on the local heating peak's location. Generally, heating increased with increasing Reynolds number.

There appeared to be two types of separated flow on the leeside of Shuttle like configurations based on results of a study by Zakkay and Miyazawa, Reference 8. The first was a free vortex layer separation characterized by one pair of separation lines where peak heating was associated with boundary layer transition. This type of separation was experienced at low angles of attack. The second was a bubble-type separation with two pairs of separation lines and peak heating associated with vortex interaction in the separation region. This circulating flow had its stagnation point on the surface centerline; as the flow moved away from the centerline, the flow separated, forming a secondary separation line. Secondary vortices were also produced. This was generally present at moderate and high angles of attack.

The analyses of the Shuttle leeside flow phenomena employed various types of data. Heat transfer data were obtained from eight tests at four ground facilities for two model scales at Mach numbers between 7 and 19, angles of attack between 20° and 45°, and Reynolds numbers between Re/ft = 4.3×10^4 and Re/ft = 1.05×10^7. Local pressure data was obtained at angles of attack between 20° and 50° and Reynolds numbers of Re/ft = 3.0×10^6 to 6.0×10^6.

With the orbiter at 20° angle of attack, the flow over the upper centerline was governed by the primary vortex impingement. Within the vortex there was a constant pressure region normal to the surface, a variation with distance in the total temperatures (due to a large in-flow of hot external air), and quite a large axial velocity. This was a turbulent boundary layer flow regime. At alpha = 30°, the vortex impingement occurred in front of and behind the canopy. The canopy and its own particular flow patterns separated these two regions. This, too, was a turbulent flow regime.

At alpha = 45°, the primary vortex impingement had moved to be located generally in front of the canopy. The strong influence of the canopy and fuselage side vortex resulted in a swirling flow pattern without the presence of the large axial velocity gradient which was common for smaller angles of attack.

Figures 17 thru 20 present oil flow data on a partial model (forebody only) showing the complex flow patterns on the fuselage side and upper surfaces. This data is for an angle of attack of 30° and a Reynolds number of 1.0×10^6. Also shown in this set of figures are the impact of the penetrations and protuberances on the orbiter forebody. On the side view, the effects of the reaction control system, RCS, nozzles, crew side hatch window, and the payload bay door hinges can be seen. On the upper surface the RCS nozzles, canopy windows, and the upper observation windows effects are shown. This data helped to understand the flow fields the penetrations experienced and some of their downstream effects.

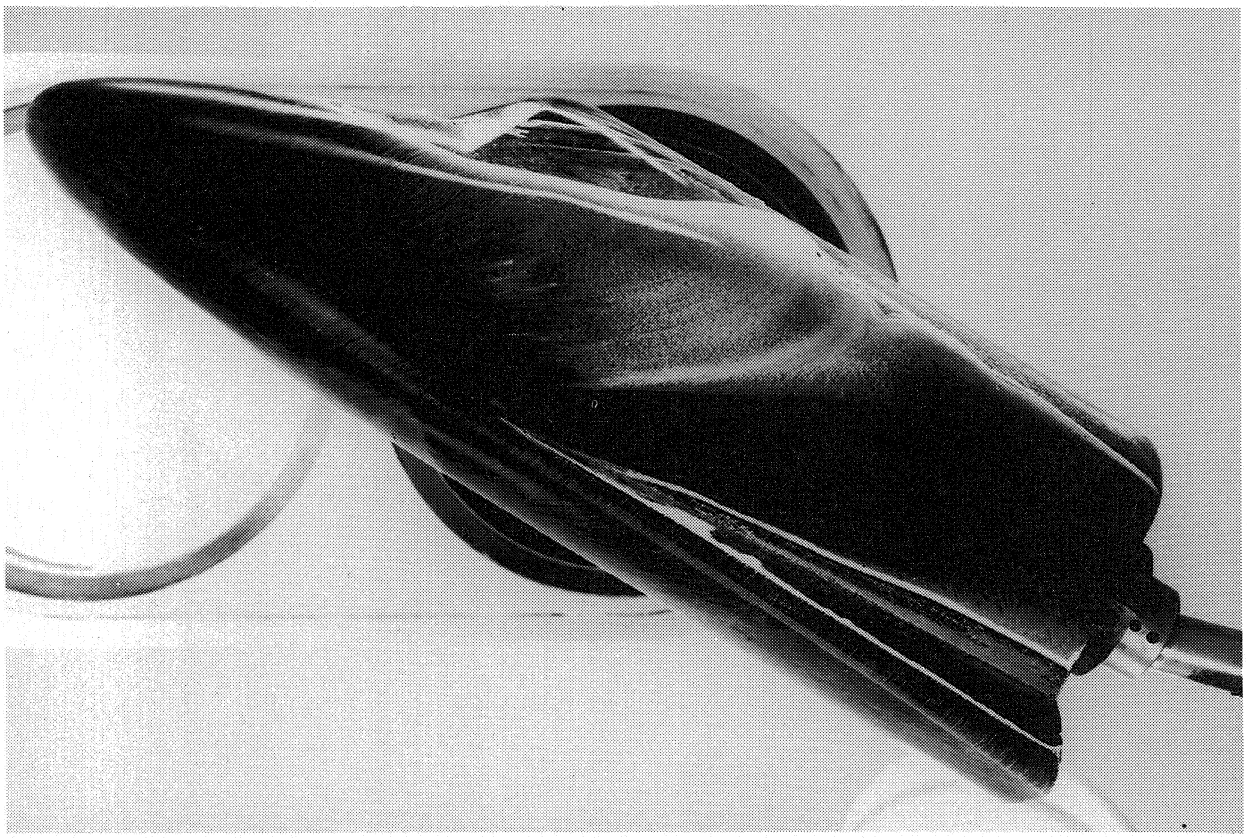

Figure 17. Oil flow patterns on the fuselage side without penetrations.

Attempts to correlate the lee side data on the orbiter involved several parameters: film coefficient ratio (h_L/h_O), Stanton number (ST), modified Stanton number (ST/M_∞), and Nusselt number (Nu) versus Reynolds number per foot (Re/ft), Reynolds number at each location ($RE_{\infty L}$) and angle of attack (α). The data trends on the orbiter upper surface were similar to that of Apollo in that the film coefficient ratio increases with increasing Reynolds number but not with the same magnitude or slope .

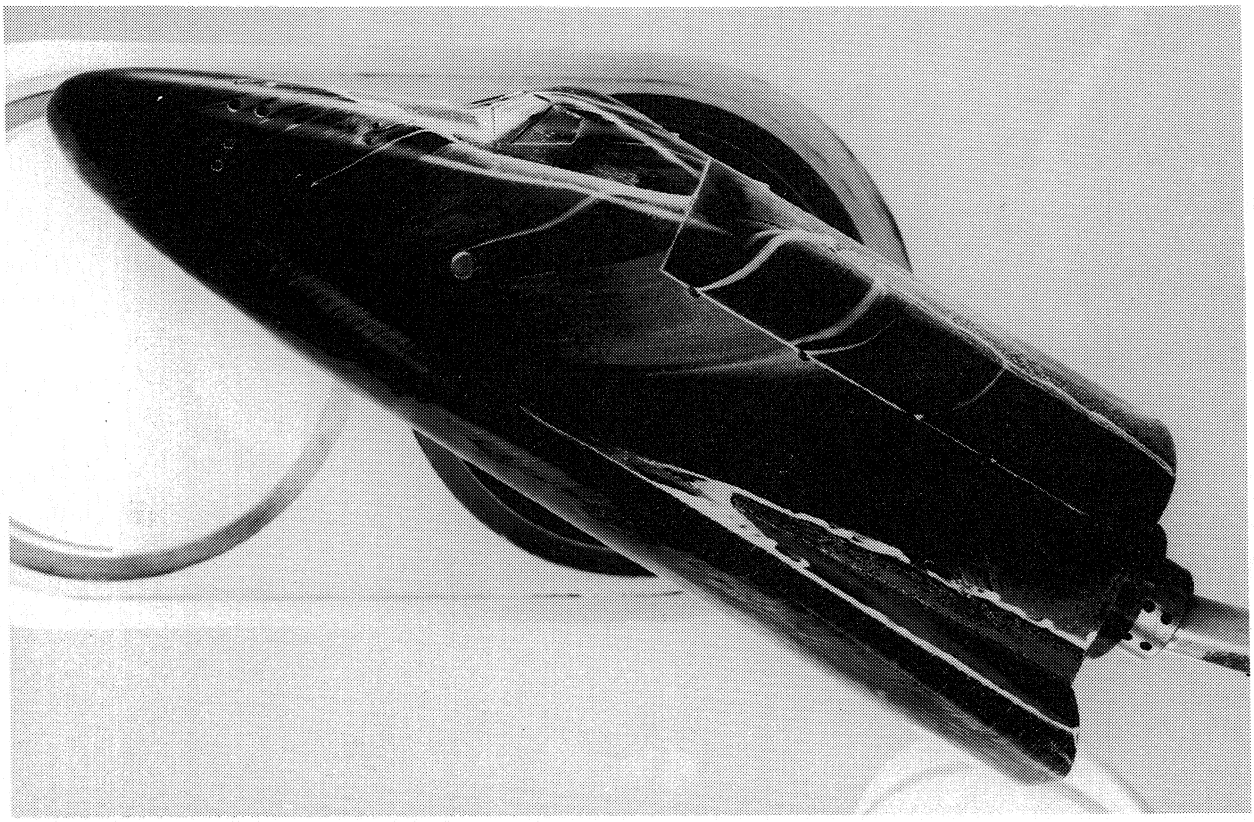

Figure 18. Oil flow patterns on the fuselage side with penetrations.

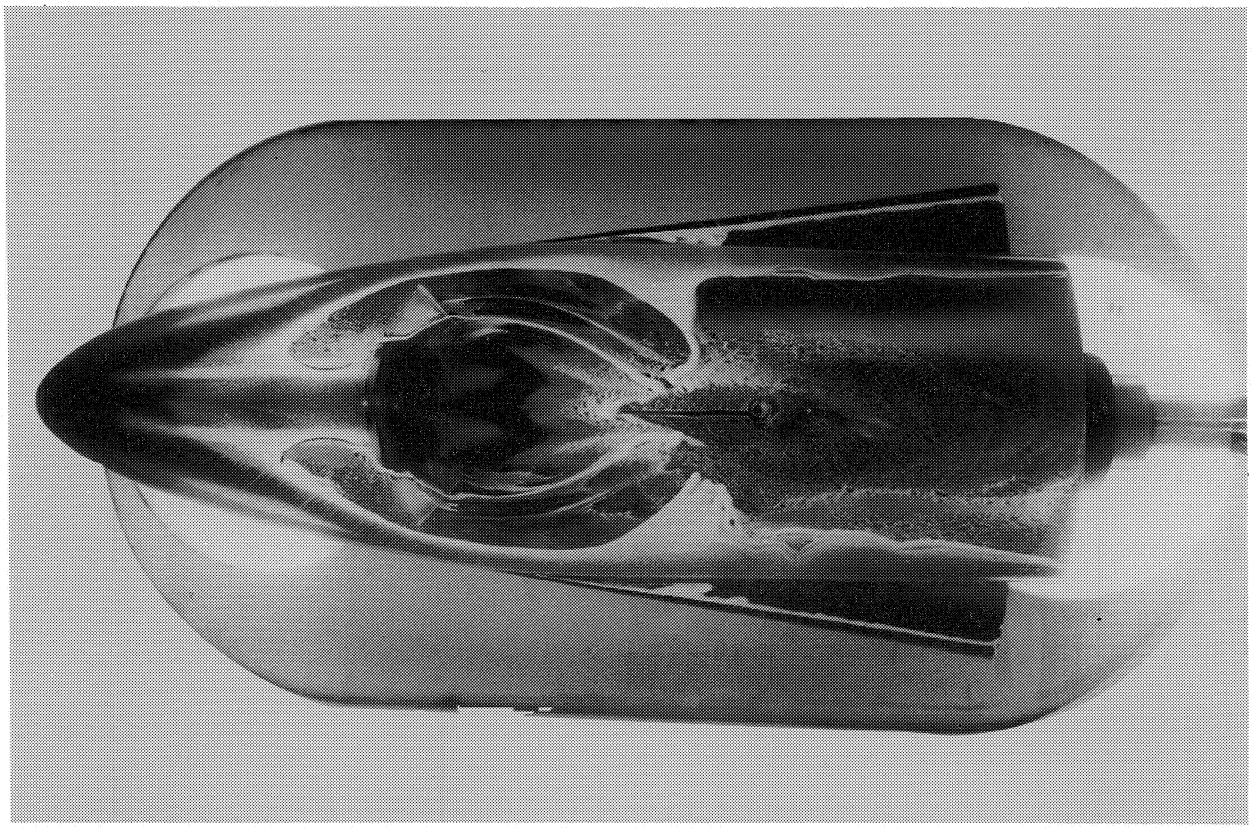

Figure 19. Oil flow patterns on the orbiter upper surface without penetrations.

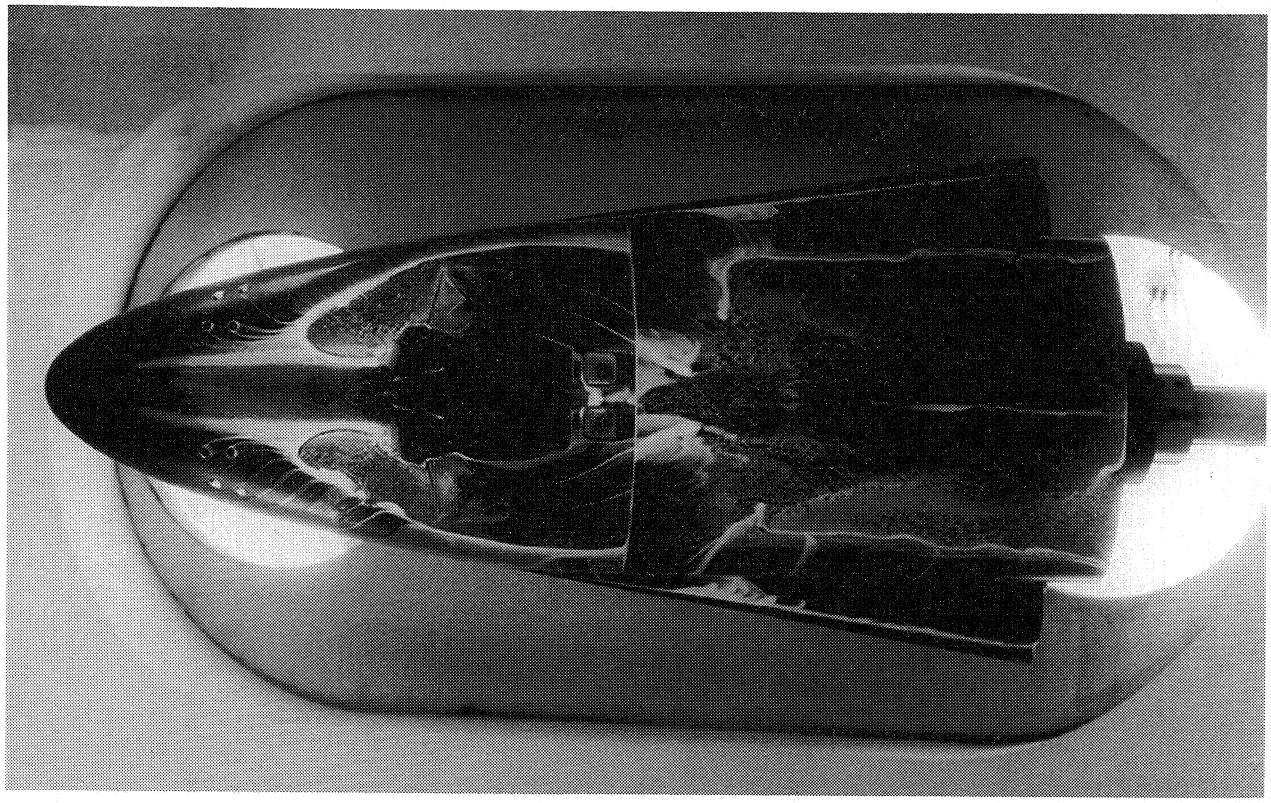

Figure 20. Oil flow patterns on the orbiter upper surface with penetrations.

For the shuttle, film coefficients were correlated in terms of ratios that vary with angle of attack and were modified to account for varying Reynolds numbers. The ratio of film coefficients with Reynolds number was fitted with one straight line per angle of attack. The ratio of the maximum heating to the minimum heating at the maximum and minimum Reynolds number was correlated as a function of angle of attack. These correlations were scaled to flight conditions based on flight freestream Reynolds numbers. Figure 21 presents this approach on the fuselage side. The portion of the figure on the left shows the heating on a sidewall trace at a constant vertical dimension for $\alpha=30°$ and $Re/Ft=0.5x10^6$. The center portion shows the X/L=.4 location with angle of attack and a fixed Re/Ft. The right portion shows the variation with Re/Ft for a fixed location and angle of attack.

A specific boundary layer transition criterion was not established for the leeward surfaces. However, the wind tunnel data which were applied directly for predicting the design heating were correlated with Reynolds number on the premise that this correlation would properly account for the effects of the boundary layer state.

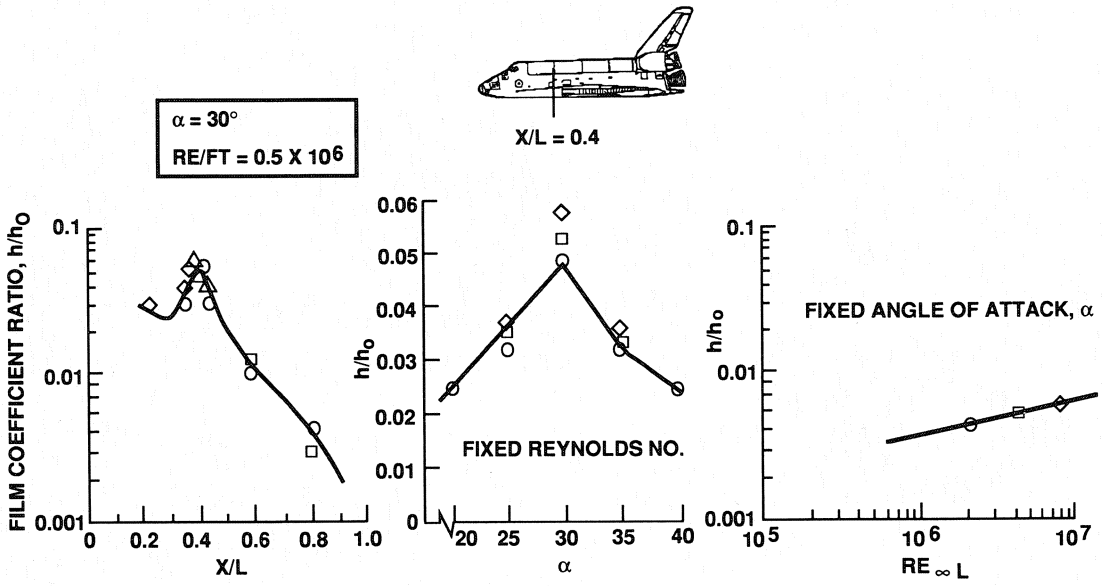

Figure 21. Typical correlation approach for the leeside regions.

Wing Upper Surface and Elevon

The wing and elevon upper surface experienced flow phenomena that complicated data correlation and extrapolation to flight conditions. The upper surface of a wing above 30° angle of attack would generally be thought of as being in separated flow. There were, however, several external forces acting upon the shuttle wing. The jet/shear layer developed due to the wing leading edge/fuselage bow shock interaction scrubbed the wing upper surface at approximately 82.5-percent semispan. This was based upon M=8 wind tunnel testing up to α=40°. Above α = 45° there appeared to be no vortex interaction effect on the wing upper surface. The scrubbing action of this disturbance is shown in the M=8 AEDC oil flow data, Figure 22. It was estimated that depending on the flight condition, the shear region would move a maximum of 10-percent of the wing span inboard compared to wind tunnel data.

This data showed the oil being scrubbed away from the leading edge region due to the relatively high shear levels compared to the rest of the wing upper surface. The effect of the vortex scrubbing was readily evident on the outboard portion of the wing.

Flow on the elevon was influenced by the recirculating wake flow and carried forward to the hinge line, causing the trailing edge to be hotter than forward chord locations. When the elevons were deflected to a positive position (into the flow), the heating was more severe than zero or negative. This was due to a more normal surface being available for the flow to impinge upon.

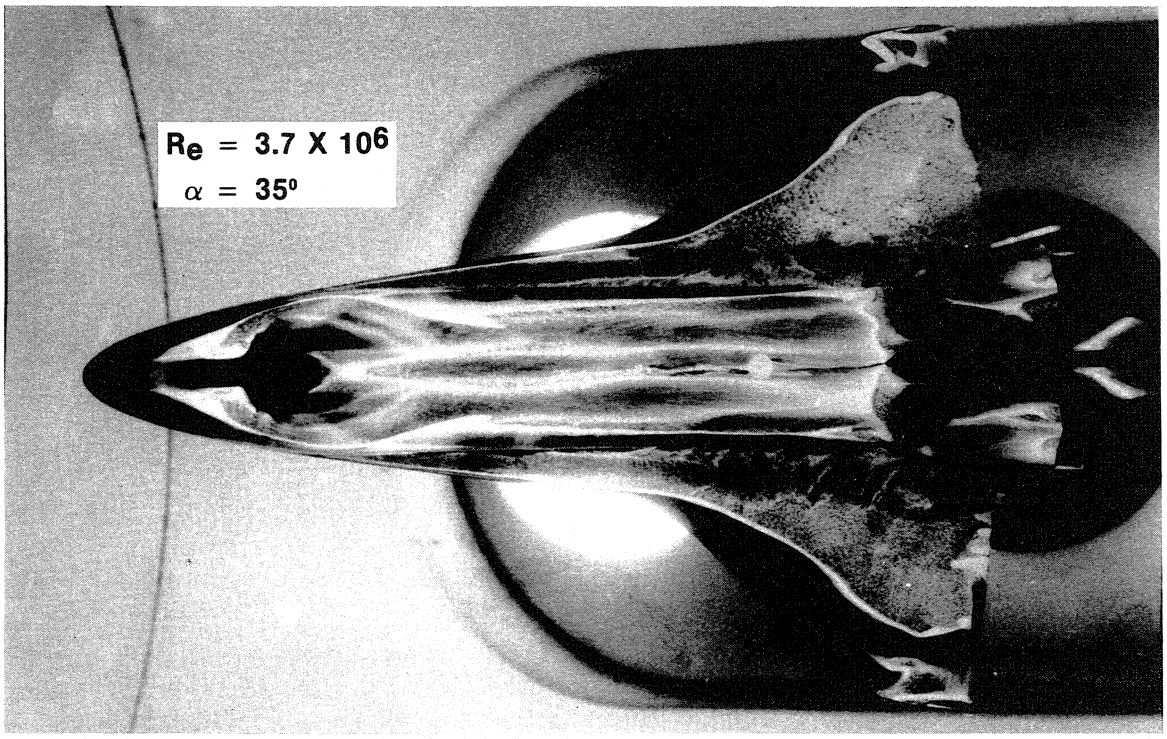

Figure 22. Oil flow visualization of wing upper surface vortex scrubbing.

Heating to the wing upper surfaces was correlated in terms of film coefficient ratios, which were a function of angle of attack and free stream Reynolds number based upon wind tunnel data. The lowest heating on the wing upper surface was at the mid-chord station, with the heating increasing fore and aft of that station. The limit on the minimum heating level was imposed at a film coefficient ratio of 0.002. This limit was based on an uncertainty analysis of the test data. Increasing alpha tended to increase the heating.

Unique Heating Phenomena

There were several unique aeroheating phenomena that impacted the orbiter aeroheating methods. Two of those are discussed in this section: surface catalytic effects and boundary layer transition. Shock impingement and vortex impingement are discussed in other sections of the paper.

Surface Catalytic Effects

The lower surface of orbiter is covered with silica tiles with a reaction cured glass, RCG, coating. This glass/silica coating inhibits to some degree the recombination of atoms in the dissociated boundary layer air. This reduction in recombination results in a reduction in energy in the boundary layer and a reduction in the surface temperature of the TPS tiles. If the surface had been an uncoated metallic TPS (fully catalytic) equilibrium temperatures would have been expected.

The design of the orbiter TPS was accomplished by predicting heating based on the assumption of equilibrium flow. This was done for two reasons: uncertainty in knowing the catalytic effects and as a design margin.

An inability at the time of TPS sizing to predict non-equilibrium boundary layer heating and a lack of knowledge about catalytic behavior of the TPS tile coating precluded a design approach based on these phenomena. However, results from plasma arc heater tests during the TPS development test program indicated the inhibiting characteristics of the tile baseline coating might reduce aerodynamic heating. As a result of the TPS development program insight into catalytic effects was developed. This was due to the fact that TPS testing was conducted in arc tunnels at NASA Ames and Johnson Space Center. To understand arc jet test heat fluxes and resulting TPS surface temperature, there was a requirement to understand the impact of the plasma arc heater disassociated air flow over the TPS test article. This was also done to understand the impact and ability to scale TPS tile step data from plasma arc testing. This resulted in the development of a relationship whereby the computed heat flux was compared with a computed radiation equilibrium heat flux. During the test program, the heating to the TPS coating in a plasma environment could be approximated by using Equation 4 of Reference 9.

$$q_{TEST} = q_{EQ}\left[\frac{H_{AW} - H_W - \eta H_D}{H_{AW} - H_W}\right] \qquad (4)$$

η was found to be 0.7 ± 0.1. However, characterization of the dissociation non-equilibrium gases produced by the arc heaters was difficult and the tile coating was often contaminated. These phenomena precluded a confident update of the aeroheating prediction methods prior to the first flight.

However, during the Shuttle's first five flights data became available to verify and enhance a predictive approach. These results are discussed later under the flight test section of this paper.

Boundary Layer Transition

Boundary layer transition was one of the major challenges for the space shuttle orbiter aeroheating methodology development as it would be for any hypersonic vehicle. However, most of the effort prior to the shuttle program had been related to cones and flat plates. These studies and research had been more experimentally directed than configuration related. Some transition data existed from the X-15 and possibly the Apollo program, but did not find their way into the shuttle program.

Today linear stability codes, which are being used on the NASP program and supersonic laminar flow control work, are available to help understand and predict transition. However, in the shuttle time frame these tools were not available. This necessitated a different approach.

Design Philosophy In addressing boundary layer transition predictions for the orbiter, the design philosophy was to assume a "smooth" surface. For the shuttle, a "smooth" surface was defined as a surface whose roughness was such that it would not result in transition earlier than that which was predicted to occur based on correlations developed based on wind tunnel models. Today someone might want to modify this approach to be transition based on that which would be experienced based on quiet tunnel testing as in the NASA Langley quiet tunnel or based on linear stability analysis.

However, it was anticipated that the wind tunnel derived transition criteria and onset locations would be conservative and accommodate some effects of vehicle roughness under actual flight conditions. This was justified due to the noise that radiated from the turbulent wind tunnel walls in the facilities where the shuttle orbiter was tested.

One thing that made boundary layer transition so difficult to model was that it was affected by many parameters: pressure gradients, surface to free stream temperature ratio, free stream Mach number, free stream turbulence noise, 2D and 3D roughness, and shock impingement.

When the basic design trades of the orbiter configuration were performed, consideration was given to the sensitivity of certain geometries featured on boundary layer transition. Some of the features considered were nose shape, wing glove position, and fuselage / wing lower surface blending.

Smooth Surface Transition Work on predicting the orbiter boundary layer transition began early in the Shuttle program with many approaches being investigated. After several studies, the $Re\theta/M_L$ parameter was selected as the design parameter for Shuttle transition prediction. Wind tunnel test data were the primary means used to determine the boundary layer transition onset criteria.

In determining boundary layer transition onset, wind tunnel test data was compared with laminar flat plate theory for different span locations on the orbiter fuselage and/or wing as shown in Figure 23. Transition onset was defined as the point where wind tunnel data departed from the theoretical laminar flow solutions.

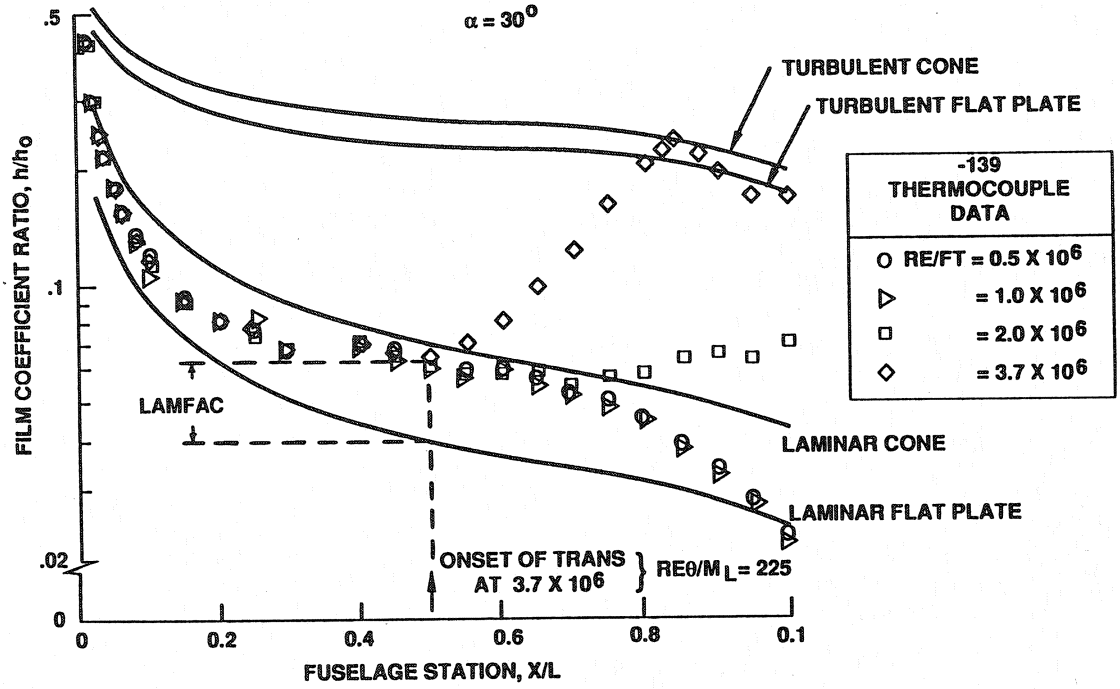

Figure 23 . Transition onset determination from heating data.

At the point where onset occurred, the $Re\theta/M_L$ values for a flat plate were calculated. The $Re\theta/M_L$ at that point was adjusted by the laminar factor by dividing the momentum thickness by LAMFAC. This resulted in the basic correlation shown in Figure 24. As the span increased the value of $Re\theta/M_L$ decreased . On the lower centerline a value of 225 was indicated while on the outboard portion of the wing $Re\theta/M_L$ was less than 100. This basic approach was further refined to separate out the angle of attack effects as wind tunnel data base was refined for the final shuttle configuration. This indicated $Re\theta/M_L$ values between 250 and 300 for the fuselage centerline which decreased to as low as 60 at the 90% wing span, due to the impact of the wing shock interaction.

Roughness Induced Transition Basic to the understanding of shuttle TPS tiles and their associated steps and gaps on transition was the orientation of the tiles to the flow streamlines. Exploratory wind tunnel tests were performed on smooth orbiter models that were grooved to simulate tile gaps. It was discovered that groves parallel (rectangular pattern) to the surface streamlines produced strong boundary-layer tripping disturbances, whereas grooves perpendicular (diamond pattern) to streamlines produced weaker disturbances, Figure 25. Subsequent experiments indicated that a 15° angle between gap and flow direction was sufficient to avoid the

parallel gap tripping effect. It was also learned from this exploratory wind tunnel data that the width of tile gaps affected transition. As the gap width increased, transition occurred at lower and lower Reynolds numbers.

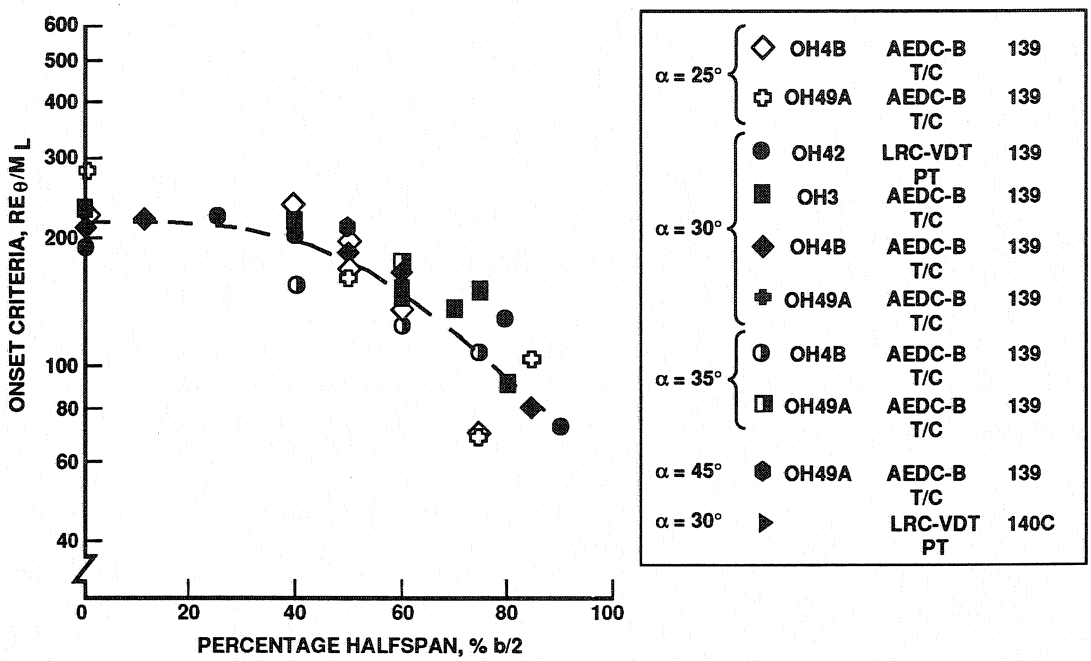

Figure 24. Basic smooth wall boundary layer transition criteria

To develop analytical techniques to define the allowable TPS installation tolerances impact of roughness on transition and further relate the completed orbiter surface configuration to the observed transition during flight, existing wind-tunnel-based boundary layer transition research was used. It was presumed that transition would be caused by single or isolated roughness elements that were three dimensional.

It had been demonstrated that in supersonic flow three-dimensional roughness (spheres) were more effective trips than two-dimensional roughness (wires perpendicular to flow). By analogy, tile edges where the step and gap were uniform would be thought of as two-dimensional roughness and tile corners or intersections as three-dimensional roughness. If the tile edge and corner steps were the same, then the corner would produce the dominant disturbance.

Figure 26 shows schematically how three-dimensional roughness size variation affects transition location. In section A of Figure 26, between 1 and 2, the roughness has little effect on the natural or smooth wall transition, indicating that the roughness disturbances do not dominate the boundary layer before they decay. The region between 2 and 3 is characterized by a small

change in roughness size, causing a large change in transition position with roughness size when transition is close to the trip. Point 3 is defined as the "effective trip" size, i.e., the smallest trip that will cause transition near the trip element. For the first flight assessment, only the left side of Figure 26, section A, up to point 3 is of interest. Section B of Figure 26 shows the effect of increasing trip size.

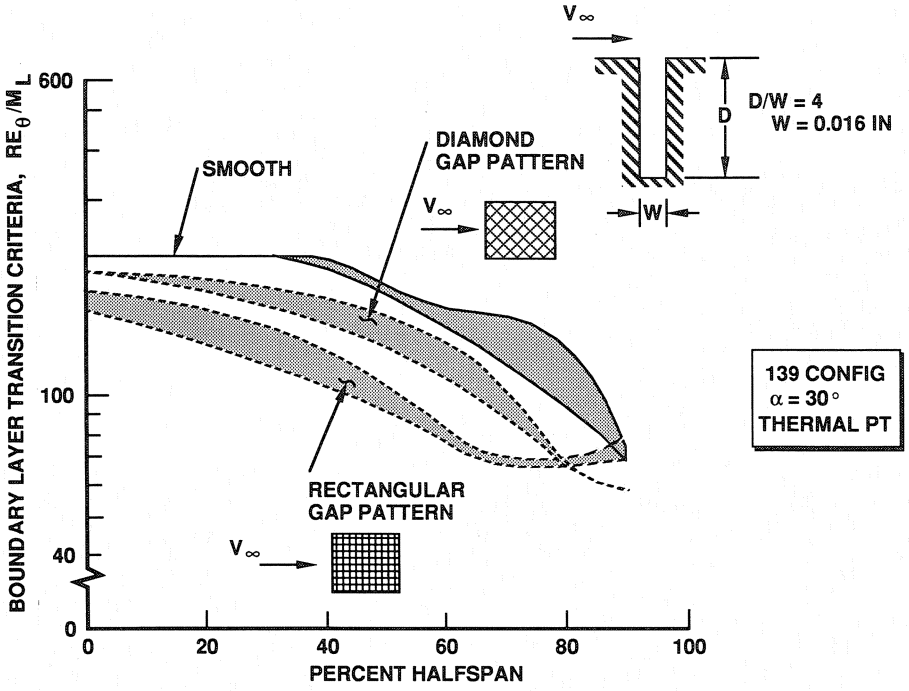

Figure 25. Effect of gap patterns on boundary layer transition.

The boundary layer was very discriminating as to the roughness sizes that affect transition. Since the roughness distribution was not expected to be uniform, a relatively small number of discrete roughnesses were expected to cause transition; and there was a low probability that these disturbances would interact with one another. The conclusion was that single-roughness-element transition research would be an appropriate basis for the analytical tools. From Reference 10, Equation 5

$$Re_k = 33.4\left[1+0.90\left(\frac{T_W}{T_\delta}-1\right)+0.28\left(\frac{T_{AW}}{T_\delta}-1\right)\right]Re_{xk}^{1/4} \qquad (5)$$

represented the conditions for an effective spherical element trip. This equation was for flow on a cone and includes variations in Mach number and heat transfer. The bracketed term in Equation 5 was nearly equal to $(\delta^*/X_k)\sqrt{Re_{xk}}$. Empirically, Equation 6 represented a slight improvement:

$$\frac{\delta^*}{x}\sqrt{Re_{xk}} = 1.09\left[1+0.90\left(\frac{T_W}{T_\delta}-1\right)+0.28\left(\frac{T_{AW}}{T_\delta}-1\right)\right] \qquad (6)$$

Substituting Equation 6 into Equation 5 yielded:

$$\frac{k}{\delta^*} = 30.7 Re_{xk}^{-1/4} \qquad (7)$$

which included heat transfer and compressibility effects for flow over a cone. Equation 7, which matched the data of References 10 and 11 about as well as the previous equations, was used to extrapolate the orbiter flight conditions.

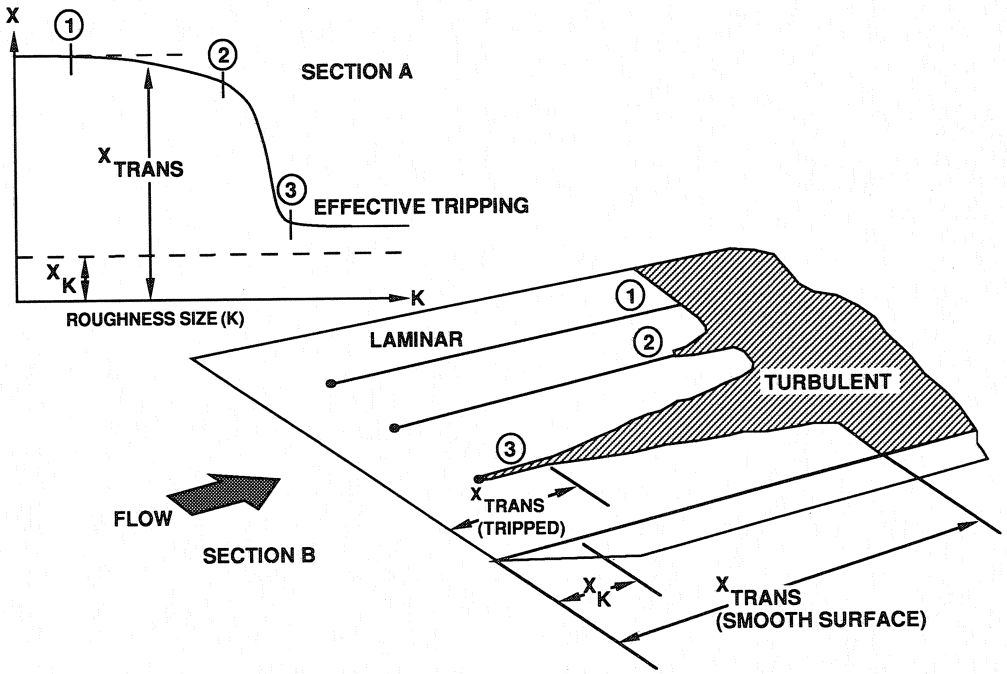

Figure 26. Description of roughness produced transition.

Wind tunnel tests were performed at the Arnold Engineering Development Center Tunnel B at M=8 to verify the applicability of Equations (5) or (7) for the orbiter configuration. These tests used a 0.04 scale model of the orbiter forebody (X/L<0.5). For the first series of tests, spherical roughness was mounted on the model at X/L=0.05, 0.11, or 0.17. The models were solid copper forward of the trip to provide an isothermal boundary layer from the stagnation point to the roughness. Aft of the trip, the models were made of an alumina-filled epoxy; and the phase change paint technique was used to obtain transition data. The roughness elements were spheres with diameters of 0.015, 0.020, 0.025, and 0.031 inch. These data are compared with the cone data of Reference 10 in Figure 27.

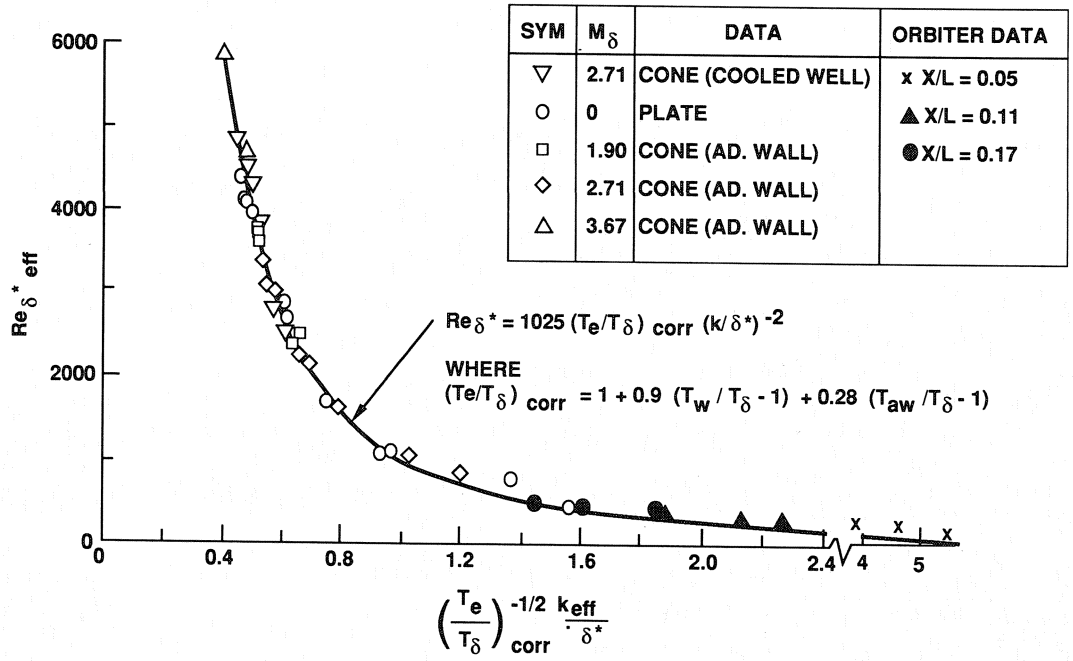

Figure 27. Effective transition data correlation including compressibility and cooling.

With the above correlation of K_{EFF}/δ^*, a means of determining a value of K with the tile system as installed or as allowed to be installed was available.

In varying from spherical trips to the TPS tile system, several factors had to be considered. Based on test data, in-line gaps between the tiles were effective trips and were influenced by both gap width and gap depth. This configuration was avoided in the orbiter tile layout wherever possible. Steps in combination with gaps (not parallel to flow) were more efficient trips than steps alone. Based on wind tunnel test data, tile steps were twice as efficient trips as spheres.

In dealing with the TPS tile system, an "equivalent" roughness was defined that incorporated the tile to tile geometry. For transverse gaps, the equivalent roughness involved tile to tile forward facing steps (K) and gap widths (G) so that the equivalent roughness became that of equation (8).

$$K_{EQ} = \sqrt{\left[K^2 + (G - 0.045)^2\right]} \qquad (8)$$

A gap width of 0.045 inch or less was assumed not to influence roughness.

For longitudinal gaps which were filled with gap fillers, the equivalent roughness was a function of the tile to tile step (K) and the area in the gap above the gap filler (A) as shown in Equation 9.

$$K_{EQ} = \sqrt{\left(K^2 + K_G^2\right)} \tag{9}$$

where

$$K_G = \sqrt{1/2 A} \tag{10}$$

Localized Flow Interactions

In addition to the orbiter acreage, localized regions of the orbiter required special attention due to severe gradients in both pressure, velocity, and thereby heating. Examples of these localized flow interactions were the elevon-elevon gap, aft OMS pod side, subsurface flow, and the SILTS pod. The elevon-elevon gap and the SILTS pod are discussed in this section. The aft OMS pod side and subsurface flow are discussed under the flight test section.

Elevon-Elevon Gap

The orbiter elevons were divided into inboard and outboard elevon sections for aerodynamic control with each section separated by a gap. This gap presented several design challenges relative to local geometry and sealing. It also created complex flow phenomena. Early wind tunnel tests did not model the gap properly but did indicate the flow phenomena based on both paint and oil flow testing. These tests were later updated with a detailed elevon-elevon wind tunnel model. Figure 28 shows the elevon-elevon gap model mounted in the wind tunnel with the upper surface of the model visible.

This test provided valuable information as to both flow field definition and heating levels. Figure 29 shows oil flow data on the elevon/elevon gap at 40° angle of attack with the inboard elevon deflected at + 5°. As can be seen from this figure several flow phenomena occur in the vicinity of the gap. Using this type of data a flow model was developed, Figure 30. This figure shows the streamline patterns in the region of the elevon-elevon gap based on both paint and oil flow data. The streamlines upstream of the gap formed approximately a 15° angle with the orbiter centerline. As the flow approached the gap it sensed a drop in pressure due to the gap and communication with the upper surface lower pressure levels. The streamlines curved between 35° and 50° with the centerline. On the outboard elevon based on oil flow tests there was a region of high shear emanating a short distance (13 inches) aft of the hinge line. It appeared that some of the oncoming boundary layer (inboard elevon) spilled into the gap; however, the outer portion of the boundary layer flow impinged on the outer elevon edge.

Heating on the inboard elevon adjacent to the elevon-elevon gap was modeled as disturbed flow, impacting both laminar and turbulent heating levels but not boundary layer transition onset. This was based on the paint data. Factors were applied to undisturbed heating levels to match the disturbed heating levels.

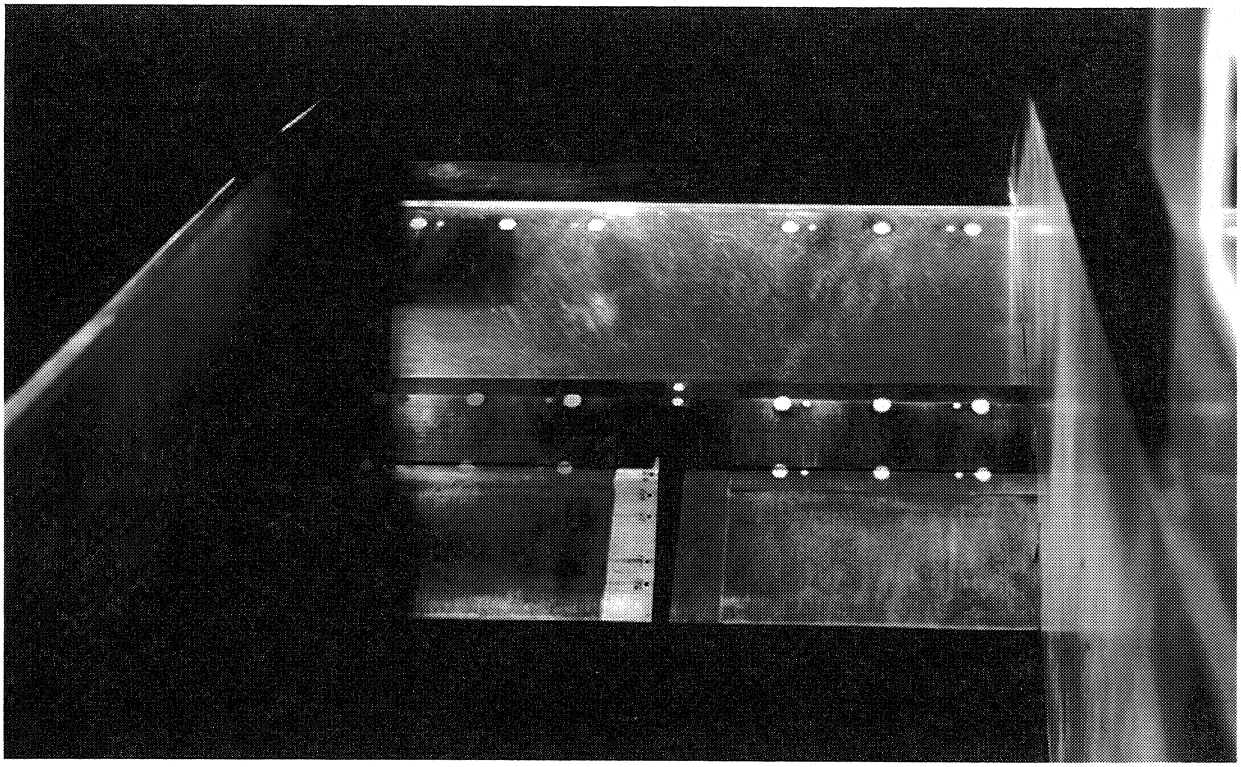

Figure 28. Elevon-elevon gap model.

The outboard elevon near the gap was influenced by tripped turbulent flow and impinging turbulent flow. The wind tunnel data was modeled by having the flow become turbulent after leaving the inboard elevon and then using a flat plate theory with a short (9-inch) running length. This method applied to the region closest to the gap.

Analysis of the elevon-elevon test data indicated a heating distribution into the gap as shown in Figure 31 based on laminar flow. This curve was referenced to the heating on the elevon lower surface and covered an angle of attack range between 30° and 40° and elevon deflections between -10° and +5°. It was assumed that the same curve would apply for turbulent reference heating. As indicated by this data, heating for up to four inches into the gap was equal to or greater than the outer elevon surface.

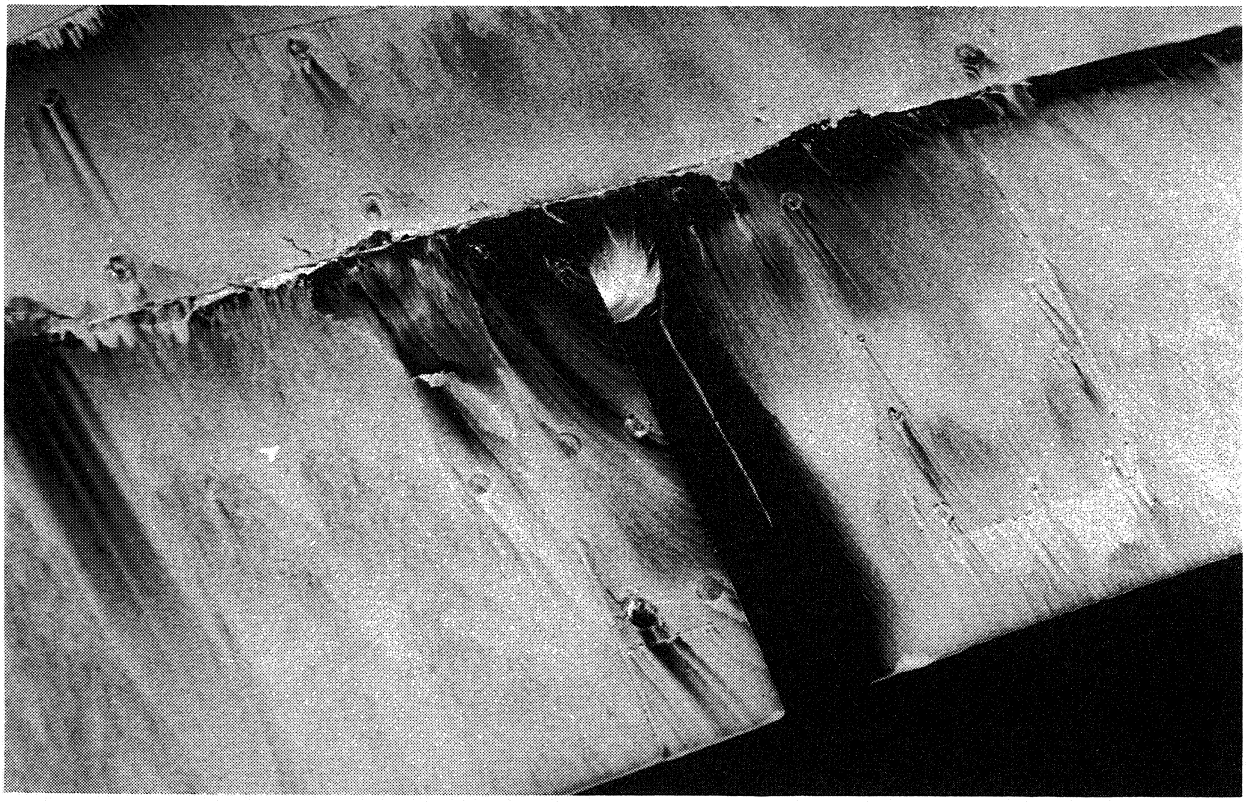

Figure 29. Elevon-elevon gap oil flow patterns.

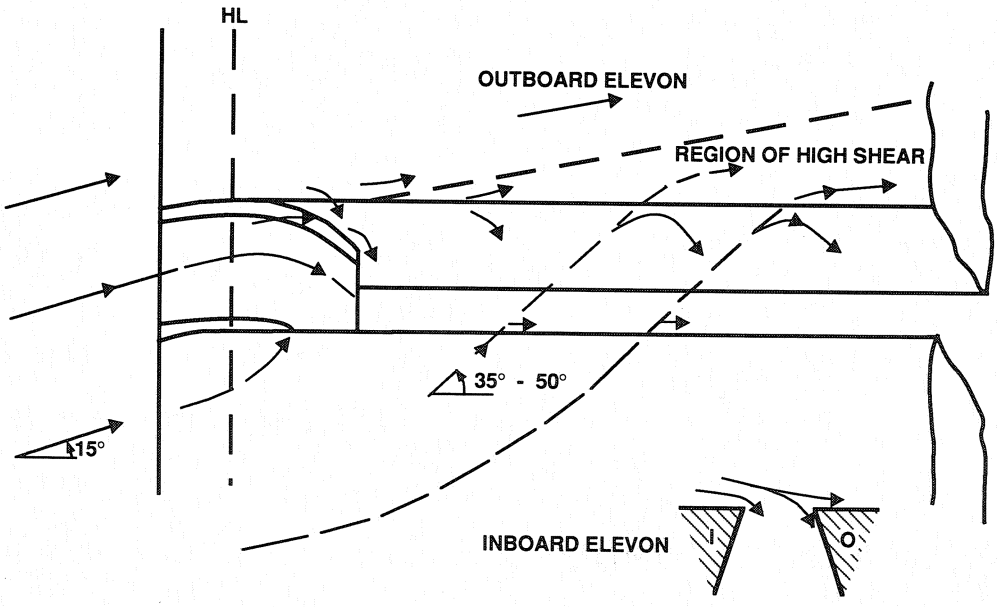

Figure 30. Elevon-elevon gap flow field patterns.

This test, however, had the flow in line with the gap and did not simulate the outboard elevon with impinging flow. For this type of flow the heating should drop off at a faster rate with distance into the gap (z). The gap heating distribution curve was modified to account for impinging flow. As will be discussed later in flight testing, this region turned out to be one of the hottest regions on the orbiter.

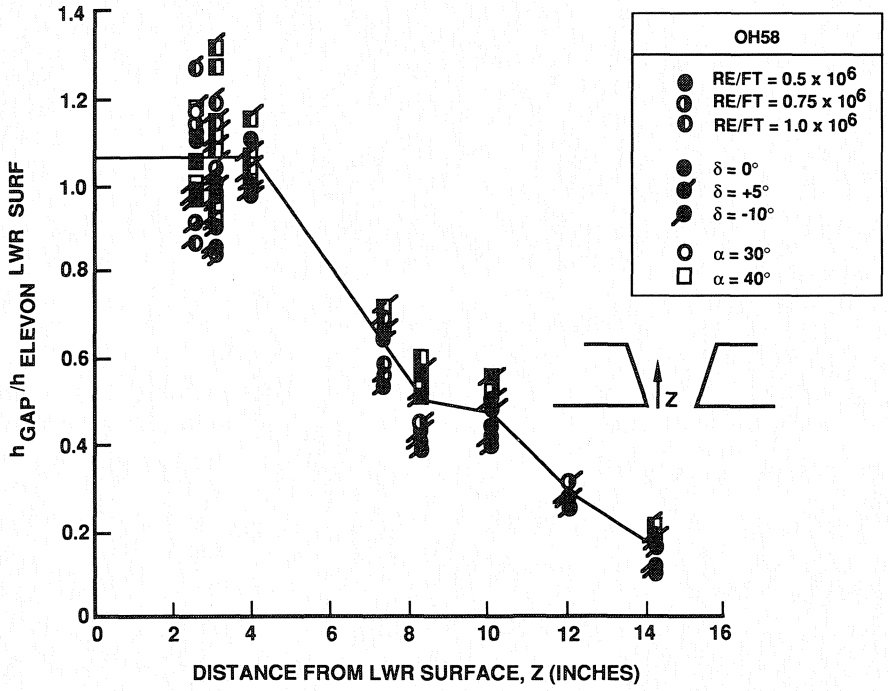

Figure 31. Elevon-elevon gap heating distributions.

SILTS Pod

One of the major Shuttle orbiter experiments, OEX, was that of the SILTS experiment. The SILTS, Shuttle Infrared Leeside Temperature Sensing, experiment consisted of a pod on the vertical tail of the orbiter to measure leeside surface temperatures to complement the TPS surface instrumentation. The pod contained an infrared camera that viewed the orbiter upper surfaces through two window cavities cooled by liquid nitrogen, Figure 32.

Wind tunnel testing was undertaken to understand the environments in the vicinity of the pod and the actual heating to the pod surfaces, especially in the vicinity of the windows. The challenge in developing methods for the front face of the pod was that of model scale. The SILTS pod relative to the entire orbiter was relatively small and therefore presented instrumentation challenges.

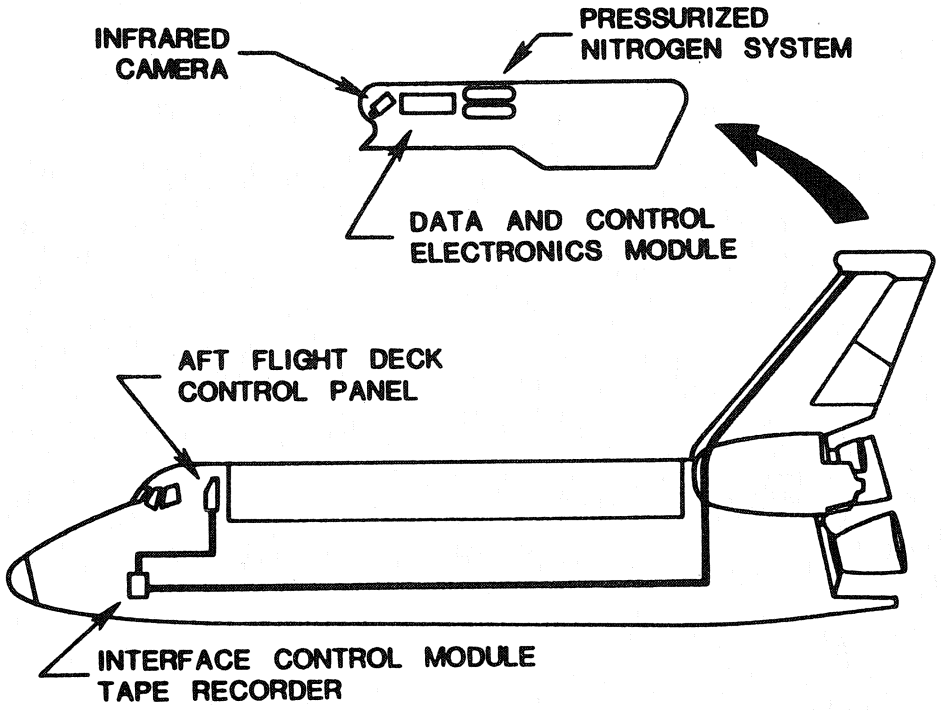

Figure 32. SILTS experiment system schematic.

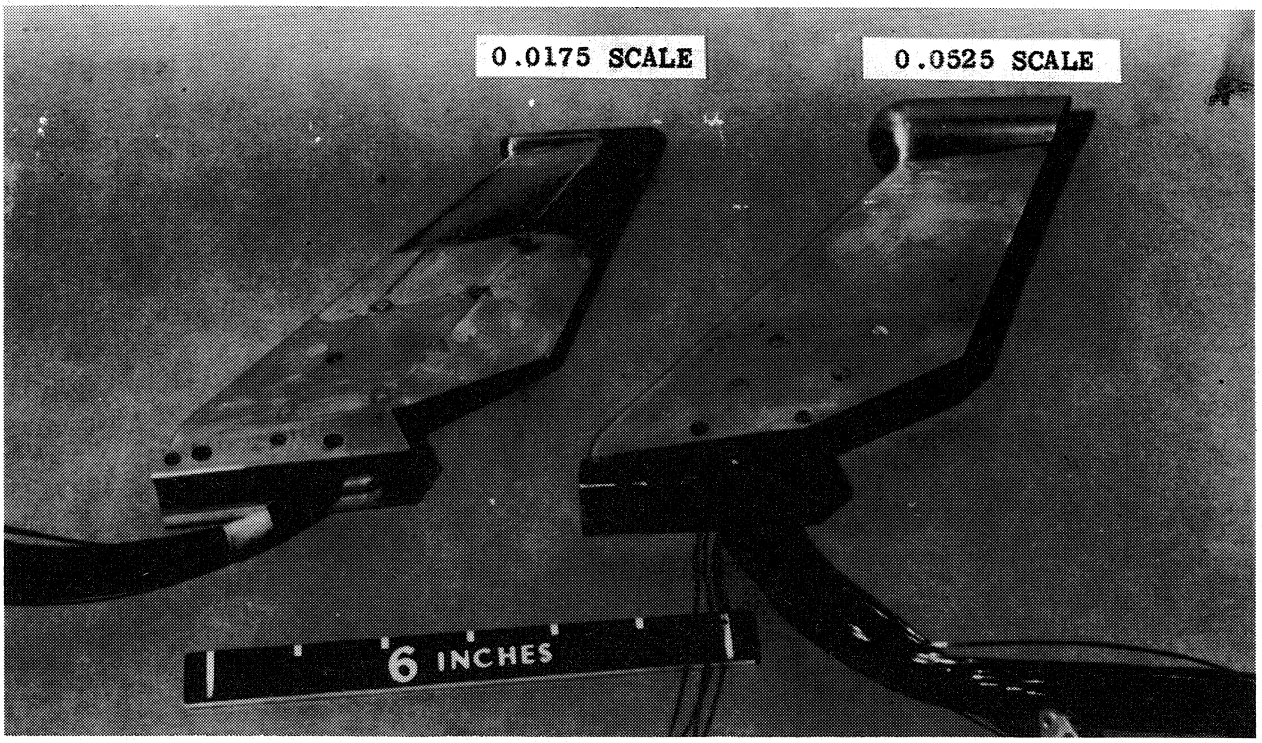

Figure 33. Comparison of two different scaled SILTS pods.

Figure 33 shows two vertical tails with the SILTS pod attached. The 0.0175 scale pod was geometrically consistent with the orbiter model on which it was attached. However the 0.0175 scale pod was so small that it couldn't be instrumented accurately with thermocouples so a larger 0.0525 pod was developed. This pod allowed more thermocouples to be installed allowing the maximum heating levels and locations to be determined as presented in Figure 34. Both vertical tail-pod combinations were tested in combination with the orbiter wind tunnel model at the AEDC facility under M=8 conditions for Reynolds numbers between Re/Ft=0.5x10^6 and 3.7x10^6. Data was obtained at angles of attack of 0°, 30°, 35°, and 40°.

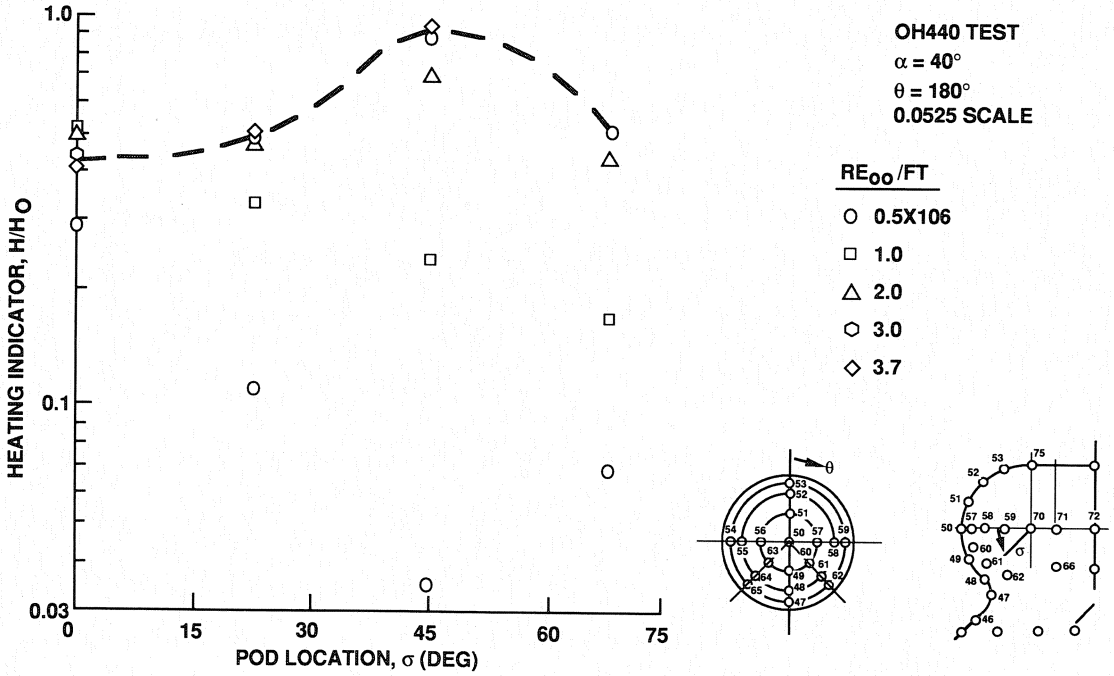

Figure 34. Heating distribution on the 0.0525 scale thermocouple pod.

A second series of tests were conducted using the thin film gauge instrumentation technique. This technique allowed high density instrumentation on the dome face and the surrounding areas, Figure 35. This model was tested at Calspan at M=11 and M=16 providing higher Mach data than had been obtained in the AEDC testing. By using a thin film gauge technique areas of peak heating were verified for the correct geometry scale. This technique also allowed interference effects to be obtained.

Test data results from ground testing at both AEDC and Calspan are shown in Figure 36. As shown all of the data indicated the peak heating to be at 45° off the horizontal. Also shown is that the 0.0175 scale thermocouple model under predicted the heating level possible due to the large

gradients and heat conduction. From a test techniques point of view, the 0.0525 thermocouple model with the larger pod situated at the correct vertical station matched the same heating levels as the smaller thin film gauge data.

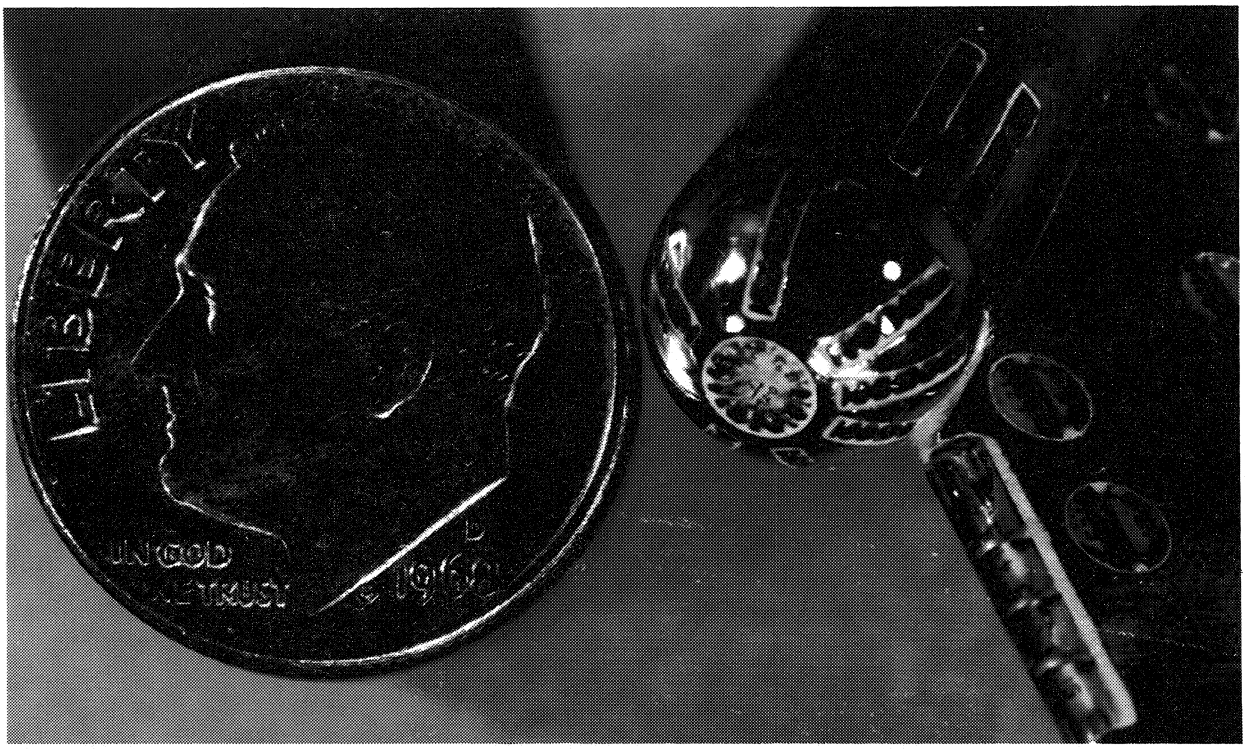

Figure 35. Thin film gauge instrumentation location on SILTS pod.

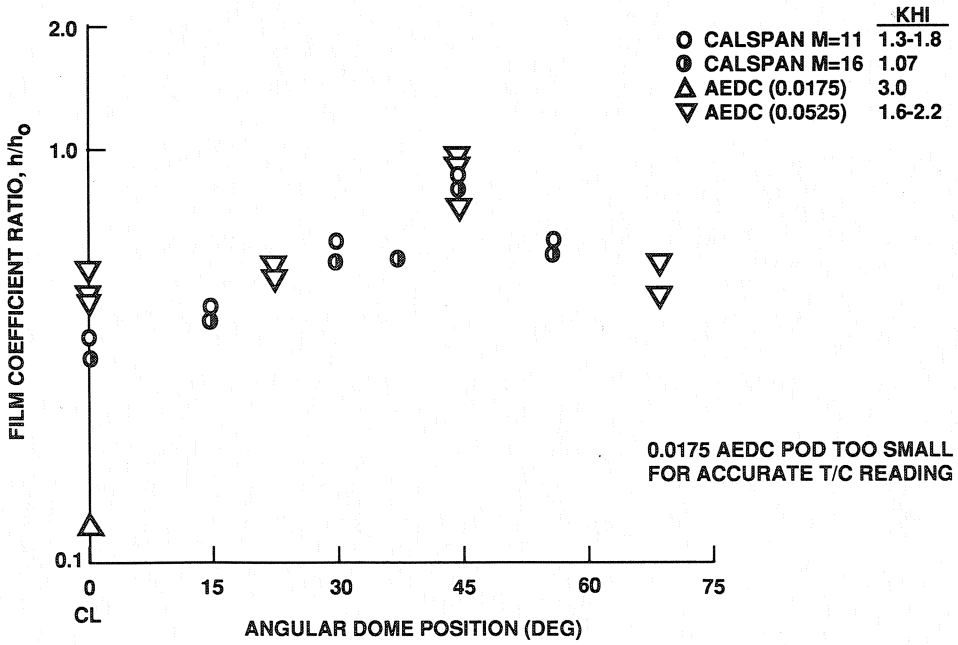

Figure 36 . CALSPAN and AEDC heating data match on the SILTS pod.

Uncertainty Definition

The philosophy for the shuttle orbiter heating methodology development was to develop methods based on nominal fits of the experimental data. Then, prior to the first flight, uncertainties would be taken into account. Heating with uncertainties would be used to assess the first flight and verify that no TPS or structural failures were anticipated and that there were no safety of flight issues.

The process of developing uncertainties on heating considered many factors. First and foremost the scatter in wind tunnel data was used. However scatter in data was not blindly used. If a few points were outside the main scatter band they were not included in the uncertainty analysis. Uncertainties in the local properties of pressure and velocity were assumed and heating uncertainties calculated. Basic theories were examined for potential uncertainties. In some instances, the origin of flow was uncertain and that was considered. Uncertainties in the impact of control surface deflections and shock impingement on heating were also considered. In the wing leading edge region, one major uncertainty was scaling to flight the effects of the double shock effects. All of the uncertainties were then root sum squared, RSS'd, together to develop an uncertainty factor. Rather than developing an uncertainty number for each heating location on the vehicle, this process was applied to regions on the orbiter as shown in Figure 37.

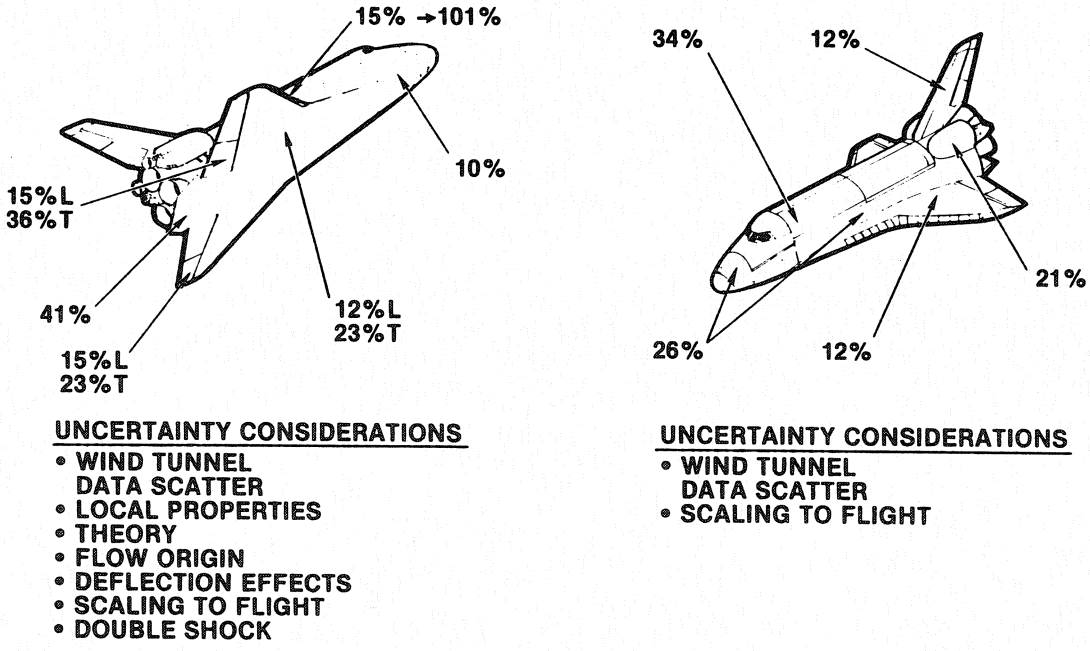

Figure 37. Aeroheating uncertainties definition for STS-1.

For the first flight, STS-1, heating estimates were made with nominal methods for both the nominal trajectory and dispersed trajectories, and uncertainties were applied to the nominal trajectory as well. Based on this analysis approach no safety of flight issues were estimated due to aerodynamic heating for the first flight of the Shuttle.

FLIGHT TEST PROGRAM

In this section the orbiter flight test program is described as well as instrumentation used to obtain aeroheating test data. Some of the flight test anomalies are identified. Emphasis is placed on comparisons of flight test data with ground test predictions.

The Shuttle flight test program to validate the aeroheating methods consisted of essentially the first five flights STS-1 through STS-5. However, due to issues that arose during these initial flights and requirements to expand the operational envelop, aeroheating data was obtained on additional operational flights.

The orbiter entry trajectories were shaped to be benign from an induced thermal point of view. This was accomplished by each flight having a vehicle angle of attack of 40° throughout most of the entry, Figure 38.

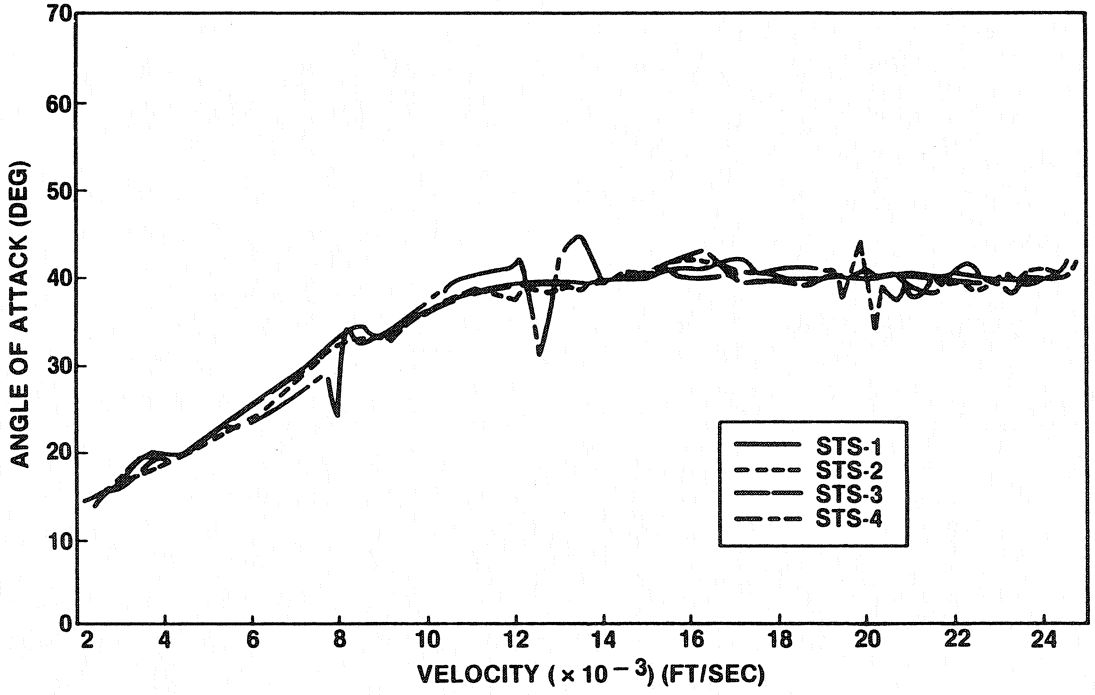

Figure 38. Angle of attack variation during the first five flights.

In addition, the orbiter entered the atmosphere from low Earth orbit inclinations between 28.5° and 40°, allowing relatively low cross ranges on the order of 720 nautical miles or less. This was important since the TPS was designed and sized for the Western Test Range,WTR. This meant the structural temperatures would be below design values. Emphasis was placed on maintaining adequate structural temperature margins during these flights. All five orbiter entry trajectories were similar, though STS-3 and STS-4 flights had slightly increased surface temperatures and reduced entry flight time. Control surface deflections varied somewhat but other than the body flap, the elevon did not reach its maximum test deflection. Several flight test maneuvers called push over-pull up, POPU, were performed which also provided additional angle of attack aeroheating data.

Unfortunately because of a malfunction of the orbiter flight data recorder, aeroheating data during STS-1 and STS-4 were lost except that which could be transmitted after black-out. Therefore, on these two flights, aeroheating was only available after approximately 950 seconds. Pressure data was obtained on two flights and calorimeter data on only one flight of the first five orbiter flights.

Flight Test Instrumentation

To support calibration of the pre STS-1 wind tunnel based methods several types of instrumentation were used. Flight test data for aeroheating focused on two areas: temperature/heating rate and pressure. For the acreage regions of the orbiter entry aeroheating data were primarily obtained from data with instruments installed in TPS tiles. However, data was also obtained with instruments in AFRSI and FRSI blankets, and radiometers for the RCC regions covering the nose and leading edge regions.

Thermocouples used in TPS tiles, such as the high temperature HRSI tiles, were installed such that the thermocouple was in contact with the reaction cured glass (RCG) tile coating. These instruments were fabricated using 10 mil platinum - platinum 13 percent rhodium wire. Thermocouples in contact with the tile coating were supposed to provide surface temperature readings. Unfortunately not all thermocouples were installed in the ideal manner. This led to the need for thermal modeling of the thermocouple later in the flight test program so that thermal lag and the actual surface conditions could be taken into account.

In addition to surface thermocouples, pressure taps through tiles or blankets were also used. Surface calorimeters were used in limited locations on the fuselage lower surface. These instrumentation locations are shown in Figures 39, 40, and 41.

For areas of the orbiter where surface temperatures were such that reinforced carbon-carbon, RCC, was used, validation of predictions was based on radiometer data. Thermocouples had been considered early in the shuttle program, but were abandoned due to concerns over degrading structural integrity of the RCC panels, the ability to bond the thermocouples, and rapid degradation of the thermocouples bond. This led to the use of radiometers, a device that functions in conjunction with a lens system that directs incident thermal energy into a thermopile sensor, to measure leading edge heating. The sensor was calibrated with a known temperature. The sensor/lens was mounted in a copper heat sink to maintain the radiometer within a specified temperature range. Five radiometers were installed on the left hand orbiter wing to measure temperature in the range of 320°F to 3000°F.

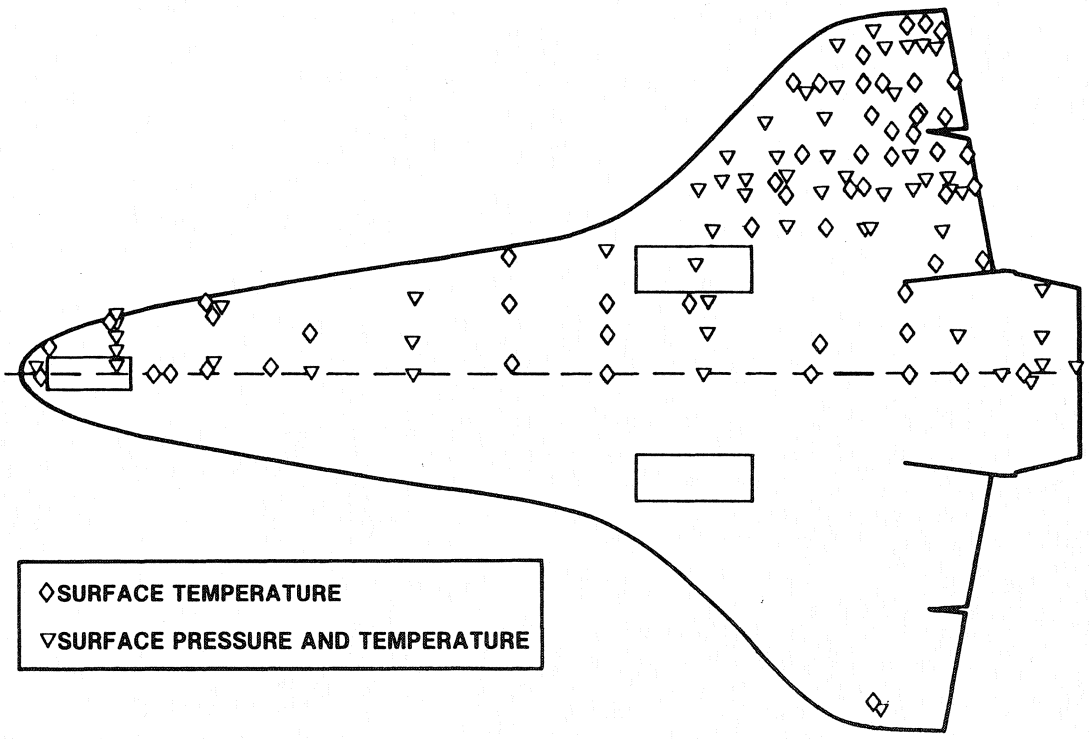

Figure 39. Orbiter lower surface instrumentation locations.

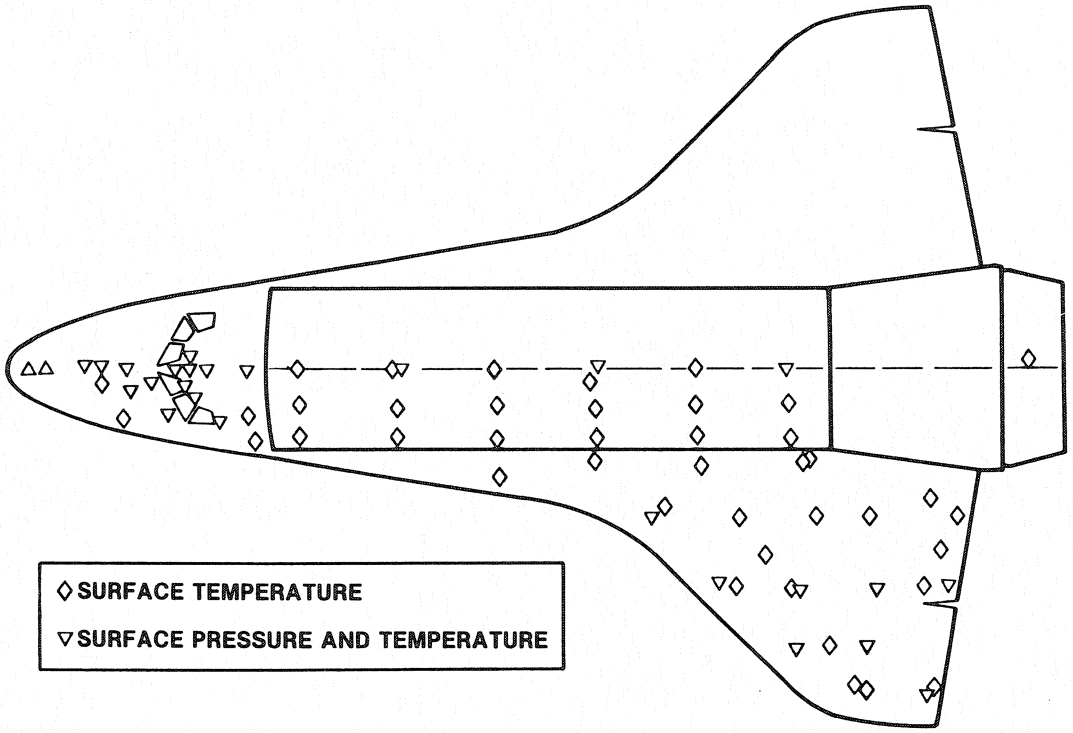

Figure 40. Orbiter upper surface instrumentation locations.

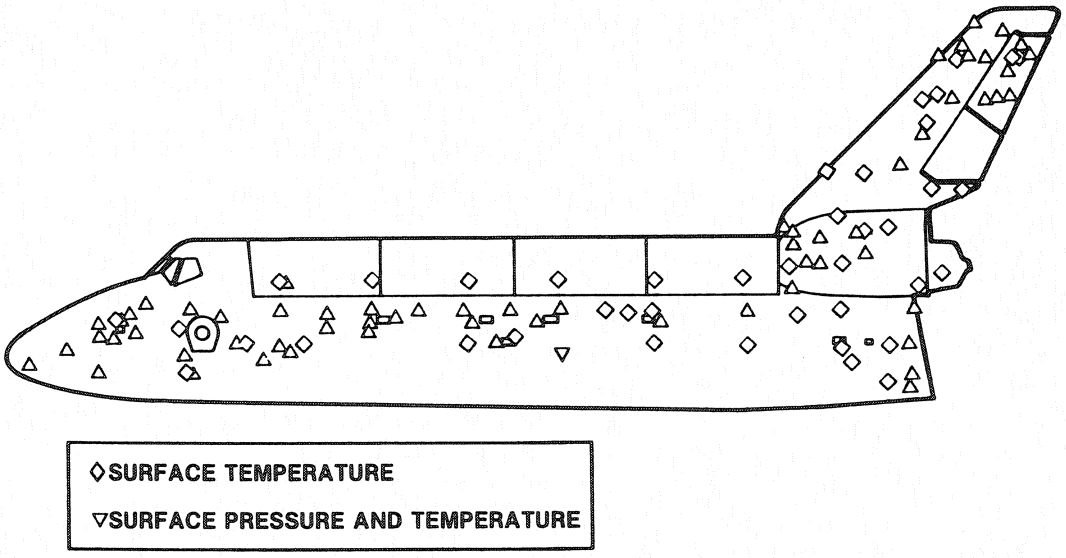

Figure 41. Orbiter side surface instrumentation locations.

Flight Test Anomalies

Several anomalies occurred during the first flight relative to aeroheating that impacted methods:

- Heating on the fuselage side due to vortex impingement was stronger than modeled with wind tunnel data resulting in an over temperature on the TPS low temperature insulation, FRSI. The area impacted by vortex impingement was also different under flight conditions. This resulted in a TPS redesign on the fuselage side.

- Impinging vortex flow on the forward OMS pod was also greater than wind tunnel derived methods. This also caused an over temperature of the FRSI and resulted in a design change by replacement of low temperature insulation with a larger region of high temperature insulation, HRSI. This vortex also served as a mechanism to trap and focus debris on the OMS pod.

- Impinging flow on the aft OMS pod side was stronger than measured in the wind tunnel either due to wind tunnel modeling, scaling to flight, or control surface deflection influences. The impact of how high energy flow could traverse significant distances was not understood prior to flight.

- Damage to TPS tiles due to debris, usually ice, resulted in premature boundary layer tripping and early transition to turbulent flow. TPS tile installation, steps and gaps, also significantly impacted transition. However, these impacts on transition were correlatable.

- Local pressure gradients set up by tile to tile steps and subsurface leak paths created charring of the TPS tile filler bars and over temperature of structure in one incident.

Flight Test Results

The first five orbiter flights provided a wealth of hypersonic flight data which were used to calibrate aeroheating methods and to enhance prediction techniques. The flight test data can be summarized by the following points.

- The simple geometry theory approach provided remarkable agreement with flight test data,
- Local pressures generally matched predictions,
- Partially catalytic effects were present,
- Boundary layer transition was impacted by surface roughness. However, transition occurred later than predicted for the first flight but sooner than for a smooth body,
- Turbulent heating levels were overestimated above M=10,
- Leading edge heating scaled directly, but the leading edge shock impingement effects were greater than direct scaling, and
- Vortex flows scaled differently than based on ground data.

Fuselage Lower Surface

In comparing the flight test data with preflight predictions on the fuselage lower surface, one obvious conclusion can be drawn. The fully catalytic (equilibrium) preflight predictions were significantly higher than the flight data, especially near the nose. As shown in Figure 42 surface temperatures at an entry time of 450 seconds were over predicted by almost 400°F and peak temperatures by 200°F for a location 2.5% aft of the nose. With increased distance from the nose the benefits of surface catalycity diminished. As indicated there was a good match between theory and data for the entire trajectory.

Another observation, Figure 43, was that using the adjusted Spalding & Chi turbulent theory was acceptable below M=10 but the theory tended to over predict for turbulent flow at higher Mach numbers. Peak turbulent temperatures were over estimated by almost 250°F using this approach. Spalding & Chi theory had provided a good match with wind tunnel test data but that was at M=8. This indicated that effort was needed to find a better match for turbulent flow at high Mach number flight. This figure also showed the reduced surface catalytic effects with increased distance from the nose.

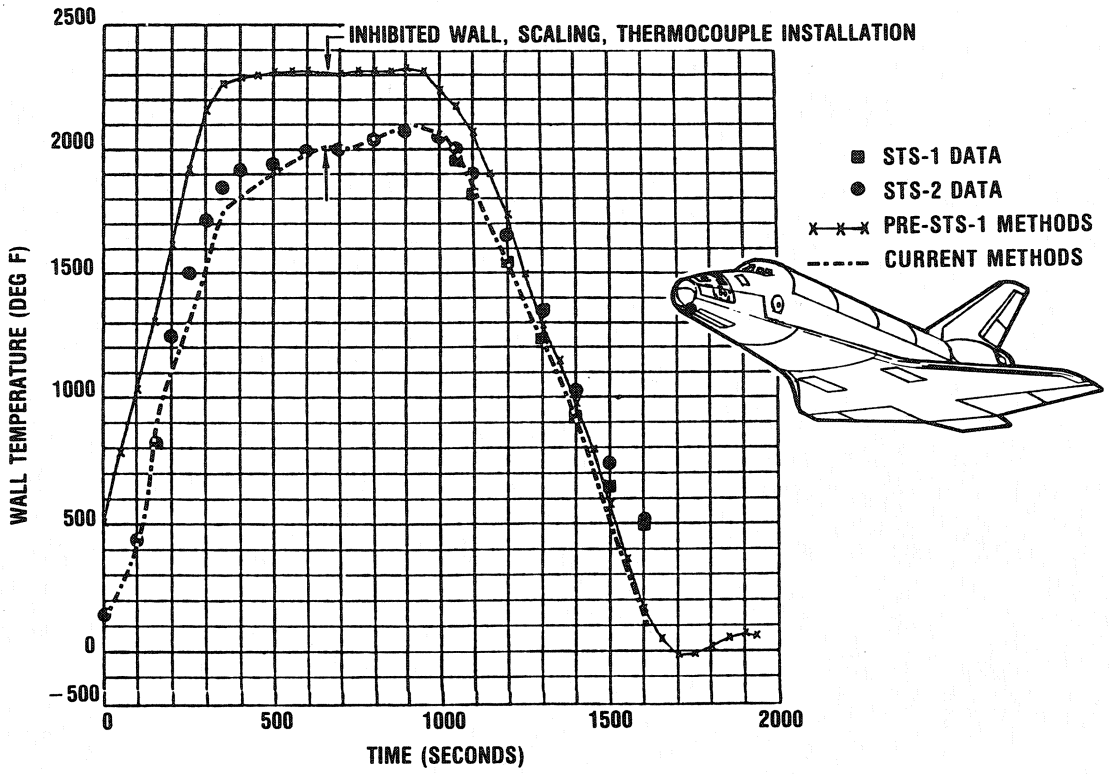

Figure 42. Fuselage lower surface temperatures at X/L=0.025.

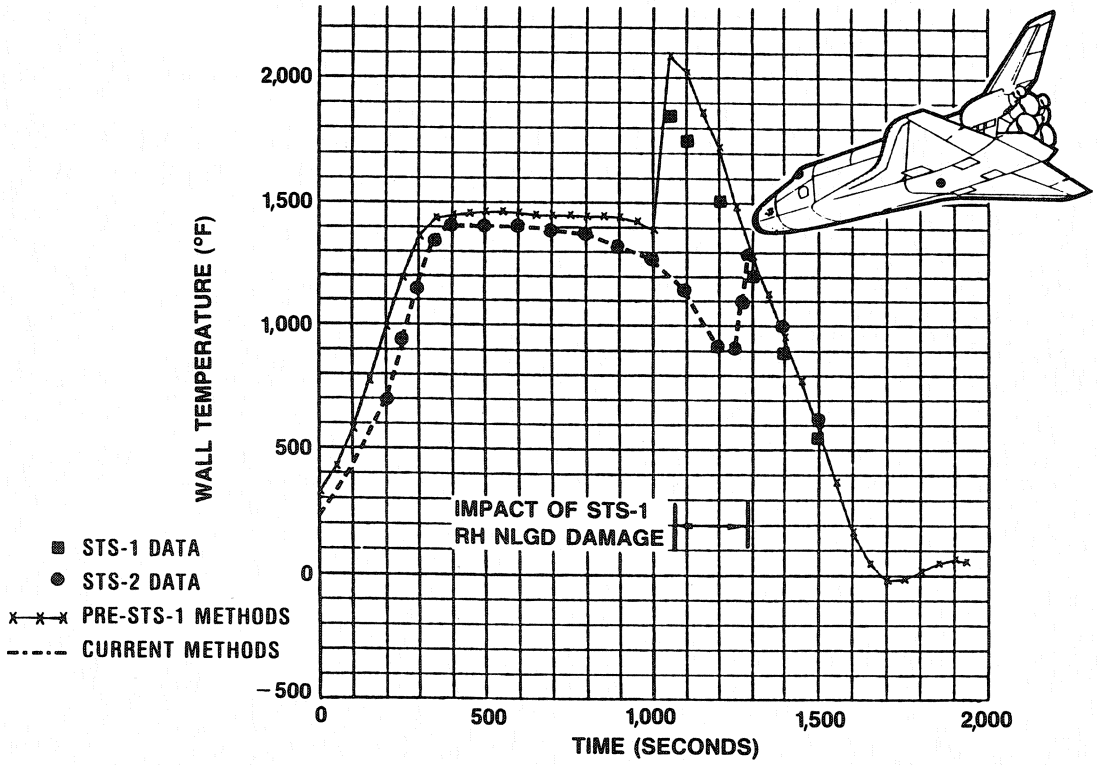

Figure 43. Fuselage lower surface temperatures at X/L=0.70.

The pre STS-1 approach of using wind tunnel verified techniques for predicting pressures did very well in matching flight test data. The local pressure levels (low pressure gradient regions) on the orbiter lower surfaces were based on P_L/P as a function of freestream Mach number, angle of attack, and local geometric angles. These correlations initially determined based on wedge and cone data were modified using orbiter wind tunnel test data as indicated in Equation 11.

$$P_L/P_\infty = 0.2397 + 1.161\ M_\infty \sin\theta + 1.060\ (M_\infty \sin\theta)^2 + 0.0487(M_\infty \sin\theta)^3 \qquad (11)$$

Data from STS-3 was compared with preflight pressure prediction approach. As indicated there was a good match between theory and pressure data. This match is shown for the first 900 seconds of the mission, Figure 44.

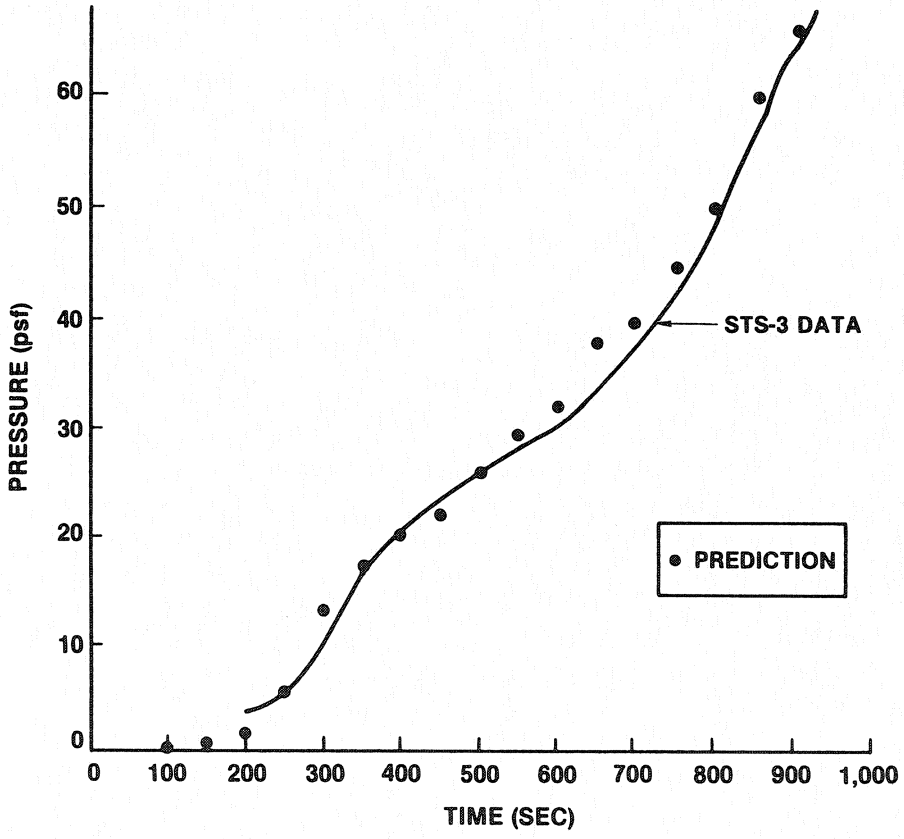

Figure 44. Comparison of pressure prediction with flight test data.

Boundary Layer Transition

In obtaining boundary layer transition flight data on the lower surface 94 thermocouples installed just under the TPS tile coating were used. Temperature data was provided at one second intervals. Figure 45 provides a typical distribution of a thermocouple time history at a location 30% aft on the fuselage from STS-2.

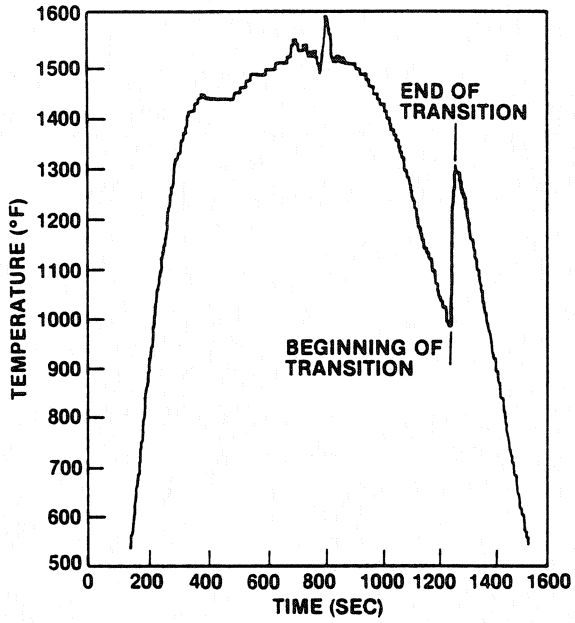

Figure 45. STS-2 Surface temperature history at X/L=0.3.

This temperature history shows that transition onset occurred at 1263 seconds while fully turbulent flow occurred at 1280 seconds. Based on the flight test data the transition period was roughly 30 seconds which equated to a transition zone of about 20% on Reynolds number. This transition zone was indicative of tripped flow. The temperature variation at approximately 800 seconds was due to a maneuver where the angle of attack was varied in a push over-pull up, POPU, maneuver.

Blumer in his analysis of the transition data, Reference 12, constructed transition patterns using turbulent spreading angles from conical flow and shuttle surface shear patterns, plus post flight inspection of roughness and TPS damage. These results are presented in Figure 46 for STS-2.

TPS tile roughness elements on the nose landing gear door resulted in the two major transition fronts on the fuselage. On the wing many transition wedges were projected due to the wing leading edge RCC attachments and tiles on carrier panels. The external tank attachment door roughness resulted in early transition in front of the body flap. Early transition on the body flap was due to the large down flap deflection on the order of 15°.

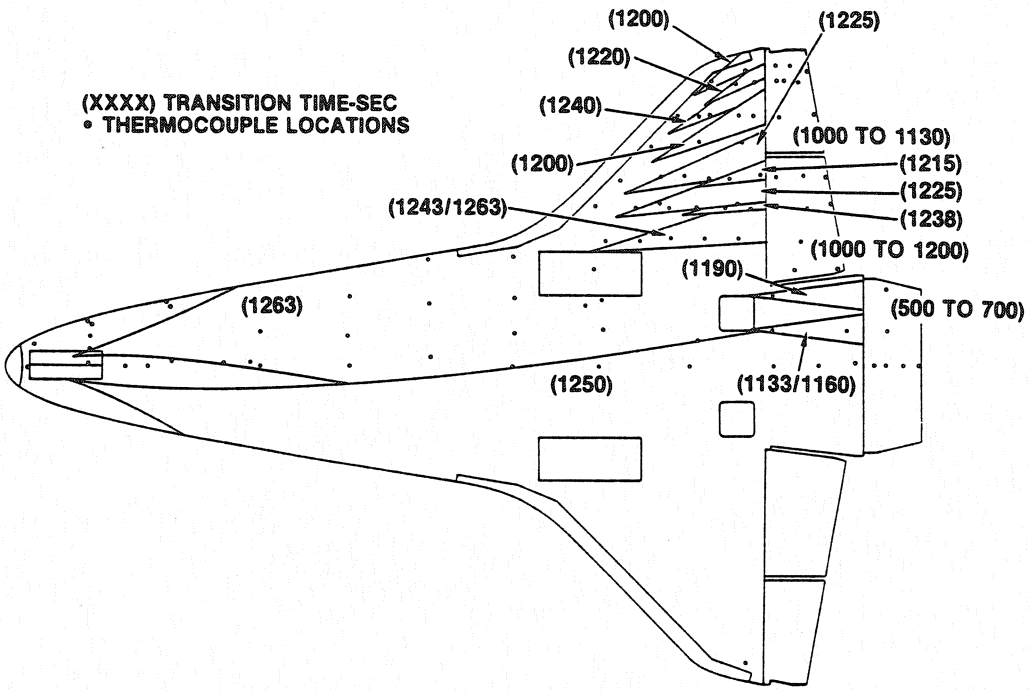

Figure 46 . STS-2 transition patterns.

In using the roughness correlation of Equation 7, the tripping data on the nose landing gear door was analyzed for each of the first five flights, Table 1. This allowed the different flight times and flight conditions to be assessed to estimate what roughness was required to predict the measured transition onset times. This approach indicated that a constant equivalent roughness of K=0.113 was present on all five flights.

Table 1 Roughness variation during the first five flights

Flight	Transition Time	Angle of Attack	Mach No.	Calculated "K"
STS-1	1252	33.6°	7.6	0.113
STS-2	1263	33.3°	8.0	0.111
STS-3	1193	32.3	7.4	0.110
STS-4	1030	40.6	10.4	0.133
STS-5	1125	36.0	8.7	0.117

Catalytic Effects

The total effects of catalytic recombination weren't really known until STS-2 due to the loss of data from STS-1. In addition to the basic tile data to understand about catalytic effects, the orbiter catalytic surface experiments sponsored by NASA Ames were conducted. These data showed a significant impact on laminar heating. By using the data from STS-2, Miller determined the impact on enthalpy of dissociation, Reference 12. He developed a semi empirical technique that modified the correlation from the arc tunnel so that heating due to catalytic effects could be estimated as shown in Equation 12. This single correlation worked for multiple locations on the orbiter and different flights. The ability of this approach to match flight test data is shown in Figures 41 and 42.

$$q_{PC} = q_{EQ}\left[\frac{H_{AWf} - Cp_f T_W - \eta H_D}{(H_{AW} - H_W)_{EQ}}\right] \tag{12}$$

$$\eta = 1 = \frac{PG\gamma_R}{h_{EQ}\sqrt{2\pi R_o Z_F T_W}} \tag{13}$$

$$\gamma_R = 0.05787 EXP\left(-6876/T_W\right) \tag{14}$$

Another phenomenon evident during the flight test program was catalytic over shoot as discussed by Stewart, Reference 13, Fully catalytic tiles were obtained by spraying standard tiles with an overcoat of black iron - cobalt - chromia spinal. The overshoot phenomena indicated that going from a partially catalytic surface to a fully catalytic surface would result in more recombination at the forward edge of the tile and less towards the back. Analysis by Rakich and Lanfranco, Reference 14, indicated 300° to 500°F above equilibrium at the front edge and 200°F at the aft end of the tile. Depending on where the flight test instrument was located on the tile would determine how much of the overshoot would be recorded. However, not all coated tiles experienced this phenomenon. Figure 47 shows the results of a possible over shoot which appeared to go away with flight test time.

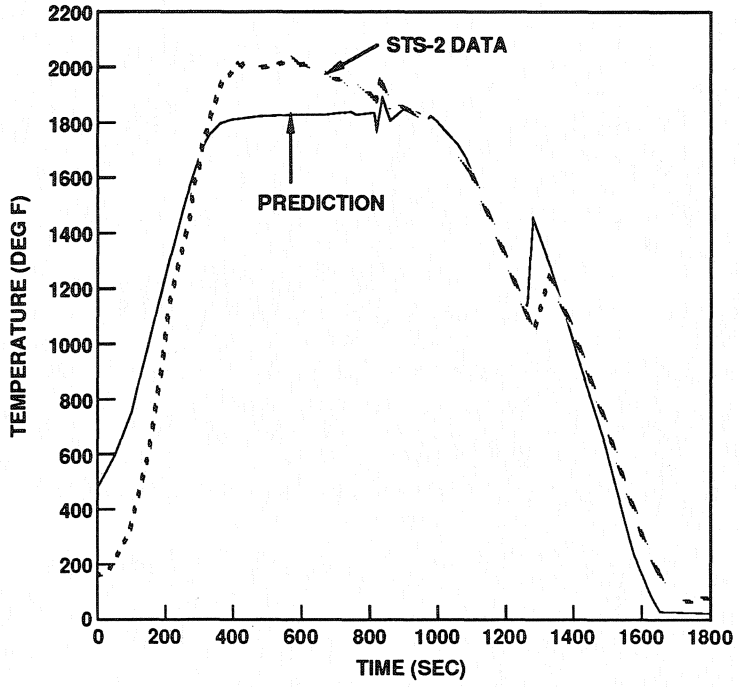

Figure 47. Potential catalytic over shoot on surface temperature.

Wing Leading Edge

Wing leading edge flight test data was obtained at four wing stations with two radiometers in the area of the fuselage bow shock impingement as discussed in Reference 15. The simple swept cylinder approach to leading edge heating resulted in excellent agreement with flight test data, Figure 48. Both STS-1 and STS-2 test data matched the preflight predictions. This data indicated agreement throughout the entry trajectory covering a wide variation in angle of attack. Based on this agreement, confidence was gained in the basic methods for moderate sweep. In areas of high sweep, ie. 40% and 98% semispan, the flight data was less than predicted. The swept cylinder approach didn't appear valid for high sweep configurations. The next issue was the impact of shock impingement.

In analyzing the flight test data within the shock impingement region it was found that using wind tunnel data directly (which worked well outside of the interaction) under predicted the temperature in this region by as much as 200°F as shown in Figure 49. However, the wind tunnel derived temperature distributions agreed well with flight data without any adjustments. The distribution around the leading edge matched the wind tunnel data but the heating level was off. To adjust for this effect a scaling to flight factor of 1.34 was required. This factor was significantly less than the factor of 2.0 estimated for the 'double shock' effects.

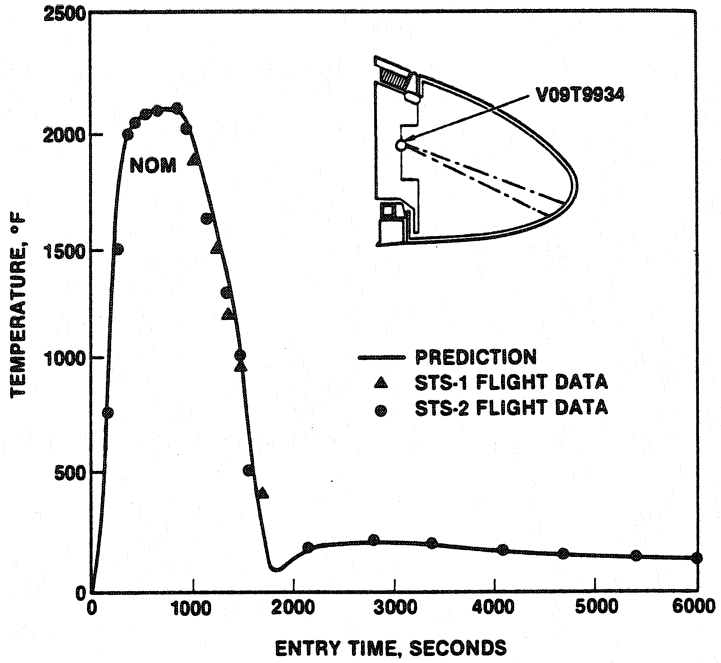

Figure 48. Radiometer temperature comparisons with preflight prediction outboard of shock impingement.

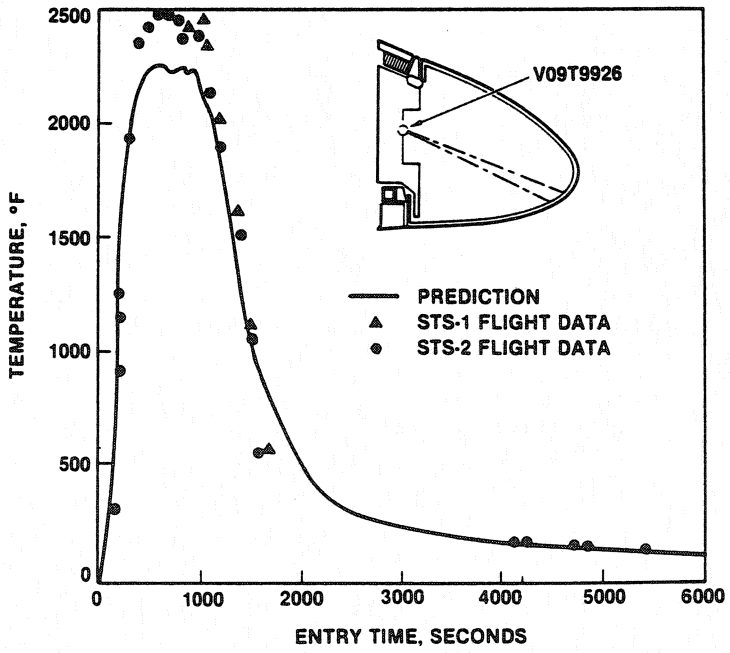

Figure 49. Wing leading edge temperatures with shock impingement .

The wing leading edge thermal analysis was a complicated procedure since there was flow into and out of the RCC panels. This did not change the RCC maximum temperature but acted as convective cooling for the attachments hardware which had to be taken into account.

Fuselage Side and Upper Surface

The fuselage side and upper surface experienced vortices that interrupted the leeside separated flow. These vortices impacted regions of the orbiter differently as illustrated in Figure 50. Zone A on the forward fuselage was more akin to attached flow. Zone B just started to pick up vortex effects. Zone C was the major area influenced by the vortex. Scaling to flight was a significant variable here. Zone D had the vortex impingement on the OMS pod.

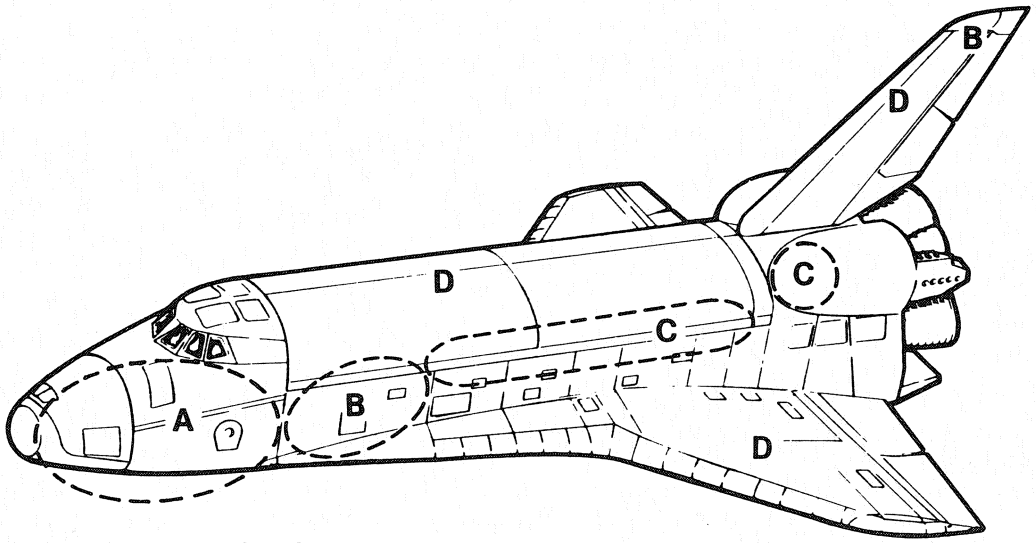

ZONE A	NO VORTEX
ZONE B	SLIGHT/MODERATE VORTEX
ZONE C	STRONG VORTEX
ZONE D	WEAK VORTEX/SEPARATED

Figure 50. Leeside vortex flows.

On the forebody side where no vortices were present wind tunnel data indicated that the nondimensional film coefficient ratios were insensitive to changes in freestream Reynolds number and some what insensitive to changes in angle of attack. This was similar to what would be expected for attached flow. However, this area did appear to benefit from partial catalytic effects. Figure 51 showed a comparison of flight data, ground data, and preflight prediction for instrument V07T9880. The data from the first five Shuttle orbiter flights were very repeatable.

Further back on the fuselage side, as on the lower surface, the effects of catalytic tiles were diminished. At 30% body length, V07T9859, there was excellent agreement between wind tunnel data and flight data in the region of matching Reynolds numbers. This was a region just upstream of the fuselage side vortex, Figure 52. Flight test data provided low Reynolds number data outside the bounds of wind tunnel conditions. Flight data at Reynolds numbers below that tested in the wind tunnel resulted in heating lower than wind tunnel values. This illustrated the need to cover the flight Reynolds number either by ground test or CFD analysis.

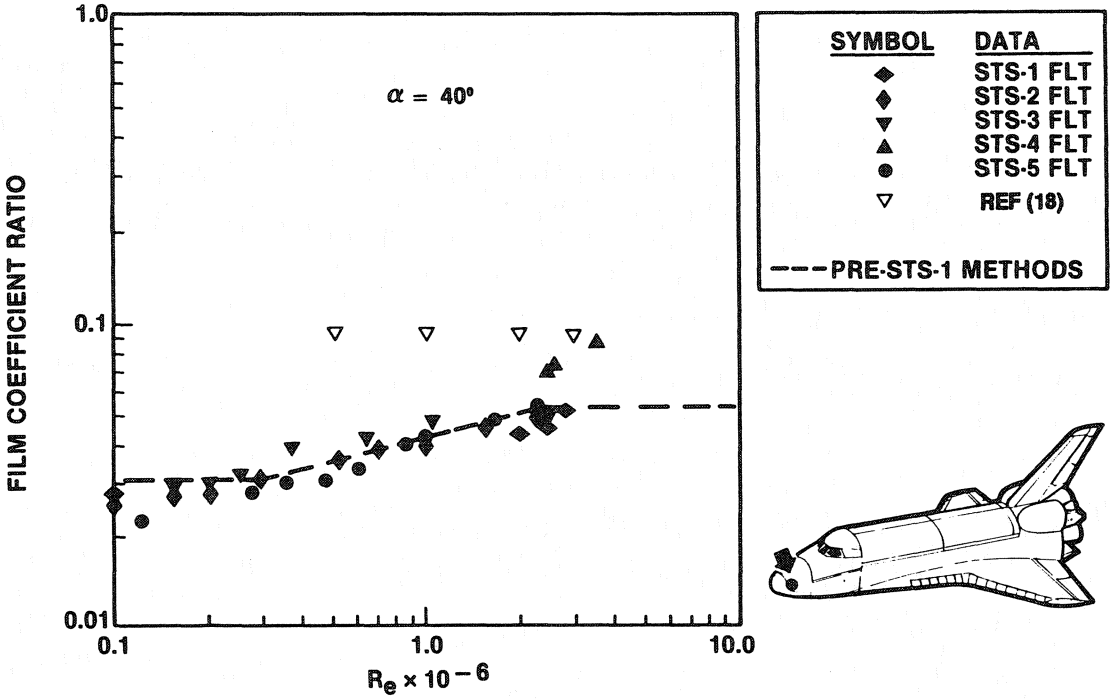

Figure 51. Fuselage side heating for instrument V07T9880.

In regions influenced by vortex scrubbing under flight conditions, the vortex impingement effect was stronger than in the wind tunnel, Figure 53. The differences got larger as the Reynolds numbers increase. This could be due to the differences in specific heats between wind tunnel and flight. The vortex moved closer to the fuselage sidewall and caused a rapid rise in temperature which became the same as at lower angles of attack. Direct application of wind tunnel data to flight conditions when vortices are present needs to be revisited. This change could also be due to a potential change in the boundary layer state as the Reynolds number increases. At lower angles of attack, 30° and 35°, the flight data was in better agreement with wind tunnel data below a Reynolds number of Re/Ft=2.0x10^6, Reference 15. However, for the higher Reynolds numbers, flight data was greater that wind tunnel data.

There was a region on the fuselage side, Figure 54, where the vortex did not impinge or scrub the side under wind tunnel conditions. But the vortex was present under flight conditions. This resulted in a significant change in heating by an order of magnitude at an angle of attack of 40°. However, for the lower angles of attack where the vortex impinged under both wind tunnel and flight conditions temperatures were in better agreement, Reference 15.

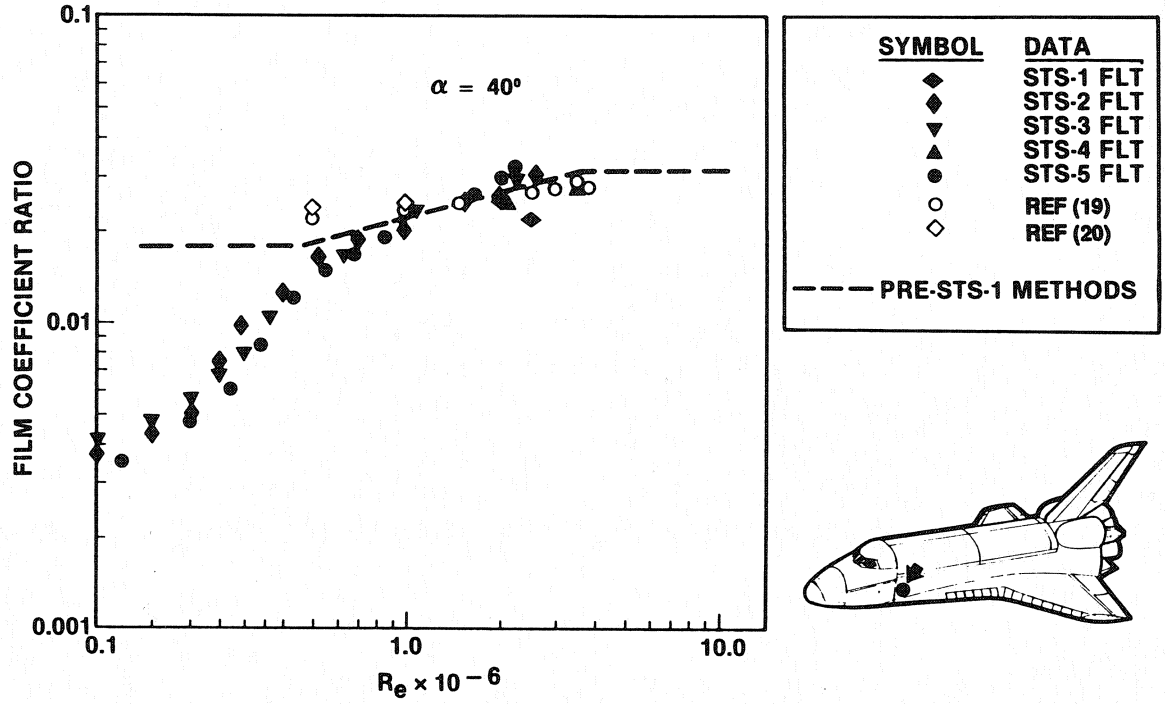

Figure 52. Fuselage side heating for instrument V07T9859.

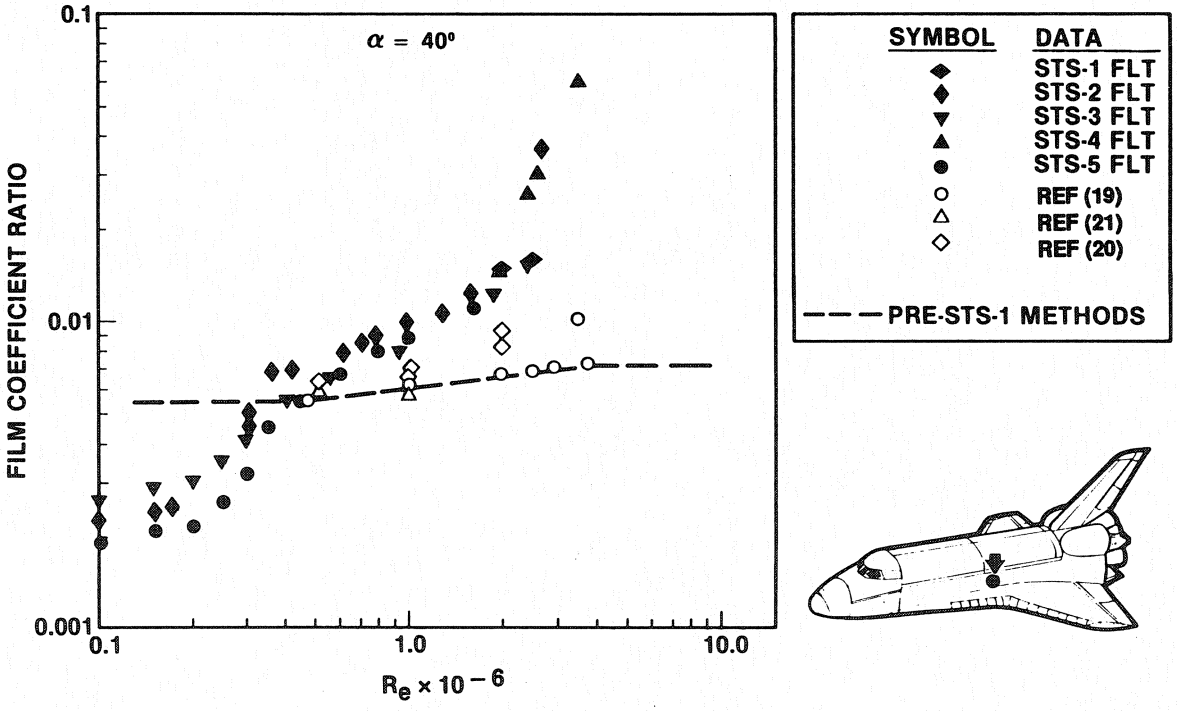

Figure 53 . Fuselage side heating for instrument V07T9905.

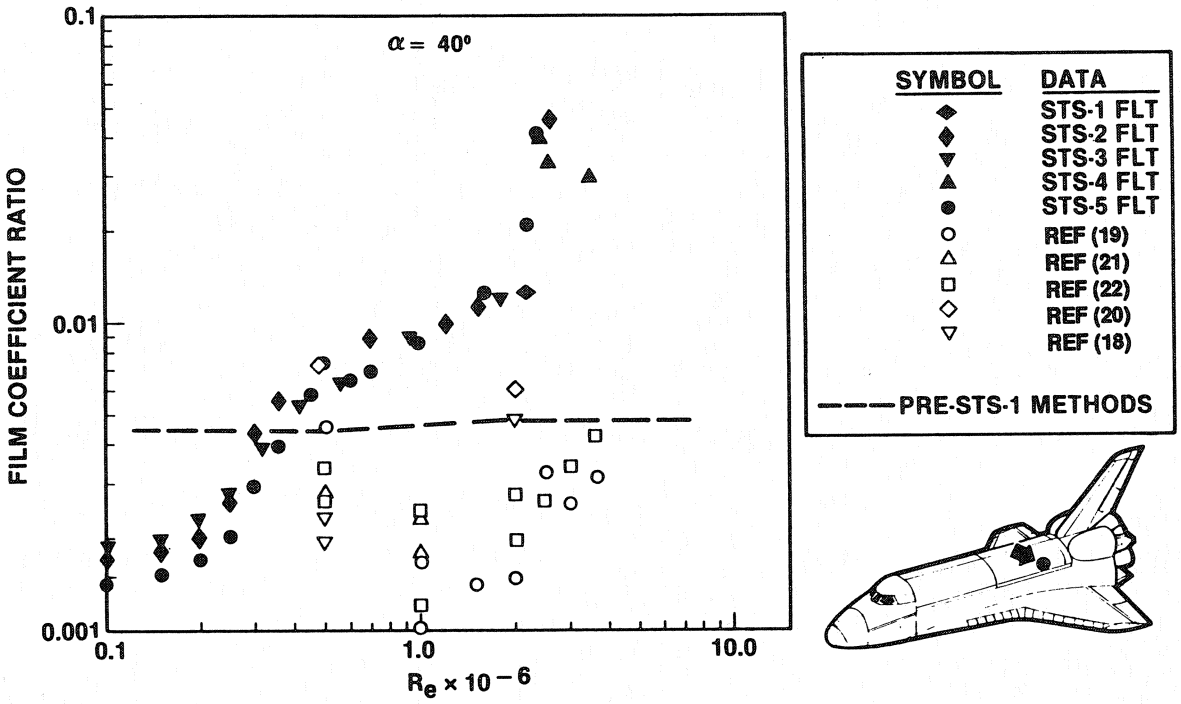

Figure 54. Fuselage side heating for instrument V07T9925.

Flight data from the first five flights indicated that it is important to obtain high Reynolds number ground test data. Ground data should match the highest Reynolds numbers planned in flight or should be carefully extrapolated to flight conditions. In addition, as a design practice, if wind tunnel test data at angle of attack below the planned flight conditions indicate vortex impingement, it should be assumed that the vortex will impinge at somewhat higher angles of attack. This will sometimes result in an over design condition.

Wing Upper Surface

The wing upper surface did not follow the same vortex scaling trend as the fuselage side. As indicated previously, in the wind tunnel a strong vortex scrubbed the outboard portion of the wing upper surface. However, flight data indicated the heating on the wing was fairly constant across the span. Flight data was an order of magnitude lower in terms of film coefficient than the wind tunnel at 90% semispan.

Inboard of the region of vortex impingement as indicated by wind tunnel data, fairly good agreement was achieved between wind tunnel and flight data. This is shown for 60% chord station in Figure 55. Both wind tunnel and flight data showed minimum heating at the 60% chord station. Heating increased towards the leading and trailing edges. In the higher wing heating regions flight data was lower than the wind tunnel data.

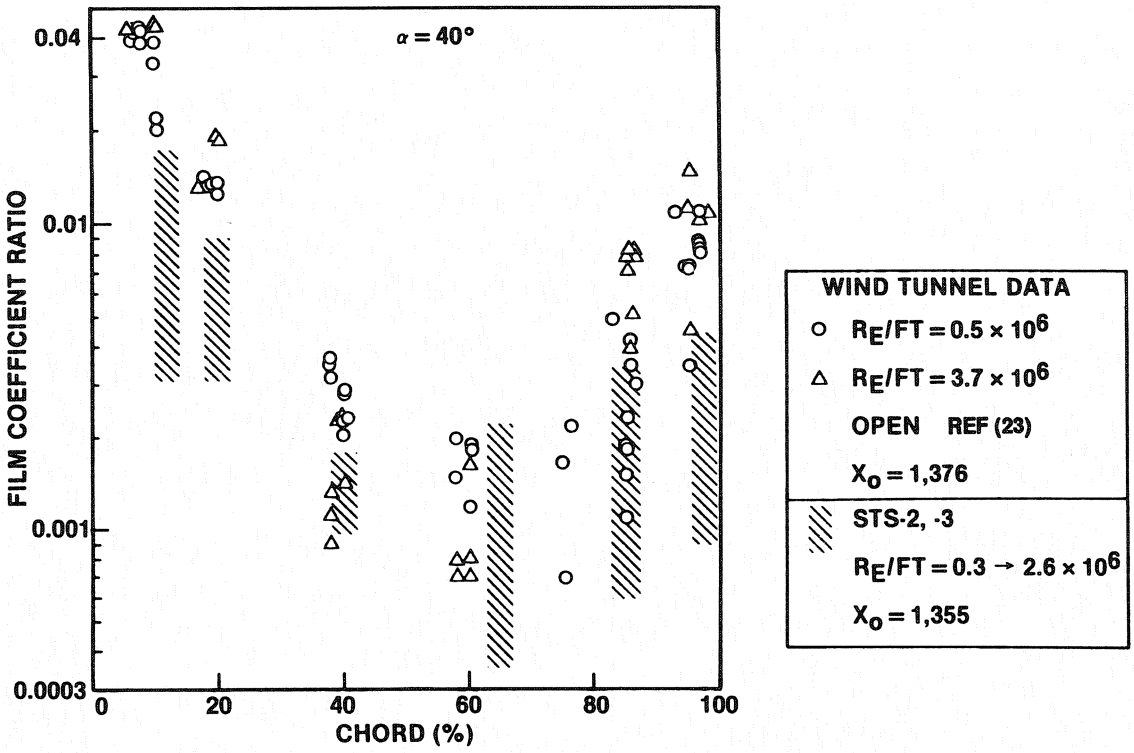

Figure 55. Wing upper surface heating comparisons.

Aft OMS Pod Side

The orbital maneuvering system, OMS, pod located on the aft side of the fuselage was known to have high heating levels on the front face due to the vortex flow impingement. However, down stream of this region the flow based on limited wind tunnel data was thought to be benign. The OMS pod heating methods were modeled consistent with the rest of the upper surface in terms of film coefficient ratios versus angle of attack, yaw, Reynolds number. It was known that some flow traversed through the elevon / fuselage gap but the influence was thought to be minor. However, the STS-1 flight corrected that opinion, Figure 56. As a result of the thermal environments, the aft lower corner of the OMS pod exceeded the TPS allowable temperatures charring the TPS outer surface and debonding the graphite epoxy structure. It was estimated that the surface temperature could have been as high as 1100°F.

A thermocouple was added in this region and data obtained on STS-3 and 5. What was discovered was that this region was sensitive to the flow going through the gap and the associated elevon deflection. Negative elevon deflections actually resulted in higher heating to this region of the OMS pod.

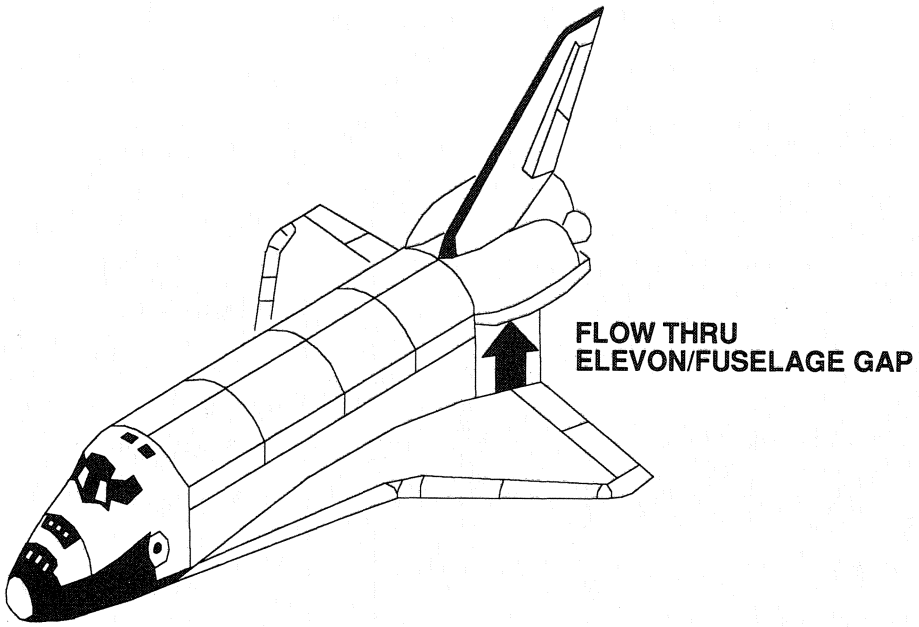

Figure 56. Aft OMS pod side flow impingement.

Using flight data from STS-3 and STS-5 a model of the environments in this area of the OMS pod was developed, Figure 57. This figure presents the results of modeling the flight data as well as presenting the wind tunnel data. As can be seen, there was an order of magnitude difference between wind tunnel and flight. Part of this difference was due to part of the wind tunnel data base not having an elevon-fuselage gap and in not properly simulating a gap. As with the fuselage side, scaling of vortex induced heating to flight conditions required more than direct application of wind tunnel data.

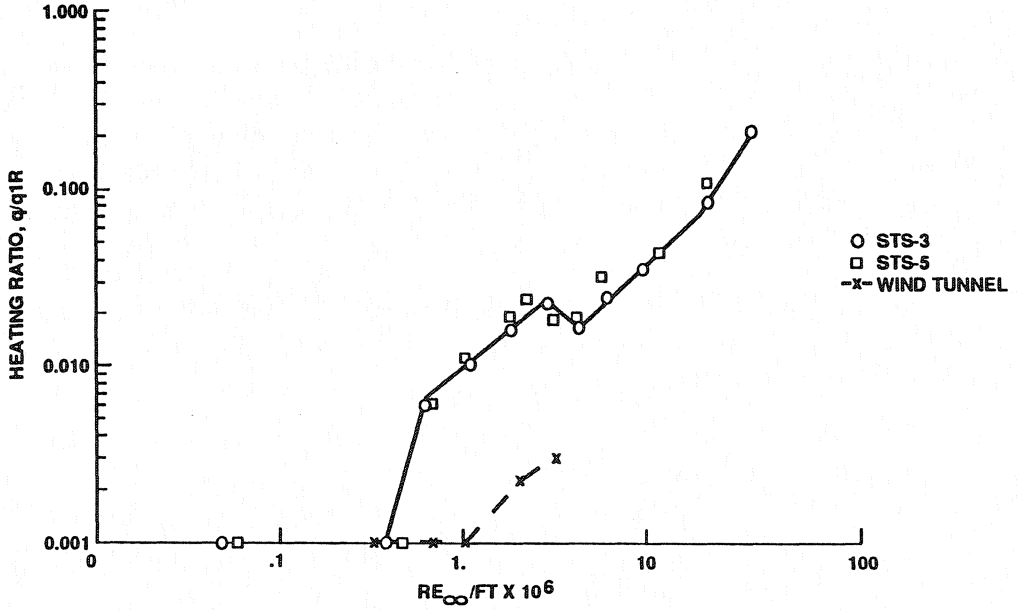

Figure 57. Aft OMS pod heating correlations .

Elevon-Elevon Gap

The elevon-elevon gap region on the wing was identified during the aeroheating methods development as a region of local flow interaction. This area was projected to experience high temperature under flight conditions. Temperatures in this area were so high that the tile corner radius slumped (increased in radius) up to 0.85 inches. Instrumentation confirmed on STS-5 that heating in the region was on the order of 2600° F for a large radius. Figure 58 presents the temperature time history for a location on the outbound elevon edge. The highest temperature recorded in this area of 2600°F was at a location slightly in front of instrument V09T9847 which was slightly outside of the main impingement region. This location had a surface temperature slightly less than 2500°F. Preflight predictions provided fair agreement with flight test data in this area of high impingement heating.

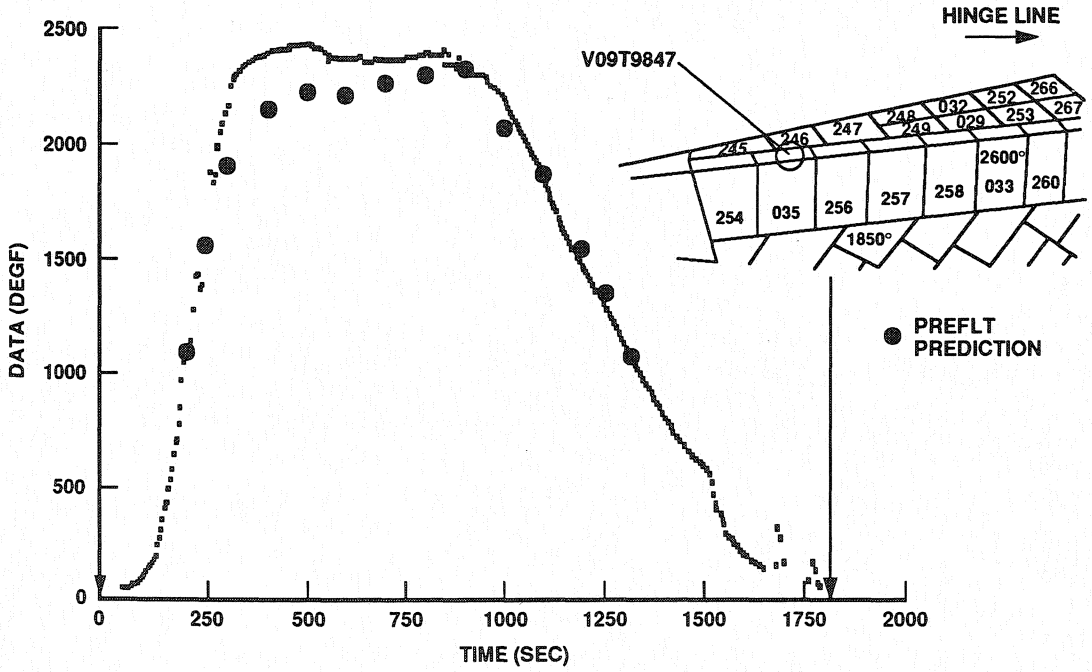

Figure 58. Elevon-elevon gap temperature history.

One approach to handle the high thermal environments in this area was to replace tiles with ablators. However, ablators that had to be replaced every flight was an expensive alternative. It turned out that if the tiles were designed with a large corner radius of 1.125 they wouldn't slump beyond that point. This allowed the high density TPS tiles to perform in this high heating area.

Subsurface Flow

One of the unique phenomena from the flight test program relative to aeroheating was that of subsurface flow. Subsurface flow was as the name implies. The external flow was able to find its way below the outer surface of the orbiter. This could be underneath the TPS tiles or into cavities such as RCC nose caps or leading edge panels. Figure 59 shows a schematic of subsurface flow relative to TPS files. In this case, a pressure gradient was formed between the outer surface of the tile and the tile/filler bar/strain isolator pad (sip) channel below the tile. By the way the tiles were installed, a pressure communication network was set up, whereby high pressure flow could seek a lower pressure several tiles away. When the external flow went below the surface the thermal energy couldn't be radiated away and the low temperature insulation components of filler bar and sip were exposed to elevated temperatures to the point of charring. It was estimated that the filler bars experience surface temperatures between 1100° and 1400°F.

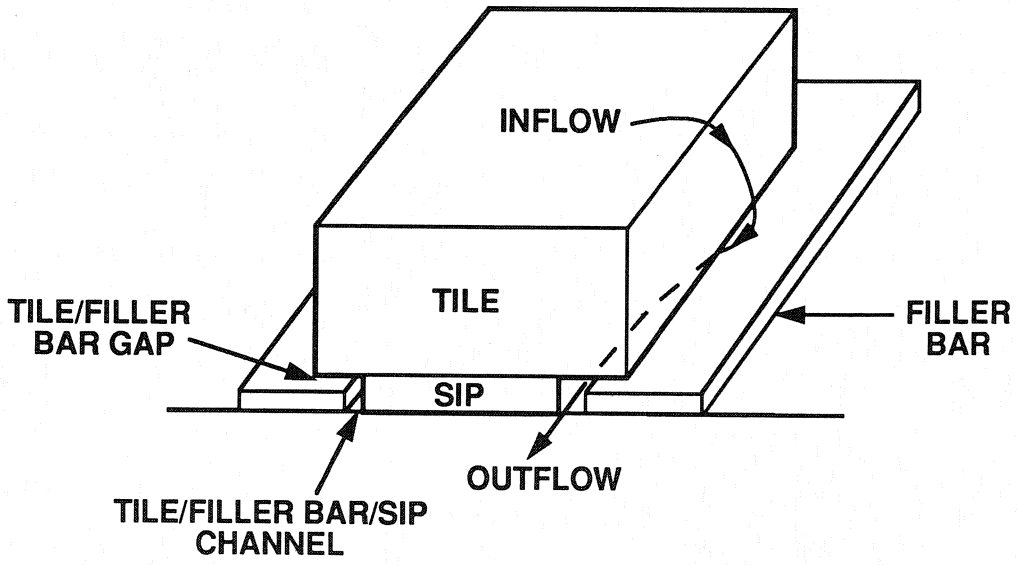

Figure 59. Subsurface flow phenomena impacts low temperature insulation.

Figure 60 shows locations of where the filler bars were charred as a result of STS-1. On STS-1 there were 614 charred filler bars and 360 charred filler bars on STS-2. As indicated in this figure the amount of charring was widespread requiring a lot of rework between flights. This phenomenon was a complex process but was correlated by accounting for the local external environments (amount of turbulent flow), tile to tile steps and gaps, tile thickness, boundary layer thickness, and tile contact with filler bars. This anomaly was eventually brought under control through redesign and roughness control.

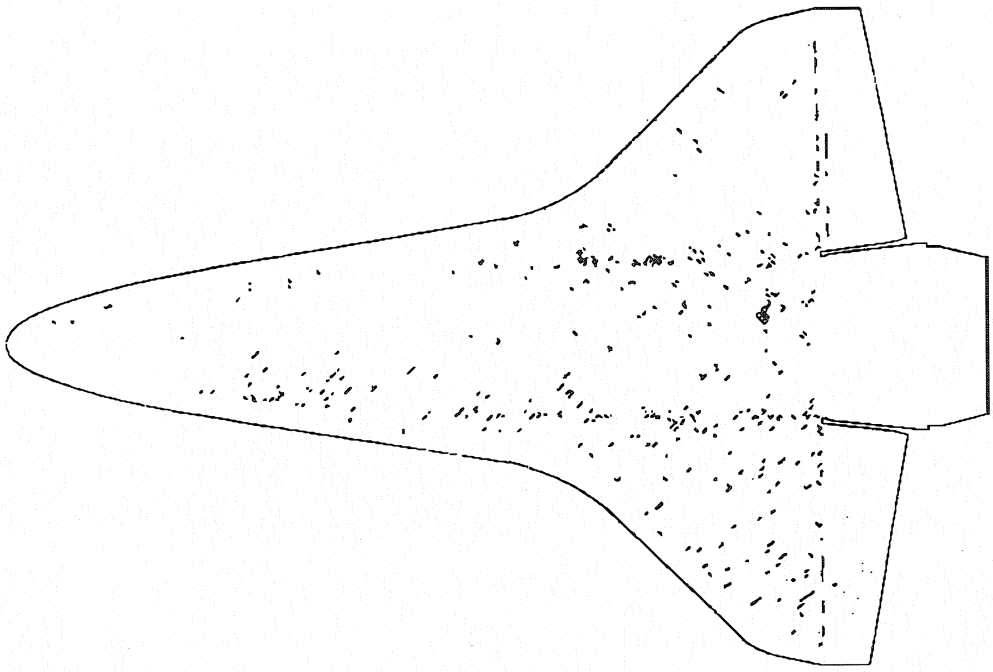

Figure 60. Locations of charred filler bar on STS-1.

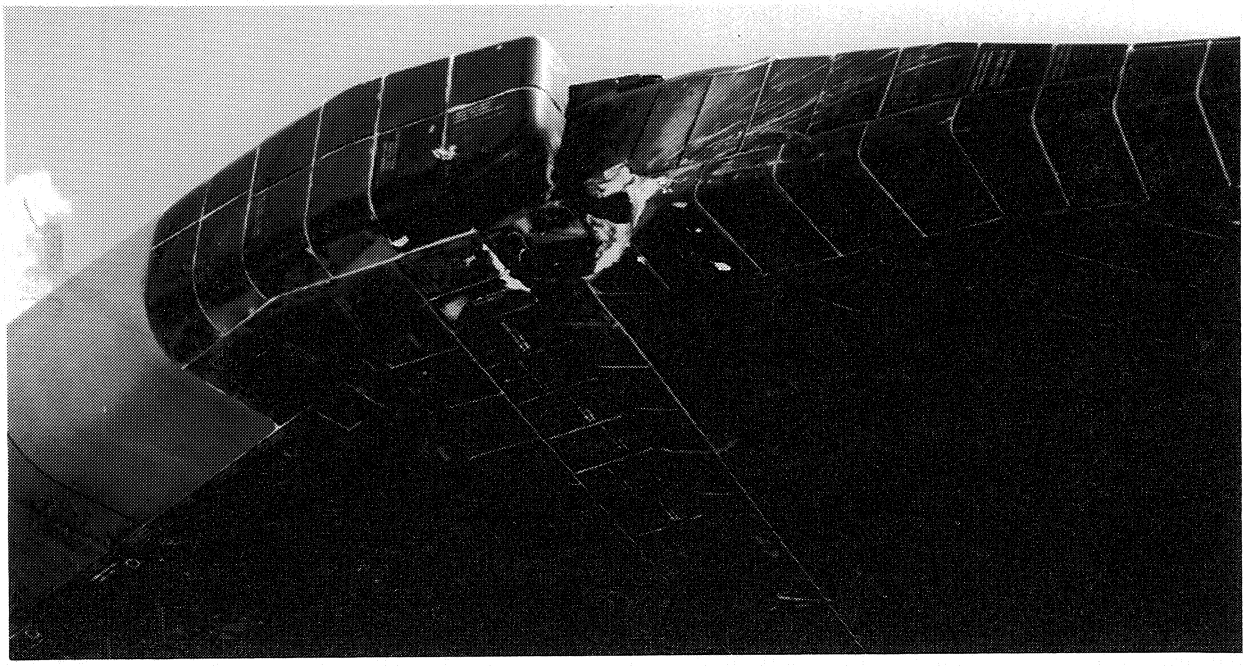

Figure 61. Outboard elevon over temperature due to subsurface flow.

A more local and dramatic example subsurface flow was that of the outboard elevon edge on STS-51D on the orbiter OV103. This phenomenon was similar to that of the general subsurface flow but was exaggerated by a more severe local environment. Reference 16 discussed this phenomenon and pointed out that the basic nature of the wing elevon gap resulted in high reattachment pressure and heating. This in combination with surface roughness resulted in tile edge slumping. When this external environment was allowed leak paths under the tile significant damage resulted. Flow entered the tile gap, progressed under the tile flowing out board, and eventually burned the tile attachment SIP, which caused the tile to become loose. This allowed more plasma to flow under the tile, resulting in the melting of the aluminium carrier panel, primary seal assembly structure, and elevon honeycomb outer face sheet, Figure 61.

The purpose of this discussion was to illustrate that there is more to aeroheating methods development than can be learned with wind tunnel data. The aeroheating analyst needs to anticipate not only the impact of the estimated environments on the surface of a vehicle but also potential leak sources. These sources must be worked with the designer, to eliminate and control the thermal impact on TPS and structure.

SUMMARY

The Space Shuttle orbiter flight test program showed that wind tunnel test data could be used to accurately model aeroheating environments for hypersonic flight within certain limitations.

In considering the design of future hypersonic vehicles several methodology/design techniques were developed.

- Simple geometric approach to modeling aeroheating environments can provide accurate windward surface results if properly correlated with wind tunnel test data.

- Catalytic surface effects of TPS can be determined and accurately predicted.

- Boundary layer transition predictions remain a challenge for hypersonic flight, especially in knowing the condition of TPS during flight. However, criteria based on conventional wind tunnel test data appear to be acceptable for design (conservative).

- Spalding and Chi turbulent theory appears to be conservative above M=10.

- Nose and leading edge heating can be accurately predicted using Fay and Riddell or swept cylinder approaches based on wind tunnel test data. However, shock impingement effects were greater than wind tunnel derived effects.

- Leeside flows correlated well with Reynolds number and angle of attack except in regions of vortex interaction.

- Ground testing needs to cover the Reynolds number range (high end) expected under flight conditions especially on the leeside.

- Extra attention needs to be paid to vortex related flows and how they scale to flight conditions.

- In the design of future hypersonic vehicles special attention needs to be given for localized regions of flow interference and subsurface flow to reduce localized damage.

- Computational fluid dynamics and linear stability theory offer hope for addressing some of these difficult scaling issues. These tools, however, need to be validated to demonstrate confidence in their ability to accurately represent flight environments.

The Space Shuttle flight test program provided a valuable set of test data to develop aeroheating methods for hypersonic flight. However, a hypersonic research vehicle is still needed to resolve many of the issues associated with slender hypersonic cruise vehicles flying at low angles of attack.

REFERENCES

1. Eckert, E.R.G.: Engineering Relations for Heat Transfer and Friction in High-Velocity Laminar and Turbulent Boundary Layer Flow Over Surface With Constant Pressure and Temperature.ASME 55-A-31, 1955.

2. Fay, J.A.; and Riddell, F.R.: Theory of Stagnation Point Heat Transfer in Dissociated Air. *T. Aero/Space Science*, vol.25, no.2, February 1958.

3. Beckwith, J.E.; and Cohen, N.B.: Application of Similar Solutions to Calculation of Laminar Heat Transfer on Bodies with Yaw and Large Pressure Gradients in High Speed Flow. NASA TN D-625, January 1961.

4. Haney, J.; and Miller,B.: Simplified Modeling of Blunt Nose Effects on Vehicle Flow Fields. AIAA -90-5259, October 1990.

5. Spalding, D.G.; and Chi, S.W.: The Drag of a Compressible Turbulent Boundary Layer on a Smooth Flat Plate With and Without Heat Transfer. *Journal of Fluid Mechanics*, vol.18, 1964, pp 117-143.

6. Keyes, J.W.; and Hains, F.D.: Analytical and Experimental Studies of Shock Interference Heating in Hypersonic Flows. NASA TN D-7139, May 1973.

7. Edney, B.: Anomalous Heat Transfer and Pressure Distribution on Blunt Bodies at Hypersonic Speeds in the Presence of an Impinging Shock. *Aeronautical Research Institute of Sweden*, FFA Report 115, February 1968.

8. Zakkay, V.; Miyozawa, M.l; and Wang, C.R.: Lee Surface Flow Phenomena Over Space Shuttle at Large Angles of Attack at M=6. NASA CR-132501, 1974.

9. Miller, B.A.: Coldarc-Dissociated Air Flow Effects During Plasma Arc Testing. *Cosmic Program Abstract*, Computer Software Management and Information Center, University of Georgia, November 1982.

10. Van Driest, E.R.; and Blumer, C.B.: Boundary-Layer Transition at Supersonic Speeds: Roughness Effects with Heat Transfer. *American Institute of Aeronautics and Astronautics Journal*, vol. 6, no.4, April 1968, pp. 603-607.

11. Van Driest, E.R.; and Blumer, C.B.: Boundary-Layer Transition at Supersonic Speeds - Three Dimensional Roughness Effects (Spheres). *Journal of the Aerospace Sciences*, vol. 29, no. 8, August 1962, pp.909-916.

12. Harthun, M.H.; Blumer, C.B.; and Miller, B.A.: Orbiter Windward Surface Entry Heating - Post Orbital Flight Test Program Update. NASA CP-2283, 1983, pp.781-805.

13. Stewart, D.A.; Rakich, J.V.; and Lanfranco, M.J.: Catalytic Surface Effects Experiment on the Space Shuttle. AIAA -81-1143, June 1981.

14. Stewart, D.A.; Rakich, J.V.; and Lanfranco, M.J.: Results of a Flight Experiment on the Catalytic Efficiency of the Space Shuttle Heat Shield. AIAA-81-0944, June 1982

15. Haney, J.W.: Orbiter Entry Heating Lessons Learned From Development Flight Test Program. NASA CP-2283, 1983, pp. 719-951.

16. Cunningham, J.A.; and Haney, J.W.: Space Shuttle Wing Leading Edge Heating Environment Prediction Derived From Development Flight Data. NASA CP-2283, 1983, pp.1083-1110.

17. Mc Bride, D.U.: Subsurface Flow Considerations in Thermal Protection Design. *STS 86-0164*, Rockwell International, June 1986.

18. Results of Heat Transfer Test in the Arnold Engineering Development Center - Von Karman Facility Tunnels A and B Utilizing Space Shuttle Orbiter Thin Skin Thermocouple Models 56-O, 60-O, and 83-O Tests: OH84B, OH105, and IH102. NASA CR-160 828, vols. 1-6, August 1981.

19. Results of Heat Transfer Tests on a 0.0175-Scale Space Shuttle Orbiter Model (56-O) on the AEDC VKF 'B' Hypersonic Wind Tunnel. NASA CR 144 596, March 1976.

20. Test Results From the NASA/Rockwell International Space Shuttle 0.0175-Scale Orbiter Forebody Models 56-O/60-O and 0.040-Scale Orbiter Forebody Model 83-O Conducted in the AEDC/VKF-B 50-Inch Hypersonic Wind Tunnel. NASA CR-167 349, vols.1-3, July 1982.

21. Test Results From the NASA/Rockwell International Space Shuttle 0.0175-Scale Orbiter Forebody Models 56-O/60-O and 0.040-Scale Orbiter Forebody Model 83-O Conducted in the NASA/ARC 3.5-Foot Hypersonic Wind Tunnel. NASA CR-160 844. October 1981.

22. An Investigation of Entry Heating on the 0.0175-Scale Space Shuttle Orbiter (Model 60-O) in the AEDC VKF Tunnel 'B'. NASA CR-160 490, vols. 1-4, July 1980.

23. Results of Test on a 0.0175-Scale Model (60-O) of the Space Shuttle Orbiter to Determine Reentry Mode Convective Heat Transfer Rates on the Upper Wing Surface and SSME Nozzles in the AEDC VKF 'B' Hypersonic Wind Tunnel (OH98). NASA CR-106 501, vols 1 and 2, September 1980.

FLIGHT EXPERIMENT DEMONSTRATING THE EFFECT OF SURFACE CATALYSIS ON THE HEATING DISTRIBUTION OVER THE SPACE SHUTTLE HEAT SHIELD

David A. Stewart
Ames Research Center
Moffett Field, CA

John V. Rakich (Retired)
Ames Research Center
Moffett Field, CA

Yih-Kanq Chen
Eloret Institute
Palo Alto, CA

SUMMARY

This paper describes flight data obtained from the Catalytic Surface Effects Experiment (CSE) during the Space Shuttle Columbia flights STS-2 through STS-5. Temperature data were compared using a correlation parameter to define equivalent flight conditions between the trajectories used by the Orbiter during the different flights. In addition, temperature data from CSE were compared with predicted values using the design trajectory 14414.1. Flight data showed that surface catalysis had a direct effect on the heating distribution over both the mid-fuselage and wing areas of the heat shield on the Orbiter.

NOMENCLATURE

C_H - heat-transfer coefficient

C_p - specific heat

C_q - constant in heating correlation

C_u - constant in velocity correlation

H_w - wall enthalpy

h - streamline metric

I_r - total enthalpy

k_w - reaction rate constant

Le - Lewis number

L - Orbiter length

M - Mach number

P - pressure

q - heat flux

R - Reynolds number

T - temperature

t - Earth entry time, from 122 km

V - flight velocity

U_e - boundary layer edge velocity

X - axial distance from nose of Orbiter

Y - span-wise distance from Orbiter centerline

α - angle of attack

γ - recombination coefficient

δ - tile thickness

σ - Stefan-Boltzmann constant

ε_{TH} - total hemispherical emittance

ϕ - roll angle

ρ - density

θ - sweep angle

Subscripts:

e - boundary layer edge

eqe - equilibrium flow

i - specie

N - nitrogen

O - oxygen

o - stagnation point

w - wall condition

∞ - free-stream condition

INTRODUCTION

The possibility of reduced heating to the Orbiter thermal protection system (TPS) during atmospheric entry has generated great interest since the first Space Shuttle flight, when surface temperatures were found to be lower than predicted (ref. 1). The thermal control coating on the Space Shuttle TPS has previously been shown to have a low catalytic efficiency during arc-jet tests (refs. 2,3). The catalytic surface effects (CSE) "OEX" experiments were designed to determine if reduced heating would persist during exposure of these TPS at flight conditions. The first phase of the CSE experiment was conducted during four of the first five flights of Columbia. The experiment used the baseline high-temperature reusable surface insulation (HRSI) which were part of the TPS covering most of the surface over the lower fuselage and wing areas of the Orbiter. The HRSI (tiles) were covered with a reaction cured glass (RCG) thermal control coating. A high catalytic efficiency overcoat developed during the pre-flight study (ref. 2) was sprayed onto selected tiles located along the mid-fuselage and wing areas to create surfaces with variable catalytic efficiency. The catalytic overcoat contained an iron-cobalt chrome spinel within a polyvinyl acetate binder. Development flight instrumentation (DFI) was used to measure surface temperature and pressure without affecting the Space Shuttle operations (ref. 4). Flight data obtained

from these surfaces were compared with predictions using a reacting boundary layer computation (refs. 5,7). High-temperature surface properties for the RCG coating and catalytic overcoat used in the computations were determined during the pre-flight study.

Post-flight test analysis for CSE includes surface properties and chemistry from RCG coated tiles removed from the Orbiter after two and five flights. Flight data from the CSE experiment are compared with predictions using a reacting boundary layer computation. A correlation parameter was used to define equivalent flight conditions for comparison of flight data with a predicted heating distribution using the design trajectory 14414.1.

FLIGHT EXPERIMENT

The catalytic surface effects experiment was planned in two phases. The first phase was completed with STS-5. It used tiles, having a single surface thermocouple, that were located along the mid-fuselage and wing areas of the Orbiter, Fig. 1. Selected tiles in these areas were sprayed with an overcoat having a high efficiency for atom recombination. During the first phase, the tiles were located along the mid fuselage at X/L = 0.15 and X/L = 0.4 for STS-2, and X/L = 0.3 and X/L = 0.4 for STS-3. For flight STS-4, the tiles were located at X/L = 0.1, 0.15, 0.2, 0.3, and 0.4; however, no data were recorded because of a system malfunction. During STS-5, tiles located at X/L = 0.1, 0.15, 0.2, 0.3, and 0.6 along the mid-fuselage and those at X/L =0.76 and X/L = 0.82 along a 60% semi-span on the wing were sprayed with the high catalytic overcoat. In addition, for STS-5, the high catalytic efficiency overcoat was sprayed on the centerline of the mid-fuselage of the Orbiter TPS to form a strip (1.52 m long by 0.22 m wide) between X/L = 0.35 and X/L = 0.4. The catalytic overcoat was sprayed with an air brush to a thickness of approximately 0.005 cm. A plastic sheet was used to mask off the surfaces surrounding the tile being sprayed with the catalytic overcoat, Fig. 2. Measured temperatures from these tiles were compared with temperatures taken from nearby tiles that were not coated with the overcoat.

Phase 2 was designed to obtain detailed temperature profile data at one location on lower mid-fuselage of the Orbiter's heat shield as the vehicle passed through several flow regions during Earth entry. The profiles would be measured using an array of surface thermocouples covering an area with and without the catalytic overcoat applied to RCG coated tiles. Typical temperature profiles calculated for location X/L = 0.27 on the mid-fuselage were made for the vehicle at altitudes of 90 km and 75 km respectively, Fig. 3. Flight data to verify these unique shaped profiles are an essential requirement in fully understanding the accuracy of advanced codes, such as Full Navier Stokes (NS), Viscous Shock Layer, (VSL) or Direct Simulation Monte-Carlo (DSMC) to compute the heating distribution over a vehicle's TPS during high speed atmospheric entry. This phase of the study was canceled due to a lack of priority and scheduling constraints.

Coating Evaluation

Pre- and post flight STS- 5 photographs of the tiles with the catalytic overcoat are shown in Figs. 4 and 5. Preflight photographs of the strip and the two tiles upstream of it X/L = 0.3 and X/L = 0.2 are shown in Fig. 4. Post-flight photographs (Fig. 5) show the catalytic overcoat sprayed on the tiles at the selected locations for STS-5 remained intact during the flight. The photograph shows that the edges of the strip were partly eroded, but the major portion of the overcoat covering this area of the vehicle TPS was unaffected by the flight environment. Visual observation showed that the color of the baseline RCG coated tiles along the mid-fuselage and wing areas of the Orbiter changed from black to gray after five flight exposures. Visual inspections prior to STS-4 did not show any noticeable change in the color of the baseline coating. A noticeable change in color of the coating occurred after STS-4 and became more pronounced after STS-5. However, a color change in the baseline coating was observed on the body flap tiles before STS-4.

Change in the color of the RCG coating indicated that contamination of the surface was possibly occurring during pre-launch and flight environments. Possible sources of contamination are sea salt, alumina, and degradation products from the bonding material for the strain isolation pad (SIP), marking paint, and gap filler coating. In addition, metallic sensors located along the mid-fuselage between X/L =0.1 and X/L = 0.2 were other sources of possible contamination, Fig. 6. The bonding material (RTV 560) consisted of a silicone rubber cured at room temperature and filled with iron oxide (Fe_2O_3). The marking paint used to identify the tiles on the Orbiter contains medium chrome yellow ($PbCrO_4$) as the major pigment and its binder is made up of organic materials (e.g., nitrocellulose, alkyd resins and plasticizers). Finally, the gap fillers used on the Orbiter TPS consisted of two types: layers of aluminoborosilicate-glass cloth bonded together with RTV 560 (nose wheel door) and aluminoborosilicate-glass cloth covered with an emittance coating. The emittance coating consisted of tetraboron- silicide and glass frit in an RTV 620 binder. Unlike the RTV 560 the RTV 620 material did not contain any fillers.

Thermogravimetric analysis (TGA) was used to measure the thermal stability of suspected contamination sources and their degradation products. Weight loss measurements were made at a fixed rate of temperature rise and over a range of temperatures from 300 K to 1500 K. These tests were conducted in air at one atmosphere. The tests showed that Fe_2O_3, SiO_2, Cr_2O_3, and PbO could all be released from these materials at temperatures below 850° K. Therefore, these oxides were probably present in the boundary layer during the launch phase of the flight (ref. 8). In addition to the tests on individual materials, post test analyses were conducted on two tiles removed from the vehicle after STS-5. The tiles were from the mid fuselage area of the vehicle at X/L = 0.138 and X/L =0.4 . X-ray diffraction (XRD) and a scanning electron microscope with an X-ray fluorescence analysis unit (ref. 9), was used to obtain qualitative chemical analysis data from the surface of the coatings. These analyses showed that not enough degradation products were adsorbed in the glassy surface of the tiles to affect their surface properties. However, the XRD analysis did show that cristobalite was present on the surface of the RCG coating and X-ray fluorescence analysis showed the presence of aluminum, silicon, sodium, and magnesium. The aluminum, probably in the form of alumina, is attributed to by-products deposited on the RCG from the burning solid rocket fuel during launch. The other elements are commonly found in sea salt.

Surface Properties

Two surface properties that are very important in determining the surface temperature on the heat shield of the Orbiter are the surface catalytic efficiency and total hemispherical emittance. During the pre-flight study for the CSE experiment, catalytic efficiencies (atom recombination coefficients) for the RCG coating were determined using arc-jet and side-arm reactor data (ref. 2) Current values for both RCG and the catalytic overcoat (ref. 2) are shown in FIG. 7.

Arc-jet tests were used to determine if sea salt contamination on the RCG coating could result in increased catalytic efficiency (ref. 9). Tests were conducted in which controlled amounts of NaCl solution were added to the RCG surface and then exposed to an arc-jet air stream for 7 min. at stagnation point conditions of H_{eo} = 17.5 MJ/kg and surface temperature of 1340 K, Table 1. These data show an increase in the catalytic efficiency (reaction rate constant) as a result of successive applications of NaCl solutions to the RCG between arc-jet exposures. Included in Table 1, are reaction rate constants (surface catalytic efficiency) that were determined during these tests for two RCG coated flight tiles. These tiles were removed from the Orbiter heat shield (in the area of the CSE experiment) after STS-2 and STS-5. They also show an increase in catalytic efficiency after exposure to the launch environment (sea salt).

Comparison of pre- and post-flight (STS-5) total hemispherical emittance for the RCG coating is plotted in Fig. 8. Included on the figure is a plot of the total hemispherical emittance for the catalytic overcoat, Fig. 8b. Total hemispherical emittance values for the coatings were calculated using both arc-jet data and room temperature spectral hemispherical reflectance data. Spectral hemispherical reflectance data were obtained using a Beckman model DK-1A (wavelength range 0.3μ to 2.3μ) and a Willey model

318 (wavelength range 2.0μ to 15μ) spectrophotometer, respectively. The arc-jet data included radiant flux and surface temperature measurements taken from disks. Radiant heat flux was measured using a radiometer and surface temperature using platinum-platinum 13% rhodium thermocouples. Pre-flight measurements of the emittance for the RCG and catalytic overcoat show them to be very similar over the temperature range of interest for the CSE experiment. However, post-flight measurements of the emittance for the RCG show a decrease of approximately 5% after five flights. Note, however, that the emittance is unchanged after exposure to only sea salt during the arc-jet tests, Table 1.

COMPUTATIONS

Flight Predictions

The effect of surface catalysis on the heating distribution over the Orbiter TPS has been estimated using a boundary layer integral matrix procedure (BLIMPK). BLIMPK simulates the reacting boundary layer next to the body using high Reynolds number equations (i.e., an asymptotic boundary layer solution) (ref. 10). Although BLIMPK does not account for interactions between the inviscid and viscous flow regimes, it does provide a more accurate estimate of the surface-to-gas interactions by using a much finer grid near the surface of the heat shield than either current Navier Stokes and Viscous Shock Layer solutions. In this study, BLIMPK solutions were conducted using the axisymmetric mode and non-isentropic option. Parameters used in BLIMPK to calculate the heating distribution over the Orbiter's windward heat shield include:

1. Boundary layer edge properties
2. Body geometry and surface pressure distribution
3. Both gas and surface kinetics

BLIMPK was originally developed by Kendall and Bartlett (ref. 11) for equilibrium multi-component flow over ablating surfaces, (BLIMP). Later the code was modified and extended by Tong (ref. 12) to include non-equilibrium boundary layer flow (KBLIMP) over the surface of the Orbiter. The code can be operated for either laminar or turbulent flows. Laminar flow exists over the Orbiter heat shield during the time of interest for CSE. Rakich and Mateer developed correlation parameters to estimate the stream metric, pressure coefficient, and species concentrations for use in BLIMPK that account for non-equilibrium edge and entropy swallowing effects on the heating distribution over the centerline of the Orbiter (refs. 5,7). These correlation parameters (eqs. 1-4) were developed assuming that they were only dependent on angle-of-attack:

streamline metric,

$$h = (\alpha) \tag{1}$$

pressure coefficient,

$$p/p_o = p_\infty/p_o + 0.5\, \rho_\infty V_\infty^2\, C_p\, (\alpha)\, /p_o \tag{2}$$

velocity due to drop in entropy,

$$U_e/U_{eo} = Cu\, (X/L)^l\, (\alpha)^m\, Re^n \tag{3}$$

and non equilibrium heating,

$$q/q_{eqe} = C_q (U_e/U_{eo})^{1/2} \quad (4)$$

where q_{eqe} results from a reacting boundary layer computation with equilibrium, isotropic edge conditions. Cq = 1 for an equilibrium boundary layer. Parameters listed in Tables 2 and 3 were calculated for several altitudes using the design trajectory 14414.

The wall pressure-stagnation pressure ratio was calculated using an inviscid non-equilibrium real-gas solution (ref. 13). Typical pressure ratios are plotted for several locations along the mid-fuselage of the Orbiter for flight STS-3, Fig. 9. Agreement between the flight data and predictions are good for all locations except X/L = 0.1 where the prediction was high. The difference in the measured and calculated values is attributed to either a local disturbance of the boundary layer or possible leakage of the pressure line to the transducer.

Early BLIMPK solutions of the heating distribution over the Orbiter TPS assumed a constant wall temperature and that the main chemical reaction was the dissociation and recombination of oxygen. Current solutions of BLIMPK use an iteration procedure between eqs. 5 and 6 below to calculate the surface heat flux to the Orbiter's TPS.

$$\gamma_i = C \varepsilon^{-E/T_w} \quad (5)$$

Expressions for oxygen and nitrogen recombination coefficients for RCG and the catalytic overcoat are given in Fig. 7.

For expressions of oxygen and nitrogen atom recombination on RCG a

$$q = \varepsilon_{th} \sigma (T_w)^4 \quad (6)$$

where s is the Stefan-Boltmann constant and e_{th} is the total hemispherical emittance of the TPS surface. Thermodynamic properties of the boundary layer gas in both earlier and current BLIMPK solutions for CSE were specified by JANAF data for each component and used Park's five species model of 20 kinetic reactions as the gas model for air (ref. 14).

Data Correlation Parameter

Normalized surface temperature and a correlation parameter were used to compare flight data with BLIMPK predictions. The normalized surface temperature, T (bar) was derived from the well-known expression for flat-plate heating with dissociated gas flow over it.

$$q_w = C_H \rho_e V_e (I_e - H_w) [(C_{pf})_{av}/(C_p)_{av} (1 - Le) + Le]^{2/3} \quad (7)$$

and assuming

$$Le = 1, \; q = \varepsilon_{TH} \sigma T_w^4$$

$$T(bar) = T_w / [\rho_\infty V_\infty^3 / 2 \sigma]^{1/4} = [C_H \rho_e V_e / \varepsilon_{TH} \rho_\infty V_\infty]^{1/4} \quad (8)$$

The hypersonic viscous interaction parameter ($M_\infty / \sqrt{R_\infty}$) was used to define equivalent flight conditions between trajectories, Fig. 10. The parameter for flight trajectories STS-2 through STS-5 are plotted as a function of time, Fig. 10a. Also, angle-of-attack and roll angles are included on the figure for the four flight cases, Fig. 10b. The figure shows that the deviations in angle-of-attack and roll angles of the

Orbiter are small for the four flight trajectories; therefore the parameter can be used to define similar flight conditions for data comparison. To illustrate the validity of this parameter, calculated heat transfer coefficients along the mid-fuselage of the Orbiter, assuming equilibrium and reacting boundary layer flows, for the design trajectory are compared with calculated values for the four flight cases, Fig. 11. Excellent agreement was obtained between the values calculated from the flight and design trajectories. Since normalized surface temperature is proportional to C_H, it follows that the flight data can also be compared using the hypersonic viscous interaction parameter to define equivalent flight conditions.

RESULTS AND DISCUSSION

Mid-fuselage Heating

The heat transfer rate histories during STS-3, at two locations on the mid-fuselage of the Orbiter, were estimated using the earlier BLIMPK solution. These calculated heating rate histories for locations at X/L = 0.15 and X/L = 0.4 are shown in Fig. 12. These computations were made assuming both equilibrium and non-equilibrium boundary layer flows. Included on the figures are the calculated wall pressure histories at these two locations. Comparisons of the two computations show that the reacting flow resulted in a 34% - 40% reduction in heat transfer rate to the vehicle at X/L = 0.15 and 25% reduction at X/L = 0.4 below the values assuming equilibrium boundary layer flow. Flight data, taken during STS-3 and STS-5, from tiles with and without the catalytic overcoat and located near or at X/L = 0.15 and X/L = 0.3 are shown in Fig. 13. These data support the computational results that show 1) the effect of surface catalysis on the heat transfer rate to the Orbiter becomes important early in trajectory (viscous boundary layer flow regime), and 2) persists until late into the trajectory where transition to turbulent flow begins.

Early BLIMPK solutions of heating distribution over the mid-fuselage of the Orbiter are compared with flight data taken at 650 s during trajectories STS-2 and STS-3, Fig. 14. Temperature distribution along the mid fuselage was predicted for assuming equilibrium and reacting boundary layer flows over the vehicle. The prediction using a reacting boundary layer resulted in a discontinuous rise in temperature on the tiles containing the catalytic overcoat. The predicted temperature rise goes above the calculated equilibrium value because of the sudden release of the energy of dissociation due to the increased surface catalytic efficiency of the tiles at both locations. Also, the predicted temperature rise is higher than the flight data taken during STS-2, and lower than the data taken during STS-3 at X/L = 0.3. The low surface temperature measured at X/L = 0.4 during STS-2 is attributed to partial removal of the catalytic overcoat during Earth entry. Better agreement between flight data and theory was observed for STS-3. Some of the CSE data was obtained from tiles located off the centerline of the lower mid-fuselage and therefore should be a little higher than the temperatures recorded for tiles located on the centerline due to cross-flow effects (ref. 7). In general, the flight data from the RCG coated tiles are lower (13% to 35%) while data from the tiles with the catalytic overcoat are higher than the temperatures computed assuming equilibrium flow over the vehicle.

Normalized temperature data, obtained from STS-2, STS-3, and STS-5, were compared with BLIMPK predictions using the design trajectory. The normalized surface temperatures were plotted against the correlation parameter, Fig. 15. They were taken from the following locations along the mid-fuselage of the Orbiter (X/L =0.15, X/L = 0.3 and X/L =0.4). Included in the figure are values of surface temperature calculated assuming equilibrium and reacting boundary layer flow in the BLIMPK predictions. Since the surface temperature across a tile with the catalytic overcoat is not constant (Fig. 3), an average value was used for comparison with the flight data (short dash line). Flight data and predictions of the temperature histories are in reasonably good agreement. The spread in the flight was the result of either a damaged thermocouple or an insufficient amount of the catalytic overcoat present on the tile (STS-2). Effect of surface catalysis on the heat transfer rate to the tiles with the catalytic overcoat is consistent throughout the flights.

Also, heating distribution data, obtained over the mid-fuselage and wing areas of the Orbiter during trajectories STS-2, STS-3 and STS-5, are plotted as a normalized surface temperature in Figs. 16 through 18. These data are compared with predictions of the surface temperature distribution over the Orbiter using the design trajectory. Again, BLIMPK predictions were made assuming equilibrium and reacting boundary flow over the surface of the vehicle. Flight data presented in figures 16 and 17 include off-centerline corrections for the surface temperature using solutions outlined in reference 6. These data agree reasonably well with the BLIMPK prediction using the reacting boundary layer flow. In addition, good agreement is shown for the data obtained from STS-2 and STS-3. Included in figure 16b, is a BLIMPK prediction assuming reacting boundary layer flow and using a temperature dependent reaction rate constant expression for oxygen on the RCG coating, (see Fig. 7). The predicted normalized surface temperature using the design trajectory was closer in agreement with the flight data from STS-2 and STS-3. These data show that the effect of surface catalysis on the heating rate decreases with decreasing Mach number and increasing distance along the mid-fuselage of the Orbiter. Flight data from STS-5 appear high for the baseline RCG coating and low for the catalytic overcoat compared to previous flight data. However, these data show that even at a distance along the mid-fuselage where the boundary layer is close to equilibrium (X/L = 0.6); surface catalysis has a pronounced effect on the heating distribution. Also, the data supports the prediction that the surface heating rate decreases downstream of the leading edge of the strip of catalytic overcoat located between X/L = 0.35 and X/L =0.4. These temperature discontinuities could result in major design levels on future TPS for advanced reentry vehicles.

In order to resolve the difference between the data taken during the STS-2 trajectory and those taken during the STS-5 trajectory, the heating distribution along the mid-fuselage was calculated using catalytic efficiency and total hemispherical emittance determined from post-flight STS-5 tiles, (see Table 1 and Fig. 8) in the BLIMPK solution, Fig. 17. Computations were made assuming equilibrium and reacting boundary layer flows over the Orbiter. These predictions show better agreement with the flight data obtained during the STS-5 trajectory.

Finally, flight data were compared with the current BLIMPK solutions using the normalized surface temperature, Fig. 18. These data were taken during trajectory STS-2 at 450 s (75 km) and during trajectory STS-3 at 200 s (91 km). The current solutions were calculated assuming reacting boundary layer flow over the fuselage of the Orbiter. These solutions include both atom recombination of nitrogen and oxygen instead of only oxygen as assumed in the earlier BLIMPK solutions. In the current computation the major portion of chemical heating to the catalytic overcoat is the result of the recombination of atomic nitrogen on the surface rather than atomic oxygen. Current predictions show better agreement with the flight data than the earlier predictions, particularly, the agreement between predicted and measured surface temperatures taken from tiles with the catalytic overcoat. Included on figure 18b, is the calculated heating distribution over the mid-fuselage of the Orbiter using a VSL code developed by Langley (ref. 16). These data were taken at an altitude of 91 km during STS-3. The predicted heating distribution is similar to the BLIMPK solution, but the absolute values are much higher the flight data. Also, the VSL solution underpredicts the temperature rise that occurs across the tiles with the catalytic overcoat. Detailed temperature profiles across the tiles with the catalytic overcoat would aide greatly in understanding the differences in the two computations (CSE phase study 2).

Wing Heating

Effect of surface catalysis on the heating distribution over the windward side of the wing was investigated by spraying the catalytic overcoat on two tiles. The tiles were located along the 60% semi-span (Y/L = 0.60). These data aide in determining the origin of the streamlines wetting the wing surface. If the streamlines originate at the nose of the Orbiter, the flow should be close to equilibrium over the wing because of the large distance from the nose and the flight data taken at X/L = 0.6 along the mid-fuselage. On the other hand, if the wing streamlines pass through the wing-leading-edge shock, then the

flow has a greater possibility of being out of equilibrium, and the effect of surface catalysis would be present. Orbiter configurations tested in wind tunnels suggest the latter possibility (ref. 17).

Because of the difficulty in exactly computing the wing flow field, a simple two-dimensional strip theory was used to analyze the wing heating. Cutting the wing at Y/L = constant yields a section shape that can be approximated by a blunt flat plate. For heating computations, the boundary layer was assumed to flow two dimensionally over the plate, starting at the stagnation line on the wing leading edge. Surface pressure was approximated with a Newtonian type distribution. Thus, the wing pressure was calculated by:

$$P_w/P_0 = \cos^2(\theta - \theta_0) \tag{9}$$

Where, due to the wing sweep, $\theta_0 = 50°$ for $a = 40°$ and P_0 is the normal shock stagnation point pressure. The pressure and normalized surface temperature are shown in Fig. 19. Heating computation includes a correction for the boundary layer swallowing effects (ref. 4).

The Newtonian pressure approximation is, of course, constant on the flat part of the wing, but agrees reasonably well with the level of flight data, STS-3, Fig. 19a. The pressure data decrease with distance as the over pressure caused by the blunted leading edge decays toward the flat-plate value.

Fig. 18b shows normalized surface temperature as a function of distance along the 60% semi-span located on the wing of the Orbiter. The prediction is compared with data obtained at the equivalent flight condition of $M_\infty/\sqrt{R_\infty} = 0.0309$ for STS-2, STS-3, and STS-5. These data show a significant effect of surface catalysis on the temperature distribution along the wing at the locations where the catalytic overcoat has been applied to the tiles (X/L = 0.76 and X/L = 0.81). The theory overpredicts the temperature rise across the tile with the overcoat but is in fair agreement with the baseline RCG coated tiles. As with the mid-fuselage data, the surface temperature over the wing is higher during STS-5 than during STS-2 or STS-3. This tendency has been discussed earlier. In summary, the effect of surface catalysis on the heating distribution over the wing is reasonably well predicted by simple two-dimensional strip theory.

CONCLUDING REMARKS

Analysis of pre- and post-flight tiles and comparison of flight data from four STS Columbia trajectories with theory resulted in the following observations:

1. Surface properties are affected by the Space Shuttle launch environment. Sea salt increased surface catalytic efficiency of RCG and alumina absorption into the RCG glass decreased its emittance.

2. Surface catalysis does affect the heating distribution along both the mid-fuselage and wing areas of the Orbiter.

3. Low surface catalytic efficiency of the RCG-coated baseline tiles resulted in lower heating during Earth entry than predicted assuming equilibrium boundary flow over the vehicle.

4. Correlation parameter and normalized surface temperatures provided a means of comparing flight data, taken from several Orbiter Earth entry trajectories, with a predicted heating distribution using a design trajectory.

REFERENCES

1. Throckmorton, D.A., "Benchmark Aerodynamic Heat transfer Data from the First Flight of the Space Shuttle Orbiter," AIAA Paper 82-003, 20th Aerospace Sciences Meeting, Orlando, FL, Jan. 1982.

2. Stewart, D. A., "Catalytic Surface Effects Experiment on Space Shuttle," Orbiter Experiments (OEX) Aerothermodynamics Symposium, Williamburg, VA, April 1993, NASA CP-3248, 1994.

3. Stewart, D. A., Rakich, J.V., and Lanfranco, M.J., "Catalytic Surface Effects Experiment on the Space Shuttle," AIAA Paper, 1981.

4. Rakich, J.V. and Lanfranco, M.J., "Numerical Computation of Space Shuttle Laminar Heating and Surface Streamlines," Journal of Spacecraft and Rockets, Vol. 14, No. 5, May 1977, pp. 265-272.

5 Rakich, J.V., Bailey, H.E., and Park, C., "Computation of Non-equilibrium Three-Dimensional Inviscid Flow over Blunt-Nosed Bodies Flying at Supersonic Speeds," AIAA Paper 75-835, 1975.

6 Rakich, J.V. and Mateer, G.G., "Calculation of Metric Coefficients for Streamline Coordinates," AIAA Journal, Vol. 10, Nov. 1972, pp 1538-1540.

7. Flowers, O. and Stewart, D.A., "Catalytic Surface Effects on Contaminated Space Shuttle Tiles in a Dissociated Nitrogen Stream," NASA TM-86770, 1985.

8. Stewart, D.A., Chen, Y.K. Henline, W.D., "Effect of Non-Equilibrium Flow Chemistry and Surface Catalysis on Surface Heating to AFE.

9. Stewart, D.A., Kolodziej, P., and Leiser, D.B., "Effect of Variable Surface Catalysis on Heating Near The Stagnation Point of a Blunt Body," AIAA Paper 85-0248, 1985.

10. Tong, H., "Non-equilibrium Chemistry Boundary Layer Integral Matrix Procedure," Aerotherm Report UM-73-37, Acurex Corporation, Mt. View, CA., 1973.

11. Kendall, R.M. and Bartlett, E.P., "Non-similar Solution of the Multi-component Laminar Boundary Layer by an Integral-Matrix Method," AIAA Journal, Vol. 6, June 1968.

12. Tong, H., Buckingham, A.C., and Curry, D.M., "Computational Procedure for Evaluation of Space Shuttle TPS Requirements," AIAA Paper 74-518, 1974.

13. Rizzi, A. and Bailey, H.E., "Reacting Non-Equilibrium Flow Around the Space Shuttle Using a Time Split Method," NASA SP-347, 1975.

14. Park, C., "A Review of Reaction Rates in High Temperature Air," AIAA Paper 89-1740, Buffalo, NY, 1989.

15. Stewart, D.A., Rakich, J.V., and Lanfranco, M.J., "Catalytic Surface Effects on Space Shuttle Thermal Protection System During Earth Entry of Flights STS-2 Through STS-5, Lessons Learned," NASA CP-2283, 1983.

16. Gupta, R.N., and Simmonds, A.L., "Stagnation Flowfield Analysis for an Aeroassist Flight Experiment Vehicle," AIAA Paper 88-2613, June 1988.

17. Marvin, J.G., Seegmiller, H.L., Lockman, W.K., Mateer, G.G., and Pappas, C.C., "Surface Flow Patterns and Aerodynamic Heating on Space Shuttle Vehicles," AIAA Paper 71-594, 1971.

Exposures	Salt g/cm^2	k_w, cm/sec	T_w, K	ε_{TH}
Arc-jet				
1	1.2×10^{-4}	200	1311	0.89
5	6.0×10^{-4}	240	1311	0.89
1	6.0×10^{-4}	200	1311	0.89
5	3.1×10^{-3}	400	1311	0.89
1	*N.D.	250	1311	0.85
1	Unc.	200	1311	0.89
Flight				
2	*N.D.	100	1200	0.89
5	*N.D.	200	1200	0.85

Table 1. Effect of salt contamination on surface properties of RCG.

Flight case	Altitude km	Velocity km/sec	Angle of attack deg	Reynolds number, $R_e \times 10^{-6}$	Cu = equilibrium	Correlation $\frac{U_e/U_{eo}}{(X/L)^{0.1}(\alpha_R)^{0.5}}$ reacting
1	74.98	7.620	41.4	0.779	15.01	15.18
2	68.88	6.614	40.2	1.423	15.16	15.35
3	64.92	5.944	34.5	2.096	15.14	15.43
4	60.66	5.121	31.8	3.034	15.24	15.32

Note: Average C_u: equilibrium flow = 15.1; reacting flow = 15.3.

Table 2. Boundary layer edge velocity correlation for design trajectory 14414.

Flight case	C_q				
Location	X/L = 0	X/L = 0.15	X/L = 0.3	X/L = 0.4	X/L = 0.6
1	1.10	1.23	1.21	1.18	1.10
2	1.04	1.13	1.14	1.11	1.09
3	1.04	1.17	1.19	1.14	1.10
4	1.03	1.07	1.12	1.09	1.10

$C_q = q / q_{eqe} (U_e/U_{eo})^{1/2}$

At X/L = 0, lim $U_e/U_{eo} = 1$.

Table 3. Surface heating correlation for nonequilibrium flow.

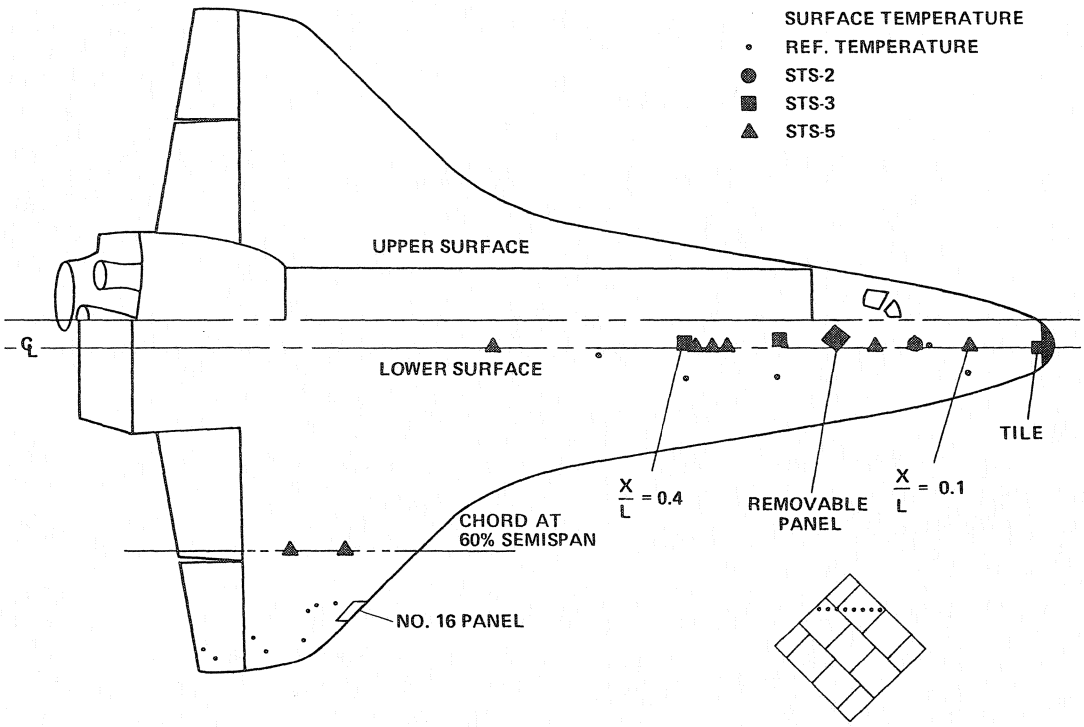

Fig. 1. CSE experiment thermocouple locations.

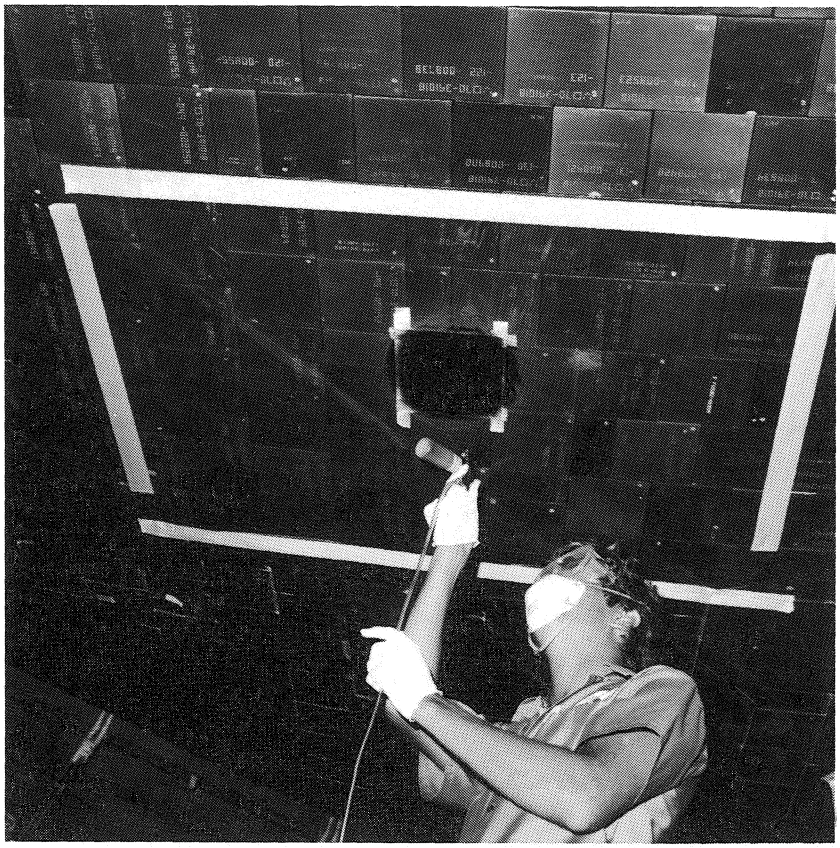

Fig. 2. Catalytic overcoat application.

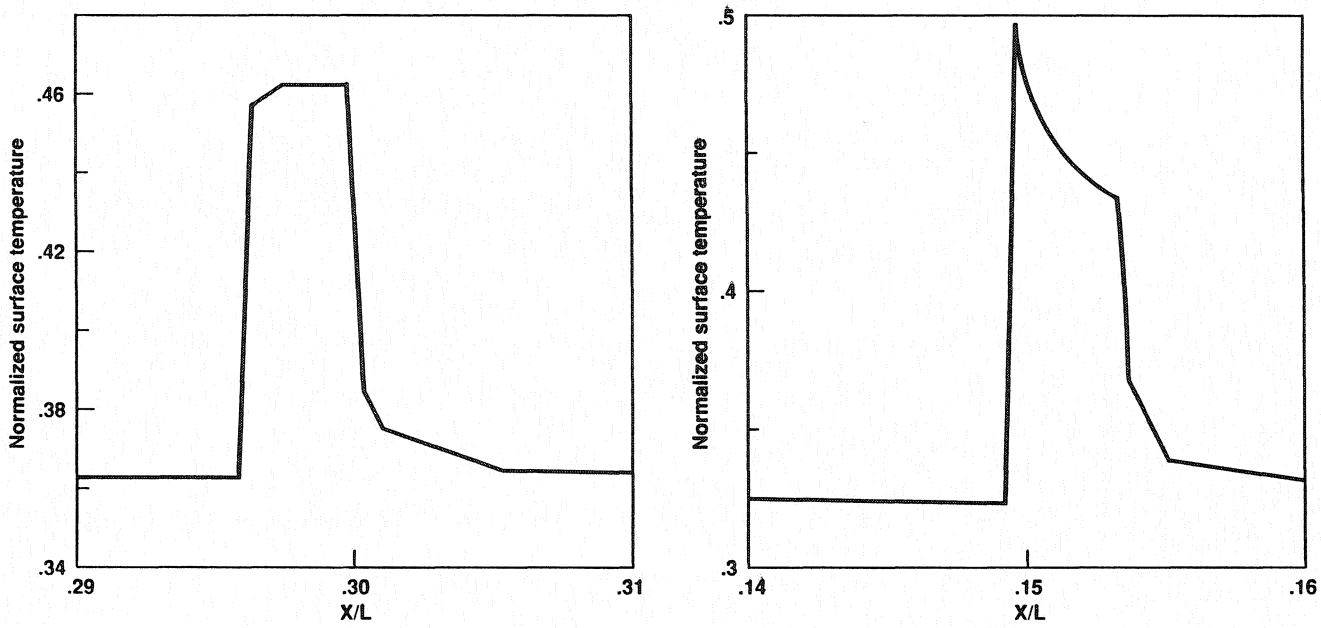

a) Alt. = 91km

b) Alt. = 75 km

Fig. 3. Temperature profiles across catalytic overcoat.

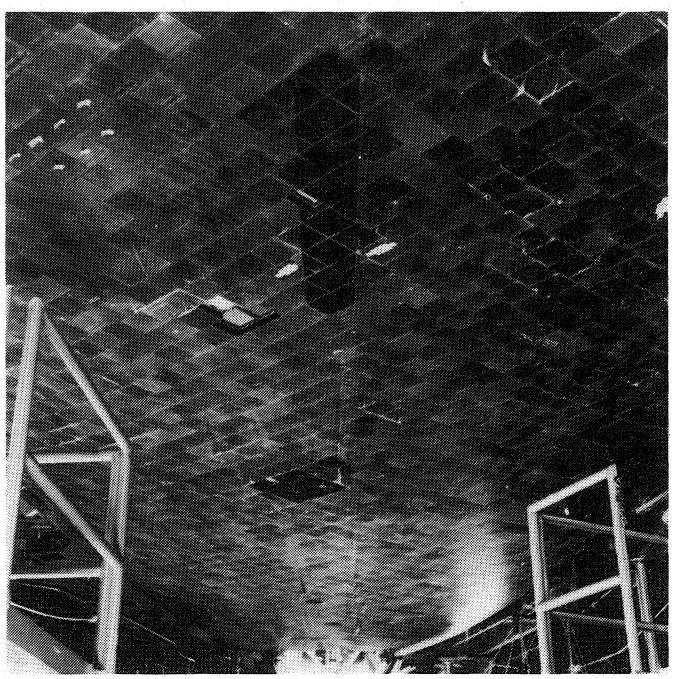

Fig. 4. Pre-flight STS-5 photographs of CSE experiment along the mid fuselage of the Orbiter.

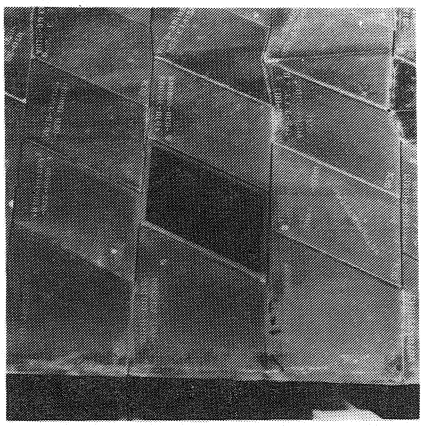

X/L = 0.1

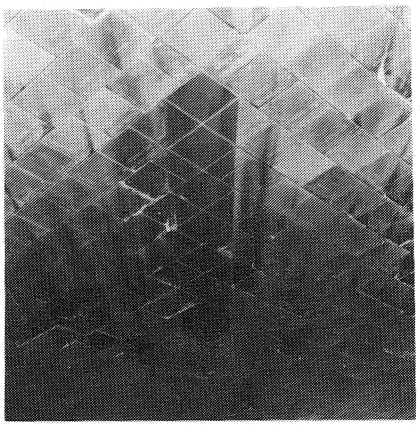

STRIP, 0.35 ≤ X/L ≤ 0.4

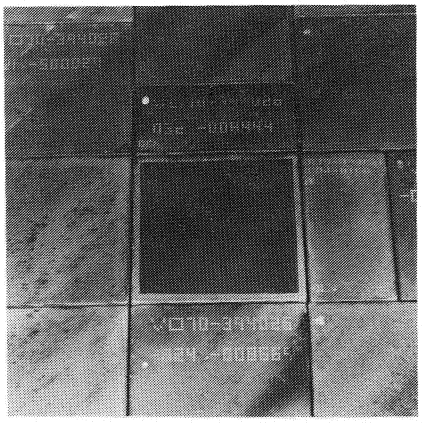

X/L = 0.6

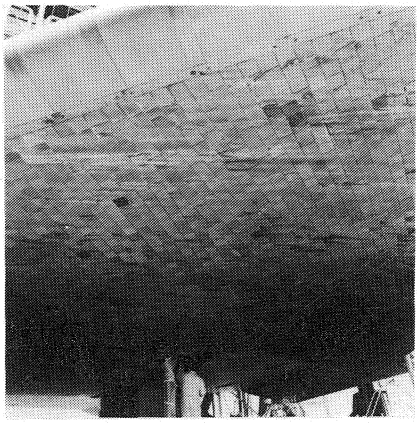

WING, 60% CHORD

Fig. 5. Post-flight photographs of selected tiles.

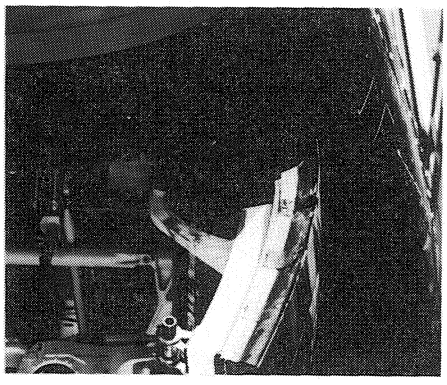

GAP FILLERS

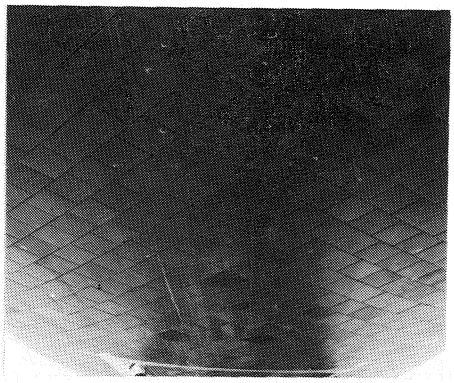

SENSORS

Fig. 6. Possible contamination sources.

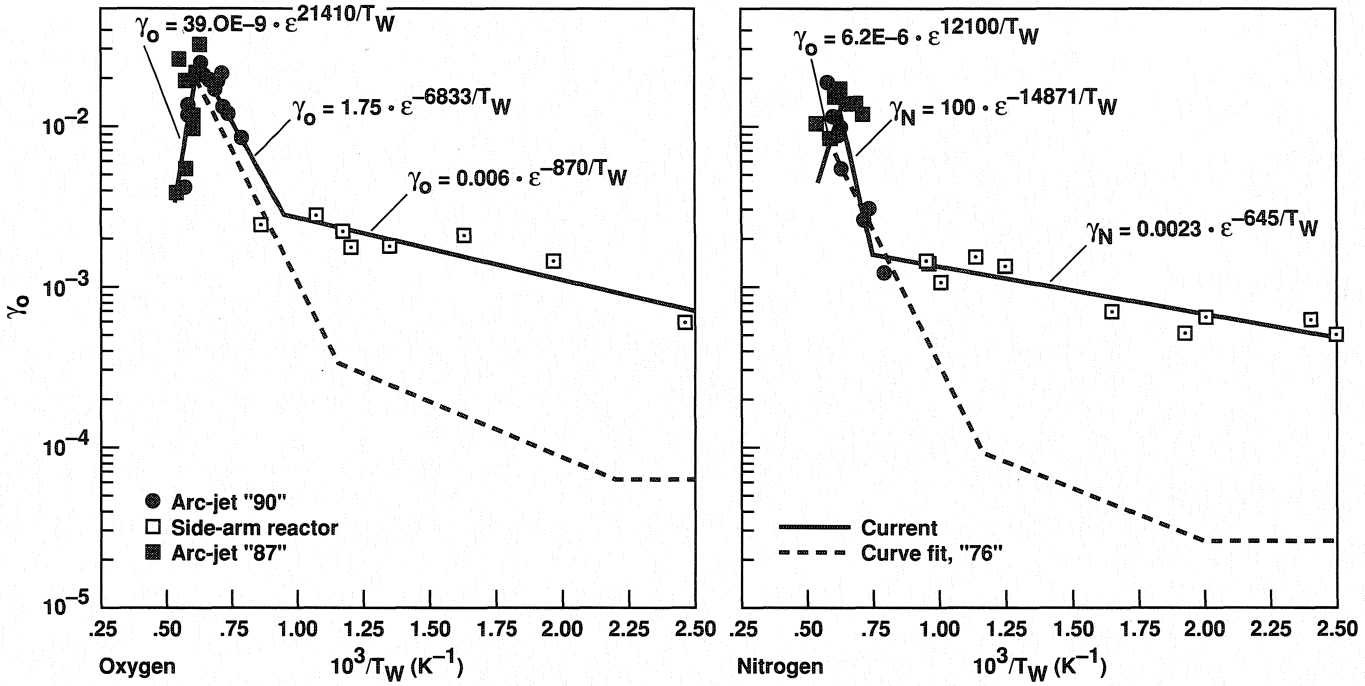

a) RCG

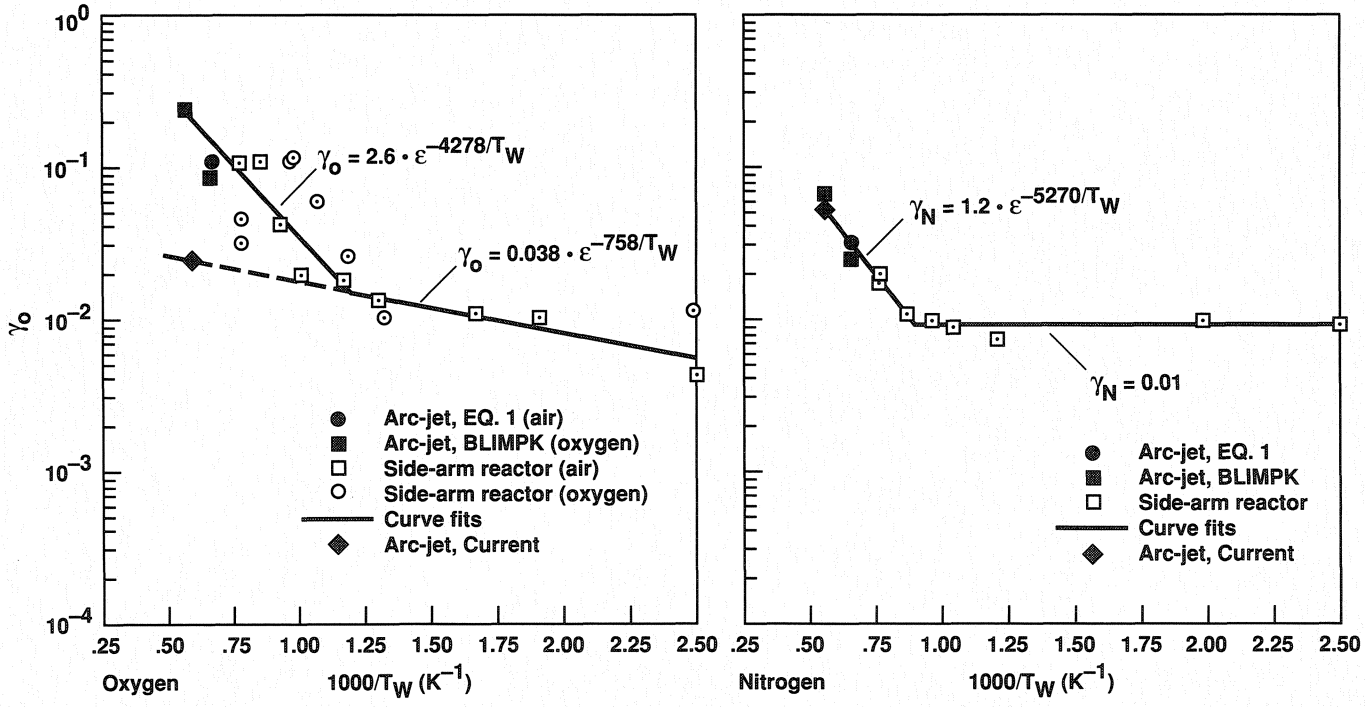

b) C-742 (spinel)

Fig. 7. Recombination coefficients.

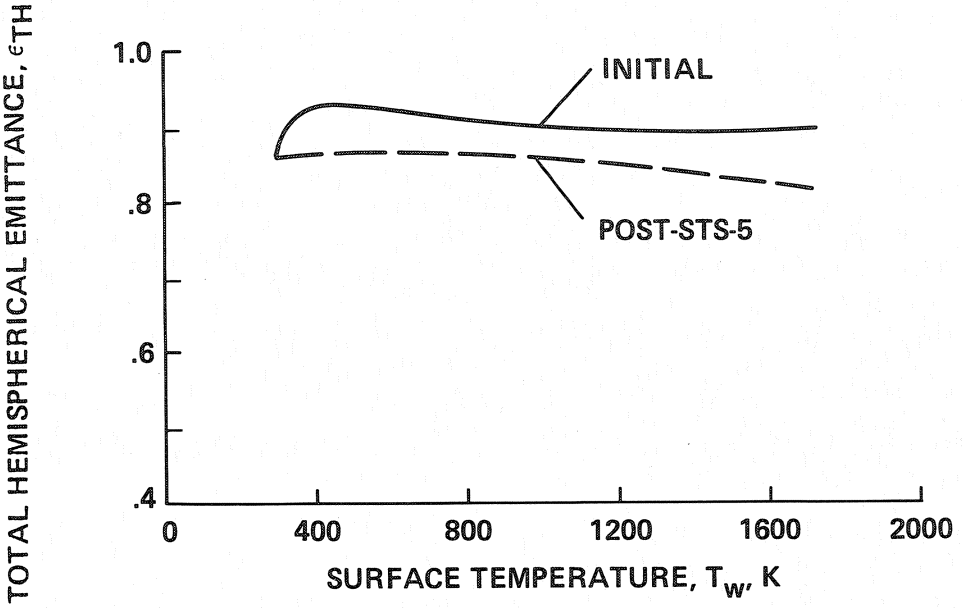

a) RCG baseline coating

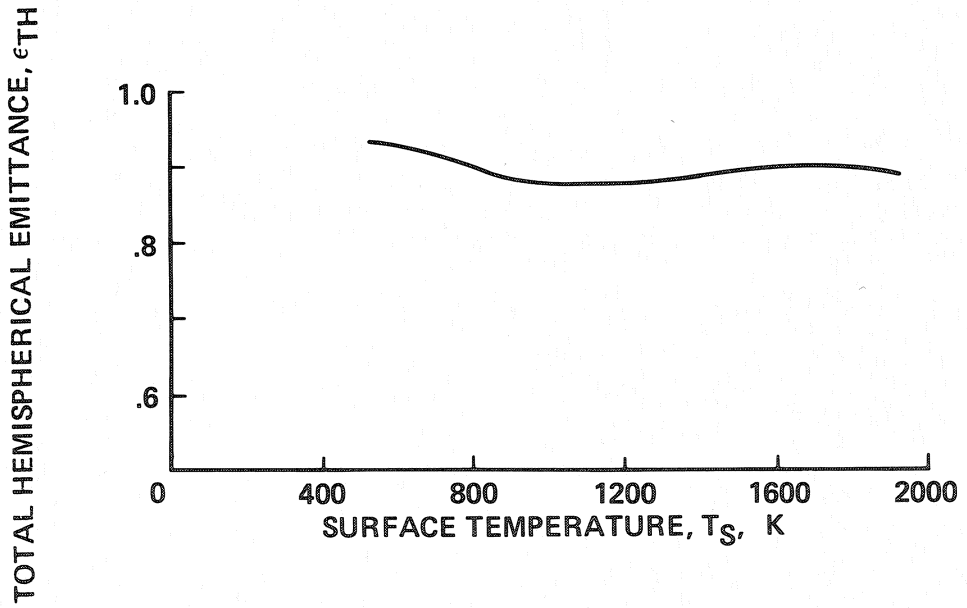

b) C-742 catalytic overcoat

Fig. 8. Total hemispherical emittance.

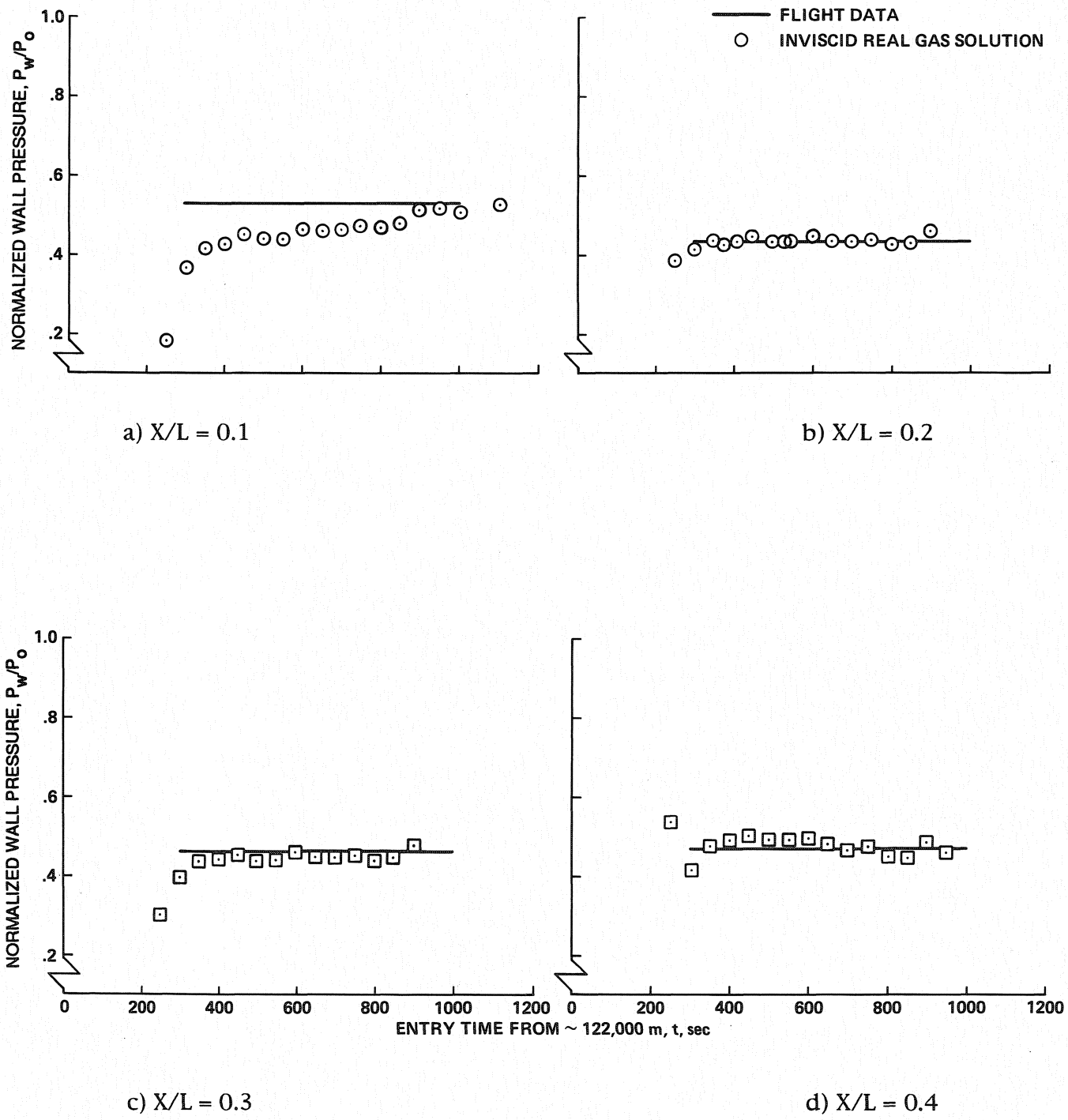

a) X/L = 0.1

b) X/L = 0.2

c) X/L = 0.3

d) X/L = 0.4

Fig. 9. Pressure history along wardward centerline during Earth entry (STS-3).

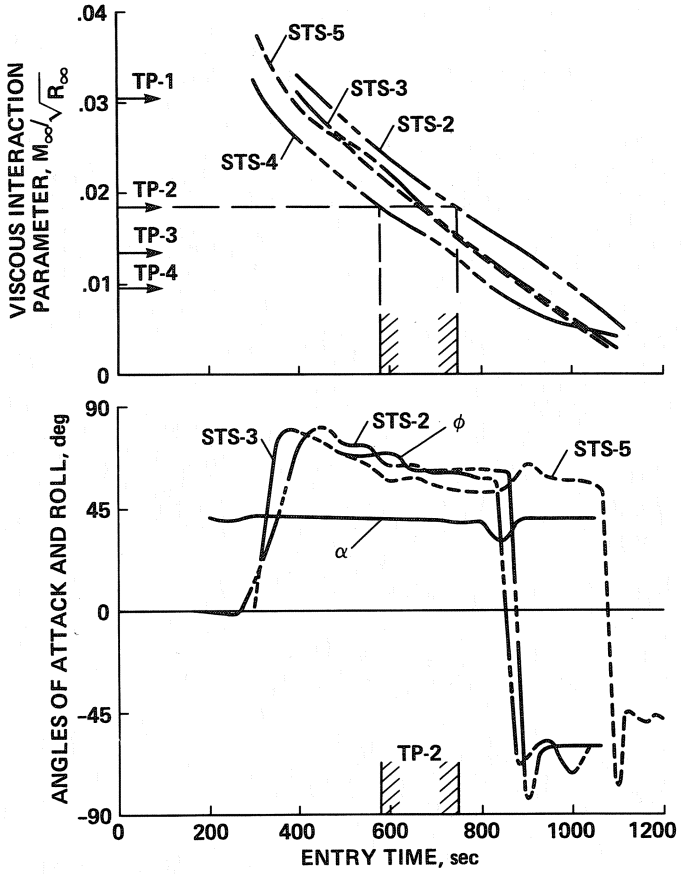

Fig. 10. Flight trajectory correlation parameter.

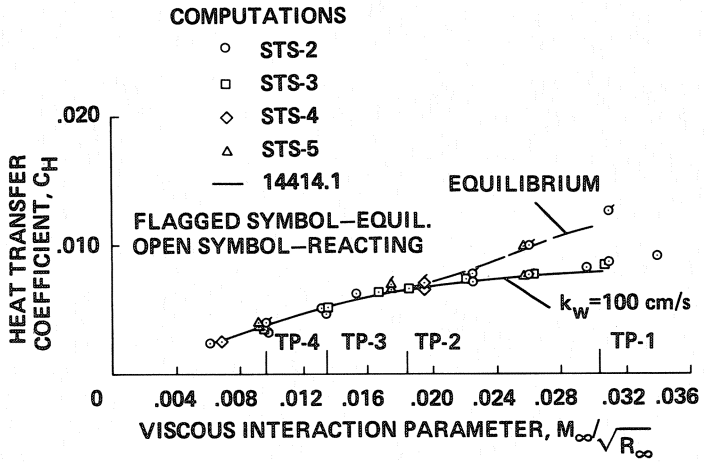

Fig. 11. Comparison of heat transfer coefficients using flight correlation parameter.

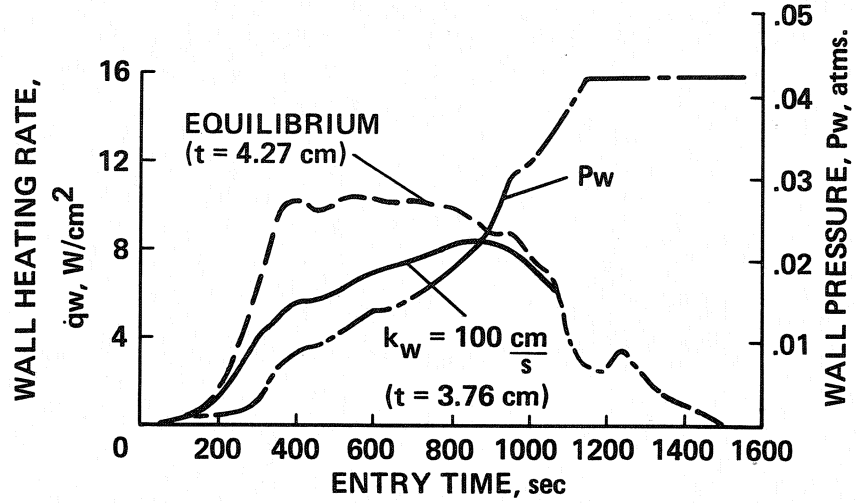

X/L = 0.15

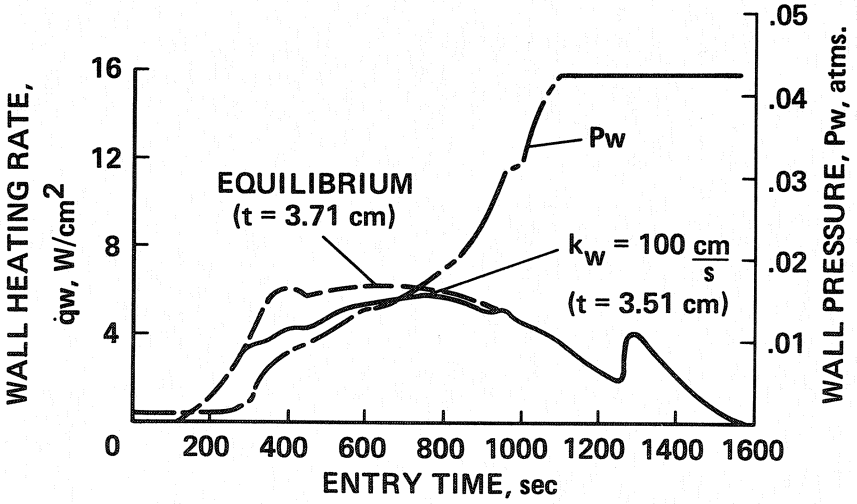

X/L = 0.4

Fig. 12. Predicted effect of surface catalysis on surface heating (STS-2).

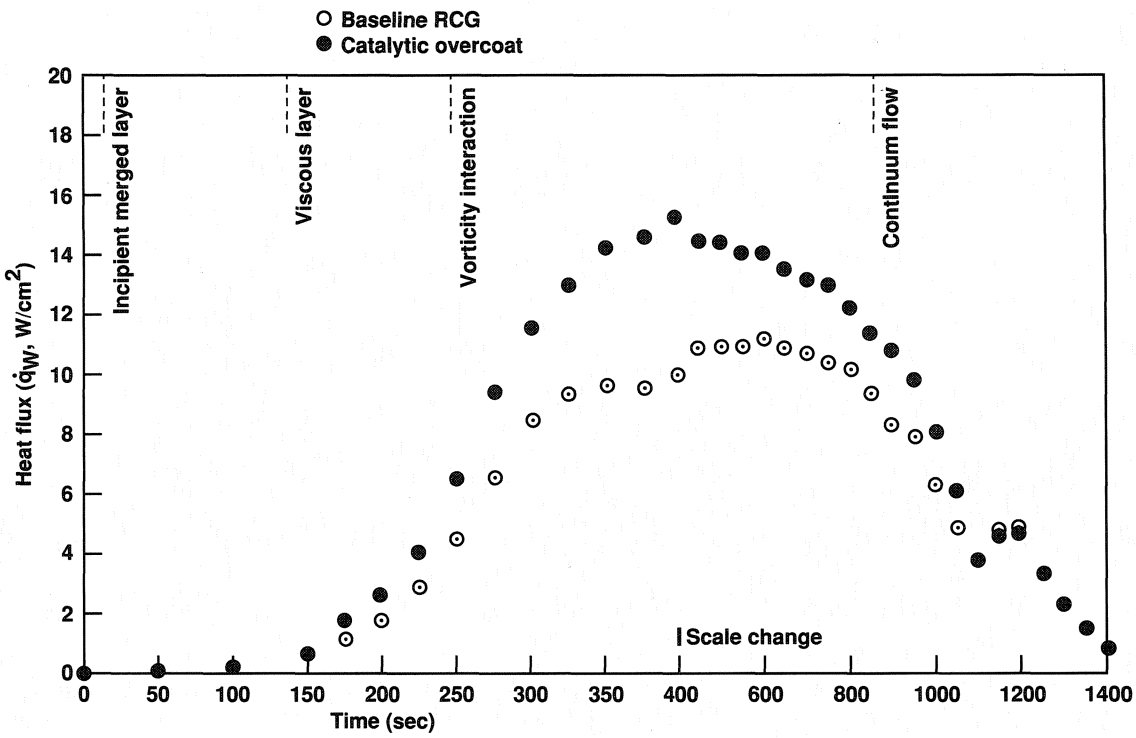

STS-5, X/L = 0.15

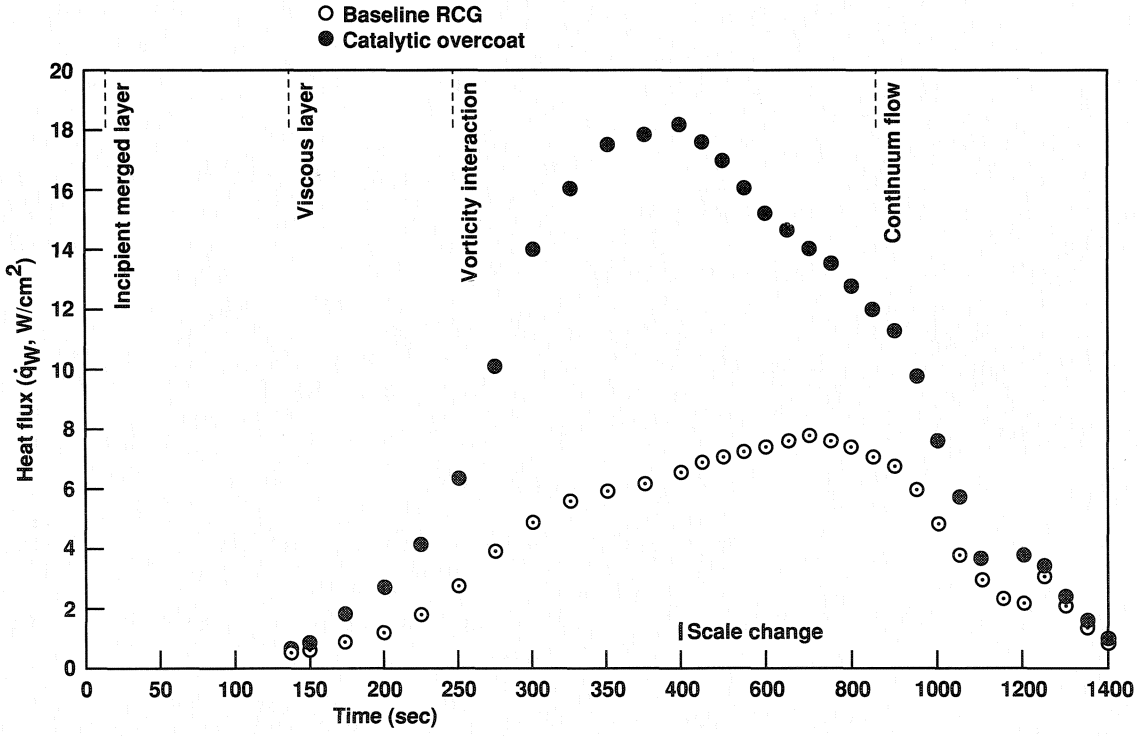

STS-3, X/L = 0.3

Fig. 13. Measured effect of surface catalysis on surface heating.

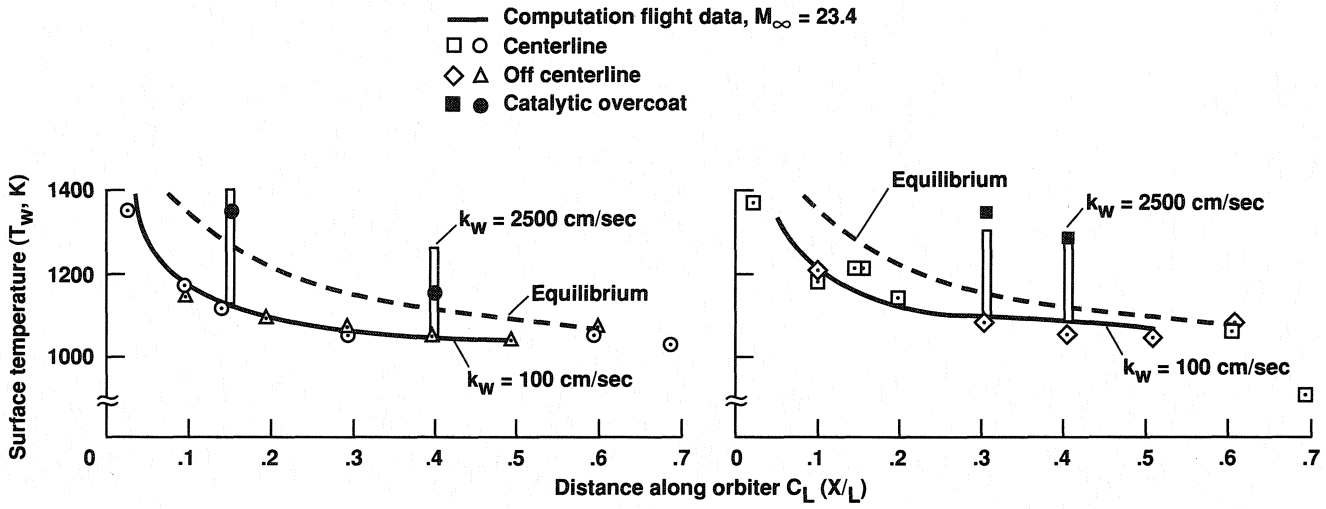

a) STS-2 b) STS-3

Fig. 14. Surface temperature distribution along mid fuselage of Orbiter.

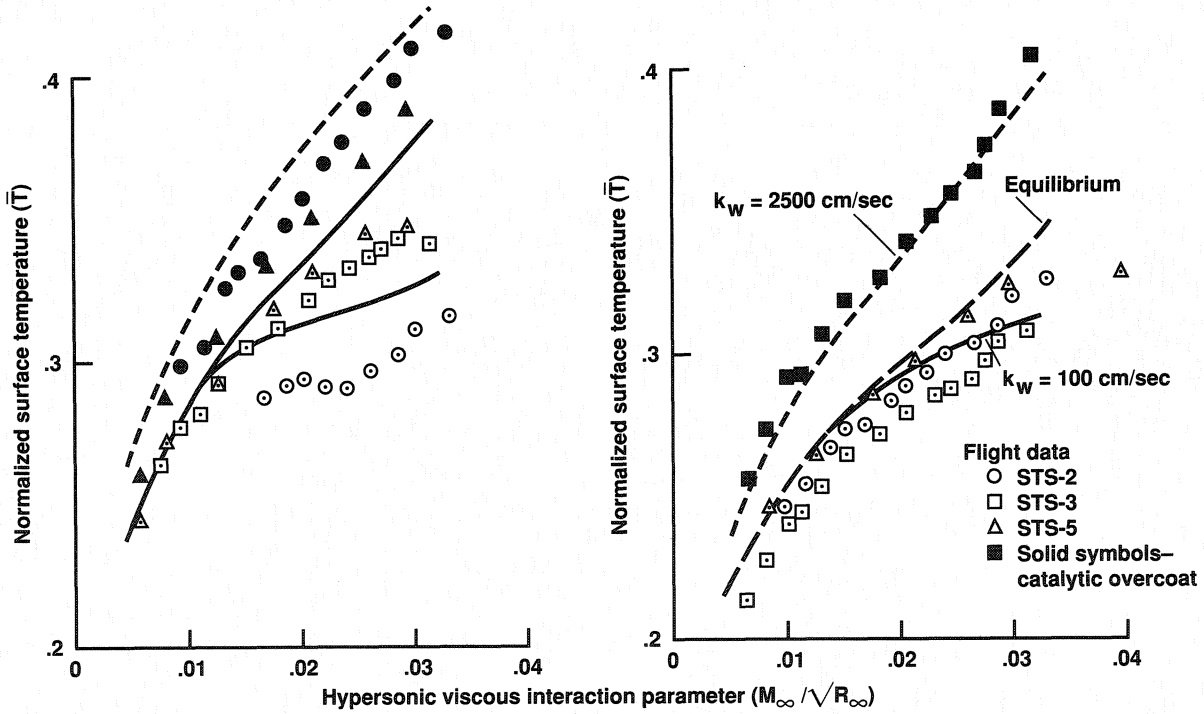

a) X/L = 0.15 b) X/L = 0.4

Fig. 15. Comparison of surface temperature at equivalent flight times.

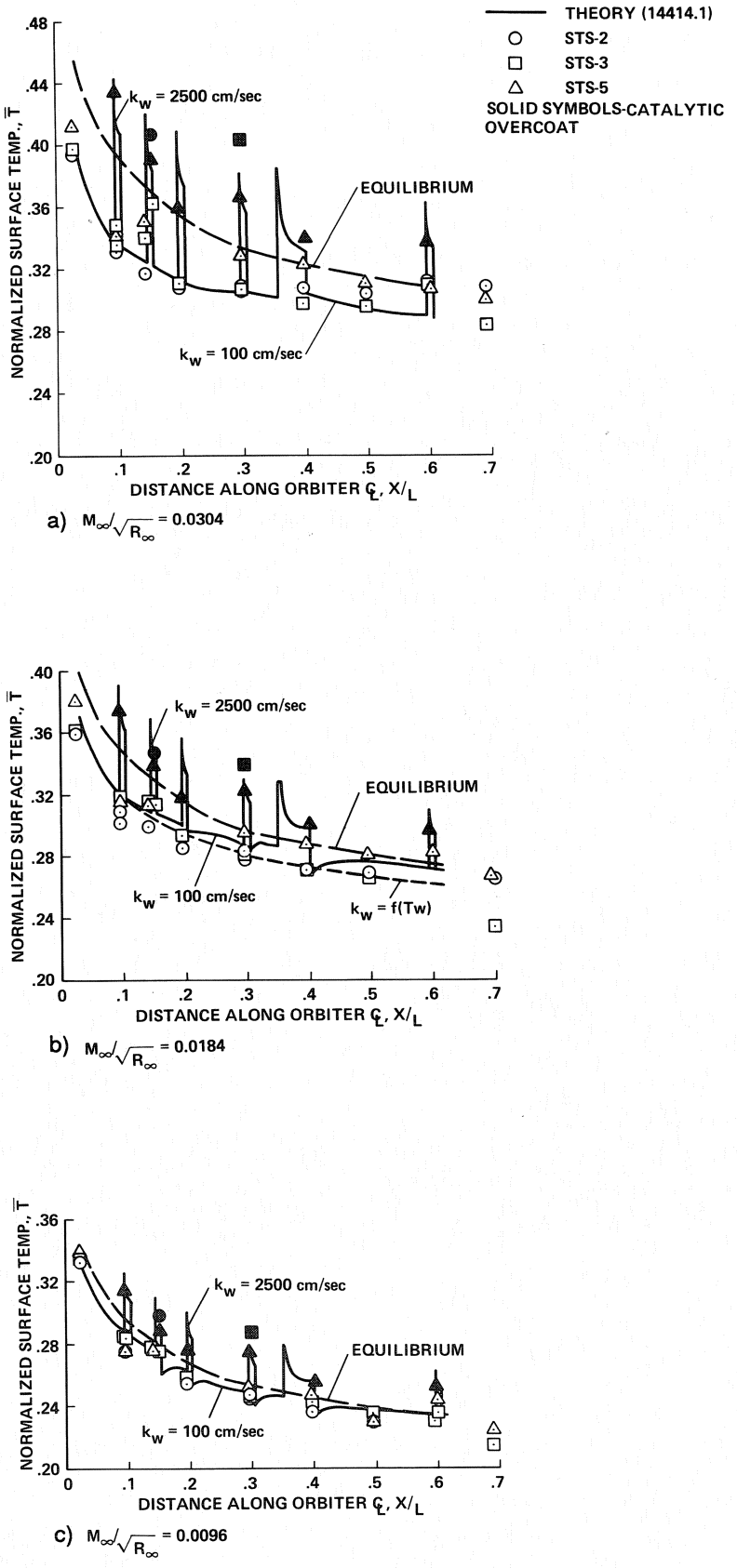

Fig. 16. Normalized surface temperature along mid fuselage.

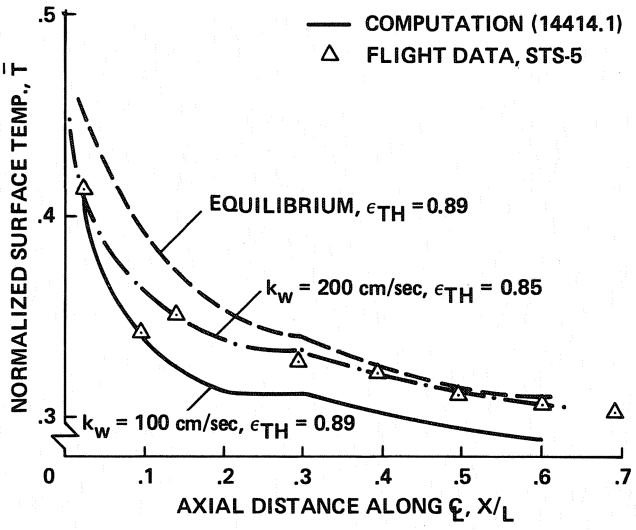

Fig. 17. Comparison of predicted and measured temperature distribution along mid fuselage of the Orbiter using STS-5 post-flight surface properties.

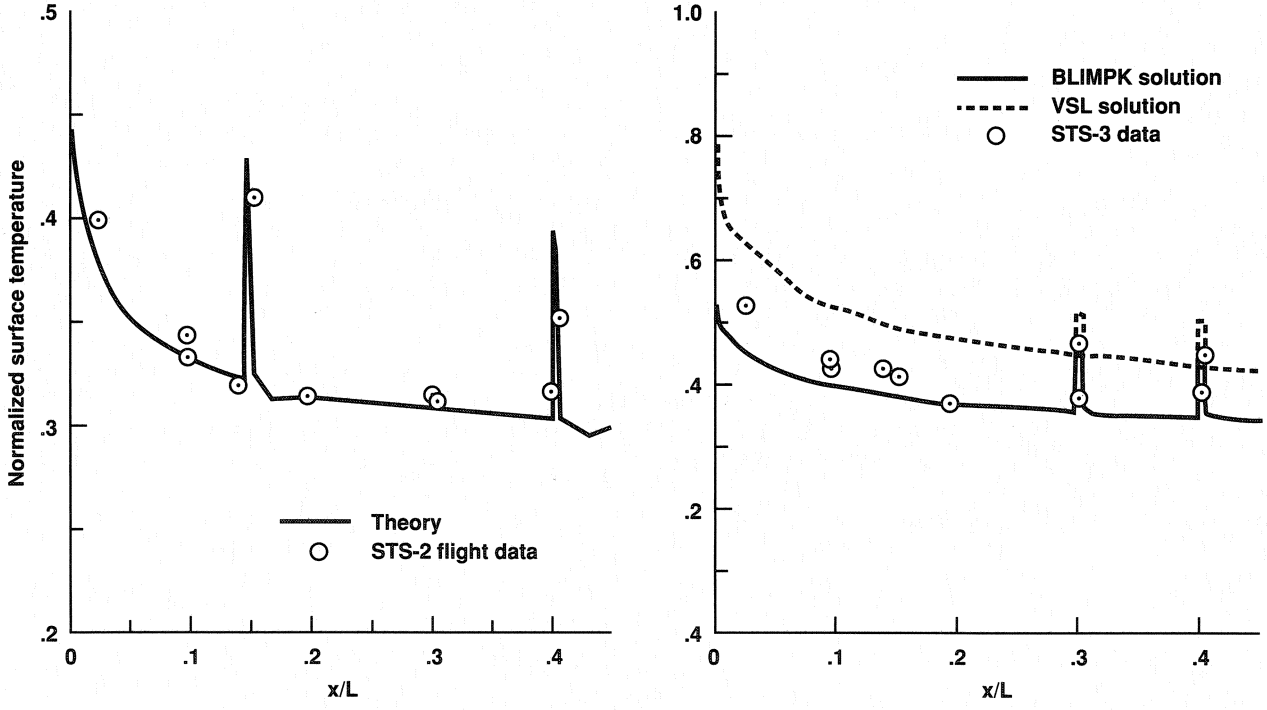

a) STS-2, Alt. 75.24 km

b) STS-3, Alt. = 91.1 km

Fig. 18. Comparison of current BLIMPK solutions with measured temperature distribution along mid fuselage of Orbiter.

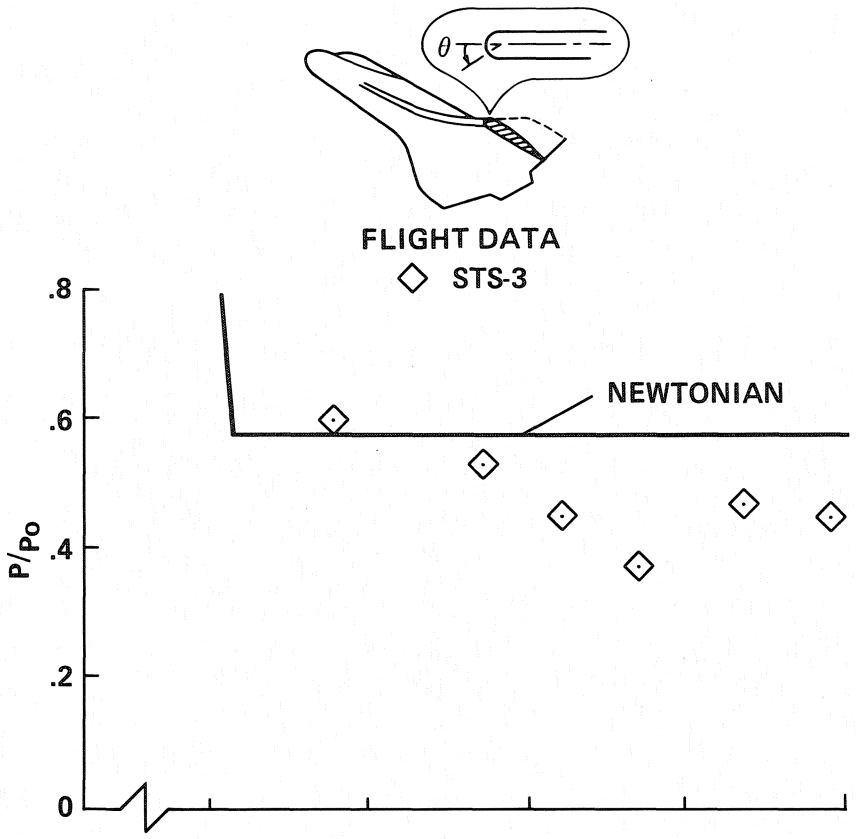

a) Wing pressure at 60% semispan

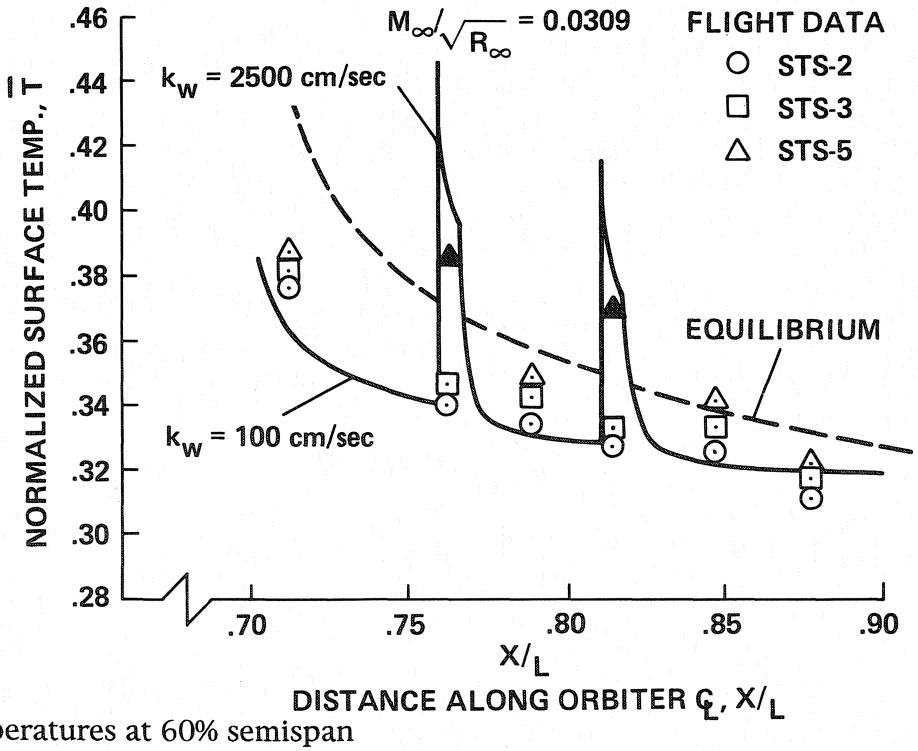

b) Wing temperatures at 60% semispan

Fig. 19. Surface pressure and temperature distribution along 60% semispan on Orbiter wing.

ORBITER WINDWARD-SURFACE BOUNDARY-LAYER TRANSITION FLIGHT DATA*

Stanley A. Bouslog and Michael Y. An
Lockheed Engineering & Sciences Company
Houston, TX

Stephen M. Derry
NASA Johnson Space Center
Houston, TX

SUMMARY

Both thermocouple data and flight-derived axial force coefficients have been used to determine the freestream flight conditions at which boundary-layer transition occurs on the windward surface of the Space Shuttle Orbiter during reentry. Boundary-layer edge local flow conditions corresponding to transition at thermocouple locations on the orbiter windward centerline have also been computed. Tables of the freestream conditions and the local flow conditions at transition are included. Transition occurred over a freestream Mach number range of 5.8 to 17.5 and Reynolds number range of 2.5×10^6 to 1.3×10^7. The roughness state of the orbiter vehicles is also discussed and correlated to the occurrence of transition. Both distributed and discrete roughness-induced transition correlations, which were based upon windtunnel test data and used in the orbiter development, have been evaluated using the flight data. Using a distributed roughness transition correlation, a flight-derived roughness height of 0.053 inches was obtained which compared well with estimates of the orbiter surface roughness. A discrete element roughness correlation applied to the orbiter was also evaluated. Flight-derived roughness heights were computed using this relation and compared to pre-flight estimates of equivalent roughness elements generated by the orbiter tile gaps and height misalignments. The derived roughness heights are comparable to the estimated pre-flight equivalent roughness. The average flight-derived equivalent roughness was computed to be 0.118 inches. Both roughness-induced transition correlations along with their respective flight-derived roughness heights can be used to predict transition with reasonable results assuming no significant changes in surface roughness occur during entry. The very early transition during the STS-28 mission, which has been attributed to two surface protuberances, is also discussed.

NOMENCLATURE

C_A	Axial force coefficient
k	Roughness height
K_{eff}	Effective roughness height
K_{eq}	Equivalent roughness height
L	Vehicle reference length, 1293 in.
M	Mach number
P	Pressure
Re_k	Local Reynolds number based on roughness height, k
Re_L	Freestream Reynolds number based on vehicle length, L
Re_x	Local Reynolds number based on wetted length, x
Re_o	Normal shock Reynolds number based on vehicle length, L
Re_θ	Local momentum thickness Reynolds number

*** Work done on contract at Lockheed Engineering & Sciences Company, NAS-9-17900.**

T	Temperature
$T_{T/C}$	Thermocouple temperature
x	Wetted axial length
X	Axial length (see fig. 2)
Y	Lateral distance in the span direction (see fig. 2)
V	Velocity
α	Angle of Attack
ρ	Density
δ^*	Displacement thickness
θ	Momentum thickness

INTRODUCTION

The Space Shuttle orbiter vehicles have flown over 50 hypersonic entries into the Earth's atmosphere. During the development of the orbiter, the variation in hypersonic reentry heating due to boundary-layer transition was a major concern in the design of the orbiter windward-surface thermal protection system (TPS). Early studies (ref. 1) demonstrated that the heat load to the windward surface increased by a factor of two if fully turbulent heating rather than laminar heating was considered. This increase in heat load would have significantly increased the weight of the TPS. Therefore, the initial orbiter design goal was to constrain the fabrication and installation of the windward-surface thermal protection tiles such that transition would not occur earlier than that obtained during smooth body windtunnel tests (refs. 2 and 3). However, it was realized that this goal imposed manufacturing and processing constraints that were not feasible. Therefore, more refined roughness-induced windtunnel-derived transition correlations were developed and used to relax the constraints on the windward-surface thermal protection system.

Today, with an operational Space Transportation System (STS), the orbiter boundary-layer transition remains an important issue. Processing the orbiter vehicle from flight to flight requires the inspection of thermal protection system repairs and maintenance to reduce the risk of an early transition. The increased heating associated with early transition can and has damaged the thermal protection system. The additional repairs associated with this damage increase the vehicle operational costs. With a better understanding of the transition phenomenon, operational procedures can be and have been modified to reduce orbiter processing costs.

After over a decade of flight and over 50 missions, a significant amount of flight boundary-layer transition flight data is available for evaluating the hypersonic transition phenomena and for evaluating roughness-induced transition correlations. Much of the flight data were obtained during the first four developmental flights (STS-1 through STS-4) and the first operational flight (STS-5). These flights provided data on the heavily instrumented Columbia vehicle. After these first five flights, a more limited set of data has been obtained on all of the orbiters, Columbia (OV-102), Discovery (OV-103), Atlantis (OV-104), Endeavour (OV-105), and Challenger (OV-099; prior to the STS-51L accident). These data provide a means to explore the long term trends of boundary-layer transition on several vehicles with nominally the same geometry. Determining boundary-layer transition from flight data has the advantage over that derived from windtunnel data in that facility noise is not introduced into the problem, and flight-derived data also have the advantage of being obtained at flight conditions as opposed to the conditions available in a windtunnel. Local flow conditions, which are usually needed for boundary-layer transition correlations, are not easily determined from either flight or windtunnel data and usually require analytical prediction. Use of flight data to evaluate transition trends from flight to flight is also complicated by the unknown roughness state of the vehicle, especially a vehicle like the orbiter which has a surface composed of thousands of fragile thermal protection tiles.

Goodrich et al (ref. 2) have used the thermocouple data from STS-1 through 5 to determine the time, the freestream conditions, and the local flow conditions at which boundary-layer transition occurs for specific locations on the orbiter during reentry. Harthun and Blumer (ref. 4) and Hartung and Throckmorton (ref. 5) have used these data to characterize the movement of the transition front on the vehicle. Unfortunately, no windward-surface thermocouple data were obtained between the STS-5 mission and the Challenger accident. However, upon return to flight (STS-26) a limited set of windward-surface thermocouple data has been obtained during all but one mission, STS-53. Furthermore, a review of the flight-derived aerodynamic coefficient data base which is obtained for most of the missions has provided an alternate method of determining the flight conditions at which the vehicle experiences transition. Step changes in the axial force during reentry indicate the onset of boundary-layer transition. Histories of the axial force coefficient, C_A, have been used to determine the time, and therefore the flight conditions, at which the boundary layer rapidly undergoes transition from laminar to turbulent.

This paper presents a summary of the freestream and predicted centerline local flow conditions at which boundary-layer transition has occurred on the windward surface of the orbiter during entry. Typical transition correlation parameters, such as the local transition Reynolds number and the momentum thickness Reynolds number, are presented in an attempt to correlate the data. A description of the roughness state of the vehicles is also provided and then compared to the flight conditions at transition. Two windtunnel-derived roughness-induced transition correlations that consider both distributed and discrete roughness, and that were used in the orbiter development, are also evaluated. Flight-data derived roughness heights, which were determined from these correlations, are presented and compared to the roughness state of the vehicle. This comparison provides an indication of the capability of windtunnel-derived correlations to predict boundary-layer transition on a hypersonic flight vehicle. Finally, the very early boundary-layer transition during the STS-28 entry is evaluated.

BOUNDARY-LAYER TRANSITION FLIGHT DATA

Thermocouple Data

As the boundary layer on the windward surface of the orbiter begins to transition from laminar to turbulent, the shear stress at the wall increases causing an increase in the convective heating rate and a corresponding increase in the wall temperature. This phenomenon is dramatically depicted by a typical history of thermocouple data on the windward surface of the orbiter, as presented in fig. 1. The rapid increase in temperature provides an indication of the onset of transition. The completion of the transition from a laminar to a turbulent boundary layer is also evident. This transition process takes approximately 20-30 seconds for a specific location on the orbiter.

During the first five flights (STS-1 through 5), the thermocouple data were obtained from the Developmental Flight Instrumentation (DFI) system which recorded the data from platinum/platinum-13% rhodium (ANSI Type R) thermocouples (ref. 6). The thermocouple junctions were placed under the Reaction Cured Glass (RCG) coating of the shuttle tiles. This coating is .015-.025 inches thick. Malfunctions of the recording equipment and data processing problems resulted in loss of much of the data during STS-1 and STS-4. Complete entry histories of the thermocouple data for STS-2, 3, and 5 are documented by Hartung and Throckmorton (ref. 6).

For flights STS-26 to present, the thermocouple data were obtained from the Modular Auxiliary Data System (MADS) which is similar to the DFI system. In fact, many of the same instruments are used on the Columbia MADS. However, the number of operational thermocouples on the windward surface of the four orbiters is very limited. Figure 2 presents a sketch of the locations of the operational MADS thermocouples on the four vehicles. Thermocouple (T/C) coordinates corresponding to the instrument locations depicted in fig. 2 are provided in Table I. Histories of the thermocouple data are obtained after each flight and have

been compiled into a data base for the present study and were reviewed to determine the time at which transition occurred.

Axial Force Data

For many of the orbiter entries the boundary-layer transition happens rapidly enough that a step change in the axial force coefficient, C_A, occurs due to a sudden increase in skin friction associated with a turbulent boundary layer. A history of the axial force coefficient for STS-5 is presented in fig. 3 and the apparent transition point is indicated. The times from entry interface at which transition onset occurs, based upon this method, have been summarized for the shuttle missions in Table II. In some cases, transition could not be determined from the C_A history. The axial force coefficients used were derived from on-board accelerometer data and trajectory data by Rockwell International. Table II also includes the range of entry times and Mach numbers at which boundary-layer transition occurs based upon thermocouple data. For most cases, both methods of predicting transition give consistent results. A comparison of the transition times as determined from the axial force coefficients with those determined locally at the thermocouple locations are presented in fig. 4 for missions STS-2 and 5. The symbols indicate the time at which transition occurred for a specific location (X/L). The data for STS-2 show that transition is indicated by the C_A data after transition has moved forward to over half of the vehicle, as determined by the thermocouple data. For STS-5, transition moves forward on the vehicle very rapidly and again the C_A data indicate transition at a consistent time.

Asymmetric Transition

In some instances, orbiter reentry has experienced anomalous elevon deflections that have been attributed to asymmetric boundary-layer transition on the orbiter windward surface. The differential skin friction between a laminar and a turbulent boundary layer induces a yawing moment on the vehicle that must be corrected. Thermocouple data have assisted in evaluating this anomaly. During STS-48, Discovery (OV-103) experienced anomalous elevon deflections, and thermocouples on the right and left side of the fuselage centerline indicated that the left side transitioned approximately 52 seconds prior to the right side. Figure 5 presents the thermocouple histories for this flight.

REVIEW OF TRANSITION FLIGHT DATA

Freestream Conditions

Prior to STS-44, a Best Estimated Trajectory (BET) was developed by the Rockwell Shuttle Operations Company that provided the history of the altitude, velocity, and angle-of-attack of the vehicle from entry interface (400,000 ft) to touchdown. Atmospheric parameters, such as density, were also provided; however, the density was often corrected by information from aerodynamic coefficient data bases. For flights STS-44 to present, the trajectory data have been obtained from the Operational Instrumentation (OI) system and the density is obtained from the dynamic pressure which is derived from accelerometer data and curve-fits of aerodynamic coefficients. These parameters can be used to establish the flight conditions existing when events, such as boundary-layer transition, occur. The freestream Reynolds number (based on orbiter length) histories are shown in fig. 6. Typical velocity/altitude histories for several missions are presented in fig. 7. Angle-of-attack and Mach number histories are presented in fig. 8. As can be seen, the entry trajectories are similar from mission to mission.

Once the transition times have been determined for each thermocouple, the corresponding freestream conditions were determined from the trajectory data base. Tables of the thermocouple locations, transition times, vehicle angle-of-attack and corresponding freestream conditions have been generated for the twenty-

eight missions, STS-26 through STS-54. Table III presents the freestream conditions for both the onset and completion of transition for the thermocouple locations on Discovery (OV-103) during STS-26. The conditions for only the onset of transition are presented in Table IV for STS-27 through STS-54. A double entry in this table for a single location indicates that the boundary layer began to transition, relaminarized, and then finally completed the transition process. The flight conditions corresponding to transition onset as determined by the available axial force coefficient data are included in Table V.

Upon reviewing the axial force and thermocouple derived transition conditions (Tables III, IV, and V), the range of freestream conditions at which transition has occurred for most of the orbiter entries has been determined. Figures 9 and 10, respectively, present the freestream Reynolds number, based on orbiter length, and Mach number at which transition has occurred on the orbiter as determined from the thermocouple data at X/L = 0.6. This location was chosen because thermocouple data was available for all of the vehicles and a significant portion of the vehicle would have a turbulent boundary layer. The normal shock Reynolds number, $Re_o \equiv \rho_\infty U_\infty L/\mu_o$, has also been computed for the transition times for this location and it is presented in fig. 11. The normal shock Reynolds number has been suggested by Ried (ref. 1) to be a flight-scaling parameter for transition testing. Considering these sets of data, the Mach number at transition varies between 5.8 and 17.5, the freestream Reynolds number range, based upon the orbiter length, varies from 2.5×10^6 to 1.3×10^7, and Re_o varies from 0.4×10^6 to 3.7×10^6. From the data presented in figs. 9 and 10, it is evident that transition occurred earlier than normal during STS-1, STS-27, STS-28, and STS-48. The early transition during STS-1 has been attributed to tile damage in the nose gear door area. Significant tile damage due to ascent debris impacts occurred on STS-27. During STS-28, protruding tile gap fillers apparently caused early transition. The early transition during STS-48 could have been caused by slumped tiles on the nose-gear door or by protruding gap fillers. Also, if the transition flight conditions determined from axial force data (Table V) are reviewed, it is seen that STS-7, 8, and 41D transitioned early. It has not been determined exactly why transition occurred early during these flights, but it is hypothesized that nose-gear door repairs increased the roughness of the nose region. If these seven missions are not considered, then the transition freestream Mach number range is reduced to 5.8 - 10.6 with an average of approximately 8.0, and the corresponding freestream Reynolds number range is 5.0×10^6 - 1.3×10^7 with an average of 8.0×10^6.

Local Flow Conditions

Typical transition correlation parameters, such as the local Reynolds number, Re_x and the momentum thickness Reynolds number, Re_θ and Re_θ/M, can be used to attempt to correlate the transition flight data. Boundary-layer edge values of Mach number, velocity, density, and viscosity, and the local momentum thickness must be determined to compute the correlation parameters. Furthermore, with the variations of velocity, density, and viscosity across the boundary layer, the roughness Reynolds number, Re_k can be calculated where the flow conditions at the roughness height, k, in the boundary layer are used. Goodrich and Derry (ref. 2) used the results of orbiter flowfield predictions (ref. 7) to generate correlations that provide the local flow conditions on the centerline of the windward surface of the orbiter. The correlations were implemented into the MINIVER code (ref. 8) by adjusting the local angle-of-attack and shock angle to match the local pressures and velocities predicted by an orbiter flowfield code (ref. 7). Boundary-layer profiles of velocity, density, and viscosity were computed in MINIVER using curve-fits of velocity and enthalpy profiles that were verified by boundary layer solutions. The correlations were updated using three equilibrium air orbiter inviscid flowfield solutions predicted by the IEC3D code (refs. 9 and 10) for entry Mach numbers of 6.6, 9.2, and 17.6. These conditions correspond to flight conditions just prior to transition during STS-30, STS-5, and STS-28, respectively, and represent the range of conditions over which transition has occurred. The MINIVER correlations were updated by matching the local pressure and local edge velocities at six locations on the windward centerline (X/L = 0.1, 0.3, 0.6, 0.7, 0.75, and 0.9). Figure 12 presents a comparison of the local Mach numbers computed by MINIVER with those obtained from IEC3D flowfield values interpolated at the boundary-layer thickness. The local flow parameters for the

thermocouple locations on the vehicle centerline for STS-26 through STS-54 were then computed using the modified MINIVER, and they are tabulated in Table VI.

With the local flow conditions at transition defined for the orbiter windward centerline, an attempt may be made to correlate the boundary-layer transition data. Goodrich et al (ref. 2) presented the local Mach number, the local Reynolds number, Re_θ/M, and a roughness Reynolds number, Re_k, at transition for thermocouple locations during the first five missions. These parameters are compared with the STS-26 to STS-54 data in figs. 13 - 16. Most of the local transition Mach numbers shown in fig. 13 fall within a band of 1.6 to 2.8 due to the similarity of entry flight conditions from flight to flight. However, the early transition during STS-28 and STS-48 results in higher local Mach numbers at transition, indicating some anomaly. Figure 14 presents the local Reynolds number, $Re_{x,tr}$, at which transition occurred, and the considerable scatter in values, especially on the aft section of the vehicle, suggests that this parameter does a poor job of correlating the data. Distributions of the Re_θ/M parameter derived from the transition flight data are presented in fig. 15 with the Re_θ/M variation at transition for a smooth body which Goodrich (ref. 2) derived from windtunnel data. Goodrich noted that Re_θ/M correlates the flight data for the front 40% of the vehicle, and the windtunnel and flight data are in fair agreement. However, considerable scatter in the data exists aft of X/L = 0.40 and is bounded by the early transition that occurred during STS-28 and the late transition that occurred during STS-49.

Both parameters, $Re_{x,tr}$ and Re_θ/M, have been used to attempt to correlate transition data using boundary-layer edge conditions; however, they do not account for the very important effects of roughness or wall temperature. The roughness Reynolds number, Re_k, accounts for these effects by using the flow conditions at the roughness height in the boundary layer. Density variations in the boundary layer due to changes in the wall temperature are accounted for by evaluating the conditions at the roughness height. The Re_k trends are presented in fig. 16 for a constant distributed-roughness height of 0.06 inches which was used by Goodrich (ref. 2). This parameter appears to provide a reasonable correlation of the data despite the constant roughness assumption. Improvements to the correlation may be possible if a method was available to characterize the roughness of the vehicle.

ROUGHNESS STATE OF THE VEHICLE

The roughness of the windward-surface of the orbiter is defined by the design and installation of the thermal protection system (TPS) and by in-flight damage or anomalies that alter the surface. The windward-surface TPS is composed of thousands of individual tiles. Gaps between the tiles and height misalignments from tile to tile result in discrete roughness elements that are distributed over the vehicle. Furthermore, the tiles themselves are delicate and very susceptible to damage. Damage to the tiles, which can be caused by debris from the External Tank and Solid Rocket Boosters, or the loosening and protrusion of fillers placed in gaps between tiles, increases the roughness of the vehicle. The roughness characteristics of each vehicle during each mission will be different and will have an effect on transition.

Pre-flight Orbiter Roughness

Goodrich (ref. 2) reviewed the available data concerning the installation of the tiles on the orbiter and estimated an averaged roughness distribution for the windward centerline. The values varied from approximately 0.04 inches for the tiled area behind the nose cap to 0.1 inches on the aft of the vehicle. To characterize the roughness of the vehicle due to tile steps and gaps, an equivalent roughness, as defined by Rockwell International (ref. 3), was used.

$$K_{eq} = \sqrt{S^2 + (G - 0.045)^2}$$

S is the step height and G is the tile gap. If the gap is less than 0.045 inches, the second term is ignored and the equivalent roughness is only a function of the tile step. The tiles are installed on the orbiter in an attempt to keep K_{eq} less than 0.110 inches in the nose region behind the nose cap. Prior to each flight since STS-26, the occurrences of K_{eq} greater than 0.110 inches near the vehicle nose or near the wing leading edges are recorded and documented. These values give an indication of the relative magnitude of discrete sources of roughness for each vehicle prior to flight. Averages of the K_{eq} values that exceed the specifications have been tabulated for each vehicle for the missions since STS-26 and are presented in Table VII. The fuselage averaged K_{eq} values in excess of 0.11 inches are approximately 0.13 inches with some variation from flight to flight due to tile repairs in the nose-gear door region. No general trend is seen in the pre-flight K_{eq} values from vehicle to vehicle.

Thermal Protection System Damage

Vehicle roughness during orbiter entries is also dependent upon flight damage or thermal protection system anomalies. After each flight, the vehicle is inspected and the number and size of tile damage sites are documented. Figure 17 presents a summary of the number of windward-surface tile damage sites for flights STS-6 to STS-54. Also, the number of locations where the damage site exceeded 1 inch in any dimension are shown. Flights STS-51G, STS-51F, STS-26, STS-27, and STS-39 experienced significant tile damage (over 200 sites). However, most of the damage on STS-26 and STS-39 consisted of small damage sites of under 1 inch in size.

Tile damage results in gouges or cavities in the surface and has potentially less effect on transition than protrusions from the surface into the flowfield. Other thermal protection system anomalies, such as the loosening of fillers placed in the gaps between some tiles, can result in protrusions from the surface into the boundary layer during orbiter entry. These protrusions produce a discrete source of disturbances that can promote transition. In one instance, STS-28, the occurrence of early transition has been attributed to gap fillers that protruded into the flow. This anomaly will be discussed in further detail in a later section.

Roughness Effects on Transition

Many studies have been conducted to obtain correlations between surface roughness and the onset of boundary-layer transition. However, the problem is complicated by defining an appropriate roughness height or distribution for a flight vehicle and whether to consider distributed or only several discrete roughness elements. Prior to flight the only knowledge about the orbiter's roughness is the general specifications used during tile installation and repair and the K_{eq} values computed near the nose and wing leading edge. During flight, the vehicle roughness can increase due to TPS damage by impacting debris or the creation of protuberances from loose tile gap fillers. It would be expected that the higher the average pre-flight K_{eq} value or the more TPS damage, transition would occur earlier. The pre-flight K_{eq} values of vehicle roughness in the nose region are correlated to the freestream Reynolds number at which transition occurred in fig. 18. However, the considerable scatter in K_{eq} data prevents any definite conclusions. Figure 19 presents the variation of transition freestream Reynolds number with number of damage sites. Again, the data are scattered but the trend appears to be that transition occurs earlier, lower freestream Reynolds number, as the damage-induced roughness of the vehicle increases. However, both flights STS-28 and 49 had a comparable number damage sites and yet STS-28 transitioned very early and STS-49 transitioned late in the entry. Furthermore, during the STS-27 flight, ablator material from one of the Solid Rocket Boosters debonded and impacted the orbiter during ascent. The result was over 600 tile damage sites and the loss of an entire tile on the windward surface of the OV-104 Orbiter. Despite this unprecedented damage, several flights with significantly less damage transitioned earlier. Therefore, general knowledge of vehicle tile damage does not directly provide a good indication of when the orbiter will transition during entry. Instead,

an evaluation of specific surface disturbances with roughness-induced transition correlations can provide a better understanding of transition on the orbiter.

ORBITER BOUNDARY-LAYER TRANSITION CORRELATIONS

In the development of the Orbiter, two types of correlations were used to evaluate boundary-layer transition on the orbiter windward surface. Both of these correlations were derived from windtunnel data and applied to the vehicle for evaluation of the thermal protection system during hypersonic entry. One correlation approached the problem by considering small distributed roughness elements on the surface as the source of transition. The other correlation accounted for transition by considering that transition was initiated by one or several discrete roughness elements located near the nose of the vehicle. These correlations have been applied to the flight conditions and compared to the transition flight data in order to evaluate their usefulness in analyzing transition on the orbiter.

Distributed Roughness Correlation

Bertin et al (ref. 11) used windtunnel data on roughened orbiter models to develop a correlation that accounted for the change in the occurrence of transition due to roughness elements distributed over most of the windward surface. From this correlation, incipient, critical, and effective roughness Reynolds numbers were defined. The incipient value, $Re_k = 30$, corresponds to the value at which the roughness has any effect on transition. The critical value, $Re_k = 110$, corresponds to the value at which the transition front is moving rapidly forward on the vehicle. The effective value, $Re_k = 180$, corresponds to the point at which the roughness elements have become effective boundary-layer trips. All of these values were derived for the local flow conditions at an X/L = 0.1. Figure 20 presents the windtunnel data Bertin used to develop this correlation. In applying this correlation to flight an average distributed roughness value must be assumed. As discussed earlier, this value is not easily obtained. Goodrich et al (ref. 2) have shown that the effective and critical values of $Re_{k,X/L=0.1}$ with k = 0.06 inches provide good predictions of transition when compared with STS-1 to 5 flight data. It was shown that for a $Re_{k,X/L=0.1} = 110$ the transition front is just starting to move forward on the body and when $Re_{k,X/L=0.1} = 180$ all of the tiles have become effective boundary-layer trips and the transition front has moved to the nose region. In order to evaluate Bertin's correlation, distributed roughness heights have been derived from the transition thermocouple flight data for STS-1 to 5 and STS-26 to 54. In this case, the roughness Reynolds number $Re_{k,X/L=0.1} = 110$ and 180 values were used since they bound the transition process on the windward surface. The effective roughness, K_{eff}, was obtained from Re_k boundary-layer profiles using the local flow conditions at X/L = 0.1 and the freestream flight conditions of transition for an X/L = 0.6. This location was chosen because thermocouple data are available and it is near the middle of the windward surface. The derived values of effective roughness are presented in Table VIII, and the average of the $Re_{k,X/L=0.1} = 110$ and 180 values are presented in fig. 21. For flights between STS-5 and STS-26, the transition conditions derived from the axial force coefficient data were used to derive an effective roughness, and these values are also provided in Table VIII.

As can be seen in fig. 21, the flight-derived values for an effective distributed roughness range from 0.043 to 0.081 inches. However, it is noted that the roughness values derived for STS-1, 4, 27, 28, and STS-48 are significantly larger than the others. Significant tile damage occurred during STS-1 and 27 which would account for the larger effective roughness values. TPS anomalies occurred during STS-28 and may have occurred during the STS-4 and STS-48 missions which may have affected the vehicle roughness. Ignoring the flight-derived roughness heights for these missions, an average roughness height range of 0.043 inches to 0.068 inches is obtained with an average of 0.053 inches. These values are well within the range of the orbiter surface roughness (0.04 to 0.1 inches) estimated by Goodrich (ref. 2), and the average is close to the 0.06 inches value Goodrich chose for his analysis.

Using a known roughness, Bertin's correlation can be used to predict when transition occurs for a specific location on the orbiter windward surface. This prediction process is described by Bertin (ref. 11) and by Goodrich (ref. 2), but it can be a complex process. Since transition moves rapidly forward on the vehicle (see fig. 4), a simpler method is to estimate the transition time by using methods, such as used by MINIVER, to compute the trajectory history of $Re_{k,X/L=0.1}$ and to use the critical value of 110 as the estimate of transition onset.

Discrete Roughness Correlation

The effect of roughness on transition has also been investigated from the point of view of discrete roughness elements located near the nose of the vehicle. Van Driest and Blumer (ref. 12) developed a spherical-element effective-roughness transition correlation based upon supersonic windtunnel test data in which a ring of spherical disturbances was placed around the nose of a sharp cone. This correlation, which accounts for compressibility and heat transfer effects, was later modified by Harthun and Blumer (ref. 4) and applied to the orbiter.

$$\frac{K_{eff}}{\delta^*} = 30.7 / Re_x^{1/4}$$

In this correlation, it is assumed that isolated roughness elements, such as protruding corners of tiles near the nose, induce transition. Furthermore, the correlation provides a prediction of the conditions for the isolated roughness to become an effective boundary-layer trip. Given the local flow conditions at transition and a relation for computing the displacement thickness, δ^*, this relation can be used to obtain a flight-derived roughness. Harthun and Blumer (ref. 4) have used their correlation to obtain a flight-derived effective roughness of 0.113 inches at X/L = 0.1 for STS-1,2,3, and 5. Transition was assumed to occur when an equivalent spherical roughness of 0.113 inches, which was located at an X/L = 0.1, satisfied the above relation. Unfortunately, the flight conditions for transition at X/L = 0.1 cannot be determined from data for the more recent flights since no thermocouple is located this far forward. However, since transition moves rapidly forward on the orbiter windward surface, the flight conditions for transition at X/L = 0.6 were used to derive an equivalent effective roughness at X/L = 0.1. Flight-derived equivalent roughnesses at X/L = 0.1 were computed and are presented in Table IX and in fig. 22. Re_x was computed by the modified MINIVER code and δ^* was computed by a relation used by Rockwell International and derived from boundary-layer code solutions (ref. 13).

$$\delta^* = 39.527\, \delta^{**} / \sqrt{Re_\infty (1/ft)}$$

$$\delta^{**} = 1.542 - 0.02375\, (\alpha(\text{degs.}))$$

The flight-derived values are compared to the pre-flight K_{eq} values in fig. 22. The flight-derived roughness values are comparable to the pre-flight K_{eq} averaged values and the flight-derived values obtained by Harthun and Blumer for STS-1 to 5. Since the pre-flight K_{eq} values are an indication of discrete sources of transition in the nose region, the flight-derived values should be reasonably close if the correlation is valid. The large flight-derived values obtained for STS-1, 28, and 48 would be expected due to the previously mentioned TPS anomalies on these flights. If these three flights are ignored, an average flight-derived K_{eq} is 0.118 inches.

EVALUATION OF EARLY TRANSITION–STS-28

As previously discussed, the presence of significant tile damage which results in a "rougher" vehicle does not necessarily result in dramatically earlier transition. The location and type of damage must also be evaluated. The STS-28 mission resulted in less than average tile damage and yet transition occurred earlier than any other mission. In this case, gap fillers located between several tiles were found protruding from the surface with burn marks which indicated that they had been protruding during entry. Two of these gap fillers which, based upon post-flight inspections, protruded approximately a quarter of an inch above the surface, were identified as potential boundary-layer trips. The location of these two gap fillers and the active thermocouples on the windward surface are shown in fig. 23. The times from entry interface at which transition onset was indicated by the thermocouple are included in parentheses next to each location. In two locations the thermocouples indicated a double transition which is not completely understood but may be due to small changes in the local flow conditions caused by angle-of-attack variations.

In order to evaluate if these gap fillers could have tripped the boundary layer at these flight conditions, the Harthun and Blumer (ref. 4) correlation can be used to estimate an equivalent roughness size for comparison to that observed post-flight. To determine the local flow conditions, an equilibrium air inviscid flowfield solution at M = 17.56 was computed using the IEC3D code (ref. 9), and surface streamlines were computed by the methods outlined by Rakich (ref. 14) using the surface velocities obtained from IEC3D. Streamlines were traced to the location of the two protruding gap fillers, and boundary-layer solutions using the BLIMP88 (ref. 15) code were obtained. Figure 23 presents the location of the STS-28 protruding gap fillers relative to predicted streamlines on the orbiter windward surface. The Re_x and δ^* were obtained from these solutions and resulted in equivalent roughness heights of 0.14 and 0.15 inches using the Harthun and Blumer correlation. Obviously, the actual dimensions of the protruding gap fillers during entry are unknown; however, since the observed heights are larger than those required to become effective boundary-layer trips, these two gap fillers could have caused the early transition during STS-28.

Poll (ref. 16) has hypothesized that roughness-induced transition emanates from roughness elements on or near an attachment line. Furthermore, he states that a disturbance on an attachment line is a more effective boundary-layer trip than one located elsewhere. An attachment line is defined as the line that separates the flow that leaves the windward surface by wrapping around the leading edge from the flow that leaves over the trailing edge. The attachment line for the forward portion of the orbiter (upstream of the wing) is indicated in fig. 23, and the aft gap filler is very close to this line. Reviewing the transition times indicated by the thermocouples downstream of this protuberance, it appears that the transition front emanates from this gap filler. Therefore, one could hypothesize that the aft gap filler caused a disturbance at the attachment line and caused the early transition.

CONCLUDING REMARKS

Both thermocouple data and flight-derived axial force coefficients have been used to determine the freestream conditions at which transition occurs during the hypersonic entry of the orbiter. Local flow conditions at transition for locations on the windward-surface centerline have also been computed. The roughness state of the vehicles has also been discussed and correlated to the occurrence of transition. Pre-flight estimates of the orbiter roughness in the nose region based upon tile step and gap measurements show no direct correlation to when transition has occurred. However, an evaluation of flight-damage induced roughness showed the expected trend of earlier transition occurring for an orbiter with more damaged tiles. But, it was also recognized that minimal tile damage does not preclude an early transition and that the specific type and location of the disturbance must be evaluated. For nominal roughness flights, the average freestream Mach number at transition is 8.0 and the average freestream Reynolds number is 8.0×10^6.

Typical transition correlation parameters were evaluated with the transition flight data, and it was concluded that only those parameters that accounted for roughness effects would correlate the data. Two of the roughness-induced transition correlations used in the development of the orbiter were evaluated to assess their ability to correlate the data. The distributed roughness transition correlation provided a flight-derived roughness height of approximately 0.053 inches which compares well with the limited knowledge of the average roughness of the orbiter windward surface. Using the discrete roughness correlation, an effective roughness height of 0.118 inches was computed, which compared well with pre-flight measurements of discrete equivalent roughness values in the nose region. These flight-derived values can be used along with the respective correlations to predict the occurrence of transition during orbiter entry. However, the occurrence of early transition due to anomalies such as occurred during STS-28 cannot be predicted. In this case, early transition has been attributed to protruding tile gap fillers. The gap filler which probably induced early transition was located near an attachment line which lends credence to the attachment-line disturbance hypothesis of Poll.

ACKNOWLEDGMENTS

The authors would like to thank E. Alexander, G. R. Kinder and other personnel at Rockwell International, Downey, CA, for providing information about the orbiter pre-flight equivalent roughness heights, the post-flight tile damage assessments, and the axial force coefficient and dynamic pressure histories. Also, the authors thank J. Colovin/LESC for modifying and running the MINIVER computer program.

REFERENCES

1. Ried, R. C., Jr.; Goodrich, W. D.; Strouhal, G.; and Curry, D. M.: The Importance of Boundary-Layer Transition to the Space Shuttle Design. Proceedings of the Boundary-Layer Transition Workshop held Nov. 3-5, 1971, Aerospace Corp. Report No. TOR-0172(S2816-16) -5, Dec. 20, 1971.

2. Goodrich, W. D.; Derry, S. M.; and Bertin, J. J.: Shuttle Orbiter Boundary-layer Transition at Flight and Wind Tunnel Conditions. *Shuttle Performance: Lessons Learned, Part 2*. NASA CP 2283, March 1983, pp.753-779.

3. Orbiter Entry Heating Prediction Methods and Data Base. Rockwell International, STS83-0948, Rev. I, July 1988.

4. Harthun, M. H.; Blumer, C. B.; and Miller, B. A.: Orbiter Windward Surface Entry Heating: Post-Orbital Flight Test Program Update. *Shuttle Performance: Lessons Learned, Part 2*. NASA CP 2283, March 1983, pp. 781-804.

5. Hartung, L. C.; and Throckmorton, D. A.: Computer Visualization of Orbiter Lower Surface Boundary-layer Transition. *Journal of Spacecraft and Rockets*, vol. 24, no. 2, March-April 1987, pp.109-114.

6. Hartung, L. C.; and Throckmorton, D. A.: Space Shuttle Entry Heating Data Book, Volumes I-III. NASA RP 1191-1193, May 1988.

7. Goodrich, W. D.; Li, C. P.; Houston, C. K.; Chiu, P. B.; and Olmedo, L.: Numerical Computations of Orbiter Flowfields and Laminar Heating Rates. *Journal of Spacecraft and Rockets*, vol. 14, no. 5, May 1977, pp.257-264.

8. Hender, D. R.: A Miniature Version of the JA70 Aerodynamic Heating Program, H800 (MINIVER). MDC-G0462, McDonnell Douglas Astronautics Co., Huntington Beach, CA, Jan. 1972.

9. Tam, L. T.: LU-SGS Implicit Scheme for Entry Vehicle Flow Computation and Comparison with Aerodynamic Data. AIAA 92-2671-CP, June 1992.

10. An, M. Y.; Wang, K. C.; and Tam, L. T.: Computation of Inviscid Flowfield Around 3-D Aerospace Vehicles and Comparison with Experimental & Flight Data. AIAA Paper 93-0885, 31st Aerospace Sciences Meeting, Jan. 1993.

11. Bertin, J. J.; Hayden, T. E.; and Goodrich, W. D.: Shuttle Boundary-Layer Transition Due to Distributed Roughness and Surface Cooling. *Journal of Spacecraft and Rockets*, vol. 19, no. 5, Sept.-Oct. 1982, pp.389-396.

12. Van Driest, E. R.; and C. B. Blumer: Boundary-Layer Transition at Supersonic Speeds: Roughness Effects with Heat Transfer. *AIAA Journal*, vol. 6, no. 4, April 1968, pp. 603-607.

13. Alexander, E.: Private Communication. Rockwell International, Downey, CA, April 1993.

14. Rakich, J. V.; and Mateer, G. G.: Calculation of Metric Coefficients for Streamline Coordinates. *AIAA Journal*, vol. 10, no. 11, Nov. 1972, pp. 1538-1540.

15. Murray, A. L.: Further Enhancements of the BLIMP Computer Code and User's Guide. AFWAL-TR-88-3010, Wright-Patterson Air Force Base, OH, June 30, 1988.

16. Poll, D. I. A.: A New Hypothesis for Transition on the Windward Face of the Space Shuttle. *Journal of Spacecraft and Rockets*, vol. 23, no. 6, Nov.-Dec. 1986, pp.605-611.

Table I. Coordinates of the Orbiter Windward Surface MADS Thermocouple Locations

T/C ID	X/L	X (in.)	Y (in.)
V07T9468	0.296	382.9	0.0
V07T9470	0.297	384.1	-51.1
V07T9478	0.592	766.0	0.0
V07T9480	0.592	766.0	-93.4
V07T9489	0.895	1157.0	0.0
V07T9492	0.986	1275.1	1.3
V07T9502	1.024	1324.3	0.0
V07T9508	1.024	1324.3	-111.1
V07T9590	0.756	978.0	0.0
V07T9591	0.683	882.7	-70.0
V07T9592	0.864	1117.1	236.4
V07T9593	0.871	1126.0	369.3
V07T9597	0.592	766.0	93.4
V07T9598	0.684	884.8	0.0
V07T9599	0.683	882.7	70.0
V07T9666	0.685	885.7	-235.5
V07T9674	0.864	1117.1	-236.4
V07T9678	0.685	885.7	235.5
V07T9683	0.297	384.1	51.1
V07T9711	0.871	1126.0	-369.3

Table II. Comparisons of Entry Time and Mach Number at Transition

Flight	Vehicle	Trans. M_∞ (C_A)*	Trans. Time (C_A)*	Trans. M_∞ (T/C)**	Trans. Time (T/C)**
STS-1	OV-102	14.5	1025	13.6-7.0	1052-1272
STS-2	OV-102	8.0	1257	8.7-7.4	1232-1289
STS-3	OV-102	8.5	1146	9.6-7.6	1107-1183
STS-4	OV-102	10.5	1022	10.3	1028-1029
STS-5	OV-102	8.9	1125	9-8.5	1122-1140
STS-6	OV-099	9.6	1090	N/A	N/A
STS-7	OV-099	13.5	1003	N/A	N/A
STS-8	OV-099	15.5	919	N/A	N/A
STS-9	OV-102	†	†	N/A	N/A
STS-41B	OV-099	†	†	N/A	N/A
STS-41C	OV-099	6.6	1213	N/A	N/A
STS-41D	OV-103	16.0	919	N/A	N/A
STS-41G	OV-099	†	†	N/A	N/A
STS-51A	OV-103	†	†	N/A	N/A
STS-51B	OV-099	†	†	N/A	N/A
STS-51D	OV-103	7.9	1156	N/A	N/A
STS-51F	OV-099	†	†	N/A	N/A
STS-51G	OV-103	7.6	1197	N/A	N/A
STS-51I	OV-103	6.9	1212	N/A	N/A
STS-61A	OV-099	10.6	1126	N/A	N/A
STS-61B	OV-104	†	†	N/A	N/A
STS-61C	OV-102	†	†	N/A	N/A
STS-26	OV-103	7.9	1172	8.6-6.9	1144-1214
STS-27	OV-104	†	†	11.0-9.4	1071-1129
STS-28	OV-102	†	†	17.9-6.4	892-1278
STS-29	OV-103	10.0	1109	10.8-8.4	1085-1157
STS-30	OV-104	6.6	1229	6.6-5.8	1227-1269
STS-31	OV-103	8.6	1141	9.4-6.0	1114-1245
STS-32	OV-102	8.3	1213	9.8-7.7	1161-1239
STS-33	OV-103	6.6	1202	7.1-6.2	1167-1231
STS-34	OV-104	9.3	1128	9.9-9.0	1111-1140
STS-35	OV-102	†	†	9.7-6.5	1147-1275
STS-36	OV-104	7.1	1237	7.1-6.3	1236-1273
STS-37	OV-104	7.0	1214	7.0-5.8	1215-1271
STS-38	OV-104	N/A	N/A	7.2-6.1	1200-1259
STS-39	OV-103	8.5	1233	8.6-7.9	1231-1255
STS-40	OV-102	8.2	1217	8.3-7.4	1213-1247
STS-41	OV-103	†	†	7.8-6.3	1183-1250
STS-42	OV-103	†	†	8.1-7.2	1216-1252
STS-43	OV-104	†	†	6.9-5.5	1269-1330
STS-44	OV-104	†	†	6.8-6.1	1231-1266
STS-45	OV-104	†	†	6.1-5.5	1292-1322
STS-46	OV-104	N/A	N/A	7.7-6.9	1250-1290
STS-47	OV-105	N/A	N/A	10.4-5.6	1147-1342
STS-48	OV-103	13.7	1008	13.7-11.1	1009-1090
STS-49	OV-105	†	†	11.3-5.1	1065-1316
STS-50	OV-102	N/A	N/A	13.6-6.0	1043-1319
STS-52	OV-102	N/A	N/A	11.5-7.2	1131-1286
STS-53	OV-103	N/A	N/A	N/A	N/A
STS-54	OV-105	N/A	N/A	8.8-4.8	1156-1342

* Axial force derived

** Thermocouple derived (Only partial data available for STS-1 and STS-4)

† Unable to determine

Table III. Flight Conditions for Transition during STS-26 Derived from Thermocouple Data
(OV-103; Entry Date: Oct. 3, 1988; Entry Interface Time: 277:16:06:33 GMT)

Time (sec)	$T_{T/C}$ (°F)	X/L	Y (in)	Alt (ft)	V_∞ (ft/sec)	M_∞	α (deg)	ρ_∞ (x10^{-6}) (slug/ft^3)	T_∞ (°R)	P_∞ (lb/ft^2)	Re_∞ (/ft)
					TRANSITION ONSET						
1137	1070	0.296	0.0	161722	9405	8.82	37.46	2.4422	477	1.817	65626
1133	1041	0.592	-93.4	162370	9524	8.93	37.59	2.3613	477	1.772	64217
1114	1021	0.592	93.4	165813	10127	9.49	38.63	1.9969	478	1.583	57678
1113	971	0.756	0.0	166023	10160	9.52	38.68	1.9802	478	1.573	57380
1137	1123	0.871	-369.3	161722	9405	8.82	37.46	2.4422	477	1.817	65626
					TRANSITION COMPLETION						
1170	1348	0.296	0.0	156005	8448	7.92	35.48	3.2256	478	2.266	77782
1168	1401	0.592	-93.4	156369	8503	7.97	35.56	3.1560	478	2.234	76604
1168	1383	0.592	93.4	156369	8503	7.97	35.56	3.1560	478	2.234	76604
1166	1366	0.756	0.0	156728	8559	8.02	35.59	3.0906	478	2.203	75506
1185	1425	0.871	-369.3	153455	8038	7.54	34.81	3.6684	477	2.500	84222

Table IV. Flight Conditions for Transition Onset Derived from Thermocouple Data

Time (sec)	$T_{T/C}$ (°F)	X/L	Y (in)	Alt (ft)	V_∞ (ft/sec)	M_∞	α (deg)	ρ_∞ (x10^{-6}) (slug/ft^3)	T_∞ (°R)	P_∞ (lb/ft^2)	Re_∞ (/ft)
					STS-27 (OV-104; Entry Date: Dec. 6, 1988; Entry Interface Time: 341:22:33:10 GMT)						
1050	1230	0.592	0.0	174562	12294	11.75	42.36	1.1552	459	0.911	41812
1049	1157	0.592	-93.4	174757	12326	11.78	42.48	1.1463	459	0.904	41605
1082	1053	0.592	93.4	169337	11297	10.79	39.99	1.4289	460	1.128	47485
1050	1091	0.683	-70.0	174562	12294	11.75	42.36	1.1552	459	0.911	41812
1052	1110	0.683	70.0	174174	12228	11.69	42.13	1.1732	460	0.926	42224
1050	1119	0.684	0.0	174562	12294	11.75	42.36	1.1552	459	0.911	41812
					STS-28 (OV-102; Entry Date: Aug. 13, 1989; Entry Interface Time: 225:12:36:50 GMT)						
1220	1012	0.296	0.0	157715	8247	7.77	36.34	2.7909	473	2.308	66238
1263	869	0.297	-51.1	147818	7157	6.73	33.74	4.0533	474	3.388	83260
906	1388	0.592	0.0	205375	17807	17.44	40.84	0.4377	438	0.362	23855
995	1281	0.592	0.0	188825	15350	14.70	40.35	0.8191	458	0.694	37125
904	1388	0.592	-99.8	205772	17856	17.50	40.91	0.4259	437	0.357	23306
959	1433	0.592	-99.8	196030	16487	15.85	40.09	0.6261	454	0.525	30669
993	1422	0.685	-235.5	189000	15384	14.74	40.49	0.8129	458	0.690	36939
913	1590	0.864	-236.4	204004	17633	17.22	40.29	0.4606	440	0.383	24744
902	1152	0.895	0.0	206170	17904	17.56	40.89	0.4149	437	0.351	22790
893	791	0.986	1.3	208148	18140	17.88	41.42	0.3835	433	0.323	21504
					STS-29 (OV-103; Entry Date: Mar. 18, 1989; Entry Interface Time: 77:13:35:10 GMT)						
1111	1119	0.296	0.0	168768	10493	9.93	39.49	1.7564	468	1.383	53440
1111	1062	0.592	-93.4	168768	10493	9.93	39.49	1.7564	468	1.383	53440
1111	1053	0.592	93.4	168768	10493	9.93	39.49	1.7564	468	1.383	53440
1111	1004	0.756	0.0	168768	10493	9.93	39.49	1.7564	468	1.383	53440
1111	1282	0.871	-369.3	168768	10493	9.93	39.49	1.7564	468	1.383	53440

Table IV. Continued

Time (sec)	$T_{T/C}$ (°F)	X/L	Y (in)	Alt (ft)	V_∞ (ft/sec)	M_∞	α (deg)	ρ_∞ (x10^{-6}) (slug/ft^3)	T_∞ (°R)	P_∞ (lb/ft^2)	Re_∞ (/ft)
STS-30 (OV-104; Entry Date: May 8, 1989; Entry Interface Time: 128:19:12:51 GMT)											
1228	769	0.592	0.0	147635	7083	6.64	32.74	4.0148	481	3.282	80673
1229	780	0.592	-93.4	147375	7059	6.62	32.65	4.0617	481	3.315	81385
1229	758	0.592	93.4	147375	7059	6.62	32.65	4.0617	481	3.315	81385
1229	737	0.683	-70.0	147114	7035	6.60	32.55	4.1053	481	3.348	82036
1227	748	0.683	70.0	147635	7083	6.64	32.74	4.0148	481	3.282	80673
1229	748	0.684	0.0	147114	7035	6.60	32.55	4.1053	481	3.348	82036
STS-31 (OV-103; Entry Date: Apr. 29, 1990; Entry Interface Time: 119:12:37:26 GMT)											
1219	822	0.296	0.0	148103	6996	6.58	33.19	3.9267	474	3.258	79181
1114	1014	0.592	-93.4	166267	9917	9.35	38.57	1.9504	472	1.591	55699
1216	737	0.592	93.4	149236	7069	6.65	33.43	3.7664	474	3.117	76526
1116	925	0.756	0.0	165925	9853	9.29	38.40	1.9841	472	1.612	56106
1116	1245	0.871	-369.3	165925	9853	9.29	38.40	1.9841	472	1.612	56106
STS-32 (OV-102; Entry Date: Jan. 20, 1990; Entry Interface Time: 20:08:30:20 GMT)											
1217	984	0.296	0.0	151049	8535	8.23	36.34	3.2890	451	2.562	83844
1217	1022	0.297	-51.1	151049	8535	8.23	36.34	3.2890	451	2.562	83844
1208	984	0.592	0.0	152470	8775	8.49	36.79	3.1039	448	2.416	81847
1215	946	0.592	-99.8	151217	8565	8.26	36.47	3.2605	451	2.544	83471
1214	1310	0.685	-235.5	151390	8595	8.30	36.51	3.2379	450	2.526	83240
1162	1362	0.864	-236.4	160329	10182	9.77	38.10	2.3612	456	1.750	71199
1199	907	0.895	0.0	154335	9079	8.82	37.41	2.9065	445	2.238	79747
STS-33 (OV-103; Entry Date: Nov. 27, 1989; Entry Interface Time: 331:23:59:27 GMT)											
1204	812	0.296	0.0	142030	6976	6.57	32.36	4.4220	473	3.660	88765
1203	769	0.592	-93.4	142271	6998	6.59	32.48	4.3741	474	3.626	87916
1188	769	0.592	93.4	145712	7334	6.80	34.13	3.6999	488	3.177	76157
1200	704	0.756	0.0	142986	7064	6.63	32.85	4.2246	477	3.528	85297
1167	1013	0.871	-369.3	150556	7847	7.14	36.87	2.9037	507	2.651	62070
STS-34 (OV-104; Entry Date: Oct. 23, 1989; Entry Interface Time: 296:15:31:40 GMT)											
1112	1024	0.592	0.0	168349	10450	9.89	40.12	1.7088	468	1.376	51757
1111	1034	0.592	-93.4	168349	10450	9.89	40.12	1.7088	468	1.376	51757
1112	1043	0.592	93.4	168122	10418	9.86	40.09	1.7210	469	1.388	51953
1112	1004	0.683	-70.0	168349	10450	9.89	40.12	1.7088	468	1.376	51757
1113	1024	0.683	70.0	167895	10387	9.83	40.00	1.7353	469	1.401	52205
1112	985	0.684	0.0	168122	10418	9.86	40.09	1.7210	469	1.388	51953
STS-35 (OV-102; Entry Date: Dec. 11, 1990; Entry Interface Time: 345:05:23:06 GMT)											
1228	888	0.296	0.0	145572	7745	7.43	34.04	4.1507	456	3.235	95172
1235	936	0.297	-51.1	144891	7570	7.26	33.75	4.2338	456	3.331	94927
1213	850	0.592	0.0	147802	8138	7.79	34.82	3.7413	458	2.945	89886
1216	850	0.592	-99.8	147250	8060	7.72	34.93	3.8173	457	3.013	90943
1192	1283	0.685	-235.5	151652	8712	8.31	36.24	3.1835	462	2.509	81330
1147	1326	0.864	-236.4	159006	10087	9.67	38.90	2.3468	457	1.838	69971
1195	772	0.895	0.0	151123	8627	8.22	36.10	3.3053	462	2.565	83564
1195	762	0.986	1.3	151123	8627	8.22	36.10	3.3053	462	2.565	83564

Table IV. Continued

Time (sec)	$T_{T/C}$ (°F)	X/L	Y (in)	Alt (ft)	V_∞ (ft/sec)	M_∞	α (deg)	ρ_∞ ($x10^{-6}$) (slug/ft^3)	T_∞ (°R)	P_∞ (lb/ft^2)	Re_∞ (/ft)
STS-36 (OV-104; Entry Date: Mar. 4, 1990; Entry Interface Time: 63:17:37:19 GMT)											
1238	812	0.592	0.0	148861	7534	7.08	34.14	3.3438	475	2.920	77309
1237	822	0.592	-93.4	149096	7559	7.10	34.25	3.3007	475	2.894	76859
1237	833	0.592	93.4	149096	7559	7.10	34.25	3.3007	475	2.894	76859
1238	780	0.683	-70.0	148861	7534	7.08	34.14	3.3438	475	2.920	77309
1236	790	0.683	70.0	149329	7584	7.13	34.31	3.2650	475	2.867	76415
1236	769	0.684	0.0	149329	7584	7.13	34.31	3.2650	475	2.867	76415
STS-37 (OV-104; Entry Date: Apr. 11, 1991; Entry Interface Time: 101:13:24:22 GMT)											
1217	822	0.592	0.0	150454	7433	6.95	34.72	3.4886	480	2.872	73747
1215	832	0.592	-93.4	150965	7485	7.00	35.19	3.4236	479	2.816	72935
1215	832	0.592	93.4	150965	7485	7.00	35.19	3.4236	479	2.816	72935
1217	801	0.683	-70.0	150454	7433	6.95	34.72	3.4886	480	2.872	73747
1217	812	0.683	70.0	150454	7433	6.95	34.72	3.4886	480	2.872	73747
1217	812	0.684	0.0	150454	7433	6.95	34.72	3.4886	480	2.872	73747
STS-38 (OV-104; Entry Date: Nov. 20, 1990; Entry Interface Time: 324:21:11:51 GMT)											
1203	822	0.592	0.0	151115	7574	7.13	34.98	3.2601	474	2.650	70925
1200	832	0.592	-93.4	151791	7659	7.21	35.15	3.1780	473	2.582	69965
1202	832	0.592	93.4	151342	7602	7.16	35.02	3.2323	474	2.627	70600
1201	780	0.683	-70.0	151568	7631	7.18	35.09	3.2049	474	2.604	70279
1203	801	0.683	70.0	151115	7574	7.13	34.98	3.2601	474	2.650	70925
1201	780	0.684	0.0	151568	7631	7.18	35.09	3.2049	474	2.604	70279
STS-39 (OV-103; Entry Date: May 6, 1991; Entry Interface Time: 126:18:23:27 GMT)											
1233	1043	0.296	0.0	161532	9237	8.53	39.40	2.4307	492	2.054	62549
1233	1033	0.592	-93.4	161532	9237	8.53	39.40	2.4307	492	2.054	62549
1233	1043	0.592	93.4	161532	9237	8.53	39.40	2.4307	492	2.054	62549
1231	945	0.756	0.0	161973	9297	8.58	39.50	2.3864	493	2.020	61741
1233	1156	0.871	-369.3	161532	9237	8.53	39.40	2.4307	492	2.054	62549
STS-40 (OV-102; Entry Date: Jun. 14, 1991; Entry Interface Time: 165:15:07:49 GMT)											
1218	1003	0.296	0.0	156449	8714	8.14	37.18	2.9354	481	2.422	72625
1218	1012	0.297	-51.1	156449	8714	8.14	37.18	2.9354	481	2.422	72625
1219	927	0.592	0.0	156244	8685	8.11	37.01	2.9583	481	2.441	72945
1219	927	0.592	-99.8	156244	8685	8.11	37.01	2.9583	481	2.441	72945
1218	1221	0.685	-235.5	156449	8714	8.14	37.18	2.9354	481	2.422	72625
1215	1059	0.864	-236.4	157060	8800	8.22	37.56	2.8684	481	2.366	71692
1217	772	0.895	0.0	156654	8743	8.17	37.34	2.9127	481	2.403	72309
1213	723	0.986	1.3	157454	8858	8.28	37.69	2.8242	481	2.330	71021
STS-41 (OV-103; Entry Date: Oct. 10, 1990; Entry Interface Time: 345:05:23:06 GMT)											
1216	832	0.592	-93.4	147157	7406	7.00	33.95	3.9051	470	3.137	83645
1217	801	0.592	93.4	146910	7380	6.98	33.84	3.9443	469	3.168	84253
1217	769	0.756	0.0	146910	7380	6.98	33.84	3.9443	469	3.168	84253
1183	1052	0.871	-369.3	154972	8319	7.77	36.57	2.8146	481	2.321	66485

Table IV. Continued

Time (sec)	$T_{T/C}$ (°F)	X/L	Y (in)	Alt (ft)	V_∞ (ft/sec)	M_∞	α (deg)	ρ_∞ ($\times 10^{-6}$) (slug/ft^3)	T_∞ (°R)	P_∞ (lb/ft^2)	Re_∞ (/ft)
STS-42 (OV-103; Entry Date: Jan. 30, 1992; Entry Interface Time: 030:15:35:44 GMT)											
1219	995	0.296	0.0	157188	8673	8.02	36.80	2.8233	487	2.361	68793
1219	965	0.592	-93.4	157188	8673	8.02	36.80	2.8233	487	2.361	68793
1217	915	0.592	93.4	157564	8728	8.07	36.92	2.7826	487	2.327	68233
1216	853	0.756	0.0	157735	8756	8.09	37.02	2.7635	487	2.311	67978
1219	1156	0.871	-369.3	157188	8673	8.02	36.80	2.8233	487	2.361	68793
STS-43 (OV-104; Entry Date:Aug. 11, 1991; Entry Interface Time: 223:11:51:52 GMT)											
1285	748	0.592	0.0	142845	6779	6.47	30.83	5.0972	460	4.027	101540
1269	801	0.592	-93.4	146828	7193	6.85	32.31	4.3255	463	3.434	91094
1291	748	0.592	93.4	141286	6625	6.33	30.43	5.4353	460	4.286	105980
1271	758	0.683	-70.0	146318	7139	6.80	31.99	4.4174	462	3.504	92379
1284	737	0.683	70.0	143098	6804	6.50	30.92	5.0443	461	3.986	100850
1284	737	0.684	0.0	143098	6804	6.50	30.92	5.0443	461	3.986	100850
STS-44 (OV-104; Entry Date: Dec. 1, 1991; Entry Interface Time: 335:22:03:23 GMT)											
1233	790	0.592	0.0	148196	7215	6.74	32.22	4.2615	476	3.485	87928
1238	801	0.592	-93.4	146888	7093	6.64	32.36	4.5798	474	3.729	93210
1231	822	0.592	93.4	148741	7264	6.78	32.46	4.1565	477	3.405	86225
1235	726	0.683	-70.0	147638	7166	6.70	32.06	4.3505	476	3.551	89287
1231	780	0.683	70.0	148741	7264	6.78	32.46	4.1565	477	3.405	86225
1233	758	0.684	0.0	148196	7215	6.74	32.22	4.2615	476	3.485	87928
STS-45 (OV-104; Entry Date: Apr. 2, 1992; Entry Interface Time: 093:10:51:49 GMT)											
1293	737	0.592	0.0	135486	6367	6.08	30.14	6.1102	457	4.794	114990
1293	737	0.592	-93.4	135486	6367	6.08	30.14	6.1102	457	4.794	114990
1292	737	0.592	93.4	135763	6390	6.09	30.22	6.0634	458	4.762	114430
1292	693	0.683	-70.0	135763	6390	6.09	30.22	6.0634	458	4.762	114430
1294	715	0.683	70.0	135210	6345	6.06	30.04	6.1816	457	4.846	116010
1293	704	0.684	0.0	135486	6367	6.08	30.14	6.1102	457	4.794	114990
STS-46 (OV-104; Entry Date: Aug. 8, 1992; Entry Interface Time: 221:12:39:52 GMT)											
1255	925	0.592	0.0	153936	8239	7.63	35.88	3.1195	485	2.597	72457
1266	894	0.592	-93.4	151108	7924	7.37	35.17	3.4338	481	2.834	77245
1250	955	0.592	93.4	155070	8372	7.74	35.79	3.0164	487	2.520	70999
1258	884	0.683	-70.0	153009	8159	7.57	35.58	3.1975	484	2.655	73716
1250	894	0.683	70.0	155070	8372	7.74	35.79	3.0164	487	2.520	70999
1254	894	0.684	0.0	154172	8266	7.65	35.94	3.0966	485	2.580	72118
STS-47 (OV-105; Entry Date: Sept. 20, 1992; Entry Interface Time: 264:12:21:42 GMT)											
1319	812	0.297	51.1	135239	6322	6.04	30.82	6.5156	457	5.108	121830
1315	790	0.296	0.0	136475	6415	6.11	31.14	6.2335	459	4.907	117880
1183	1147	0.297	-51.1	167448	10076	9.31	40.90	1.9092	487	1.597	54047
1303	780	0.592	93.4	139402	6691	6.34	32.23	5.5097	463	4.379	107840
1217	935	0.592	0.0	160309	9025	8.34	38.97	2.5055	487	2.095	63529
1303	1062	0.685	235.5	139402	6691	6.34	32.23	5.5097	463	4.379	107840
1182	1396	0.685	-235.5	167574	10107	9.34	40.59	1.9069	487	1.595	54149
1184	975	0.756	0.0	167310	10045	9.28	41.12	1.9115	487	1.599	53946
1220	1157	0.871	369.3	159481	8937	8.26	38.67	2.5686	487	2.148	64496
1150	1157	0.864	236.4	169895	11158	10.31	38.78	1.7643	487	1.475	55308
1181	1110	0.864	-236.4	170470	11251	10.40	38.61	1.7318	487	1.448	54744
1182	1310	0.871	-369.3	167574	10107	9.34	40.59	1.9069	487	1.595	54149

Table IV. Concluded

Time (sec)	$T_{T/C}$ (°F)	X/L	Y (in)	Alt (ft)	V_∞ (ft/sec)	M_∞	α (deg)	ρ_∞ ($x10^{-6}$) (slug/ft^3)	T_∞ (°R)	P_∞ (lb/ft^2)	Re_∞ (/ft)
STS-48 (OV-103; Entry Date: Sept. 18, 1991; Entry Interface Time: 261:07:07:43 GMT)											
1062	1274	0.296	0.0	181579	12735	12.01	40.18	1.1123	472	0.901	40800
1010	1248	0.592	-93.4	186876	14403	13.64	38.52	0.9094	468	0.731	37977
1062	1175	0.592	93.4	181579	12735	12.01	40.18	1.1123	472	0.901	40800
1011	1166	0.756	0.0	186795	14371	13.60	38.47	0.9122	468	0.733	38005
1009	1576	0.871	-369.3	186957	14436	13.67	38.54	0.9066	468	0.728	37949
STS-49 (OV-105; Entry Date: May 16, 1992; Entry Interface Time: 137:20:27:03 GMT)											
1296	715	0.297	51.1	129405	5673	5.47	27.34	8.4466	448	6.494	143970
1278	715	0.296	0.0	134243	6053	5.79	28.94	6.8223	455	5.331	122470
1280	758	0.297	-51.1	133733	6010	5.75	28.69	6.9453	454	5.418	123950
1278	693	0.592	93.4	134243	6053	5.79	28.94	6.8223	455	5.331	122470
1279	649	0.592	0.0	133988	6030	5.77	28.82	6.8928	455	5.381	123350
1279	995	0.685	-235.5	133988	6030	5.77	28.82	6.8928	455	5.381	123350
1279	615	0.756	0.0	133988	6030	5.77	28.82	6.8928	455	5.381	123350
1165	1062	0.871	369.3	156851	8947	8.27	37.26	2.4218	487	2.025	60878
1182	915	0.864	236.4	153455	8450	7.83	35.95	2.8108	484	2.337	67044
1065	1175	0.864	-236.4	176161	12115	11.25	40.33	1.2598	483	1.044	43195
1171	995	0.871	-369.3	155765	8779	8.11	37.00	2.5639	487	2.144	63234
STS-50 (OV-102; Entry Date: Jun. 29, 1992; Entry Interface Time: 191:11:10:46 GMT)											
1300	821	0.296	0.0	137454	6663	6.34	31.36	5.7182	460	4.516	112020
1302	830	0.297	-51.1	136922	6618	6.30	31.14	5.8503	459	4.612	114000
1205	1012	0.592	0.0	156382	9190	8.49	36.12	2.8500	487	2.383	73583
1278	791	0.592	-99.8	144550	7197	6.77	33.71	4.5396	471	3.669	94306
1249	1184	0.685	-235.5	150296	7941	7.40	34.92	3.5179	480	2.896	79474
1154	1097	0.864	-236.4	166908	10802	9.98	39.23	1.9149	487	1.601	58111
1043	1520	0.895	0.0	187124	14426	13.56	42.85	0.9074	471	0.733	37785
STS-52 (OV-102; Entry Date: Nov. 1, 1992; Entry Interface Time: 306:13:33:52 GMT)											
1243	1022	0.296	0.0	158953	8835	8.17	36.78	2.7317	487	2.284	67807
1264	965	0.297	-51.1	154637	8242	7.63	34.71	3.2980	486	2.752	76501
1231	955	0.592	0.0	161055	9202	8.51	37.50	2.4513	487	2.050	63373
1234	965	0.592	-99.8	160578	9116	8.43	37.44	2.5252	487	2.112	64677
1243	1257	0.685	-235.5	158953	8835	8.17	36.78	2.7317	487	2.284	67807
1231	1022	0.864	-236.4	161055	9202	8.51	37.50	2.4513	487	2.050	63373
1230	888	0.895	0.0	161200	9230	8.53	37.51	2.4360	487	2.037	63169
1131	683	0.986	1.3	176038	12392	11.51	38.64	1.3965	483	1.157	48967
STS-54 (OV-105; Entry Date: Jan. 19, 1993; Entry Interface Time: 019:13:06:59 GMT)											
1281	864	0.297	51.1	137412	6230	5.93	30.65	5.7199	460	4.517	104780
1227	905	0.296	0.0	150880	7534	7.01	35.04	3.3315	480	2.747	71296
1300	801	0.297	-51.1	132203	5829	5.59	29.09	6.9140	452	5.366	120180
1226	894	0.592	93.4	151102	7557	7.03	35.12	3.3064	481	2.729	70938
1221	853	0.592	0.0	152232	7678	7.13	35.40	3.1912	483	2.643	69371
1227	1147	0.685	235.5	150880	7534	7.01	35.04	3.3315	480	2.747	71296
1229	1119	0.685	-235.5	150396	7485	6.97	34.91	3.4346	480	2.828	73118
1209	832	0.756	0.0	155152	7977	7.38	36.51	2.9103	487	2.432	65252
1192	1004	0.871	369.3	158245	8441	7.80	36.39	2.5904	487	2.166	61434
1222	945	0.864	236.4	152013	7654	7.11	35.35	3.2150	482	2.661	69704
1156	1091	0.864	-236.4	162279	9501	8.78	37.50	2.1830	487	1.826	58272
1188	985	0.871	-369.3	158637	8547	7.90	36.72	2.5744	487	2.153	61816
1220	801	0.895	0.0	152564	7703	7.15	35.47	3.1690	483	2.627	69052

Table V. Flight Conditions for Transition Derived from C_A Data

Flight	Time (sec)	M_∞	Alt (ft)	V_∞ (ft/sec)	α (deg)	ρ_∞ (x10^{-6}) (slug/ft^3)	T_∞ (^oR)	P_∞ (lb/ft^2)	Re_∞ (/ft)
STS-1	1025	14.5	189180	15008	40.04	0.7867	451	0.628	36147
STS-2	1257	8.0	149840	8506	33.29	3.2067	474	2.650	79656
STS-3	1146	8.5	154081	9113	33.90	2.9406	482	2.455	76654
STS-4	1022	10.5	177204	11176	40.60	1.4060	474	1.103	43542
STS-5	1125	8.9	157646	9297	36.52	2.5385	458	1.965	68606
STS-6	1090	9.6	169430	10260	39.16	1.7404	480	1.440	50987
STS-7	1003	13.5	187942	14312	39.19	0.8972	471	0.745	38051
STS-8	919	15.5	194040	15953	40.03	0.6873	445	0.522	33001
STS-41C	1213	6.6	145120	6988	32.93	4.0754	470	3.416	85432
STS-41D	919	16.0	197776	16523	39.71	0.5787	448	0.431	27877
STS-51D	1156	7.9	157381	8340	35.99	2.8930	471	2.105	62853
STS-51G	1197	7.6	154431	8080	35.06	3.1551	475	2.541	72189
STS-51I	1212	6.9	148868	7277	33.88	3.8868	465	3.062	81441
STS-61A	1126	10.6	168896	11192	40.07	1.5902	468	1.261	50977
STS-26	1172	7.9	155634	8393	35.41	2.8223	478	2.298	67179
STS-29	1109	10.0	169152	10560	39.57	1.7074	468	1.363	52060
STS-30	1229	6.6	147114	7035	32.55	4.1053	481	3.348	81158
STS-31	1141	8.6	161893	9090	36.60	2.2804	471	1.886	60782
STS-32	1213	8.3	151567	8625	36.43	3.1993	450	2.508	83838
STS-33	1202	6.6	142511	7020	32.60	4.3305	475	3.593	88792
STS-34	1128	9.3	164419	9908	39.26	1.9295	472	1.601	56400
STS-36	1237	7.1	149096	7559	34.25	3.3007	475	2.894	76859
STS-37	1214	7.0	151220	7512	35.29	3.3879	479	2.788	72582
STS-39	1233	8.5	161532	9237	39.40	2.3159	492	2.054	62550
STS-40	1217	8.2	156654	8743	37.34	2.9411	481	2.403	72309
STS-48	1008	13.7	187039	14468	38.54	0.9144	468	0.726	37920

Table VI. Local Flow Conditions at Transition Along Orbiter Windward Centerline

X_{tr}/L	Time (sec)	M	Re_x (x10^6)	Re_θ/M	T_w (^oR)	T_w/T_o	Re_k 0.03 in	Re_k 0.06 in	Re_k 0.10 in
				STS-26					
0.296	1137	2.00	1.490	206.5	1530	0.2954	46	132	269
0.756	1113	2.40	5.052	330.2	1431	0.2620	49	143	296
				STS-27					
0.594	1050	2.39	3.001	241.6	1690	0.2674	40	109	220
0.684	1050	2.45	3.594	260.1	1579	0.2498	42	114	228
				STS-28					
0.296	1220	1.89	1.659	227.6	1472	0.3144	47	140	293
0.594	995	2.92	3.445	240.8	1741	0.1976	43	113	225
0.894	902	3.29	2.598	194.7	1347	0.1390	20	50	95

Table VI. Continued

X_{tr}/L	Time (sec)	M	Re_x ($x10^6$)	Re_θ/M	T_w (^oR)	T_w/T_o	Re_k 0.03 in	Re_k 0.06 in	Re_k 0.10 in
				STS-29					
0.296	1111	2.03	1.347	191.3	1579	0.2834	44	121	240
0.756	1111	2.41	4.749	318.5	1464	0.2627	46	134	276
				STS-30					
0.594	1228	2.25	5.710	374.2	1229	0.3113	55	170	376
0.684	1229	2.32	7.131	409.0	1208	0.3088	55	173	384
				STS-31					
0.296	1219	1.94	2.112	253.9	1282	0.3305	54	163	351
0.756	1116	2.37	5.092	334.8	1385	0.2591	49	144	298
				STS-32					
0.296	1217	1.96	2.052	247.6	1444	0.2986	64	185	381
0.594	1208	2.23	5.272	355.1	1444	0.2923	64	191	404
0.894	1199	2.54	6.604	363.6	1347	0.2654	41	126	270
				STS-33					
0.296	1204	1.99	2.416	264.7	1272	0.3290	62	187	403
0.756	1200	2.35	8.737	448.7	1164	0.2959	64	196	432
				STS-34					
0.594	1112	2.26	3.388	280.0	1484	0.2672	46	132	269
0.684	1112	2.32	4.092	303.3	1445	0.2607	47	135	275
				STS-35					
0.296	1228	2.00	2.411	266.7	1348	0.3058	69	204	429
0.594	1213	2.27	5.991	376.3	1310	0.2826	71	212	451
0.894	1195	2.57	7.254	377.7	1347	0.2761	41	129	280
				STS-36					
0.594	1238	2.23	5.400	361.6	1272	0.2965	56	173	376
0.684	1237	2.29	6.488	389.3	1229	0.2846	57	176	382
				STS-37					
0.594	1217	2.18	5.126	357.3	1282	0.3045	53	164	358
0.684	1217	2.23	6.246	386.9	1272	0.3021	53	164	359
				STS-38					
0.594	1203	2.18	4.882	347.9	1282	0.2977	51	158	343
0.684	1201	2.25	5.885	374.9	1240	0.2859	52	160	348
				STS-39					
0.296	1233	1.81	1.505	219.0	1503	0.2932	51	145	292
0.756	1231	2.20	5.561	367.5	1405	0.2729	55	162	338

Table VI. Continued

X_{tr}/L	Time (sec)	M	Re_x ($x10^6$)	Re_θ/M	T_w (^oR)	T_w/T_o	Re_k 0.03 in	Re_k 0.06 in	Re_k 0.10 in
				STS-40					
0.296	1218	1.90	1.791	234.5	1463	0.2977	57	164	336
0.594	1219	2.19	4.812	344.7	1387	0.2830	60	179	375
0.894	1217	2.48	6.440	365.8	1347	0.2734	39	121	261
				STS-41					
0.756	1217	2.32	8.133	432.7	1229	0.2948	61	188	412
				STS-42					
0.296	1219	1.92	1.726	229.2	1455	0.2974	54	155	318
0.756	1216	2.29	6.309	383.1	1313	0.2665	58	173	365
				STS-43					
0.594	1285	2.38	7.530	418.5	1208	0.3250	67	208	465
0.756	1284	2.48	10.505	478.5	1197	0.3205	66	206	464
				STS-44					
0.594	1233	2.31	6.328	387.6	1250	0.3088	61	188	415
0.756	1233	2.42	8.884	445.3	1218	0.3009	61	190	422
				STS-45					
0.594	1293	2.36	8.656	452.1	1197	0.3523	72	229	518
0.684	1293	2.42	10.566	490.6	1164	0.3426	73	232	525
				STS-46					
0.594	1255	2.20	4.893	346.7	1385	0.2950	55	168	360
0.684	1254	2.25	5.921	374.8	1354	0.2874	56	170	365
				STS-47					
0.296	1315	2.01	3.197	304.7	1250	0.3637	77	236	519
0.594	1217	2.10	4.093	325.5	1395	0.2767	55	161	335
0.756	1184	2.21	4.795	331.9	1435	0.2649	50	146	301
				STS-48					
0.296	1062	2.31	1.256	170.2	1734	0.2616	37	100	199
0.756	1011	3.09	4.379	258.8	1626	0.1990	39	103	207
				STS-49					
0.296	1278	2.13	3.507	320.2	1175	0.3720	75	232	518
0.594	1279	2.38	9.309	472.7	1109	0.3530	76	242	548
0.756	1279	2.45	12.730	541.9	1075	0.3422	76	242	549

Table VI. Concluded

X_{tr}/L	Time (sec)	M	Re_x ($x10^6$)	Re_θ/M	T_w (^oR)	T_w/T_o	Re_k 0.03 in	Re_k 0.06 in	Re_k 0.10 in
				STS-50					
0.296	1300	2.04	3.057	293.5	1281	0.3525	74	227	497
0.594	1205	2.33	5.001	336.9	1472	0.2870	61	179	377
0.894	1043	2.90	3.635	234.1	1347	0.1640	29	77	151
				STS-52					
0.296	1243	1.95	1.708	225.8	1482	0.2986	53	152	312
0.594	1231	2.23	4.208	317.7	1415	0.2768	53	157	328
0.894	1230	2.53	5.535	334.0	1347	0.2629	34	105	225
				STS-54					
0.296	1227	1.87	1.799	241.0	1365	0.3183	49	146	311
0.594	1221	2.16	4.754	345.9	1313	0.3007	50	155	338
0.756	1209	2.21	6.085	385.6	1292	0.2852	50	153	331
0.894	1220	2.50	6.610	366.4	1347	0.3076	30	98	222

Table VII. Average Pre-Flight Fuselage Roughness (K_{eq}) Values

FLIGHT	VEHICLE	PRE-FLT K_{eq} (in.)
STS-26	OV-103	0.135
STS-27	OV-104	0.122
STS-28	OV-102	0.140
STS-29	OV-103	0.134
STS-30	OV-104	0.148
STS-31	OV-103	0.129
STS-32	OV-102	0.131
STS-33	OV-103	0.128
STS-34	OV-104	0.127
STS-35	OV-102	0.130
STS-36	OV-104	0.129
STS-37	OV-104	0.127
STS-38	OV-104	0.128
STS-39	OV-103	0.126
STS-40	OV-102	0.127
STS-41	OV-103	0.129
STS-42	OV-103	0.127
STS-43	OV-104	0.127
STS-44	OV-104	0.128
STS-45	OV-104	0.128
STS-46	OV-104	0.128
STS-47	OV-105	0.131
STS-48	OV-103	0.127
STS-49	OV-105	0.127
STS-50	OV-102	0.129
STS-52	OV-102	0.127
STS-53	OV-103	0.125
STS-54	OV-105	0.126

Note: Data obtained from Rockwell International

Table VIII. Flight-Derived Effective Roughness Heights, K_{eff}, using Bertin's Correlation

T/C Derived				C_A Derived			
Flight	Vehicle	Flight-Derived K_{eff} (in.)		Flight	Vehicle	Flight-Derived K_{eff} (in.)	
		$Re_{k,X/L=0.1}=110$	$Re_{k,X/L=0.1}=180$			$Re_{k,X/L=0.1}=110$	$Re_{k,X/L=0.1}=180$
STS-1	OV-102	0.061	0.088	STS-1	OV-102	0.066	0.095
STS-2	OV-102	0.039	0.056	STS-2	OV-102	0.041	0.059
STS-3	OV-102	0.039	0.057	STS-3	OV-102	0.041	0.058
STS-4	OV-102	0.058	0.086	STS-4	OV-102	0.061	0.092
STS-5	OV-102	0.042	0.061	STS-5	OV-102	0.045	0.066
STS-26	OV-103	0.051	0.075	STS-6	OV-099	0.054	0.080
STS-27	OV-104	0.063	0.095	STS-7	OV-099	0.062	0.090
STS-28	OV-102	0.059	0.085	STS-8	OV-099	0.070	0.101
STS-29	OV-103	0.054	0.080	STS-41C	OV-099	0.042	0.059
STS-30	OV-104	0.044	0.062	STS-41D	OV-103	0.079	0.114
STS-31	OV-103	0.052	0.076	STS-51D	OV-103	0.050	0.072
STS-32	OV-102	0.040	0.058	STS-51G	OV-103	0.045	0.064
STS-33	OV-103	0.040	0.057	STS-51I	OV-103	0.044	0.061
STS-34	OV-104	0.054	0.080	STS-61A	OV-099	0.054	0.080
STS-35	OV-102	0.038	0.054	STS-26	OV-103	0.047	0.067
STS-36	OV-104	0.044	0.062	STS-29	OV-103	0.054	0.080
STS-37	OV-104	0.046	0.064	STS-30	OV-104	0.044	0.061
STS-38	OV-104	0.047	0.066	STS-31	OV-103	0.050	0.072
STS-39	OV-103	0.047	0.069	STS-32	OV-102	0.040	0.057
STS-40	OV-102	0.043	0.062	STS-33	OV-103	0.041	0.057
STS-41	OV-103	0.040	0.056	STS-34	OV-104	0.051	0.076
STS-42	OV-103	0.044	0.063	STS-36	OV-104	0.044	0.062
STS-43	OV-104	0.039	0.053	STS-37	OV-104	0.046	0.065
STS-44	OV-104	0.041	0.057	STS-39	OV-103	0.047	0.069
STS-45	OV-104	0.036	0.050	STS-40	OV-102	0.043	0.062
STS-46	OV-104	0.044	0.063	STS-48	OV-103	0.063	0.091
STS-47	OV-105	0.047	0.069				
STS-48	OV-103	0.064	0.092				
STS-49	OV-105	0.036	0.049				
STS-50	OV-102	0.041	0.060				
STS-52	OV-102	0.047	0.068				
STS-54	OV-105	0.047	0.067				

Table IX. Flight-Derived Equivalent Roughness Heights, K_{eq}, using Harthun/Blumer Correlation

Flight	Vehicle	Flt-Derived K_{eq} (in.)	Flight	Vehicle	Flt-Derived K_{eq} (in.)
STS-1	OV-102	0.150	STS-37	OV-104	0.121
STS-2	OV-102	0.121	STS-38	OV-104	0.124
STS-3	OV-102	0.121	STS-39	OV-103	0.116
STS-4	OV-102	0.134	STS-40	OV-102	0.114
STS-5	OV-102	0.113	STS-41	OV-103	0.113
STS-26	OV-103	0.128	STS-42	OV-103	0.119
STS-27	OV-104	0.134	STS-43	OV-104	0.107
STS-28	OV-102	0.220	STS-44	OV-104	0.114
STS-29	OV-103	0.130	STS-45	OV-104	0.099
STS-30	OV-104	0.121	STS-46	OV-104	0.118
STS-31	OV-103	0.129	STS-47	OV-105	0.117
STS-32	OV-102	0.105	STS-48	OV-103	0.162
STS-33	OV-103	0.118	STS-49	OV-105	0.096
STS-34	OV-104	0.128	STS-50	OV-102	0.115
STS-35	OV-102	0.105	STS-52	OV-102	0.123
STS-36	OV-104	0.119	STS-54	OV-105	0.124

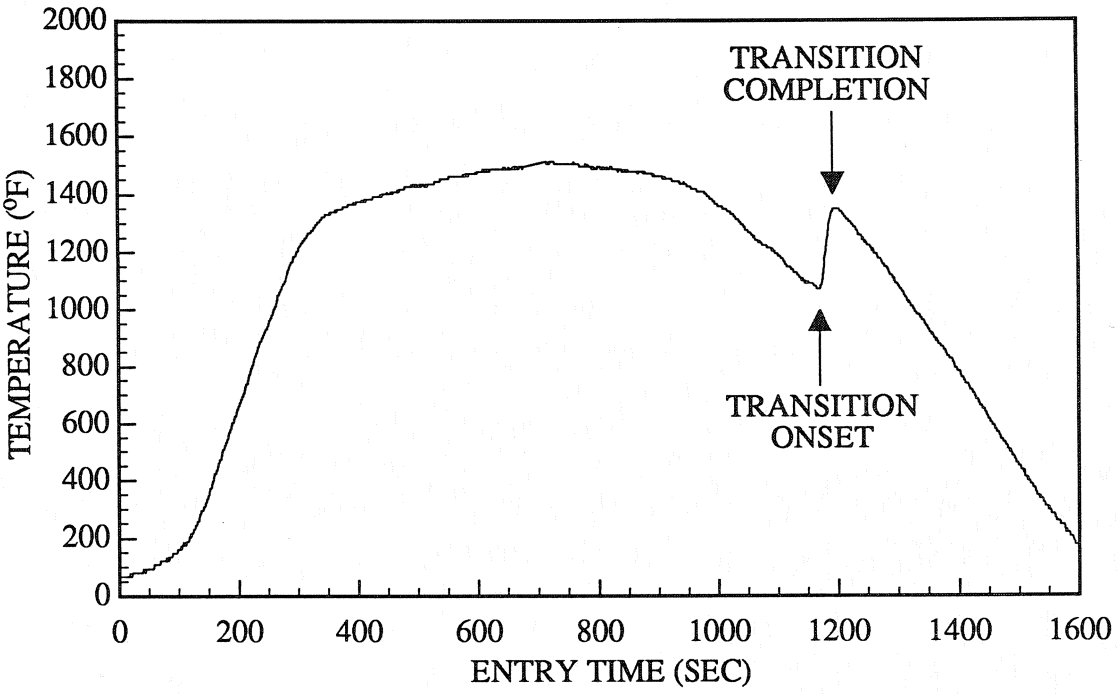

Figure 1. Measured temperature history on OV-103 windward surface during STS-26 entry.

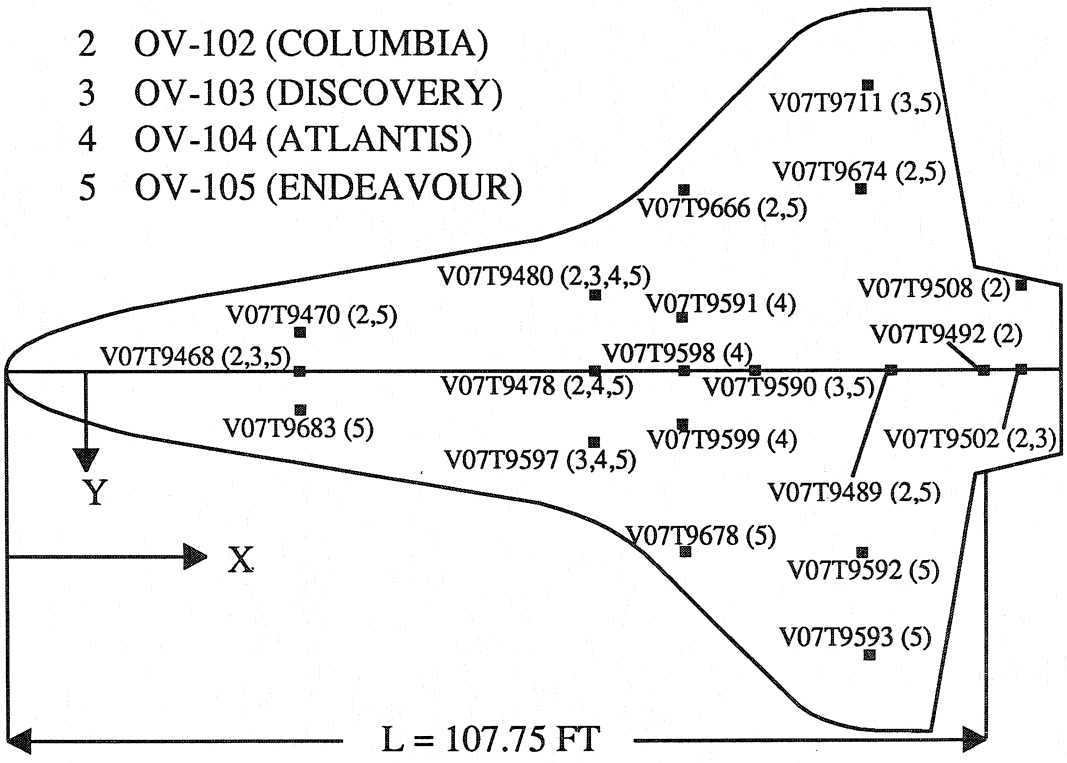

Figure 2. Sketch of thermocouple locations.

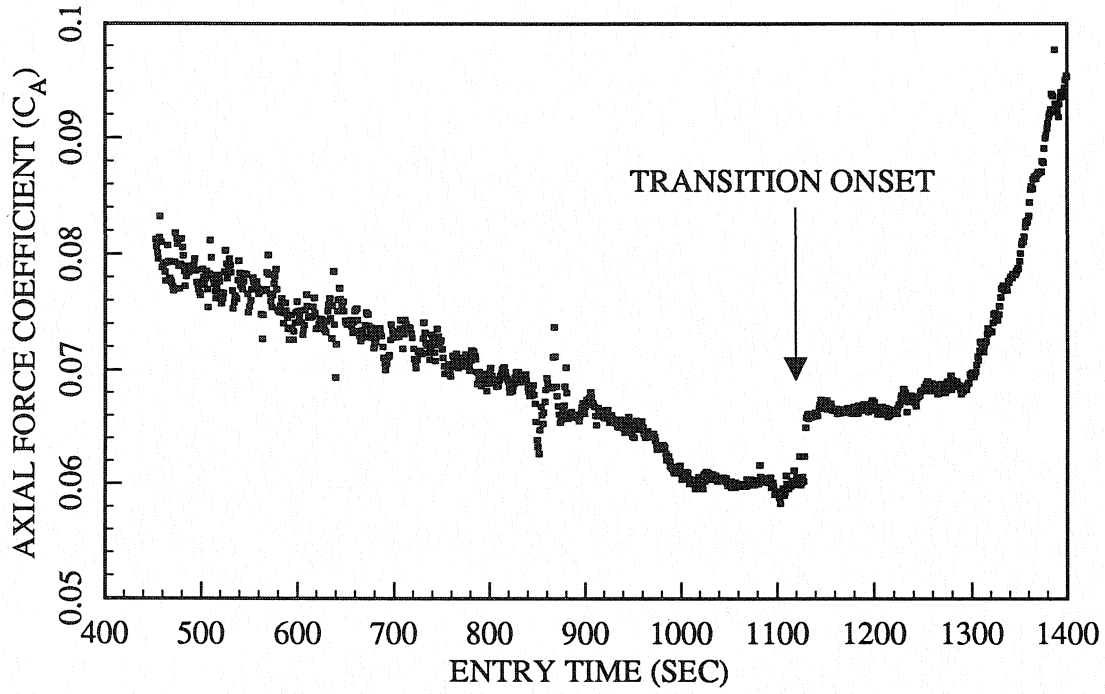

Figure 3. Axial force coefficient history for STS-5.

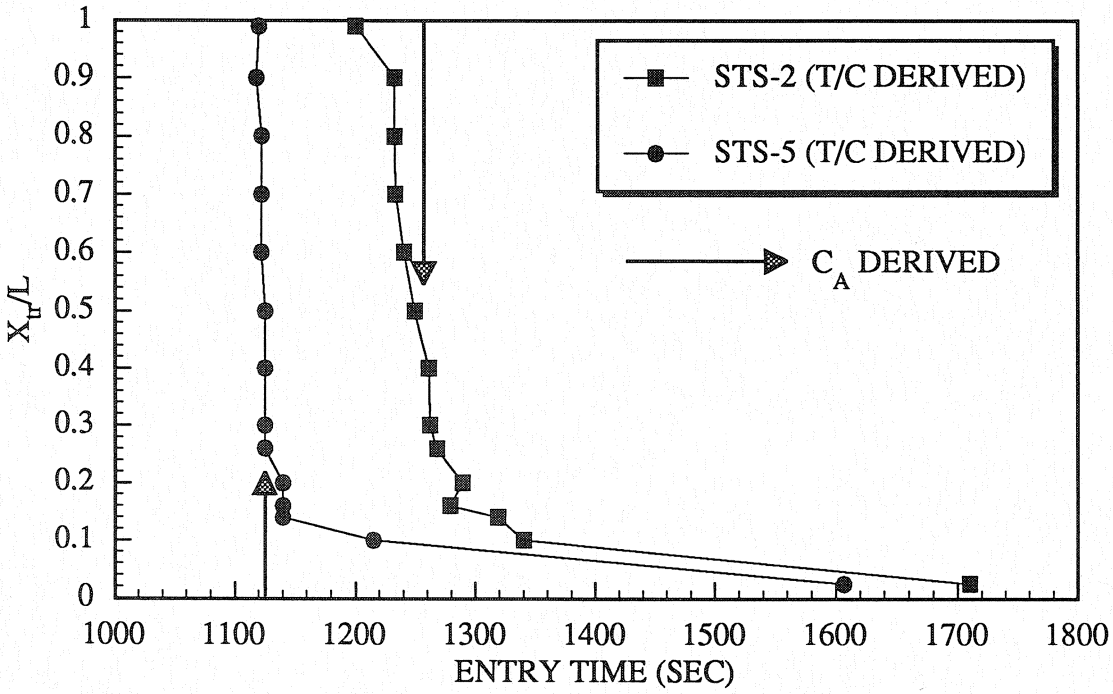

Figure 4. Comparison of transition time derived from C_A data and thermocouple data.

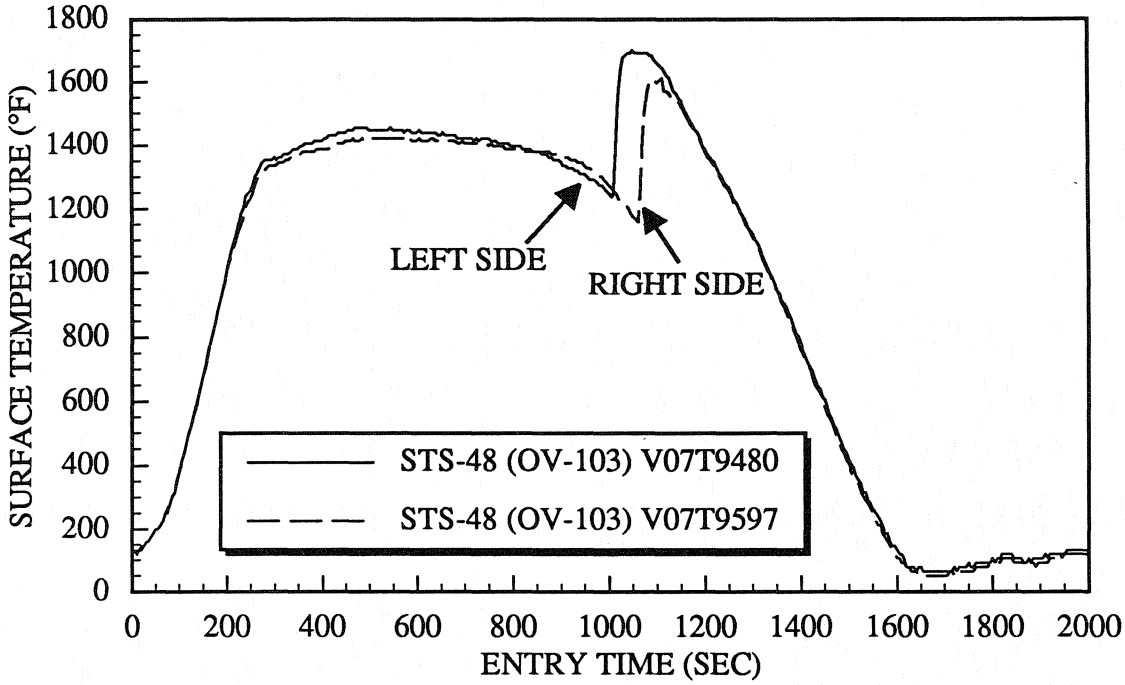

Figure 5. Asymmetric boundary layer transition on STS-48.

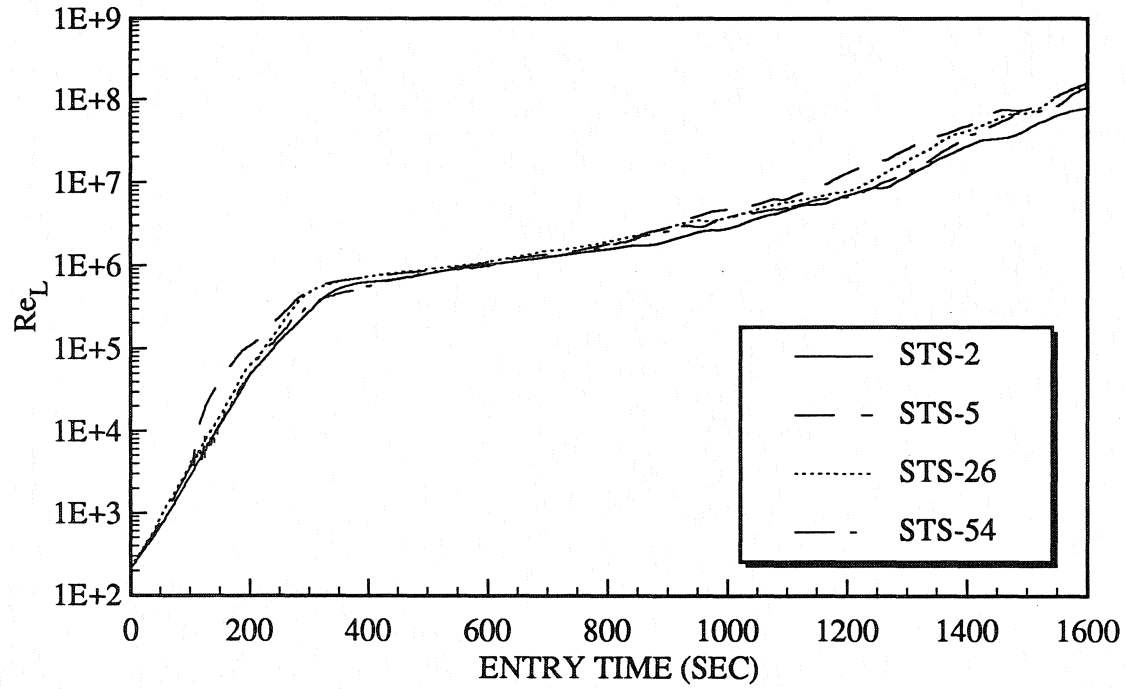

Figure 6. Typical orbiter entry Reynolds number histories.

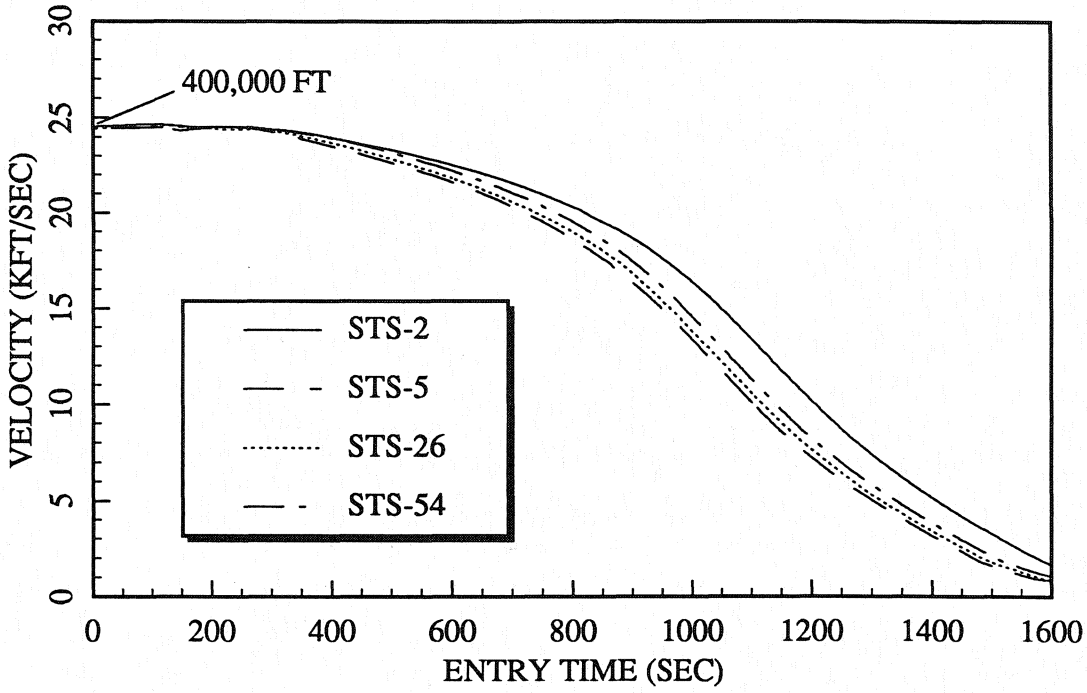

Figure 7(a). Typical orbiter entry velocity histories.

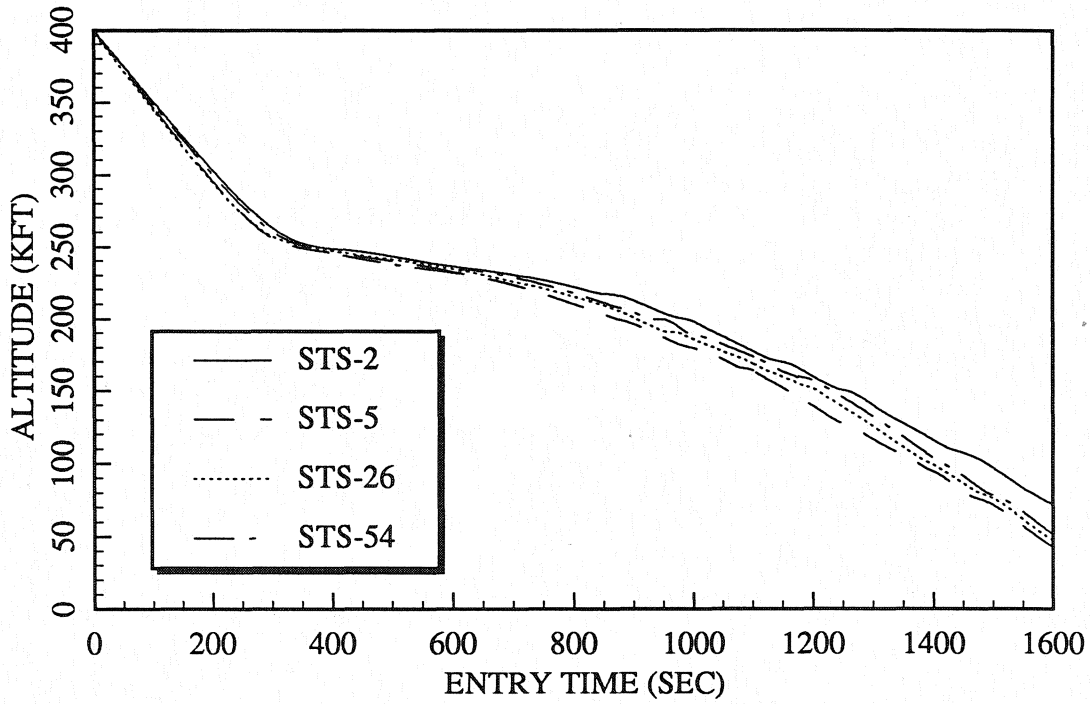

Figure 7(b). Typical orbiter entry altitude histories.

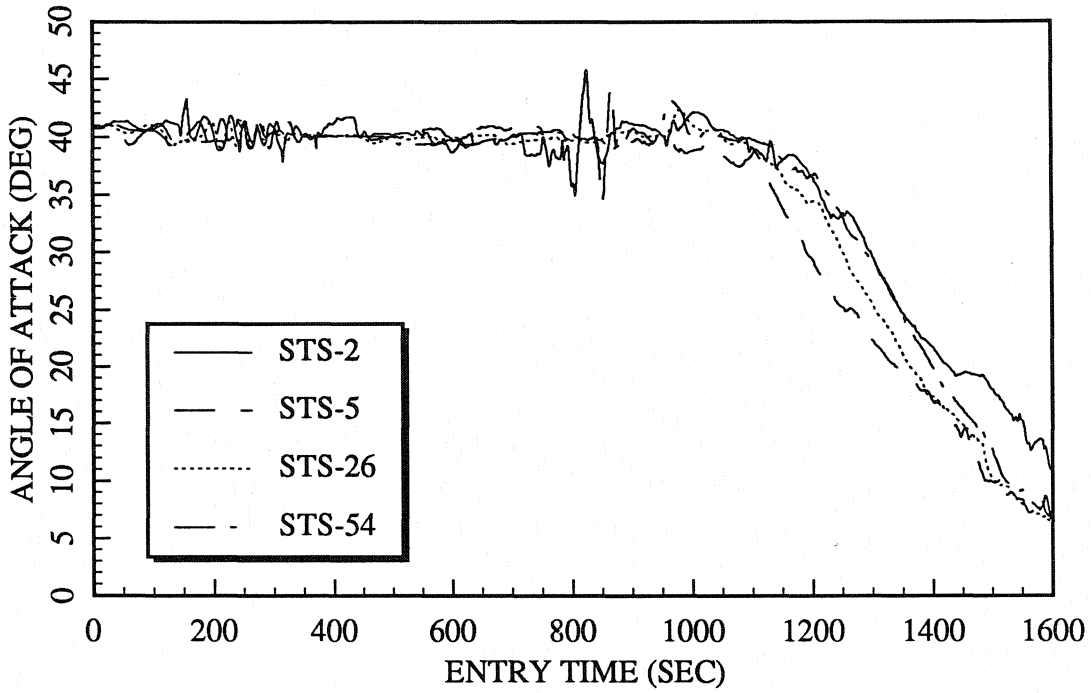

Figure 8(a). Typical orbiter entry angle-of-attack histories.

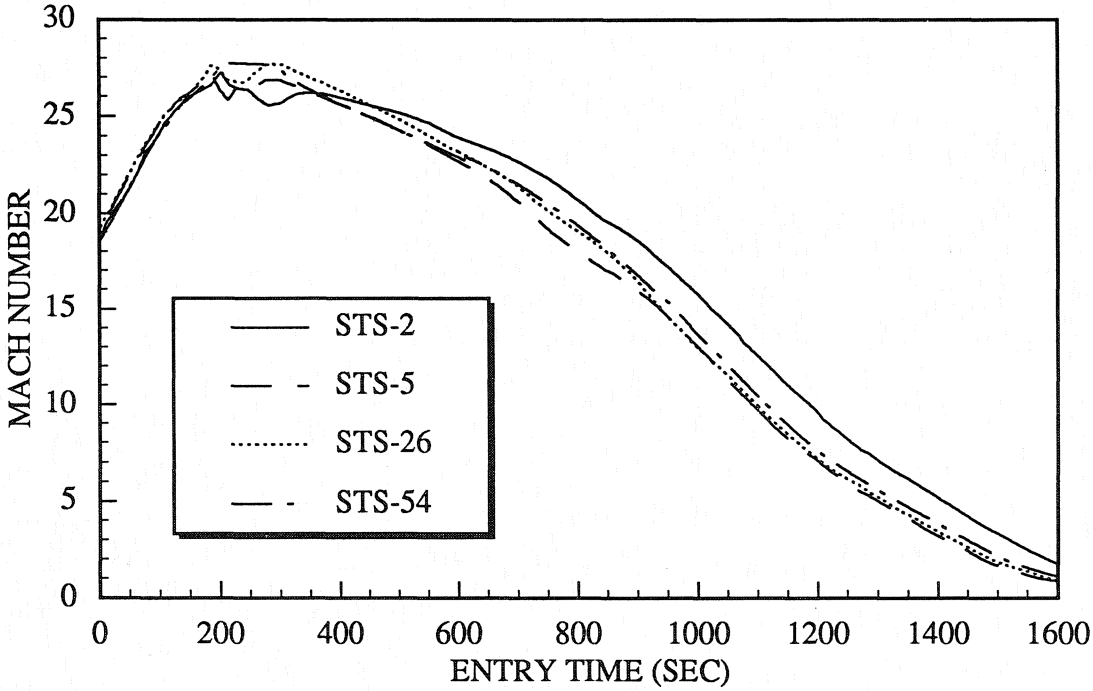

Figure 8(b). Typical orbiter entry Mach number histories.

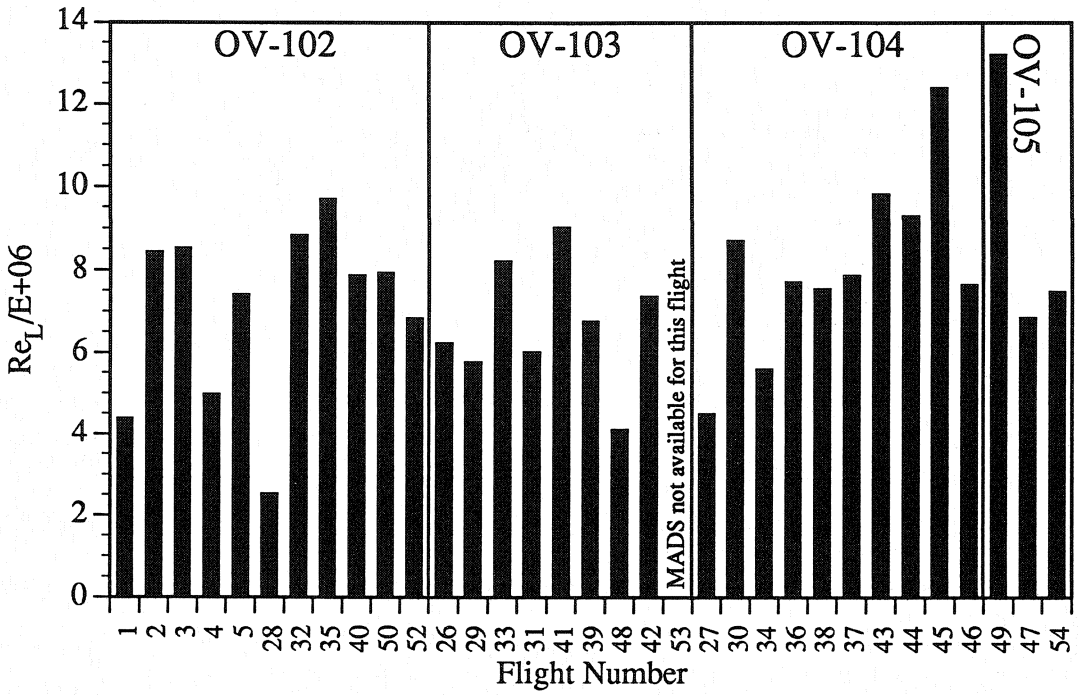

Figure 9. Freestream Reynolds number at transition based on thermocouple data, X/L=0.6.

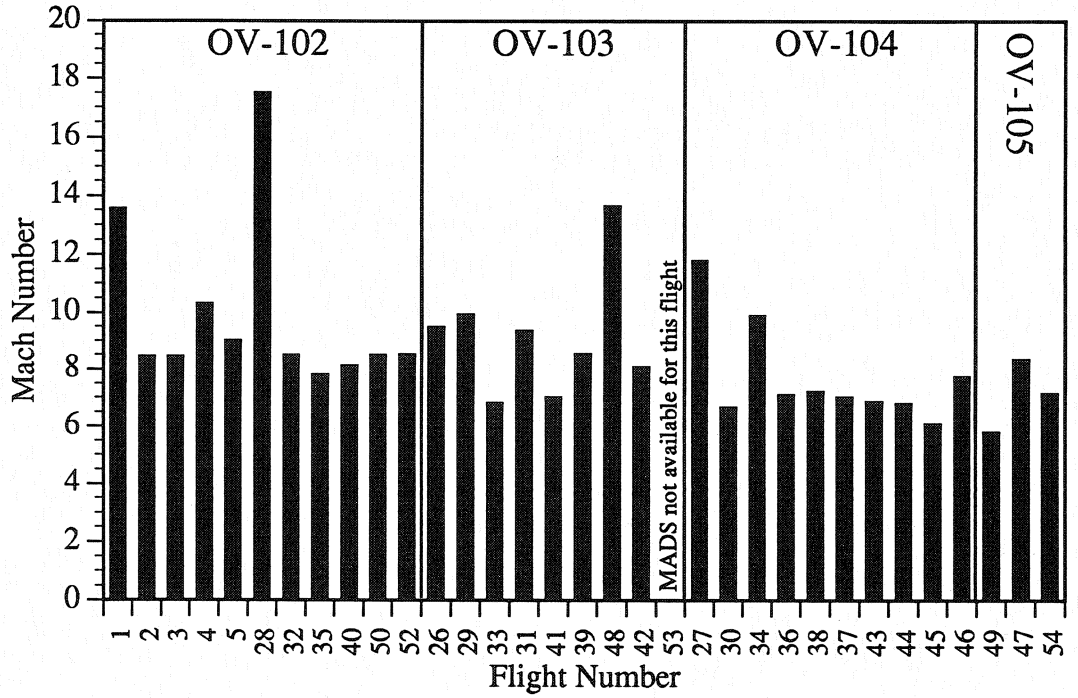

Figure 10. Freestream Mach number at transition based on thermocouple data, X/L=0.6.

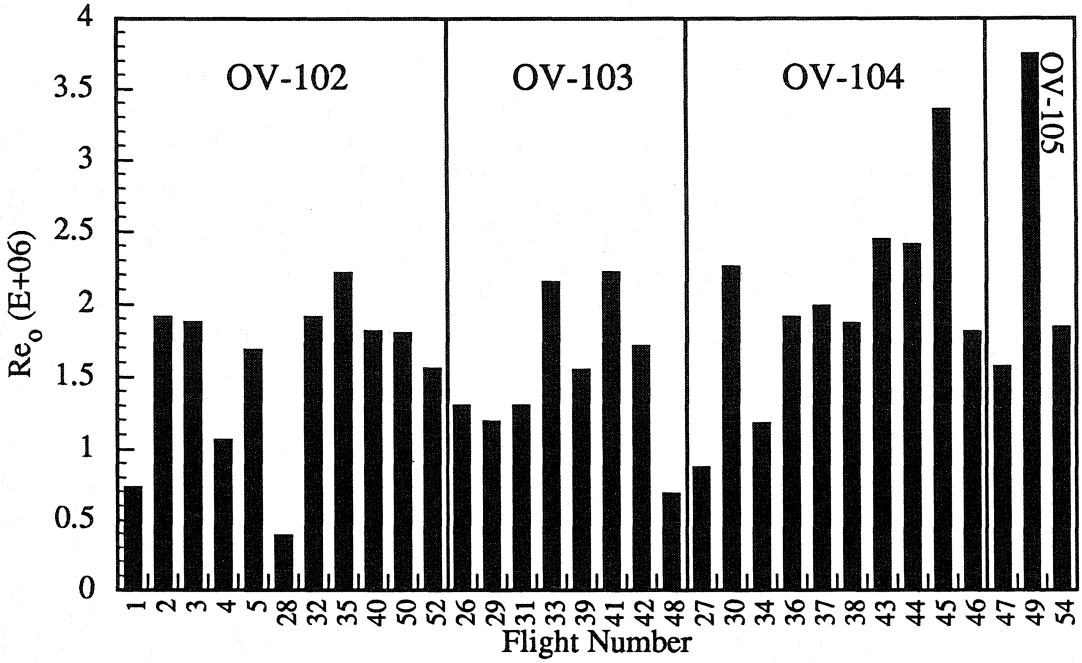

Figure 11. Normal shock Reynolds number at transition based on thermocouple data, X/L=0.6.

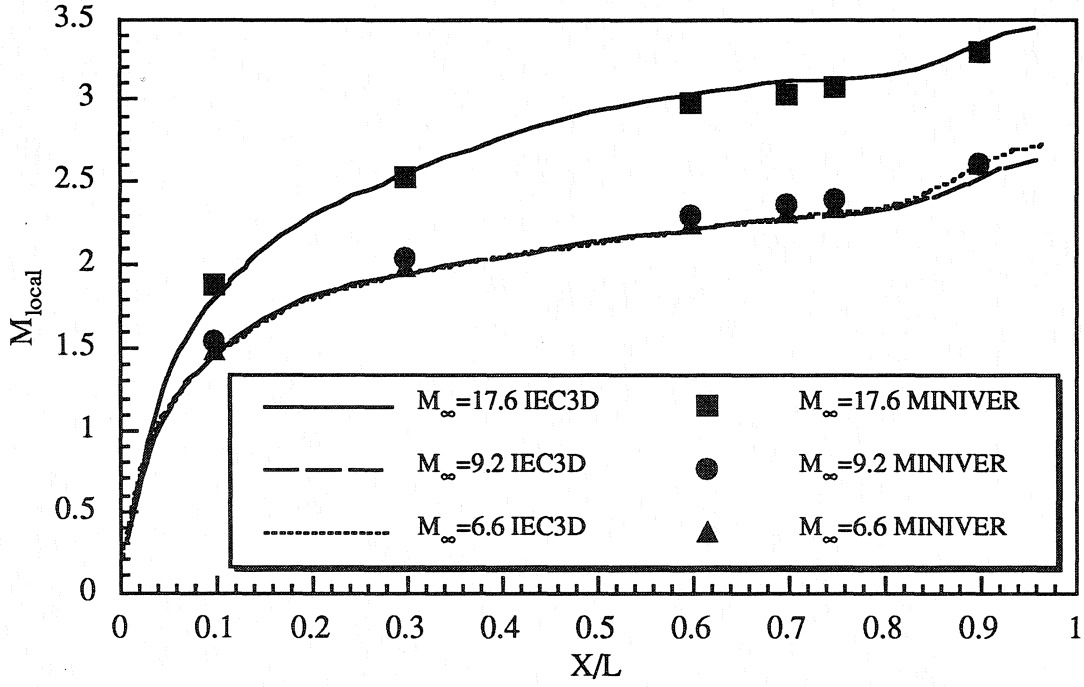

Figure 12. Local Mach number computed by MINIVER and an inviscid flowfield solution.

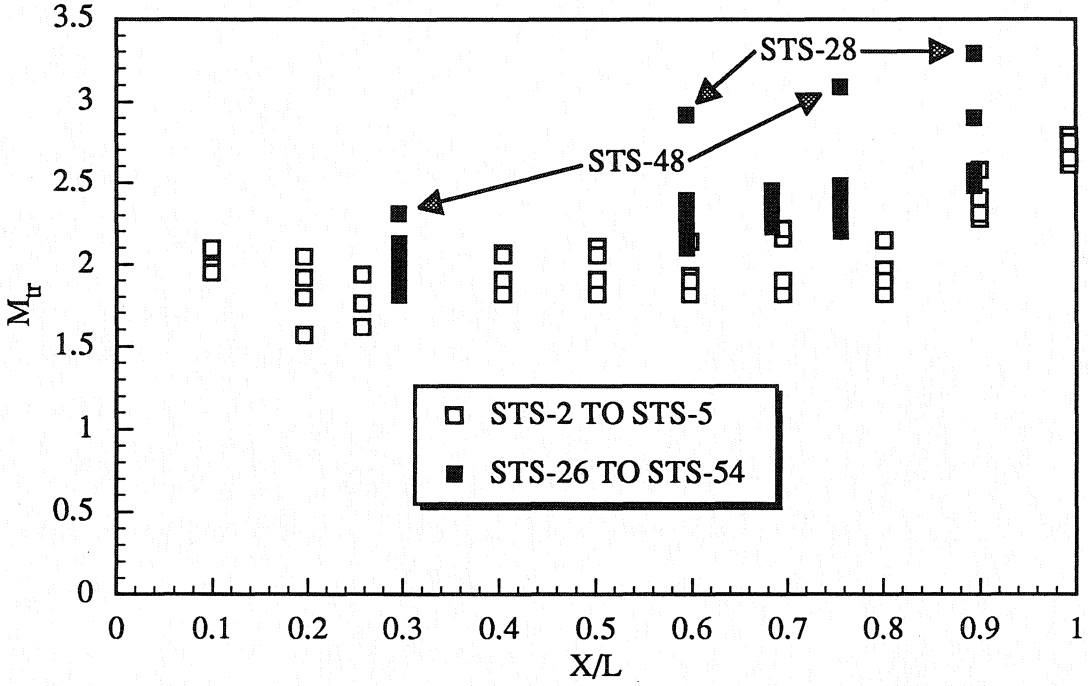

Figure 13. Local Mach number at transition.

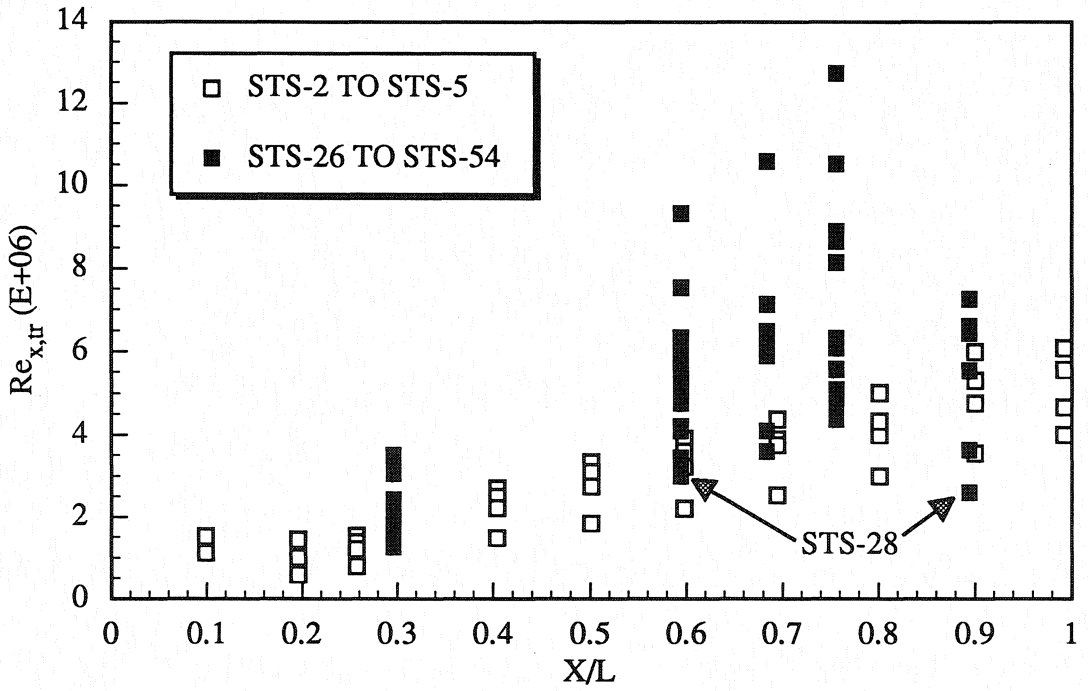

Figure 14. Local Reynolds number at transition.

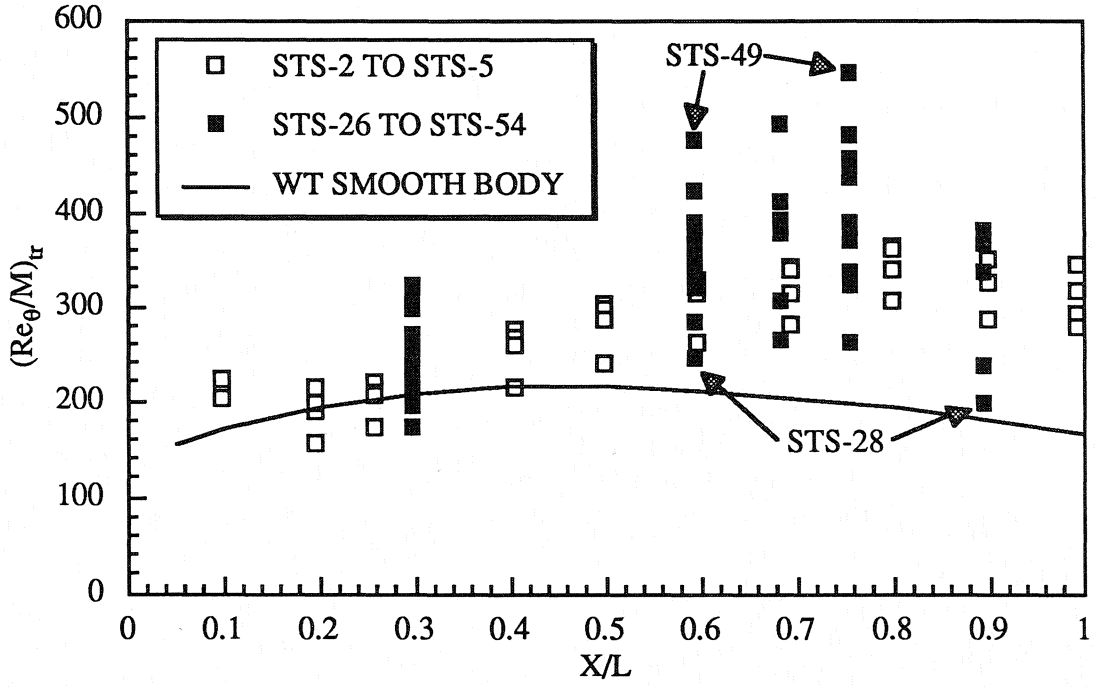

Figure 15. Momentum thickness Reynolds number at transition.

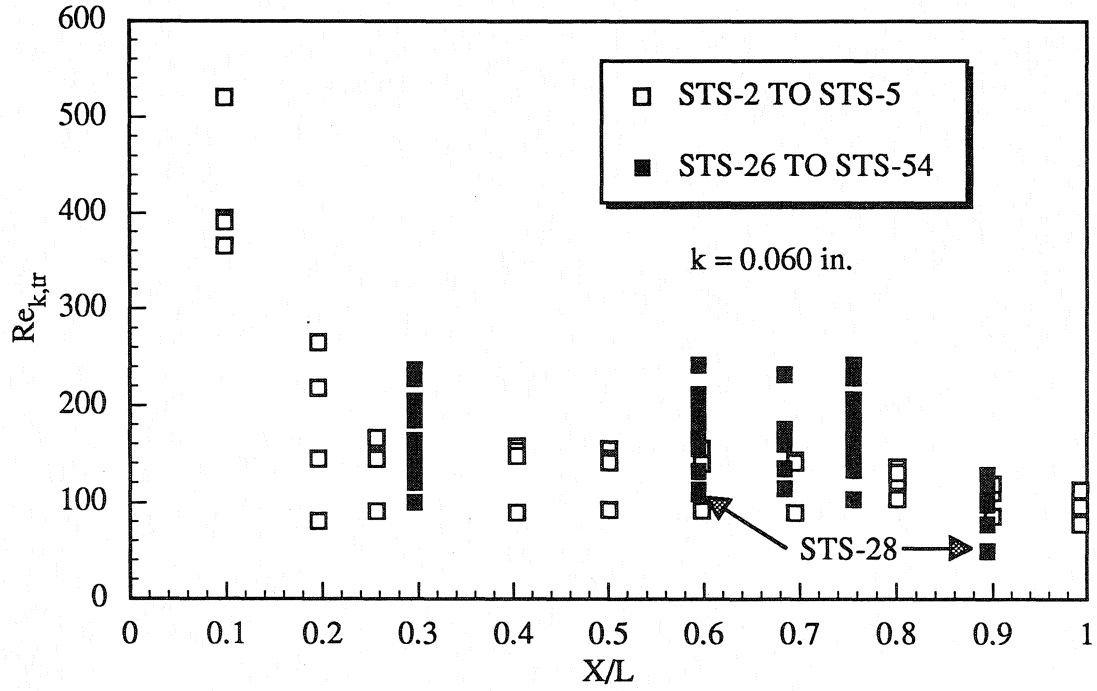

Figure 16. Roughness Reynolds number at transition.

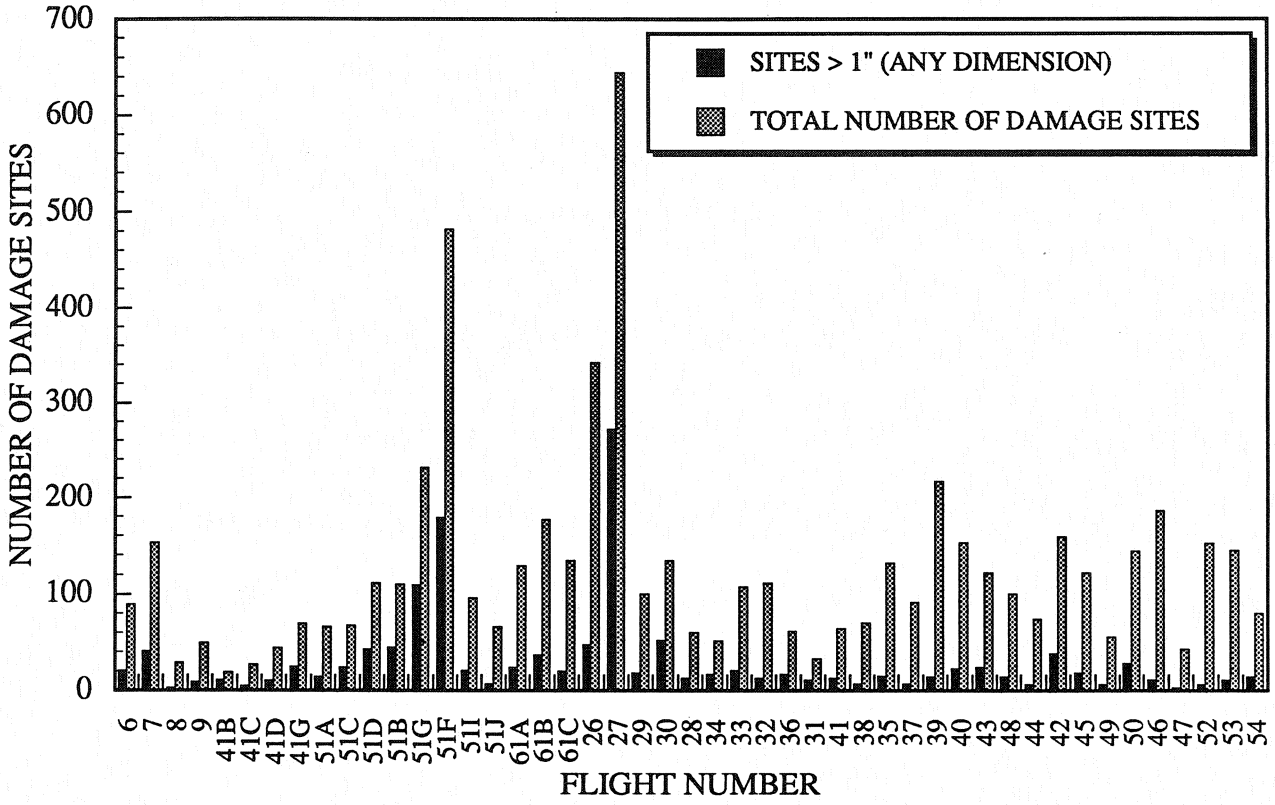

Figure 17. Summary of orbiter windward-surface tile damage.

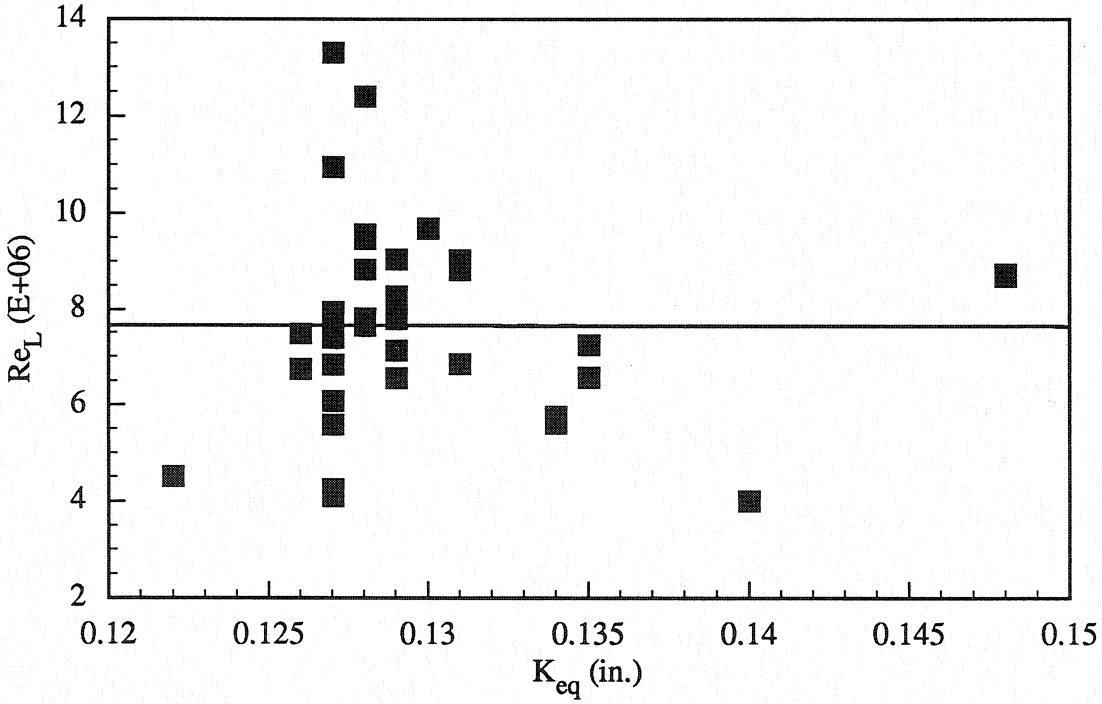

Figure 18. Correlation between nose pre-flight K_{eq} and transition freestream Reynolds number.

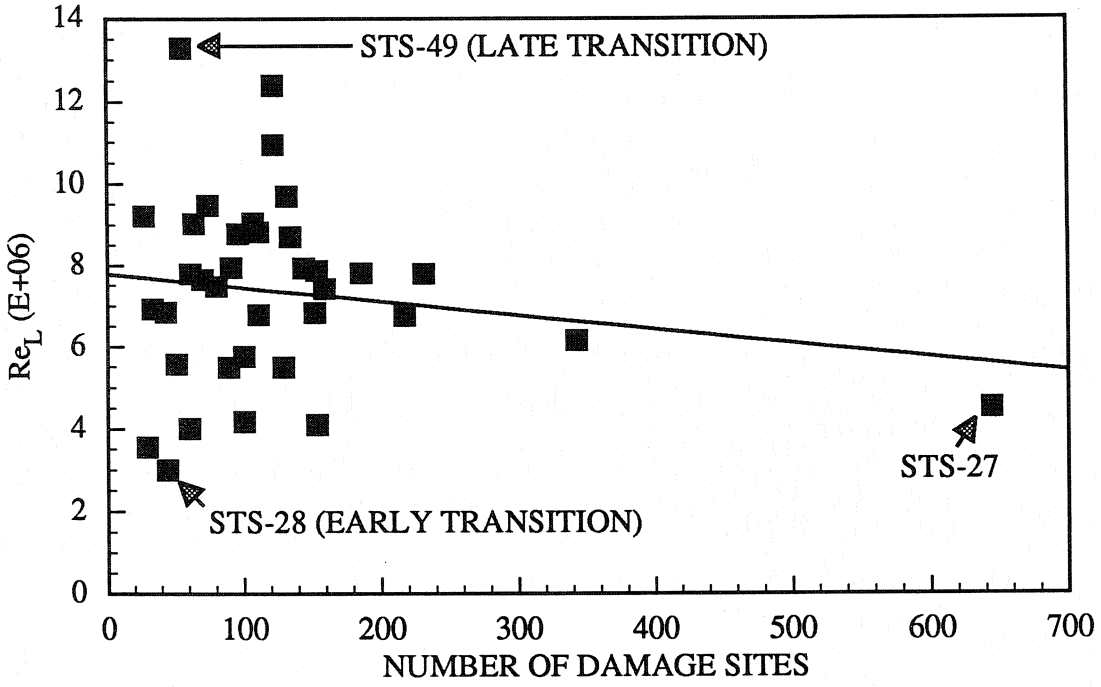

Figure 19. Correlation between freestream Reynolds number and number of damage sites.

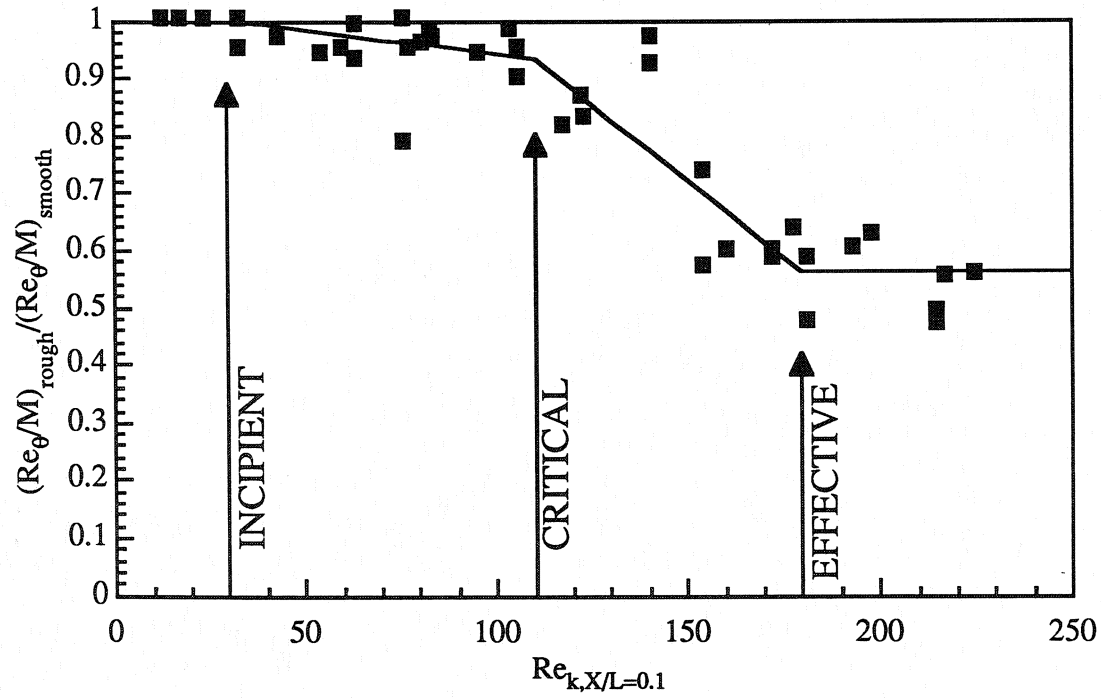

Figure 20. Bertin's roughness-induced transition correlation.

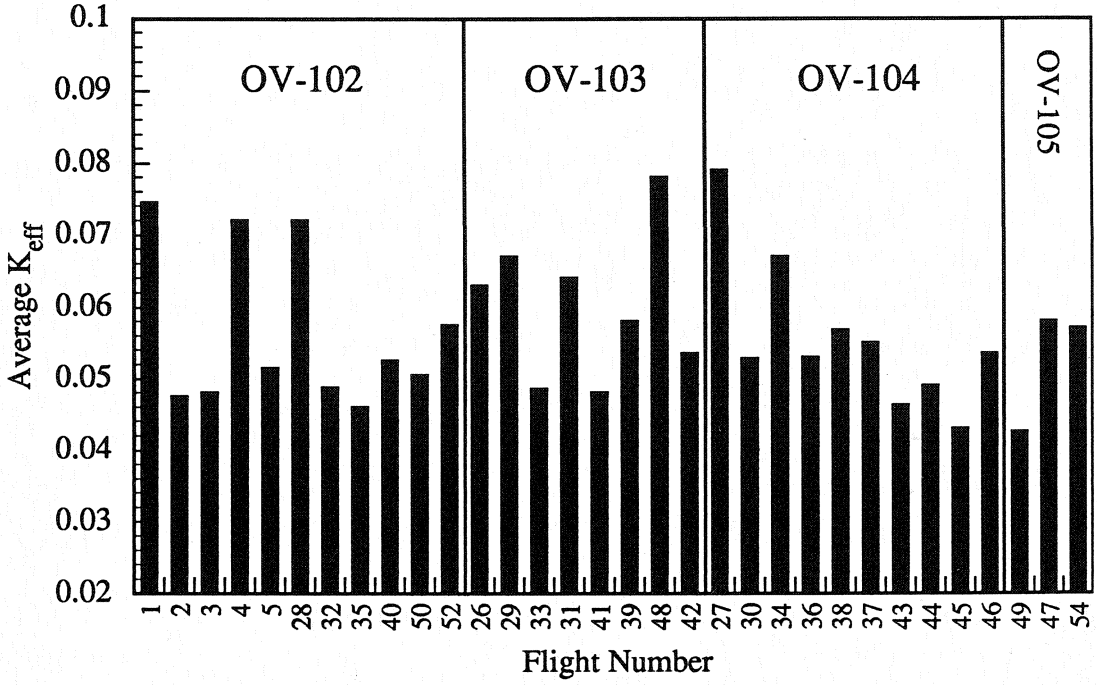

Figure 21. Roughness heights derived from flight data using Bertin's correlation.

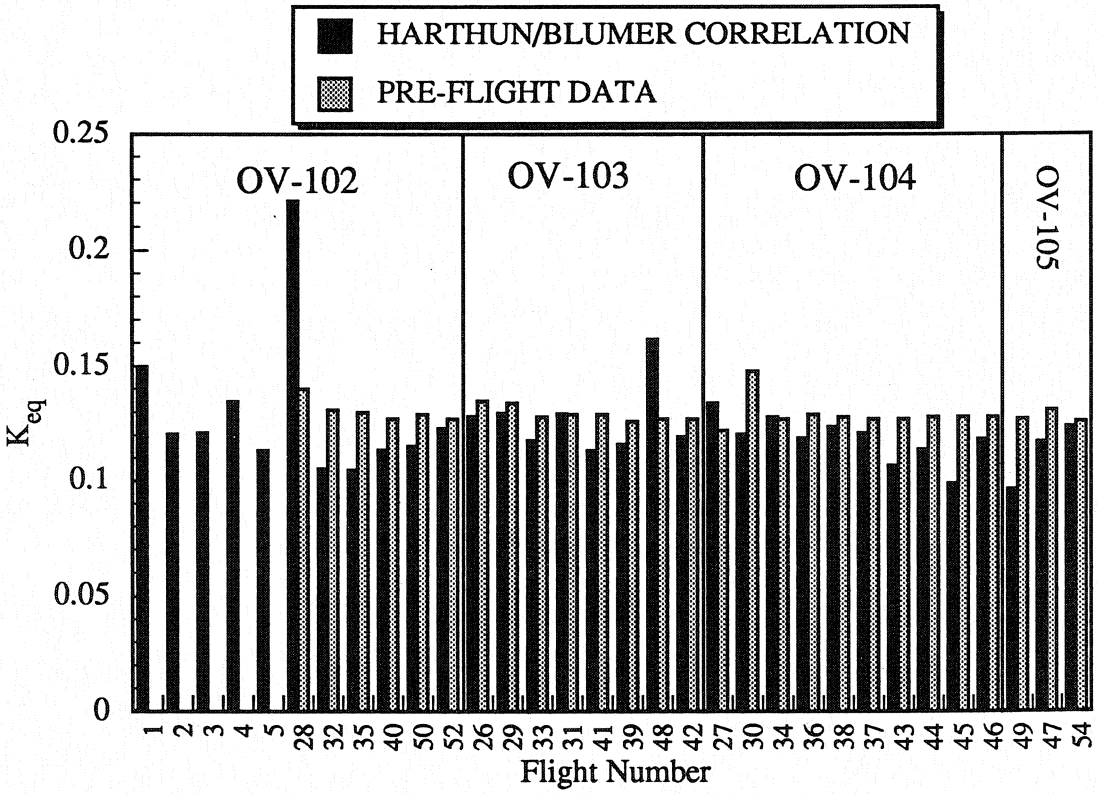

Figure 22. Roughness heights derived from flight data using Harthun/Blumer correlation.

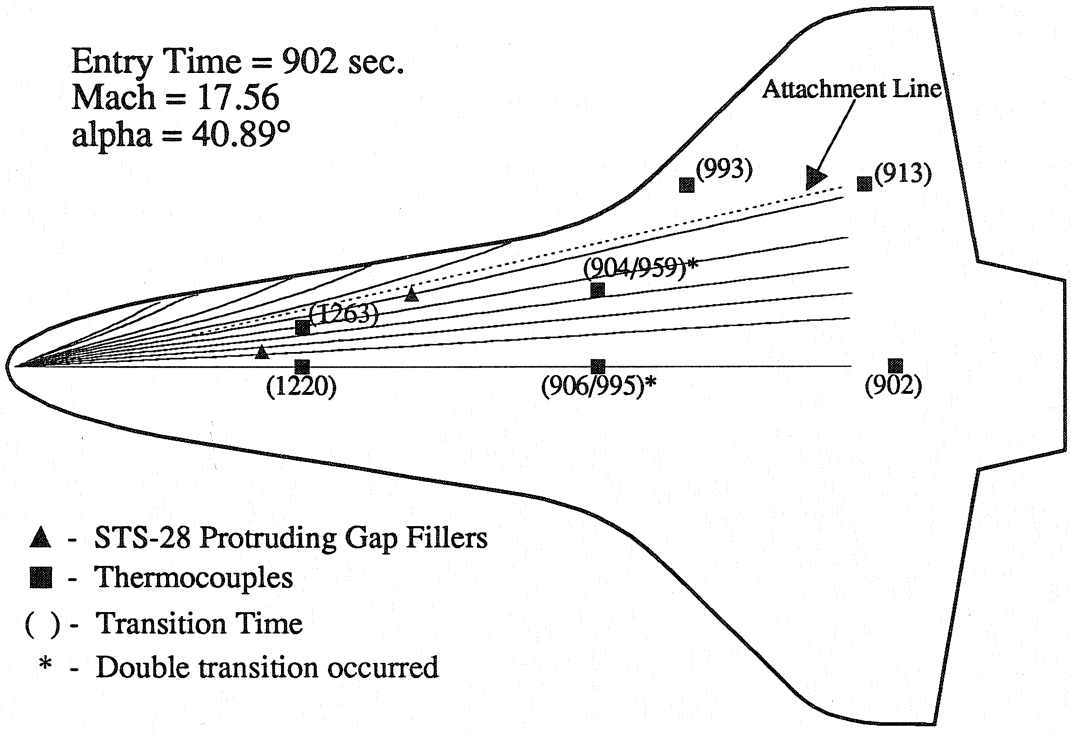

Figure 23. Orbiter windward-surface streamlines and gap filler/thermocouple locations for STS-28.

SPACE SHUTTLE ORBITER WING LEADING EDGE HEATING PREDICTIONS AND MEASUREMENTS*

John DeVenezia and K.C. Wang
Lockheed Engineering & Sciences Company
Houston, TX

Jose M. Caram
NASA Johnson Space Center
Houston, TX

SUMMARY

Aerothermodynamic heating in the shock interaction region of the Space Shuttle Orbiter wing leading edge was investigated in order to develop a more robust engineering model for future trajectory analyses. An aerodynamic heating code has been modified in an attempt to calculate the heating in this region for nominal re-entries and transoceanic abort landings of the Orbiter. The development and validation of this methodology progressed from heating calculations for simple geometries at wind tunnel conditions, to wind tunnel tests on a 0.025 scale Orbiter model, to Orbiter nose cap flight calculations, and finally to wing leading edge flight calculations . Comparisons are made with radiometer flight data for three flights in the wing leading edge region.

INTRODUCTION

The Space Shuttle Orbiter is the first spacecraft which uses a reusable thermal protection system to protect it from the extreme temperatures produced during re-entry into the Earth's atmosphere. The wings of the Orbiter are used to generate aerodynamic drag while in the hypersonic phase of re-entry and aerodynamic lift while at low supersonic and subsonic speeds. It is during the hypersonic portion of the re-entry that the Orbiter leading edge surfaces can reach temperatures of 2800°F as a result of aerodynamic heating. These leading edge surfaces, which consist of the nose cap and the wing leading edge (WLE) of the Orbiter, make up the Leading Edge Structural Subsystem (LESS)[1,2]. The hottest areas of the LESS are the stagnation point on the Orbiter nose cap and the shock interaction regions on the leading edge of the wings. It is the shock interaction heating to the WLE that is currently constraining flight designers who generate Transoceanic Abort Landing (TAL) trajectories for the Space Shuttle Program. The objective of this study was to develop an improved shock interaction heating model which contains more of the flow field physics as compared to the reference sphere based engineering models currently being used by flight designers.

Although primarily designed to satisfy the aerodynamic requirements for a vehicle which flies through the entire atmospheric flight regime, the Orbiter double–delta wing planform also minimizes the shock interaction heating to the WLE[3]. The shock interaction heating is a result of the bow shock, which is generated at the nose of the vehicle, intersecting with the shock generated by the WLE as shown in Figure 1. This intersection of shocks is clearly visible in Schlieren photographs from a wind tunnel test of an Orbiter model at re-entry conditions as seen in Figure 2. Six types of shock interference patterns were first described by Edney[4] and shown in Figure 3. The type of shock interaction which develops on a body is a function of the angle in which the impinging shock intersects the secondary shock. Because of the

* Work done on contract at Lockheed Engineering & Sciences Company, NAS-9-17900

45° leading edge sweep angle of the Orbiter wing, the bow shock intersects the wing shock at an obtuse angle which results in a Type V shock interference pattern[5]. The type V interference pattern, as shown in Figure 4, has a detached supersonic jet and shear layer. The peak heating is a result of the transmitted shock interacting with the boundary layer on the WLE.

The complexity of the Orbiter wing design and the flow field of the shock interaction region prevented engineers from obtaining accurate predictions of the WLE heating using computational fluid dynamic (CFD) techniques that were available during the mid – 1970s. In experimental studies of shock interference effects[6-11] engineers used wedges at various half angles as the impingement shock generator and either wedges or cylinders to generate the secondary shock. Pressure and heat transfer data were obtained on the secondary geometries. These studies showed that type V interference patterns could result in between two to four times the heating as compared to the heating generated by a leading edge shock only at similar freestream conditions. These investigations were used to develop engineering codes [2-14] which calculated the heating for these simple geometries. Experimental heat transfer results for a 0.025 scale Orbiter configuration were obtained in 1978[15]. In these tests, surface temperature measurements were made at both spanwise and circumferential locations of the WLE. The reduced heating data showed the location and magnitude of the shock interaction heating on the Orbiter at various angles of attack and were used in the development of the engineering model being discussed in this report.

Because of the high surface temperatures expected along the WLE as well as the nose of the Orbiter, Reinforced Carbon–Carbon (RCC) was used to form the leading edge structure. RCC is a carbon composite possessing reasonable strength and a low coefficient of thermal expansion which provides it with excellent resistance to thermal stress and shock[16]. In order to prevent oxidation of the carbon-carbon, the RCC is impregnated with tetraethyl – ortho silicate (TEOS) and coated with silicon carbide (SiC). As well as having good emittance characteristics[17] the SiC coating has been shown to be partially catalytic[18-21] which prevents much of the chemical energy in the flow field from being transferred to the surface. Unfortunately, data on RCC recombination rates is very limited and can vary from 100 – 1000 cm/sec for specific material temperatures. However, any heating model should take advantage of the partially catalytic property of the RCC when calculating the heating to surfaces where this material is being used.

The current engineering model[22] being used by trajectory designers to calculate the heating to the Orbiter WLE in the shock interaction region was developed from the XF0002 aerothermodynamic heating code[23]. This model is incorporated into an engineering code known as the Wing Leading Edge Thermal Indicator (WLETI) and is based on heating to a one foot reference sphere in equilibrium air which is then modified with wind tunnel and flight derived correction factors. Pre STS–1 predictions of heating to the WLE were made using wind tunnel derived correction factors only. Development flight instrumentation (DFI) data that was obtained during the Orbiter Flight Test (OFT) program[1] showed that the heating to the WLE in the shock interaction region was underpredicted. Adjustments to the code were done through the use of flight derived correction factors. Since thermocouples could not be mounted to the RCC, optical radiometers were used to measure the inner mold line (IML) surface temperature of the wing panel where the effects of the shock interaction would be observed. Two-dimensional thermal analysis models[24-25] of the WLE were used to calculate the outer mold line (OML) temperatures and heat fluxes experienced during re-entry. The flight correction factors were then iterated upon by comparing the predicted heating rates to the heating rates inferred from the flight data. This approach eliminated the need to model the shock interaction flow field, the variation in heating due to changes in angle of attack, and the effects of the partially catalytic surface property of the RCC because they are all incorporated in the correction factors. However, this model is limited to those flight conditions from which the data was obtained; i.e. nominal end of mission re-entries flown at 40° angle of attack.

The current design trajectory for TAL's modulate the Orbiter's angle of attack from 43° to 40° whereas the flight procedure for Contingency TAL's dictate a 40°/28° modulation for additional downrange capability. The peak aerodynamic heating for these trajectories is more severe than nominal end of mission re-entry trajectories. If a TAL is declared, it would be necessary for the Orbiter to fly faster at lower altitudes in order to achieve the downrange needed to make a safe landing at the abort sites

across the Atlantic. Especially for Contingency TAL flight conditions, the shock interaction heating to the wings can become so severe that the predicted RCC temperatures would exceed the single mission use limits for the material. Thus, trajectories would have to be designed so that the amount of time that the predicted temperatures are at or slightly above the single mission use temperatures of 3230°F is limited to 30 seconds or less.

The objective of this work was to develop an engineering heating model of the shock interaction region of the Space Shuttle Orbiter wing which includes more of the physics of the shock interaction flowfield, the effects of shock interaction heating with changes in angle of attack, and the partially catalytic surface of the RCC material. CFD analyses of the Orbiter at wind tunnel and flight conditions, in addition to more recent studies of shock interaction heating, were applied in this study. The following report documents the methodology, theory, and validation techniques used in developing this engineering model.

ENGINEERING METHODOLOGY

Lanmin Model

In this study the Lanmin code[26] was used as a quick and versatile tool to generate heating rate and temperature histories encountered along End of Mission (EOM) and TAL trajectories. The Lanmin code is a NASA Langley Research Center derivative of the MINIVER aerothermodynamic code which itself is a modification of the JA70 Aerodynamic Heating Code. These codes have been in existence for decades and have proven themselves to be speedy, robust and accurate. They basically consist of fluid property routines, flowfield routines and heating routines. The heating routines are coded from generally accepted engineering correlation heating methodologies and use predicted flowfields for the problem on hand. Lanmin was modified to handle multiple shocks by using the upstream shock's post-shock flowfield properties as the input conditions for the subsequent shock.

Validation of Lanmin for Shock-Shock interaction type cases

Because of the complexity of the viscid-inviscid interaction phenomenon, many experimental investigations of the shock-interaction phenomenon have used models consisting of basic configurations. The Lanmin code was run for several simple-geometry wind tunnel tests in order to check the Lanmin model for the shock-shock interaction type of problem. These open-literature wind tunnel tests used simple geometries at a variety of Mach numbers. A representative shock-wave impingement on leading-edge test was performed by Hiers and Loubsky at the Ames 1-foot shock tunnel[8]. The geometry for this case was a cylindrical leading edge of a blunted flat-plate model with sharp flat-plate shock generator. Figure 5 (see fig. 7a) shows the layout and freestream conditions of this wind tunnel test. The Lanmin code was used to model the shock generated by the sharp flat-plate with a wedge and then the swept cylindrical leading edge of the blunted flat-plate as a parallel shock. Lanmin was then used to calculate the modified Beckwith and Gallagher swept cylinder heating for this using the downstream conditions of the previously calculated shocks. The Lanmin predictions for one of the wind tunnel runs for this test are presented in Table 1. The calculated results are well within the measured data's accuracy band of ±20%.

Another wind tunnel test to estimate the aerothermodynamic environment for the shuttle entry configuration was performed by Bertin and Hinkle at the University of Texas Supersonic Wind Tunnel in 1974.[9] Figure 6a and 6b outline the geometry for this test and the freestream conditions at which the test was conducted. The Lanmin code was used to model the double wedge configuration and predict the pressure in two of the zones as shown in Figure 6b, specifically zone 3 and zone 7. For zone 7, in addition to the double wedge shocks, the transmitted shock was modeled as a standing normal shock. The comparison of the measured and predicted data is shown in Table 2. Again, Lanmin predicts with reasonable accuracy the shock-shock interaction flow.

A wind tunnel test with a wedge-cylinder configuration was run by Barnette in 1976.[10] Figure 7a shows the configuration of the test article. A wedge, inclined 15° to the freestream, generated the bow shock wave and a slab plate with a hemi-cylindrical leading edge represented the wing leading-edge in this test. Pressure data was obtained along the axis of symmetry of the hemi-cylindrical leading-edge and off the plane of symmetry at three transverse locations. The Lanmin code was run with a wedge shock and a parallel shock for the swept cylinder for a variety of sweep angles. The results of this test are shown in Figure 7b. Good agreement is seen for the entire set of sweep angles, 30° to 70°.

Effective Radius Technique

It has been shown that the modifications to Lanmin allow it to accurately produce shock interaction heating rates for simple geometric configurations at wind tunnel conditions. Because of the complexity of the Orbiter design, specifically the Orbiter's WLE, correction factors had to be developed to account for the differences between a simple cone–swept cylinder combination to that of the double-delta WLE with a variable radius of curvature. These correction factors were derived using the heating data obtained from the OH–66 wind tunnel test[15]. The data was obtained for freestream conditions of around Mach 10 and at four different Reynolds Numbers. The 0.025 scaled Orbiter was swept through angle of attack from 0° to 45° and yaw angles from -2° to 4°. Since the Orbiter rarely flies with any yaw angle, the 0° yaw angle data was primarily used to develop the flowfield correction factors. Figure 8 shows the maximum heating to the WLE for these cases at angles of attack between 25° and 45°. In general, the shock interaction heating decreases as the angle of attack increases. The spread in the data is due to the various Reynolds Numbers at which the tests were conducted. No Reynolds number correlation could be found in the data for the shock interaction region.

As was mentioned previously, data were obtained in both the spanwise and circumferential directions. Figure 9 shows the measurement locations on the model. The circles indicate where only single thin film gauges were located and the rectangles indicate where the gauges were distributed circumferentially about the leading edge. In order to accurately measure the heating to the WLE while at angle of attack, the single gauges were displaced 30° down along the surface of the leading edge of the wing. The location of the maximum shock interference heating was shown to be at the 55% halfspan of the wing for angles of attack of 30° and more. This 55% half span corresponds to the WLE panel #9 as shown in Figure 10. Blueprint drawings of the panel #9 were used to obtain the geometric radius of curvature for this location. It was also noted that the circumferential distribution of the heating at the 55% halfspan location indicated the maximum heating was not at the surface location that was perpendicular to the freestream. The data showed that the stagnation line for the wing was shifted downward about 5° along the surface. This phenomenon can be explained by the shifting of the maximum entropy streamline as the flow passes through the WLE shock[27].

The shift in the stagnation line and the variable radius of curvature of the WLE had to be modeled before the flowfield correction factors could be developed. The geometric radius of curvature for the inboard section of panel #9 was curvefit as a function of angle of attack. As the angle of attack changes, the radius of curvature that is used to calculate the heating to the swept cylinder (i.e. WLE) will also change. To account for the shift in the maximum entropy streamline, a 5° increment is added to the angle of attack. This added increment increases the radius of curvature, thus decreasing the calculated heating rate.

Considering these local flowfield effects at the surface of the WLE, the flowfield correction factors were developed by comparing the calculated heating from the cone/swept-cylinder model using the variable radius of curvature, at 0.025 scale, to the heating rates obtained from the wind tunnel data. In order to calculate the heating rates it was first necessary to determine what cone half angle should be used which would give the proper bow shock angle before the shock intercepts the wing shock. This was accomplished with high fidelity computer solutions for the OH-66 wind tunnel test.

A three-dimensional, shock capturing, inviscid CFD code, Inviscid Equilibrium Computation in 3-Dimensions (IEC3D)[28], was used in computing an inviscid flowfield solution for the OH-66 test conditions. The IEC3D code is a general purpose three-dimensional Euler solution CFD code, which can compute inviscid flowfield solutions around general three-dimensional geometries over a wide range of flight conditions and angles-of-attack. IEC3D utilizes an upwind-biased, finite-volume high order Total Variation Diminishing (TVD) scheme. Both Van Leer's Monotone Upstream-centered Scheme for Conservation Laws (MUSCL) type of flux-vector splitting[29, 30] and Roe's characteristic-based flux-difference splitting[31] are combined. An improved implicit solution algorithm called Lower-Upper Symmetric Gauss-Seidel (LU-SGS)[32] has also been incorporated. This code has been validated with wind tunnel and various flight data.[33]

Because the quality of a CFD solution is highly influenced by the quality of the grid used, the following procedure was adopted to ensure proper grid resolution at the regions needed. An initial grid was used to get approximate shock shape and location. An outer grid boundary adjustment program was then used to push the outer boundary inward toward the shock. Finally, the Multidimensional Self-Adaptive Grid Code (SAGE)[34] was applied to adapt the grid based on flowfield variable of adjusted grid solution. The Mach number was used as the adaptations variable for this work.

CFD solutions were generated at wind tunnel conditions for 30° and 40° angle of attack. Mach contours were then used, Figure 11, to determine the angle of the bow shock from the centerline of the vehicle just before it is intersected by the interaction zone. The shock angles that resulted were 11.3° and 13° for the 30° and 40° angle of attack cases, respectively. Because the shock generator in the engineering model is a cone, the cone half angles to generate those shock half angles at Mach 10 were 8.8° and 10.6°, respectively, and were obtained in Chart 5 of ref. 35. The modified Lanmin code alters the geometry so that it is 90° out of plane with the angle of attack and will change the planform of the geometry as the angle of attack increases. Because of this and the cone half angles that were mentioned above, a cone half angle of 8.5° was chosen to generate the impingement shock. This was verified by calculating the shock angles generated off an 8.5° cone at the wind tunnel freestream conditions listed in the OH–66 report.

For these same conditions, heating rates were calculated and compared to the measured data. Flowfield correction factors were then generated by knowing that the heating rates will vary as the inverse of the square root of the radius. Since the scaled geometric radius was known, a correction factor in the form of $R_{effective} / R_{geometric}$ was determined for each wind tunnel case run. Figure 12 shows these factors. The average at each angle of attack was used to generate the flowfield correction factor variation. A piecewise linear fit to the average factors was input into the code, and the wind tunnel cases were rerun. The results of these predictions are presented in the validation section of this report.

Effect of Partially Catalytic Surfaces

Surface chemistry effects of the SiC coating on the RCC were modeled using Goulard's[36] theory of heat transfer on a hypersonic stagnation point with partially catalytic surfaces. This theory assumes that the boundary layer is chemically frozen such that the mass fractions of the different components of air at the edge of the boundary layer remain constant to the surface. In order to account for finite catalytic recombination rates at the wall, Goulard introduced a nonsimilar boundary condition which can be reduced to similarity for stagnation flows. The solution was extended to the general case of partially catalytic wall efficiency by the introduction of a correction factor which is a function of the flight condition, the nose radius, and the recombination rate of the material. The final output is a ratio of partially catalytic wall heating to fully catalytic wall heating.

It has been shown that fully catalytic heating is comparable to equilibrium air heating[37]. The heating rates produced by Lanmin are calculated using equilibrium air tables. However, the species concentrations that are needed to determine the amount of chemical energy that can be recovered by recombination on a surface are not provided by the code. A seven species equilibrium air model was

incorporated into the Goulard algorithm which calculates the species concentrations based on the pressure and temperature calculated in the Lanmin code. Since the code will use equilibrium edge conditions, it is expected that for an uncalibrated case the effects of using a partially catalytic surface will be over estimated due to over estimation of atomic species as compared to those in nonequilibrium flow. This is because at nonequilibrium flight conditions, chemical reaction rates are not as fast as when in equilibrium flight conditions. Thus, there will not be as much atomic oxygen and nitrogen produced by the time the flow reaches the edge of the boundary layer.

In order to use Goulard's theory it is necessary to have information on the recombination rates of the material to be flown. Recombination rates for RCC vary[18-20] between 100 to 1000 cm/sec; however, it was shown in a more recent work by Stewart et al.[38] that at lower wall temperatures the SiC coating of the RCC behaved similarly to Reaction Cured Glass (RCG) coating of the Shuttle tiles. These recombination rates were used as an initial estimate to the effects of a partially catalytic wall. Along with these rates, the capability was added so that the heating ratio could be determined using a single constant recombination rate for both atomic oxygen and nitrogen. In addition to these latter two items, a single recombination rate for both atomic oxygen and nitrogen for RCC was backed out by comparing reduced OFT nose cap data to calculated equilibrium heating rates for the stagnation point of the nose cap.

Stagnation point heating rates for the nose cap were reduced from DFI radiometer data for STS–5[1,2], Figure 13. These heating rates are referred to as flight derived heating rates which automatically take into account the effects of nonequilibrium edge conditions and surface catalysis. The equilibrium heating rate for the nose cap for the STS–5 entry trajectory is also presented in Figure 13 and was used to back out a single recombination rate for RCC that varies with wall temperature. The equilibrium stagnation point heating to the Orbiter was calculated by the BLIMP88 code[39]. The BLIMP88 code is a multi-chemical reaction code which uses an integral matrix procedure to solve the axisymmetric boundary layer equations. The equilibrium heating was obtained for a 2.36 foot radius sphere, which is the radius of curvature of the nose cap at 40° angle of attack. The ratio of the flight data to the equilibrium heating data was then used to back out a single recombination rate for RCC, using Lanmin calculated freestream properties. This recombination rate could then be used for the WLE heating calculations.

In order to verify the inferred recombination rates, nose cap heating rates were again calculated, this time using the Goulard algorithm. An initial guess wall temperature is used to calculate the recombination rates at the wall. Use of these rates result in a ratio of partially catalytic to fully catalytic heating which is then multiplied by the equilibrium heating rate. This new heating rate is then used to obtain a new wall temperature and wall emittance factor. The new wall temperature is then used to calculate a new wall recombination rates for the next time point in the trajectory. This approach is valid as long as the time between trajectory points remains small. The calculated heating rates using the inferred rates are compared to the original flight derived heating rates and are shown in Figure 14. The results, as was expected, are in good agreement to the flight derived data for the nose cap of the Orbiter.

VALIDATION

Wind Tunnel Test

Lanmin OH–66 test results

Results of the OH–66 wind tunnel test for a variety of cases using the flowfield correction factor described previously can be seen in Figure 15. The comparison between the measured and calculated heating rates for the OH–66 test shows good agreement. Statistical analysis indicated a standard deviation of 4.95% for the 0° yaw cases. When all of the wind tunnel cases are considered, Figure 16, the standard deviation increases to 7.76%. However, recall that the Orbiter normally flies with 0° yaw angle.

CFD OH–66 test results

As a part of the validation effort, a high fidelity two-layer method was used to predict leading edge heating and compare with the OH-66 test results. The CFD two-layer method uses the axisymmetric analog methodology for three dimensional boundary layer developed by Cooke[40]. Following that approach, the general three-dimensional boundary layer equations are written in a streamline coordinate system and the cross-flow is assumed to be small and can be neglected. This reduces the three-dimensional boundary layer equations to a form that is identical to those of axisymmetric flow, provided that the distance along a streamline is interpreted as the distance along an "equivalent body", and the metric coefficient that describes the spreading of streamlines is interpreted as the radius of the equivalent body. This method allows the existing axisymmetric boundary layer codes to be used to compute the approximate three-dimensional heating rate along a streamline.

In order to apply the axisymmetric analog technique in computing approximate heating of three-dimensional bodies, the inviscid surface streamline paths and the metric coefficients need to be computed. DeJarnette and Davis[41] calculated the streamlines as the lines of steepest descent emanating from the stagnation point. DeJarnette and Hamilton[42] developed a simple method for calculating streamlines from the known pressure distribution. However, this approach has proven difficult to apply, unless the surface geometry and pressures can be described analytically. More success has been achieved in using the three-dimensional inviscid flowfield solution surface velocities to compute surface streamlines and metric coefficients.[43–47] But, the disadvantage of this approach is that it requires more computer time than the engineering approximate methods described in references 41 and 42. The majority of the computer time is spent in obtaining the three-dimensional inviscid flowfield solution.

A streamline code, which uses surface velocity components in Cartesian coordinates as input, has been developed to trace streamline paths and compute metric coefficients along the path. A boundary code, BLIMP88[39] was used to evaluate the heating along a streamline. To trace surface streamlines paths and evaluate metric coefficients along the path, requires the solving of a system of five ordinary differential equations. A fourth order variable step Runge-Kutta integrator was used to integrate the ordinary differential equations.

Surface streamlines emanate from the stagnation point and spread all over the body surface. It is very difficult to start a streamline path from the stagnation point and have it pass through a specific point on the body. Since heating rates at specific locations on the leading edge are of interest, a procedure was developed to trace streamlines in a backward fashion, starting at a specific location and tracing the streamline toward the stagnation point. This can be done easily be reversing the sign of velocity components while integrating the streamline equations. Streamline coordinates and the integration step size are saved for each integration step. The process can then be reversed at a point very close to the stagnation point (the stagnation point can never be reached) and re-trace the streamline in a forward fashion and compute metric coefficients along the streamline path until the point of interest is reached. The streamline location, metric coefficient and pressure distribution along the streamline can then be passed to a boundary layer code to evaluate heating. This procedure was applied to calculate the leading edge heating 0.025 scale model Space Shuttle Orbiter configuration at a wind tunnel condition of Mach 10 and angles of attack of 30 and 40 degrees. Figure 17 shows the comparison between predicted and measured heating rates for the 30 degree angle of attack case. The predictions compare well with the experimental data except at $x/L = 0.6620$ and $x/L = 0.7703$ locations where the predicted value is about 15% less then measurements. Figure 18 shows the comparison between computed and measured heating rates for the 40 degree angle of attack case. Again the predictions compare well with the experimental data except at $x/L = 0.6530$. A heating rate of more the 135 Btu/ft^2-sec was measured while the prediction is about 62.5 Btu/ft^2-sec. Because of the unreasonably high heating rate measured, we suspect the accuracy of the measurement at this location.

Flight Data

Description of Radiometer

The Wing Leading Edge Structural Subsystem uses a non-contact temperature-measuring device that operates similar to a pyrometer; this device is termed a radiometer, Figure 19a. The radiometer is a thermoelectric instrument that functions in conjunction with a lens system that collimates incident thermal energy to a thermopile sensor, Figure 19b. The sensor millivolt output is calibrated as a known function of source temperature and emittance and, in operation, provides a continuous readout of temperature. Radiometers were used on Columbia (OV–102) during the OFT program, and a single radiometer is currently being used on Discovery (OV–103). The temperature of the IML of RCC wing panel #9 on OV–103 is measured by a radiometer that is mounted on the wing structure, Figure 16c. The Orbiter radiometers are total radiation radiometers. The primary purpose of the radiometers is to provide temperature data that is used to calculate OML heat rate histories and heating distributions experienced by the RCC surface during entry. The conversion of IML temperature data to OML heat flux predictions required detailed thermal analysis of the radiation enclosure formed by the leading edge cavity that consists of the panel IML and the spar insulation surface. Two dimensional thermal math models (TMM) were developed by Rockwell International to convert radiometer temperatures to surface heating[24]. A reduced but calibrated form of this TMM was incorporated into the Lanmin model used in this analysis.

Recently an effort was completed to recalibrate the panel #9 radiometer from OV–103. High temperature outgassing of the RCC shell and wing cavity insulation blankets contaminated the radiometer's sapphire window causing the indicated temperature to be lower then the actual value. A calibration was performed on the radiometer in the contaminated and cleaned state. A multiplication factor of 1.077 to recorded radiometer voltage was recommended to compensate for window contamination[48].

Comparison of Goulard-Lanmin model with flight data

As a final validation attempt the Goulard-Lanmin model was compared to flight derived data for the STS-2, 5, and 30 flight trajectories. The STS–2 best estimated trajectory (BET) was run with the Lanmin model in both equilibrium and partially catalytic mode. It was seen that in order to match the equilibrium portion of the trajectory, taken to be at an entry interface time of about 1000 seconds, a scaling factor of 1.17 needed to be applied. This is thought to be due to the fact that the effective radius is correlated for the WLE from wind tunnel data and a tunnel-to-flight correction factor is needed. It is seen in Figure 20 that the equilibrium model is overpredicting in the high heating region. When the Goulard partial catalycity model is applied the predictions match the flight data very well. This Goulard-Lanmin model was then applied to the BET for STS–5. In this case it is seen that the partial catalytic Lanmin model is underpredicting, Figure 21. Actually the equilibrium calculation in this case gives the best agreement with the radiometer data. This is in contradiction to the STS–2 results and this inconsistency is currently under investigation. For the STS-30 trajectory the results were similar to STS–2. The equilibrium calculation overpredicted and the inclusion of partial catalycity brought the calculation in line with those values computed by the WLETI program, Figure 22. The WLETI program is correlated with entry flight data and is consider to match the radiometer data well for normal re-entry EOM mission.

CONCLUSIONS

The wing leading heating calculation methodology presented in this paper has several advantages over the present design model. It includes more flowfield physics, uses actual Orbiter and WLE geometries and is applicable beyond the correlation envelope of flight data. The Lanmin code has been shown to be useful in modeling objects with basic geometry in a shock interaction environment. A

generic partial catalycity model has been incorporated into the Lanmin code that relieves excessive conservatism from analyses by removing the equilibrium heating assumption. The integrated model has achieved good correlation to wind tunnel and flight cases. However some questions still remain in regard to the results. The scaling of OH–66 wind tunnel data to flight continues to be of concern, and the discrepancy between the predictions for STS–2 and STS–5 needs to be investigated. Work continues on this project with the analysis being extended to the 80% span wing location. Since at the 80% span location the flow is free of the shock interaction phenomenon, looking there should identify whether the dissimilarity between the STS-2 and STS-5 predictions is due to flowfield characteristics or the partially catalytic model. Future shock-shock interaction CFD work for flight cases will also help validate the new engineering method.

The radiometer flight data was seen to be valuable in identifying problems in the proposed methodology. It is the flight data that contains all the effects of shock interaction and partial catalycity and the flight data will be used as the final word as to the validity of any method.

REFERENCES

1. Curry, D. M.; Cunningham, J. A.; and Frahm, J. R: Space Shuttle Orbiter – Leading Edge Structural Subsystem Thermal Performance. AIAA-82–0004, AIAA 20st Aerospace Sciences Meeting, January 11–14, 1982.

2. Curry, D. M.; Latchem, J. W.; and Whisenhunt, G. B.: Space Shuttle Orbiter Leading Edge Structural Subsystem Development. AIAA-83–0483, AIAA 21st Aerospace Sciences Meeting, January 10–13, 1983.

3. Young, J. C.; Underwood, J. M.; Romere, P. O.; et al.: The Aerodynamic Challenges of the Design and Development of the Space Shuttle Orbiter. NASA CP-2342, Part 1, June 28–30, 1983, pp. 209–263.

4. Edney, B. E.: Anomalous Heat Transfer and Pressure Distributions on Blunt Bodies at Hypersonic Speeds in the Presence of an Impinging Shock. FFA Rept. 115, Feb. 1968, The Aeronautical Research Inst. of Sweden, Stockholm, Sweden.

5. Bertin, J. J.; Graumann, B. W.; and Goodrich, W. D.: Aerothermodynamic Aspects of Shock–Interference Patterns for Shuttle Configurations During Entry. AIAA-73–238, Washington, D.C., 1973.

6. Cunningham, J. A.; and Haney, J. W.: Space Shuttle Wing Leading Edge Heating Environment Prediction Derived from Development Flight Data. *Shuttle Performance: Lessons Learned,* NASA CP-2283, Part 2, March 8–10, 1983, pp. 1083–1110.

7. Hains, F. D.; and Keyes, J. W.: Shock Interference Heating in Hypersonic Flows. *AIAA Journal,* vol. 10, Nov. 1972, pp. 1441–1447.

8. Hiers, R. S.; and Loubsky, W. J.: Effects of Shockwave Impingement on the Heat Transfer on a Cylindrical Leading Edge. NASA TN-D–3859, 1967.

9. Bertin, J. J.; and Hinkle, J. C.: *An Experimental Investigation of the Flowfield for Double Wedge Configurations in a Mach 4.97 Stream.* Aerospace Engineering Report 74003, The University of Texas, June 1974.

10. Barnette, D. W.: *An Experimental Investigation of Supersonic Flowfield Past a Wedge-Cylinder Configuration.* Aerospace Engineering Report 76002, The University of Texas, April 1976.

11. Wieting, A. R.; and Holden, M. S.: Experimental Shock-Wave Interference Heating on a Cylinder at Mach 6 and 8. *AIAA Journal*, vol. 27, Nov. 1989, pp. 1557–1565.

12. Bertin, J. J.; Graumann; B. W., and Goodrich, W. D: High Velocity and Real-Gas Effects on Weak Two-Dimensional Shock-Interaction Patterns. *Journal of Spacecraft and Rockets*, Vol. 12, March 1975, pp. 155–161.

13. Bertin, J. J.; Mosso, S. J.; Barnette, D. W.; and Goodrich, W. D: Engineering Flowfields and Heating Rates for Highly Swept Wing Leading Edges. *Journal of Spacecraft and Rockets*, Vol. 13, Sept. 1976, pp. 540–546.

14. Amirkabirian, I.; Bertin, J. J; and Mezines, S. A.: The Aerothermodynamic Environment for Hypersonic Flow Past a Simulated Wing Leading Edge. AIAA Paper 86–0389, AIAA 24th Aerospace Sciences Meeting, January 6–9, 1986.

15. Wittliff, C. E.; and Berthold, C. L.: *Results of Heat Transfer Testing of an 0.025–Scale Model (66–0) of the Space Shuttle Orbiter Configuration 140B in the Calspan Hypersonic Shock Tunnel (OH66)*. DMS–DR–22359, (NASA–CR–151,405), January 1978, Data Management Services.

16. Curry, D. M.; and Webster, C. N.: Material Characteristics of Space Shuttle Reinforced Carbon-Carbon. *24th National SAMPE Symposium*, San Francisco, CA, May 8–10, 1979.

17. Caram, J. M.; Bouslog, S. A.; and Cunnington, G. R.: Emittance Measurements of Space Shuttle Orbiter Reinforced Carbon–Carbon. NASA TP – 3293, December 1992.

18. Stewart, D. A.; Rakich, J. V.; and Lanfranco, M. J.: Catalytic Surface Effects Experiment on the Space Shuttle. AIAA–81–1143, AIAA 16th Thermophysics Conference, Palo Alto, CA., June 23–25, 1981.

19. Zwan, A. D.; Crocks, R. S.; and Whatley, W. J.: Arcjet Validation of Surface Catalycity using Viscous Shock Approach. AGARD–CP–437, Validation of Computational Fluid Dynamics, Lisbon, Portugal, May 2–5, 1988.

20. Curry, D. M.; Rochelle, W. C.; Chao, D. C.; and Ting, P. C.: Space Shuttle Orbiter Nose Cap Thermal Analysis. AIAA Paper 86–0388, AIAA 24th Aerospace Sciences Meeting, Reno, NV, January 6–9, 1986.

21. Stewart, D. A.; Henline, W. D.; Kolodziej, P.; and Pincha, E. M.: Effect of Surface Catalysis on Heating to Ceramic Coated Thermal Protection Systems for Transatmospheric Vehicles. AIAA–88–2706, AIAA Thermophysics, Plasmadynamics, and Lasers Conference, June 27–29, 1988.

22. Flores, R. B.: *Wing Leading Edge Temperature Indicator*. Rockwell International Report STS89–0635A, October 1991.

23. Miller, B. A.: *XF0002 Aeroheating Computer Program Engineering Description and User's Guide*. SOD 80–0150, August 1982 rev.

24. Chao, D. M.; Battley, H. H.; Gallegos, J. J.; and Curry, D. M.: Thermal Mathematical Modeling and System Simulation of Space Shuttle LESS Subsystem. AIAA-84–1772, AIAA 19th Thermophysics Conference, June 25–28, 1984.

25. Williams, S. D.; and Curry, D. M.: Assessing the Orbiter Thermal Environment Using Flight Data. *Journal of Spacecraft and Rockets*, vol. 21, Nov.–Dec. 1984, pp. 534–541.

26. Engel, Carl D.; and Praharaj, Sarat C.: *MINIVER Upgrade for the Avid System.* REMTECH, Inc. Huntsville, AL, Aug. 1983.

27. Anderson, Jr., J. D.: *Hypersonic and High Temperature Gas Dynamics.* New York, 1989.

28. Tam, L. T.: LU-SGS Implicit Scheme for Entry Vehicle Flow Computation and Comparison with Aerodynamic Data. AIAA–92–2671, June 1992.

29. Van Leer, B.: Flux-Vector Splitting for the Euler Equations. *Lecture Notes in Physics*, vol. 170, 1982, pp. 507–512.

30. Anderson, W. K.; Thomas, L. J.; and Van Leer, B.: Comparison of Finite Volume Flux Vector Splitting for the Euler Equations. *AIAA Journal,* vol. 24, no. 9, Sept. 1986, pp. 1453–1460.

31. Roe, P. L.: Characteristic-Based Schemes for the Euler Equations. *Annual Review of Fluid Mechanics*, 1986, pp. 337–356.

32. Jamerson, A.; and Yoon, S.: Lower-Upper Implicit Schemes with Multiple Grids for the Euler Equations. *AIAA Journal*, vol. 25, 1987, pp. 929–935.

33. An, M. Y.; Wang, K. C.; and Tam L. T.: Computation of Inviscid Flowfield around 3-D Aerospace Vehicles and Comparison with Experimental and Flight Data. AIAA–93–0885, Reno NV, Jan. 1993.

34. Davie, C. B.; and Venkatpathy, E.: The Multidimensional Self-Adaptive Grid Code, SAGE. NASA TM–103905, July 1992.

35. *Equations, Tables, and Charts for Compressible Flow.* NACA 1135, NASA Ames Research Center, Moffett Field, CA., 1953.

36. Goulard, R. J.: On Catalytic Recombination Rates in Hypersonic Stagnation Heat Transfer. *Jet Propulsion*, vol. 28, Nov. 1958, pp. 737–745.

37. Rochelle, W. C.; Mueller, S. R.; Colovin, J. E.: *AFE Stagnation Point Heating Predictions as a Function of Time for 4100-LB Vehicle Trajectory.* Lockheed Engineering and Sciences Company, APD 277, July 7, 1988.

38. Stewart, D. A.; Chen, Y. K.; and Henline, W. D.: Effect of Non-Equilibrium Flow Chemistry and Surface Catalysis on Surface Heating to AFE. AIAA–91–1373, AIAA 26th Thermophysics Conference, June 24–26, 1991.

39. Murray, A. L.,: *Further Enhancements of the BLIMP Computer Code and User's Guide.* AFWAL–TR–88–3010, June 30,1988.

40. Cooke, J. C.: An Axially Symmetric Analogue for General Three-Dimensional Boundary Layers. British A.R.C., R&M No. 3200, 1959.

41. DeJarnette, F. R.; and Davis, R. M.: A Simplified Method for Calculating Laminar Heat Transfer over Bodies at an Angle-Of-Attack. NASA TN D-4720, 1968.

42. DeJarnette, F. R.; and Hamilton, H. H. II: Inviscid Surface Streamlines and Heat Transfer on Shuttle-Type Configurations. *Journal of Spacecraft and Rockets*, vol. 10, May 1973, pp. 314–321.

43. Goodrich, W. D.; Li, C. P.; Houston, D. K.; Chiu, P. B.; and Olmedo, L.: Numerical Computations of Orbiter Flowfields and Laminar Heating Rates, *Journal of Spacecraft and Rockets*, vol. 14, May 1977, pp. 257–264.

44. Rakich, J. V.; and Lanfranco, M. J.: Numerical Computation of Space Shuttle Laminar Heating and Surface Streamlines. *Journal of Spacecraft and Rockets*, vol. 14, May 1977, pp. 265–272.

45. Hamilton, H. H. II: Calculation of Laminar Heating Rates on Three-Dimensional Configurations using the Axisymmetric Analogue. NASA TP-1698, Sept. 1980.

46. Hamilton, H. H. II; DeJarnette, F. R.; and Weilmuenster, K. J.: Application of Axisymmetric Analogue for Calculating Heating in Three-Dimensional Flows. AIAA-85-0242, Reno NV, Jan. 1985.

47. Hamilton, H. H. II; Greene, F. A.; and Weilmuenster, K. J.: Comparison of Heating Rate Calculations and Experimental Data on a Modified Shuttle Orbiter at Mach 6. AIAA-91-1347, Honolulu, Hawaii, June 1991.

48. Milhoan, J. D.; and Rarick, D.: Calibration of Orbiter Wing Leading Edge Radiometer S/N 2276. Thermal Branch Report JSC-25971, July 1992.

Table 1. Hiers and Loubsky Results

$M_\infty=14,\ \Lambda=45°,\ \delta = 10°$	
q_{Lanmin} / q_0	$q_{measured} / q_0$
2.07	2.00

Table 2. Bertin and Hinkle Results

	$M_\infty=4.97,\ \Lambda=51°,\ \delta = 15°$	
	p_{Lanmin} / p_∞	$p_{measured} / p_\infty$
zone 3	44.2	41.0
zone 7	61.2	68.0

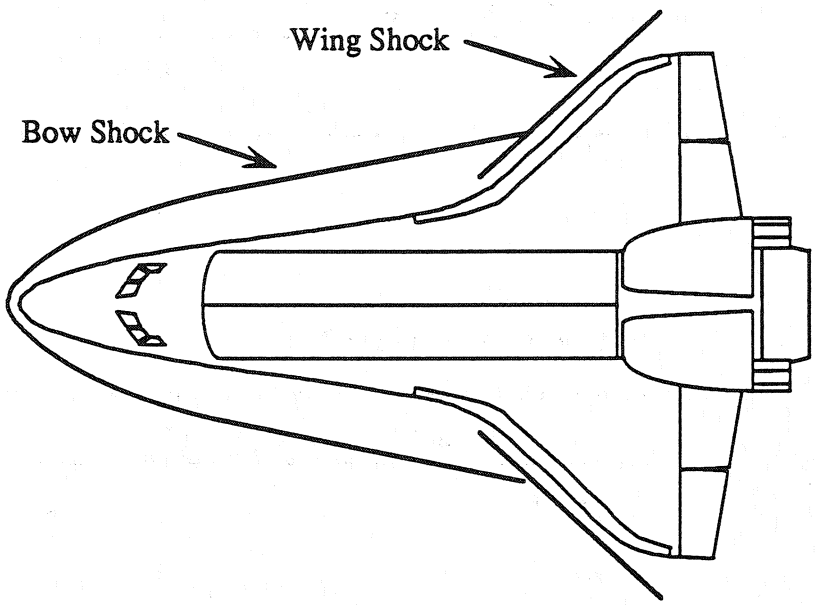

Figure 1. Space Shuttle Orbiter shock structure.

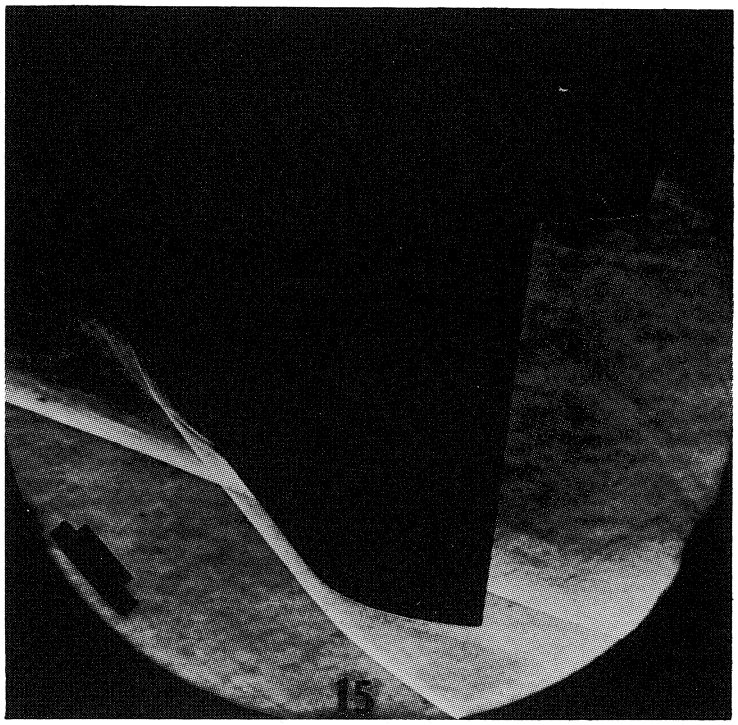

Figure 2. Schlieren Photograph of Shock Interaction Near Wing Leading Edge[15]

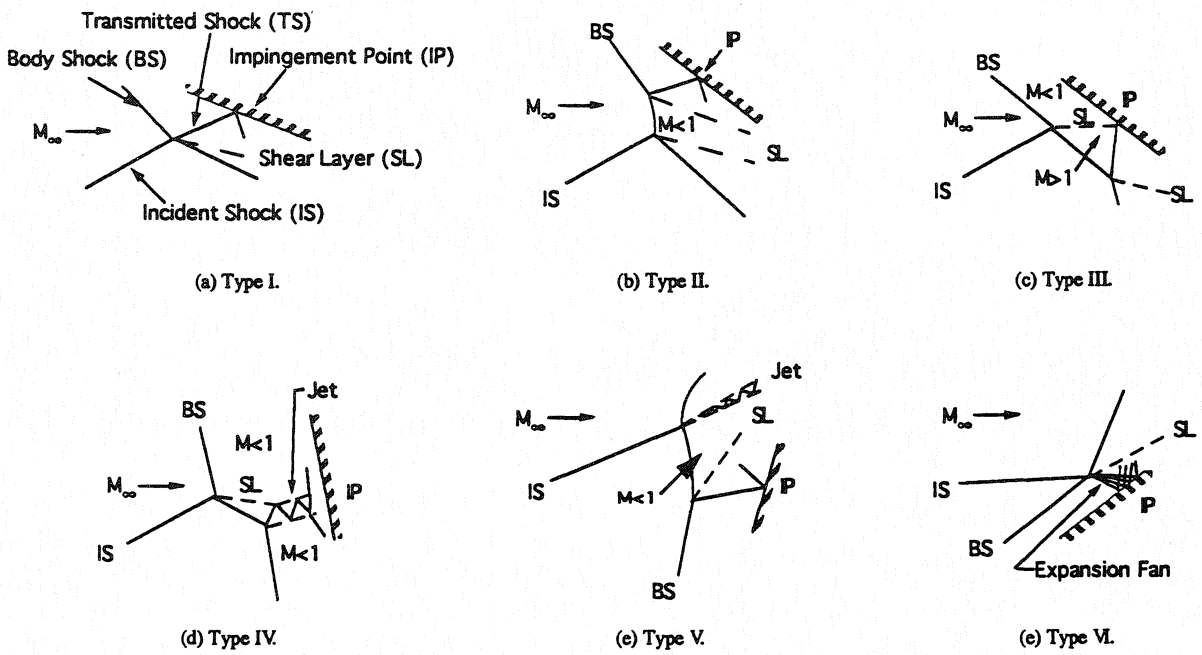

(a) Type I. (b) Type II. (c) Type III.

(d) Type IV. (e) Type V. (e) Type VI.

Figure 3. Six types of shock interaction patterns.

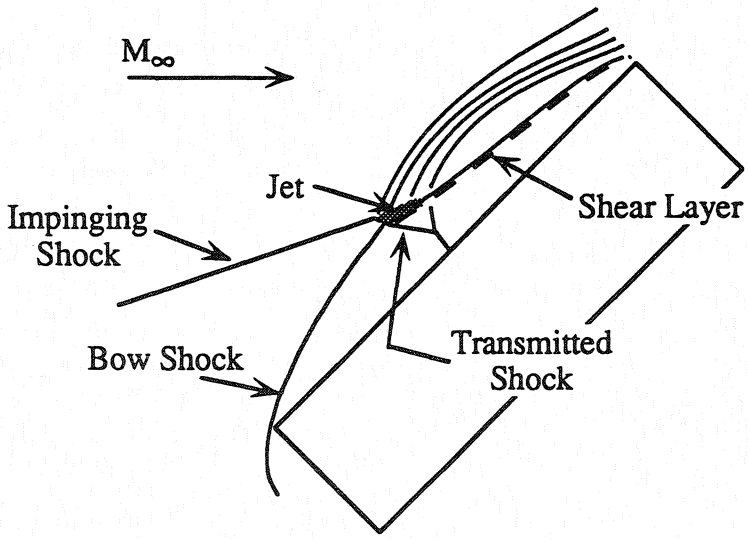

Figure 4. Flowfield of a type V interference pattern.

Figure 5 is included as a portion of figure 7a.

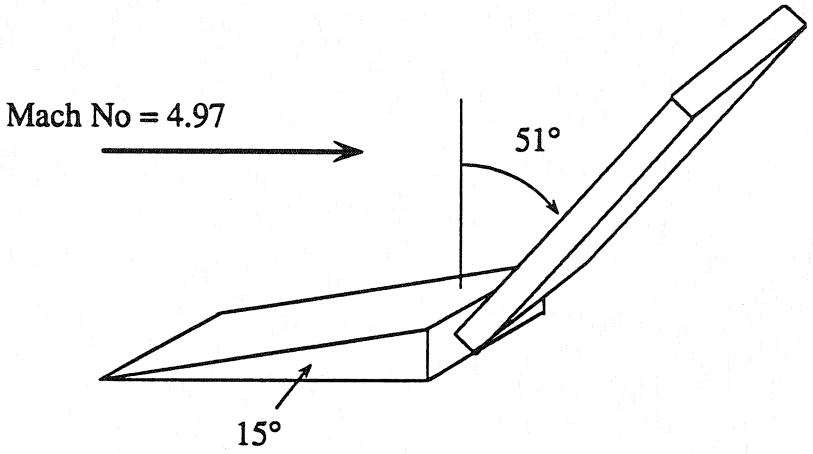

Figure 6a. Bertin and Hinkle test geometry.

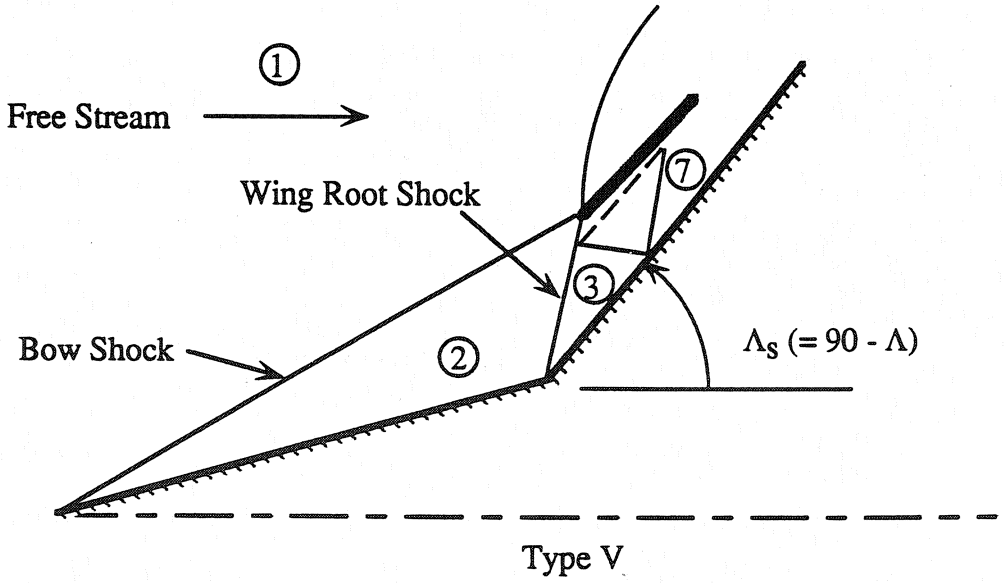

Figure 6b. Bertin and Hinkle test flowfield elements.

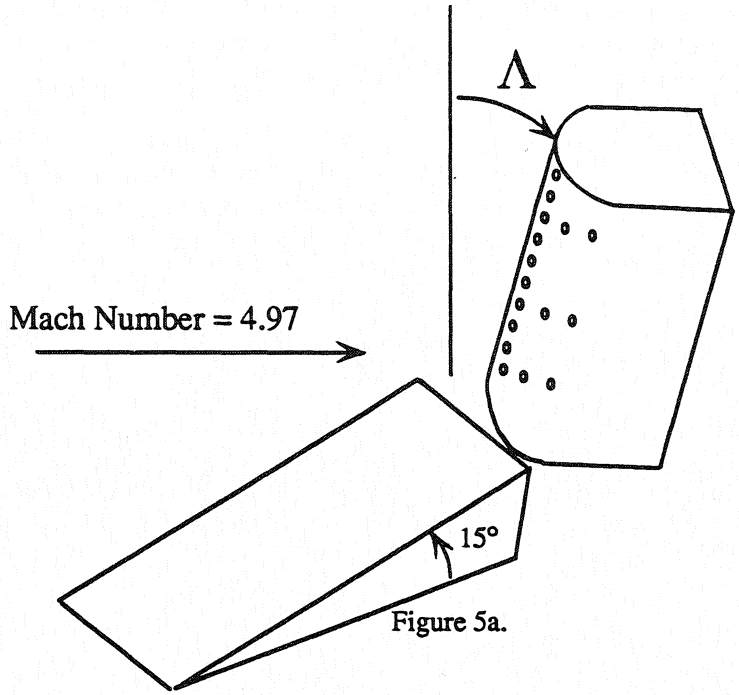

Figure 5a.

Figure 7a. Barnette wedge-cylinder test geometry.

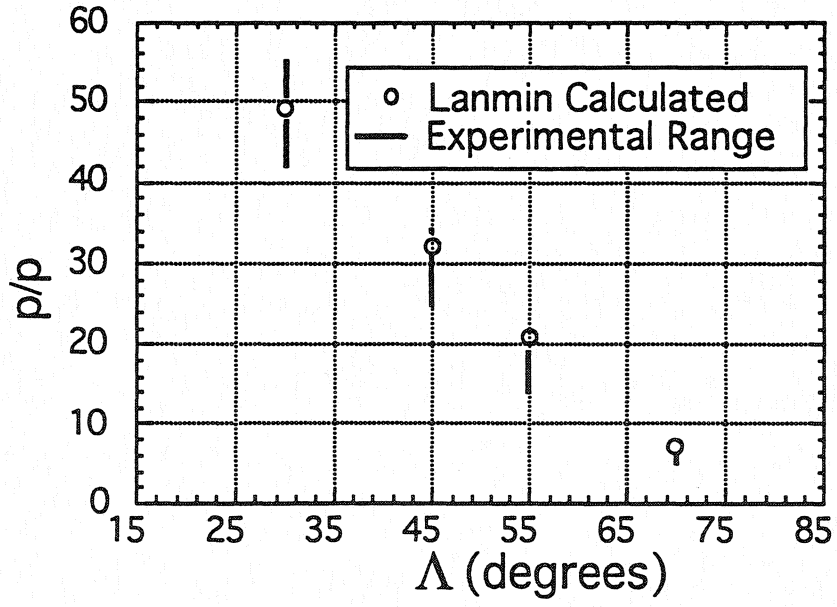

Figure 7b. Barnette wedge-cylinder test results.

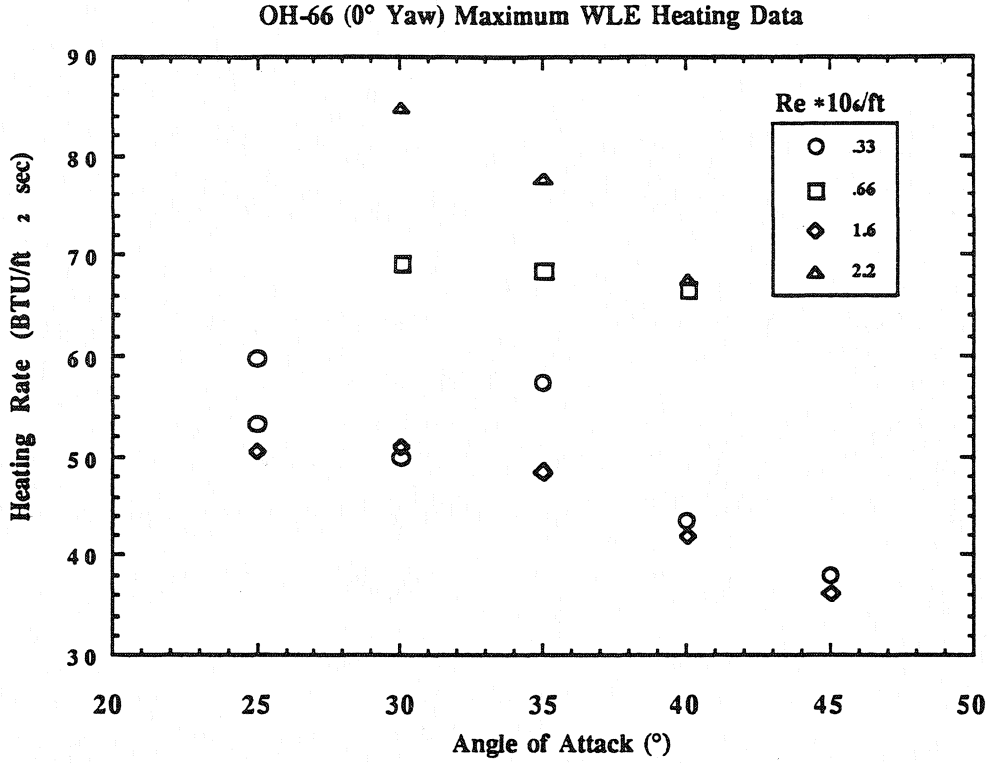

Figure 8. Heating data from OH-66 test.

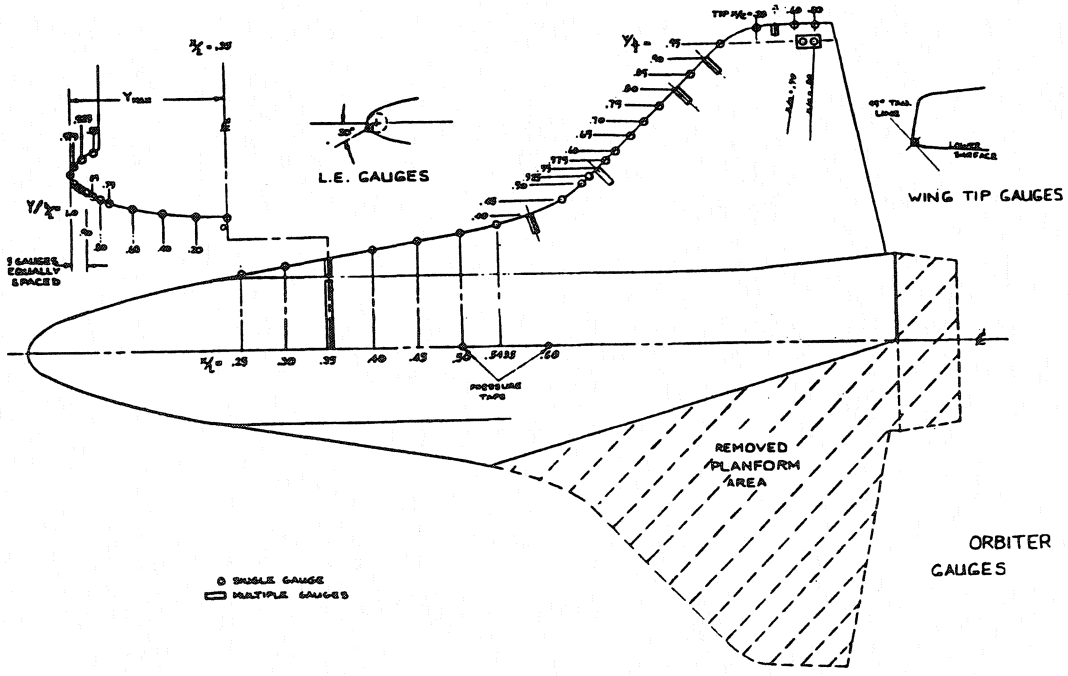

Figure 9. Measurement locations for OH-66 test.[15]

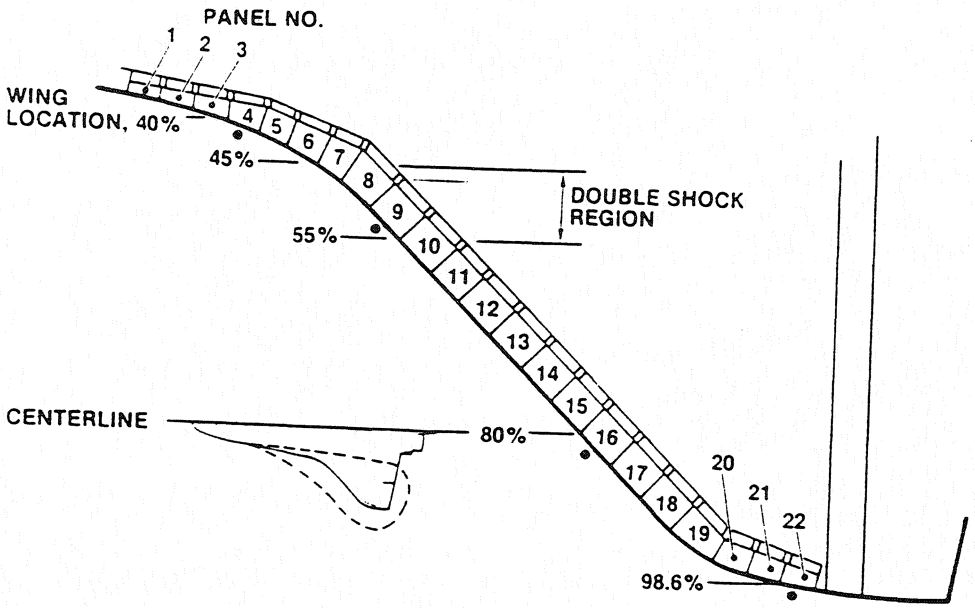

Figure 10. Panel location for 55% span.

Mach Number Contours

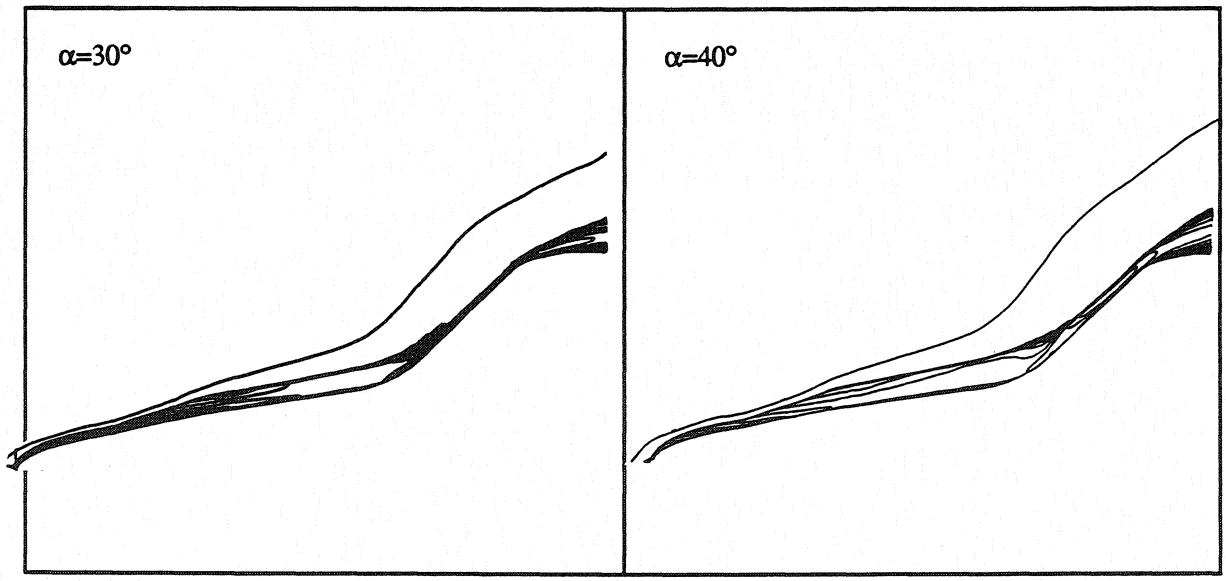

Figure 11. CFD solutions for OH-66 test.

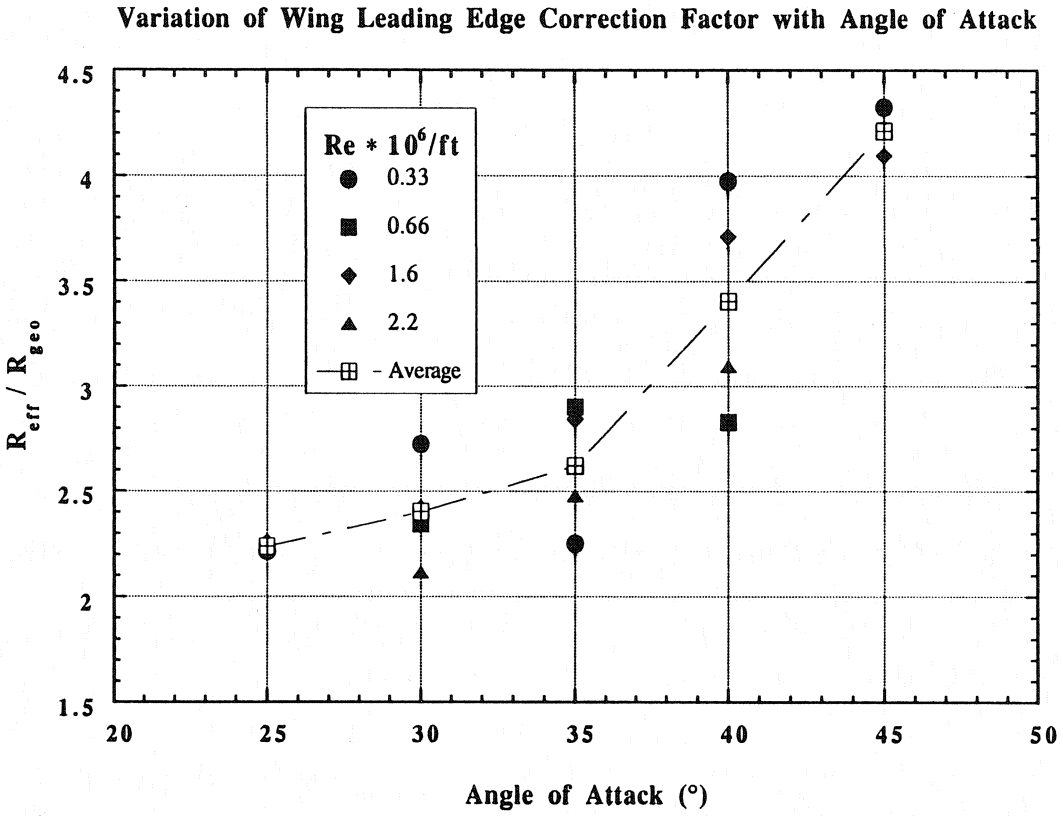

Figure 12. OH-66 derived effective radius to geometric radius ratio.

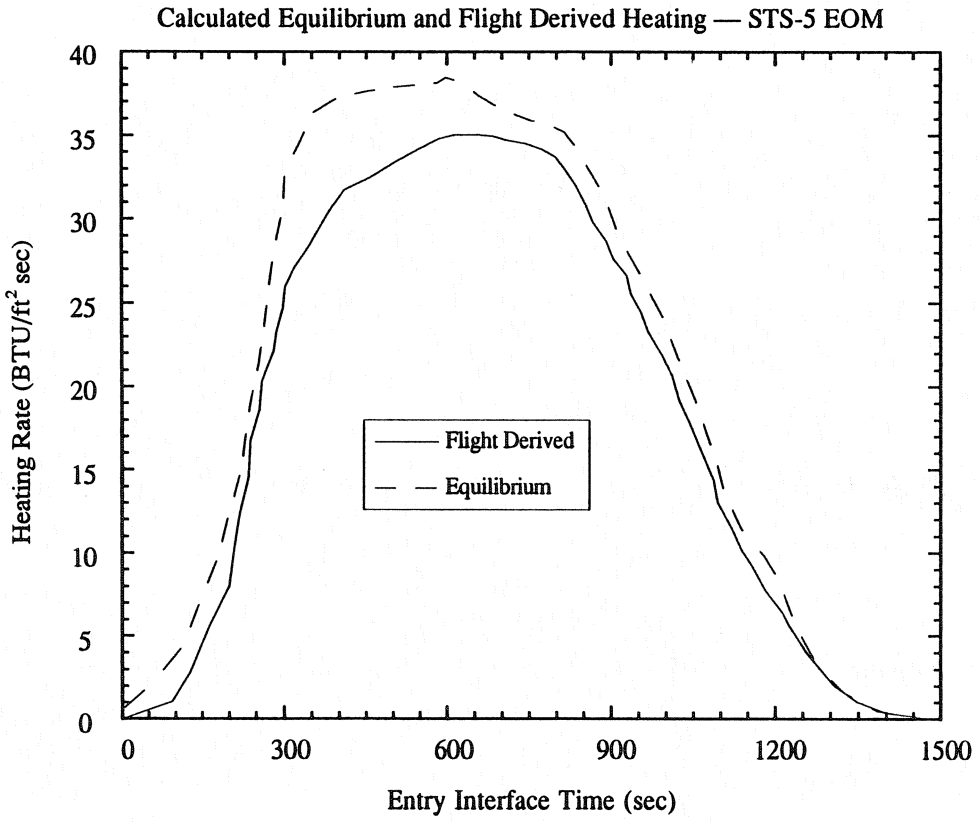

Figure 13. Equilibrium and flight derived stagnation point heating rates for STS-5.

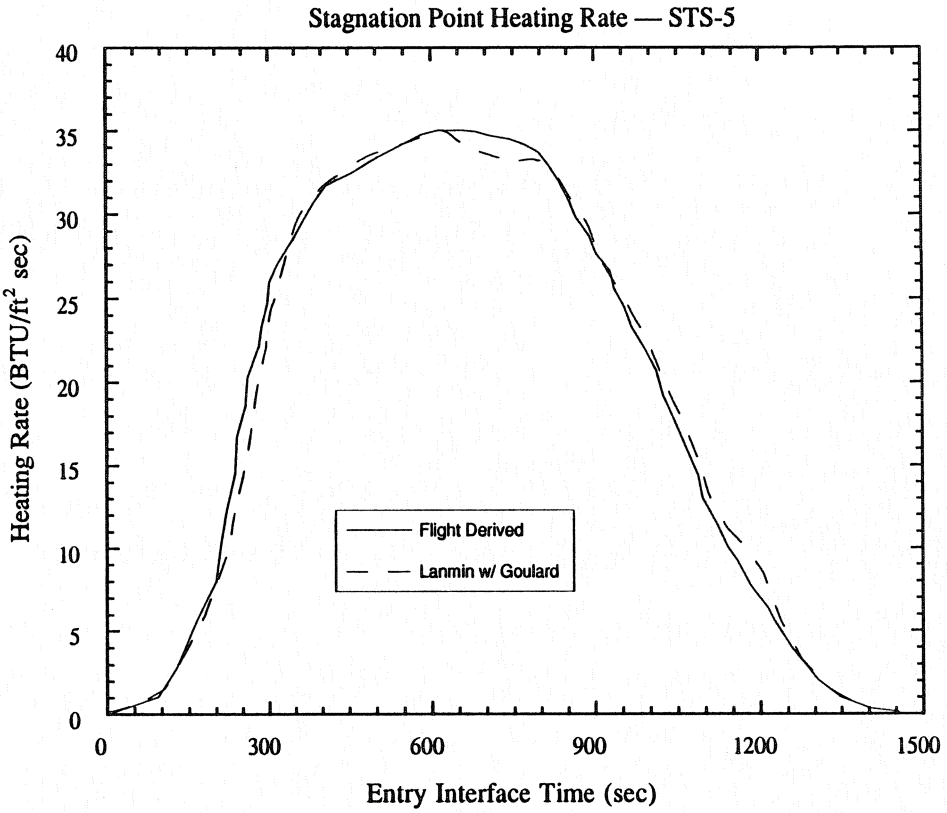

Figure 14. Partially catalytic and flight derived stagnation point heating rates for STS-5.

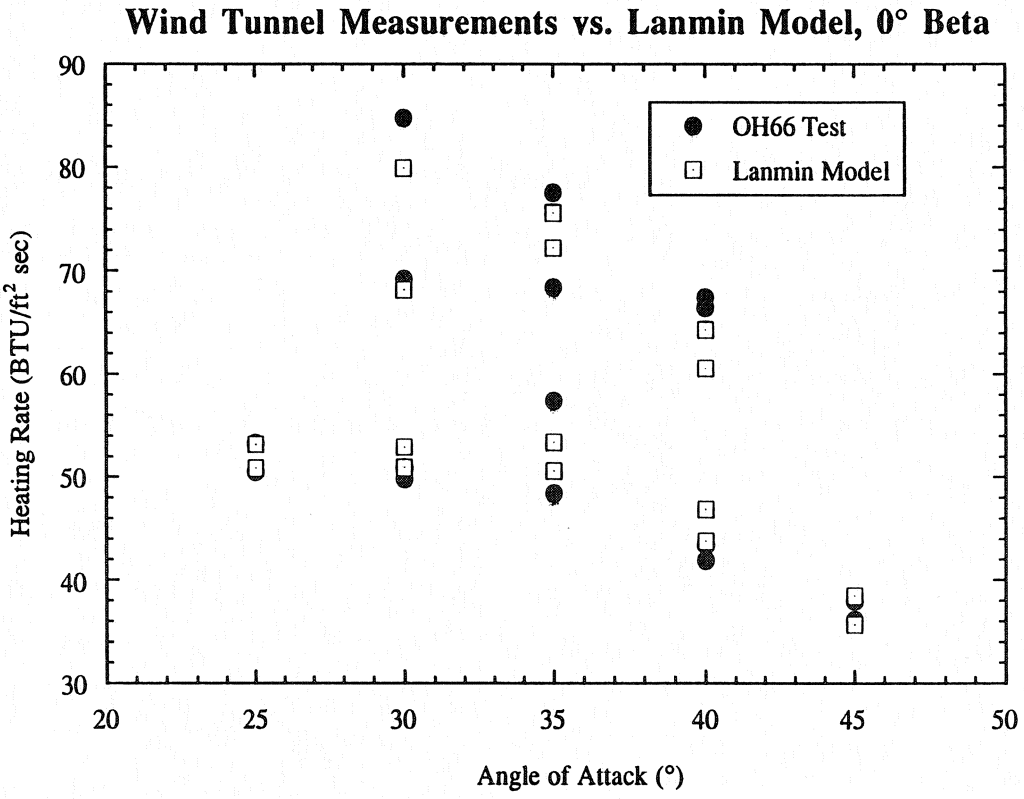

Figure 15. Calculated and measured heating rates for the OH-66 wind tunnel test ($\beta = 0°$).

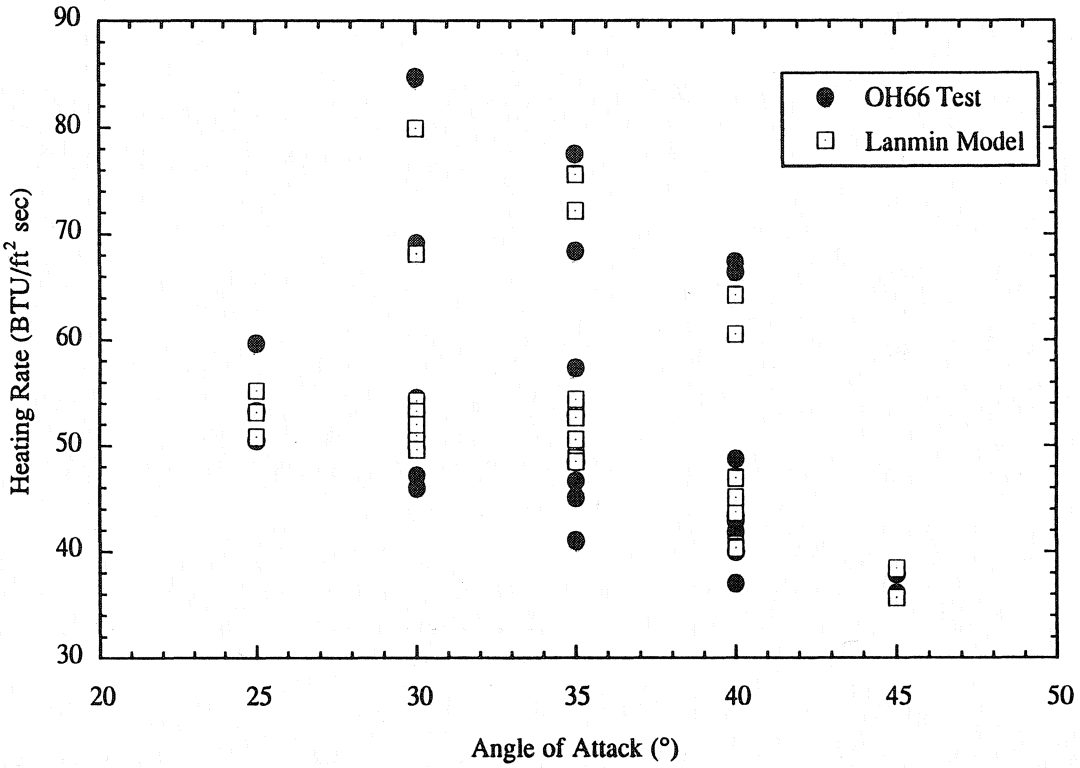

Figure 16. Calculated and measured heating rates for the OH-66 wind tunnel test, all cases.

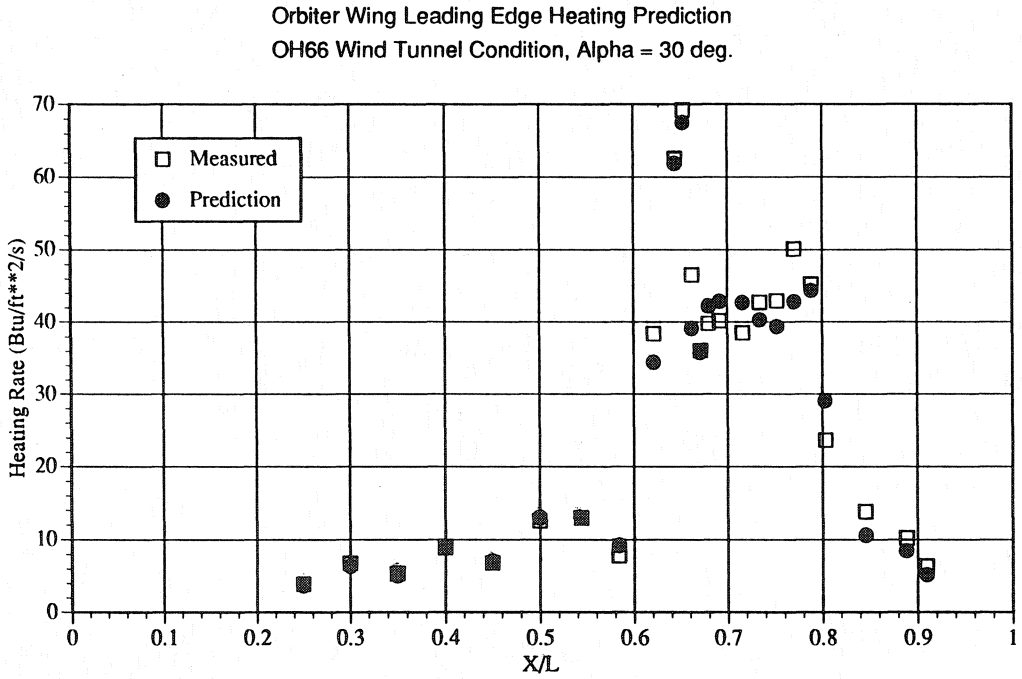

Figure 17. CFD results for angle of attack = 30° OH-66 test.

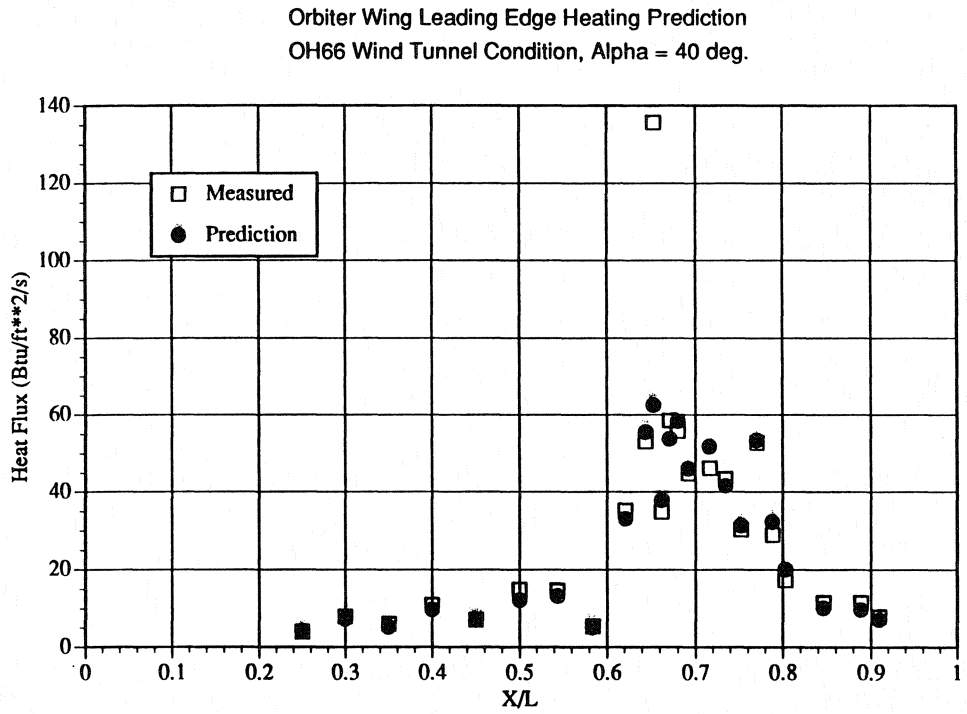

Figure 18. CFD results for angle of attack = 40° OH-66 test.

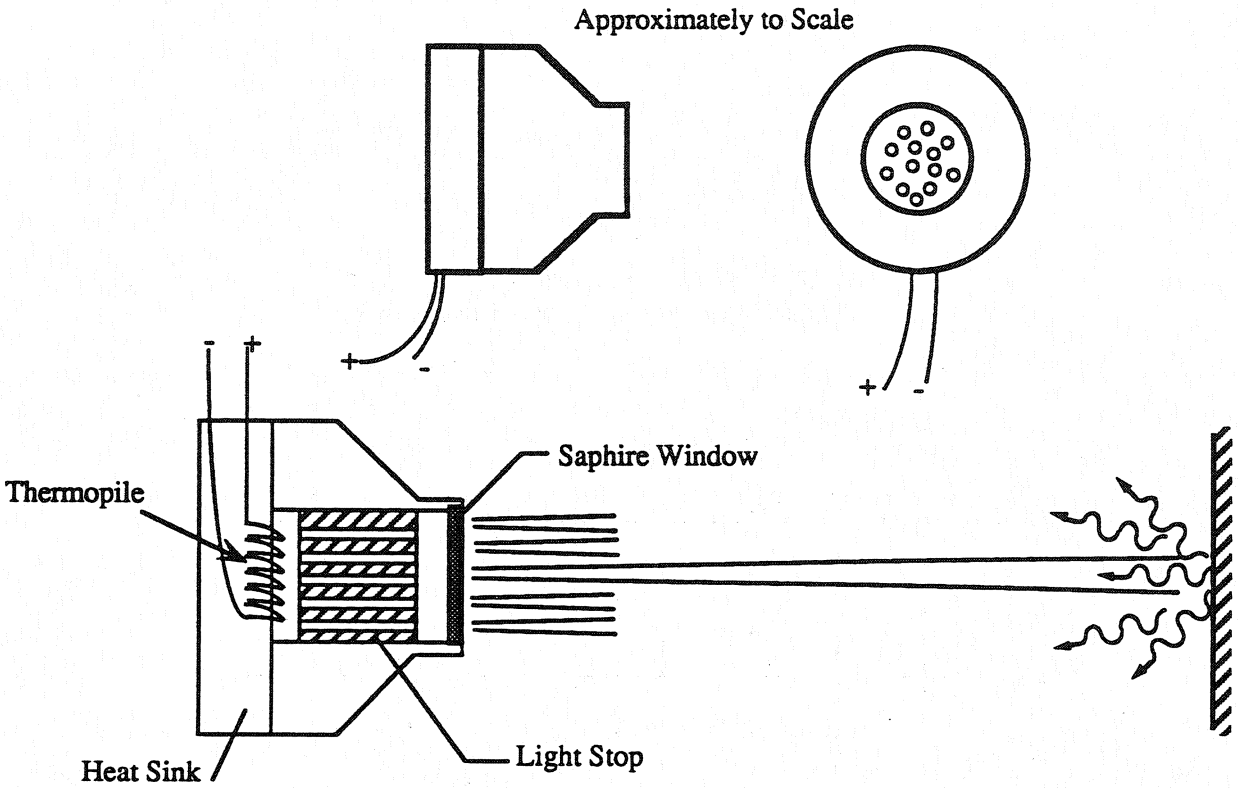

Figure 19a. Approximate internal constructions of total radiometer.

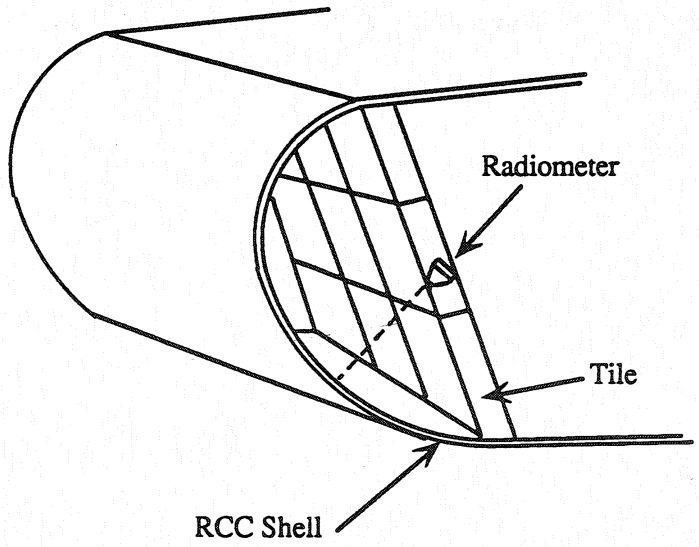

Figure 19b. Location of radiometer in wing leading edge.

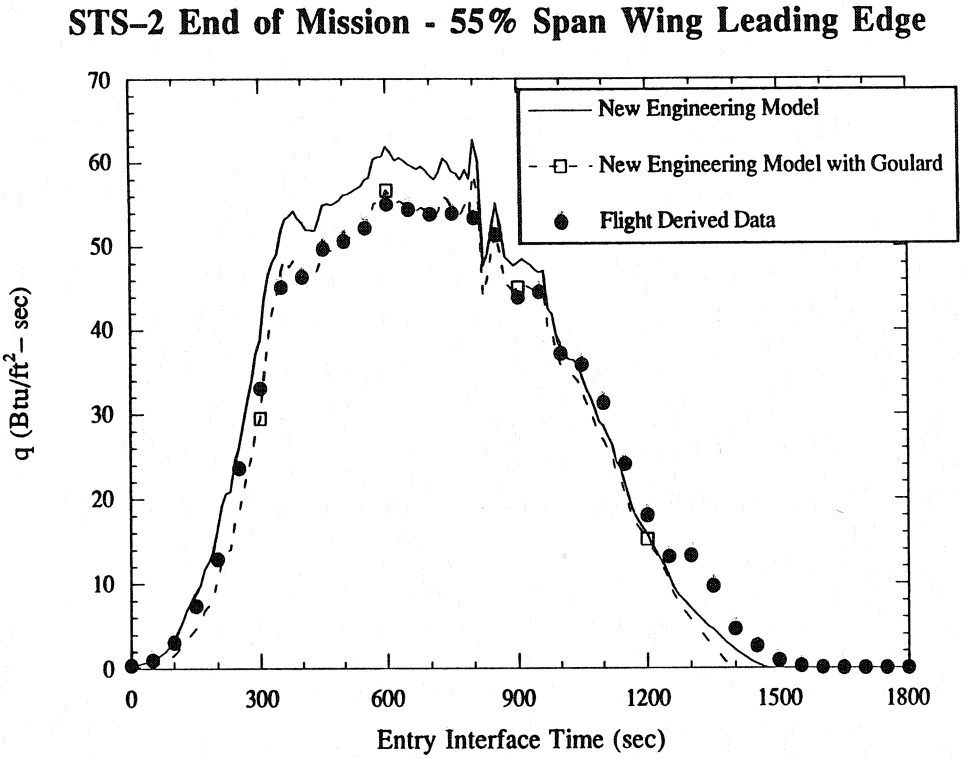

Figure 20. New Lanmin model with and without Goulard model compared with flight data, STS-2.

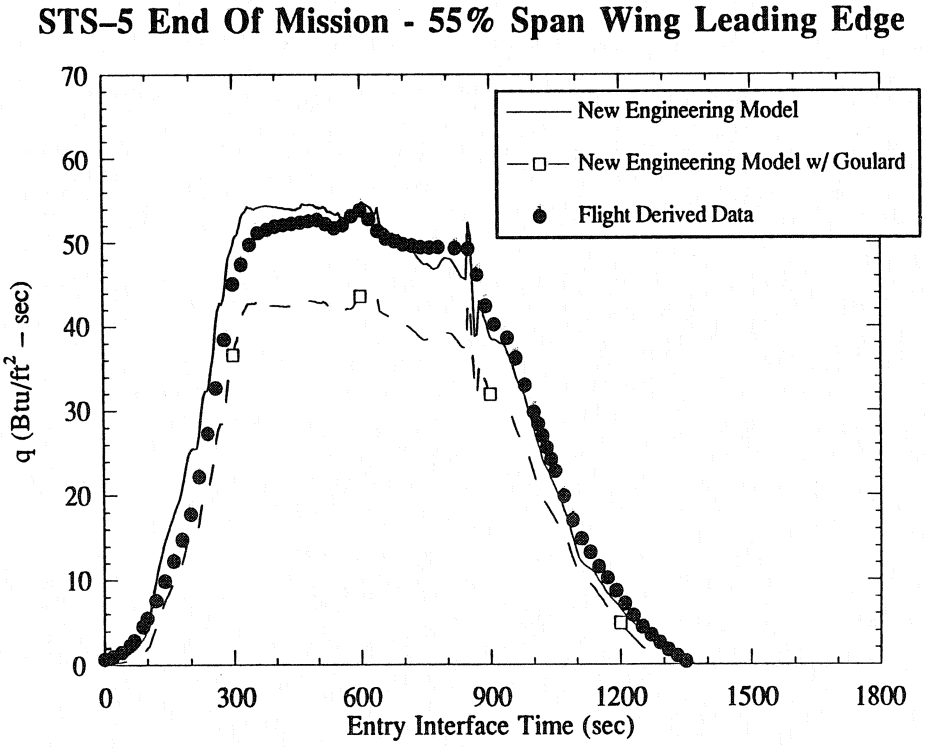

Figure 21. New Lanmin model with and without Goulard model compared with flight data, STS-5.

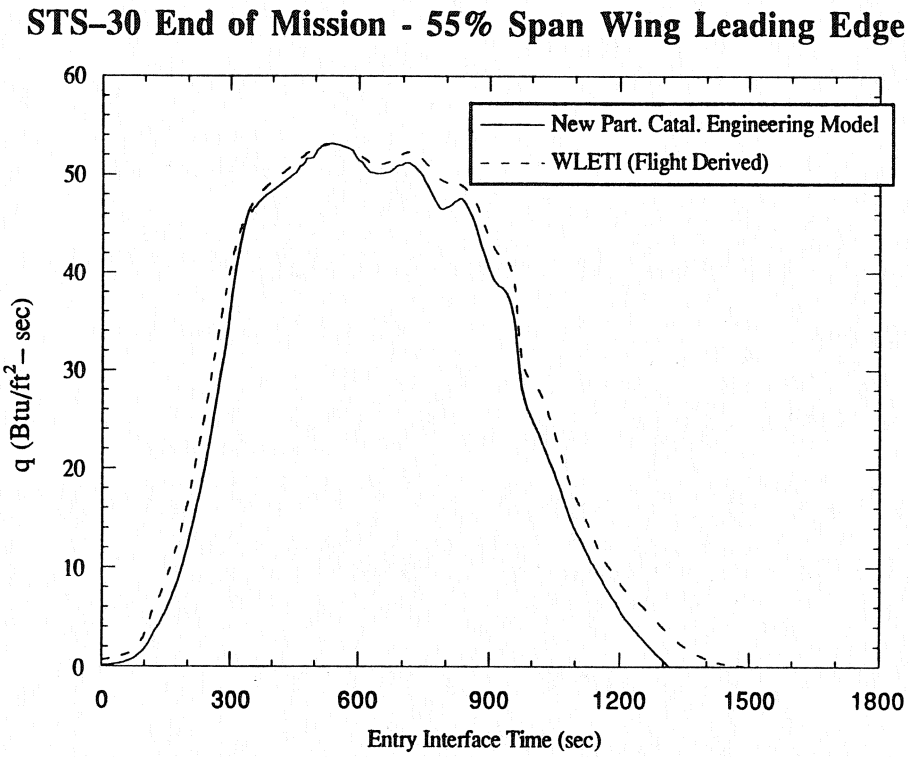

Figure 22. New Lanmin model compared with current model, STS-30.

Appendix A

Table A.1 contains the 55% span wing leading edge radiometer data and corresponding Best Estimated Trajectory (BET) for all available flights. The BET data presented is entry interface elapsed time, altitude (h), Orbiter freestream velocity, Orbiter angle of attack (α), freestream density and freestream temperature (T_∞). The inner mold line (IML) temperature data is taken from the radiometer located in the panel 9 of the wing leading edge structure and has the measurement ID number of v09T9926a. The first three flights listed: STS-2,3 and 5, are of OV-102 (Columbia) and use the instrument calibration specific to that vehicle. The OV-102 calibration is given as IML temp $= (\text{counts} \times 3.372 * 10^{11})^{0.25} - 460$. The calibration used for the OV-103 flights is a combination from two sources. The high temperature portion of the calibration is from work recently completed at NASA/JSC (ref. 48). The raw count radiometer data is first corrected for the contamination found on the radiometer's sapphire window. A correction factor of 1.077 is applied to the uncalibrated data and then the data is calibrated with the suggested formula IML temp $= (-5.90037 * 10^{-8}) * \text{cnts}^4 + (1.2084 * 10^{-4}) * \text{cnts}^3 - 0.05958 * \text{cnts}^2 + 15.3771 * \text{cnts} + 1201.65$. This calibration for OV-103 was formulated for temperatures above 1800 °F and so the more appropriate previous calibration of IML temp $= (\text{counts} \times 5.615329 * 10^{11}) - 460$ was used for the lower temperature portion of entry. Electronic copies of this data are available from the author through electronic mail. Send requests to `devenzia@euler.jsc.nasa.gov`.

Table A.1 Wing Leading Edge Data

STS-2 BET and Radiometer Data

time (sec)	$h*10^{-3}$ (ft)	vel. (ft/sec)	α (°)	density ($slug/ft^3$)	T_∞ (°F)	IML temp (°F)
0	399.65	24523	41.05	3.906e-11	737	-460
5	397.16	24530	40.95	4.262e-11	717	-460
10	394.68	24537	40.89	4.647e-11	698	-460
15	392.20	24543	40.88	5.088e-11	679	-460
20	389.73	24548	40.92	5.578e-11	660	-460
25	387.25	24554	41.00	6.124e-11	642	-460
30	384.78	24561	41.13	6.743e-11	624	-460
35	382.31	24567	41.33	7.425e-11	607	-460
40	379.84	24571	41.29	8.234e-11	590	-460
45	377.37	24576	41.29	9.140e-11	574	-460
50	374.91	24585	41.32	1.019e-10	559	-460
55	372.45	24599	41.33	1.144e-10	545	-460
60	369.99	24613	41.30	1.283e-10	531	-460
65	367.53	24621	41.08	1.437e-10	517	-460
70	365.08	24629	40.90	1.610e-10	503	-460
75	362.63	24634	40.74	1.813e-10	490	-460
80	360.18	24639	40.66	2.049e-10	479	-460
85	357.74	24643	40.60	2.317e-10	468	-460
90	355.30	24649	40.57	2.634e-10	458	-460
95	352.86	24654	40.58	2.994e-10	448	-460
100	350.42	24656	40.67	3.403e-10	438	-460
105	347.99	24657	40.78	3.868e-10	428	-460
110	345.57	24656	40.90	4.402e-10	419	-460
115	343.14	24644	41.07	5.032e-10	413	-460
120	340.72	24632	41.33	5.750e-10	406	-460
125	338.31	24621	41.36	6.580e-10	400	-460
130	335.90	24611	41.23	7.531e-10	395	-460
135	333.50	24602	41.15	8.615e-10	389	-460
140	331.10	24596	41.09	9.845e-10	384	-460
145	328.70	24592	40.47	1.125e-09	378	-460
150	326.32	24574	41.79	1.283e-09	375	-187
155	323.94	24552	43.09	1.464e-09	372	302
160	321.56	24533	41.20	1.668e-09	369	302
165	319.20	24523	39.86	1.897e-09	366	446
170	316.84	24513	39.86	2.156e-09	364	446
175	314.49	24503	40.41	2.451e-09	361	543
180	312.16	24493	41.30	2.784e-09	359	570
185	309.83	24484	41.74	3.161e-09	356	640
190	307.52	24489	41.65	3.620e-09	351	733
195	305.21	24494	41.23	4.142e-09	346	795
200	302.93	24501	40.38	4.737e-09	341	872
205	300.66	24507	39.22	5.327e-09	342	958
210	298.41	24512	38.84	5.890e-09	348	1023
215	296.17	24517	38.87	6.492e-09	354	1095
220	293.96	24518	39.58	7.193e-09	358	1178
225	291.77	24516	41.02	7.980e-09	360	1250
230	289.60	24514	41.83	8.759e-09	361	1329
235	287.46	24515	41.20	9.652e-09	362	1398
240	285.34	24519	39.70	1.067e-08	362	1449
245	283.26	24523	38.71	1.182e-08	363	1517
250	281.20	24525	41.03	1.305e-08	365	1570
255	279.18	24525	41.31	1.434e-08	369	1628
260	277.20	24523	40.27	1.573e-08	373	1681
265	275.25	24517	39.48	1.714e-08	377	1723
270	273.35	24500	40.23	1.866e-08	379	1770
275	271.50	24482	41.01	2.028e-08	381	1814
280	269.70	24464	39.88	2.199e-08	383	1849
285	267.95	24448	39.27	2.392e-08	383	1896
290	266.27	24434	40.07	2.602e-08	382	1940
295	264.64	24418	41.14	2.822e-08	381	1981
300	263.09	24401	40.88	3.051e-08	379	2015
305	261.61	24388	40.30	3.300e-08	377	2045
310	260.21	24376	39.33	3.566e-08	374	2074
315	258.89	24365	38.53	3.837e-08	370	2105
320	257.66	24351	39.75	4.108e-08	368	2139
325	256.51	24334	40.31	4.377e-08	365	2164
330	255.47	24318	40.18	4.638e-08	363	2186
335	254.52	24302	40.65	4.884e-08	362	2207
340	253.67	24282	40.91	5.115e-08	361	2216
345	252.93	24261	40.45	5.327e-08	360	2222
350	252.28	24239	40.10	5.517e-08	359	2235
355	251.70	24215	40.14	5.689e-08	358	2252
360	251.18	24191	39.85	5.849e-08	358	2273
365	250.69	24165	39.80	6.002e-08	358	2289
370	250.25	24139	39.67	6.144e-08	357	2309
375	249.85	24112	40.31	6.274e-08	357	2321
380	249.50	24084	40.15	6.390e-08	357	2331
385	249.20	24054	40.70	6.489e-08	357	2335
390	248.95	24022	40.84	6.570e-08	357	2339
395	248.74	23991	41.14	6.639e-08	357	2339
400	248.56	23958	41.14	6.699e-08	357	2339
405	248.40	23927	41.43	6.754e-08	357	2343
410	248.24	23895	41.62	6.806e-08	357	2346
415	248.07	23863	41.49	6.863e-08	358	2343
420	247.88	23830	41.64	6.927e-08	358	2344
425	247.68	23797	41.68	6.997e-08	358	2346
430	247.47	23764	41.70	7.073e-08	358	2350
435	247.24	23731	41.67	7.154e-08	358	2354
440	246.99	23699	40.70	7.241e-08	358	2354
445	246.73	23668	39.95	7.336e-08	358	2358
450	246.45	23637	40.16	7.439e-08	358	2363
455	246.16	23605	40.37	7.548e-08	358	2370
460	245.87	23574	39.96	7.659e-08	358	2380
465	245.58	23543	40.05	7.771e-08	359	2380
470	245.28	23511	40.26	7.888e-08	359	2384
475	244.97	23479	40.27	8.012e-08	359	2387
480	244.64	23447	40.25	8.143e-08	359	2392
485	244.30	23414	40.26	8.282e-08	359	2398
490	243.95	23381	40.27	8.428e-08	359	2402
495	243.60	23348	40.25	8.579e-08	359	2403
500	243.24	23315	40.14	8.734e-08	359	2406
505	242.88	23281	40.21	8.894e-08	359	2407
510	242.51	23245	40.28	9.051e-08	360	2409
515	242.15	23209	40.29	9.209e-08	360	2409
520	241.78	23173	40.30	9.371e-08	360	2413
525	241.42	23136	40.31	9.535e-08	361	2418
530	241.06	23097	40.24	9.701e-08	361	2423

STS-2 BET and Radiometer Data (continued)

time (sec)	h*10^{-3} (ft)	vel. (ft/sec)	α (°)	density (slug/ft^3)	T_∞ (°F)	IML temp (°F)
535	240.70	23059	40.14	9.868e-08	361	2427
540	240.35	23020	40.34	1.004e-07	362	2430
545	239.99	22980	40.40	1.021e-07	362	2434
550	239.61	22941	40.14	1.040e-07	362	2434
555	239.22	22901	40.33	1.058e-07	363	2437
560	238.83	22860	40.34	1.076e-07	364	2441
565	238.44	22818	39.76	1.094e-07	365	2444
570	238.07	22777	39.44	1.111e-07	366	2448
575	237.72	22736	39.33	1.128e-07	367	2451
580	237.38	22695	39.42	1.144e-07	368	2454
585	237.06	22653	39.48	1.160e-07	369	2458
590	236.75	22611	39.40	1.175e-07	370	2458
595	236.44	22567	39.04	1.190e-07	371	2461
600	236.16	22524	38.65	1.204e-07	372	2461
605	235.89	22481	38.76	1.219e-07	372	2468
610	235.62	22437	39.03	1.234e-07	372	2468
615	235.37	22393	39.57	1.248e-07	373	2468
620	235.12	22345	39.32	1.263e-07	373	2465
625	234.87	22300	39.09	1.278e-07	373	2465
630	234.62	22254	39.23	1.293e-07	373	2465
635	234.36	22208	39.28	1.309e-07	374	2465
640	234.09	22161	39.33	1.325e-07	374	2465
645	233.81	22115	39.39	1.342e-07	374	2465
650	233.52	22067	39.56	1.360e-07	374	2465
655	233.23	22018	39.61	1.379e-07	374	2465
660	232.93	21970	39.67	1.399e-07	375	2465
665	232.62	21920	39.74	1.418e-07	375	2465
670	232.32	21868	39.73	1.437e-07	376	2463
675	232.01	21818	39.32	1.457e-07	376	2460
680	231.69	21767	39.66	1.477e-07	377	2458
685	231.37	21716	39.64	1.499e-07	377	2454
690	231.02	21663	39.72	1.521e-07	378	2454
695	230.67	21609	39.81	1.545e-07	378	2454
700	230.32	21555	40.05	1.570e-07	379	2451
705	229.95	21498	40.20	1.595e-07	380	2451
710	229.59	21438	40.16	1.620e-07	380	2448
715	229.24	21377	40.31	1.644e-07	381	2448
720	228.90	21315	39.12	1.668e-07	382	2448
725	228.56	21256	38.42	1.692e-07	382	2448
730	228.22	21197	38.37	1.716e-07	383	2448
735	227.86	21138	38.46	1.743e-07	384	2451
740	227.46	21078	38.36	1.771e-07	385	2448
745	227.03	21017	38.54	1.802e-07	386	2449
750	226.59	20955	39.22	1.835e-07	387	2454
755	226.15	20887	39.62	1.867e-07	388	2451
760	225.71	20821	38.38	1.898e-07	389	2446
765	225.26	20759	37.90	1.929e-07	391	2444
770	224.80	20694	38.85	1.963e-07	392	2441
775	224.32	20628	38.16	1.998e-07	394	2437
780	223.83	20563	38.03	2.034e-07	395	2437
785	223.33	20494	39.40	2.072e-07	397	2436
790	222.83	20427	38.67	2.110e-07	399	2433
795	222.34	20359	38.94	2.146e-07	401	2429
800	221.84	20297	35.73	2.184e-07	403	2427
805	221.31	20239	34.95	2.224e-07	405	2427
810	220.76	20179	37.54	2.267e-07	407	2423
815	220.19	20103	41.08	2.312e-07	409	2420
820	219.62	20012	43.92	2.360e-07	411	2416
825	219.07	19913	45.80	2.411e-07	412	2408
830	218.54	19815	41.65	2.460e-07	413	2390
835	218.02	19728	41.38	2.509e-07	414	2375
840	217.57	19643	39.69	2.552e-07	415	2370
845	217.24	19563	38.38	2.584e-07	416	2374
850	217.06	19487	37.76	2.601e-07	416	2380
855	216.95	19413	37.96	2.610e-07	416	2385
860	216.81	19338	38.72	2.623e-07	417	2387
865	216.58	19258	40.18	2.644e-07	417	2382
870	216.26	19175	40.37	2.676e-07	418	2375
875	215.84	19091	40.72	2.720e-07	418	2364
880	215.33	19006	40.76	2.776e-07	419	2356
885	214.72	18918	41.35	2.845e-07	420	2350
890	214.03	18829	41.28	2.925e-07	420	2345
895	213.26	18737	41.22	3.016e-07	421	2335
900	212.44	18644	41.14	3.114e-07	422	2327
905	211.59	18549	41.05	3.220e-07	424	2322
910	210.72	18452	41.04	3.332e-07	425	2315
915	209.84	18354	41.00	3.448e-07	426	2311
920	208.97	18250	41.00	3.560e-07	429	2311
925	208.08	18144	40.90	3.676e-07	431	2311
930	207.19	18036	40.75	3.796e-07	433	2310
935	206.29	17926	40.61	3.924e-07	435	2308
940	205.40	17812	40.62	4.062e-07	436	2308
945	204.52	17695	40.47	4.204e-07	437	2308
950	203.68	17578	40.16	4.343e-07	438	2308
955	202.91	17463	40.04	4.468e-07	439	2311
960	202.20	17352	39.55	4.575e-07	441	2315
965	201.56	17236	40.42	4.674e-07	444	2319
970	201.00	17114	41.39	4.762e-07	445	2319
975	200.52	16990	40.83	4.838e-07	447	2318
980	200.12	16869	40.70	4.904e-07	448	2311
985	199.73	16748	41.05	4.971e-07	449	2308
990	199.28	16625	41.40	5.053e-07	450	2304
995	198.70	16499	41.74	5.159e-07	450	2298
1000	197.97	16371	42.01	5.298e-07	452	2290
1005	197.07	16240	42.10	5.475e-07	453	2279
1010	196.03	16105	42.09	5.675e-07	456	2270
1015	194.91	15969	42.01	5.894e-07	459	2259
1020	193.74	15830	41.93	6.132e-07	462	2250
1025	192.55	15686	41.70	6.413e-07	463	2242
1030	191.40	15538	41.19	6.714e-07	463	2233
1035	190.32	15391	40.77	7.009e-07	462	2224
1040	189.31	15240	40.64	7.287e-07	463	2220
1045	188.34	15088	40.56	7.560e-07	463	2216
1050	187.37	14934	40.57	7.844e-07	464	2211
1055	186.37	14777	40.50	8.144e-07	465	2205
1060	185.34	14620	40.44	8.460e-07	465	2196
1065	184.32	14460	40.16	8.791e-07	466	2189
1070	183.30	14300	40.07	9.105e-07	469	2180
1075	182.31	14144	39.85	9.360e-07	474	2173
1080	181.33	13987	39.83	9.680e-07	475	2164
1085	180.35	13828	39.93	1.005e-06	475	2155
1090	179.35	13667	39.79	1.044e-06	475	2145

STS-2 BET and Radiometer Data (continued)

time (sec)	h*10^{-3} (ft)	vel. (ft/sec)	α (°)	density (slug/ft^3)	T_∞ (°F)	IML temp (°F)
1095	178.34	13509	38.63	1.086e-06	475	2136
1100	177.30	13352	38.96	1.130e-06	475	2126
1105	176.26	13192	38.84	1.176e-06	475	2118
1110	175.22	13031	38.77	1.224e-06	475	2108
1115	174.21	12869	38.44	1.273e-06	475	2101
1120	173.26	12709	38.20	1.320e-06	475	2091
1125	172.41	12551	37.93	1.361e-06	476	2081
1130	171.68	12387	39.52	1.398e-06	477	2067
1135	171.08	12214	38.86	1.429e-06	477	2060
1140	170.59	12052	37.50	1.454e-06	478	2044
1145	170.17	11898	37.57	1.477e-06	477	2028
1150	169.78	11742	37.85	1.501e-06	477	2017
1155	169.32	11586	38.06	1.529e-06	476	2002
1160	168.73	11430	38.30	1.567e-06	476	1989
1165	167.97	11275	38.37	1.616e-06	475	1971
1170	167.04	11119	38.39	1.680e-06	474	1953
1175	165.95	10962	38.19	1.756e-06	472	1938
1180	164.77	10805	37.84	1.843e-06	471	1923
1185	163.54	10649	37.52	1.937e-06	470	1904
1190	162.29	10494	37.34	2.034e-06	470	1887
1195	161.01	10338	36.89	2.138e-06	470	1874
1200	159.72	10180	36.54	2.234e-06	473	1860
1205	158.45	10023	36.05	2.326e-06	477	1847
1210	157.27	9868	35.61	2.415e-06	481	1833
1215	156.19	9712	34.72	2.522e-06	480	1819
1220	155.19	9561	34.37	2.627e-06	479	1809
1225	154.22	9413	33.72	2.732e-06	478	1797
1230	153.23	9269	33.24	2.845e-06	476	1790
1235	152.21	9129	33.21	2.966e-06	475	1780
1240	151.33	8985	33.02	3.075e-06	474	1767
1245	150.72	8843	32.86	3.152e-06	474	1757
1250	150.35	8701	33.31	3.197e-06	474	1744
1255	150.02	8560	33.12	3.238e-06	474	1733
1260	149.50	8423	33.46	3.302e-06	474	1720
1265	148.74	8288	33.17	3.402e-06	474	1709
1270	147.74	8155	32.83	3.535e-06	474	1712
1275	146.60	8027	32.30	3.730e-06	470	1728
1280	145.39	7903	31.69	3.960e-06	464	1739
1285	144.16	7781	31.22	4.209e-06	458	1747
1290	142.86	7654	30.50	4.436e-06	458	1755
1295	141.44	7529	30.08	4.696e-06	458	1760
1300	139.95	7402	29.58	5.004e-06	456	1760
1305	138.49	7271	29.09	5.336e-06	454	1760
1310	137.10	7147	28.46	5.672e-06	452	1760
1315	135.78	7031	27.96	6.006e-06	450	1757
1320	134.52	6916	27.58	6.343e-06	449	1752
1325	133.28	6802	27.13	6.703e-06	447	1749
1330	132.07	6688	26.62	7.078e-06	445	1744
1335	130.88	6574	26.08	7.477e-06	443	1736
1340	129.70	6456	25.53	7.952e-06	437	1728
1345	128.54	6340	25.02	8.448e-06	433	1720
1350	127.41	6225	24.63	8.945e-06	429	1712
1355	126.31	6112	24.27	9.423e-06	427	1695
1360	125.22	6001	23.96	9.921e-06	425	1687
1365	124.15	5890	23.59	1.044e-05	423	1678
1370	123.08	5781	23.46	1.098e-05	421	1661
1375	122.01	5673	23.00	1.156e-05	420	1643
1380	120.90	5569	22.52	1.219e-05	418	1630
1385	119.73	5464	22.40	1.290e-05	416	1612
1390	118.51	5359	22.24	1.369e-05	414	1592
1395	117.27	5255	21.92	1.449e-05	413	1566
1400	116.05	5153	21.64	1.528e-05	414	1546
1405	114.86	5050	21.31	1.609e-05	414	1526
1410	113.71	4949	20.92	1.700e-05	413	1506
1415	112.60	4849	20.52	1.795e-05	411	1487
1420	111.52	4750	20.22	1.892e-05	409	1464
1425	110.53	4649	20.05	1.980e-05	409	1444
1430	109.74	4548	19.74	2.052e-05	409	1419
1435	109.14	4448	19.44	2.108e-05	409	1393
1440	108.58	4351	19.16	2.163e-05	409	1366
1445	107.94	4256	19.25	2.226e-05	409	1338
1450	107.22	4161	19.40	2.300e-05	409	1323
1455	106.47	4065	19.48	2.379e-05	409	1293
1460	105.74	3970	19.38	2.459e-05	409	1271
1465	105.01	3875	19.26	2.541e-05	409	1244
1470	104.21	3783	19.30	2.639e-05	408	1227
1475	103.29	3693	19.22	2.758e-05	408	1190
1480	102.24	3605	19.14	2.899e-05	407	1164
1485	101.06	3518	19.16	3.068e-05	405	1131
1490	99.79	3433	18.77	3.266e-05	404	1110
1495	98.44	3350	18.30	3.489e-05	402	1087
1500	97.06	3262	17.95	3.737e-05	400	1064
1505	95.66	3174	17.60	4.006e-05	398	1040
1510	94.27	3086	17.38	4.296e-05	396	1014
1515	92.90	2995	16.99	4.604e-05	394	987
1520	91.56	2906	16.52	4.925e-05	393	958
1525	90.22	2821	16.11	5.230e-05	394	928
1530	88.88	2738	15.78	5.557e-05	395	895
1535	87.51	2656	15.14	5.931e-05	395	895
1540	86.10	2574	15.53	6.356e-05	393	860
1545	84.67	2492	15.66	6.820e-05	392	822
1550	83.30	2407	15.18	7.297e-05	391	822
1555	82.10	2324	14.29	7.744e-05	390	779
1560	81.00	2249	13.16	8.181e-05	389	762
1565	79.90	2177	12.57	8.644e-05	389	733
1570	78.76	2107	13.06	9.151e-05	387	733
1575	77.61	2034	13.37	9.670e-05	387	679
1580	76.47	1959	13.57	1.021e-04	387	679
1585	75.36	1883	13.40	1.077e-04	388	618
1590	74.26	1811	12.77	1.140e-04	386	618
1595	73.19	1743	11.19	1.206e-04	384	618
1600	72.09	1680	11.38	1.277e-04	383	543
1605	70.99	1615	10.64	1.348e-04	382	543
1610	69.87	1554	10.16	1.424e-04	382	543
1615	68.69	1501	9.80	1.510e-04	382	543
1620	67.45	1451	9.00	1.610e-04	380	446
1625	66.13	1399	7.90	1.726e-04	379	446
1630	64.70	1349	7.92	1.861e-04	377	446
1635	63.16	1301	8.25	2.018e-04	376	446
1640	61.57	1256	8.06	2.195e-04	374	446
1645	59.95	1205	8.03	2.389e-04	372	356
1650	58.32	1143	8.34	2.597e-04	370	392

STS-2 BET and Radiometer Data (concluded)

time (sec)	$h*10^{-3}$ (ft)	vel. (ft/sec)	α (°)	density ($slug/ft^3$)	T_∞ (°F)	IML temp (°F)
1655	56.73	1104	8.05	2.829e-04	368	302
1660	55.19	1056	7.65	3.064e-04	367	302
1665	53.68	1028	7.45	3.291e-04	369	302
1670	52.21	985	7.07	3.538e-04	369	302
1675	50.75	952	5.78	3.800e-04	369	302
1680	49.21	927	6.30	4.098e-04	369	302
1685	47.66	910	7.23	4.439e-04	369	302
1690	46.19	886	8.12	4.750e-04	371	302
1695	44.85	858	7.09	5.046e-04	374	302
1700	43.52	840	6.49	5.363e-04	375	302
1705	42.13	834	6.18	5.712e-04	377	302
1710	40.65	842	5.01	6.087e-04	381	302
1715	39.08	857	3.52	6.467e-04	387	302
1720	37.39	834	6.18	6.898e-04	393	302
1725	35.62	818	7.44	7.373e-04	400	302
1730	33.78	801	7.93	7.903e-04	406	302
1735	31.94	783	8.08	8.465e-04	413	302
1740	30.16	764	7.32	9.024e-04	419	-174
1745	28.39	753	7.28	9.564e-04	428	-174
1750	26.72	731	6.53	1.009e-03	436	302

STS-3 BET and Radiometer Data

time (sec)	$h*10^{-3}$ (ft)	vel. (ft/sec)	α (°)	density ($slug/ft^3$)	T_∞ (°F)	IML temp (°F)
0	399.60	24457	40.96	3.805e-11	717	-460
5	397.11	24460	40.91	4.158e-11	698	-460
10	394.61	24463	40.77	4.543e-11	680	-460
15	392.12	24465	40.68	4.976e-11	662	-460
20	389.62	24468	40.68	5.456e-11	644	-460
25	387.13	24470	40.78	5.996e-11	626	-460
30	384.63	24473	40.93	6.618e-11	609	-460
35	382.14	24477	41.06	7.305e-11	591	-460
40	379.65	24477	40.90	8.118e-11	576	-460
45	377.15	24477	40.78	9.025e-11	560	-460
50	374.65	24475	40.69	1.009e-10	546	-460
55	372.16	24471	40.65	1.135e-10	533	-460
60	369.66	24467	40.67	1.275e-10	520	-460
65	367.16	24467	40.72	1.434e-10	506	-460
70	364.66	24466	40.80	1.612e-10	493	-460
75	362.16	24465	40.90	1.820e-10	481	-460
80	359.66	24464	41.04	2.056e-10	470	-460
85	357.16	24464	41.09	2.330e-10	459	-460
90	354.66	24465	41.04	2.658e-10	450	-460
95	352.17	24466	41.00	3.031e-10	441	-460
100	349.67	24468	40.94	3.459e-10	433	-460
105	347.17	24471	40.86	3.946e-10	423	-460
110	344.67	24473	40.77	4.514e-10	416	-460
115	342.18	24474	40.69	5.173e-10	409	-460
120	339.68	24475	40.66	5.931e-10	402	-460
125	337.19	24478	40.57	6.813e-10	396	-460
130	334.70	24481	40.43	7.825e-10	391	-460
135	332.21	24484	40.28	8.985e-10	385	-460
140	329.73	24488	40.08	1.031e-09	379	-315
145	327.25	24494	39.81	1.182e-09	375	302
150	324.77	24505	39.50	1.350e-09	371	302
155	322.30	24516	39.34	1.542e-09	368	446
160	319.83	24536	39.35	1.787e-09	361	465
165	317.37	24557	39.49	2.075e-09	354	543
170	314.91	24578	39.79	2.408e-09	346	618
175	312.46	24599	40.22	2.794e-09	339	690
180	310.02	24597	40.87	3.185e-09	338	742
185	307.59	24584	41.48	3.600e-09	341	822
190	305.16	24571	41.32	4.068e-09	343	895
195	302.75	24558	40.85	4.595e-09	345	958
200	300.34	24534	40.11	5.225e-09	345	1014
205	297.95	24503	39.26	5.963e-09	343	1069
210	295.57	24473	39.11	6.801e-09	341	1135
215	293.20	24467	39.27	7.704e-09	341	1194
220	290.85	24463	39.92	8.712e-09	342	1261
225	288.53	24461	41.14	9.826e-09	343	1323
230	286.23	24478	41.49	1.091e-08	348	1383
235	283.96	24495	40.15	1.211e-08	353	1447
240	281.72	24513	39.37	1.344e-08	357	1507
245	279.51	24540	39.83	1.504e-08	357	1570
250	277.35	24564	40.97	1.679e-08	357	1636
255	275.22	24587	40.99	1.875e-08	356	1689
260	273.15	24608	39.82	2.108e-08	353	1746
265	271.13	24627	39.38	2.362e-08	349	1800
270	269.16	24644	40.22	2.639e-08	346	1857

STS-3 BET and Radiometer Data (continued)

time (sec)	$h*10^{-3}$ (ft)	vel. (ft/sec)	α (°)	density ($slug/ft^3$)	T_∞ (°F)	IML temp (°F)
275	267.27	24646	41.21	2.917e-08	346	1903
280	265.44	24645	40.64	3.211e-08	346	1945
285	263.70	24643	39.43	3.519e-08	346	1987
290	262.04	24637	39.43	3.831e-08	347	2036
295	260.47	24620	40.80	4.124e-08	349	2079
300	259.00	24601	41.04	4.420e-08	352	2104
305	257.63	24580	40.24	4.714e-08	354	2118
310	256.37	24558	39.96	5.002e-08	356	2118
315	255.23	24530	40.23	5.255e-08	359	2107
320	254.20	24497	40.35	5.477e-08	362	2081
325	253.29	24464	40.40	5.680e-08	366	2044
330	252.51	24428	40.85	5.862e-08	368	2012
335	251.84	24393	40.11	6.023e-08	370	2008
340	251.25	24359	39.53	6.167e-08	372	2015
345	250.72	24325	39.60	6.301e-08	374	2024
350	250.22	24291	39.81	6.430e-08	376	2042
355	249.75	24256	40.07	6.557e-08	377	2062
360	249.30	24220	40.18	6.680e-08	378	2083
365	248.87	24183	40.16	6.810e-08	379	2110
370	248.46	24145	40.14	6.937e-08	379	2155
375	248.07	24106	40.13	7.061e-08	380	2209
380	247.70	24067	40.12	7.182e-08	380	2256
385	247.34	24028	40.11	7.302e-08	380	2288
390	246.99	23988	40.07	7.421e-08	380	2308
395	246.64	23947	40.04	7.541e-08	380	2324
400	246.29	23906	40.04	7.663e-08	381	2339
405	245.94	23864	40.06	7.787e-08	381	2351
410	245.60	23823	40.08	7.911e-08	381	2362
415	245.27	23780	40.09	8.036e-08	381	2373
420	244.94	23737	40.09	8.161e-08	381	2377
425	244.61	23694	40.09	8.287e-08	381	2384
430	244.28	23650	40.08	8.416e-08	381	2395
435	243.95	23605	40.21	8.547e-08	382	2402
440	243.61	23560	40.20	8.685e-08	382	2403
445	243.26	23514	40.28	8.831e-08	382	2413
450	242.91	23468	40.20	8.982e-08	382	2420
455	242.55	23423	40.28	9.146e-08	381	2427
460	242.19	23377	40.31	9.316e-08	381	2428
465	241.84	23331	40.32	9.488e-08	380	2430
470	241.49	23283	40.20	9.661e-08	380	2434
475	241.14	23237	40.01	9.836e-08	380	2437
480	240.79	23189	40.09	1.001e-07	379	2441
485	240.44	23142	39.92	1.020e-07	379	2444
490	240.09	23093	39.74	1.038e-07	378	2448
495	239.75	23044	39.56	1.057e-07	378	2455
500	239.42	22996	39.58	1.075e-07	377	2455
505	239.11	22946	39.57	1.093e-07	377	2458
510	238.80	22896	39.52	1.110e-07	376	2461
515	238.50	22846	39.30	1.127e-07	376	2461
520	238.21	22797	39.22	1.145e-07	376	2461
525	237.93	22746	39.27	1.162e-07	375	2465
530	237.64	22696	39.32	1.179e-07	375	2465
535	237.35	22645	39.38	1.197e-07	375	2465
540	237.06	22593	39.43	1.215e-07	374	2461
545	236.77	22542	39.52	1.233e-07	374	2458
550	236.49	22489	39.67	1.252e-07	374	2454
555	236.21	22436	39.71	1.270e-07	373	2448
560	235.92	22383	39.77	1.288e-07	373	2444
565	235.61	22329	39.83	1.306e-07	374	2444
570	235.30	22276	39.88	1.326e-07	374	2448
575	234.98	22222	39.94	1.346e-07	374	2448
580	234.64	22167	39.99	1.366e-07	374	2451
585	234.30	22113	40.04	1.388e-07	375	2451
590	233.96	22058	40.10	1.410e-07	375	2455
595	233.60	22003	40.21	1.433e-07	375	2455
600	233.22	21946	40.41	1.458e-07	376	2455
605	232.82	21890	40.44	1.485e-07	376	2455
610	232.40	21832	40.49	1.514e-07	377	2455
615	231.95	21773	40.54	1.545e-07	377	2455
620	231.49	21713	40.42	1.577e-07	378	2458
625	231.02	21653	40.25	1.611e-07	379	2459
630	230.55	21592	40.28	1.646e-07	379	2461
635	230.07	21530	40.16	1.681e-07	380	2461
640	229.60	21468	39.89	1.718e-07	381	2461
645	229.13	21403	39.95	1.753e-07	382	2465
650	228.66	21337	39.99	1.788e-07	383	2465
655	228.19	21270	40.09	1.823e-07	384	2465
660	227.73	21202	39.72	1.858e-07	385	2461
665	227.25	21133	40.19	1.896e-07	386	2461
670	226.76	21063	39.60	1.934e-07	387	2461
675	226.25	20995	39.94	1.975e-07	388	2465
680	225.74	20925	40.07	2.017e-07	389	2461
685	225.22	20854	39.83	2.061e-07	391	2461
690	224.70	20783	39.94	2.105e-07	392	2461
695	224.19	20709	39.82	2.149e-07	393	2458
700	223.68	20636	39.57	2.193e-07	395	2455
705	223.19	20562	39.64	2.237e-07	396	2455
710	222.71	20488	39.58	2.275e-07	398	2455
715	222.23	20413	39.65	2.312e-07	400	2451
720	221.75	20335	39.74	2.349e-07	403	2450
725	221.26	20258	39.75	2.388e-07	405	2448
730	220.76	20180	39.78	2.428e-07	407	2448
735	220.26	20100	39.81	2.469e-07	409	2444
740	219.76	20021	39.88	2.511e-07	411	2441
745	219.24	19939	40.02	2.555e-07	414	2437
750	218.70	19857	40.04	2.602e-07	416	2433
755	218.14	19772	40.06	2.651e-07	419	2430
760	217.55	19688	40.11	2.705e-07	421	2427
765	216.94	19601	40.21	2.761e-07	424	2423
770	216.32	19513	40.00	2.819e-07	426	2420
775	215.69	19427	39.98	2.878e-07	429	2416
780	215.06	19340	39.77	2.938e-07	431	2413
785	214.43	19252	39.89	3.000e-07	433	2412
790	213.79	19161	39.98	3.064e-07	436	2406
795	213.14	19069	39.81	3.131e-07	438	2402
800	212.48	18976	40.02	3.200e-07	441	2401
805	211.83	18878	39.56	3.270e-07	443	2399
810	211.18	18781	39.42	3.341e-07	445	2395
815	210.55	18683	39.22	3.411e-07	448	2395
820	209.94	18583	39.29	3.481e-07	450	2391
825	209.32	18481	39.32	3.576e-07	449	2388
830	208.66	18379	39.29	3.688e-07	448	2383

STS-3 BET and Radiometer Data (continued)

time (sec)	$h*10^{-3}$ (ft)	vel. (ft/sec)	α (°)	density ($slug/ft^3$)	T_∞ (°F)	IML temp (°F)
835	207.96	18273	39.28	3.810e-07	446	2380
840	207.25	18167	39.31	3.941e-07	444	2376
845	206.52	18059	39.58	4.078e-07	442	2369
850	205.80	17947	39.49	4.221e-07	440	2362
855	205.07	17833	39.43	4.371e-07	438	2350
860	204.34	17719	39.43	4.526e-07	436	2347
865	203.63	17600	39.43	4.682e-07	434	2350
870	202.93	17479	39.47	4.832e-07	433	2347
875	202.37	17357	39.33	4.942e-07	433	2346
880	202.05	17236	39.47	5.006e-07	433	2339
885	201.99	17116	39.89	5.018e-07	433	2335
890	202.07	16995	40.35	5.002e-07	433	2327
895	202.11	16873	40.80	4.994e-07	433	2319
900	201.93	16747	41.41	5.032e-07	433	2307
905	201.45	16617	42.32	5.128e-07	433	2291
910	200.69	16481	42.82	5.287e-07	434	2274
915	199.65	16339	43.02	5.510e-07	435	2254
920	198.42	16191	43.26	5.789e-07	436	2242
925	197.08	16040	42.94	6.108e-07	437	2228
930	195.71	15895	42.69	6.410e-07	442	2215
935	194.37	15752	42.23	6.704e-07	447	2206
940	193.10	15606	41.86	7.000e-07	450	2198
945	191.91	15458	41.55	7.290e-07	453	2188
950	190.79	15306	41.15	7.572e-07	456	2180
955	189.70	15154	40.89	7.857e-07	460	2171
960	188.63	15000	40.68	8.144e-07	462	2184
965	187.60	14844	40.56	8.431e-07	465	2184
970	186.88	14686	40.51	8.637e-07	467	2180
975	185.58	14526	40.52	9.022e-07	471	2175
980	184.52	14362	40.27	9.363e-07	473	2175
985	183.58	14200	39.95	9.715e-07	473	2171
990	182.79	14040	39.59	1.004e-06	472	2170
995	182.13	13881	39.45	1.031e-06	472	2166
1000	181.55	13723	39.39	1.053e-06	472	2161
1005	180.99	13565	39.47	1.074e-06	473	2152
1010	180.42	13407	39.50	1.098e-06	473	2146
1015	179.80	13247	39.54	1.125e-06	473	2137
1020	179.17	13088	39.58	1.153e-06	473	2123
1025	178.50	12928	39.59	1.183e-06	472	2113
1030	177.78	12769	39.50	1.217e-06	472	2103
1035	177.03	12609	39.78	1.253e-06	472	2092
1040	176.26	12447	39.64	1.291e-06	472	2073
1045	175.45	12288	39.60	1.332e-06	472	2061
1050	174.64	12129	39.51	1.374e-06	472	2045
1055	173.80	11969	39.45	1.419e-06	472	2029
1060	172.92	11807	39.25	1.468e-06	472	2014
1065	171.99	11647	39.06	1.521e-06	472	2001
1070	171.01	11487	38.98	1.580e-06	473	1985
1075	169.99	11327	38.83	1.643e-06	473	1972
1080	168.92	11166	38.73	1.709e-06	474	1956
1085	167.78	11006	38.64	1.781e-06	475	1942
1090	166.60	10844	38.31	1.860e-06	476	1925
1095	165.37	10684	38.02	1.945e-06	477	1912
1100	164.12	10524	37.75	2.036e-06	478	1894
1105	162.86	10361	37.37	2.132e-06	479	1881
1110	161.59	10201	36.91	2.234e-06	481	1873
1115	160.33	10040	36.49	2.340e-06	482	1854
1120	159.15	9879	35.87	2.446e-06	482	1840
1125	158.12	9723	34.99	2.544e-06	482	1825
1130	157.19	9573	34.67	2.637e-06	482	1812
1135	156.27	9426	34.19	2.730e-06	482	1789
1140	155.32	9283	33.74	2.831e-06	482	1760
1145	154.29	9142	33.90	2.945e-06	482	1767
1150	153.30	8998	33.54	3.058e-06	482	1766
1155	152.56	8855	33.39	3.146e-06	482	1750
1160	152.09	8710	33.54	3.202e-06	482	1743
1165	151.76	8566	33.29	3.243e-06	482	1728
1170	151.31	8427	33.47	3.299e-06	482	1712
1175	150.62	8289	33.35	3.386e-06	482	1695
1180	149.69	8154	33.15	3.517e-06	481	1678
1185	148.48	8021	32.87	3.708e-06	478	1668
1190	147.04	7890	32.49	3.960e-06	474	1661
1195	145.57	7760	31.88	4.233e-06	470	1661
1200	144.24	7632	31.27	4.498e-06	466	1663
1205	143.00	7503	30.75	4.743e-06	464	1678
1210	141.80	7375	30.21	4.990e-06	463	1689
1215	140.59	7249	29.80	5.251e-06	461	1695
1220	139.37	7125	29.38	5.537e-06	459	1695
1225	138.10	7006	29.14	5.861e-06	456	1695
1230	136.80	6885	28.88	6.212e-06	453	1704
1235	135.49	6764	28.30	6.564e-06	452	1695
1240	134.17	6643	27.59	6.924e-06	452	1695
1245	132.87	6525	27.07	7.310e-06	452	1687
1250	131.61	6409	26.57	7.772e-06	448	1687
1255	130.38	6294	26.16	8.278e-06	442	1678
1260	129.15	6177	25.69	8.772e-06	439	1670
1265	127.91	6061	25.40	9.295e-06	437	1661
1270	126.65	5947	25.04	9.808e-06	437	1641
1275	125.38	5834	24.63	1.033e-05	437	1625
1280	124.08	5722	24.30	1.092e-05	437	1615
1285	122.76	5612	23.97	1.160e-05	435	1604
1290	121.46	5502	23.53	1.232e-05	433	1586
1295	120.17	5393	22.95	1.307e-05	432	1566
1300	118.90	5289	22.52	1.384e-05	430	1546
1305	117.65	5187	22.28	1.459e-05	431	1533
1310	116.41	5085	21.93	1.538e-05	431	1511
1315	115.18	4986	21.62	1.623e-05	430	1489
1320	113.96	4888	21.51	1.715e-05	430	1466
1325	112.75	4790	21.24	1.811e-05	429	1442
1330	111.55	4693	21.02	1.915e-05	427	1417
1335	110.36	4595	20.72	2.024e-05	425	1391
1340	109.24	4496	20.42	2.132e-05	424	1366
1345	108.33	4397	19.96	2.224e-05	423	1338
1350	107.62	4298	19.79	2.297e-05	422	1323
1355	107.00	4200	19.51	2.364e-05	421	1308
1360	106.32	4105	19.49	2.436e-05	421	1290
1365	105.55	4011	19.55	2.515e-05	422	1261
1370	104.68	3919	19.41	2.606e-05	423	1227
1375	103.70	3827	19.35	2.737e-05	421	1209
1380	102.65	3736	19.12	2.891e-05	417	1187
1385	101.54	3646	18.69	3.061e-05	414	1151
1390	100.37	3560	18.44	3.231e-05	413	1127

STS-3 BET and Radiometer Data (concluded)

time (sec)	$h*10^{-3}$ (ft)	vel. (ft/sec)	α (°)	density ($slug/ft^3$)	T_∞ (°F)	IML temp (°F)
1395	99.18	3474	18.16	3.415e-05	413	1087
1400	97.96	3390	18.09	3.620e-05	411	1064
1405	96.72	3309	17.71	3.860e-05	408	1040
1410	95.48	3228	17.54	4.119e-05	405	1014
1415	94.24	3147	17.00	4.384e-05	402	987
1420	92.98	3067	16.79	4.651e-05	402	958
1425	91.72	2985	16.43	4.934e-05	401	952
1430	90.46	2896	15.86	5.231e-05	401	921
1435	89.19	2809	15.72	5.549e-05	401	888
1440	87.90	2723	15.65	5.894e-05	401	860
1445	86.58	2638	15.09	6.268e-05	401	822
1450	85.21	2559	15.43	6.758e-05	397	813
1455	83.83	2479	15.37	7.308e-05	391	779
1460	82.60	2394	14.76	7.740e-05	391	770
1465	81.53	2310	14.34	8.136e-05	392	733
1470	80.51	2223	15.17	8.531e-05	392	722
1475	79.57	2135	14.86	8.918e-05	392	679
1480	78.69	2050	14.26	9.297e-05	392	667
1485	77.86	1975	13.13	9.674e-05	392	618
1490	77.01	1906	12.15	1.007e-04	392	618
1495	76.10	1843	11.64	1.052e-04	392	603
1500	75.10	1783	11.19	1.104e-04	392	543
1505	74.00	1728	10.75	1.164e-04	392	543
1510	72.80	1675	10.44	1.232e-04	392	543
1515	71.52	1622	10.58	1.312e-04	391	446
1520	70.17	1567	10.28	1.404e-04	390	446
1525	68.77	1514	10.15	1.506e-04	389	446
1530	67.33	1459	10.10	1.622e-04	387	446
1535	65.88	1404	9.56	1.751e-04	384	446
1540	64.41	1349	9.20	1.893e-04	382	446
1545	62.93	1296	9.05	2.047e-04	379	302
1550	61.44	1245	9.03	2.216e-04	376	302
1555	59.95	1193	8.94	2.369e-04	378	302
1560	58.47	1139	9.04	2.519e-04	382	302
1565	57.02	1084	9.02	2.675e-04	386	302
1570	55.60	1023	9.02	2.900e-04	382	302
1575	54.21	973	7.60	3.125e-04	379	302
1580	52.75	956	6.65	3.402e-04	375	302
1585	51.19	948	7.98	3.690e-04	373	302
1590	49.66	931	8.23	3.958e-04	375	302
1595	48.21	908	8.93	4.205e-04	379	302
1600	46.86	877	8.75	4.429e-04	385	302
1605	45.62	867	6.58	4.647e-04	389	302
1610	44.36	845	5.91	4.890e-04	393	302
1615	43.04	827	6.21	5.191e-04	394	302
1620	41.67	813	5.35	5.543e-04	394	302
1625	40.26	800	4.71	6.054e-04	386	302
1630	38.83	765	5.39	6.508e-04	384	302
1635	37.32	762	5.26	6.864e-04	392	-308
1640	35.81	760	4.83	7.243e-04	399	150
1645	34.27	758	4.56	7.655e-04	405	302
1650	32.67	762	4.76	8.100e-04	412	-460
1655	31.03	774	4.39	8.620e-04	417	-460
1660	29.39	767	4.39	9.209e-04	420	-460
1665	27.76	770	4.34	9.786e-04	425	-460
1670	26.21	763	4.92	1.029e-03	432	-460
1675	24.76	750	4.86	1.077e-03	440	-460
1680	23.40	725	5.79	1.123e-03	446	-460
1685	22.16	705	5.54	1.172e-03	450	-460
1690	21.02	673	6.57	1.223e-03	453	-460
1695	19.98	646	6.38	1.264e-03	457	-460
1700	19.00	620	7.62	1.302e-03	462	-460
1705	18.05	619	7.38	1.339e-03	466	-460
1710	17.01	627	5.89	1.381e-03	471	-460
1715	15.87	636	7.35	1.428e-03	476	-460
1720	14.85	638	8.26	1.471e-03	481	-460
1725	14.03	620	4.55	1.506e-03	485	-460
1730	13.18	606	5.07	1.544e-03	489	-460
1735	12.27	592	4.85	1.586e-03	493	-460
1740	11.29	588	5.77	1.633e-03	497	-460
1745	10.33	596	5.27	1.682e-03	500	-460
1750	9.38	580	5.50	1.753e-03	497	-460

STS-5 BET and Radiometer Data

time (sec)	$h*10^{-3}$ (ft)	vel. (ft/sec)	α (°)	density ($slug/ft^3$)	T_∞ (°F)	IML temp (°F)
0	390.00	24393	30.29	7.190e-11	724	-460
5	387.22	24393	30.52	8.370e-11	724	-460
10	384.80	24394	30.74	9.550e-11	724	-460
15	382.38	24394	30.97	1.073e-10	724	-460
20	379.97	24395	31.19	1.191e-10	706	-460
25	377.55	24396	31.42	1.309e-10	687	-460
30	375.13	24396	31.64	1.427e-10	667	-460
35	372.72	24397	31.87	1.545e-10	648	-460
40	370.30	24397	32.09	1.663e-10	629	-460
45	367.88	24398	32.32	1.781e-10	611	-460
50	365.47	24399	32.54	1.899e-10	592	-460
55	363.05	24399	32.76	2.297e-10	577	-460
60	360.63	24400	32.99	2.695e-10	561	-460
65	358.22	24401	33.22	3.092e-10	547	-460
70	355.80	24401	33.44	3.490e-10	533	-460
75	353.38	24402	33.67	3.888e-10	520	-460
80	350.97	24402	33.89	4.286e-10	506	-460
85	348.55	24403	34.12	4.684e-10	493	-460
90	346.13	24404	34.34	5.081e-10	481	-460
95	343.72	24404	34.57	5.479e-10	470	-460
100	341.30	24405	34.79	5.877e-10	460	-460
105	338.88	24405	35.01	7.595e-10	451	-460
110	336.47	24406	35.24	9.314e-10	443	-460
115	334.05	24407	35.46	1.103e-09	434	-460
120	331.63	24407	35.69	1.275e-09	425	-460
125	329.22	24408	35.91	1.447e-09	418	-460
130	326.80	24409	36.13	1.619e-09	412	302
135	324.38	24409	36.36	1.791e-09	406	302
140	321.97	24410	36.58	1.962e-09	402	302
145	319.55	24411	36.81	2.134e-09	397	446
150	317.13	24411	37.03	2.306e-09	392	453
155	314.72	24412	37.28	2.732e-09	387	543
160	312.30	24412	37.54	3.157e-09	384	618
165	309.89	24413	37.79	3.583e-09	381	683
170	307.47	24413	38.04	4.008e-09	379	779
175	305.05	24414	38.29	4.434e-09	377	824
180	302.64	24415	38.55	4.859e-09	374	895
185	300.22	24415	38.80	5.284e-09	372	958
190	297.81	24416	39.05	5.710e-09	369	1016
195	295.39	24416	39.31	6.136e-09	367	1087
200	292.98	24417	39.56	6.561e-09	365	1151
205	290.73	24423	39.67	7.972e-09	361	1227
210	288.48	24429	39.77	9.383e-09	361	1278
215	286.23	24436	39.88	1.079e-08	360	1339
220	283.98	24442	39.99	1.220e-08	360	1394
225	281.73	24448	40.10	1.362e-08	359	1457
230	279.49	24455	40.20	1.503e-08	359	1514
235	277.24	24461	40.31	1.644e-08	358	1577
240	274.99	24467	40.42	1.785e-08	358	1634
245	272.74	24473	40.52	1.926e-08	357	1687
250	270.49	24480	40.63	2.067e-08	356	1737
255	268.86	24454	40.59	2.359e-08	355	1783
260	267.22	24428	40.56	2.652e-08	354	1834
265	265.59	24402	40.52	2.944e-08	353	1894
270	263.96	24376	40.48	3.237e-08	352	1944
275	262.32	24351	40.44	3.529e-08	351	1986
280	260.69	24325	40.41	3.821e-08	350	2025
285	259.06	24299	40.37	4.114e-08	349	2068
290	257.42	24273	40.33	4.406e-08	348	2104
295	255.79	24248	40.30	4.699e-08	347	2138
300	254.16	24222	40.26	4.991e-08	346	2162
305	253.53	24187	40.23	5.182e-08	346	2180
310	252.91	24152	40.19	5.372e-08	347	2198
315	252.29	24118	40.16	5.563e-08	347	2207
320	251.66	24083	40.13	5.754e-08	347	2225
325	251.04	24049	40.10	5.945e-08	347	2246
330	250.41	24014	40.06	6.135e-08	347	2271
335	249.79	23979	40.03	6.326e-08	348	2292
340	249.17	23945	40.00	6.517e-08	348	2312
345	248.54	23910	39.96	6.707e-08	348	2328
350	247.92	23875	39.93	6.898e-08	348	2339
355	247.62	23836	39.94	7.010e-08	348	2350
360	247.31	23797	39.95	7.122e-08	349	2362
365	247.01	23758	39.95	7.234e-08	349	2369
370	246.71	23719	39.96	7.346e-08	349	2380
375	246.41	23680	39.97	7.457e-08	350	2388
380	246.10	23641	39.98	7.569e-08	350	2395
385	245.80	23602	39.99	7.681e-08	350	2406
390	245.50	23563	39.99	7.793e-08	350	2413
395	245.20	23524	40.00	7.905e-08	351	2420
400	244.90	23485	40.01	8.017e-08	351	2430
405	244.62	23443	40.02	8.132e-08	351	2438
410	244.33	23402	40.02	8.246e-08	352	2448
415	244.05	23361	40.03	8.361e-08	352	2455
420	243.77	23319	40.03	8.476e-08	353	2461
425	243.49	23278	40.04	8.591e-08	353	2465
430	243.21	23236	40.05	8.705e-08	353	2468
435	242.93	23195	40.05	8.820e-08	354	2471
440	242.65	23153	40.06	8.935e-08	354	2471
445	242.37	23112	40.06	9.049e-08	355	2475
450	242.09	23071	40.07	9.164e-08	355	2475
455	241.80	23026	40.07	9.294e-08	356	2481
460	241.51	22982	40.06	9.423e-08	356	2481
465	241.22	22938	40.06	9.553e-08	357	2482
470	240.93	22893	40.05	9.682e-08	357	2488
475	240.64	22849	40.05	9.812e-08	358	2488
480	240.35	22805	40.05	9.942e-08	358	2495
485	240.06	22760	40.04	1.007e-07	359	2498
490	239.77	22716	40.04	1.020e-07	360	2498
495	239.48	22672	40.03	1.033e-07	360	2501
500	239.19	22627	40.03	1.046e-07	361	2501
505	238.85	22580	40.09	1.062e-07	362	2501
510	238.51	22533	40.15	1.079e-07	363	2501
515	238.17	22486	40.21	1.096e-07	364	2501
520	237.83	22439	40.27	1.112e-07	364	2501
525	237.49	22392	40.33	1.129e-07	365	2501
530	237.15	22345	40.39	1.145e-07	366	2501
535	236.81	22298	40.45	1.161e-07	367	2501
540	236.47	22252	40.51	1.178e-07	368	2501
545	236.13	22204	40.57	1.195e-07	369	2501
550	235.79	22157	40.63	1.211e-07	370	2498
555	235.35	22104	40.54	1.233e-07	371	2498

STS-5 BET and Radiometer Data (continued)

time (sec)	$h*10^{-3}$ (ft)	vel. (ft/sec)	α (°)	density (slug/ft^3)	T_∞ (°F)	IML temp (°F)
560	234.92	22051	40.44	1.256e-07	373	2495
565	234.48	21998	40.35	1.278e-07	375	2495
570	234.05	21944	40.25	1.301e-07	376	2491
575	233.61	21891	40.16	1.323e-07	378	2491
580	233.18	21838	40.07	1.345e-07	379	2491
585	232.74	21785	39.97	1.368e-07	381	2488
590	232.31	21731	39.88	1.390e-07	382	2488
595	231.87	21678	39.78	1.413e-07	384	2488
600	231.44	21625	39.69	1.435e-07	385	2491
605	231.03	21564	39.79	1.457e-07	387	2492
610	230.62	21503	39.90	1.479e-07	389	2495
615	230.21	21442	40.01	1.501e-07	391	2495
620	229.80	21381	40.11	1.523e-07	393	2498
625	229.39	21320	40.22	1.545e-07	395	2495
630	228.98	21258	40.32	1.567e-07	397	2494
635	228.57	21197	40.42	1.589e-07	399	2491
640	228.16	21136	40.53	1.611e-07	401	2491
645	227.75	21075	40.64	1.633e-07	403	2488
650	227.34	21014	40.74	1.655e-07	404	2485
655	226.83	20941	40.71	1.683e-07	407	2481
660	226.33	20868	40.69	1.712e-07	410	2478
665	225.82	20795	40.66	1.741e-07	412	2475
670	225.32	20722	40.64	1.769e-07	415	2471
675	224.81	20649	40.61	1.798e-07	417	2468
680	224.31	20575	40.58	1.826e-07	420	2465
685	223.80	20502	40.56	1.854e-07	423	2461
690	223.30	20429	40.53	1.883e-07	425	2461
695	222.79	20356	40.51	1.911e-07	428	2458
700	222.29	20283	40.48	1.940e-07	430	2455
705	221.66	20196	40.46	1.994e-07	431	2454
710	221.04	20109	40.45	2.047e-07	432	2448
715	220.41	20022	40.43	2.101e-07	433	2444
720	219.79	19935	40.42	2.154e-07	434	2441
725	219.16	19848	40.40	2.208e-07	435	2437
730	218.54	19761	40.38	2.262e-07	436	2437
735	217.91	19674	40.37	2.315e-07	437	2430
740	217.28	19587	40.35	2.369e-07	437	2427
745	216.66	19500	40.34	2.422e-07	438	2423
750	216.03	19413	40.32	2.476e-07	439	2420
755	215.34	19321	40.27	2.553e-07	440	2416
760	214.65	19230	40.23	2.629e-07	441	2416
765	213.95	19139	40.18	2.706e-07	442	2413
770	213.26	19047	40.14	2.783e-07	442	2409
775	212.56	18956	40.09	2.860e-07	443	2406
780	211.87	18864	40.04	2.936e-07	444	2402
785	211.17	18773	40.00	3.013e-07	445	2399
790	210.48	18682	39.95	3.090e-07	445	2395
795	209.78	18590	39.91	3.166e-07	446	2395
800	209.09	18499	39.86	3.243e-07	447	2395
805	208.38	18398	39.45	3.347e-07	448	2395
810	207.67	18296	39.04	3.450e-07	448	2391
815	206.96	18195	38.62	3.554e-07	449	2391
820	206.24	18093	38.21	3.657e-07	449	2387
825	205.53	17992	37.80	3.761e-07	450	2380
830	204.82	17891	37.39	3.865e-07	451	2377
835	204.11	17789	36.98	3.968e-07	451	2376
840	203.40	17688	36.56	4.072e-07	452	2369
845	202.69	17587	36.15	4.175e-07	452	2369
850	201.98	17485	35.74	4.279e-07	453	2365
855	201.29	17359	36.24	4.410e-07	454	2377
860	200.61	17232	36.74	4.540e-07	454	2384
865	199.93	17106	37.24	4.671e-07	454	2373
870	199.25	16980	37.74	4.801e-07	455	2346
875	198.57	16853	38.24	4.932e-07	455	2323
880	197.89	16727	38.74	5.062e-07	455	2319
885	197.21	16600	39.24	5.193e-07	456	2319
890	196.52	16474	39.74	5.323e-07	456	2316
895	195.84	16348	40.24	5.454e-07	457	2308
900	195.16	16221	40.74	5.584e-07	457	2295
905	194.22	16080	40.60	5.835e-07	457	2270
910	193.27	15939	40.46	6.086e-07	458	2199
915	192.33	15798	40.32	6.338e-07	458	2033
920	191.39	15658	40.18	6.589e-07	458	2222
925	190.44	15517	40.04	6.840e-07	459	2234
930	189.50	15376	39.90	7.091e-07	459	2242
935	188.56	15235	39.76	7.342e-07	459	2241
940	187.61	15094	39.62	7.594e-07	460	2233
945	186.67	14953	39.48	7.845e-07	460	2224
950	185.73	14812	39.34	8.096e-07	460	2216
955	185.03	14652	39.29	8.354e-07	460	2207
960	184.33	14492	39.24	8.613e-07	460	2202
965	183.64	14332	39.20	8.871e-07	460	2193
970	182.94	14171	39.15	9.130e-07	461	2184
975	182.24	14011	39.10	9.388e-07	461	2175
980	181.54	13851	39.05	9.646e-07	461	2165
985	180.85	13691	39.00	9.905e-07	461	2157
990	180.15	13531	38.96	1.016e-06	461	2147
995	179.45	13371	38.91	1.042e-06	461	2138
1000	178.76	13210	38.86	1.068e-06	461	2132
1005	177.96	13050	38.80	1.109e-06	461	2118
1010	177.16	12890	38.74	1.149e-06	461	2113
1015	176.35	12730	38.68	1.190e-06	461	2098
1020	175.55	12570	38.62	1.230e-06	461	2088
1025	174.75	12409	38.56	1.271e-06	460	2073
1030	173.95	12249	38.50	1.312e-06	460	2062
1035	173.15	12089	38.44	1.352e-06	460	2051
1040	172.35	11929	38.38	1.393e-06	460	2035
1045	171.55	11769	38.32	1.433e-06	460	2024
1050	170.75	11608	38.26	1.474e-06	460	2008
1055	169.99	11444	38.30	1.528e-06	460	1996
1060	169.23	11280	38.35	1.581e-06	460	1979
1065	168.47	11115	38.39	1.635e-06	459	1967
1070	167.71	10951	38.44	1.689e-06	459	1956
1075	166.95	10786	38.48	1.742e-06	459	1944
1080	166.19	10622	38.52	1.796e-06	459	1931
1085	165.43	10458	38.57	1.850e-06	459	1919
1090	164.67	10293	38.61	1.904e-06	458	1906
1095	163.91	10129	38.66	1.957e-06	458	1893
1100	163.15	9964	38.70	2.011e-06	458	1874
1105	161.94	9814	38.17	2.142e-06	457	1860
1110	160.74	9663	37.64	2.272e-06	457	1839
1115	159.54	9512	37.10	2.403e-06	456	1819

STS-5 BET and Radiometer Data (continued)

time (sec)	h*10^{-3} (ft)	vel. (ft/sec)	α (°)	density (slug/ft^3)	T_∞ (°F)	IML temp (°F)
1120	158.33	9362	36.57	2.534e-06	456	1805
1125	157.13	9211	36.04	2.665e-06	455	1790
1130	155.93	9060	35.51	2.795e-06	454	1783
1135	154.73	8910	34.98	2.926e-06	454	1791
1140	153.52	8759	34.44	3.057e-06	453	1812
1145	152.32	8609	33.91	3.187e-06	453	1827
1150	151.12	8458	33.38	3.318e-06	452	1840
1155	149.85	8326	32.94	3.556e-06	451	1847
1160	148.59	8195	32.49	3.794e-06	450	1854
1165	147.33	8063	32.05	4.031e-06	450	1854
1170	146.06	7931	31.60	4.269e-06	449	1854
1175	144.80	7800	31.16	4.507e-06	448	1853
1180	143.53	7668	30.71	4.745e-06	447	1847
1185	142.27	7536	30.27	4.983e-06	446	1840
1190	141.01	7405	29.82	5.220e-06	445	1833
1195	139.74	7273	29.38	5.458e-06	444	1826
1200	138.48	7141	28.93	5.696e-06	444	1818
1205	137.33	7023	28.53	6.069e-06	443	1805
1210	136.19	6905	28.13	6.442e-06	442	1805
1215	135.04	6786	27.73	6.816e-06	441	1797
1220	133.90	6668	27.33	7.189e-06	440	1797
1225	132.75	6549	26.92	7.562e-06	439	1783
1230	131.60	6431	26.52	7.935e-06	438	1767
1235	130.46	6313	26.12	8.308e-06	437	1752
1240	129.31	6195	25.72	8.682e-06	436	1744
1245	128.17	6076	25.32	9.055e-06	435	1728
1250	127.02	5958	24.92	9.428e-06	434	1719
1255	125.89	5857	24.63	1.005e-05	433	1703
1260	124.77	5756	24.34	1.068e-05	432	1687
1265	123.65	5655	24.04	1.130e-05	431	1669
1270	122.52	5554	23.75	1.192e-05	430	1651
1275	121.40	5453	23.46	1.255e-05	429	1633
1280	120.27	5353	23.17	1.317e-05	429	1614
1285	119.15	5252	22.88	1.380e-05	428	1586
1290	118.02	5151	22.58	1.442e-05	427	1566
1295	116.90	5050	22.29	1.505e-05	426	1546
1300	115.77	4949	22.00	1.567e-05	425	1525
1305	114.67	4852	21.72	1.671e-05	424	1503
1310	113.57	4756	21.44	1.775e-05	423	1480
1315	112.47	4659	21.17	1.880e-05	422	1456
1320	111.37	4563	20.89	1.984e-05	421	1432
1325	110.27	4466	20.61	2.088e-05	420	1407
1330	109.17	4370	20.33	2.192e-05	419	1380
1335	108.06	4273	20.05	2.296e-05	418	1352
1340	106.96	4176	19.78	2.401e-05	417	1337
1345	105.86	4080	19.50	2.505e-05	416	1293
1350	104.76	3983	19.22	2.609e-05	415	1276
1355	103.66	3892	18.99	2.787e-05	414	1244
1360	102.57	3801	18.76	2.965e-05	413	1227
1365	101.47	3710	18.53	3.143e-05	412	1190
1370	100.37	3619	18.30	3.321e-05	411	1171
1375	99.28	3528	18.08	3.499e-05	410	1150
1380	98.18	3436	17.85	3.676e-05	409	1110
1385	97.08	3345	17.62	3.854e-05	408	1087
1390	95.98	3254	17.39	4.032e-05	407	1064
1395	94.89	3163	17.16	4.210e-05	406	1040
1400	93.79	3072	16.93	4.388e-05	405	1014
1405	92.36	2992	16.69	4.826e-05	404	987
1410	90.93	2911	16.45	5.264e-05	403	958
1415	89.50	2831	16.20	5.702e-05	402	955
1420	88.07	2751	15.96	6.140e-05	401	895
1425	86.64	2671	15.72	6.578e-05	400	895
1430	85.21	2591	15.48	7.016e-05	399	860
1435	83.78	2511	15.24	7.454e-05	398	822
1440	82.35	2431	14.99	7.892e-05	397	818
1445	80.91	2351	14.75	8.330e-05	396	779
1450	79.48	2271	14.51	8.768e-05	395	733
1455	78.61	2200	14.05	9.240e-05	394	733
1460	77.73	2128	13.58	9.712e-05	393	728
1465	76.85	2057	13.12	1.018e-04	393	679
1470	75.97	1986	12.65	1.066e-04	392	618
1475	75.09	1915	12.19	1.113e-04	392	618
1480	74.21	1843	11.73	1.160e-04	391	618
1485	73.34	1772	11.26	1.207e-04	391	543
1490	72.46	1701	10.80	1.255e-04	390	543
1495	71.58	1630	10.33	1.302e-04	390	543
1500	70.70	1558	9.87	1.349e-04	389	543
1505	69.23	1512	9.67	1.493e-04	388	446
1510	67.76	1466	9.48	1.637e-04	388	446
1515	66.29	1420	9.28	1.781e-04	387	446
1520	64.82	1373	9.08	1.925e-04	387	446
1525	63.35	1327	8.89	2.069e-04	386	446
1530	61.88	1281	8.69	2.213e-04	385	302
1535	60.41	1235	8.49	2.357e-04	385	302
1540	58.94	1188	8.29	2.501e-04	384	302
1545	57.47	1142	8.10	2.645e-04	384	302
1550	56.00	1096	7.90	2.789e-04	383	302
1555	54.60	1070	7.83	3.063e-04	383	302
1560	53.20	1045	7.75	3.336e-04	383	302
1565	51.80	1020	7.68	3.610e-04	383	302
1570	50.40	994	7.60	3.884e-04	383	302
1575	49.00	969	7.53	4.158e-04	383	302
1580	47.60	943	7.45	4.431e-04	383	302
1585	46.20	918	7.38	4.705e-04	383	302
1590	44.80	892	7.30	4.979e-04	383	-460
1595	43.40	867	7.23	5.252e-04	383	302
1600	42.00	841	7.15	5.526e-04	383	302
1605	40.59	830	7.18	5.939e-04	387	-460
1610	39.19	819	7.21	6.352e-04	391	-460
1615	37.78	808	7.23	6.766e-04	395	-460
1620	36.37	797	7.26	7.179e-04	399	227
1625	34.97	787	7.29	7.592e-04	403	-460
1630	33.56	775	7.32	8.005e-04	407	-460
1635	32.15	765	7.35	8.418e-04	411	-460
1640	30.75	754	7.37	8.832e-04	415	-460
1645	29.34	743	7.40	9.245e-04	419	-460
1650	27.93	732	7.43	9.658e-04	423	-460
1655	26.93	719	7.36	1.003e-03	427	-460
1660	25.92	707	7.29	1.040e-03	432	-460
1665	24.92	694	7.22	1.078e-03	436	-460
1670	23.92	682	7.15	1.115e-03	440	-460
1675	22.91	670	7.07	1.152e-03	444	-460

STS-5 BET and Radiometer Data (concluded)

time (sec)	$h*10^{-3}$ (ft)	vel. (ft/sec)	α (°)	density ($slug/ft^3$)	T_∞ (°F)	IML temp (°F)
1680	21.91	657	7.00	1.190e-03	449	-460
1685	20.91	645	6.93	1.227e-03	453	-460
1690	19.90	632	6.86	1.264e-03	457	-460
1695	18.90	620	6.79	1.302e-03	461	-460
1700	17.90	608	6.72	1.339e-03	466	-460
1705	16.96	602	6.47	1.385e-03	469	-460
1710	16.03	596	6.22	1.431e-03	472	-460
1715	15.10	591	5.98	1.477e-03	475	-460
1720	14.16	585	5.73	1.523e-03	479	-460
1725	13.23	579	5.48	1.568e-03	482	-460
1730	12.30	574	5.23	1.614e-03	485	-460
1735	11.36	568	4.98	1.660e-03	488	-460
1740	10.43	563	4.74	1.706e-03	492	-460
1745	9.50	557	4.49	1.752e-03	495	-460
1750	8.56	552	4.24	1.798e-03	498	-460

STS-26 BET and Radiometer Data

time (sec)	$h*10^{-3}$ (ft)	vel. (ft/sec)	α (°)	density ($slug/ft^3$)	T_∞ (°F)	IML temp (°F)
0	398.51	24447	40.89	3.894e-11	683	-460
5	395.76	24450	40.87	4.302e-11	664	-460
10	393.02	24452	40.88	4.756e-11	645	-460
15	390.29	24456	40.90	5.273e-11	626	-460
20	387.56	24459	40.89	5.850e-11	608	-460
25	384.84	24463	40.93	6.520e-11	591	-460
30	382.12	24466	40.95	7.265e-11	574	-460
35	379.41	24468	40.93	8.129e-11	558	-460
40	376.70	24471	40.71	9.090e-11	542	-460
45	374.00	24476	40.52	1.055e-10	529	422
50	371.31	24482	40.37	1.240e-10	516	220
55	368.62	24485	40.30	1.426e-10	503	-460
60	365.94	24487	40.27	1.611e-10	490	422
65	363.26	24489	40.34	1.820e-10	478	-460
70	360.59	24492	40.45	2.061e-10	467	-460
75	357.93	24493	40.58	2.333e-10	456	422
80	355.28	24493	40.70	2.644e-10	447	422
85	352.63	24493	40.85	2.995e-10	438	422
90	349.99	24491	41.01	3.406e-10	430	422
95	347.35	24490	41.05	3.876e-10	421	422
100	344.73	24504	41.00	4.409e-10	414	589
105	342.11	24538	40.92	5.012e-10	408	460
110	339.50	24568	40.77	5.696e-10	403	422
115	336.89	24571	40.53	6.483e-10	397	-258
120	334.30	24573	40.16	7.375e-10	392	-460
125	331.72	24573	39.65	8.403e-10	388	-460
130	329.14	24572	39.17	9.573e-10	383	-460
135	326.58	24574	39.22	1.089e-09	380	-460
140	324.02	24577	39.49	1.237e-09	377	-460
145	321.48	24577	39.56	1.407e-09	374	88
150	318.95	24565	39.59	1.615e-09	369	-126
155	316.43	24553	39.57	1.853e-09	365	422
160	313.92	24542	39.59	2.125e-09	360	525
165	311.43	24532	39.56	2.437e-09	355	589
170	308.95	24523	39.69	2.795e-09	350	701
175	306.49	24513	39.88	3.204e-09	344	754
180	304.04	24501	40.02	3.702e-09	338	859
185	301.61	24483	40.26	4.312e-09	330	920
190	299.20	24468	40.74	4.884e-09	331	1005
195	296.82	24452	41.31	5.524e-09	332	1067
200	294.46	24436	41.17	6.179e-09	334	1132
205	292.12	24420	40.23	6.783e-09	339	1202
210	289.81	24405	39.22	7.444e-09	343	1264
215	287.53	24393	39.08	8.273e-09	346	1347
220	285.28	24385	40.05	9.293e-09	346	1419
225	283.07	24376	41.26	1.042e-08	347	1484
230	280.89	24373	40.97	1.166e-08	348	1543
235	278.76	24375	39.68	1.301e-08	348	1614
240	276.67	24376	39.14	1.449e-08	349	1669
245	274.63	24380	39.96	1.619e-08	347	1724
250	272.64	24386	41.18	1.816e-08	344	1752
255	270.71	24390	40.96	2.035e-08	340	1785
260	268.85	24393	39.72	2.274e-08	336	1820
265	267.06	24396	39.36	2.530e-08	333	1860
270	265.35	24396	40.35	2.802e-08	330	1903

STS-26 BET and Radiometer Data (continued)

time (sec)	h*10^{-3} (ft)	vel. (ft/sec)	α (°)	density (slug/ft^3)	T_∞ (°F)	IML temp (°F)
275	263.72	24392	40.94	3.092e-08	328	1956
280	262.18	24385	40.21	3.390e-08	326	2005
285	260.74	24373	39.78	3.680e-08	325	2052
290	259.40	24359	40.18	3.972e-08	325	2097
295	258.16	24343	40.46	4.261e-08	325	2123
300	257.05	24324	40.43	4.541e-08	324	2157
305	256.05	24303	40.51	4.806e-08	324	2189
310	255.17	24277	40.16	5.030e-08	325	2226
315	254.40	24249	40.13	5.229e-08	326	2252
320	253.72	24221	39.81	5.413e-08	327	2274
325	253.10	24193	39.61	5.584e-08	328	2296
330	252.53	24164	40.07	5.746e-08	329	2322
335	252.00	24134	40.25	5.901e-08	330	2337
340	251.51	24104	40.18	6.050e-08	331	2350
345	251.04	24073	40.13	6.194e-08	332	2364
350	250.59	24041	40.13	6.335e-08	333	2375
355	250.17	24009	40.13	6.471e-08	333	2382
360	249.77	23975	40.12	6.604e-08	334	2389
365	249.38	23942	40.12	6.734e-08	335	2402
370	249.01	23906	40.12	6.855e-08	335	2408
375	248.66	23870	40.11	6.972e-08	336	2414
380	248.32	23833	40.11	7.087e-08	336	2420
385	247.99	23796	40.11	7.200e-08	337	2425
390	247.66	23759	40.11	7.313e-08	338	2431
395	247.35	23722	40.11	7.427e-08	339	2432
400	247.03	23683	40.11	7.541e-08	339	2432
405	246.72	23645	40.10	7.658e-08	340	2432
410	246.40	23606	40.11	7.776e-08	341	2438
415	246.08	23567	40.11	7.898e-08	342	2444
420	245.75	23528	40.13	8.023e-08	342	2450
425	245.43	23488	40.15	8.149e-08	343	2450
430	245.11	23447	40.14	8.275e-08	344	2456
435	244.79	23406	40.15	8.401e-08	345	2456
440	244.49	23365	40.15	8.525e-08	345	2462
445	244.19	23322	40.18	8.648e-08	346	2467
450	243.90	23279	40.08	8.771e-08	347	2467
455	243.61	23236	39.75	8.893e-08	348	2473
460	243.32	23192	39.61	9.016e-08	348	2473
465	243.03	23149	39.40	9.141e-08	349	2484
470	242.75	23106	39.43	9.265e-08	350	2490
475	242.47	23063	39.45	9.386e-08	350	2496
480	242.20	23019	39.56	9.504e-08	351	2500
485	241.93	22975	39.60	9.620e-08	352	2501
490	241.67	22931	39.71	9.738e-08	352	2502
495	241.39	22886	39.85	9.861e-08	353	2507
500	241.11	22840	39.88	9.988e-08	354	2507
505	240.82	22793	39.92	1.012e-07	355	2511
510	240.52	22746	39.95	1.026e-07	356	2512
515	240.21	22699	39.97	1.040e-07	356	2512
520	239.90	22650	40.01	1.055e-07	357	2512
525	239.59	22602	39.81	1.069e-07	358	2513
530	239.28	22553	39.79	1.084e-07	359	2518
535	238.97	22504	39.82	1.099e-07	360	2518
540	238.66	22455	39.84	1.114e-07	361	2516
545	238.35	22406	39.87	1.130e-07	362	2509
550	238.03	22356	39.89	1.146e-07	363	2513
555	237.69	22305	39.91	1.163e-07	364	2512
560	237.34	22253	39.92	1.181e-07	365	2512
565	236.98	22201	39.96	1.199e-07	366	2512
570	236.62	22148	39.91	1.219e-07	367	2512
575	236.25	22094	39.88	1.238e-07	368	2512
580	235.88	22041	39.75	1.258e-07	369	2512
585	235.52	21987	39.78	1.279e-07	370	2518
590	235.17	21933	39.81	1.300e-07	370	2512
595	234.82	21878	39.84	1.322e-07	371	2518
600	234.46	21823	39.88	1.343e-07	371	2517
605	234.11	21767	39.90	1.365e-07	372	2518
610	233.74	21711	39.92	1.389e-07	372	2512
615	233.36	21653	39.94	1.413e-07	373	2512
620	232.97	21596	39.95	1.439e-07	373	2512
625	232.56	21538	39.97	1.466e-07	374	2512
630	232.13	21478	39.99	1.494e-07	375	2512
635	231.70	21417	40.03	1.523e-07	375	2512
640	231.26	21356	40.05	1.553e-07	376	2511
645	230.82	21294	40.08	1.584e-07	377	2512
650	230.37	21231	40.12	1.616e-07	378	2511
655	229.92	21167	40.13	1.648e-07	379	2511
660	229.45	21102	40.15	1.682e-07	380	2510
665	228.97	21037	40.13	1.718e-07	380	2509
670	228.48	20972	40.11	1.756e-07	381	2508
675	227.98	20904	40.02	1.796e-07	382	2508
680	227.48	20837	39.71	1.837e-07	382	2507
685	226.98	20768	39.74	1.878e-07	383	2501
690	226.50	20698	39.46	1.919e-07	383	2496
695	226.03	20629	39.33	1.956e-07	385	2501
700	225.57	20559	39.36	1.988e-07	387	2501
705	225.13	20489	39.38	2.019e-07	389	2507
710	224.68	20418	39.46	2.051e-07	391	2506
715	224.22	20346	39.56	2.085e-07	393	2502
720	223.75	20272	39.59	2.119e-07	395	2507
725	223.27	20197	39.62	2.156e-07	397	2501
730	222.78	20121	39.65	2.193e-07	399	2501
735	222.29	20046	39.67	2.234e-07	401	2501
740	221.80	19970	39.70	2.275e-07	402	2501
745	221.31	19892	39.72	2.318e-07	404	2501
750	220.81	19813	39.72	2.363e-07	405	2500
755	220.29	19733	39.73	2.410e-07	406	2496
760	219.76	19652	39.76	2.459e-07	408	2496
765	219.22	19571	39.83	2.513e-07	409	2496
770	218.66	19490	39.92	2.569e-07	410	2491
775	218.10	19406	39.93	2.627e-07	411	2490
780	217.53	19320	39.73	2.688e-07	412	2490
785	216.95	19233	39.72	2.752e-07	413	2490
790	216.37	19146	39.65	2.817e-07	414	2490
795	215.79	19058	39.66	2.885e-07	414	2490
800	215.22	18968	39.66	2.954e-07	415	2490
805	214.64	18877	39.67	3.025e-07	415	2490
810	214.06	18784	39.65	3.099e-07	416	2484
815	213.46	18690	39.67	3.176e-07	416	2480
820	212.85	18594	39.54	3.258e-07	417	2479
825	212.22	18497	39.49	3.343e-07	418	2473
830	211.60	18399	39.50	3.431e-07	418	2467

STS-26 BET and Radiometer Data (continued)

time (sec)	$h*10^{-3}$ (ft)	vel. (ft/sec)	α (°)	density ($slug/ft^3$)	T_∞ (°F)	IML temp (°F)
835	210.98	18298	39.48	3.521e-07	419	2463
840	210.34	18197	39.51	3.615e-07	419	2466
845	209.70	18095	39.58	3.713e-07	420	2462
850	209.03	17991	39.77	3.808e-07	421	2456
855	208.35	17884	39.97	3.909e-07	423	2451
860	207.63	17776	40.07	4.017e-07	424	2450
865	206.88	17665	40.21	4.134e-07	426	2439
870	206.08	17552	40.34	4.261e-07	427	2438
875	205.25	17437	40.38	4.400e-07	429	2427
880	204.39	17319	40.36	4.549e-07	430	2426
885	203.50	17200	40.39	4.707e-07	432	2415
890	202.59	17073	40.38	4.868e-07	434	2408
895	201.64	16940	40.50	5.035e-07	436	2407
900	200.67	16805	40.48	5.214e-07	439	2397
905	199.68	16665	40.42	5.403e-07	441	2390
910	198.67	16522	40.25	5.601e-07	444	2383
915	197.67	16378	40.06	5.805e-07	446	2383
920	196.69	16233	39.97	6.013e-07	449	2376
925	195.73	16092	39.91	6.217e-07	451	2370
930	194.78	15950	40.01	6.423e-07	454	2364
935	193.83	15805	40.05	6.636e-07	457	2357
940	192.85	15657	40.07	6.857e-07	460	2356
945	191.89	15509	40.03	7.078e-07	463	2350
950	191.10	15358	39.98	7.263e-07	466	2344
955	190.63	15203	40.00	7.373e-07	467	2337
960	190.49	15049	40.27	7.404e-07	468	2330
965	190.52	14894	40.85	7.395e-07	468	2318
970	190.44	14738	41.46	7.412e-07	468	2303
975	190.02	14581	42.04	7.511e-07	470	2281
980	189.24	14420	42.35	7.725e-07	471	2267
985	188.25	14257	42.22	8.006e-07	472	2245
990	187.23	14094	41.76	8.307e-07	473	2231
995	186.28	13932	41.37	8.613e-07	473	2215
1000	185.42	13772	41.04	8.919e-07	473	2206
1005	184.62	13613	40.87	9.216e-07	472	2192
1010	183.83	13456	40.68	9.516e-07	471	2183
1015	183.05	13297	40.58	9.821e-07	470	2175
1020	182.26	13137	40.45	1.013e-06	470	2160
1025	181.45	12979	40.51	1.046e-06	470	2143
1030	180.62	12820	40.56	1.082e-06	470	2135
1035	179.75	12662	40.59	1.119e-06	470	2125
1040	178.85	12502	40.58	1.160e-06	469	2109
1045	177.93	12340	40.45	1.203e-06	469	2097
1050	177.03	12179	40.10	1.256e-06	469	2081
1055	176.18	12017	39.72	1.311e-06	470	2071
1060	175.41	11857	39.47	1.363e-06	470	2063
1065	174.68	11697	39.31	1.411e-06	471	2046
1070	173.98	11539	39.35	1.458e-06	471	2045
1075	173.26	11381	39.45	1.504e-06	472	2028
1080	172.48	11223	39.56	1.553e-06	473	2018
1085	171.63	11063	39.54	1.605e-06	473	2009
1090	170.70	10903	39.43	1.659e-06	474	2007
1095	169.73	10741	39.30	1.714e-06	475	1988
1100	168.72	10579	39.03	1.769e-06	476	1977
1105	167.70	10418	38.91	1.825e-06	477	1958
1110	166.66	10257	38.78	1.882e-06	478	1938
1115	165.60	10095	38.57	1.941e-06	478	1918
1120	164.61	9934	38.14	1.997e-06	478	1907
1125	163.70	9768	37.84	2.051e-06	478	1886
1130	162.86	9615	37.67	2.121e-06	478	1875
1135	162.05	9464	37.52	2.191e-06	477	1865
1140	161.23	9315	37.34	2.264e-06	476	1844
1145	160.39	9166	37.06	2.341e-06	476	1832
1150	159.53	9017	36.65	2.418e-06	476	1820
1155	158.65	8870	36.14	2.499e-06	477	1809
1160	157.78	8727	35.80	2.583e-06	477	1799
1165	156.91	8587	35.61	2.670e-06	478	1785
1170	156.00	8448	35.48	2.765e-06	478	1783
1175	155.07	8310	35.43	2.866e-06	478	1771
1180	154.18	8173	35.10	2.966e-06	478	1771
1185	153.46	8038	34.81	3.054e-06	477	1771
1190	152.87	7905	34.43	3.128e-06	476	1785
1195	152.25	7778	34.18	3.209e-06	476	1773
1200	151.44	7653	34.37	3.317e-06	475	1769
1205	150.44	7529	34.37	3.454e-06	474	1758
1210	149.25	7405	34.25	3.609e-06	475	1758
1215	147.94	7281	33.87	3.787e-06	476	1756
1220	146.60	7158	33.27	3.995e-06	476	1756
1225	145.28	7034	32.71	4.226e-06	474	1746
1230	143.97	6913	32.08	4.466e-06	472	1744
1235	142.68	6794	31.64	4.718e-06	470	1732
1240	141.38	6676	31.30	4.985e-06	468	1729
1245	140.06	6557	30.65	5.285e-06	465	1715
1250	138.74	6442	30.00	5.615e-06	461	1700
1255	137.43	6327	29.57	5.965e-06	457	1671
1260	136.13	6204	28.87	6.356e-06	453	1635
1265	134.85	6085	28.26	6.768e-06	448	1606
1270	133.58	5966	27.81	7.178e-06	445	1571
1275	132.29	5847	27.48	7.593e-06	444	1515
1280	130.98	5728	27.05	8.044e-06	443	1050
1285	129.63	5616	26.67	8.542e-06	441	589
1290	128.25	5505	26.30	9.084e-06	440	604
1295	126.84	5398	25.89	9.710e-06	437	1398
1300	125.41	5293	25.42	1.041e-05	433	1492
1305	123.99	5190	24.89	1.113e-05	430	1512
1310	122.58	5091	24.50	1.183e-05	430	1495
1315	121.18	4993	24.19	1.256e-05	430	1512
1320	119.77	4895	23.86	1.333e-05	430	1492
1325	118.36	4798	23.43	1.415e-05	431	1471
1330	116.94	4702	23.07	1.503e-05	431	1474
1335	115.52	4605	22.65	1.596e-05	431	1471
1340	114.10	4508	22.12	1.702e-05	430	1450
1345	112.68	4411	21.65	1.828e-05	426	1447
1350	111.28	4315	20.99	1.963e-05	422	1428
1355	109.88	4214	20.58	2.108e-05	418	1405
1360	108.49	4115	20.08	2.262e-05	414	1381
1365	107.11	4022	19.74	2.415e-05	413	1360
1370	105.72	3933	19.46	2.570e-05	412	1356
1375	104.35	3843	19.27	2.735e-05	412	1356
1380	103.09	3751	18.82	2.894e-05	412	1334
1385	102.05	3659	18.19	3.034e-05	412	1331
1390	101.11	3570	17.55	3.168e-05	412	1304

STS-26 BET and Radiometer Data (concluded)

time (sec)	$h*10^{-3}$ (ft)	vel. (ft/sec)	α (°)	density ($slug/ft^3$)	T_∞ (°F)	IML temp (°F)
1395	100.16	3484	17.44	3.317e-05	410	1275
1400	99.13	3398	17.34	3.486e-05	409	1246
1405	98.02	3312	17.21	3.675e-05	408	1214
1410	96.86	3223	16.89	3.884e-05	407	1186
1415	95.64	3136	16.54	4.112e-05	406	1181
1420	94.40	3051	16.25	4.360e-05	406	1146
1425	93.14	2965	16.10	4.626e-05	405	1146
1430	91.85	2880	15.84	4.915e-05	404	1108
1435	90.54	2798	15.66	5.231e-05	404	1108
1440	89.21	2716	15.36	5.573e-05	403	1103
1445	87.86	2636	15.04	5.943e-05	402	1067
1450	86.50	2556	14.79	6.341e-05	401	1029
1455	85.12	2478	14.45	6.770e-05	400	1029
1460	83.76	2399	13.72	7.244e-05	399	1023
1465	82.50	2322	14.01	7.713e-05	397	974
1470	81.38	2240	13.61	8.146e-05	396	974
1475	80.40	2159	13.62	8.534e-05	396	974
1480	79.53	2079	13.13	8.894e-05	396	927
1485	78.75	2000	12.69	9.233e-05	395	927
1490	77.99	1926	11.50	9.589e-05	395	920
1495	77.18	1860	10.69	9.986e-05	395	920
1500	76.26	1798	10.15	1.045e-04	394	920
1505	75.21	1741	9.76	1.102e-04	393	912
1510	74.02	1686	9.66	1.170e-04	393	920
1515	72.71	1633	9.57	1.249e-04	392	920
1520	71.29	1584	9.53	1.342e-04	391	974
1525	69.80	1541	9.43	1.448e-04	389	974
1530	68.26	1495	9.12	1.568e-04	386	920
1535	66.69	1444	8.78	1.703e-04	384	920
1540	65.10	1394	8.42	1.852e-04	381	867
1545	63.50	1345	8.15	2.019e-04	379	859
1550	61.90	1297	7.94	2.200e-04	376	787
1555	60.32	1249	7.71	2.394e-04	373	849
1560	58.76	1201	7.31	2.602e-04	371	787
1565	57.23	1147	7.23	2.815e-04	370	787
1570	55.72	1094	7.32	3.040e-04	370	711
1575	54.28	1044	7.07	3.273e-04	370	787
1580	52.88	997	6.92	3.516e-04	369	701
1585	51.50	959	6.82	3.752e-04	371	701
1590	50.14	924	6.85	3.984e-04	374	701
1595	48.77	902	6.72	4.231e-04	377	701
1600	47.40	881	7.91	4.485e-04	380	701
1605	46.06	871	4.92	4.749e-04	383	701
1610	44.56	868	6.70	5.063e-04	387	602
1615	43.08	859	6.46	5.398e-04	389	701
1620	41.66	846	6.00	5.743e-04	392	701
1625	40.28	835	5.21	6.099e-04	394	701
1630	38.92	818	5.35	6.465e-04	395	701
1635	37.57	790	5.65	6.823e-04	395	701
1640	36.20	778	5.19	7.242e-04	399	701
1645	34.82	758	7.15	7.657e-04	405	701
1650	33.44	747	7.53	8.002e-04	411	602
1655	32.11	740	7.20	8.310e-04	417	701
1660	30.82	728	7.52	8.557e-04	421	701
1665	29.59	714	7.30	8.948e-04	426	711
1670	28.40	700	7.26	9.410e-04	432	701
1675	27.24	678	7.58	9.838e-04	437	787
1680	26.10	669	7.63	1.026e-03	443	701
1685	24.97	666	7.51	1.064e-03	449	701
1690	23.89	661	7.54	1.100e-03	454	589
1695	22.90	650	7.68	1.135e-03	458	589
1700	22.00	643	7.48	1.168e-03	462	569
1705	21.17	632	7.18	1.199e-03	465	422
1710	20.40	622	7.47	1.229e-03	468	589
1715	19.65	614	7.42	1.256e-03	471	422
1720	18.92	608	7.29	1.266e-03	474	589
1725	18.16	604	6.52	1.309e-03	477	422
1730	17.30	609	6.36	1.343e-03	480	589
1735	16.37	614	6.34	1.378e-03	484	589
1740	15.36	616	6.65	1.433e-03	489	589
1745	14.31	619	5.51	1.479e-03	493	589
1750	13.27	617	4.79	1.532e-03	495	589

STS-29 BET and Radiometer Data

time (sec)	$h*10^{-3}$ (ft)	vel. (ft/sec)	α (°)	density ($slug/ft^3$)	T_∞ (°F)	IML temp (°F)
0	399.48	24441	40.77	3.834e-11	723	-460
5	396.76	24443	40.98	4.217e-11	702	-460
10	394.03	24447	40.93	4.636e-11	681	-460
15	391.32	24450	40.79	5.130e-11	661	-460
20	388.60	24454	40.75	5.676e-11	642	-460
25	385.89	24456	40.82	6.308e-11	622	-460
30	383.19	24458	40.93	7.018e-11	603	-460
35	380.50	24459	40.97	7.879e-11	585	-460
40	377.81	24460	40.99	8.935e-11	568	-460
45	375.12	24460	40.91	1.047e-10	552	-460
50	372.44	24456	40.78	1.301e-10	537	-460
55	369.77	24452	40.67	1.600e-10	523	-460
60	367.11	24452	40.60	1.809e-10	508	-460
65	364.45	24451	40.54	2.045e-10	494	-460
70	361.80	24451	40.54	2.316e-10	482	-460
75	359.15	24452	40.58	2.623e-10	470	-460
80	356.51	24453	40.62	2.972e-10	459	-460
85	353.88	24454	40.62	3.369e-10	450	-460
90	351.26	24457	40.60	3.825e-10	440	-460
95	348.64	24461	40.55	4.360e-10	431	-460
100	346.03	24464	40.52	4.969e-10	422	-460
105	343.43	24467	40.43	5.662e-10	415	-460
110	340.83	24470	40.27	6.449e-10	408	-460
115	338.25	24474	40.06	7.359e-10	401	-460
120	335.67	24477	39.77	8.401e-10	395	-460
125	333.10	24480	39.35	9.603e-10	389	-460
130	330.54	24484	39.31	1.101e-09	383	-460
135	327.99	24488	39.44	1.261e-09	376	-460
140	325.46	24497	39.66	1.438e-09	373	-460
145	322.93	24505	39.66	1.639e-09	370	-460
150	320.42	24509	39.72	1.869e-09	368	61
155	317.91	24512	39.83	2.133e-09	365	422
160	315.43	24514	39.89	2.433e-09	363	422
165	312.95	24516	39.91	2.772e-09	361	422
170	310.50	24517	39.91	3.156e-09	358	589
175	308.05	24519	39.98	3.590e-09	356	701
180	305.63	24520	40.14	4.080e-09	354	752
185	303.22	24519	40.52	4.634e-09	352	829
190	300.84	24521	41.14	5.248e-09	351	895
195	298.47	24529	41.35	5.916e-09	352	942
200	296.13	24537	40.74	6.662e-09	353	1023
205	293.81	24539	39.48	7.488e-09	354	1067
210	291.52	24538	38.96	8.401e-09	354	1146
215	289.26	24537	39.63	9.412e-09	355	1214
220	287.02	24534	41.00	1.052e-08	356	1292
225	284.82	24531	41.14	1.173e-08	357	1346
230	282.66	24526	39.93	1.306e-08	358	1405
235	280.54	24529	39.42	1.450e-08	359	1475
240	278.47	24532	40.04	1.608e-08	360	1531
245	276.46	24535	41.10	1.778e-08	360	1597
250	274.49	24535	40.40	1.962e-08	360	1656
255	272.59	24534	39.65	2.162e-08	360	1709
260	270.76	24532	40.32	2.372e-08	360	1766
265	268.99	24528	40.93	2.594e-08	360	1816
270	267.29	24519	40.45	2.831e-08	359	1860
275	265.68	24509	39.67	3.078e-08	359	1892
280	264.14	24498	39.84	3.336e-08	358	1934
285	262.69	24485	40.50	3.600e-08	357	1968
290	261.33	24469	40.54	3.865e-08	356	2007
295	260.07	24451	40.20	4.127e-08	356	2032
300	258.91	24432	40.12	4.382e-08	355	2067
305	257.87	24409	40.59	4.626e-08	355	2095
310	256.94	24384	40.46	4.854e-08	355	2125
315	256.13	24359	39.99	5.063e-08	355	2155
320	255.41	24330	39.78	5.247e-08	355	2183
325	254.77	24299	39.75	5.413e-08	355	2206
330	254.19	24267	40.17	5.567e-08	356	2223
335	253.66	24234	40.29	5.711e-08	356	2249
340	253.17	24200	40.25	5.847e-08	357	2267
345	252.72	24167	40.21	5.975e-08	357	2279
350	252.30	24132	40.18	6.097e-08	358	2296
355	251.91	24098	40.15	6.213e-08	358	2303
360	251.54	24063	40.14	6.324e-08	358	2314
365	251.20	24028	40.13	6.430e-08	358	2323
370	250.87	23993	40.11	6.533e-08	359	2337
375	250.55	23958	40.09	6.634e-08	359	2341
380	250.24	23922	40.10	6.734e-08	359	2348
385	249.93	23886	40.06	6.832e-08	360	2357
390	249.64	23850	40.07	6.930e-08	360	2364
395	249.35	23813	40.08	7.028e-08	360	2366
400	249.06	23776	40.11	7.120e-08	360	2374
405	248.77	23739	40.10	7.212e-08	361	2379
410	248.48	23702	40.09	7.305e-08	361	2383
415	248.18	23664	40.07	7.402e-08	362	2389
420	247.88	23626	40.07	7.503e-08	363	2389
425	247.56	23587	40.07	7.608e-08	363	2392
430	247.24	23548	40.07	7.718e-08	364	2389
435	246.91	23508	40.04	7.831e-08	364	2392
440	246.58	23469	40.09	7.947e-08	365	2389
445	246.25	23428	40.08	8.065e-08	365	2395
450	245.92	23387	40.11	8.183e-08	366	2395
455	245.60	23346	40.10	8.300e-08	367	2395
460	245.29	23303	40.10	8.415e-08	367	2395
465	244.99	23261	40.12	8.529e-08	368	2398
470	244.69	23218	40.15	8.642e-08	368	2402
475	244.40	23174	40.18	8.754e-08	369	2402
480	244.11	23130	40.20	8.869e-08	369	2404
485	243.81	23085	40.14	8.986e-08	370	2406
490	243.51	23040	39.93	9.106e-08	370	2408
495	243.20	22995	39.79	9.232e-08	371	2408
500	242.89	22950	39.82	9.361e-08	371	2408
505	242.57	22904	39.83	9.493e-08	372	2408
510	242.25	22857	39.74	9.626e-08	372	2408
515	241.93	22810	39.64	9.760e-08	373	2408
520	241.61	22764	39.60	9.896e-08	374	2408
525	241.30	22717	39.63	1.003e-07	374	2410
530	240.99	22670	39.66	1.017e-07	375	2414
535	240.69	22622	39.70	1.030e-07	375	2414
540	240.39	22573	39.74	1.043e-07	376	2414
545	240.09	22524	39.79	1.056e-07	376	2418
550	239.79	22475	39.81	1.070e-07	377	2414
555	239.49	22425	39.84	1.085e-07	377	2414

STS-29 BET and Radiometer Data (continued)

time (sec)	h*10^{-3} (ft)	vel. (ft/sec)	α (°)	density (slug/ft^3)	T_∞ (°F)	IML temp (°F)
560	239.17	22375	39.86	1.100e-07	378	2414
565	238.83	22324	39.88	1.115e-07	379	2414
570	238.49	22273	39.92	1.132e-07	379	2414
575	238.13	22222	39.94	1.150e-07	380	2414
580	237.77	22169	39.97	1.168e-07	381	2414
585	237.39	22116	40.01	1.187e-07	381	2414
590	237.01	22063	40.04	1.207e-07	382	2414
595	236.63	22008	40.07	1.227e-07	383	2414
600	236.25	21953	39.88	1.247e-07	383	2410
605	235.88	21897	39.93	1.268e-07	384	2410
610	235.51	21841	39.95	1.289e-07	384	2414
615	235.14	21783	39.99	1.311e-07	384	2414
620	234.77	21725	40.01	1.333e-07	385	2414
625	234.40	21666	40.05	1.355e-07	385	2414
630	234.02	21607	40.08	1.379e-07	385	2418
635	233.70	21559	40.09	1.399e-07	385	2418
640	233.29	21498	40.05	1.425e-07	385	2414
645	232.88	21436	40.07	1.452e-07	386	2414
650	232.45	21374	40.11	1.480e-07	386	2414
655	232.02	21312	40.15	1.509e-07	386	2414
660	231.60	21248	40.18	1.539e-07	387	2414
665	231.16	21184	40.15	1.570e-07	387	2414
670	230.72	21119	40.18	1.601e-07	387	2414
675	230.27	21053	40.20	1.635e-07	387	2408
680	229.81	20987	40.22	1.670e-07	387	2408
685	229.32	20919	40.24	1.708e-07	388	2414
690	228.83	20851	40.28	1.747e-07	388	2408
695	228.22	20769	40.24	1.796e-07	388	2408
700	227.71	20699	40.28	1.838e-07	388	2408
705	227.21	20629	40.31	1.881e-07	389	2408
710	226.71	20558	40.34	1.924e-07	389	2402
715	226.21	20487	40.38	1.968e-07	389	2402
720	225.70	20415	40.42	2.005e-07	391	2402
725	225.19	20341	40.44	2.043e-07	393	2402
730	224.66	20267	40.46	2.082e-07	395	2402
735	224.11	20192	40.48	2.124e-07	397	2399
740	223.54	20115	40.39	2.169e-07	399	2395
745	222.96	20038	40.36	2.215e-07	401	2395
750	222.36	19962	40.25	2.258e-07	404	2395
755	221.76	19885	40.47	2.302e-07	407	2395
760	221.15	19807	40.48	2.348e-07	410	2395
765	220.52	19727	40.59	2.397e-07	413	2393
770	219.87	19646	40.59	2.448e-07	417	2395
775	219.20	19564	40.60	2.505e-07	419	2395
780	218.52	19481	40.61	2.569e-07	421	2389
785	217.83	19395	40.58	2.634e-07	423	2389
790	217.14	19309	40.34	2.701e-07	425	2383
795	216.46	19222	40.22	2.769e-07	426	2383
800	215.79	19132	40.21	2.836e-07	428	2383
805	215.12	19041	40.06	2.903e-07	430	2380
810	214.45	18948	39.95	2.972e-07	432	2380
815	213.77	18853	39.92	3.044e-07	434	2379
820	213.08	18757	39.84	3.118e-07	436	2376
825	212.39	18660	39.70	3.195e-07	438	2372
830	211.70	18561	39.63	3.273e-07	440	2374
835	211.01	18461	39.62	3.353e-07	442	2372
840	210.34	18359	39.58	3.433e-07	444	2370
845	209.66	18256	39.57	3.514e-07	446	2364
850	208.99	18152	39.60	3.607e-07	446	2364
855	208.30	18045	39.55	3.705e-07	447	2359
860	207.60	17936	39.46	3.807e-07	447	2359
865	206.89	17827	39.42	3.915e-07	447	2350
870	206.18	17715	39.40	4.027e-07	448	2350
875	205.46	17601	39.38	4.143e-07	448	2348
880	204.73	17487	39.58	4.265e-07	448	2344
885	203.99	17369	39.73	4.394e-07	448	2341
890	203.23	17249	39.91	4.531e-07	448	2337
895	202.44	17129	39.88	4.671e-07	449	2330
900	201.63	17007	39.88	4.819e-07	449	2319
905	200.79	16882	39.84	4.977e-07	450	2317
910	199.93	16756	39.80	5.142e-07	451	2310
915	199.07	16627	39.76	5.314e-07	452	2307
920	198.22	16496	39.69	5.490e-07	452	2303
925	197.37	16363	39.68	5.671e-07	453	2296
930	196.51	16227	39.59	5.861e-07	454	2291
935	195.65	16085	39.52	6.075e-07	453	2289
940	194.77	15942	39.57	6.298e-07	453	2281
945	193.89	15796	39.66	6.533e-07	452	2274
950	193.02	15649	39.92	6.778e-07	452	2270
955	192.26	15502	39.79	7.003e-07	451	2255
960	191.80	15352	39.63	7.143e-07	450	2252
965	191.67	15203	39.79	7.183e-07	450	2245
970	191.75	15055	40.15	7.157e-07	450	2240
975	191.80	14906	40.73	7.140e-07	450	2230
980	191.57	14758	41.64	7.213e-07	450	2209
985	190.95	14604	42.69	7.410e-07	449	2194
990	189.99	14446	43.06	7.725e-07	447	2178
995	188.84	14286	43.07	8.069e-07	449	2158
1000	187.68	14124	42.79	8.432e-07	450	2128
1005	186.63	13961	42.25	8.776e-07	451	2116
1010	185.71	13795	41.75	9.083e-07	453	2096
1015	184.90	13630	41.59	9.365e-07	454	2090
1020	184.13	13467	41.42	9.641e-07	455	2066
1025	183.34	13302	41.30	9.932e-07	455	2057
1030	182.51	13137	41.10	1.025e-06	456	2045
1035	181.66	12972	40.97	1.060e-06	456	2036
1040	180.78	12807	40.86	1.096e-06	457	2020
1045	179.89	12641	40.82	1.134e-06	458	2007
1050	179.00	12474	40.74	1.174e-06	458	1991
1055	178.14	12308	40.46	1.213e-06	459	1978
1060	177.33	12141	40.30	1.252e-06	460	1962
1065	176.55	11978	40.15	1.289e-06	460	1948
1070	175.80	11819	40.10	1.326e-06	461	1931
1075	175.07	11659	40.15	1.363e-06	462	1921
1080	174.31	11500	40.15	1.403e-06	462	1907
1085	173.50	11341	40.20	1.445e-06	463	1897
1090	172.66	11179	40.15	1.492e-06	464	1886
1095	171.77	11018	40.04	1.543e-06	465	1875
1100	170.85	10856	39.89	1.597e-06	465	1854
1105	169.91	10693	39.71	1.653e-06	466	1843
1110	168.96	10527	39.55	1.710e-06	468	1832
1115	167.99	10360	39.33	1.771e-06	469	1820

STS-29 BET and Radiometer Data (continued)

time (sec)	$h*10^{-3}$ (ft)	vel. (ft/sec)	α (°)	density ($slug/ft^3$)	T_∞ (°F)	IML temp (°F)
1120	166.99	10195	39.15	1.835e-06	471	1798
1125	165.97	10030	39.18	1.903e-06	472	1798
1130	165.00	9866	39.01	1.971e-06	474	1785
1135	164.09	9704	38.82	2.037e-06	475	1575
1140	163.23	9544	38.45	2.101e-06	476	1531
1145	162.42	9388	38.09	2.163e-06	477	1550
1150	161.63	9234	37.94	2.225e-06	478	1544
1155	160.83	9081	37.81	2.289e-06	479	1531
1160	160.01	8931	37.52	2.357e-06	480	1677
1165	159.16	8782	37.32	2.430e-06	481	1708
1170	158.27	8635	36.98	2.508e-06	482	1700
1175	157.35	8490	36.64	2.592e-06	483	1700
1180	156.40	8349	36.33	2.689e-06	483	1715
1185	155.43	8210	36.29	2.793e-06	482	1744
1190	154.50	8070	36.05	2.896e-06	482	1744
1195	153.73	7934	35.75	2.983e-06	481	1729
1200	153.06	7801	35.52	3.056e-06	482	1744
1205	152.34	7673	35.25	3.137e-06	483	1722
1210	151.44	7546	35.27	3.241e-06	483	1722
1215	150.34	7420	35.19	3.378e-06	483	1715
1220	149.10	7294	34.90	3.552e-06	482	1700
1225	147.79	7169	34.41	3.744e-06	481	1685
1230	146.49	7043	33.94	3.952e-06	479	1669
1235	145.19	6917	33.43	4.174e-06	477	1654
1240	143.88	6793	32.94	4.410e-06	475	1637
1245	142.54	6670	32.50	4.667e-06	473	1637
1250	141.16	6550	32.06	4.946e-06	470	1621
1255	139.76	6430	31.64	5.263e-06	467	1621
1260	138.33	6309	31.19	5.611e-06	463	1586
1265	136.89	6189	30.75	5.968e-06	461	1569
1270	135.47	6070	30.21	6.323e-06	461	1550
1275	134.08	5952	29.63	6.686e-06	461	1531
1280	132.73	5842	29.08	7.043e-06	462	1531
1285	131.39	5733	28.83	7.416e-06	462	1531
1290	130.03	5627	28.32	7.811e-06	464	1512
1295	128.62	5525	28.04	8.236e-06	465	1512
1300	127.18	5423	27.72	8.714e-06	465	1492
1305	125.70	5321	27.28	9.264e-06	464	1482
1310	124.20	5220	26.78	9.879e-06	463	1471
1315	122.69	5118	26.21	1.060e-05	459	1457
1320	121.17	5018	25.75	1.137e-05	455	1435
1325	119.67	4923	25.28	1.220e-05	452	1412
1330	118.16	4828	24.79	1.309e-05	449	1412
1335	116.67	4733	24.17	1.404e-05	446	1405
1340	115.19	4639	23.46	1.504e-05	443	1381
1345	113.72	4548	23.00	1.610e-05	440	1373
1350	112.25	4456	22.53	1.724e-05	438	1339
1355	110.78	4365	21.95	1.847e-05	435	1331
1360	109.31	4274	21.38	1.983e-05	432	1331
1365	107.85	4183	20.73	2.129e-05	429	1304
1370	106.39	4088	20.18	2.290e-05	426	1275
1375	104.95	3994	19.64	2.460e-05	422	1246
1380	103.53	3902	19.26	2.642e-05	419	1225
1385	102.11	3810	18.90	2.836e-05	416	1225
1390	100.70	3719	18.57	3.046e-05	413	1181
1395	99.37	3627	18.39	3.259e-05	410	1181
1400	98.26	3533	17.87	3.451e-05	407	1146
1405	97.31	3442	17.24	3.614e-05	406	1146
1410	96.36	3356	17.05	3.782e-05	406	1146
1415	95.35	3270	16.98	3.970e-05	405	1108
1420	94.28	3184	16.80	4.190e-05	404	1108
1425	93.16	3098	16.48	4.443e-05	401	1081
1430	91.99	3013	16.18	4.721e-05	399	1067
1435	90.78	2929	15.79	5.020e-05	397	1053
1440	89.54	2846	15.56	5.343e-05	396	1023
1445	88.28	2765	15.40	5.693e-05	394	1023
1450	86.99	2684	15.22	6.072e-05	393	1023
1455	85.69	2603	14.98	6.483e-05	392	974
1460	84.37	2522	14.66	6.923e-05	391	974
1465	83.04	2439	14.62	7.394e-05	390	974
1470	81.75	2357	13.72	7.878e-05	389	974
1475	80.61	2275	14.09	8.344e-05	389	937
1480	79.62	2192	13.55	8.767e-05	388	920
1485	78.76	2109	13.55	9.154e-05	387	920
1490	78.00	2028	13.13	9.505e-05	387	920
1495	77.30	1950	11.99	9.839e-05	387	901
1500	76.57	1880	11.06	1.020e-04	387	859
1505	75.76	1816	10.51	1.061e-04	387	859
1510	74.82	1757	10.18	1.111e-04	386	810
1515	73.75	1700	10.11	1.171e-04	386	859
1520	72.56	1645	10.19	1.241e-04	386	859
1525	71.28	1592	10.08	1.322e-04	386	836
1530	69.92	1541	9.93	1.413e-04	385	810
1535	68.51	1489	9.90	1.516e-04	385	787
1540	67.07	1441	9.61	1.638e-04	382	760
1545	65.62	1394	9.32	1.771e-04	379	787
1550	64.17	1340	8.97	1.906e-04	378	728
1555	62.70	1285	8.78	2.049e-04	378	787
1560	61.23	1234	8.58	2.203e-04	378	701
1565	59.77	1187	8.41	2.369e-04	378	787
1570	58.32	1141	8.28	2.539e-04	379	728
1575	56.89	1097	8.41	2.707e-04	381	701
1580	55.50	1054	7.94	2.881e-04	383	760
1585	54.13	1013	7.81	3.075e-04	384	701
1590	52.77	975	7.87	3.281e-04	384	701
1595	51.41	941	7.84	3.505e-04	384	701
1600	50.05	919	7.78	3.749e-04	384	701
1605	48.69	899	8.56	4.010e-04	383	624
1610	47.39	877	9.00	4.271e-04	383	701
1615	46.17	862	7.69	4.533e-04	383	589
1620	44.94	850	7.67	4.835e-04	382	623
1625	43.68	839	7.09	5.176e-04	379	701
1630	42.41	832	6.62	5.539e-04	377	589
1635	41.11	829	6.30	5.902e-04	378	623
1640	39.83	821	5.35	6.286e-04	378	666
1645	38.52	814	5.11	6.682e-04	379	701
1650	37.20	805	5.03	7.017e-04	385	589
1655	35.88	787	5.16	7.365e-04	391	623
1660	34.60	768	5.10	7.726e-04	396	589
1665	33.30	755	5.37	8.102e-04	402	623
1670	31.94	741	6.41	8.496e-04	408	589
1675	30.44	728	7.80	8.937e-04	415	589

STS-29 BET and Radiometer Data (concluded)

time (sec)	h*10^{-3} (ft)	vel. (ft/sec)	α (°)	density (slug/ft^3)	T_∞ (°F)	IML temp (°F)
1680	28.86	718	7.97	9.443e-04	421	589
1685	27.24	704	8.25	9.946e-04	430	623
1690	25.70	691	6.81	1.045e-03	437	701
1695	24.30	685	7.02	1.093e-03	443	701
1700	23.04	665	7.62	1.139e-03	449	666
1705	21.93	644	7.48	1.181e-03	453	666
1710	20.94	629	7.34	1.220e-03	456	589
1715	20.03	627	6.91	1.256e-03	460	666
1720	19.12	630	6.59	1.293e-03	463	623
1725	18.21	629	6.26	1.328e-03	468	701
1730	17.27	629	6.20	1.364e-03	473	589
1735	16.28	625	6.46	1.406e-03	477	701
1740	15.30	617	6.01	1.453e-03	480	701
1745	14.34	613	5.65	1.502e-03	482	760
1750	13.42	606	4.63	1.549e-03	484	701

STS-33 BET and Radiometer Data

time (sec)	h*10^{-3} (ft)	vel. (ft/sec)	α (°)	density (slug/ft^3)	T_∞ (°F)	IML temp (°F)
0	399.62	24652	40.82	4.117e-11	753	-460
5	396.33	24661	40.86	4.626e-11	726	-460
10	393.05	24668	40.91	5.217e-11	699	-460
15	389.78	24675	40.90	5.915e-11	673	-460
20	386.53	24681	40.93	6.720e-11	647	-460
25	383.30	24686	40.85	7.655e-11	623	-460
30	380.08	24688	40.75	8.746e-11	600	-460
35	376.89	24688	40.71	1.001e-10	579	-460
40	373.71	24693	40.70	1.148e-10	559	-460
45	370.55	24699	40.78	1.317e-10	540	-460
50	367.41	24719	40.88	1.521e-10	521	-460
55	364.29	24741	41.00	1.759e-10	502	-460
60	361.19	24731	40.79	2.043e-10	486	-460
65	358.11	24720	40.44	2.370e-10	470	-460
70	355.05	24724	40.10	2.763e-10	455	-460
75	352.00	24729	39.81	3.217e-10	441	-460
80	348.98	24734	39.56	3.779e-10	427	-460
85	345.98	24739	39.30	4.434e-10	414	-460
90	343.00	24736	39.41	5.191e-10	404	-460
95	340.03	24733	39.47	6.069e-10	395	-460
100	337.09	24734	39.50	7.118e-10	386	-460
105	334.17	24735	39.52	8.337e-10	379	-460
110	331.28	24729	39.64	9.808e-10	371	-460
115	328.40	24721	39.73	1.153e-09	363	-460
120	325.55	24732	39.72	1.343e-09	360	-460
125	322.72	24745	39.58	1.561e-09	357	-460
130	319.92	24758	39.50	1.822e-09	354	-460
135	317.15	24773	39.52	2.129e-09	350	-460
140	314.40	24788	39.61	2.484e-09	347	422
145	311.67	24804	39.76	2.893e-09	344	308
150	308.98	24820	40.06	3.365e-09	340	567
155	306.31	24836	40.59	3.909e-09	337	589
160	303.68	24844	41.24	4.601e-09	330	589
165	301.07	24844	41.33	5.402e-09	324	701
170	298.51	24844	41.17	6.117e-09	330	787
175	295.97	24844	40.81	6.915e-09	335	912
180	293.48	24843	40.16	7.700e-09	344	920
185	291.02	24842	39.25	8.517e-09	353	1017
190	288.60	24841	39.18	9.406e-09	362	1097
195	286.23	24838	39.95	1.044e-08	367	1141
200	283.91	24835	41.18	1.157e-08	371	1214
205	281.64	24829	41.00	1.284e-08	374	1300
210	279.42	24822	39.74	1.444e-08	371	1353
215	277.27	24813	39.29	1.618e-08	368	1425
220	275.18	24802	40.07	1.805e-08	366	1492
225	273.16	24776	41.05	1.998e-08	365	1534
230	271.21	24749	40.56	2.198e-08	366	1604
235	269.33	24722	39.49	2.404e-08	367	1654
240	267.54	24691	39.67	2.619e-08	368	1713
245	265.82	24659	40.69	2.843e-08	369	1758
250	264.21	24624	40.94	3.071e-08	370	1796
255	262.70	24589	39.90	3.301e-08	371	1830
260	261.30	24558	39.52	3.532e-08	371	1865
265	260.01	24526	40.25	3.758e-08	372	1906
270	258.84	24493	40.75	3.976e-08	372	1947

STS-33 BET and Radiometer Data (continued)

time (sec)	$h*10^{-3}$ (ft)	vel. (ft/sec)	α (°)	density (slug/ft^3)	T_∞ (°F)	IML temp (°F)
275	257.80	24460	40.74	4.180e-08	372	1977
280	256.88	24427	39.99	4.369e-08	373	2007
285	256.08	24395	39.74	4.542e-08	373	2044
290	255.37	24365	40.13	4.704e-08	373	2063
295	254.74	24336	39.81	4.858e-08	372	2090
300	254.16	24306	39.62	5.002e-08	372	2108
305	253.62	24276	40.02	5.139e-08	372	2125
310	253.12	24245	40.23	5.272e-08	371	2142
315	252.64	24214	40.07	5.400e-08	371	2158
320	252.19	24182	39.98	5.525e-08	371	2174
325	251.76	24149	40.10	5.646e-08	371	2183
330	251.35	24116	40.12	5.765e-08	370	2198
335	250.95	24083	40.05	5.882e-08	370	2206
340	250.57	24049	40.03	5.996e-08	370	2214
345	250.21	24014	40.04	6.107e-08	370	2229
350	249.85	23980	40.06	6.217e-08	370	2237
355	249.51	23945	40.05	6.327e-08	369	2245
360	249.17	23911	40.06	6.437e-08	369	2259
365	248.84	23877	40.08	6.552e-08	369	2260
370	248.50	23844	40.06	6.669e-08	368	2273
375	248.16	23811	40.03	6.790e-08	368	2281
380	247.81	23778	40.05	6.916e-08	368	2289
385	247.45	23744	40.14	7.048e-08	367	2289
390	247.08	23709	40.13	7.186e-08	367	2289
395	246.71	23673	40.10	7.329e-08	366	2296
400	246.33	23636	40.10	7.476e-08	366	2303
405	245.96	23599	40.09	7.625e-08	366	2310
410	245.59	23562	40.10	7.774e-08	365	2317
415	245.23	23525	40.10	7.924e-08	365	2323
420	244.87	23488	40.11	8.075e-08	365	2330
425	244.52	23450	40.12	8.226e-08	364	2331
430	244.18	23411	40.12	8.377e-08	364	2337
435	243.84	23372	40.11	8.528e-08	363	2344
440	243.50	23333	40.15	8.678e-08	363	2344
445	243.16	23293	40.15	8.829e-08	362	2351
450	242.83	23253	40.16	8.982e-08	362	2363
455	242.49	23213	40.17	9.133e-08	362	2370
460	242.15	23175	40.17	9.286e-08	361	2376
465	241.81	23136	40.34	9.442e-08	361	2376
470	241.47	23095	40.41	9.601e-08	361	2376
475	241.12	23053	40.19	9.763e-08	361	2383
480	240.79	23011	39.94	9.924e-08	361	2383
485	240.46	22967	39.59	1.008e-07	361	2389
490	240.15	22924	39.22	1.024e-07	361	2395
495	239.85	22881	38.94	1.039e-07	361	2402
500	239.56	22838	38.92	1.053e-07	361	2408
505	239.29	22794	38.93	1.067e-07	361	2413
510	239.02	22749	38.93	1.080e-07	361	2414
515	238.76	22705	38.94	1.094e-07	361	2414
520	238.50	22661	39.13	1.108e-07	361	2420
525	238.24	22615	39.37	1.122e-07	361	2420
530	237.97	22568	39.39	1.136e-07	361	2420
535	237.70	22521	39.42	1.151e-07	361	2420
540	237.42	22474	39.43	1.166e-07	361	2420
545	237.13	22427	39.46	1.182e-07	361	2420
550	236.83	22379	39.84	1.200e-07	361	2420
555	236.51	22331	40.05	1.218e-07	361	2420
560	236.17	22281	40.06	1.238e-07	361	2420
565	235.81	22231	40.09	1.256e-07	362	2414
570	235.44	22180	40.12	1.276e-07	363	2414
575	235.05	22128	40.15	1.296e-07	364	2408
580	234.66	22076	40.17	1.318e-07	365	2408
585	234.25	22022	40.24	1.340e-07	366	2408
590	233.85	21968	40.22	1.363e-07	367	2402
595	233.44	21913	40.23	1.386e-07	368	2402
600	233.02	21858	40.26	1.411e-07	368	2408
605	232.60	21802	40.29	1.436e-07	370	2402
610	232.16	21744	40.31	1.462e-07	371	2402
615	231.71	21686	40.34	1.488e-07	372	2395
620	231.25	21627	40.36	1.517e-07	373	2395
625	230.78	21568	40.27	1.546e-07	374	2395
630	230.30	21507	40.32	1.576e-07	376	2395
635	229.83	21446	40.35	1.607e-07	377	2395
640	229.35	21383	40.36	1.639e-07	378	2395
645	228.86	21320	40.38	1.673e-07	379	2389
650	228.35	21255	40.39	1.708e-07	380	2389
655	227.82	21189	40.41	1.746e-07	381	2389
660	227.28	21123	40.42	1.786e-07	381	2383
665	226.73	21055	40.36	1.828e-07	382	2383
670	226.17	20986	40.36	1.872e-07	383	2383
675	225.60	20915	40.37	1.917e-07	384	2376
680	225.04	20843	40.21	1.963e-07	385	2376
685	224.49	20771	40.20	2.010e-07	386	2376
690	223.95	20698	40.22	2.056e-07	387	2376
695	223.41	20624	40.23	2.104e-07	387	2376
700	222.88	20548	40.24	2.152e-07	388	2376
705	222.34	20473	40.25	2.198e-07	390	2376
710	221.79	20395	40.31	2.245e-07	391	2376
715	221.23	20316	40.15	2.294e-07	393	2371
720	220.65	20235	40.15	2.346e-07	395	2376
725	220.05	20156	40.06	2.400e-07	396	2376
730	219.45	20069	40.25	2.450e-07	399	2370
735	218.84	19970	40.01	2.496e-07	402	2370
740	218.21	19869	40.14	2.543e-07	406	2370
745	217.58	19765	39.81	2.592e-07	410	2370
750	216.95	19660	39.76	2.642e-07	413	2370
755	216.30	19555	39.72	2.698e-07	416	2371
760	215.64	19461	39.88	2.771e-07	417	2370
765	214.97	19366	39.90	2.848e-07	418	2370
770	214.27	19269	39.73	2.929e-07	418	2364
775	213.57	19171	39.78	3.013e-07	419	2364
780	212.87	19071	39.66	3.099e-07	420	2364
785	212.17	18970	39.49	3.187e-07	421	2364
790	211.49	18868	39.40	3.275e-07	422	2364
795	210.82	18765	39.31	3.365e-07	423	2369
800	210.14	18662	39.49	3.457e-07	424	2364
805	209.45	18558	39.65	3.544e-07	425	2364
810	208.73	18453	39.80	3.630e-07	428	2364
815	207.99	18344	39.94	3.723e-07	430	2358
820	207.21	18232	39.87	3.823e-07	433	2357
825	206.40	18118	39.64	3.929e-07	436	2351
830	205.59	18003	39.49	4.040e-07	438	2350

STS-33 BET and Radiometer Data (continued)

time (sec)	h*10^{-3} (ft)	vel. (ft/sec)	α (°)	density (slug/ft^3)	T_∞ (°F)	IML temp (°F)
835	204.79	17887	39.57	4.154e-07	441	2350
840	203.98	17769	39.60	4.271e-07	443	2344
845	203.16	17649	39.62	4.396e-07	446	2338
850	202.32	17534	39.66	4.543e-07	446	2338
855	201.46	17416	39.83	4.699e-07	447	2337
860	200.57	17295	39.81	4.866e-07	447	2330
865	199.67	17171	39.76	5.042e-07	448	2330
870	198.76	17046	39.70	5.227e-07	448	2317
875	197.85	16919	39.72	5.419e-07	449	2323
880	196.93	16791	39.77	5.620e-07	449	2317
885	196.03	16654	40.15	5.830e-07	450	2310
890	195.29	16513	39.88	6.005e-07	450	2310
895	194.86	16373	39.90	6.111e-07	450	2303
900	194.73	16233	40.22	6.143e-07	450	2296
905	194.78	16093	40.71	6.133e-07	449	2289
910	194.77	15950	41.25	6.137e-07	449	2281
915	194.47	15807	41.85	6.212e-07	449	2267
920	193.80	15657	42.82	6.382e-07	449	2260
925	192.75	15500	43.33	6.655e-07	450	2238
930	191.40	15334	43.07	7.026e-07	450	2222
935	189.92	15167	42.63	7.452e-07	450	2199
940	188.50	14998	42.14	7.896e-07	451	2191
945	187.33	14829	41.35	8.281e-07	451	2183
950	186.51	14663	41.03	8.556e-07	451	2175
955	185.92	14498	40.60	8.746e-07	452	2167
960	185.39	14339	40.29	8.923e-07	453	2159
965	184.80	14180	40.50	9.123e-07	453	2158
970	184.11	14019	40.74	9.358e-07	454	2150
975	183.34	13856	40.85	9.639e-07	455	2134
980	182.50	13692	40.89	9.974e-07	455	2125
985	181.62	13527	40.78	1.033e-06	455	2116
990	180.75	13361	40.49	1.070e-06	455	2099
995	179.92	13195	40.18	1.107e-06	455	2082
1000	179.15	13032	39.94	1.142e-06	455	2073
1005	178.44	12869	39.83	1.175e-06	455	2063
1010	177.76	12707	39.73	1.208e-06	455	2054
1015	177.07	12545	39.75	1.242e-06	455	2045
1020	176.37	12385	39.82	1.272e-06	457	2036
1025	175.63	12223	39.86	1.303e-06	460	2017
1030	174.87	12061	39.77	1.336e-06	462	2008
1035	174.09	11898	39.70	1.371e-06	465	1997
1040	173.32	11735	39.49	1.406e-06	467	1978
1045	172.57	11572	39.34	1.440e-06	470	1968
1050	171.86	11411	39.22	1.474e-06	472	1958
1055	171.16	11251	39.26	1.508e-06	474	1929
1060	170.44	11092	39.31	1.543e-06	476	1928
1065	169.67	10932	39.42	1.584e-06	478	1907
1070	168.82	10773	39.51	1.629e-06	480	1897
1075	167.89	10613	39.55	1.679e-06	483	1881
1080	166.88	10452	39.59	1.737e-06	485	1875
1085	165.78	10288	39.55	1.800e-06	488	1854
1090	164.60	10125	39.55	1.870e-06	491	1832
1095	163.38	9959	39.59	1.952e-06	493	1832
1100	162.22	9795	39.27	2.046e-06	491	1820
1105	161.17	9635	39.02	2.136e-06	489	1798
1110	160.20	9477	38.66	2.215e-06	489	1785
1115	159.29	9321	38.29	2.277e-06	492	1772
1120	158.41	9169	37.94	2.339e-06	495	1758
1125	157.54	9020	37.79	2.401e-06	499	1744
1130	156.64	8873	37.63	2.468e-06	501	1729
1135	155.69	8730	37.59	2.542e-06	504	1715
1140	154.80	8585	37.42	2.613e-06	506	1700
1145	154.08	8442	37.19	2.673e-06	509	1685
1150	153.49	8303	37.11	2.730e-06	509	1684
1155	152.85	8169	37.01	2.796e-06	508	1668
1160	152.02	8035	37.40	2.883e-06	508	1639
1165	151.00	7900	37.11	2.995e-06	507	1636
1170	149.87	7771	36.48	3.144e-06	504	1621
1175	148.70	7646	36.18	3.312e-06	500	1604
1180	147.52	7520	35.39	3.490e-06	495	1604
1185	146.38	7402	34.55	3.679e-06	490	1569
1190	145.27	7288	33.96	3.876e-06	486	1569
1195	144.14	7175	33.42	4.084e-06	482	1550
1200	142.99	7064	32.85	4.313e-06	477	1550
1205	141.79	6954	32.22	4.564e-06	472	1516
1210	140.56	6847	31.70	4.838e-06	467	1531
1215	139.29	6739	31.32	5.144e-06	462	1527
1220	137.99	6632	30.88	5.479e-06	457	1531
1225	136.67	6518	30.29	5.833e-06	453	1531
1230	135.34	6401	29.71	6.207e-06	449	1535
1235	134.01	6285	29.21	6.605e-06	446	1550
1240	132.67	6166	28.77	7.024e-06	443	1550
1245	131.33	6047	28.32	7.472e-06	440	1535
1250	130.00	5934	27.81	7.922e-06	440	1531
1255	128.66	5823	27.39	8.386e-06	439	1516
1260	127.35	5714	26.80	8.894e-06	438	1512
1265	126.04	5613	26.29	9.489e-06	434	1512
1270	124.74	5511	25.59	1.011e-05	430	1492
1275	123.47	5409	24.89	1.075e-05	428	1492
1280	122.21	5308	24.50	1.140e-05	425	1471
1285	120.96	5208	24.08	1.210e-05	423	1471
1290	119.68	5103	23.78	1.287e-05	421	1450
1295	118.40	4999	23.49	1.371e-05	419	1445
1300	117.09	4895	23.10	1.460e-05	416	1428
1305	115.76	4792	22.75	1.557e-05	414	1405
1310	114.42	4690	22.31	1.662e-05	412	1386
1315	113.06	4590	21.95	1.779e-05	409	1386
1320	111.70	4489	21.47	1.906e-05	406	1356
1325	110.33	4394	20.97	2.033e-05	405	1336
1330	108.97	4301	20.64	2.164e-05	405	1351
1335	107.62	4207	20.38	2.305e-05	404	1310
1340	106.29	4111	19.82	2.462e-05	403	1304
1345	104.95	4018	19.32	2.628e-05	401	1277
1350	103.66	3923	19.22	2.798e-05	399	1275
1355	102.55	3828	18.82	2.953e-05	398	1246
1360	101.64	3734	18.42	3.087e-05	396	1244
1365	100.76	3645	17.97	3.217e-05	396	1214
1370	99.82	3559	17.91	3.362e-05	395	1183
1375	98.80	3473	17.80	3.526e-05	395	1181
1380	97.71	3389	17.50	3.707e-05	395	1148
1385	96.55	3308	17.22	3.899e-05	396	1146
1390	95.34	3227	16.80	4.108e-05	398	1146

STS-33 BET and Radiometer Data (concluded)

time (sec)	$h*10^{-3}$ (ft)	vel. (ft/sec)	α (°)	density ($slug/ft^3$)	T_∞ (°F)	IML temp (°F)
1395	94.12	3145	16.46	4.343e-05	398	1108
1400	92.88	3063	16.13	4.600e-05	397	1106
1405	91.63	2981	15.95	4.874e-05	397	1106
1410	90.39	2897	15.57	5.176e-05	396	1067
1415	89.14	2814	15.23	5.498e-05	395	1067
1420	87.87	2733	15.07	5.844e-05	394	1023
1425	86.60	2651	14.86	6.215e-05	393	1023
1430	85.32	2570	14.58	6.613e-05	392	977
1435	84.02	2489	14.26	7.050e-05	391	974
1440	82.74	2407	13.83	7.515e-05	390	974
1445	81.56	2326	13.99	7.968e-05	388	923
1450	80.53	2239	13.93	8.379e-05	388	923
1455	79.63	2154	13.45	8.752e-05	387	920
1460	78.85	2070	13.63	9.095e-05	387	920
1465	78.15	1989	12.84	9.419e-05	386	920
1470	77.47	1916	11.80	9.749e-05	385	920
1475	76.73	1850	11.01	1.012e-04	385	859
1480	75.89	1788	10.59	1.056e-04	384	859
1485	74.91	1730	10.34	1.109e-04	383	859
1490	73.81	1677	10.23	1.173e-04	382	859
1495	72.58	1624	10.14	1.249e-04	381	791
1500	71.25	1573	10.06	1.335e-04	380	856
1505	69.84	1522	9.98	1.434e-04	380	859
1510	68.38	1470	9.86	1.543e-04	379	787
1515	66.90	1420	9.50	1.663e-04	378	787
1520	65.39	1371	9.13	1.793e-04	377	787
1525	63.88	1319	8.87	1.935e-04	376	787
1530	62.36	1269	8.62	2.088e-04	376	787
1535	60.84	1218	9.64	2.250e-04	376	787
1540	59.41	1160	10.51	2.414e-04	376	704
1545	58.16	1100	11.05	2.564e-04	376	701
1550	57.10	1042	10.51	2.695e-04	377	704
1555	56.17	987	10.52	2.815e-04	378	784
1560	55.31	937	9.84	2.929e-04	379	704
1565	54.45	895	9.80	3.049e-04	379	701
1570	53.55	862	11.74	3.181e-04	380	701
1575	52.61	833	11.80	3.324e-04	380	696
1580	51.50	816	12.04	3.498e-04	381	701
1585	50.17	814	12.80	3.712e-04	383	701
1590	48.65	816	11.67	3.977e-04	385	593
1595	46.92	826	12.60	4.328e-04	384	593
1600	44.99	821	12.37	4.736e-04	385	696
1605	42.96	831	10.95	5.220e-04	386	589
1610	40.89	827	10.40	5.737e-04	388	589
1615	38.89	837	8.94	6.322e-04	388	701
1620	37.07	820	8.63	6.860e-04	390	589
1625	35.51	788	7.65	7.316e-04	394	589
1630	34.17	759	7.07	7.739e-04	397	428
1635	32.99	730	7.00	8.126e-04	400	589
1640	31.90	716	7.34	8.452e-04	404	589
1645	30.85	702	7.14	8.776e-04	409	582
1650	29.83	671	8.32	9.093e-04	413	428
1655	28.91	643	8.37	9.428e-04	416	589
1660	28.06	641	8.35	9.695e-04	420	589
1665	27.23	640	7.86	9.964e-04	424	589
1670	26.41	639	7.85	1.024e-03	427	589
1675	25.59	637	7.78	1.052e-03	431	589
1680	24.79	635	7.48	1.083e-03	434	589
1685	23.99	635	7.24	1.114e-03	437	589
1690	23.19	626	7.14	1.144e-03	440	589
1695	22.37	617	7.33	1.177e-03	443	589
1700	21.54	617	6.95	1.210e-03	446	589
1705	20.70	621	6.73	1.242e-03	450	589
1710	19.84	622	7.00	1.275e-03	454	610
1715	18.96	624	6.54	1.309e-03	458	592
1720	18.06	619	6.34	1.346e-03	462	592
1725	17.11	616	6.69	1.387e-03	466	589
1730	16.13	608	6.74	1.432e-03	469	592
1735	15.14	609	6.05	1.475e-03	474	701
1740	14.15	609	5.30	1.519e-03	478	697
1745	13.18	603	4.33	1.563e-03	482	701
1750	12.20	612	4.41	1.611e-03	486	701

STS-31 BET and Radiometer Data

time (sec)	$h*10^{-3}$ (ft)	vel. (ft/sec)	α (°)	density ($slug/ft^3$)	T_∞ (°F)	IML temp (°F)
0	399.90	24749	40.86	3.834e-11	716	-460
5	396.33	24749	40.90	4.245e-11	690	-460
10	392.79	24749	40.72	4.823e-11	664	-460
15	389.27	24752	40.55	5.491e-11	640	-460
20	385.77	24756	40.43	6.284e-11	615	-460
25	382.30	24759	40.35	7.211e-11	592	-460
30	378.85	24759	40.32	8.201e-11	570	-460
35	375.43	24761	40.32	9.205e-11	549	-460
40	372.04	24769	40.36	9.874e-11	530	-460
45	368.67	24775	40.44	1.099e-10	511	-460
50	365.33	24781	40.55	1.284e-10	493	-460
55	362.02	24786	40.69	1.509e-10	475	-460
60	358.73	24790	41.05	1.779e-10	457	-460
65	355.46	24795	41.13	2.098e-10	442	-460
70	352.23	24799	41.02	2.472e-10	429	-460
75	349.02	24803	40.89	2.936e-10	415	-460
80	345.84	24807	40.81	3.485e-10	401	-460
85	342.69	24800	40.76	4.134e-10	391	-460
90	339.56	24794	40.74	4.898e-10	381	-460
95	336.47	24790	40.77	5.814e-10	373	-460
100	333.40	24787	40.83	6.903e-10	365	-460
105	330.36	24787	40.95	8.245e-10	356	-460
110	327.35	24783	40.92	9.804e-10	349	-460
115	324.38	24766	40.75	1.152e-09	347	-460
120	321.43	24753	40.59	1.356e-09	344	-460
125	318.52	24768	40.63	1.620e-09	338	-460
130	315.64	24785	40.88	1.932e-09	333	-122
135	312.80	24802	41.00	2.299e-09	327	68
140	309.99	24821	40.95	2.729e-09	321	406
145	307.21	24840	40.83	3.233e-09	316	569
150	304.48	24857	40.85	3.806e-09	312	569
155	301.78	24858	40.85	4.405e-09	315	612
160	299.13	24859	40.86	4.996e-09	323	731
165	296.52	24859	40.87	5.655e-09	330	807
170	293.95	24859	40.86	6.352e-09	337	895
175	291.43	24858	40.91	7.081e-09	346	948
180	288.95	24856	40.86	7.878e-09	354	1039
185	286.53	24854	40.83	8.777e-09	359	1102
190	284.17	24851	40.90	9.760e-09	364	1171
195	281.86	24847	40.52	1.085e-08	367	1244
200	279.61	24843	39.56	1.224e-08	364	1298
205	277.42	24838	38.95	1.376e-08	361	1375
210	275.31	24835	39.25	1.545e-08	358	1428
215	273.26	24847	40.09	1.750e-08	351	1487
220	271.29	24858	40.73	1.976e-08	345	1549
225	269.40	24866	40.33	2.223e-08	338	1599
230	267.60	24869	39.50	2.471e-08	335	1646
235	265.89	24869	39.21	2.724e-08	334	1698
240	264.30	24865	39.64	2.981e-08	333	1746
245	262.81	24857	40.59	3.240e-08	332	1790
250	261.45	24844	41.35	3.483e-08	332	1837
255	260.23	24827	40.42	3.712e-08	333	1871
260	259.13	24810	39.53	3.928e-08	334	1914
265	258.18	24790	40.34	4.126e-08	335	1955
270	257.36	24767	40.82	4.305e-08	336	1988
275	256.65	24744	39.76	4.466e-08	336	2026
280	256.05	24721	39.17	4.611e-08	336	2053
285	255.51	24696	39.60	4.743e-08	337	2079
290	255.01	24669	40.68	4.867e-08	337	2100
295	254.55	24640	41.02	4.986e-08	337	2113
300	254.11	24611	40.09	5.100e-08	338	2129
305	253.70	24583	39.65	5.209e-08	338	2145
310	253.31	24554	40.07	5.315e-08	338	2161
315	252.94	24525	40.26	5.419e-08	339	2176
320	252.59	24496	40.03	5.520e-08	339	2187
325	252.24	24466	39.89	5.620e-08	339	2199
330	251.90	24436	40.03	5.721e-08	339	2206
335	251.56	24404	40.13	5.821e-08	339	2221
340	251.23	24372	40.07	5.922e-08	340	2228
345	250.90	24340	39.97	6.024e-08	340	2239
350	250.58	24307	39.98	6.127e-08	340	2246
355	250.25	24273	40.07	6.232e-08	340	2257
360	249.93	24239	40.11	6.338e-08	341	2257
365	249.61	24204	40.00	6.443e-08	341	2271
370	249.30	24169	39.96	6.547e-08	341	2277
375	249.00	24133	39.95	6.652e-08	341	2287
380	248.71	24097	39.95	6.757e-08	341	2298
385	248.42	24061	39.98	6.863e-08	341	2304
390	248.12	24023	39.99	6.971e-08	341	2304
395	247.82	23985	39.96	7.081e-08	341	2318
400	247.52	23946	39.93	7.196e-08	341	2318
405	247.21	23907	39.94	7.313e-08	341	2324
410	246.90	23867	39.98	7.434e-08	341	2331
415	246.59	23827	39.96	7.556e-08	342	2337
420	246.29	23786	39.97	7.679e-08	342	2343
425	245.99	23744	39.93	7.801e-08	342	2350
430	245.69	23703	39.84	7.922e-08	342	2350
435	245.41	23661	39.86	8.041e-08	342	2356
440	245.13	23618	39.85	8.158e-08	342	2362
445	244.86	23576	39.72	8.274e-08	342	2366
450	244.59	23533	39.73	8.392e-08	342	2375
455	244.31	23491	39.72	8.515e-08	343	2375
460	244.03	23448	39.72	8.642e-08	343	2377
465	243.73	23405	39.82	8.777e-08	343	2381
470	243.42	23362	39.86	8.919e-08	343	2381
475	243.09	23318	39.85	9.070e-08	343	2385
480	242.76	23273	39.87	9.228e-08	344	2383
485	242.42	23228	40.02	9.378e-08	344	2387
490	242.07	23181	40.06	9.530e-08	345	2387
495	241.72	23134	40.08	9.685e-08	346	2387
500	241.37	23085	39.96	9.841e-08	346	2389
505	241.03	23036	39.70	9.998e-08	347	2391
510	240.70	22989	39.52	1.015e-07	348	2393
515	240.37	22941	39.62	1.031e-07	349	2399
520	240.04	22892	39.81	1.047e-07	349	2405
525	239.72	22843	39.81	1.062e-07	350	2405
530	239.40	22793	39.83	1.078e-07	351	2403
535	239.08	22741	39.83	1.095e-07	351	2401
540	238.75	22688	39.47	1.111e-07	352	2399
545	238.43	22636	39.13	1.128e-07	353	2399
550	238.11	22584	39.03	1.145e-07	353	2399
555	237.80	22531	39.04	1.161e-07	354	2399

STS-31 BET and Radiometer Data (continued)

time (sec)	h*10^{-3} (ft)	vel. (ft/sec)	α (°)	density (slug/ft^3)	T_∞ (°F)	IML temp (°F)
560	237.50	22479	39.04	1.178e-07	355	2399
565	237.21	22427	39.39	1.194e-07	355	2399
570	236.92	22373	39.50	1.210e-07	356	2399
575	236.62	22318	39.53	1.227e-07	356	2393
580	236.31	22264	39.55	1.245e-07	357	2393
585	235.98	22209	39.79	1.264e-07	358	2389
590	235.64	22153	39.77	1.286e-07	358	2383
595	235.27	22096	39.81	1.309e-07	358	2381
600	234.88	22039	39.82	1.334e-07	358	2381
605	234.47	21980	39.86	1.361e-07	359	2375
610	234.06	21920	39.85	1.389e-07	359	2375
615	233.63	21860	39.85	1.419e-07	359	2369
620	233.20	21799	39.87	1.449e-07	360	2369
625	232.78	21736	39.75	1.479e-07	360	2362
630	232.36	21673	39.45	1.508e-07	360	2365
635	231.96	21611	39.46	1.536e-07	361	2366
640	231.56	21547	39.47	1.565e-07	362	2366
645	231.16	21482	39.49	1.593e-07	362	2362
650	230.76	21417	39.49	1.623e-07	363	2366
655	230.34	21352	39.51	1.654e-07	364	2362
660	229.91	21286	39.53	1.687e-07	365	2362
665	229.46	21218	39.55	1.721e-07	366	2362
670	229.01	21150	39.56	1.756e-07	367	2356
675	228.54	21079	40.01	1.793e-07	368	2356
680	228.08	21010	38.58	1.830e-07	368	2356
685	227.61	20941	39.10	1.869e-07	369	2356
690	227.13	20870	39.48	1.908e-07	370	2356
695	226.66	20798	39.48	1.948e-07	371	2356
700	226.18	20725	39.57	1.990e-07	372	2356
705	225.70	20650	39.62	2.032e-07	373	2350
710	225.22	20575	39.62	2.075e-07	374	2350
715	224.75	20500	39.65	2.118e-07	375	2350
720	224.27	20423	39.67	2.161e-07	376	2347
725	223.80	20346	39.83	2.207e-07	377	2346
730	223.31	20267	40.19	2.254e-07	378	2341
735	222.81	20185	40.21	2.302e-07	379	2341
740	222.30	20105	40.17	2.347e-07	381	2337
745	221.75	20022	40.15	2.395e-07	383	2333
750	221.18	19939	40.14	2.447e-07	386	2331
755	220.58	19855	40.13	2.502e-07	388	2331
760	219.96	19770	40.15	2.561e-07	390	2324
765	219.31	19685	40.16	2.622e-07	393	2324
770	218.65	19603	40.17	2.683e-07	396	2320
775	217.99	19520	40.18	2.746e-07	399	2318
780	217.33	19435	40.18	2.810e-07	402	2318
785	216.67	19348	40.09	2.876e-07	404	2318
790	216.01	19259	40.09	2.945e-07	407	2315
795	215.35	19165	40.11	3.017e-07	409	2318
800	214.68	19068	40.09	3.093e-07	411	2318
805	213.98	18968	39.99	3.172e-07	413	2313
810	213.30	18866	39.85	3.252e-07	415	2313
815	212.64	18763	40.86	3.331e-07	417	2307
820	212.03	18660	39.33	3.406e-07	419	2311
825	211.47	18555	39.88	3.477e-07	421	2311
830	210.91	18449	39.75	3.549e-07	423	2311
835	210.31	18342	39.99	3.627e-07	425	2313
840	209.66	18232	40.21	3.716e-07	426	2311
845	208.96	18122	40.37	3.817e-07	428	2307
850	208.20	18009	40.50	3.930e-07	429	2302
855	207.41	17893	40.49	4.052e-07	430	2298
860	206.57	17776	40.46	4.185e-07	432	2289
865	205.70	17656	40.47	4.327e-07	433	2291
870	204.80	17534	40.49	4.480e-07	435	2284
875	203.87	17410	40.47	4.643e-07	436	2282
880	202.93	17282	40.45	4.817e-07	438	2277
885	201.97	17152	40.26	5.003e-07	439	2271
890	201.01	17019	39.98	5.194e-07	440	2266
895	200.08	16884	39.70	5.388e-07	440	2271
900	199.19	16747	39.54	5.580e-07	441	2264
905	198.35	16609	39.44	5.768e-07	442	2264
910	197.55	16468	39.36	5.952e-07	443	2264
915	196.78	16326	39.28	6.136e-07	444	2257
920	196.01	16184	39.38	6.325e-07	445	2257
925	195.22	16039	39.47	6.524e-07	445	2252
930	194.41	15892	39.64	6.737e-07	446	2245
935	193.64	15741	39.89	6.948e-07	446	2238
940	193.09	15587	39.93	7.101e-07	447	2228
945	192.90	15431	40.21	7.157e-07	447	2223
950	193.02	15275	40.70	7.121e-07	447	2214
955	193.28	15119	41.40	7.047e-07	446	2209
960	193.38	14963	41.88	7.018e-07	446	2191
965	193.12	14807	42.48	7.090e-07	447	2176
970	192.48	14649	43.18	7.278e-07	447	2161
975	191.51	14486	43.10	7.569e-07	447	2140
980	190.40	14322	42.73	7.918e-07	447	2121
985	189.30	14153	42.38	8.265e-07	448	2104
990	188.28	13983	42.06	8.597e-07	449	2090
995	187.35	13813	41.88	8.912e-07	450	2079
1000	186.46	13646	41.54	9.217e-07	451	2064
1005	185.61	13480	41.20	9.517e-07	453	2055
1010	184.78	13317	41.26	9.820e-07	454	2047
1015	183.95	13154	41.11	1.013e-06	455	2035
1020	183.10	12992	40.98	1.045e-06	456	2026
1025	182.24	12832	40.99	1.076e-06	458	2017
1030	181.35	12672	40.84	1.109e-06	461	2007
1035	180.46	12511	40.70	1.144e-06	463	1998
1040	179.58	12350	40.59	1.179e-06	465	1988
1045	178.73	12190	40.51	1.214e-06	467	1972
1050	177.90	12030	40.52	1.249e-06	469	1959
1055	177.09	11869	40.54	1.284e-06	471	1949
1060	176.27	11702	40.42	1.322e-06	472	1932
1065	175.44	11533	40.38	1.363e-06	473	1922
1070	174.57	11363	40.28	1.407e-06	474	1901
1075	173.68	11192	40.07	1.453e-06	475	1887
1080	172.78	11025	39.91	1.505e-06	475	1868
1085	171.87	10858	39.69	1.561e-06	475	1865
1090	170.95	10692	39.48	1.619e-06	474	1842
1095	170.00	10529	39.43	1.681e-06	474	1830
1100	169.02	10369	39.43	1.748e-06	473	1818
1105	167.99	10207	39.37	1.821e-06	473	1807
1110	167.00	10046	38.63	1.895e-06	472	1794
1115	166.09	9885	38.49	1.964e-06	472	1782

STS-31 BET and Radiometer Data (continued)

time (sec)	h*10^{-3} (ft)	vel. (ft/sec)	α (°)	density (slug/ft^3)	T_∞ (°F)	IML temp (°F)
1120	165.27	9724	38.18	2.029e-06	472	1773
1125	164.47	9569	38.55	2.095e-06	472	1757
1130	163.67	9414	37.46	2.162e-06	471	1757
1135	162.87	9265	37.63	2.231e-06	471	1744
1140	162.06	9118	37.20	2.303e-06	471	1730
1145	161.23	8987	36.57	2.379e-06	471	1730
1150	160.41	8820	39.14	2.457e-06	471	1730
1155	159.66	8660	37.34	2.533e-06	470	1721
1160	159.04	8518	35.85	2.597e-06	470	1730
1165	158.57	8382	36.37	2.648e-06	470	1730
1170	158.11	8244	36.44	2.698e-06	469	1726
1175	157.49	8109	36.55	2.767e-06	469	1717
1180	156.73	7969	36.78	2.847e-06	470	1713
1185	156.02	7832	36.25	2.921e-06	470	1703
1190	155.42	7700	35.76	2.985e-06	471	1689
1195	154.83	7573	35.08	3.049e-06	472	1689
1200	154.03	7453	34.25	3.139e-06	473	1675
1205	152.87	7334	34.05	3.280e-06	474	1660
1210	151.37	7214	33.87	3.474e-06	474	1660
1215	149.61	7093	33.51	3.719e-06	474	1646
1220	147.72	6972	33.12	4.003e-06	474	1630
1225	145.81	6852	32.87	4.318e-06	474	1615
1230	143.95	6731	32.48	4.648e-06	473	1604
1235	142.21	6609	32.05	4.982e-06	472	1599
1240	140.59	6488	31.59	5.312e-06	472	1599
1245	139.09	6373	31.08	5.630e-06	472	1583
1250	137.70	6257	30.29	5.942e-06	472	1566
1255	136.40	6142	29.57	6.291e-06	470	1549
1260	135.12	6030	29.18	6.660e-06	467	1549
1265	133.81	5918	28.95	7.057e-06	464	1537
1270	132.46	5806	28.63	7.489e-06	461	1531
1275	131.09	5695	28.41	7.959e-06	458	1513
1280	129.74	5585	27.18	8.447e-06	456	1513
1285	128.42	5479	27.52	8.954e-06	454	1495
1290	127.08	5375	26.66	9.482e-06	453	1476
1295	125.71	5272	26.32	1.004e-05	452	1456
1300	124.29	5171	25.77	1.066e-05	452	1448
1305	122.85	5071	25.04	1.135e-05	450	1436
1310	121.39	4973	24.52	1.210e-05	448	1436
1315	119.94	4874	24.10	1.297e-05	444	1415
1320	118.49	4774	23.78	1.393e-05	440	1400
1325	117.03	4675	23.34	1.496e-05	436	1393
1330	115.56	4576	23.17	1.606e-05	431	1371
1335	114.10	4478	22.56	1.723e-05	428	1371
1340	112.65	4383	22.03	1.841e-05	426	1330
1345	111.20	4290	21.52	1.968e-05	425	1323
1350	109.77	4194	21.61	2.095e-05	425	1298
1355	108.37	4102	20.49	2.228e-05	425	1279
1360	106.96	4012	20.04	2.373e-05	424	1252
1365	105.53	3922	19.67	2.529e-05	424	1244
1370	104.09	3833	19.41	2.698e-05	423	1223
1375	102.65	3743	19.10	2.879e-05	422	1214
1380	101.20	3654	18.61	3.074e-05	421	1214
1385	99.79	3565	18.17	3.289e-05	419	1184
1390	98.52	3475	17.46	3.495e-05	417	1151
1395	97.43	3384	16.82	3.676e-05	416	1151
1400	96.42	3294	16.41	3.852e-05	416	1151
1405	95.38	3206	16.38	4.041e-05	415	1116
1410	94.29	3119	16.30	4.253e-05	414	1105
1415	93.14	3031	16.15	4.490e-05	413	1079
1420	91.94	2945	15.88	4.752e-05	412	1079
1425	90.69	2861	15.74	5.054e-05	410	1079
1430	89.39	2777	15.84	5.393e-05	408	1039
1435	88.04	2692	14.98	5.769e-05	405	1009
1440	86.64	2613	14.85	6.187e-05	403	996
1445	85.22	2534	14.43	6.641e-05	400	996
1450	83.81	2452	14.65	7.116e-05	399	996
1455	82.49	2368	14.14	7.590e-05	398	962
1460	81.33	2283	14.04	8.028e-05	397	948
1465	80.34	2198	13.70	8.423e-05	396	948
1470	79.48	2113	13.54	8.779e-05	396	948
1475	78.74	2031	12.90	9.102e-05	395	911
1480	78.04	1955	11.76	9.429e-05	395	948
1485	77.29	1887	10.88	9.799e-05	395	895
1490	76.44	1825	10.43	1.024e-04	394	895
1495	75.46	1767	10.11	1.077e-04	393	895
1500	74.34	1711	9.99	1.141e-04	392	895
1505	73.11	1657	10.02	1.216e-04	392	877
1510	71.77	1603	9.92	1.303e-04	391	834
1515	70.37	1549	9.94	1.397e-04	390	834
1520	68.91	1494	10.08	1.502e-04	389	834
1525	67.44	1444	9.62	1.615e-04	388	834
1530	65.95	1396	9.17	1.738e-04	387	764
1535	64.44	1342	8.87	1.878e-04	385	813
1540	62.93	1288	8.91	2.032e-04	383	764
1545	61.42	1237	8.75	2.197e-04	382	764
1550	59.93	1190	8.43	2.370e-04	380	764
1555	58.47	1141	8.24	2.555e-04	379	764
1560	57.04	1084	8.47	2.758e-04	377	705
1565	55.66	1030	8.58	2.968e-04	375	679
1570	54.32	974	8.41	3.159e-04	376	705
1575	53.00	926	8.16	3.360e-04	378	739
1580	51.64	896	8.33	3.578e-04	379	679
1585	50.24	902	7.76	3.809e-04	382	679
1590	48.85	901	7.68	4.053e-04	384	679
1595	47.51	882	7.81	4.325e-04	384	679
1600	46.18	872	6.77	4.618e-04	383	679
1605	44.78	859	6.97	4.939e-04	384	679
1610	43.36	842	7.28	5.285e-04	384	602
1615	41.95	842	6.54	5.649e-04	385	646
1620	40.53	848	5.75	6.038e-04	386	569
1625	39.11	845	5.49	6.452e-04	387	602
1630	37.71	824	5.10	6.827e-04	391	602
1635	36.32	811	4.66	7.168e-04	398	602
1640	34.91	787	5.68	7.482e-04	407	569
1645	33.47	772	6.60	7.860e-04	413	569
1650	31.94	755	6.87	8.303e-04	419	569
1655	30.39	741	7.32	8.720e-04	427	569
1660	28.83	719	8.03	9.183e-04	434	569
1665	27.30	710	7.36	9.645e-04	441	569
1670	25.86	692	7.46	1.012e-03	447	569
1675	24.57	682	7.10	1.057e-03	451	569

STS-31 BET and Radiometer Data (concluded)

time (sec)	$h*10^{-3}$ (ft)	vel. (ft/sec)	α (°)	density ($slug/ft^3$)	T_∞ (°F)	IML temp (°F)
1680	23.43	664	7.09	1.097e-03	456	569
1685	22.47	641	7.34	1.131e-03	460	569
1690	21.64	621	8.13	1.161e-03	463	569
1695	20.92	607	8.18	1.191e-03	465	569
1700	20.29	596	7.00	1.217e-03	466	646
1705	19.64	592	6.38	1.245e-03	468	569
1710	18.87	595	6.47	1.277e-03	470	602
1715	18.02	596	7.30	1.310e-03	474	569
1720	17.14	598	7.06	1.345e-03	478	569
1725	16.27	602	6.39	1.380e-03	482	569
1730	15.38	606	6.09	1.422e-03	487	569
1735	14.47	608	5.50	1.465e-03	492	602
1740	13.52	607	4.86	1.492e-03	495	569
1745	12.52	609	5.28	1.544e-03	497	569
1750	11.49	606	5.67	1.599e-03	498	602

STS-41 BET and Radiometer Data

time (sec)	$h*10^{-3}$ (ft)	vel. (ft/sec)	α (°)	density ($slug/ft^3$)	T_∞ (°F)	IML temp (°F)
0	408.03	24391	41.01	4.616e-11	724	-460
5	405.42	24394	41.01	4.618e-11	724	-460
10	402.82	24398	40.98	4.620e-11	724	-460
15	400.22	24401	40.94	4.622e-11	724	-460
20	397.63	24424	40.90	5.036e-11	706	-36
25	395.04	24428	40.91	5.536e-11	687	-460
30	392.45	24432	40.92	6.107e-11	667	-460
35	389.86	24435	40.91	6.753e-11	648	-460
40	387.28	24438	40.75	7.477e-11	629	-460
45	384.70	24441	40.67	8.315e-11	611	-460
50	382.13	24445	40.66	9.243e-11	592	-460
55	379.55	24449	40.75	1.030e-10	577	-460
60	376.99	24452	40.90	1.148e-10	561	-460
65	374.42	24454	41.07	1.281e-10	547	-460
70	371.86	24453	41.03	1.432e-10	533	-11
75	369.30	24452	40.92	1.603e-10	520	-460
80	366.75	24451	40.89	1.803e-10	506	-460
85	364.20	24450	40.90	2.027e-10	493	-460
90	361.66	24443	40.93	2.286e-10	481	-460
95	359.12	24434	40.98	2.578e-10	470	-460
100	356.58	24424	40.93	2.907e-10	460	-460
105	354.05	24413	40.87	3.278e-10	451	-460
110	351.53	24400	40.86	3.699e-10	443	-460
115	349.01	24393	40.83	4.197e-10	434	-460
120	346.49	24386	40.83	4.761e-10	425	-460
125	343.98	24367	40.80	5.392e-10	418	-460
130	341.48	24343	40.78	6.102e-10	412	-460
135	338.98	24321	40.76	6.906e-10	406	-460
140	336.49	24304	40.70	7.817e-10	402	-460
145	334.00	24286	40.60	8.844e-10	397	-460
150	331.52	24280	40.44	1.005e-09	392	-460
155	329.05	24275	40.20	1.141e-09	387	-28
160	326.59	24258	39.89	1.292e-09	384	-460
165	324.14	24227	39.51	1.461e-09	381	-460
170	321.70	24198	39.32	1.651e-09	379	-10
175	319.26	24193	39.38	1.872e-09	377	422
180	316.84	24190	39.43	2.121e-09	374	422
185	314.42	24187	39.83	2.401e-09	372	505
190	312.02	24185	40.18	2.717e-09	369	645
195	309.63	24182	40.47	3.073e-09	367	701
200	307.25	24192	40.69	3.472e-09	365	787
205	304.89	24218	40.87	3.921e-09	364	787
210	302.54	24247	40.98	4.424e-09	362	889
215	300.20	24278	40.99	4.991e-09	361	947
220	297.89	24310	41.00	5.626e-09	360	974
225	295.59	24342	40.98	6.336e-09	359	1067
230	293.31	24360	41.02	7.111e-09	358	1127
235	291.05	24374	40.80	7.968e-09	358	1181
240	288.82	24388	40.57	8.917e-09	358	1246
245	286.61	24398	40.23	9.968e-09	358	1290
250	284.42	24408	39.86	1.113e-08	358	1356
255	282.27	24418	39.51	1.240e-08	358	1416
260	280.15	24424	39.54	1.378e-08	359	1461
265	278.07	24430	40.38	1.528e-08	360	1522
270	276.02	24434	41.36	1.691e-08	360	1578

STS-41 BET and Radiometer Data (continued)

time (sec)	$h*10^{-3}$ (ft)	vel. (ft/sec)	α (°)	density ($slug/ft^3$)	T_∞ (°F)	IML temp (°F)
275	274.03	24437	41.45	1.864e-08	361	1629
280	272.08	24439	40.82	2.050e-08	362	1677
285	270.20	24440	39.54	2.252e-08	362	1729
290	268.38	24440	38.96	2.465e-08	362	1778
295	266.63	24436	39.52	2.690e-08	362	1832
300	264.96	24429	40.74	2.924e-08	362	1881
305	263.38	24419	41.22	3.163e-08	362	1923
310	261.89	24406	40.04	3.408e-08	362	1973
315	260.50	24389	39.28	3.659e-08	362	2012
320	259.22	24371	39.83	3.907e-08	361	2054
325	258.04	24350	41.01	4.148e-08	361	2094
330	256.98	24326	41.48	4.379e-08	360	2121
335	256.03	24301	40.57	4.594e-08	360	2158
340	255.20	24276	39.37	4.797e-08	359	2187
345	254.45	24250	39.57	4.985e-08	359	2218
350	253.78	24223	40.03	5.161e-08	358	2249
355	253.16	24195	39.83	5.329e-08	358	2263
360	252.59	24167	39.86	5.489e-08	358	2285
365	252.05	24138	40.49	5.643e-08	357	2299
370	251.54	24106	40.86	5.792e-08	357	2317
375	251.06	24074	40.14	5.937e-08	357	2327
380	250.61	24042	39.77	6.077e-08	356	2344
385	250.18	24011	40.05	6.212e-08	356	2357
390	249.77	23978	40.21	6.345e-08	356	2373
395	249.37	23945	40.09	6.476e-08	356	2383
400	248.98	23914	40.01	6.617e-08	355	2389
405	248.60	23882	40.09	6.762e-08	354	2399
410	248.23	23848	40.13	6.906e-08	353	2405
415	247.87	23814	40.09	7.050e-08	352	2414
420	247.52	23779	40.11	7.193e-08	352	2420
425	247.18	23743	40.12	7.334e-08	351	2429
430	246.84	23707	40.12	7.475e-08	350	2438
435	246.52	23671	40.14	7.615e-08	349	2444
440	246.20	23634	40.27	7.754e-08	349	2453
445	245.88	23596	40.75	7.895e-08	348	2462
450	245.56	23557	40.69	8.039e-08	347	2464
455	245.24	23518	40.54	8.186e-08	347	2467
460	244.92	23478	40.36	8.338e-08	346	2473
465	244.59	23439	40.33	8.495e-08	345	2479
470	244.26	23401	40.55	8.657e-08	344	2484
475	243.92	23361	40.72	8.824e-08	344	2490
480	243.58	23319	40.69	8.995e-08	343	2490
485	243.24	23277	40.36	9.170e-08	342	2490
490	242.90	23234	40.02	9.349e-08	342	2496
495	242.56	23191	39.67	9.521e-08	341	2501
500	242.23	23146	39.40	9.665e-08	342	2507
505	241.91	23102	39.27	9.806e-08	342	2512
510	241.60	23058	39.24	9.941e-08	343	2520
515	241.31	23013	39.28	1.007e-07	344	2523
520	241.04	22968	39.31	1.019e-07	344	2532
525	240.79	22922	39.35	1.030e-07	345	2534
530	240.55	22876	39.35	1.041e-07	345	2539
535	240.32	22830	39.34	1.052e-07	346	2544
540	240.10	22783	39.37	1.063e-07	346	2547
545	239.87	22736	39.38	1.073e-07	346	2549
550	239.63	22689	39.42	1.085e-07	347	2549
555	239.38	22642	39.44	1.097e-07	347	2549
560	239.13	22594	39.45	1.109e-07	348	2549
565	238.86	22547	39.48	1.122e-07	348	2552
570	238.59	22498	39.52	1.136e-07	349	2555
575	238.31	22450	39.63	1.150e-07	350	2555
580	238.03	22400	39.76	1.165e-07	350	2555
585	237.75	22350	39.78	1.180e-07	351	2557
590	237.45	22300	39.82	1.195e-07	351	2555
595	237.14	22249	40.03	1.212e-07	352	2557
600	236.81	22198	40.05	1.230e-07	352	2557
605	236.46	22146	40.08	1.250e-07	353	2555
610	236.09	22094	40.30	1.271e-07	354	2555
615	235.71	22038	40.30	1.294e-07	354	2549
620	235.32	21979	40.26	1.318e-07	355	2549
625	234.93	21921	39.87	1.342e-07	355	2549
630	234.55	21864	39.93	1.367e-07	355	2547
635	234.16	21806	40.20	1.392e-07	355	2549
640	233.76	21747	40.43	1.418e-07	356	2549
645	233.35	21688	40.44	1.446e-07	356	2547
650	232.92	21627	40.46	1.476e-07	357	2544
655	232.47	21565	40.45	1.508e-07	357	2544
660	232.00	21501	40.18	1.541e-07	358	2539
665	231.53	21438	40.13	1.576e-07	358	2539
670	231.05	21374	40.04	1.612e-07	359	2539
675	230.56	21309	40.07	1.648e-07	359	2539
680	230.08	21242	39.92	1.686e-07	360	2536
685	229.61	21176	39.96	1.724e-07	360	2536
690	229.13	21109	39.96	1.758e-07	362	2536
695	228.65	21043	39.98	1.791e-07	363	2539
700	228.16	20976	39.99	1.825e-07	365	2536
705	227.66	20908	40.02	1.861e-07	367	2534
710	227.15	20840	40.04	1.898e-07	368	2534
715	226.63	20770	40.06	1.937e-07	370	2531
720	226.10	20700	40.07	1.976e-07	372	2528
725	225.57	20632	40.11	2.006e-07	376	2526
730	225.04	20563	40.14	2.036e-07	380	2525
735	224.50	20493	40.16	2.066e-07	384	2523
740	223.97	20423	40.19	2.097e-07	388	2523
745	223.44	20350	40.04	2.128e-07	392	2523
750	222.90	20277	39.90	2.160e-07	396	2518
755	222.36	20205	39.95	2.194e-07	399	2517
760	221.81	20132	39.82	2.228e-07	403	2518
765	221.27	20058	39.55	2.263e-07	406	2512
770	220.72	19983	39.49	2.298e-07	409	2518
775	220.19	19906	39.32	2.334e-07	413	2515
780	219.67	19830	39.12	2.369e-07	416	2515
785	219.17	19751	39.14	2.417e-07	416	2521
790	218.67	19672	39.15	2.466e-07	417	2518
795	218.17	19592	39.16	2.516e-07	417	2518
800	217.67	19511	39.43	2.568e-07	418	2518
805	217.15	19429	39.64	2.622e-07	418	2515
810	216.61	19345	39.78	2.681e-07	419	2515
815	216.03	19258	39.93	2.741e-07	420	2509
820	215.43	19168	40.02	2.803e-07	421	2507
825	214.81	19077	40.17	2.870e-07	422	2501
830	214.15	18984	40.16	2.941e-07	424	2496

STS-41 BET and Radiometer Data (continued)

time (sec)	$h*10^{-3}$ (ft)	vel. (ft/sec)	α (°)	density (slug/ft^3)	T_∞ (°F)	IML temp (°F)
835	213.47	18890	40.34	3.017e-07	425	2490
840	212.76	18794	40.49	3.098e-07	426	2484
845	212.03	18696	40.51	3.184e-07	428	2479
850	211.27	18597	40.54	3.276e-07	429	2473
855	210.48	18495	40.51	3.375e-07	431	2467
860	209.67	18391	40.37	3.480e-07	432	2464
865	208.84	18286	40.35	3.596e-07	433	2459
870	208.01	18178	40.18	3.715e-07	434	2456
875	207.18	18069	39.99	3.839e-07	435	2450
880	206.35	17959	39.98	3.967e-07	435	2450
885	205.53	17847	39.95	4.099e-07	436	2447
890	204.70	17733	39.93	4.236e-07	436	2444
895	203.87	17617	39.89	4.378e-07	437	2442
900	203.04	17497	39.76	4.527e-07	437	2438
905	202.20	17374	39.75	4.685e-07	438	2435
910	201.37	17248	39.59	4.847e-07	438	2432
915	200.56	17121	39.50	5.009e-07	438	2432
920	199.76	16993	39.45	5.175e-07	438	2430
925	198.96	16862	39.47	5.347e-07	438	2426
930	198.15	16730	39.50	5.528e-07	438	2426
935	197.31	16595	39.57	5.722e-07	438	2420
940	196.43	16458	39.60	5.930e-07	439	2418
945	195.52	16321	39.59	6.150e-07	439	2411
950	194.59	16182	39.58	6.386e-07	440	2408
955	193.63	16041	39.70	6.636e-07	440	2396
960	192.67	15893	39.74	6.886e-07	441	2392
965	191.69	15740	39.76	7.144e-07	443	2386
970	190.68	15584	39.81	7.418e-07	444	2377
975	189.66	15430	39.76	7.714e-07	446	2370
980	188.63	15282	39.83	8.039e-07	446	2363
985	187.58	15131	39.80	8.383e-07	446	2352
990	186.51	14976	39.93	8.749e-07	447	2347
995	185.43	14810	39.94	9.119e-07	448	2337
1000	184.42	14641	39.65	9.479e-07	449	2324
1005	183.56	14474	39.19	9.802e-07	450	2317
1010	182.84	14310	38.90	1.007e-06	451	2303
1015	182.24	14148	38.75	1.030e-06	451	2303
1020	181.70	13987	38.68	1.052e-06	452	2291
1025	181.18	13825	38.71	1.072e-06	452	2281
1030	180.67	13662	38.59	1.093e-06	453	2274
1035	180.16	13502	38.76	1.114e-06	453	2267
1040	179.74	13339	38.97	1.132e-06	454	2260
1045	179.59	13177	39.14	1.139e-06	454	2245
1050	179.76	13017	39.57	1.131e-06	454	2230
1055	180.13	12857	40.17	1.115e-06	453	2222
1060	180.47	12699	40.82	1.101e-06	453	2207
1065	180.51	12543	41.37	1.099e-06	453	2186
1070	180.18	12385	42.53	1.113e-06	453	2170
1075	179.47	12223	42.86	1.143e-06	454	2137
1080	178.49	12058	42.82	1.186e-06	455	2111
1085	177.39	11891	42.37	1.237e-06	456	2094
1090	176.35	11725	41.74	1.284e-06	458	2063
1095	175.39	11559	41.38	1.327e-06	460	2045
1100	174.52	11393	41.30	1.367e-06	462	2023
1105	173.72	11228	41.40	1.406e-06	464	2001
1110	172.92	11065	40.96	1.449e-06	465	1978
1115	172.04	10903	41.02	1.499e-06	465	1968
1120	171.04	10741	41.01	1.558e-06	465	1952
1125	169.92	10577	40.98	1.625e-06	466	1948
1130	168.68	10409	40.72	1.699e-06	469	1932
1135	167.38	10241	40.34	1.779e-06	471	1938
1140	166.09	10085	40.16	1.867e-06	472	1924
1145	164.96	9932	39.47	1.948e-06	472	1917
1150	164.04	9781	38.87	2.017e-06	473	1901
1155	163.22	9632	38.55	2.079e-06	474	1880
1160	162.43	9483	38.44	2.140e-06	474	1869
1165	161.62	9336	38.33	2.206e-06	475	1847
1170	160.75	9190	38.25	2.277e-06	476	1843
1175	159.85	9037	38.10	2.354e-06	476	1832
1180	158.91	8881	37.84	2.437e-06	477	1820
1185	157.92	8727	37.54	2.526e-06	478	1809
1190	156.90	8576	37.14	2.623e-06	479	1798
1195	155.84	8433	36.80	2.726e-06	480	1785
1200	154.75	8291	36.51	2.837e-06	481	1772
1205	153.62	8149	36.23	2.959e-06	481	1763
1210	152.47	8005	35.74	3.100e-06	480	1758
1215	151.29	7865	35.44	3.250e-06	479	1738
1220	150.10	7726	35.14	3.418e-06	477	1721
1225	148.88	7591	34.53	3.606e-06	474	1715
1230	147.65	7459	34.08	3.808e-06	471	1700
1235	146.41	7327	33.66	4.021e-06	468	1685
1240	145.17	7194	33.13	4.247e-06	466	1676
1245	143.93	7064	32.39	4.485e-06	463	1685
1250	142.73	6934	32.01	4.730e-06	461	1679
1255	141.66	6807	31.34	4.960e-06	458	1691
1260	140.77	6684	30.91	5.160e-06	457	1694
1265	139.93	6564	30.59	5.353e-06	455	1685
1270	138.96	6446	30.65	5.586e-06	454	1691
1275	137.80	6326	30.43	5.877e-06	452	1685
1280	136.49	6208	30.05	6.217e-06	451	1685
1285	135.13	6090	29.39	6.590e-06	450	1676
1290	133.77	5978	28.81	7.005e-06	447	1660
1295	132.43	5866	28.50	7.482e-06	443	1654
1300	131.07	5754	27.97	7.998e-06	439	1654
1305	129.70	5649	27.66	8.494e-06	438	1637
1310	128.32	5550	26.79	9.018e-06	437	1611
1315	126.94	5452	26.30	9.572e-06	436	1586
1320	125.54	5354	25.77	1.016e-05	436	1586
1325	124.12	5255	25.33	1.082e-05	435	1586
1330	122.69	5151	24.83	1.160e-05	431	1576
1335	121.27	5050	24.30	1.244e-05	428	1558
1340	119.85	4950	23.94	1.321e-05	428	1550
1345	118.43	4849	23.55	1.403e-05	429	1531
1350	117.01	4749	23.18	1.489e-05	429	1512
1355	115.61	4649	22.67	1.580e-05	430	1492
1360	114.21	4552	22.28	1.679e-05	429	1471
1365	112.84	4457	21.82	1.794e-05	427	1450
1370	111.47	4363	21.35	1.915e-05	424	1450
1375	110.12	4268	20.99	2.045e-05	421	1428
1380	108.76	4174	20.62	2.183e-05	419	1405
1385	107.41	4082	20.40	2.328e-05	417	1391
1390	106.05	3991	19.86	2.479e-05	416	1356

STS-41 BET and Radiometer Data (concluded)

time (sec)	$h*10^{-3}$ (ft)	vel. (ft/sec)	α (°)	density ($slug/ft^3$)	T_∞ (°F)	IML temp (°F)
1395	104.67	3903	19.53	2.641e-05	415	1341
1400	103.28	3817	19.08	2.817e-05	414	1314
1405	101.86	3727	18.88	3.008e-05	413	1304
1410	100.43	3635	18.21	3.224e-05	411	1287
1415	99.01	3544	17.97	3.458e-05	409	1275
1420	97.75	3452	17.59	3.672e-05	408	1258
1425	96.67	3363	16.92	3.851e-05	408	1246
1430	95.65	3277	16.69	4.029e-05	409	1214
1435	94.59	3192	16.64	4.230e-05	409	1195
1440	93.48	3110	16.38	4.475e-05	407	1181
1445	92.32	3030	16.22	4.748e-05	404	1160
1450	91.11	2948	16.01	5.038e-05	403	1146
1455	89.85	2865	15.74	5.338e-05	403	1108
1460	88.58	2783	15.40	5.663e-05	403	1108
1465	87.28	2702	15.36	6.013e-05	403	1067
1470	85.97	2620	15.10	6.386e-05	403	1067
1475	84.68	2537	14.63	6.789e-05	403	1067
1480	83.37	2449	14.76	7.242e-05	401	1041
1485	82.12	2360	13.85	7.706e-05	399	1023
1490	80.99	2276	13.95	8.166e-05	397	1004
1495	80.01	2192	13.62	8.601e-05	395	994
1500	79.14	2108	13.67	9.004e-05	393	974
1505	78.38	2028	12.97	9.374e-05	392	953
1510	77.65	1956	11.88	9.734e-05	391	942
1515	76.89	1891	10.79	1.013e-04	390	920
1520	76.01	1832	10.34	1.061e-04	389	883
1525	74.99	1777	10.15	1.118e-04	388	920
1530	73.85	1723	9.99	1.186e-04	387	920
1535	72.59	1670	9.88	1.265e-04	386	859
1540	71.24	1618	9.69	1.355e-04	385	859
1545	69.81	1567	9.49	1.459e-04	384	859
1550	68.31	1518	9.38	1.574e-04	383	816
1555	66.79	1467	9.06	1.702e-04	382	816
1560	65.24	1416	8.69	1.841e-04	381	830
1565	63.68	1364	8.30	1.994e-04	380	787
1570	62.10	1314	8.06	2.161e-04	379	823
1575	60.52	1261	7.77	2.349e-04	377	744
1580	58.96	1209	7.58	2.556e-04	374	787
1585	57.42	1151	7.35	2.794e-04	370	787
1590	55.90	1094	7.40	3.053e-04	365	787
1595	54.43	1039	7.51	3.286e-04	366	701
1600	53.00	991	7.23	3.524e-04	367	787
1605	51.60	947	7.28	3.772e-04	368	744
1610	50.21	915	7.21	4.021e-04	370	701
1615	48.80	895	7.94	4.289e-04	373	701
1620	47.42	876	8.26	4.562e-04	375	645
1625	46.10	861	7.33	4.841e-04	377	701
1630	44.78	847	6.57	5.190e-04	376	589
1635	43.43	835	6.74	5.502e-04	379	645
1640	42.07	830	6.38	5.782e-04	385	701
1645	40.71	825	6.13	6.106e-04	390	701
1650	39.36	820	5.59	6.433e-04	394	589
1655	38.02	816	5.18	6.759e-04	400	645
1660	36.66	806	5.12	7.107e-04	405	645
1665	35.32	793	4.79	7.450e-04	410	701
1670	33.96	783	4.65	7.795e-04	417	645
1675	32.48	775	6.58	8.208e-04	423	589
1680	30.92	755	7.51	8.660e-04	429	589
1685	29.33	751	8.54	9.194e-04	433	656
1690	27.81	733	7.49	9.705e-04	438	633
1695	26.44	703	7.84	1.012e-03	445	589
1700	25.22	679	7.11	1.050e-03	451	701
1705	24.11	663	7.34	1.087e-03	456	656
1710	23.08	645	7.87	1.123e-03	460	633
1715	22.16	629	8.24	1.158e-03	464	701
1720	21.30	621	9.07	1.192e-03	466	633
1725	20.51	612	8.76	1.224e-03	469	656
1730	19.78	602	8.29	1.254e-03	471	656
1735	19.08	595	8.12	1.282e-03	473	656
1740	18.38	590	8.17	1.311e-03	476	701
1745	17.67	588	6.86	1.340e-03	479	701
1750	16.86	592	6.37	1.372e-03	483	589

STS-39 BET and Radiometer Data

time (sec)	$h*10^{-3}$ (ft)	vel. (ft/sec)	α (°)	density ($slug/ft^3$)	T_∞ (°F)	IML temp (°F)
0	407.87	24912	40.72	4.643e-11	749	-460
5	405.64	24914	40.53	4.641e-11	749	-460
10	403.41	24917	40.39	4.639e-11	749	-460
15	401.17	24920	40.34	4.637e-11	748	-460
20	398.94	24911	40.27	4.796e-11	741	-460
25	396.71	24912	40.28	5.196e-11	723	-460
30	394.48	24913	40.41	5.629e-11	704	-460
35	392.25	24915	40.53	6.120e-11	687	-460
40	390.02	24916	40.66	6.661e-11	669	-460
45	387.79	24918	40.93	7.252e-11	652	-460
50	385.56	24919	41.03	7.933e-11	635	-460
55	383.33	24921	40.95	8.678e-11	619	-460
60	381.10	24923	40.96	9.506e-11	602	-460
65	378.88	24925	40.82	1.044e-10	587	-460
70	376.65	24926	40.78	1.148e-10	572	-460
75	374.43	24930	40.79	1.263e-10	558	-460
80	372.21	24935	40.82	1.392e-10	544	-460
85	369.99	24940	40.86	1.535e-10	531	-460
90	367.77	24944	40.95	1.702e-10	517	-460
95	365.55	24948	40.87	1.889e-10	504	-460
100	363.34	24952	40.77	2.097e-10	491	-460
105	361.12	24955	40.73	2.330e-10	480	-460
110	358.91	24957	40.72	2.590e-10	470	-460
115	356.70	24959	40.75	2.878e-10	460	-460
120	354.49	24962	40.76	3.200e-10	452	-460
125	352.28	24965	40.79	3.558e-10	444	-460
130	350.07	24966	40.82	3.973e-10	435	-460
135	347.87	24968	40.87	4.441e-10	427	-460
140	345.67	24969	40.93	4.965e-10	419	-460
145	343.47	24965	40.92	5.560e-10	412	-460
150	341.27	24961	40.87	6.225e-10	406	-460
155	339.08	24958	40.78	6.977e-10	399	-460
160	336.89	24956	40.65	7.833e-10	393	-460
165	334.70	24954	40.42	8.794e-10	387	-460
170	332.52	24954	40.13	9.911e-10	381	-460
175	330.33	24955	39.83	1.119e-09	375	-460
180	328.16	24956	39.41	1.264e-09	369	422
185	325.99	24951	39.20	1.433e-09	363	422
190	323.82	24943	39.28	1.624e-09	357	422
195	321.65	24937	39.70	1.838e-09	352	470
200	319.50	24947	40.04	2.053e-09	352	470
205	317.35	24958	40.23	2.292e-09	352	589
210	315.20	24968	40.35	2.559e-09	352	701
215	313.06	24979	40.32	2.855e-09	352	762
220	310.93	24991	40.15	3.185e-09	353	787
225	308.81	25002	39.91	3.552e-09	353	859
230	306.70	25014	39.63	3.958e-09	353	920
235	304.59	25024	39.38	4.407e-09	354	1023
240	302.50	25025	39.32	4.892e-09	355	1080
245	300.42	25025	39.68	5.430e-09	355	1130
250	298.36	25025	40.09	6.026e-09	356	1224
255	296.31	25024	40.56	6.681e-09	356	1304
260	294.28	25023	41.09	7.403e-09	357	1364
265	292.27	25021	41.39	8.199e-09	357	1412
270	290.29	25019	40.80	9.070e-09	357	1477
275	288.32	25017	39.56	1.002e-08	357	1531
280	286.39	25014	38.94	1.105e-08	358	1586
285	284.48	25011	39.13	1.217e-08	358	1642
290	282.60	25007	39.74	1.338e-08	358	1689
295	280.75	25011	40.92	1.474e-08	357	1758
300	278.95	25018	41.55	1.623e-08	356	1801
305	277.19	25023	41.22	1.783e-08	355	1846
310	275.48	25027	39.99	1.954e-08	353	1889
315	273.82	25025	39.09	2.148e-08	350	1921
320	272.22	25022	39.34	2.354e-08	348	1958
325	270.68	25016	40.53	2.572e-08	345	2000
330	269.20	25007	41.35	2.799e-08	343	2036
335	267.80	24996	40.29	3.020e-08	342	2059
340	266.48	24985	39.26	3.241e-08	342	2086
345	265.24	24973	39.30	3.463e-08	342	2119
350	264.08	24958	40.56	3.683e-08	342	2144
355	263.02	24941	41.40	3.898e-08	342	2175
360	262.05	24922	41.19	4.100e-08	343	2199
365	261.17	24902	39.80	4.276e-08	344	2214
370	260.37	24882	39.03	4.442e-08	345	2230
375	259.64	24862	39.57	4.600e-08	347	2240
380	258.96	24841	39.69	4.752e-08	348	2254
385	258.32	24818	39.64	4.900e-08	349	2269
390	257.71	24795	39.86	5.043e-08	350	2284
395	257.14	24771	40.09	5.184e-08	351	2291
400	256.59	24746	40.01	5.322e-08	352	2310
405	256.06	24721	39.77	5.458e-08	352	2324
410	255.55	24696	39.79	5.592e-08	353	2324
415	255.07	24670	39.97	5.725e-08	354	2330
420	254.59	24645	39.91	5.857e-08	354	2346
425	254.13	24618	39.85	5.990e-08	355	2350
430	253.67	24591	39.96	6.123e-08	355	2359
435	253.22	24563	39.94	6.258e-08	356	2372
440	252.77	24534	39.84	6.393e-08	356	2378
445	252.33	24506	39.88	6.529e-08	357	2385
450	251.90	24476	39.90	6.666e-08	357	2389
455	251.48	24446	39.88	6.804e-08	358	2402
460	251.06	24416	39.88	6.943e-08	358	2408
465	250.64	24385	39.91	7.083e-08	359	2414
470	250.23	24353	39.93	7.227e-08	359	2420
475	249.81	24321	39.93	7.373e-08	360	2426
480	249.39	24289	39.92	7.523e-08	360	2428
485	248.97	24256	39.94	7.679e-08	360	2434
490	248.55	24223	39.95	7.842e-08	360	2444
495	248.13	24188	39.96	8.008e-08	361	2450
500	247.72	24153	39.98	8.175e-08	361	2458
505	247.31	24117	39.96	8.342e-08	361	2467
510	246.92	24080	39.97	8.507e-08	361	2473
515	246.54	24043	39.97	8.668e-08	361	2479
520	246.18	24005	39.97	8.826e-08	361	2486
525	245.83	23967	39.97	8.980e-08	361	2490
530	245.50	23928	39.99	9.132e-08	361	2496
535	245.17	23889	39.97	9.283e-08	361	2501
540	244.84	23849	39.97	9.434e-08	361	2503
545	244.52	23809	39.99	9.589e-08	361	2507
550	244.19	23770	39.98	9.748e-08	362	2512
555	243.85	23730	39.96	9.913e-08	362	2512

STS-39 BET and Radiometer Data (continued)

time (sec)	h*10^{-3} (ft)	vel. (ft/sec)	α (°)	density (slug/ft^3)	T_∞ (°F)	IML temp (°F)
560	243.51	23689	39.98	1.008e-07	362	2518
565	243.15	23649	39.99	1.026e-07	362	2518
570	242.80	23607	39.98	1.044e-07	362	2528
575	242.45	23564	40.01	1.062e-07	362	2530
580	242.11	23521	39.97	1.079e-07	363	2534
585	241.78	23477	39.74	1.095e-07	363	2539
590	241.46	23434	39.86	1.111e-07	364	2539
595	241.14	23391	40.12	1.127e-07	365	2539
600	240.82	23346	40.14	1.143e-07	365	2544
605	240.50	23301	40.18	1.160e-07	365	2544
610	240.18	23255	40.12	1.177e-07	366	2546
615	239.84	23209	39.84	1.195e-07	367	2549
620	239.50	23163	39.88	1.214e-07	367	2549
625	239.15	23115	39.91	1.233e-07	368	2555
630	238.79	23068	39.72	1.253e-07	368	2555
635	238.44	23021	39.78	1.274e-07	369	2556
640	238.08	22973	39.80	1.294e-07	370	2558
645	237.73	22925	39.84	1.315e-07	370	2555
650	237.39	22876	39.89	1.336e-07	371	2555
655	237.04	22826	39.93	1.357e-07	371	2560
660	236.69	22775	39.94	1.379e-07	372	2560
665	236.34	22724	39.65	1.401e-07	372	2560
670	235.98	22673	39.33	1.423e-07	373	2565
675	235.63	22620	39.52	1.441e-07	375	2565
680	235.29	22566	39.41	1.460e-07	376	2565
685	234.95	22512	39.28	1.478e-07	377	2565
690	234.62	22458	39.34	1.496e-07	379	2565
695	234.28	22403	39.33	1.515e-07	380	2565
700	233.94	22348	39.38	1.534e-07	382	2565
705	233.59	22292	39.39	1.554e-07	383	2563
710	233.23	22236	39.43	1.574e-07	385	2560
715	232.87	22181	39.92	1.596e-07	386	2556
720	232.49	22123	40.21	1.618e-07	388	2555
725	232.10	22064	40.21	1.641e-07	390	2555
730	231.69	22005	40.25	1.665e-07	391	2549
735	231.26	21944	40.27	1.684e-07	391	2548
740	230.80	21882	40.30	1.705e-07	391	2544
745	230.32	21820	40.31	1.727e-07	390	2549
750	229.84	21754	40.19	1.750e-07	390	2549
755	229.36	21689	39.61	1.773e-07	390	2553
760	228.89	21624	39.40	1.795e-07	390	2549
765	228.43	21560	39.43	1.818e-07	390	2549
770	227.97	21495	39.77	1.840e-07	390	2544
775	227.51	21429	40.00	1.863e-07	390	2544
780	227.04	21360	40.04	1.886e-07	389	2544
785	226.56	21291	40.05	1.911e-07	389	2542
790	226.06	21220	39.81	1.941e-07	389	2539
795	225.55	21148	39.84	1.986e-07	389	2539
800	225.04	21073	39.43	2.032e-07	390	2537
805	224.55	21000	39.41	2.078e-07	390	2535
810	224.08	20926	39.39	2.123e-07	390	2534
815	223.66	20850	38.62	2.164e-07	390	2534
820	223.28	20775	39.70	2.201e-07	391	2534
825	222.92	20699	39.50	2.237e-07	391	2528
830	222.55	20623	39.55	2.274e-07	391	2532
835	222.15	20546	39.54	2.313e-07	392	2528
840	221.73	20468	39.71	2.356e-07	392	2528
845	221.27	20388	39.90	2.403e-07	393	2523
850	220.80	20307	39.90	2.453e-07	393	2518
855	220.30	20226	39.98	2.507e-07	394	2518
860	219.77	20143	40.10	2.565e-07	394	2518
865	219.22	20058	40.18	2.626e-07	395	2516
870	218.65	19971	40.00	2.690e-07	396	2512
875	218.05	19884	39.85	2.758e-07	397	2510
880	217.43	19796	39.87	2.830e-07	398	2507
885	216.81	19705	39.94	2.905e-07	399	2503
890	216.18	19613	39.80	2.982e-07	400	2501
895	215.54	19518	39.83	3.061e-07	401	2496
900	214.88	19421	39.85	3.144e-07	402	2494
905	214.20	19323	39.83	3.233e-07	404	2490
910	213.51	19222	39.82	3.325e-07	405	2490
915	212.81	19119	39.76	3.422e-07	406	2484
920	212.10	19017	39.71	3.522e-07	407	2483
925	211.39	18913	39.93	3.626e-07	408	2477
930	210.67	18809	40.10	3.734e-07	409	2471
935	209.92	18702	40.44	3.850e-07	411	2462
940	209.14	18594	40.72	3.958e-07	413	2464
945	208.31	18480	40.77	4.070e-07	417	2462
950	207.46	18362	40.32	4.188e-07	420	2462
955	206.63	18246	39.92	4.307e-07	424	2460
960	205.82	18130	39.96	4.426e-07	427	2460
965	205.01	18010	39.93	4.546e-07	430	2462
970	204.21	17887	39.78	4.671e-07	433	2458
975	203.40	17763	39.62	4.799e-07	437	2456
980	202.59	17645	39.58	4.940e-07	439	2454
985	201.78	17527	39.54	5.087e-07	441	2450
990	200.97	17408	39.57	5.239e-07	442	2448
995	200.15	17287	39.65	5.396e-07	444	2440
1000	199.33	17163	39.75	5.559e-07	446	2436
1005	198.49	17037	39.83	5.730e-07	448	2430
1010	197.63	16909	39.88	5.920e-07	450	2420
1015	196.73	16779	39.96	6.136e-07	452	2412
1020	195.79	16642	40.07	6.379e-07	453	2402
1025	194.81	16501	40.19	6.642e-07	454	2389
1030	193.80	16356	40.28	6.922e-07	455	2380
1035	192.76	16209	40.55	7.222e-07	456	2374
1040	191.69	16056	40.47	7.541e-07	457	2361
1045	190.61	15903	40.14	7.876e-07	458	2348
1050	189.54	15747	40.10	8.229e-07	459	2334
1055	188.47	15586	39.97	8.602e-07	460	2321
1060	187.38	15422	39.91	8.995e-07	460	2291
1065	186.29	15253	39.86	9.402e-07	461	2271
1070	185.32	15083	39.18	9.783e-07	462	2234
1075	184.54	14917	38.80	1.010e-06	462	2179
1080	183.94	14751	38.61	1.035e-06	463	2130
1085	183.46	14588	38.19	1.056e-06	464	2047
1090	183.05	14427	38.44	1.073e-06	465	2024
1095	182.71	14264	38.57	1.088e-06	466	2056
1100	182.44	14098	38.30	1.099e-06	467	1974
1105	182.23	13937	38.92	1.109e-06	467	1787
1110	182.03	13776	38.94	1.119e-06	468	1640
1115	181.74	13616	39.26	1.131e-06	469	1227

STS-39 BET and Radiometer Data (continued)

time (sec)	$h*10^{-3}$ (ft)	vel. (ft/sec)	α (°)	density (slug/ft^3)	T_∞ (°F)	IML temp (°F)
1120	181.33	13455	39.56	1.149e-06	470	1732
1125	180.79	13292	39.91	1.173e-06	472	1858
1130	180.13	13125	40.04	1.202e-06	473	1956
1135	179.41	12960	39.92	1.234e-06	475	2067
1140	178.65	12794	39.75	1.269e-06	476	2054
1145	177.88	12629	39.58	1.305e-06	478	1774
1150	177.10	12464	39.47	1.343e-06	480	2088
1155	176.32	12296	39.42	1.384e-06	481	2104
1160	175.52	12128	39.44	1.427e-06	481	2045
1165	174.72	11959	39.49	1.472e-06	482	2063
1170	173.92	11789	39.48	1.519e-06	482	2043
1175	173.11	11623	39.41	1.570e-06	482	2063
1180	172.30	11458	39.48	1.624e-06	482	2050
1185	171.54	11292	39.67	1.676e-06	481	2032
1190	171.00	11126	39.79	1.715e-06	481	2022
1195	170.73	10963	40.03	1.737e-06	480	2003
1200	170.63	10801	40.41	1.746e-06	480	1988
1205	170.47	10639	40.69	1.759e-06	480	1978
1210	170.01	10481	41.16	1.790e-06	481	1958
1215	169.19	10322	41.60	1.842e-06	483	1944
1220	168.04	10159	41.59	1.916e-06	486	1928
1225	166.81	10001	41.07	1.998e-06	489	1917
1230	165.70	9855	40.51	2.074e-06	491	1897
1235	164.73	9711	39.95	2.142e-06	494	1882
1240	163.80	9570	39.81	2.212e-06	496	1871
1245	162.81	9418	39.61	2.304e-06	495	1860
1250	161.75	9267	39.42	2.408e-06	493	1854
1255	160.61	9116	39.18	2.526e-06	491	1849
1260	159.42	8959	38.79	2.635e-06	492	1832
1265	158.30	8802	37.86	2.740e-06	494	1820
1270	157.32	8650	37.45	2.836e-06	496	1805
1275	156.39	8518	36.95	2.931e-06	497	1798
1280	155.40	8390	36.66	3.033e-06	499	1793
1285	154.31	8264	36.65	3.151e-06	500	1772
1290	153.10	8134	36.49	3.316e-06	498	1744
1295	151.84	8003	35.93	3.510e-06	493	1729
1300	150.59	7872	35.21	3.714e-06	489	1715
1305	149.39	7732	34.59	3.911e-06	486	1721
1310	148.20	7596	34.22	4.117e-06	484	1729
1315	146.98	7459	33.86	4.330e-06	482	1744
1320	145.72	7326	33.31	4.542e-06	483	1744
1325	144.44	7195	33.05	4.769e-06	483	1744
1330	143.11	7063	32.63	5.014e-06	484	1744
1335	141.75	6933	32.24	5.277e-06	484	1744
1340	140.37	6802	31.76	5.573e-06	484	1729
1345	138.98	6673	31.23	5.913e-06	481	1729
1350	137.58	6546	30.77	6.278e-06	479	1729
1355	136.16	6420	30.33	6.652e-06	477	1715
1360	134.74	6296	29.90	7.051e-06	476	1700
1365	133.31	6183	29.34	7.463e-06	476	1691
1370	131.88	6077	28.91	7.895e-06	475	1685
1375	130.43	5969	28.57	8.394e-06	473	1669
1380	128.97	5859	28.25	8.991e-06	468	1654
1385	127.61	5748	27.82	9.575e-06	463	1644
1390	126.46	5630	27.22	1.005e-05	462	1631
1395	125.41	5515	26.82	1.049e-05	461	1614
1400	124.29	5409	26.46	1.101e-05	460	1604
1405	123.00	5318	26.43	1.169e-05	456	1586
1410	121.56	5227	26.32	1.252e-05	452	1569
1415	120.04	5119	25.38	1.336e-05	450	1550
1420	118.53	5008	24.74	1.421e-05	450	1531
1425	117.04	4901	24.30	1.512e-05	450	1512
1430	115.54	4797	23.90	1.611e-05	449	1512
1435	114.03	4692	23.62	1.720e-05	448	1492
1440	112.51	4587	22.98	1.840e-05	446	1471
1445	111.01	4484	22.40	1.969e-05	443	1450
1450	109.52	4388	21.74	2.110e-05	440	1428
1455	108.03	4293	21.11	2.259e-05	438	1405
1460	106.56	4192	20.66	2.418e-05	435	1381
1465	105.09	4091	20.09	2.588e-05	433	1366
1470	103.64	3992	19.61	2.768e-05	431	1356
1475	102.20	3893	19.25	2.958e-05	429	1331
1480	100.78	3799	18.79	3.156e-05	427	1304
1485	99.36	3710	18.43	3.364e-05	426	1275
1490	97.96	3623	17.94	3.583e-05	425	1264
1495	96.57	3539	17.57	3.807e-05	425	1246
1500	95.18	3455	17.06	4.045e-05	425	1233
1505	93.81	3364	16.66	4.334e-05	422	1214
1510	92.46	3272	16.25	4.648e-05	417	1181
1515	91.14	3183	15.79	4.961e-05	415	1181
1520	89.85	3097	15.53	5.255e-05	414	1146
1525	88.69	3010	15.22	5.537e-05	414	1146
1530	87.67	2923	14.73	5.794e-05	414	1108
1535	86.69	2838	14.64	6.054e-05	414	1067
1540	85.66	2755	14.79	6.339e-05	414	1067
1545	84.58	2674	14.60	6.678e-05	413	1041
1550	83.44	2601	14.41	7.082e-05	410	1023
1555	82.24	2529	14.29	7.531e-05	407	1023
1560	81.02	2444	14.53	8.052e-05	403	994
1565	79.87	2354	14.07	8.589e-05	398	974
1570	78.86	2264	13.76	9.092e-05	394	953
1575	77.98	2180	13.00	9.542e-05	392	974
1580	77.15	2101	12.39	9.967e-05	390	953
1585	76.35	2025	12.05	1.040e-04	389	920
1590	75.53	1952	11.44	1.086e-04	388	883
1595	74.65	1886	10.80	1.138e-04	386	920
1600	73.68	1823	10.44	1.198e-04	385	883
1605	72.59	1763	10.26	1.269e-04	383	859
1610	71.40	1705	10.12	1.352e-04	381	859
1615	70.11	1649	9.89	1.447e-04	379	859
1620	68.74	1593	9.80	1.556e-04	377	859
1625	67.31	1538	9.55	1.679e-04	374	830
1630	65.84	1483	9.37	1.814e-04	372	787
1635	64.35	1427	9.17	1.964e-04	370	787
1640	62.86	1371	8.88	2.126e-04	369	787
1645	61.37	1317	8.53	2.299e-04	368	787
1650	59.87	1263	8.31	2.486e-04	367	787
1655	58.39	1210	9.44	2.688e-04	366	787
1660	57.02	1153	10.19	2.890e-04	365	761
1665	55.85	1091	10.77	3.076e-04	364	787
1670	54.90	1021	11.14	3.218e-04	365	787
1675	54.13	954	10.84	3.335e-04	366	701

STS-39 BET and Radiometer Data (concluded)

time (sec)	$h*10^{-3}$ (ft)	vel. (ft/sec)	α (°)	density ($slug/ft^3$)	T_∞ (°F)	IML temp (°F)
1680	53.46	902	9.44	3.441e-04	367	701
1685	52.72	869	10.69	3.561e-04	368	701
1690	51.92	842	10.84	3.697e-04	369	701
1695	51.04	823	10.92	3.845e-04	371	701
1700	50.09	807	11.32	4.009e-04	373	667
1705	49.05	800	9.71	4.196e-04	376	667
1710	47.85	807	9.83	4.463e-04	375	667
1715	46.47	815	11.04	4.808e-04	373	667
1720	44.91	818	11.30	5.177e-04	374	701
1725	43.23	814	11.97	5.575e-04	378	622
1730	41.51	816	10.80	5.974e-04	383	667
1735	39.78	820	8.98	6.405e-04	389	622
1740	38.09	811	9.49	6.803e-04	396	667
1745	36.41	801	7.63	7.241e-04	403	633
1750	34.69	789	7.84	7.721e-04	409	589

STS-48 BET and Radiometer Data

time (sec)	$h*10^{-3}$ (ft)	vel. (ft/sec)	α (°)	density ($slug/ft^3$)	T_∞ (°F)	IML temp (°F)
0	410.12	25231	40.77	3.726e-11	729	-460
5	406.75	25235	41.00	3.725e-11	729	-460
10	403.41	25239	40.88	3.725e-11	729	-460
15	400.09	25243	40.78	3.725e-11	728	-460
20	396.78	25248	40.71	4.160e-11	704	-460
25	393.50	25249	40.69	4.672e-11	679	-460
30	390.24	25250	40.70	5.291e-11	656	-460
35	387.01	25251	40.80	5.988e-11	633	-460
40	383.79	25253	40.97	6.772e-11	610	-460
45	380.60	25254	40.99	7.668e-11	588	-460
50	377.42	25255	40.95	8.697e-11	566	-460
55	374.27	25257	40.89	9.929e-11	545	-460
60	371.14	25258	40.81	1.140e-10	526	-460
65	368.04	25260	40.88	1.308e-10	507	-460
70	364.95	25261	40.94	1.499e-10	488	-460
75	361.89	25261	40.76	1.730e-10	471	-460
80	358.85	25259	40.53	2.001e-10	454	-460
85	355.83	25257	40.31	2.322e-10	439	-460
90	352.84	25255	40.12	2.696e-10	425	-460
95	349.87	25254	39.93	3.135e-10	411	-460
100	346.92	25254	39.77	3.644e-10	398	-460
105	343.99	25252	39.61	4.266e-10	387	-460
110	341.09	25249	39.44	5.007e-10	377	-460
115	338.21	25248	39.39	5.881e-10	368	-460
120	335.36	25248	39.41	6.907e-10	360	-460
125	332.53	25249	39.51	8.102e-10	352	-389
130	329.73	25250	39.53	9.492e-10	344	351
135	326.95	25251	39.59	1.112e-09	338	422
140	324.20	25253	39.63	1.306e-09	335	422
145	321.48	25254	39.57	1.529e-09	333	422
150	318.78	25258	39.56	1.777e-09	333	422
155	316.11	25262	39.51	2.062e-09	333	599
160	313.47	25265	39.50	2.390e-09	334	701
165	310.85	25268	39.68	2.765e-09	334	787
170	308.27	25271	39.88	3.196e-09	335	794
175	305.72	25274	39.92	3.688e-09	335	920
180	303.20	25276	39.84	4.242e-09	335	979
185	300.71	25279	39.56	4.849e-09	337	1067
190	298.26	25281	39.48	5.533e-09	338	1149
195	295.85	25283	39.42	6.300e-09	339	1246
200	293.47	25284	39.66	7.156e-09	341	1306
205	291.14	25285	39.99	8.109e-09	342	1383
210	288.86	25285	40.47	9.161e-09	343	1450
215	286.62	25285	40.95	1.029e-08	345	1531
220	284.44	25284	41.07	1.152e-08	346	1586
225	282.31	25282	40.50	1.286e-08	347	1655
230	280.23	25280	39.49	1.431e-08	349	1715
235	278.22	25278	39.22	1.587e-08	350	1759
240	276.27	25273	39.91	1.753e-08	351	1810
245	274.40	25267	41.15	1.925e-08	353	1855
250	272.59	25258	41.29	2.104e-08	354	1907
255	270.87	25248	40.27	2.291e-08	355	1948
260	269.23	25238	39.24	2.484e-08	356	1997
265	267.68	25227	39.64	2.682e-08	357	2026
270	266.21	25214	40.88	2.880e-08	358	2063

STS-48 BET and Radiometer Data (continued)

time (sec)	h*10^{-3} (ft)	vel. (ft/sec)	α (°)	density (slug/ft^3)	T_∞ (°F)	IML temp (°F)
275	264.85	25200	41.15	3.079e-08	359	2089
280	263.58	25184	40.11	3.273e-08	360	2116
285	262.43	25167	39.64	3.462e-08	360	2142
290	261.39	25148	40.85	3.641e-08	361	2174
295	260.46	25126	40.89	3.807e-08	361	2206
300	259.64	25104	40.10	3.960e-08	362	2237
305	258.91	25082	39.99	4.103e-08	362	2259
310	258.24	25059	39.68	4.238e-08	363	2281
315	257.62	25036	39.66	4.366e-08	363	2296
320	257.04	25013	40.14	4.491e-08	364	2310
325	256.49	24988	40.32	4.611e-08	364	2330
330	255.96	24963	39.93	4.730e-08	364	2343
335	255.46	24938	39.92	4.841e-08	365	2357
340	254.98	24912	40.17	4.950e-08	365	2363
345	254.51	24886	40.12	5.058e-08	365	2377
350	254.05	24859	39.99	5.165e-08	365	2389
355	253.61	24832	39.99	5.272e-08	366	2396
360	253.18	24803	40.04	5.378e-08	366	2407
365	252.76	24774	40.03	5.485e-08	366	2414
370	252.35	24745	40.00	5.591e-08	367	2420
375	251.95	24715	40.01	5.699e-08	367	2426
380	251.54	24684	40.05	5.808e-08	367	2438
385	251.14	24653	39.99	5.919e-08	367	2444
390	250.73	24622	39.98	6.033e-08	368	2451
395	250.32	24590	40.03	6.151e-08	368	2456
400	249.91	24558	40.05	6.273e-08	368	2462
405	249.49	24525	40.00	6.399e-08	369	2468
410	249.07	24491	39.97	6.527e-08	369	2473
415	248.64	24457	40.01	6.658e-08	369	2479
420	248.23	24422	40.07	6.791e-08	370	2490
425	247.82	24386	40.04	6.924e-08	370	2490
430	247.42	24350	40.02	7.057e-08	370	2496
435	247.03	24314	40.01	7.190e-08	370	2501
440	246.65	24277	40.00	7.322e-08	371	2507
445	246.27	24238	40.00	7.455e-08	371	2512
450	245.90	24200	40.02	7.590e-08	371	2518
455	245.52	24161	40.01	7.727e-08	372	2522
460	245.15	24121	40.00	7.869e-08	372	2523
465	244.77	24081	40.01	8.014e-08	372	2529
470	244.39	24039	40.00	8.163e-08	373	2534
475	244.01	23997	40.01	8.314e-08	373	2539
480	243.63	23955	40.04	8.464e-08	373	2544
485	243.26	23911	40.05	8.613e-08	374	2549
490	242.90	23868	40.06	8.762e-08	374	2549
495	242.55	23825	40.07	8.909e-08	375	2549
500	242.20	23781	40.08	9.056e-08	375	2555
505	241.87	23736	40.09	9.202e-08	375	2560
510	241.54	23691	40.09	9.346e-08	376	2560
515	241.21	23645	39.96	9.497e-08	376	2560
520	240.88	23598	39.98	9.654e-08	376	2560
525	240.55	23551	39.99	9.816e-08	377	2570
530	240.21	23503	39.93	9.984e-08	377	2575
535	239.86	23454	39.84	1.016e-07	378	2575
540	239.51	23406	39.58	1.034e-07	378	2580
545	239.15	23358	39.55	1.052e-07	379	2580
550	238.80	23309	39.58	1.070e-07	379	2580
555	238.46	23259	39.59	1.089e-07	379	2580
560	238.12	23210	39.60	1.107e-07	380	2585
565	237.79	23159	39.62	1.125e-07	380	2585
570	237.46	23107	39.49	1.143e-07	381	2590
575	237.14	23056	39.20	1.162e-07	381	2590
580	236.82	23004	39.18	1.180e-07	381	2590
585	236.50	22952	39.18	1.199e-07	382	2595
590	236.17	22899	39.20	1.218e-07	382	2600
595	235.85	22845	39.09	1.238e-07	382	2600
600	235.52	22791	38.50	1.257e-07	383	2600
605	235.21	22738	38.72	1.277e-07	383	2595
610	234.91	22685	38.77	1.296e-07	383	2600
615	234.61	22629	38.99	1.315e-07	384	2601
620	234.32	22572	38.78	1.334e-07	384	2600
625	234.04	22516	38.52	1.353e-07	384	2605
630	233.76	22460	38.42	1.372e-07	385	2601
635	233.47	22403	38.80	1.391e-07	385	2605
640	233.19	22345	38.62	1.411e-07	385	2605
645	232.91	22285	38.35	1.430e-07	386	2605
650	232.63	22226	38.15	1.450e-07	386	2605
655	232.37	22168	37.98	1.469e-07	386	2600
660	232.11	22110	38.83	1.488e-07	386	2600
665	231.84	22049	38.90	1.508e-07	387	2600
670	231.57	21987	39.18	1.528e-07	387	2600
675	231.29	21924	39.21	1.549e-07	387	2600
680	230.99	21860	39.07	1.571e-07	388	2600
685	230.67	21796	39.00	1.595e-07	388	2596
690	230.35	21731	39.00	1.620e-07	388	2595
695	230.01	21666	39.02	1.646e-07	389	2595
700	229.65	21601	39.11	1.674e-07	389	2590
705	229.29	21535	39.38	1.703e-07	390	2590
710	228.91	21467	39.64	1.734e-07	390	2585
715	228.51	21399	39.64	1.766e-07	390	2580
720	228.09	21331	39.79	1.801e-07	391	2584
725	227.63	21261	39.92	1.838e-07	392	2576
730	227.15	21190	40.07	1.879e-07	392	2575
735	226.63	21117	40.08	1.924e-07	393	2575
740	226.08	21044	40.05	1.972e-07	394	2574
745	225.52	20969	39.97	2.022e-07	395	2570
750	224.94	20892	39.85	2.073e-07	395	2566
755	224.37	20816	39.71	2.126e-07	396	2565
760	223.80	20737	39.67	2.180e-07	397	2565
765	223.24	20658	39.40	2.234e-07	398	2565
770	222.70	20577	39.28	2.288e-07	399	2565
775	222.16	20496	38.91	2.342e-07	400	2564
780	221.64	20414	39.02	2.395e-07	401	2560
785	221.13	20331	38.88	2.449e-07	402	2560
790	220.63	20247	38.80	2.503e-07	403	2555
795	220.13	20162	38.85	2.558e-07	403	2559
800	219.63	20076	38.83	2.615e-07	404	2555
805	219.13	19989	38.85	2.672e-07	405	2555
810	218.63	19901	38.96	2.730e-07	405	2555
815	218.14	19810	38.95	2.789e-07	406	2549
820	217.64	19720	38.94	2.850e-07	407	2544
825	217.13	19628	38.94	2.913e-07	408	2544
830	216.61	19535	39.16	2.977e-07	409	2539

STS-48 BET and Radiometer Data (continued)

time (sec)	h*10^{-3} (ft)	vel. (ft/sec)	α (°)	density (slug/ft^3)	T_∞ (°F)	IML temp (°F)
835	216.07	19441	39.33	3.041e-07	410	2538
840	215.50	19345	39.42	3.108e-07	412	2533
845	214.91	19249	39.52	3.180e-07	413	2528
850	214.30	19150	39.63	3.257e-07	415	2524
855	213.65	19049	39.76	3.338e-07	417	2523
860	212.97	18947	39.66	3.425e-07	419	2518
865	212.27	18841	39.67	3.517e-07	421	2518
870	211.54	18733	39.41	3.615e-07	423	2518
875	210.82	18625	39.16	3.715e-07	425	2517
880	210.10	18516	39.06	3.816e-07	427	2512
885	209.40	18405	39.08	3.918e-07	429	2507
890	208.70	18291	39.06	4.021e-07	431	2502
895	208.00	18176	39.04	4.128e-07	433	2501
900	207.29	18059	39.09	4.238e-07	435	2496
905	206.58	17940	39.15	4.351e-07	436	2490
910	205.85	17819	39.08	4.470e-07	438	2484
915	205.10	17697	39.23	4.596e-07	440	2474
920	204.32	17573	39.47	4.730e-07	442	2467
925	203.50	17446	39.77	4.873e-07	444	2462
930	202.65	17315	39.83	5.033e-07	446	2455
935	201.75	17181	39.97	5.208e-07	447	2444
940	200.79	17045	39.93	5.398e-07	449	2438
945	199.79	16906	39.93	5.604e-07	451	2432
950	198.77	16763	39.80	5.824e-07	452	2426
955	197.75	16618	39.65	6.052e-07	454	2425
960	196.74	16471	39.55	6.284e-07	456	2415
965	195.77	16320	39.31	6.517e-07	457	2414
970	194.83	16169	39.18	6.748e-07	459	2408
975	193.91	16016	39.20	6.981e-07	460	2401
980	193.01	15861	39.17	7.219e-07	462	2394
985	192.10	15704	39.23	7.466e-07	463	2383
990	191.18	15544	39.37	7.725e-07	464	2377
995	190.29	15380	39.28	7.984e-07	465	2370
1000	189.49	15215	39.00	8.231e-07	466	2362
1005	188.81	15053	38.82	8.447e-07	466	2356
1010	188.23	14890	38.77	8.634e-07	467	2344
1015	187.74	14727	38.53	8.800e-07	467	2337
1020	187.29	14565	38.54	8.951e-07	468	2337
1025	186.88	14403	38.52	9.094e-07	468	2344
1030	186.47	14242	38.37	9.235e-07	469	2350
1035	186.07	14082	38.45	9.379e-07	469	2350
1040	185.67	13922	38.59	9.525e-07	469	2356
1045	185.25	13762	38.74	9.680e-07	469	2350
1050	184.80	13602	38.94	9.846e-07	470	2342
1055	184.32	13443	39.15	1.003e-06	470	2330
1060	183.79	13284	39.44	1.023e-06	470	2324
1065	183.20	13123	39.61	1.046e-06	471	2315
1070	182.56	12963	39.78	1.072e-06	471	2301
1075	181.87	12801	40.04	1.100e-06	472	2289
1080	181.13	12637	39.94	1.131e-06	472	2280
1085	180.35	12472	39.69	1.165e-06	473	2273
1090	179.58	12308	39.48	1.199e-06	474	2260
1095	178.83	12146	39.37	1.233e-06	474	2245
1100	178.10	11984	39.43	1.268e-06	475	2230
1105	177.36	11822	39.45	1.303e-06	475	2220
1110	176.60	11661	39.53	1.341e-06	476	2205
1115	175.79	11500	39.68	1.382e-06	476	2191
1120	174.93	11337	39.81	1.427e-06	477	2181
1125	174.01	11172	39.79	1.477e-06	478	2165
1130	173.07	11005	39.61	1.530e-06	478	2157
1135	172.27	10838	39.31	1.578e-06	478	2142
1140	171.71	10673	39.13	1.612e-06	479	2125
1145	171.33	10512	39.21	1.635e-06	479	2108
1150	170.89	10352	39.29	1.663e-06	479	2090
1155	170.20	10193	39.93	1.707e-06	479	2081
1160	169.27	10031	40.19	1.769e-06	479	2070
1165	168.20	9870	39.96	1.843e-06	479	2052
1170	167.11	9711	39.51	1.920e-06	480	2036
1175	166.05	9554	39.17	1.999e-06	480	2024
1180	165.02	9398	38.64	2.080e-06	480	2017
1185	163.99	9244	38.15	2.163e-06	480	2007
1190	162.98	9093	37.66	2.247e-06	481	1990
1195	161.99	8944	37.16	2.332e-06	481	1978
1200	161.00	8800	36.73	2.419e-06	482	1968
1205	160.00	8658	36.53	2.513e-06	482	1948
1210	158.95	8518	36.46	2.617e-06	482	1938
1215	157.82	8379	36.33	2.733e-06	482	1926
1220	156.63	8239	36.09	2.864e-06	481	1915
1225	155.39	8100	35.53	3.008e-06	480	1907
1230	154.18	7962	34.85	3.157e-06	480	1897
1235	153.01	7826	34.11	3.308e-06	479	1886
1240	151.88	7696	33.69	3.461e-06	478	1875
1245	150.73	7567	33.46	3.623e-06	478	1865
1250	149.52	7439	33.28	3.802e-06	477	1854
1255	148.24	7309	32.81	4.001e-06	476	1851
1260	146.92	7180	32.19	4.220e-06	475	1843
1265	145.60	7053	31.53	4.457e-06	474	1832
1270	144.29	6929	31.07	4.703e-06	473	1820
1275	143.00	6806	30.60	4.961e-06	471	1809
1280	141.70	6685	30.06	5.235e-06	470	1798
1285	140.37	6565	29.68	5.535e-06	468	1785
1290	139.03	6446	29.26	5.868e-06	466	1772
1295	137.65	6328	28.87	6.229e-06	464	1761
1300	136.25	6213	28.41	6.614e-06	462	1744
1305	134.82	6099	27.99	7.031e-06	460	1729
1310	133.37	5985	27.56	7.497e-06	458	1712
1315	131.89	5872	27.11	8.009e-06	455	1700
1320	130.42	5759	26.62	8.555e-06	452	1697
1325	128.99	5646	25.96	9.122e-06	450	1669
1330	127.70	5535	25.40	9.664e-06	447	1654
1335	126.63	5426	25.05	1.014e-05	446	1650
1340	125.67	5318	24.82	1.058e-05	445	1634
1345	124.66	5214	24.41	1.107e-05	443	1604
1350	123.54	5111	24.72	1.164e-05	442	1586
1355	122.31	5008	24.39	1.230e-05	440	1569
1360	120.98	4907	24.01	1.305e-05	439	1550
1365	119.58	4806	23.66	1.390e-05	437	1527
1370	118.13	4707	23.12	1.484e-05	436	1512
1375	116.67	4609	22.72	1.585e-05	434	1492
1380	115.20	4512	22.23	1.694e-05	432	1471
1385	113.73	4415	21.77	1.812e-05	430	1467
1390	112.28	4319	21.24	1.938e-05	428	1428

STS-48 BET and Radiometer Data (concluded)

time (sec)	$h*10^{-3}$ (ft)	vel. (ft/sec)	α (°)	density ($slug/ft^3$)	T_∞ (°F)	IML temp (°F)
1395	110.85	4225	20.88	2.070e-05	427	1409
1400	109.43	4130	20.48	2.207e-05	426	1381
1405	108.02	4036	20.07	2.351e-05	425	1356
1410	106.64	3940	19.76	2.503e-05	424	1356
1415	105.28	3845	19.24	2.662e-05	423	1331
1420	103.92	3751	18.91	2.832e-05	422	1325
1425	102.57	3658	18.48	3.013e-05	421	1304
1430	101.23	3566	17.91	3.206e-05	420	1270
1435	99.89	3476	17.78	3.412e-05	419	1246
1440	98.55	3386	17.49	3.632e-05	417	1246
1445	97.21	3295	17.17	3.867e-05	416	1214
1450	95.86	3206	16.91	4.120e-05	415	1208
1455	94.55	3116	16.42	4.382e-05	414	1181
1460	93.38	3027	15.61	4.626e-05	413	1146
1465	92.35	2941	14.95	4.856e-05	412	1146
1470	91.30	2857	14.88	5.101e-05	411	1108
1475	90.18	2774	14.97	5.383e-05	410	1108
1480	88.99	2690	14.73	5.699e-05	409	1067
1485	87.74	2608	14.25	6.052e-05	408	1067
1490	86.42	2529	14.14	6.449e-05	406	1059
1495	85.04	2449	14.39	6.889e-05	405	1059
1500	83.70	2370	13.42	7.352e-05	404	1013
1505	82.45	2292	13.73	7.808e-05	402	984
1510	81.34	2211	13.38	8.241e-05	401	1013
1515	80.34	2132	13.03	8.650e-05	400	974
1520	79.43	2055	12.32	9.041e-05	400	931
1525	78.54	1981	11.41	9.448e-05	399	931
1530	77.61	1912	10.71	9.898e-05	398	920
1535	76.60	1849	10.06	1.042e-04	397	920
1540	75.47	1789	9.63	1.102e-04	395	920
1545	74.22	1731	9.57	1.174e-04	394	920
1550	72.87	1674	9.25	1.257e-04	392	871
1555	71.42	1621	9.11	1.353e-04	391	859
1560	69.89	1574	8.86	1.465e-04	388	859
1565	68.31	1526	8.75	1.593e-04	385	801
1570	66.69	1476	8.51	1.728e-04	384	787
1575	65.06	1426	8.17	1.869e-04	384	844
1580	63.43	1376	7.88	2.021e-04	384	787
1585	61.81	1322	7.55	2.206e-04	381	787
1590	60.20	1271	7.51	2.413e-04	377	787
1595	58.62	1217	7.18	2.610e-04	377	787
1600	57.08	1164	7.06	2.824e-04	376	787
1605	55.57	1115	6.90	3.066e-04	373	787
1610	54.11	1068	6.95	3.298e-04	373	701
1615	52.71	1024	6.78	3.553e-04	371	787
1620	51.35	980	6.38	3.794e-04	372	770
1625	50.02	939	6.58	4.047e-04	373	701
1630	48.69	904	6.55	4.310e-04	374	701
1635	47.36	888	8.14	4.576e-04	376	701
1640	46.11	868	6.39	4.817e-04	380	701
1645	44.85	856	6.11	5.106e-04	382	678
1650	43.54	840	6.66	5.436e-04	382	701
1655	42.26	825	6.81	5.732e-04	386	678
1660	41.03	811	6.11	6.038e-04	388	701
1665	39.82	800	5.99	6.349e-04	391	701
1670	38.56	786	7.63	6.682e-04	395	589
1675	37.34	764	7.90	7.010e-04	399	611
1680	36.21	745	7.43	7.302e-04	403	701
1685	35.10	737	7.39	7.619e-04	407	589
1690	33.96	734	7.73	7.942e-04	411	589
1695	32.80	728	7.77	8.228e-04	418	589
1700	31.67	719	6.99	8.536e-04	424	701
1705	30.58	708	6.84	8.864e-04	428	611
1710	29.50	697	7.15	9.190e-04	433	611
1715	28.42	688	7.59	9.505e-04	438	589
1720	27.37	682	6.67	9.813e-04	444	701
1725	26.33	679	7.36	1.013e-03	449	678
1730	25.28	666	7.92	1.047e-03	454	701
1735	24.24	653	8.20	1.083e-03	458	701
1740	23.27	645	7.55	1.119e-03	460	701
1745	22.37	636	7.76	1.153e-03	464	701
1750	21.52	629	7.84	1.185e-03	467	701

STS-42 BET and Radiometer Data

time (sec)	$h*10^{-3}$ (ft)	vel. (ft/sec)	α (°)	density ($slug/ft^3$)	T_∞ (°F)	IML temp (°F)
0	399.91	24961	40.15	1.941e-11	718	-460
5	397.30	24964	40.15	7.061e-12	689	-460
10	394.69	24967	40.21	3.401e-11	660	-460
15	392.01	24971	40.29	6.507e-11	640	-460
20	388.98	24974	40.43	6.864e-11	623	-460
25	386.40	24977	40.60	1.789e-11	609	-460
30	383.82	24981	40.86	1.812e-10	595	-460
35	381.25	24984	41.11	8.021e-11	581	-460
40	378.17	24987	41.10	3.456e-11	564	-460
45	375.62	24990	40.84	1.357e-10	550	-460
50	373.07	24994	40.64	1.187e-10	536	-460
55	370.53	24997	40.51	6.449e-11	522	-460
60	368.00	25000	40.41	2.368e-10	508	-460
65	364.97	25003	40.35	2.199e-10	492	-460
70	362.45	25006	40.31	2.366e-10	478	-460
75	359.94	25009	40.34	1.681e-10	462	-460
80	357.44	25012	40.42	2.943e-10	455	-460
85	354.95	25015	40.56	3.140e-10	448	-460
90	351.96	25019	40.69	3.509e-10	440	-460
95	349.49	25021	40.84	3.371e-10	433	-460
100	347.02	25025	41.04	2.097e-10	426	-460
105	344.57	25028	40.84	5.426e-10	420	-460
110	342.12	25030	40.62	4.517e-10	413	-460
115	339.19	25033	40.39	6.918e-10	405	-460
120	336.76	25036	40.14	9.383e-10	398	-460
125	334.35	25039	39.79	9.199e-10	391	-460
130	331.94	25041	39.44	1.089e-09	385	-460
135	329.46	25044	39.23	1.275e-09	378	-460
140	326.68	25046	39.28	1.568e-09	377	-460
145	324.31	25049	39.83	1.528e-09	373	-460
150	321.95	25051	40.41	1.650e-09	369	43
155	319.60	25053	40.81	1.827e-09	365	422
160	316.80	25055	41.14	1.969e-09	361	-460
165	314.48	25057	41.22	1.940e-09	357	422
170	312.17	25059	40.94	2.371e-09	353	422
175	309.88	25060	40.50	2.819e-09	349	494
180	307.60	25062	40.08	3.117e-09	345	652
185	304.89	25063	39.62	3.476e-09	341	701
190	302.65	25064	39.19	4.150e-09	337	819
195	300.43	25064	39.19	4.932e-09	334	859
200	298.22	25065	39.34	5.635e-09	330	944
205	296.04	25064	39.66	6.342e-09	326	1023
210	293.45	25064	40.31	7.065e-09	325	1085
215	291.33	25063	41.29	7.853e-09	325	1181
220	289.23	25060	41.52	9.153e-09	325	1259
225	287.16	25058	40.77	9.994e-09	325	1316
230	285.12	25055	39.47	1.137e-08	325	1392
235	282.72	25052	38.96	1.266e-08	325	1471
240	280.76	25048	39.06	1.429e-08	325	1550
245	278.84	25042	39.90	1.592e-08	325	1611
250	276.97	25036	41.23	1.687e-08	325	1669
255	275.08	25029	41.38	1.879e-08	325	1736
260	273.02	25021	40.24	2.032e-08	325	1791
265	271.32	25011	39.24	2.322e-08	325	1830
270	269.67	25001	39.20	2.601e-08	325	1880
275	268.09	24990	40.32	2.819e-08	325	1917
280	266.29	24977	41.33	3.006e-08	325	1958
285	264.88	24962	41.26	3.184e-08	325	1996
290	263.55	24944	40.02	3.438e-08	325	2030
295	262.30	24929	39.24	3.732e-08	325	2067
300	261.14	24912	40.01	3.923e-08	328	2094
305	259.87	24894	40.86	4.076e-08	331	2129
310	258.92	24873	40.88	4.341e-08	333	2158
315	258.07	24848	40.01	4.559e-08	335	2178
320	257.30	24827	39.41	4.830e-08	336	2199
325	256.61	24805	39.75	4.871e-08	338	2225
330	255.85	24783	39.84	4.940e-08	339	2256
335	255.28	24759	40.36	5.038e-08	340	2281
340	254.74	24730	40.61	5.150e-08	342	2299
345	254.23	24706	40.01	5.227e-08	343	2313
350	253.76	24682	39.79	5.304e-08	344	2330
355	253.22	24657	39.99	5.433e-08	345	2344
360	252.79	24631	40.18	5.568e-08	346	2357
365	252.37	24600	40.07	5.659e-08	347	2366
370	251.98	24573	39.95	5.917e-08	348	2379
375	251.58	24546	40.03	5.906e-08	348	2389
380	251.15	24518	40.12	6.048e-08	349	2396
385	250.79	24486	40.06	6.246e-08	350	2402
390	250.43	24455	40.01	6.410e-08	351	2408
395	250.08	24425	40.02	6.537e-08	352	2414
400	249.67	24395	40.04	6.574e-08	352	2423
405	249.33	24365	40.06	6.563e-08	353	2429
410	249.00	24328	40.05	6.742e-08	354	2436
415	248.67	24297	40.03	6.842e-08	355	2438
420	248.34	24266	40.02	6.946e-08	355	2447
425	247.95	24234	40.03	7.092e-08	356	2453
430	247.63	24202	40.03	7.190e-08	357	2456
435	247.30	24163	40.04	7.277e-08	358	2462
440	246.98	24130	40.05	7.372e-08	358	2467
445	246.65	24097	40.06	7.462e-08	359	2470
450	246.27	24063	40.04	7.548e-08	360	2479
455	245.95	24029	40.03	7.608e-08	360	2479
460	245.63	23988	40.03	7.693e-08	361	2484
465	245.31	23954	40.04	7.772e-08	362	2490
470	244.98	23920	40.04	7.876e-08	363	2490
475	244.57	23885	40.04	7.994e-08	364	2496
480	244.23	23849	40.04	8.120e-08	364	2498
485	243.87	23806	40.03	8.303e-08	365	2501
490	243.51	23769	40.04	8.676e-08	366	2507
495	243.13	23730	40.08	8.972e-08	366	2507
500	242.71	23691	40.08	9.049e-08	367	2512
505	242.36	23647	40.06	9.203e-08	368	2518
510	242.03	23603	40.06	9.355e-08	369	2523
515	241.71	23563	40.07	9.528e-08	370	2528
520	241.34	23521	40.03	9.772e-08	370	2528
525	241.04	23479	40.06	9.836e-08	371	2534
530	240.75	23429	40.08	9.973e-08	372	2536
535	240.46	23386	40.11	1.011e-07	372	2541
540	240.17	23343	40.12	1.020e-07	373	2544
545	239.82	23300	40.15	1.029e-07	374	2549
550	239.53	23256	40.17	1.038e-07	374	2549
555	239.23	23203	40.19	1.055e-07	375	2549

STS-42 BET and Radiometer Data (continued)

time (sec)	$h*10^{-3}$ (ft)	vel. (ft/sec)	α (°)	density ($slug/ft^3$)	T_∞ (°F)	IML temp (°F)
560	238.93	23159	40.22	1.060e-07	376	2555
565	238.62	23114	40.24	1.073e-07	376	2555
570	238.24	23069	40.27	1.084e-07	377	2557
575	237.92	23024	40.31	1.096e-07	378	2560
580	237.60	22969	40.34	1.117e-07	378	2560
585	237.28	22922	40.38	1.133e-07	379	2560
590	236.95	22875	40.41	1.148e-07	380	2560
595	236.56	22827	40.43	1.171e-07	381	2560
600	236.22	22779	40.38	1.177e-07	381	2560
605	235.88	22721	40.42	1.205e-07	382	2560
610	235.52	22672	40.42	1.221e-07	383	2560
615	235.15	22622	40.23	1.246e-07	384	2560
620	234.71	22572	40.14	1.261e-07	385	2560
625	234.32	22516	40.20	1.288e-07	385	2562
630	233.94	22461	40.22	1.303e-07	386	2562
635	233.54	22409	40.20	1.310e-07	387	2565
640	233.08	22358	40.22	1.329e-07	388	2565
645	232.69	22306	40.23	1.342e-07	389	2565
650	232.49	22243	40.26	1.375e-07	389	2565
655	233.29	22189	40.28	1.398e-07	388	2565
660	232.98	22135	40.30	1.418e-07	388	2562
665	232.55	22080	40.32	1.443e-07	389	2560
670	232.18	22024	40.34	1.468e-07	390	2560
675	231.76	21957	40.30	1.493e-07	391	2557
680	231.33	21900	40.23	1.528e-07	392	2555
685	230.89	21842	40.25	1.559e-07	393	2555
690	230.34	21784	40.10	1.575e-07	394	2555
695	229.92	21726	40.18	1.602e-07	395	2555
700	229.50	21655	40.21	1.623e-07	396	2555
705	229.13	21596	40.28	1.641e-07	397	2552
710	228.72	21534	40.31	1.702e-07	398	2552
715	228.20	21473	40.13	1.722e-07	399	2549
720	227.77	21411	40.21	1.741e-07	400	2547
725	227.33	21335	40.23	1.795e-07	400	2544
730	226.87	21271	40.20	1.847e-07	401	2544
735	226.36	21205	39.93	1.916e-07	403	2539
740	225.74	21138	39.70	1.966e-07	404	2539
745	225.23	21064	39.52	1.996e-07	405	2544
750	224.74	20991	39.57	2.040e-07	406	2544
755	224.24	20922	39.58	2.089e-07	407	2544
760	223.67	20853	39.52	2.125e-07	408	2539
765	223.20	20783	39.54	2.155e-07	409	2541
770	222.74	20699	39.53	2.184e-07	410	2539
775	222.30	20628	39.69	2.217e-07	411	2539
780	221.85	20556	39.85	2.258e-07	412	2536
785	221.30	20482	39.86	2.310e-07	413	2534
790	220.82	20407	39.90	2.346e-07	414	2534
795	220.33	20317	39.91	2.374e-07	415	2531
800	219.83	20242	40.15	2.403e-07	417	2528
805	219.35	20165	40.35	2.433e-07	418	2523
810	218.72	20086	40.51	2.484e-07	419	2523
815	218.18	20006	40.53	2.543e-07	420	2515
820	217.64	19909	40.56	2.601e-07	421	2512
825	217.05	19826	40.52	2.674e-07	423	2507
830	216.40	19740	41.58	2.749e-07	424	2501
835	215.60	19654	40.51	2.856e-07	426	2498
840	214.85	19566	40.45	2.928e-07	427	2496
845	214.09	19460	40.09	3.025e-07	429	2496
850	213.36	19371	40.08	3.108e-07	430	2496
855	212.67	19280	40.06	3.205e-07	432	2496
860	211.87	19187	39.95	3.304e-07	434	2493
865	211.21	19083	39.60	3.401e-07	435	2493
870	210.59	18981	39.68	3.496e-07	436	2496
875	209.95	18884	39.72	3.613e-07	438	2496
880	209.16	18784	39.67	3.731e-07	440	2493
885	208.53	18684	39.53	3.822e-07	441	2496
890	207.89	18563	39.54	3.923e-07	442	2496
895	207.26	18460	39.54	4.038e-07	444	2496
900	206.63	18356	39.53	4.128e-07	445	2493
905	205.87	18251	39.71	4.218e-07	447	2490
910	205.21	18143	39.86	4.312e-07	448	2490
915	204.53	18011	39.99	4.472e-07	450	2484
920	203.85	17897	39.98	4.685e-07	451	2484
925	203.10	17780	39.80	4.844e-07	453	2476
930	202.16	17663	39.76	4.989e-07	455	2479
935	201.40	17543	39.73	5.147e-07	455	2476
940	200.62	17398	39.70	5.347e-07	456	2473
945	199.84	17273	39.76	5.536e-07	457	2473
950	199.04	17146	39.71	5.737e-07	458	2465
955	198.06	17017	39.65	5.937e-07	459	2465
960	197.21	16886	39.67	6.151e-07	460	2456
965	196.35	16725	39.75	6.346e-07	461	2456
970	195.51	16589	39.89	6.512e-07	462	2450
975	194.61	16450	40.04	6.773e-07	463	2444
980	193.55	16307	40.09	6.976e-07	464	2441
985	192.64	16146	40.18	7.224e-07	465	2432
990	191.67	15985	40.33	7.515e-07	466	2423
995	190.65	15831	40.60	7.873e-07	467	2414
1000	189.40	15672	40.41	8.269e-07	468	2405
1005	188.29	15508	40.85	8.778e-07	470	2399
1010	187.09	15312	39.55	9.291e-07	471	2389
1015	185.93	15147	38.94	9.734e-07	472	2383
1020	184.92	14988	37.91	1.007e-06	473	2377
1025	184.13	14833	37.60	1.034e-06	474	2373
1030	183.70	14679	37.42	1.050e-06	475	2373
1035	182.93	14489	37.60	1.068e-06	475	2367
1040	183.12	14342	37.86	1.078e-06	475	2363
1045	182.87	14188	38.04	1.093e-06	475	2348
1050	182.57	14035	38.26	1.103e-06	476	2329
1055	182.36	13880	38.67	1.117e-06	476	2303
1060	182.31	13695	38.83	1.114e-06	476	2230
1065	182.55	13542	39.27	1.106e-06	476	2166
1070	183.07	13391	39.85	1.085e-06	475	2026
1075	183.85	13240	40.92	1.059e-06	474	1564
1080	184.32	13091	41.52	1.022e-06	474	810
1085	184.43	12913	42.64	1.012e-06	474	787
1090	184.08	12762	43.24	1.018e-06	474	1001
1095	183.24	12614	42.98	1.046e-06	475	1356
1100	181.88	12464	42.85	1.112e-06	476	1798
1105	180.50	12290	42.99	1.192e-06	478	1225
1110	179.13	12115	42.59	1.261e-06	479	1837
1115	177.95	11955	41.88	1.321e-06	481	1988

STS-42 BET and Radiometer Data (continued)

time (sec)	$h*10^{-3}$ (ft)	vel. (ft/sec)	α (°)	density ($slug/ft^3$)	T_∞ (°F)	IML temp (°F)
1120	176.79	11794	41.44	1.382e-06	482	2007
1125	175.96	11637	40.81	1.428e-06	483	1998
1130	175.14	11451	40.76	1.481e-06	484	1983
1135	174.26	11295	40.70	1.534e-06	485	1998
1140	173.34	11139	40.57	1.589e-06	486	2002
1145	172.17	10980	41.24	1.656e-06	487	2007
1150	171.14	10824	40.20	1.722e-06	487	2007
1155	170.09	10637	39.95	1.792e-06	487	1998
1160	169.02	10483	39.81	1.849e-06	487	1988
1165	167.92	10328	39.79	1.917e-06	487	1973
1170	166.53	10173	39.78	1.991e-06	487	1958
1175	165.42	10016	39.40	2.085e-06	487	1948
1180	164.38	9831	38.93	2.188e-06	487	1928
1185	163.41	9679	38.35	2.270e-06	487	1912
1190	162.55	9531	38.02	2.343e-06	487	1912
1195	161.57	9384	37.90	2.412e-06	487	1897
1200	160.69	9239	37.57	2.482e-06	487	1881
1205	159.85	9068	37.39	2.589e-06	487	1875
1210	158.99	8922	37.46	2.653e-06	487	1854
1215	158.05	8783	37.10	2.756e-06	487	1848
1220	157.01	8645	36.74	2.853e-06	487	1837
1225	156.07	8493	36.59	2.981e-06	487	1832
1230	155.05	8345	36.18	3.113e-06	487	1837
1235	153.98	8211	35.86	3.225e-06	485	1843
1240	152.68	8080	35.61	3.331e-06	483	1854
1245	151.48	7950	35.50	3.457e-06	481	1848
1250	149.76	7797	35.19	3.602e-06	479	1848
1255	148.60	7670	34.86	3.736e-06	477	1843
1260	147.41	7545	34.80	3.948e-06	475	1843
1265	145.98	7418	34.21	4.111e-06	473	1826
1270	144.76	7294	33.70	4.339e-06	471	1820
1275	143.55	7147	33.20	4.616e-06	469	1820
1280	142.35	7027	32.56	4.879e-06	467	1815
1285	141.16	6909	32.01	5.145e-06	466	1798
1290	139.70	6791	31.61	5.448e-06	463	1798
1295	138.58	6674	30.91	5.860e-06	462	1785
1300	137.58	6532	30.08	6.347e-06	460	1778
1305	136.69	6420	29.20	6.598e-06	459	1772
1310	135.76	6309	28.99	6.992e-06	458	1758
1315	134.49	6200	28.69	7.222e-06	456	1744
1320	133.33	6092	28.46	7.628e-06	454	1729
1325	132.06	5962	28.08	8.166e-06	452	1715
1330	130.71	5854	27.55	8.771e-06	450	1715
1335	129.17	5748	27.01	9.282e-06	447	1700
1340	127.25	5647	26.42	9.993e-06	445	1685
1345	125.58	5530	25.94	1.090e-05	442	1669
1350	123.97	5420	24.80	1.159e-05	440	1654
1355	122.55	5321	24.34	1.231e-05	437	1629
1360	120.96	5222	23.98	1.292e-05	435	1621
1365	119.69	5123	23.67	1.366e-05	433	1604
1370	118.44	5006	23.37	1.459e-05	431	1586
1375	117.21	4908	22.97	1.553e-05	429	1569
1380	115.99	4811	22.55	1.645e-05	428	1559
1385	114.51	4715	22.19	1.734e-05	425	1541
1390	113.31	4620	21.87	1.848e-05	423	1522
1395	112.09	4505	21.66	1.985e-05	422	1492
1400	110.85	4410	21.00	2.121e-05	420	1471
1405	109.65	4315	20.57	2.278e-05	418	1471
1410	108.20	4223	20.18	2.370e-05	416	1450
1415	106.98	4132	20.04	2.512e-05	414	1428
1420	105.66	4021	19.71	2.739e-05	412	1405
1425	104.33	3930	19.15	2.921e-05	411	1381
1430	102.98	3841	18.86	3.074e-05	410	1356
1435	101.42	3751	18.58	3.256e-05	409	1343
1440	100.21	3662	18.37	3.457e-05	409	1331
1445	99.077	3553	18.04	3.742e-05	408	1304
1450	98.070	3462	17.44	3.968e-05	408	1275
1455	97.168	3374	16.84	4.143e-05	407	1261
1460	96.109	3289	16.68	4.343e-05	406	1261
1465	95.073	3196	16.71	4.541e-05	406	1246
1470	93.985	3105	16.64	4.784e-05	405	1214
1475	92.815	3023	16.52	5.033e-05	405	1181
1480	91.270	2942	16.28	5.299e-05	404	1164
1485	89.964	2862	16.06	5.635e-05	403	1146
1490	88.597	2765	16.63	6.012e-05	402	1125
1495	87.156	2690	15.36	6.433e-05	402	1108
1500	85.689	2613	15.13	6.885e-05	401	1084
1505	84.031	2536	14.85	7.366e-05	400	1067
1510	82.634	2447	14.61	8.537e-05	399	1067
1515	81.246	2365	14.58	8.086e-05	398	1023
1520	79.986	2280	14.70	8.495e-05	398	1023
1525	78.979	2193	14.37	9.055e-05	397	1023
1530	78.016	2105	14.32	9.703e-05	397	1004
1535	77.251	2021	14.06	1.037e-04	396	994
1540	76.505	1940	13.01	1.069e-04	396	953
1545	75.793	1866	11.70	1.084e-04	395	953
1550	75.074	1801	11.13	1.094e-04	395	920
1555	74.191	1741	10.90	1.136e-04	395	920
1560	73.160	1683	10.74	1.215e-04	394	920
1565	72.034	1629	10.64	1.300e-04	393	883
1570	70.808	1576	10.55	1.406e-04	393	859
1575	69.463	1526	10.51	1.451e-04	392	859
1580	68.000	1476	10.96	1.500e-04	391	859
1585	66.602	1426	10.92	1.623e-04	390	859
1590	65.189	1376	10.49	1.758e-04	390	816
1595	63.755	1328	10.15	1.911e-04	390	787
1600	62.272	1283	9.83	2.103e-04	390	830
1605	60.838	1238	9.47	2.294e-04	390	816
1610	59.393	1194	9.25	2.448e-04	390	830
1615	57.932	1152	9.30	2.603e-04	390	787
1620	56.531	1110	8.99	2.791e-04	390	787
1625	55.103	1068	8.88	2.982e-04	390	787
1630	53.749	1029	8.59	3.255e-04	390	787
1635	52.372	992	8.35	3.513e-04	390	753
1640	50.955	960	8.61	3.697e-04	390	787
1645	49.539	930	8.30	3.923e-04	390	735
1650	48.228	903	8.44	4.091e-04	390	735
1655	46.943	883	9.10	4.348e-04	390	735
1660	45.682	861	9.11	4.608e-04	390	701
1665	44.507	841	9.14	4.877e-04	390	701
1670	43.376	825	8.62	5.165e-04	390	633
1675	42.269	808	7.97	5.422e-04	390	701

STS-42 BET and Radiometer Data (concluded)

time (sec)	$h*10^{-3}$ (ft)	vel. (ft/sec)	α (°)	density ($slug/ft^3$)	T_∞ (°F)	IML temp (°F)
1680	41.119	791	7.34	5.685e-04	390	701
1685	40.010	776	6.33	6.041e-04	390	701
1690	38.831	753	5.26	6.328e-04	390	701
1695	37.610	735	6.05	6.679e-04	390	633
1700	36.351	718	6.12	7.097e-04	390	633
1705	35.133	703	5.91	7.500e-04	394	701
1710	33.924	688	6.50	7.806e-04	398	589
1715	32.744	674	7.19	8.121e-04	402	701
1720	31.594	663	7.45	8.456e-04	406	701
1725	30.559	646	7.51	8.835e-04	410	701
1730	29.561	630	7.30	9.111e-04	413	701
1735	28.558	619	7.91	9.405e-04	417	633
1740	27.578	612	8.10	9.711e-04	420	701
1745	26.567	610	8.72	1.004e-03	424	701
1750	25.622	613	8.66	1.036e-03	427	701

STS-56 BET and Radiometer Data

time (sec)	$h*10^{-3}$ (ft)	vel. (ft/sec)	α (°)	density ($slug/ft^3$)	T_∞ (°F)	IML temp (°F)
0	400.17	24946	40.77	9.346e-11	721	-460
5	397.69	24949	40.76	2.497e-11	693	-460
10	395.22	24952	40.87	3.191e-11	666	-460
15	392.25	24955	40.99	9.311e-11	641	-460
20	389.78	24958	40.82	7.342e-11	628	-460
25	387.31	24962	40.64	2.716e-11	614	-460
30	384.85	24965	40.55	1.572e-10	601	-460
35	382.39	24968	40.51	1.156e-10	587	-460
40	379.44	24971	40.54	7.871e-11	571	-460
45	376.98	24974	40.59	1.624e-11	558	-460
50	374.53	24977	40.69	6.397e-11	544	-460
55	372.08	24980	40.85	1.446e-10	531	-460
60	369.64	24983	41.04	2.254e-10	517	-460
65	366.70	24986	41.07	1.285e-10	501	-460
70	364.27	24989	40.93	1.527e-10	488	-460
75	361.83	24992	40.64	1.275e-10	474	-460
80	359.40	24995	40.42	2.049e-10	460	-460
85	356.97	24998	40.31	1.318e-10	454	-460
90	354.06	25001	40.24	2.076e-10	445	-460
95	351.64	25004	40.23	3.391e-10	439	-460
100	349.23	25007	40.26	3.004e-10	432	-460
105	346.82	25010	40.31	4.139e-10	426	-460
110	344.31	25013	40.35	4.139e-10	419	-460
115	341.53	25016	40.40	4.946e-10	411	-460
120	339.13	25019	40.42	4.629e-10	404	-460
125	336.74	25021	40.40	6.425e-10	398	-460
130	334.35	25024	40.35	6.944e-10	391	-460
135	331.49	25027	40.27	8.277e-10	384	-460
140	329.12	25029	40.18	9.442e-10	377	-460
145	326.75	25032	40.13	1.204e-09	377	-460
150	324.38	25034	40.07	1.233e-09	373	-460
155	322.03	25037	39.98	1.496e-09	369	-460
160	319.21	25039	39.92	1.615e-09	365	406
165	316.87	25041	39.85	1.759e-09	361	7
170	314.54	25043	39.78	2.241e-09	357	406
175	312.22	25045	39.79	2.581e-09	353	494
180	309.91	25046	39.94	3.091e-09	349	569
185	307.15	25047	40.25	3.497e-09	345	569
190	304.86	25048	40.77	3.921e-09	341	679
195	302.59	25049	41.29	4.266e-09	337	764
200	300.33	25049	41.18	4.688e-09	333	834
205	298.09	25049	41.04	5.129e-09	330	924
210	295.42	25049	40.86	5.593e-09	325	996
215	293.21	25049	40.78	6.262e-09	325	1061
220	291.03	25047	40.88	7.454e-09	325	1133
225	288.86	25046	40.80	8.379e-09	325	1198
230	286.63	25044	40.59	9.396e-09	325	1271
235	284.19	25041	40.11	1.066e-08	325	1334
240	282.11	25038	39.44	1.194e-08	325	1403
245	280.07	25033	39.27	1.398e-08	325	1476
250	278.06	25028	39.92	1.535e-08	325	1540
255	275.70	25022	40.71	1.664e-08	325	1606
260	273.79	25015	41.04	1.818e-08	325	1667
265	271.92	25006	40.29	1.991e-08	325	1730
270	270.10	24997	39.29	2.153e-08	325	1788

STS-56 BET and Radiometer Data (continued)

time (sec)	h*10^{-3} (ft)	vel. (ft/sec)	α (°)	density (slug/ft^3)	T_∞ (°F)	IML temp (°F)
275	268.34	24988	39.20	2.329e-08	325	1836
280	266.30	24978	39.76	2.619e-08	325	1871
285	264.67	24966	41.07	2.780e-08	325	1921
290	263.12	24949	41.55	3.076e-08	325	1949
295	261.64	24933	40.90	3.273e-08	327	1991
300	260.24	24918	39.56	3.473e-08	330	2030
305	258.67	24902	39.17	3.617e-08	333	2064
310	257.46	24885	39.95	3.806e-08	336	2098
315	256.33	24862	40.88	4.001e-08	338	2126
320	255.30	24841	40.53	4.271e-08	340	2149
325	254.37	24820	40.10	4.525e-08	342	2172
330	253.38	24798	40.31	4.690e-08	345	2198
335	252.65	24774	40.38	4.869e-08	346	2216
340	251.99	24745	39.74	5.047e-08	348	2241
345	251.39	24721	39.27	5.165e-08	349	2265
350	250.81	24696	39.82	5.250e-08	350	2292
355	250.20	24670	40.46	5.420e-08	351	2305
360	249.71	24639	40.32	5.527e-08	352	2321
365	249.24	24610	39.88	5.586e-08	353	2337
370	248.80	24582	40.22	5.728e-08	354	2352
375	248.29	24554	40.58	5.770e-08	355	2365
380	247.89	24525	40.16	5.840e-08	356	2377
385	247.49	24491	39.80	6.029e-08	357	2386
390	247.11	24462	40.03	6.087e-08	358	2397
395	246.74	24431	40.16	6.508e-08	359	2397
400	246.29	24399	40.06	6.588e-08	360	2406
405	245.92	24367	40.00	6.686e-08	361	2415
410	245.56	24329	40.04	6.796e-08	361	2423
415	245.20	24296	40.06	7.011e-08	362	2431
420	244.86	24262	40.09	6.999e-08	363	2440
425	244.46	24229	40.10	7.020e-08	364	2442
430	244.13	24195	40.10	7.160e-08	364	2453
435	243.81	24154	40.10	7.262e-08	365	2453
440	243.49	24119	40.10	7.469e-08	366	2459
445	243.17	24083	40.10	7.579e-08	366	2467
450	242.78	24048	40.07	7.598e-08	367	2475
455	242.45	24012	40.06	7.659e-08	368	2480
460	242.13	23969	40.08	7.843e-08	369	2485
465	241.80	23932	40.09	7.973e-08	369	2485
470	241.48	23894	40.10	8.180e-08	370	2493
475	241.13	23856	40.10	8.221e-08	371	2496
480	240.83	23813	40.11	8.426e-08	371	2501
485	240.54	23770	40.14	8.579e-08	372	2506
490	240.26	23730	40.17	8.879e-08	373	2506
495	239.93	23689	40.03	9.127e-08	373	2511
500	239.66	23647	39.60	9.316e-08	374	2516
505	239.39	23600	39.38	8.938e-08	375	2526
510	239.11	23560	39.83	9.024e-08	375	2531
515	238.84	23518	40.15	9.391e-08	376	2531
520	238.51	23476	40.02	9.440e-08	376	2536
525	238.24	23434	39.83	9.519e-08	377	2536
530	237.96	23383	39.97	9.663e-08	378	2538
535	237.67	23340	39.99	9.712e-08	378	2543
540	237.37	23297	40.03	9.888e-08	379	2543
545	237.00	23254	40.05	9.933e-08	380	2546
550	236.68	23209	40.10	1.010e-07	380	2548
555	236.36	23156	40.14	1.019e-07	381	2553
560	236.03	23111	40.19	1.027e-07	382	2555
565	235.70	23066	40.24	1.047e-07	383	2553
570	235.30	23020	40.19	1.065e-07	383	2558
575	234.97	22973	40.00	1.102e-07	384	2555
580	234.65	22917	39.78	1.103e-07	385	2563
585	234.32	22870	39.81	1.122e-07	385	2565
590	233.99	22824	39.86	1.118e-07	386	2570
595	233.63	22776	39.91	1.146e-07	387	2567
600	233.31	22722	39.97	1.157e-07	388	2570
605	233.00	22670	40.01	1.191e-07	388	2570
610	232.67	22620	39.85	1.210e-07	389	2570
615	232.28	22570	39.84	1.233e-07	390	2570
620	231.95	22519	39.67	1.260e-07	390	2570
625	231.62	22458	39.45	1.293e-07	391	2572
630	231.29	22406	39.47	1.311e-07	392	2574
635	230.96	22354	39.52	1.329e-07	393	2577
640	230.25	22302	39.38	1.361e-07	394	2577
645	229.53	22249	39.15	1.388e-07	396	2579
650	229.21	22184	39.19	1.416e-07	396	2579
655	228.85	22130	39.09	1.431e-07	397	2581
660	228.50	22076	39.10	1.448e-07	398	2584
665	228.14	22021	39.16	1.467e-07	399	2586
670	227.84	21965	39.20	1.481e-07	399	2588
675	227.53	21898	39.25	1.508e-07	400	2584
680	227.23	21841	39.30	1.549e-07	401	2584
685	226.90	21783	39.34	1.570e-07	401	2584
690	226.51	21725	39.38	1.557e-07	402	2584
695	226.21	21666	39.54	1.594e-07	403	2584
700	225.87	21595	39.55	1.632e-07	404	2584
705	225.50	21534	39.58	1.672e-07	404	2584
710	225.09	21472	39.55	1.710e-07	405	2584
715	224.60	21409	39.39	1.735e-07	406	2579
720	224.19	21339	39.47	1.755e-07	407	2579
725	223.79	21270	39.85	1.799e-07	408	2581
730	223.44	21203	40.21	1.821e-07	409	2579
735	223.15	21136	40.32	1.850e-07	409	2574
740	223.03	21068	40.02	1.847e-07	410	2572
745	222.99	20989	39.96	1.822e-07	410	2572
750	222.94	20923	40.33	1.831e-07	410	2570
755	222.79	20856	40.75	1.869e-07	410	2563
760	222.48	20786	41.40	1.896e-07	411	2555
765	222.10	20714	41.65	1.916e-07	412	2546
770	221.62	20628	41.46	1.955e-07	413	2541
775	221.10	20554	41.50	2.012e-07	414	2533
780	220.53	20479	41.37	2.064e-07	415	2526
785	219.80	20404	41.17	2.103e-07	417	2524
790	219.18	20329	41.21	2.152e-07	418	2521
795	218.55	20243	40.99	2.245e-07	419	2516
800	217.90	20157	40.75	2.337e-07	421	2511
805	217.24	20075	40.50	2.413e-07	422	2508
810	216.45	19993	40.26	2.488e-07	424	2511
815	215.81	19912	40.05	2.539e-07	425	2511
820	215.19	19813	40.08	2.625e-07	427	2511
825	214.57	19729	39.96	2.675e-07	428	2511
830	213.93	19644	39.99	2.730e-07	429	2511

STS-56 BET and Radiometer Data (continued)

time (sec)	h*10^{-3} (ft)	vel. (ft/sec)	α (°)	density (slug/ft^3)	T_∞ (°F)	IML temp (°F)
835	213.22	19558	40.01	2.818e-07	431	2508
840	212.60	19459	39.93	2.872e-07	432	2506
845	211.98	19364	39.97	2.941e-07	433	2506
850	211.35	19275	39.98	2.990e-07	435	2503
855	210.60	19183	40.13	3.109e-07	436	2501
860	209.96	19089	39.95	3.195e-07	438	2498
865	209.31	18976	39.95	3.296e-07	439	2493
870	208.64	18879	39.89	3.394e-07	441	2490
875	207.97	18781	39.85	3.467e-07	442	2490
880	207.19	18683	39.84	3.533e-07	444	2483
885	206.53	18584	39.96	3.591e-07	445	2480
890	205.87	18462	40.14	3.714e-07	447	2480
895	205.23	18357	40.19	3.797e-07	448	2469
900	204.52	18253	40.25	3.871e-07	450	2469
905	203.64	18146	40.49	3.970e-07	451	2459
910	202.92	18036	40.55	4.135e-07	453	2453
915	202.08	17899	40.44	4.368e-07	455	2448
920	201.24	17782	40.08	4.619e-07	456	2442
925	200.42	17663	39.70	4.742e-07	456	2437
930	199.46	17544	39.56	4.918e-07	458	2437
935	198.68	17424	39.51	5.061e-07	458	2437
940	197.95	17277	39.55	5.212e-07	459	2431
945	197.21	17153	39.66	5.336e-07	460	2431
950	196.43	17027	39.84	5.490e-07	461	2423
955	195.51	16898	39.98	5.698e-07	462	2417
960	194.70	16749	40.03	5.934e-07	463	2409
965	193.85	16602	39.93	6.176e-07	464	2403
970	193.02	16461	40.09	6.325e-07	465	2400
975	192.04	16322	39.79	6.601e-07	466	2391
980	191.25	16180	39.69	6.788e-07	466	2386
985	190.46	16009	39.77	6.998e-07	467	2386
990	189.64	15863	39.82	7.381e-07	468	2374
995	188.77	15713	39.82	7.609e-07	469	2371
1000	187.67	15560	39.92	7.894e-07	470	2356
1005	186.75	15405	40.10	8.128e-07	471	2346
1010	185.85	15215	39.99	8.484e-07	472	2337
1015	185.02	15056	39.71	8.757e-07	473	2328
1020	184.29	14897	39.49	9.096e-07	474	2318
1025	183.54	14739	39.30	9.286e-07	475	2305
1030	183.00	14581	39.12	9.498e-07	475	2292
1035	182.53	14394	39.06	9.673e-07	476	2279
1040	182.09	14241	38.83	9.751e-07	476	2269
1045	181.66	14090	39.13	9.957e-07	477	2255
1050	181.07	13935	39.40	1.012e-06	477	2234
1055	180.53	13779	39.68	1.042e-06	478	2220
1060	179.98	13589	39.62	1.082e-06	479	2195
1065	179.42	13430	39.05	1.114e-06	479	2169
1070	178.86	13273	39.32	1.146e-06	480	2146
1075	178.27	13111	40.41	1.200e-06	480	2134
1080	177.69	12925	38.66	1.210e-06	481	2114
1085	177.12	12766	38.26	1.241e-06	482	2110
1090	176.57	12613	38.79	1.282e-06	482	2098
1095	175.80	12456	38.94	1.323e-06	483	2086
1100	175.15	12299	38.91	1.342e-06	484	2065
1105	174.49	12113	38.98	1.382e-06	485	2048
1110	173.83	11957	39.08	1.416e-06	485	2039
1115	173.19	11802	39.08	1.441e-06	486	2030
1120	172.42	11646	39.18	1.471e-06	487	2022
1125	171.74	11491	39.28	1.508e-06	487	1991
1130	171.03	11305	39.36	1.551e-06	487	1972
1135	170.28	11148	39.41	1.615e-06	487	1982
1140	169.47	10992	39.29	1.651e-06	487	1977
1145	168.45	10837	39.30	1.699e-06	487	1954
1150	167.56	10682	39.32	1.745e-06	487	1945
1155	166.69	10492	39.39	1.845e-06	487	1945
1160	165.94	10332	38.91	1.938e-06	487	1929
1165	165.43	10175	38.61	1.980e-06	487	1926
1170	165.04	10023	38.50	1.988e-06	487	1906
1175	164.68	9876	38.42	2.001e-06	487	1897
1180	164.19	9701	38.88	2.033e-06	487	1887
1185	163.54	9556	39.05	2.065e-06	487	1867
1190	162.68	9410	39.38	2.119e-06	487	1857
1195	161.63	9266	39.01	2.175e-06	487	1840
1200	160.66	9107	38.73	2.271e-06	487	1826
1205	159.67	8955	38.20	2.404e-06	487	1805
1210	158.54	8818	36.75	2.538e-06	487	1794
1215	157.26	8682	37.21	2.599e-06	487	1782
1220	156.16	8546	36.77	2.727e-06	487	1770
1225	155.11	8388	36.37	2.832e-06	487	1757
1230	154.11	8257	36.03	2.948e-06	485	1736
1235	153.11	8128	35.72	3.087e-06	484	1717
1240	151.87	7999	35.09	3.275e-06	482	1717
1245	150.84	7872	34.64	3.361e-06	480	1695
1250	149.82	7723	34.53	3.537e-06	479	1689
1255	148.78	7598	34.45	3.656e-06	477	1681
1260	147.72	7477	33.92	3.858e-06	476	1675
1265	146.37	7356	33.35	4.002e-06	474	1689
1270	145.07	7236	33.05	4.276e-06	472	1689
1275	143.39	7097	32.39	4.533e-06	469	1698
1280	142.25	6983	31.37	4.740e-06	467	1703
1285	141.14	6871	31.26	4.879e-06	466	1703
1290	139.79	6760	31.15	5.071e-06	464	1695
1295	138.62	6649	30.91	5.364e-06	462	1689
1300	137.42	6516	30.48	5.701e-06	460	1689
1305	136.21	6405	30.00	5.976e-06	458	1675
1310	134.94	6295	29.64	6.294e-06	456	1675
1315	133.55	6188	29.23	6.633e-06	454	1669
1320	132.30	6067	28.83	7.060e-06	452	1660
1325	131.08	5954	28.30	7.480e-06	450	1646
1330	129.84	5849	27.90	7.982e-06	449	1630
1335	128.35	5743	27.37	8.453e-06	446	1615
1340	127.12	5640	26.95	8.850e-06	444	1605
1345	125.91	5520	26.68	9.412e-06	443	1599
1350	124.67	5417	26.32	9.907e-06	441	1583
1355	123.42	5316	25.94	1.047e-05	439	1566
1360	121.90	5216	25.63	1.105e-05	437	1549
1365	120.61	5119	25.31	1.162e-05	435	1538
1370	119.29	4999	25.06	1.250e-05	433	1521
1375	117.96	4902	24.50	1.340e-05	430	1513
1380	116.60	4804	23.92	1.426e-05	428	1495
1385	114.98	4710	23.51	1.502e-05	426	1476
1390	113.64	4614	23.20	1.601e-05	424	1456

STS-56 BET and Radiometer Data (concluded)

time (sec)	$h*10^{-3}$ (ft)	vel. (ft/sec)	α (°)	density ($slug/ft^3$)	T_∞ (°F)	IML temp (°F)
1395	112.28	4502	22.73	1.727e-05	422	1436
1400	110.90	4408	22.27	1.851e-05	420	1415
1405	109.53	4314	21.67	1.991e-05	418	1393
1410	108.06	4220	21.03	2.129e-05	415	1380
1415	107.00	4128	20.27	2.283e-05	414	1357
1420	105.91	4022	19.99	2.404e-05	412	1347
1425	104.74	3934	19.79	2.548e-05	411	1323
1430	103.49	3846	19.55	2.708e-05	410	1298
1435	102.02	3758	19.10	2.878e-05	410	1298
1440	100.68	3663	18.82	3.035e-05	409	1271
1445	99.38	3572	18.53	3.253e-05	408	1255
1450	98.12	3485	18.13	3.461e-05	408	1214
1455	96.60	3403	17.59	3.689e-05	407	1214
1460	95.36	3320	17.65	3.947e-05	406	1184
1465	94.15	3216	17.00	4.213e-05	405	1151
1470	92.88	3138	16.06	4.539e-05	405	1130
1475	91.60	3058	16.14	4.812e-05	404	1116
1480	90.13	2976	16.04	5.088e-05	403	1094
1485	88.88	2894	15.70	5.407e-05	403	1079
1490	87.62	2797	15.45	5.777e-05	402	1039
1495	86.46	2716	14.59	6.079e-05	401	1039
1500	85.31	2639	14.86	6.460e-05	401	1022
1505	84.08	2560	14.72	6.838e-05	400	996
1510	82.86	2470	14.62	7.263e-05	399	967
1515	81.63	2389	14.35	7.565e-05	399	977
1520	80.53	2308	14.54	7.741e-05	398	948
1525	79.52	2225	14.62	8.199e-05	397	927
1530	78.64	2141	14.74	8.585e-05	397	916
1535	77.73	2058	14.63	9.174e-05	396	871
1540	76.88	1979	14.00	9.652e-05	396	895
1545	75.91	1907	12.94	1.027e-04	395	871
1550	74.99	1842	11.89	1.083e-04	395	834
1555	73.91	1781	11.07	1.145e-04	394	834
1560	72.74	1723	10.41	1.218e-04	394	834
1565	71.54	1668	9.96	1.307e-04	393	806
1570	70.17	1615	9.71	1.414e-04	392	792
1575	68.53	1564	9.78	1.490e-04	391	764
1580	67.11	1514	9.95	1.558e-04	391	764
1585	65.58	1460	9.68	1.675e-04	390	730
1590	63.96	1408	9.54	1.806e-04	390	764
1595	62.47	1356	9.19	1.968e-04	390	730
1600	61.00	1305	8.67	2.161e-04	390	764
1605	59.49	1254	8.20	2.382e-04	390	679
1610	58.07	1207	8.53	2.565e-04	390	713
1615	56.57	1163	7.96	2.782e-04	390	679
1620	55.06	1117	7.92	2.960e-04	390	679
1625	53.58	1073	8.54	3.160e-04	390	613
1630	52.38	1037	8.43	3.491e-04	390	679
1635	50.77	1003	7.78	3.751e-04	390	613
1640	49.43	971	7.78	3.942e-04	390	613
1645	48.07	951	8.73	4.049e-04	390	679
1650	46.79	936	9.07	4.362e-04	390	613
1655	45.57	922	9.05	4.655e-04	390	613
1660	44.34	916	8.49	4.914e-04	390	679
1665	43.13	918	8.18	5.214e-04	390	679
1670	41.86	921	7.85	5.489e-04	390	679
1675	40.52	929	7.10	5.817e-04	390	613
1680	39.20	935	6.74	6.248e-04	390	635
1685	37.83	939	6.21	6.633e-04	390	679
1690	36.45	935	5.76	7.042e-04	390	613
1695	35.00	925	5.61	7.454e-04	394	679
1700	33.63	914	4.99	7.814e-04	399	613
1705	32.26	904	4.98	8.224e-04	404	679
1710	30.96	893	4.96	8.635e-04	408	679
1715	29.64	874	4.75	9.023e-04	413	635
1720	28.23	841	6.37	9.479e-04	418	635
1725	26.75	789	7.69	1.004e-03	423	679
1730	25.17	736	8.26	1.061e-03	429	679
1735	23.67	697	6.99	1.114e-03	434	679
1740	22.36	660	7.26	1.159e-03	439	679
1745	21.24	619	7.70	1.200e-03	443	679
1750	20.35	580	7.62	1.250e-03	446	679

ORBITER LEESIDE SURFACE AEROHEATING ENVIRONMENT CHARACTERIZATION

David A. Throckmorton
NASA Langley Research Center
Hampton, VA

A written version of this paper was not provided by the author.
Copies of presentation materials used at the Symposium are presented herein.

LEESIDE FLOWFIELD CHARACTERISTICS

- Three-Dimensional, Separated Flow
- Laminar or Transitional or Turbulent
- Vortex Scrubbing and Impingement
- Hysteresis

FIGURE 1

DFI LEESIDE TEMPERATURE MEASUREMENT LOCATIONS

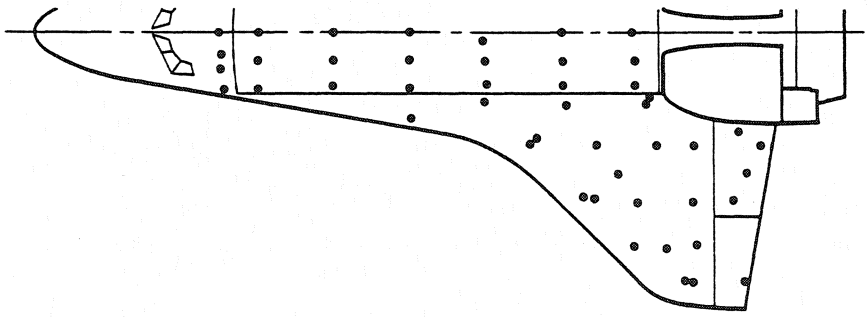

FIGURE 2

LEESIDE CENTERLINE HEAT TRANSFER

(X/L ≈ 0.4, α ≈ 40°)

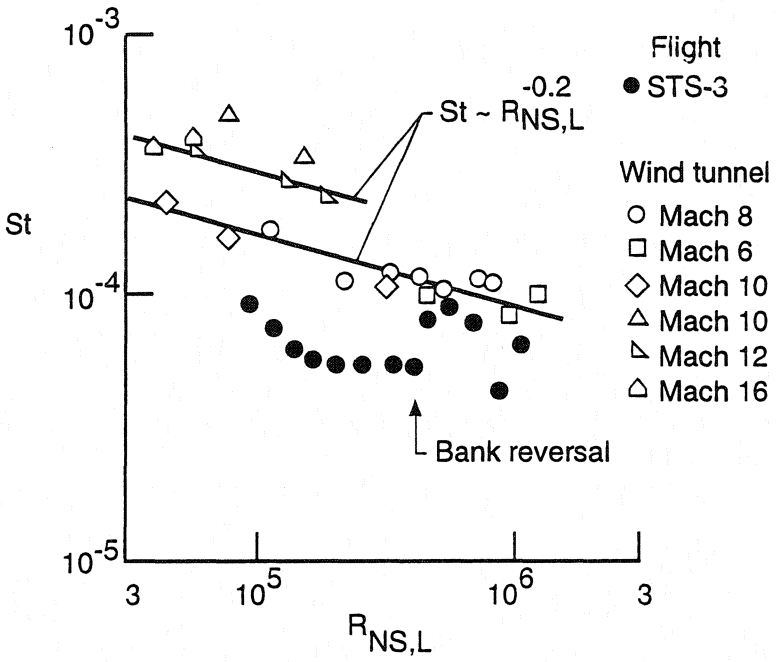

FIGURE 3

LEESIDE CENTERLINE HEAT TRANSFER

(X/L ≈ 0.6, α ≈ 40°)

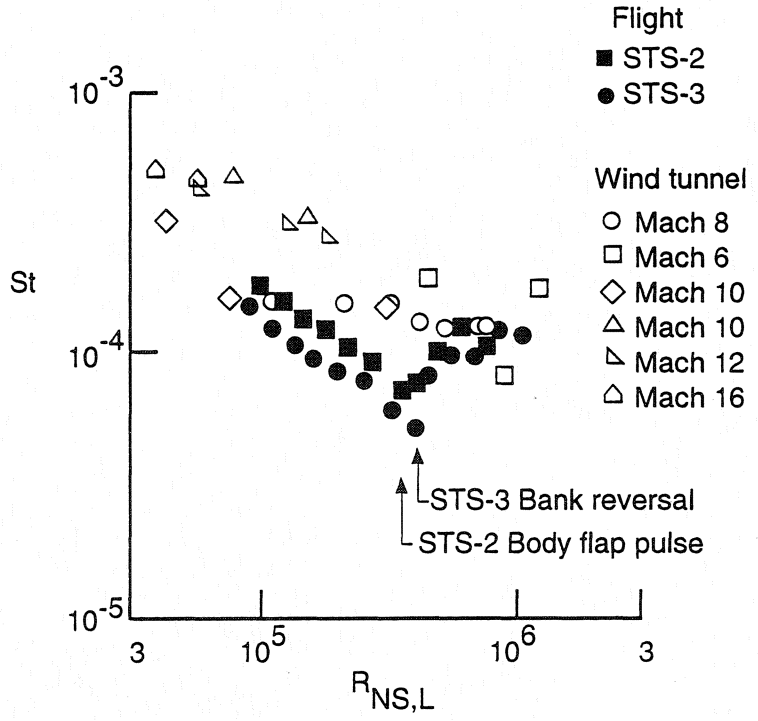

FIGURE 4

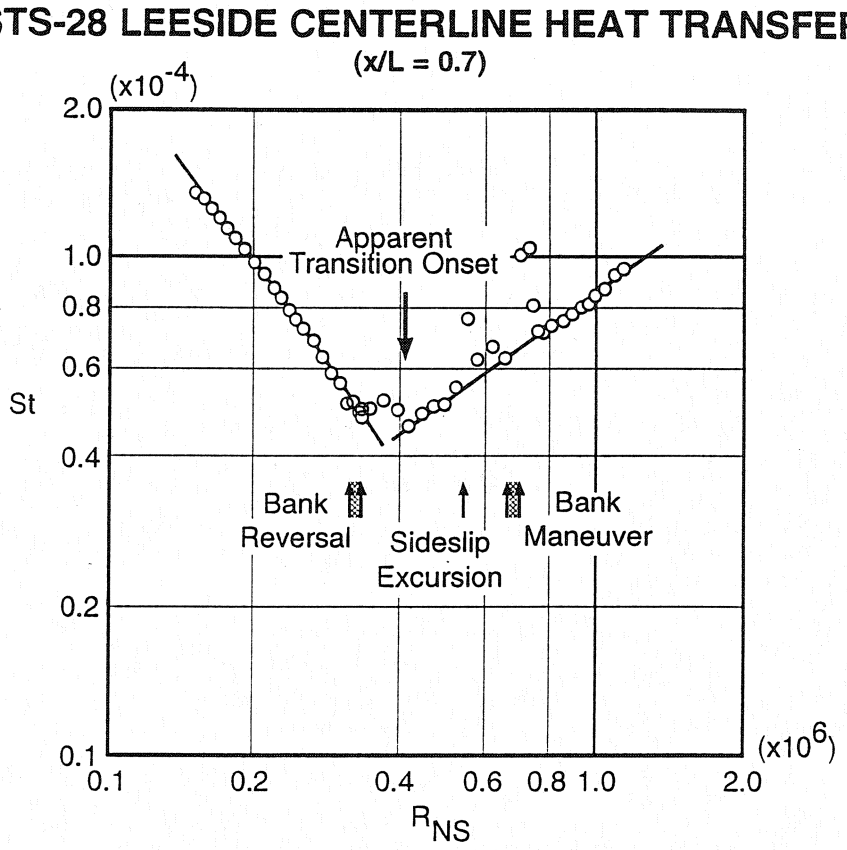

FIGURE 5

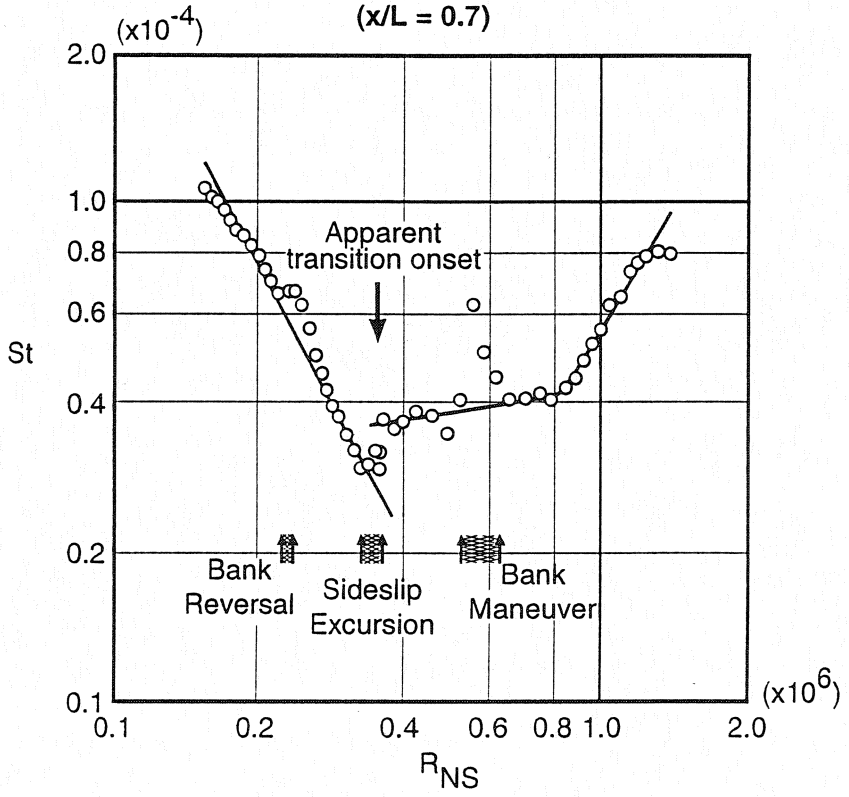

FIGURE 6

WING LEESIDE HEAT TRANSFER

(Y/b/2 ≈ 0.4, x/c ≈ 0.4, α ≈ 40°)

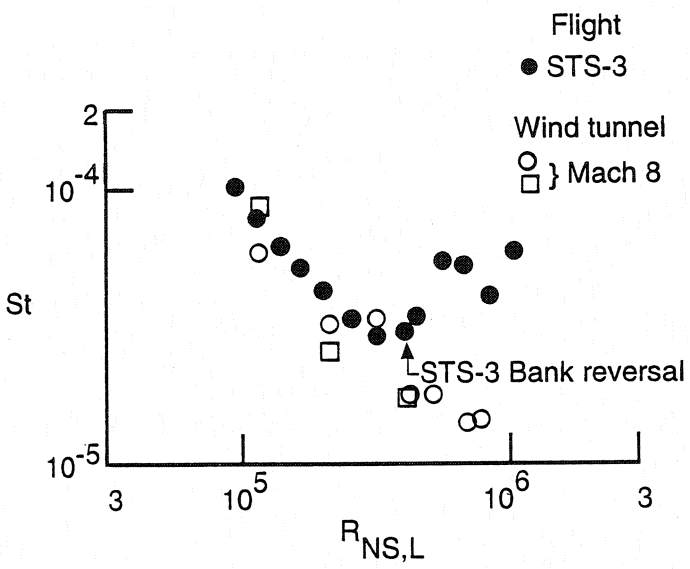

FIGURE 7

(Y/b/2 ≈ 0.9, x/c ≈ 0.4, α ≈ 40°)

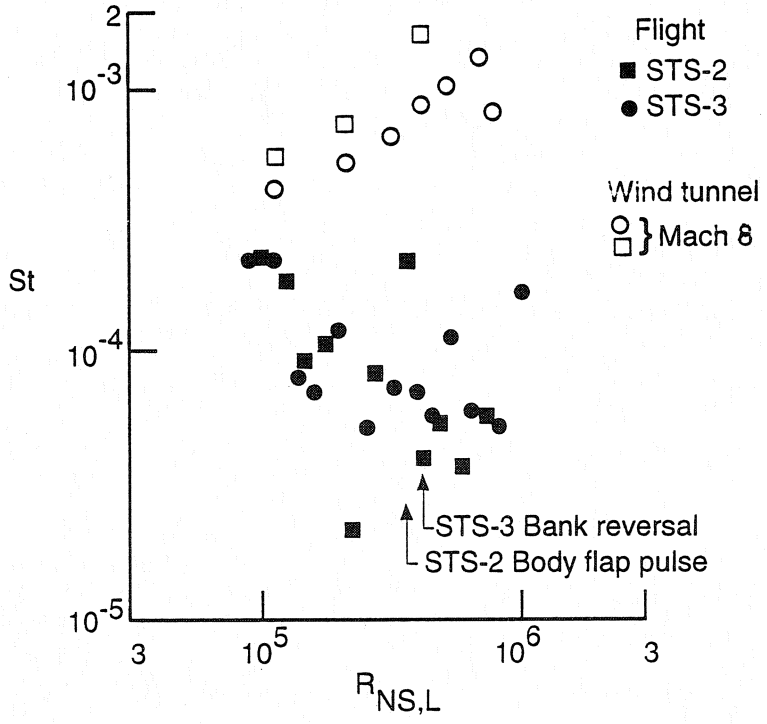

FIGURE 8

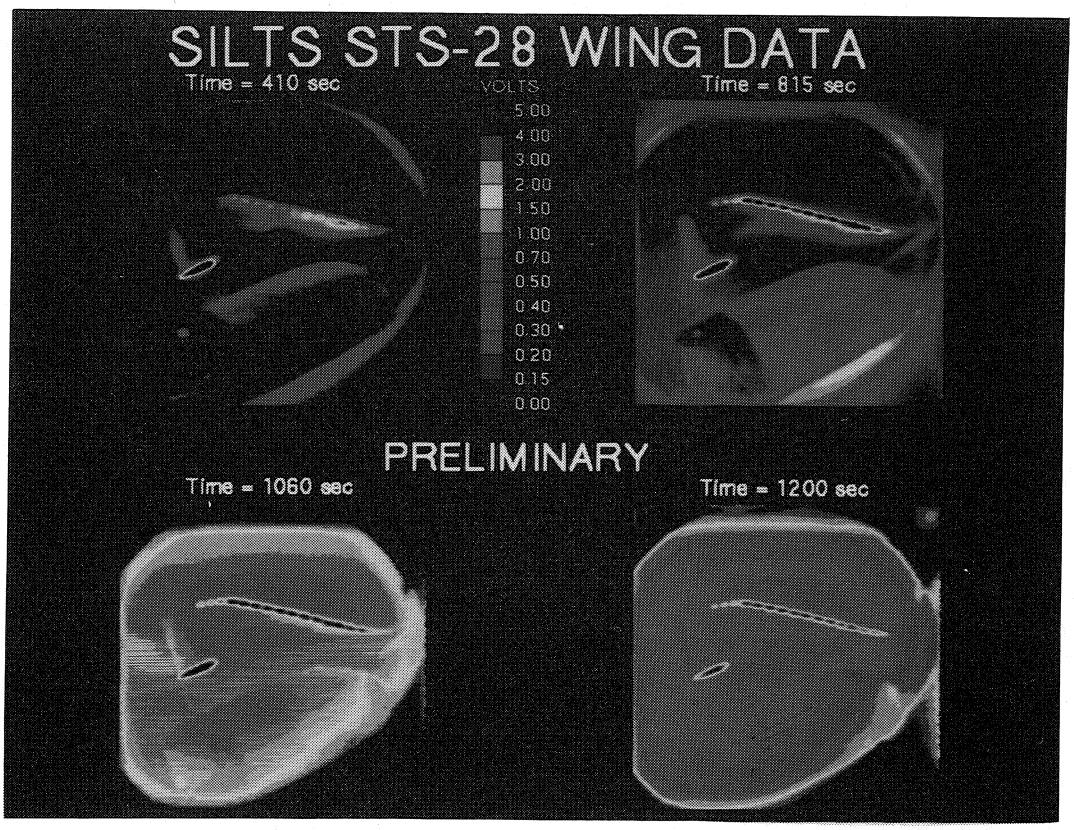

(See page 947 for color version of this figure.)

FIGURE 9

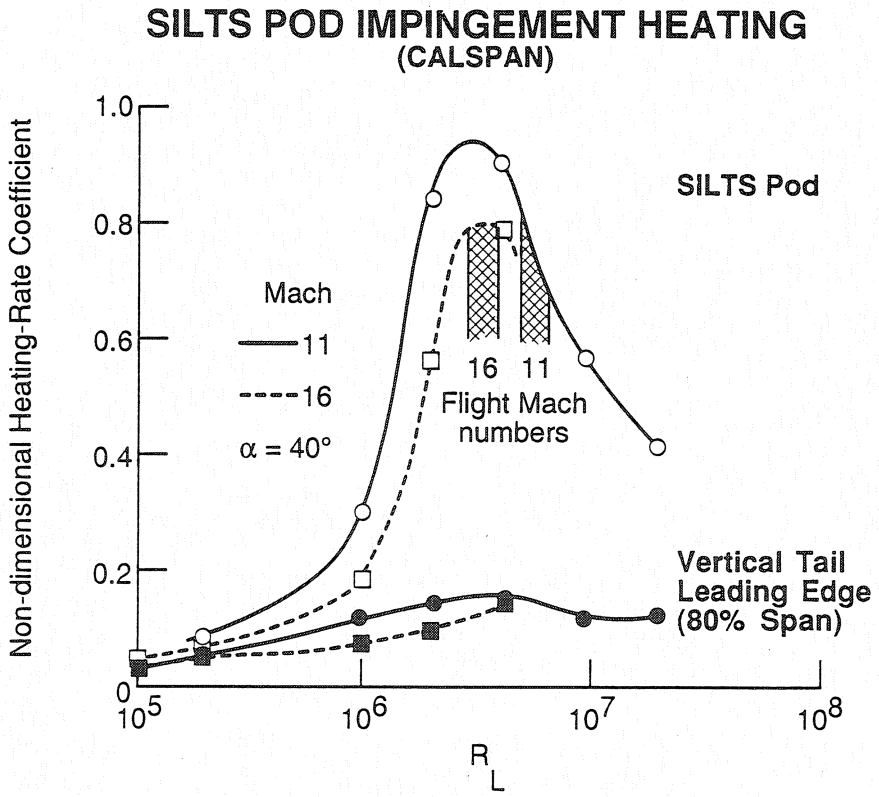

FIGURE 10

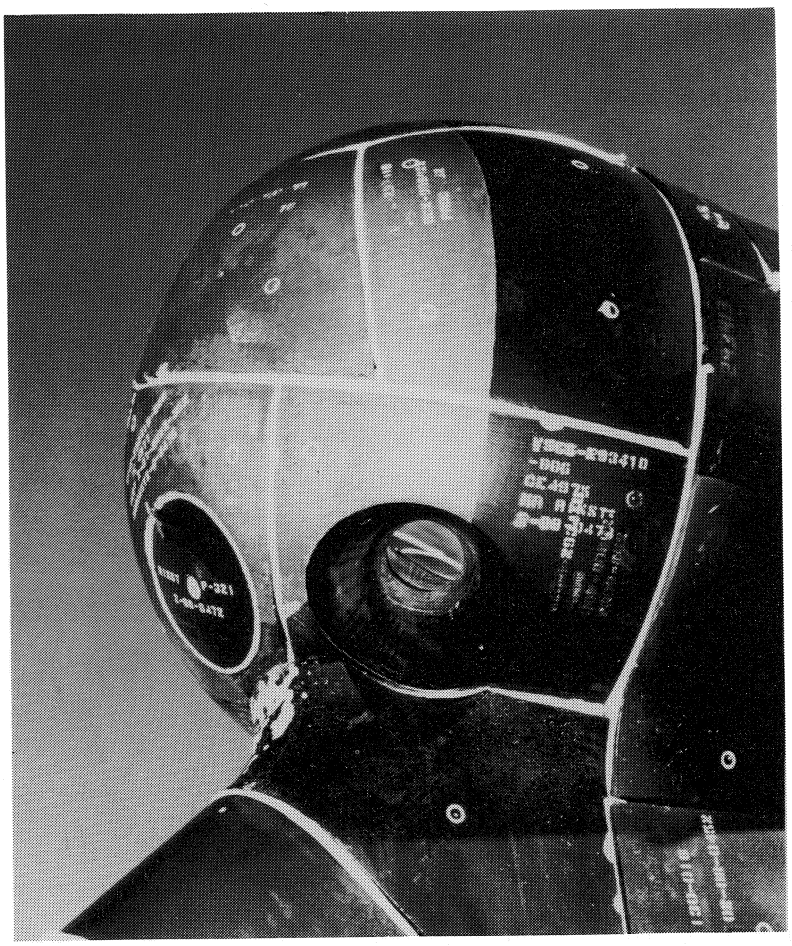

FIGURE 11

LEESIDE HEATING METHODOLOGY OVERPREDICTS IMPINGEMENT HEATING TO SILTS DOME

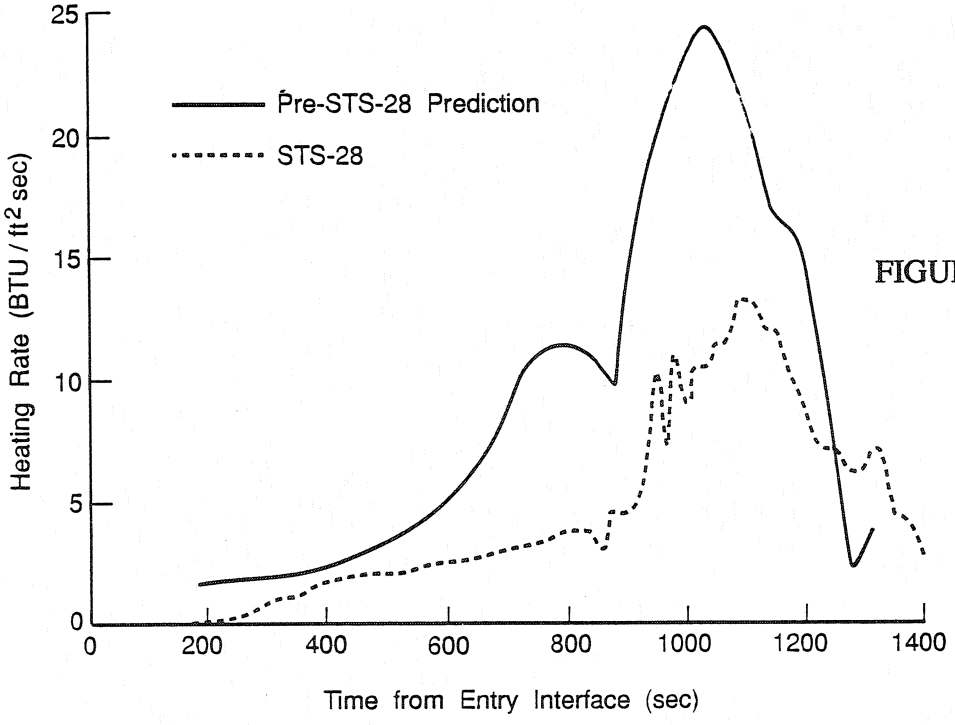

FIGURE 12

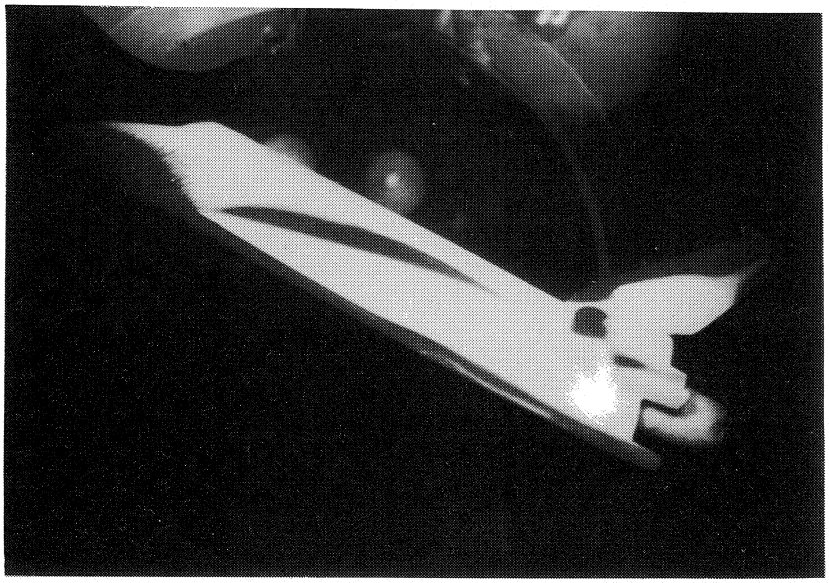

FIGURE 13

(See page 948 for color version of this figure.)

ORBITER SIDE FUSELAGE HEAT TRANSFER

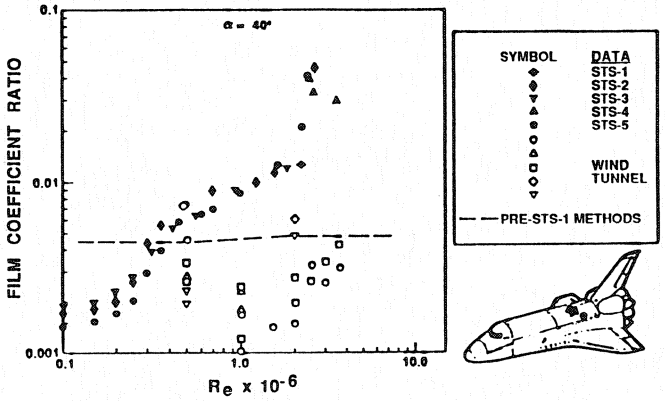

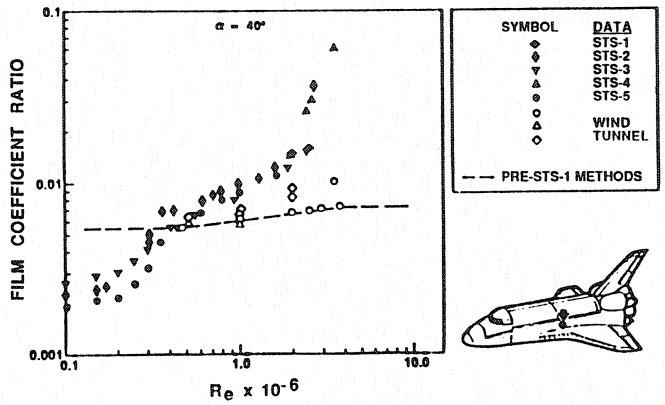

FIGURE 14

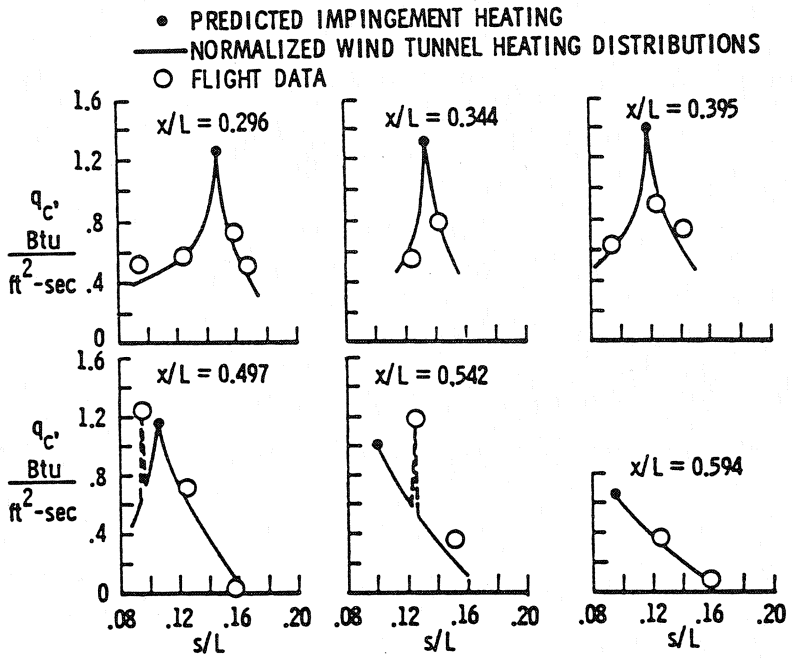

FIGURE 15

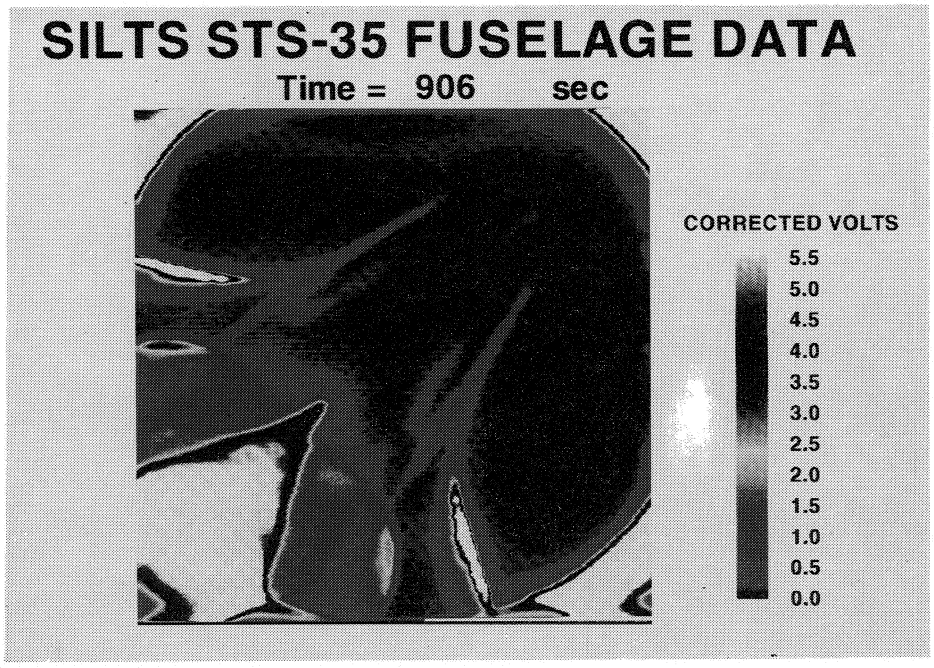

(See page 948 for color version of this figure.)

FIGURE 16

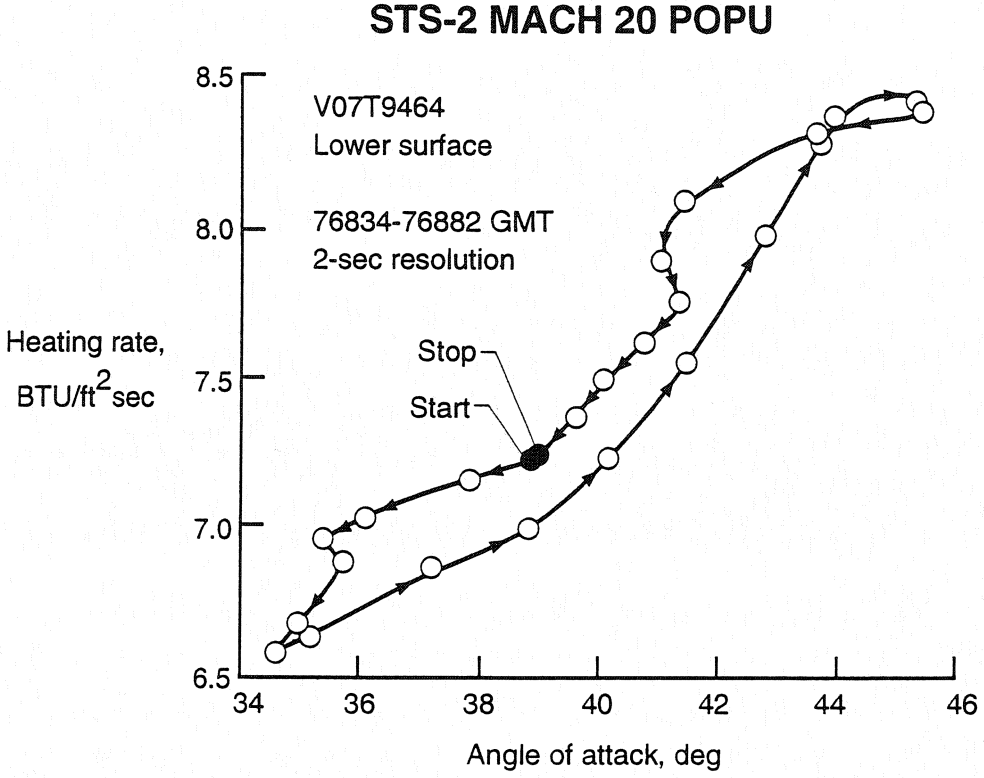

FIGURE 17

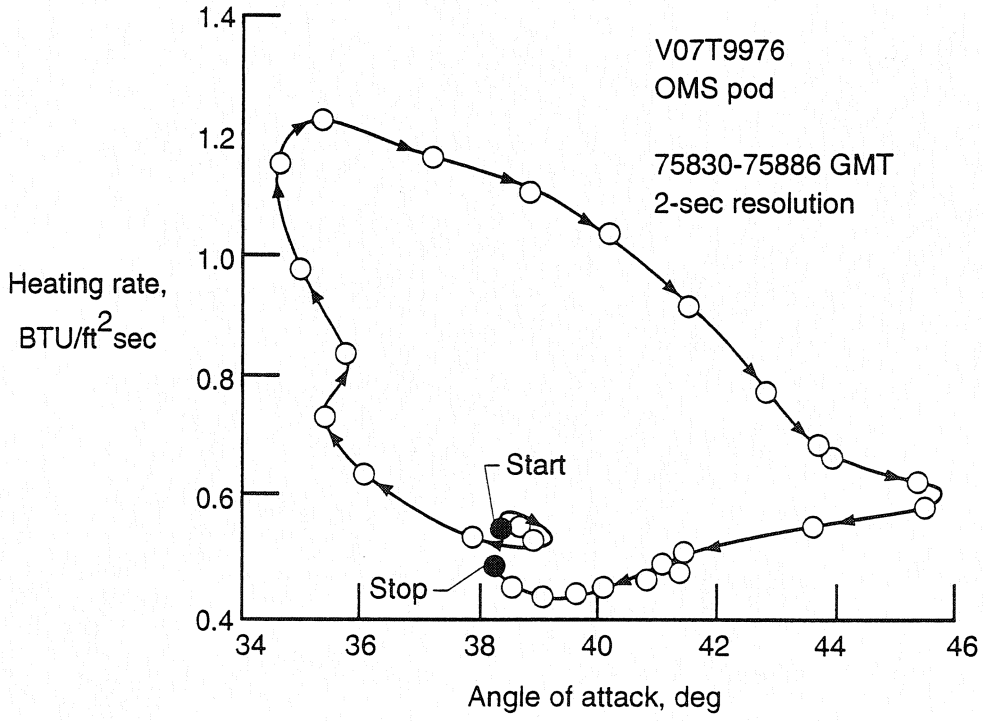

FIGURE 18

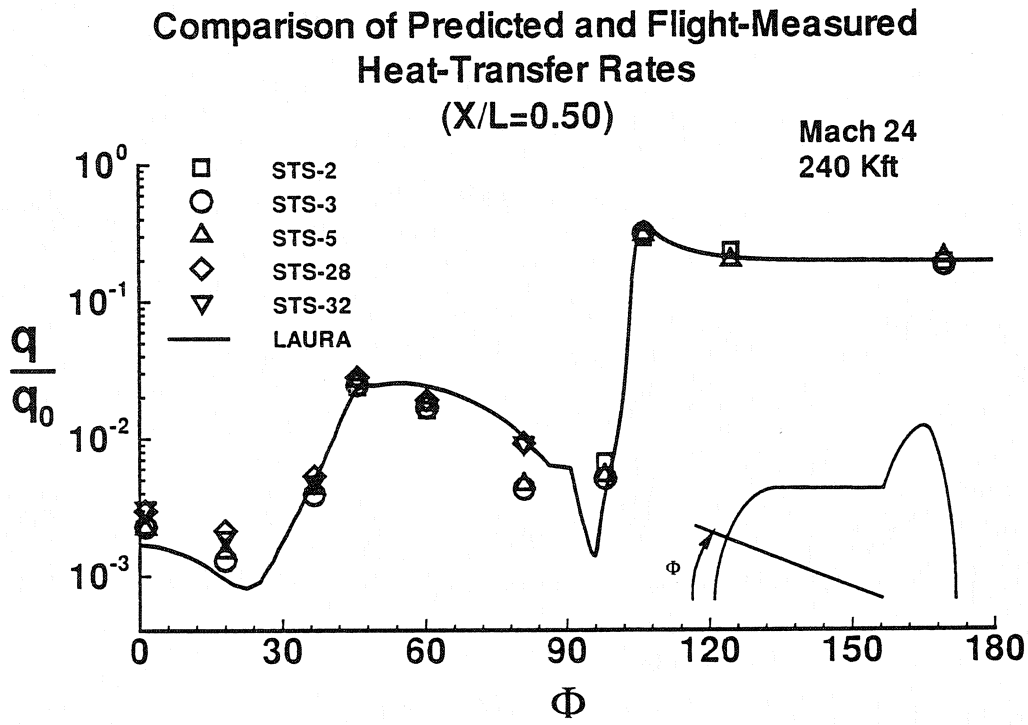

FIGURE 19

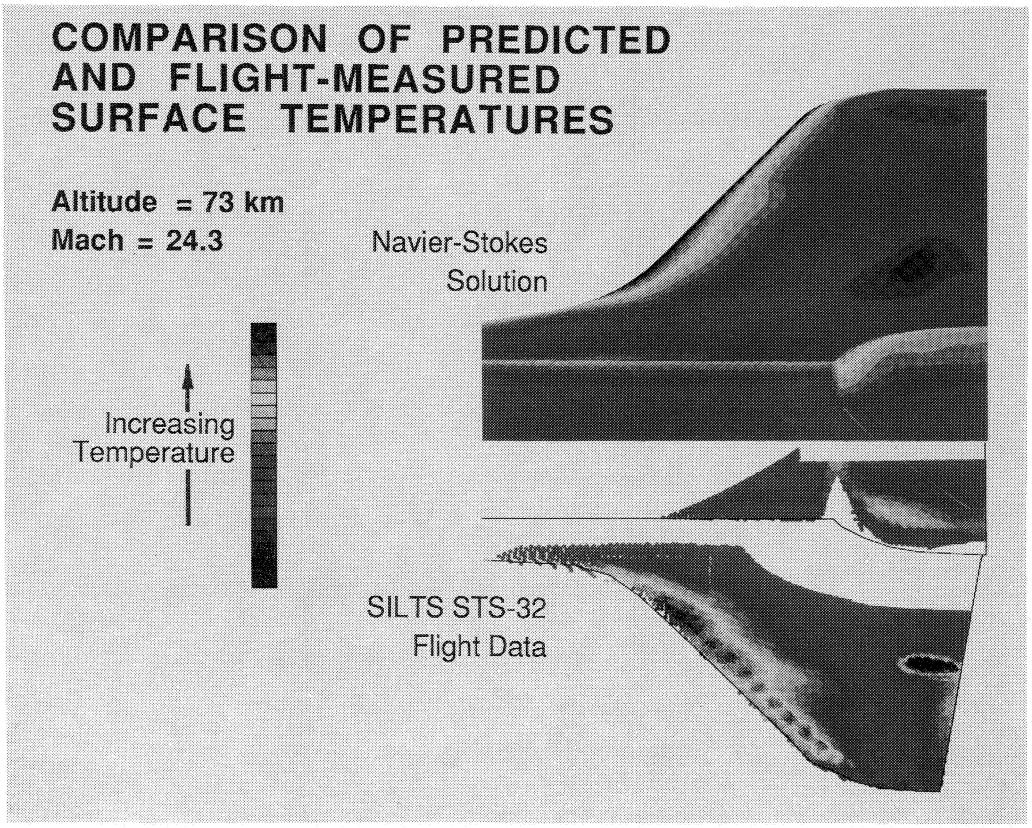

(See page 949 for color version of this figure.)
FIGURE 20

CONCLUDING REMARKS

- Leeside Heating Environment No Less Perplexing Today Than 20 Years Ago
- Flight Data Exhibit "Laminar" Behavior at Mach $\geq$ 16-17, at Which Condition a "Transitional Phenomenon" is Evident
- Vortex Impingement is of Significant Influence and is Not Well Modeled
- Modern CFD Shows Promise for Modeling the Leeside Flowfield Structure and Heat Transfer (Laminar)

FIGURE 21

ENGINEERING HEATING ANALYSES WITH APPLICATION TO SHUTTLE ORBITER

H. H. Hamilton II, E. V. Zoby, and C. J. Riley
NASA Langley Research Center
Hampton, VA

INTRODUCTION

The prediction of aerodynamic heating on advanced entry vehicles, such as the Shuttle orbiter, is a challenging design problem. These vehicles are in general three-dimensional (see Fig. 1) and can operate at large angles of attack during periods of peak heating. Ground-based facilities cannot completely simulate the flight environment; thus, it is necessary to rely heavily on computational fluid dynamic (CFD) codes to predict heating. The Shuttle orbiter traverses the atmosphere from entry interface to landing, passing through all flight regimes from free molecule to continuum; but, peak heating occurs in the continuum regime; thus, only continuum methods are considered in this paper.

Two types of codes, "benchmark" and "engineering," are used to predict heating in various phases of vehicle design. The best modern benchmark codes are usually based on finite-difference or finite-volume solutions of the Navier-Stokes (NS) equations[1,2] and include the accurate treatment of thermodynamic and transport phenomena. These codes yield surface heating predictions as well as detailed information about the entire flowfield, but require long run times on today's computers. Because of their long run times, the NS codes are not practical for most conceptual design applications but can provide detailed information needed for final design. Engineering codes,[3] on the other hand, use approximate solution techniques and treatment of thermodynamic and transport phenomena and provide reasonably accurate results and much shorter run times than benchmark codes. Thus, they are ideally suited for use in conceptual design studies.

Before any code can be used with confidence, it must be "validated" by comparing with experimental data.[4] Under ideal conditions, this task would involve comparing predictions with experimental data measured on the vehicle of interest at both wind-tunnel

and flight conditions. Obviously, this approach is not always possible. For the Shuttle orbiter, however, there exists an extensive flight-data base that was obtained during the development flights using the Development Flight Instrumentation (DFI)[5,6] as well as a large body of wind-tunnel data. The Shuttle orbiter, thus, offers a unique opportunity in code development and validation.

The purpose of the present paper is to describe several engineering codes used in the Aerothermodynamics Branch of the Space Systems Division at the NASA Langley Research Center and to present comparisons of heating predictions made using these codes with both wind-tunnel and flight data on the Shuttle orbiter. In addition, it will be shown that the approach for calculating heating on the Shuttle orbiter, described in this paper, can be applied to other three-dimensional entry vehicles such as the HL-20.

SYMBOLS

h	metric coefficient, static enthalpy or heat transfer coefficient
L	axial length
M	Mach number
p	pressure
q	convective heating rate
r, ϕ, z	cylindrical coordinates
s	coordinate on surface aligned with streamline direction or surface distance
R_B	base radius
R_e	unit Reynolds number
R_N	nose radius
T	static temperature
u, v, w	velocity components
V_∞	freestream velocity
x, y, z	cartesian coordinates
α	angle of attack
β	coordinate on surface normal to streamline direction
θ_C	cone half angle
θ_H	hyperboloid asymptotic angle
ρ	density

ξ, ζ, η	generalized coordinates

Subscripts:

b	body surface
e	boundary-layer edge
ref	reference
w	wall
$*$	dimensional
∞	freestream

BACKGROUND

Over the last two decades, engineering codes have been demonstrated to be of practical importance in supporting aerothermodynamic studies for both outer planetary and Earth entry vehicles. These methods were used not only in parametric studies but also in the design phase. Although CFD codes are now available for application to complex geometries and reacting-gas chemistry flows, these codes use large computer storage and have large run time requirements. Also, the size and complexity of CFD codes require a user to devote a large amount of time to understand the codes and to apply them. The engineering codes are characterized by low computer storage and run times and should continue to contribute in the future to the mission study and design process.

For this paper, engineering codes are loosely classified into three categories based on various levels of approximation: (1) simple engineering methods, (2) approximate flowfield solution methods, and (3) "equivalent axisymmetric" body methods. The simple engineering methods compute the local flow conditions based on normal-shock or oblique-shock entropy conditions over simple shapes such as wedges and cones. These methods can be employed at the conceptual study level by an experienced researcher to model the flow over regions of a vehicle surface for both aerodynamic and aerothermodynamic calculations. The approximate flowfield solution methods provide a more detailed procedure for computing the aerodynamic heating on the actual body shape and are useful in performing parametric studies needed during preliminary design. The limitation of these methods is strongly dependent on the accuracy of the inviscid flowfield

analysis and the method used to compute the heating. The equivalent axisymmetric body methods use an axisymmetric body to approximate a certain region of a three-dimensional vehicle, such as the windward symmetry plane, and apply a flowfield code to compute the flow over the approximate body shape. While this approach does not provide information about the entire vehicle, it does provide detailed information about a limited region of the vehicle which can be very helpful at the preliminary design stage. The accuracy of this approach obviously depends on the degree to which the flow over the equivalent body approximates the flow over the actual body. Engineering codes, applicable to each of these categories, have been used extensively to compute the heating on the Shuttle orbiter and other advanced entry vehicles.

Simple Engineering Methods

Prior to the early 1970's, the engineering methods were the primary source for predicting the aerothermal environment in the actual design phase of an entry vehicle. The engineering methods included approximate analyses for computing the stagnation point and the local laminar and turbulent heating rates. Representative methods for these calculations are presented for the laminar stagnation-point analysis[7–11] and for the local laminar[8,10,12–14] and turbulent[15–20] calculations. The approximate turbulent heat-transfer expressions are based on relating skin-friction to the Stanton number through Reynolds analogy. For the local heating-rate calculations, the flow properties were based on normal-shock or oblique-shock entropy conditions, and pressure distributions were either input or computed by analytic expressions. Boundary-layer calculations[21,22] or limited ground-test data provided the benchmark comparisons for testing the reliability of the results computed by the methods. The previously mentioned approximate techniques or similar expressions continue to be employed throughout the aeronautical community.

Today, the simple engineering techniques are used by industry and government aerospace agencies in the conceptual studies phase. The conceptual study starts with a vehicle geometry description based on the experience of the designer or the mission requirements. Portions of the actual vehicle are usually modeled with simple geometric shapes (see Fig. 2) which are much easier to analyze than the actual geometry. This geometry modeling process is coupled in the conceptual design phase with a range of programs with the capability to compute pertinent aerodynamic, aeroheating, thermal/structures, propulsion, performance/trajectory, and operations/cost parameters. This iterative process at the conceptual level aids in the definition and possibly resolution

of significant deficiencies in a vehicle concept before a major commitment to the project is initiated. Two codes which can account for several components in the conceptual study process and which are widely used by the aerospace community are MINIVER[23] and APAS[24] (Aerodynamic Preliminary Analysis System).

The MINIVER program provides to the user a menu for selection of methods to compute post-shock and local flow properties as well as laminar and turbulent heating-rate values. Options are available in the code to compute the heating at the stagnation point of a vehicle, over swept leading edges, interference and boundary-layer transition regions as well as over sharp nose wedges and cones. The heating expressions for the wedges or cones are based on incompressible skin-friction relations which employ the Eckert reference temperature (enthalpy) method to account for compressibility effects. The skin-friction expressions are related to heat transfer by a Reynolds analogy factor. The calculations can be based on perfect gas or equilibrium air chemistry, and angle-of-attack effects are included through use of an equivalent cone or an approximate cross-flow option. The heating rates can be computed for two- or three-dimensional (3-D) surfaces where 3-D effects are included by a flat-plate to sharp-cone correction, and the flow calculations are based on normal-shock or sharp-cone entropy conditions. An illustration of the different heating levels which can be computed by the code options is shown in Fig. 3. The heating rates are computed along the windward symmetry plane of the Shuttle Orbiter for the STS-2 trajectory at 47.7 km altitude. The experimental flight data[6] are also shown.

The APAS program employs a finite surface element method and computes separate inviscid and viscous solutions on each element. These quantities are integrated to obtain total vehicle forces and moments. The inviscid solutions are based on an array of pressure options which are applicable to simple geometries, e.g., sharp wedges or cones, and the viscous results are computed with approximate laminar or turbulent skin-friction relations. A major advantage of the APAS code over other similar engineering analyses is that vehicle aerodynamics are predicted over the supersonic and hypersonic speed range with the same geometry model. The properties in the skin-friction relations are also based on the Eckert reference temperature (enthalpy) method to account for compressibility effects. The skin-friction relations are related to heating rates through a Reynolds analogy factor, and the calculations can be based on perfect gas or equilibrium air chemistry conditions.

The approximate flowfield methods provide an engineering approach in aerothermodynamic studies to couple the inviscid and viscous flows where the viscous flow can be computed by finite-difference or integral boundary-layer methods. In 1960, Ferri[25] demonstrated the influence of the inviscid local flow properties over blunted vehicles on surface heat transfer. Streamlines that pass through different points on the curved shock, which is generated by the blunt nose, are characterized by different entropy levels, and these streamlines are gradually entrained in the boundary layer as the layer grows over the surface (Fig. 4). This process has been referred to as "entropy-layer swallowing." For regions of the vehicle surface affected by this process, the variable-entropy boundary-layer edge conditions were demonstrated to increase the local heating rates, especially the turbulent rates, over corresponding rates computed with normal-shock entropy conditions. Typically, the entropy-layer swallowing effects are approximately accounted for in an inviscid-viscous analysis, e. g., Refs. 26 and 27, by mass balancing. The iterative mass balancing procedure equates the mass flow in the boundary layer at the body point of interest to a stream tube of equal mass in the freestream. Another iterative method was suggested by Popinski[28] to overcome inherent difficulties involved with applying mass balancing to three-dimensional flow problems. Popinski suggested that variable-entropy effects be locally included by moving out in the inviscid flowfield a distance equal to the boundary-layer thickness and using these properties as the boundary-layer edge properties. This concept was incorporated in an approximate flowfield method[29] and predicted surface pressures and heating-rate results at 0 deg angle-of-attack conditions were shown to be in good agreement with experimental data and with CFD predictions. An example of this effort is shown in Fig. 5 where the Reentry F flight data[30] are compared with results of approximate[29] and detailed[31] analysis. The approximate flowfield method uses a second-order Maslen pressure relation[32] and an iterative method to converge the inviscid flowfield over the desired body.

Approximate flowfield techniques were not used extensively in design calculations through the 1960's, however, due primarily to the existing state of the art in computational capabilities. Also, since the mission requirements and vehicle performance capabilities allowed for reasonably large design safety factors, predictions based on conservative assumptions could be employed. The vehicle designer had significant flexibility in payload design to insure that the science objectives were successfully met. Although advances in computational capabilities even in the late 1960's reduced the concern of excessive

computer costs, the major drivers in a wider implementation of the approximate flowfield methods were technology issues which required more detailed and accurate analysis than afforded by the simple engineering methods. Examples of these technology issues were encountered in the outer-planetary probe studies conducted in the 1970's and are found currently in the design studies of the proposed air-breathing transatmospheric vehicle (TAV). The outer-planetary probes were based on high-energy entry conditions (in excess of 100 km/sec for the Galileo project) and resulted in large radiative and convective fluxes. A reliable design of an ablative heat shield is not possible for this type of thermal environment without the knowledge of the flow property distributions in the shock layer. The TAV has limited design margins, since present performance capabilities are not sufficient to meet mission requirements and relatively accurate predictions are even required in the preliminary design phase. Thus, not only has the use of the approximate flowfield analyses increased, but also the level of analysis in some of these methods has likewise improved. For instance, approximate predictions of outer-planetary inviscid radiative heating levels[33] and of convective heating rates at both outer-planetary and Earth entry conditions[29] have been shown to be in good agreement with a Viscous Shock Layer (VSL) analysis.[34] These methods were applied to axisymmetric bodies only. An illustration of the results of these investigations is shown in Fig. 6. Predicted convective heating rates from an approximate[29] and detailed[34] method are compared for a Saturn entry condition.

Since most entry configurations, such as the Shuttle orbiter, are three dimensional, an approximate flowfield for computing heating on three-dimensional bodies is needed. One such method is based on the axisymmetric analog developed by Cooke.[35] Following that approach, the three-dimensional boundary-layer equations are written in a streamline coordinate system, and the cross-flow velocity in the boundary layer which is tangent to the surface and normal to the inviscid streamline direction is assumed to be zero. The resulting boundary-layer equations are identical in form to the axisymmetric boundary-layer equations if the distance along a streamline is interpreted as surface distance and the metric coefficient associated with the coordinate direction normal to the streamline direction, h (see Fig. 7), is equated to the axisymmetric body radius. These assumptions allow any axisymmetric heating method to be used to compute the heating along an inviscid surface streamline. Thus, by considering multiple streamlines the heating on an entire vehicle can be computed. Hayes[36] has shown that the assumption of small cross flow in the boundary is valid when the streamline curvature is small; and further, Vaglio-Laurin[13] has shown that when the wall is highly cooled, as it is in most flight applications, the small cross flow assumption is valid even for cases where the streamline curvature may not be small.

The most time consuming aspect of applying this technique is that of computing the three-dimensional inviscid flowfield from which the surface streamlines and metrics are determined. DeJarnette and Hamilton[37] presented a relatively simple and fast method for calculating the streamline information used in the heating calculations which is based on an input pressure distribution. The input pressure distribution can be obtained from correlations, other calculations or experimental data. The edge properties used in this approach were based on normal shock entropy. In References 38 and 39, DeJarnette presents improved methods of computing the streamlines and metrics from known pressure distributions and extends the approach to include entropy-layer swallowing. The approximate method[38] was developed for simple shapes defined by conic sections. This method is known as AEROHEAT and is widely used by the aerospace community. However, an investigation[40] demonstrated that the heating predictions were not satisfactory for small half-angle cones, especially less than 15 deg, and the deficiency was attributed to the use of Newtonian pressures. (Unlike the analysis of Ref. 29 which computes flowfield and surface pressures, these procedures of DeJarnette and associates employ an assumed pressure distribution). Significant improvements in the heating predictions were attained by pressure correlations that were developed[41] for half-angle cones less than 15 deg. While the approach of using a known pressure distribution to compute the streamlines and metrics is relatively simple and works well for axisymmetric bodies, it does not, in general, work as well for a shape, such as the Shuttle orbiter, which has a relatively flat lower surface. This is due in part to the fact that, for these shapes, the streamlines are very sensitive to the input pressure distribution, making it very difficult to obtain pressures that are sufficiently accurate to yield good streamline and heating results. Zoby, *et al.*[42] used an algebraic expression for the streamline metric, derived from the Newtonian streamline concept,[43] to modify the engineering code[29] for calculating the heating on the windward and leeward symmetry planes of spherically-blunted cones at angle of attack, and the predicted results compared well with available experimental data for cone half angles greater than 15 deg.

An improved engineering inviscid-boundary layer method[44,45] has been recently developed by combining a simplified three-dimensional (3-D) inviscid technique[44] with the axisymmetric analog[35] and a set of approximate convective heating equations.[29] This algorithm is referred to as THINBL (Three-dimensional Hypersonic Inviscid-Boundary Layer method). The inviscid technique, which is similar to the thin shock layer method of Maslen[32] significantly improves the 3-D capabilities of existing engineering methods. The method is applicable to perfect gas and equilibrium air flows at both laminar and turbulent

conditions. The 3-D inviscid analysis is simplified by using approximate stream functions in the shock layer and by using an explicit expression developed by Maslen for the pressure across the shock layer. Like Maslen's method, this technique is an inverse method; *i.e.* for an assumed shock shape, the corresponding body shape is calculated. The solution procedure involves iteratively changing the shock shape in the subsonic-transonic region until the correct body shape is obtained. Beyond this region, the shock surface is determined using a marching technique. The 3-D boundary-layer analysis is simplified by using the axisymmetric analog as is done in most engineering aerothermal methods. Surface streamlines are determined by solving the inviscid momentum equations along the body surface using the body geometry and the surface pressure distribution generated by the approximate 3-D inviscid analysis. Along each streamline, the approximate convective heating equations of Zoby[29] are used to calculate the surface heating rates. Boundary-layer edge conditions are found, similar to Ref. 29, by interpolating in the inviscid solution a distance away from the wall equal to the boundary-layer thickness to approximately account for the effects of entropy-layer swallowing. Solutions have been obtained for axisymmetric shapes (paraboloids, sphere-cones) and simple 3-D shapes (blunted elliptic cones) at angle of attack.[45] Comparisons with experimental data[46] and Navier-Stokes solutions[1] have shown good agreement as noted in Figs. 8 and 9. Thus, this engineering method provides a unique capability for flowfield solutions over 3-D blunted noses as well as 3-D afterbodies. In addition, the method is much faster than numerical solutions of the full inviscid flowfield equations.

To get around the problem associated with using assumed pressure distributions, a method was developed[47] and improved[48,49] for calculating the inviscid surface streamlines and metrics from the velocity components obtained from an inviscid flowfield solution.[50,51] This approach provides a more accurate way of calculating the streamline information and thus the heating. Using this approach along with the approximate heating relationships of Zoby,[29] an engineering heating code, AA3DBL[48] (Axisymmetric Analog for 3D Boundary Layers), has been developed which is applicable to a wider range of vehicle shapes. Heating predictions from AA3DBL have been shown to compare well with experimental data and results from other benchmark calculations. However, because the streamline and heating calculations for most of the body are performed in a cylindrical coordinate system there are still certain types of bodies that can not be defined (namely, those bodies whose cross section can not be described with a single valued function in cylindrical coordinates – see Fig. 10).

To remove the restrictions associated with using a cylindrical coordinate system, a new engineering heating code, LATCH[52] (Langley Approximate Three-Dimensional Convective Heating), has been developed which uses a generalized body-fitted coordinate system (see Fig. 11) to calculate streamline location and heating. This coordinate system is compatible with the one used in the LAURA (Langley Aerothermodynamic Upwind Relaxation Algorithm) code; and since the inviscid version of LAURA can be used to compute the inviscid flowfield over almost any body shape, the LATCH code, coupled with the flowfield output from LAURA, can also be used to compute the heating over almost any shape. Results of calculations for the Shuttle orbiter using both AA3DBL and LATCH will be discussed in detail in a later section.

The engineering codes that have been described thus far are applicable to conditions where the fluid is an ideal gas or in chemical equilibrium. Obviously, with future missions that encompass significant nonequilibrium chemistry effects, the level of sophistication in engineering codes will further increase. Although the axisymmetric analog concept is still applicable for nonequilibrium chemistry, some significant changes will have to be made in the way the boundary layer is calculated and possibly in the way that the edge properties are obtained from the inviscid solution. However, a relatively simple method (the equivalent axisymmetric body method), described in the next section, is applicable to certain body shapes, such as the Shuttle orbiter, and can be used to make heating calculations where nonequilibrium chemistry effects are important.

Equivalent Axisymmetric Body Methods

The engineering methods discussed thus far use the actual vehicle shape and then apply some form of approximate solution technique to compute the heating. Another useful approach is to use an "equivalent axisymmetric" body to represent a limited region of the vehicle, such as the windward symmetry plane, and then apply either an approximate or detailed flowfield code to compute the heating. Adams, *et al.*[53] used a hyperboloid of revolution (see Fig. 12) to approximate the windward symmetry plane of the Shuttle orbiter at large angle of attack ($\alpha = 30$ deg) and demonstrated that the shock shape, pressure, heating, and flowfield calculated on this body compared well with experimental data. Murray, *et al.*[54] used a similar approach to calculate the flowfield and heating on the Shuttle orbiter for 15 deg $\leq \alpha \leq$ 45 deg and found that the results were much better at the larger angles of attack ($\alpha \geq 30$ deg).

The equivalent axisymmetric body concept of Adams, *et al.*[53] was extended[55] to include an angle of attack range of 25-45 deg. For known longitudinal and cross-sectional measurements, a nose radius and asymptotic half angle (θ_H) were computed for an axisymmetric hyperboloid which modeled the Shuttle orbiter's windward symmetry plane at an angle of attack.

The equivalent body results were incorporated in approximate[55] and detailed[56] axisymmetric flowfield codes and the heating predictions were compared with Shuttle ground[57] and flight-test data[6] as well as results of other CFD predictions.[58,59] Typical results of these comparisons are shown in Figs. 13 and 14, and the agreement is very good. The reason that the equivalent body concept is successful for the Shuttle orbiter is that it has a relatively wide, flat lower surface with a smoothly decreasing slope in the longitudinal direction and thus the hyperboloids can model both the Shuttle orbiter longitudinal and circumferential cross sections at different angles of attack with reasonably accuracy. However, the equivalent axisymmetric body concept is not always applicable. For example, an equivalent cone angle ($\alpha + \theta_c$) does not provide adequate modeling for a small half-angle cone at angle of attack. Viscous Shock Layer[31] laminar and turbulent heating rates computed for perfect gas and equilibrium air chemistry conditions for a spherically blunted 5 deg half-angle cone were presented in Ref. 60 and show the influence of angle of attack (cross flow) on cone heating. Poor comparisons are obtained when an equivalent cone ($\alpha + \theta_c$) is used to compute the laminar heating for the 5 deg cone at 10 deg angle of attack (see Fig. 15). However, for either chemistry condition, the turbulent heating levels for the cone at angle of attack and the equivalent cone are essentially the same. This result is expected, and as explained in Ref. 61, the reason for the smaller cross-flow effect in turbulent flow than in laminar flow is because the turbulent shear stress is so large it dominates all other effects.

APPLICATION OF THE AXISYMMETRIC ANALOG

In the remainder of the paper, heating calculations from LATCH[52] are compared with experimental data and with results from other calculations. As discussed previously, LATCH is an approximate three-dimensional heating code based on the axisymmetric analog[35] which is written in a generalized, body-fitted coordinate system ξ, ζ, η (see Fig. 11). The coordinate system is defined numerically, based on cartesian coordinates x, y, z, such that $\xi = \xi(x, y, z)$, $\zeta = \zeta(x, y, z)$, and $\eta = \eta(x, y, z)$. In this paper, flowfield data obtained from an inviscid version of LAURA[1] have been used with LATCH to perform the

heating calculations, but flowfield data from any three-dimensional inviscid code can be used.

Geometry Description

The geometry used in the Shuttle orbiter calculations in this paper is the "HALIS" orbiter geometry and is shown in Fig. 16 along with the complete Shuttle orbiter geometry. This geometry model was developed initially for use with the HALIS[51] inviscid flowfield code to simplify shuttle flowfield calculations. The HALIS orbiter models the lower surface of the Shuttle orbiter back to $x/L = 0.94$ and has the same upper symmetry plane profile as the Shuttle orbiter (except for canopy and vertical tail). However, the upper surface has been modified by filling in the region between the leading edge of the strake or wing and the upper symmetry plane with elliptical segments. This simplifies the leeside geometry and makes calculations in this region much easier; but it does not affect calculations on the windward side, because, at the angles of attack of interest, the crossflow velocity at the leading edge is supersonic.

Shuttle Orbiter

In this section, heating calculations from LATCH are presented for the Shuttle orbiter and are compared with other computations and with experimental data. The heating comparisons are presented first at wind tunnel conditions and then in flight. The wind tunnel case considered here is for an angle of attack of 30 deg, a Mach number of 5.83, and a unit Reynolds number of 1.94 x 10^6/m. The remaining freestream conditions for this case are given in Table I (case 1). The inviscid data used in LATCH to perform the heating calculations for this case were obtained from an inviscid version of LAURA.[1] A grid of 145 points down the body, 81 points around the body, and 41 points between the body and outer computational boundary was used and the solution required approximately 5-10 hours on a Cray-YMP computer. The LATCH heating computations used 201 streamlines and required approximately 30 minutes on a Sun SPARCstation 2. The heating results for the windward symmetry plane are presented in Fig. 17 and are compared with calculations from AA3DBL[49], LAURA[1] and experimental data.[62] The experimental data used for comparison were obtained in air on a 0.0075 scale model of the HALIS orbiter which was designed to provide a large number of high quality heat-transfer measurements for

comparison with CFD predictions. Although there are some slight differences, the LATCH calculations are in general in very good agreement with the other data.

A comparison of heating in a circumferential direction around the body is presented in Fig. 18 at $x/L = 0.55$. The results are plotted as q_w vs s/L, where s is the surface distance around the body measured normal to the symmetry plane (starting on the lower surface and increasing toward the upper surface). The heating first increases in a direction away from lower symmetry plane, reaches a peak near the leading edge, and finally decreases rapidly on the leeside. The peak in heating near the leading edge is caused by a strong divergence of the surface streamlines in this region combined with a rapid acceleration of the flow. This general pattern of circumferential heating has been observed[49] at all axial stations. The LATCH heating predictions are in good agreement with the other results near the symmetry plane but are lower than the other results in the vicinity of the leading edge. AA3DBL and LATCH are very similar codes and although they are written in different coordinate systems they would be expected to produce almost identical results for this case. The primary difference between these two heating predictions is in the inviscid solutions that were used. AA3DBL used inviscid data from HALIS while LATCH used data from an inviscid version of LAURA. Some differences have been noted in the pressures and surface velocities near the leading edge and these differences probably cause the difference in predicted heating.

The maximum heating rate near the wing (or fuselage) leading edge for this case is presented in Fig. 19 as a function of x/L. The experimental values of heating are shown only for those cross sections where a gauge was located near the leading edge. It should be noted that the experimental measurements, although dense compared with other experimental studies, may not be sufficiently dense to capture the "absolute maximum" leading-edge heating, and thus the actual peak values are probably higher than those shown. In addition, surface conduction is usually a problem near a small leading edge such as this and conduction would tend to produce measured heating rates that are lower than the actual heating rate. The rapid rise in heating near $x/L = 0.6$ is associated with the beginning of the wing. The leading edge heating reaches a sharply defined peak near $x/L = 0.7$, which approaches the stagnation point value. This peak in heating is located just downstream of the start of the wing shock (see Fig. 20). Further downstream, the heating first decreases rapidly, levels out near the start of the bow-shock wing-shock interaction ($x/L = 0.75$), and then decreases rapidly again as the wing turns more parallel to the flow. There are some differences in the LATCH and AA3DBL heating predictions

which are thought to be due to differences in the inviscid solutions used in each case (see previous paragraph), but both predictions track the experimental data reasonably well.

Several points on the STS-2 trajectory were analyzed in Ref. 56 using an equivalent axisymmetric body approach with a nonequilibrium viscous shock-layer code, and it was concluded that the flow over the windward side of the Shuttle orbiter remained in chemical nonequilibrium down to an altitude of approximately 50 km. Since, at the present time, LATCH does not include chemical nonequilibrium effects, two STS-2 trajectory points were chosen for analysis where the flow is expected to be near chemical equilibrium. The first is at an altitude of 46.67 km, and the second is at an altitude of 52.97 km (see cases 2 and 3 in Table I). For these two altitudes, heating predictions on the windward side of the Shuttle orbiter are presented (at the locations shown in Fig. 21) and compared with STS-2 flight data. All of the inviscid data used in LATCH to perform the heating calculations for these two cases were obtained from an inviscid version of LAURA using a grid 145 points down the body, 81 points around the body, and 65 points between the body and the outer computational boundary. Each inviscid solution required approximately 5-10 hours of computational time on a Cray-YMP. Each LATCH solution was obtained using 201 streamlines and required approximately 45 minutes of computing time on a Sun SPARCstation 2.

The heating calculations from LATCH along the windward symmetry plane are presented in Fig. 22 along with the STS-2 flight data for comparison. These calculations assume that the flow is laminar and that it is in chemical equilibrium. There is some apparent scatter in the experimental data, but, in general, the LATCH predictions are in very good agreement.

Lateral heating distributions in planes normal to the axis of the Shuttle orbiter at x/L stations of 0.1, 0.4, 0.5, 0.6, and 0.7 (see Fig. 21) are presented in Figs. 23 through 27, respectively. The results are plotted as q_w vs z/L. Again, there appears to be some scatter in the data; but, except for $x/L = 0.5$, the predicted values are in reasonably good overall agreement with the STS-2 flight data. At $x/L = 0.5$, the two out board data points are significantly higher than the predicted values. Other investigations (e. g. see Refs. 1, 48, and 59) have noted similar "problems" with these two measurements when comparing heating predictions with the shuttle flight data. Examination of the time histories of these two thermocouples shows that they are laminar and that there is nothing unusual about their time traces that would suggest that the thermocouples are bad. The reasons for these large differences are unknown.

Off symmetry-plane heating distributions along lines parallel to the windward symmetry plane at z/L values of 0.075, 0.145, and 0.290 (see Fig. 21) are presented in Figs. 28 through 30, respectively. In the first (Fig. 28), the results are located on the fuselage; in the second (Fig. 29), the results are located in the wing root area; and in the third (Fig. 30), the results are located out toward the wing tip. At $z/L = 0.145$ and 0.290, Figs 29 and 30, the predicted heating is in reasonably good agreement with the flight data where the flow is laminar, but near the trailing edge where transition has occurred in flight[6] the data are higher than the laminar calculations as would be expected. In fact, at $z/L = 0.290$ (Fig. 30) the heating near the trailing edge has been shown to reach a fully turbulent level.[48] A turbulent calculation capability is not presently included in LATCH. At $z/L = 0.075$ (Fig. 28) the data at the two forward thermocouples are significantly higher than the predictions. One of the measurements (at $x/L = 0.5$) is the same as that discussed in the previous paragraph. The time history traces for the other thermocouple (at $x/L = 0.2$) indicate the flow is laminar and give no indications that the thermocouple is bad. The reasons for these differences are also unknown. Note that the most outboard measurements in Figs. 26 and 27 are also somewhat higher than the predictions.

The maximum heating along the leading edge of the fuselage and wing is presented in Fig. 31. This heating distribution is similar to that for the wind tunnel case presented in Fig. 19 except that the peak heating point occurs slightly further upstream for the flight case ($x/L \approx 0.65$) than the wind tunnel case ($x/L \approx 0.7$). This result is because the shock layer is much thinner in flight than in the wind tunnel, and the bow-shock wave is much closer to the body. The peak heating on the wing leading edge is higher than the stagnation value. A general trend in predicted heating near the wing leading edge has been noted both in the wind tunnel and in flight that suggests that the actual heating on the wing leading edge is probably 20 to 30 percent higher than the LATCH predictions. One reason for this is probably that the approximate heating relations currently used in the LATCH do not include velocity gradient effects which if included would increase the predicted heating in this region. However, the heating predictions near the leading edge require further investigation.

Similar heating comparisons are presented in Figs. 32-41 for the second STS-2 trajectory point at an altitude of 52.97 km (see case 3 in Table I for freestream flow conditions). The heating comparison along the windward symmetry plane (Fig. 32) indicates that LATCH over predicts the heating over the forward portion of the body but is in better agreement with the data near the end of the body. This suggests that the flow for

this case is still in chemical nonequilibrium (at least over the forward portion of the body) and coupled with the finite catalycity of the surface tiles causes a reduction in the flight heating below the equilibrium level. This same conclusion was reached in Ref. 56 from a windward symmetry plane heating analysis of this and other STS-2 trajectory points. This same general trend is noted in all of the heating results for this case. Note that, for this higher altitude, the data appear to be laminar at all locations except near the trailing edge of the wing tip (Fig. 40). This result is confirmed by an examination of the time history traces of the flight data. One final note, the two outboard thermocouples in the lateral heating distribution at $x/L = 0.5$ (Fig. 35) now "appear" to agree much better with the predicted values than in the previous case. This is probably fortuitous because they are still significantly higher than the other measurements; but as a result of finite catalytic surface effects their level has been reduced closer to the equilibrium level predicted by LATCH.

HL-20

LATCH uses a generalized body-fitted coordinate system as a frame of reference for performing heating calculations. All of the results presented thus far in the paper could have been obtained using AA3DBL,[47–49] which uses cylindrical coordinates. However, as discussed previously, there are certain body shapes with cross sections that can not be described in cylindrical coordinates (e. g. see Fig. 10). For these types of shapes, a more general coordinate system such as that used in LATCH is required. One such configuration is the HL-20 which is shown in Fig. 42. The cross sections aft of $x/L \approx 0.6$ can not be described in a cylindrical coordinate system such as that used in AA3DBL. However, this type of body can be easily defined in the generalized coordinate system used in LATCH. The application of LATCH to the HL-20 is demonstrated with the windward symmetry plane heating presented in Fig. 43 along with the heating predictions from LAURA and experimental data.[1] The LATCH results are in good agreement with both LAURA and the experimental data. A circumferential heating distribution at $x/L = 0.5$ is presented in Fig. 44. The LATCH predictions are in good agreement with LAURA except near the leading edge where they underpredict the LAURA results by approximately 30 percent. A similar trend was noted earlier for the Shuttle orbiter.

[1]Experimental heating data obtained using a thermal phosphor technique was provided by Ron Merski, Experimental Hypersonics Branch, SSD, LaRC

CONCLUDING REMARKS

Several engineering codes used in the Aerothermodynamics Branch of the Space Systems Division have been described. These codes have been used to analyze both planetary and Earth entry vehicles including Apollo, Galileo, and Shuttle orbiter and the experience gained by the branch in the application of these codes is unique in the aerospace community and enhances the capability to develop new engineering codes that will be useful in the analysis of future advanced entry vehicles. These codes provide useful tools for defining the aerothermodynamic environment during preliminary design and serve a complementary role with benchmark codes for detailed design.

The development of a new engineering code (LATCH) based on the axisymmetric analog is described. The code is written in a generalized, body-fitted coordinate system and uses a three-dimensional inviscid flowfield along with approximate heating relations to calculate heating on general three-dimensional bodies. Heating calculations on the Shuttle orbiter at both wind tunnel and flight conditions are presented. The results of these heating calculations are compared with Navier-Stokes calculations and with both wind tunnel and STS-2 flight data. The heating predictions are, in general, in good agreement with both the wind tunnel and flight data over most of the windward side of the Shuttle orbiter. However, there are some regions of the Shuttle orbiter where the flight data are significantly higher than the predictions. The reasons for these differences are unexplained.

Heating predictions on the HL-20, an advanced entry vehicle, are also presented at wind tunnel conditions. The predictions are compared with experimental data and with Navier-Stokes calculations. In general, the predictions are in good agreement with these data. These results show that the new engineering code, which uses a generalized body-fitted coordinate system, can be applied to bodies that are too complex for previous engineering codes.

ACKNOWLEDGMENTS

The authors thank K. James Weilmuenster, Francis A. Greene and Richard A. Thompson of the Aerothermodynamics Branch, Kathryn E. Wurster of the Vehicle Analysis Branch and Dr. Fred R. DeJarnette of North Carolina State University for their technical advice and assistance.

REFERENCES

1. Gnoffo, P. A.; Weilmuenster, K. James; and Alter, Stephen J.: A Multiblock Analysis for Shuttle Orbiter Re-heating from Mach 24 to Mach 12, Orbiter Experiments (OEX) Aerothermodynamics Symposium, NASA CP-3248, 1993.

2. Vatsa, V. N.; Thomas, J. L.; and Wedan, B. W.: Navier-Stokes Computations of a Prolate Spheroid at Angle of Attack, *Journal of Aircraft* , Vol. 26, No. 11, 1989, pp. 986-993.

3. DeJarnette, F. R.; Hamilton, H. H.; Weilmuenster, K. J.; and Cheatwood, F. M.: A Review of Some Approximate Methods Used in Aerodynamic Heating Analysis, *Journal of Thermophysics and Heat Transfer,* vol. 1, no. 1, January 1987, pp. 5–12.

4. Sutton, Kenneth; Zoby, Ernest V.; and Hamilton, H. Harris: Overview of CFD Methods and Comparisons with Flight Aerothermal Data, Presented at the AGARD Symposium on Validation of Computational Fluid Dynamics, Lisbon, Portugal, May 2-5, 1988.

5. Throckmorton, David A.: Benchmark Determination of Shuttle Orbiter Entry Aerodynamic Heat-Transfer Data, *Journal of Spacecraft and Rockets,* vol. 20, no. 3, May-June 1983, pp.219–224.

6. Hartung, Lin C.; and Throckmorton, David A.: Space Shuttle Entry Heating Data Book, Vol. I - STS-2, NASA RP-1191, Vol. II – STS-3, NASA RP-1192, Vol. III – STS-5, NASA RP-1193, May 1988.

7. Fay, J. A.; and Riddell, F. R.: Theory of Stagnation-Point Heat Transfer in Dissociated Air, *Journal of Aerospace Sciences,*vol. 25, no. 2, Feb. 1958, pp. 73-85, 121.

8. Cohen, N. B.: Boundary-Layer Similar Solutions and Correlation Equations for Laminar Heat-Transfer Distribution in Equilibrium Air at Velocities Up to 41,100 Feet Per Second, NASA TR R-118, 1961.

9. Kemp, N. H.; Rose, P. H.; and Detra, R. W.: Laminar Heat Transfer Around Blunt Bodies in Dissociated Air, *Journal of Aerospace Sciences,* vol. 26, no. 7, July 1959, pp. 421-430.

10. Sutton, K.; and Graves, R. A., Jr.: A General Stagnation Point Convective Heating Equation for Arbitrary Gas Mixtures, NASA TR R-376, Nov. 1971.

11. Marvin, J. G.; and Deiwert, G. S.: Convective Heat Transfer in Planetary Gases, NASA TR R-224, July 1965.

12. Lees, L.: Laminar Heat Transfer Over Blunt Bodies at Hypersonic Flight Speeds, *Jet Propulsion,* vol. 26, no. 4, April 1956, pp. 259-269, 274.

13. Vaglio-Laurin, R.: Laminar Heat Transfer on Three-Dimensional Blunt Bodies in Hypersonic Flow, *ARS Journal,* vol. 29, no. 2, Feb. 1959, pp. 123-129.

14. Zoby, E. V.: Approximate Relations for Laminar Heat Transfer and Shear Stress Functions in Equilibrium Dissociated Air, NASA TN D-4484, April 1968.

15. Phillips, R. L.: A Summary of Several Techniques Used in the Analysis of High Enthalpy Level, High Cooling Ratio Turbulent Boundary Layers on Blunt Bodies of Revolution, Ramo Wooldrige Corp., GM-TM-194, Sept. 1957.

16. Vaglio-Laurin, R.: Turbulent Heat Transfer on Blunt Nosed Bodies in Two-Dimensional and General Three-Dimensional Hypersonic Flow, *Journal of Aerospace Sciences,* vol. 27, no. 1, Jan. 1960, pp. 27-36.

17. Cresci, R. J.; MacKenzie, D. A.; and Libby, P. A.: An Investigation of Laminar, Transitional, and Turbulent Heat Transfer on Blunt-Nosed Bodies in Hypersonic Flow, *Journal of Aerospace Sciences,* vol. 27, no. 6, June 1960, pp. 401-414.

18. Hartley, D. L.; and Witze, P. D.: Turbulent Heating From a Compressible Boundary Layer With Pressure Gradient, Sandia Labs., SCL RR-69-70, Oct. 1969.

19. Spalding, D. B.; and Chi, S. W.: The Drag of a Compressible Turbulent Boundary Layer on a Smooth Flat Plate With and Without Heat Transfer, *Journal of Fluid Mechanics,* vol. 18, pt. 1, Jan. 1964, pp. 117-143.

20. Van Driest, E. R.: The Problem of Aerodynamic Heating, *Aeronautical Engineering Review,* vol. 15, no. 10, Oct. 1956, pp. 26-41.

21. Harris, J. E.: Numerical Solutions of the Equations for Compressible Laminar, Transitional, and Turbulent Boundary Layers and Comparisons With Experimental Data, NASA TR R-368, Aug. 1971.

22. Anderson, E. C.; and Lewis, C. H.: Laminar or Turbulent Boundary-Layer Flows of Perfect Gases or Reacting Gas Mixtures in Chemical Equilibrium, NASA CR-1893, Oct. 1971.

23. Engle, C. D.; and Praharaj, S. C.: MINIVER Upgrade for the AVID System, Vol. I: LANMIN User's Manual, NASA CR-172212, Aug. 1982.

24. Cruz, C. I.; and Wilhite, A. W.: Prediction of Transatmospheric Vehicle High-Speed Aerodynamic Characteristics Using the Aerodynamic Preliminary Analysis System, AIAA Paper No. 89-2173, July 1989.

25. Ferri, A.: Some Heat-Transfer Problems in Hypersonic Flow," *Aeronautics and Astronautics,* Pergamon Press, New York, 1960, pp. 344- 377.

26. Witze, P. O.; and Hartley, D. C.: Assessment of the Proper Boundary Conditions at the Outer Edge of the Turbulent Boundary Layer on Spherically Blunted Conical Bodies, Sandia Labs., SCL-RR-69-67, Sept. 1969.

27. Edquist, C. T.: A Technique for Predicting Shock Induced Vorticity Effects During Venus Entry, Martin Marietta Corp., R-70-48671-006, Aug. 1970.

28. Popinski, Z.: Compressible Laminar Boundary Layers on Sharp Cones at Incidence With Entropy Swallowing, *AIAA Journal,* vol. 13, no. 9, Sept. 1975, pp. 1135-1136.

29. Zoby, E. V.; Moss, J. N.; and Sutton, K.: Approximate Convective Heating Equations for Hypersonic Flows, *Journal of Spacecraft and Rockets,* vol. 18, Jan. 1981, pp. 64-70.

30. Howard, F. G.; Thermal Analysis Methods and Basic Heat-Transfer Data for a Turbulent Heating Flight Experiment at Mach 20 (Reentry F), NASA TMX-2282, May 1971.

31. Thareja, R. R.; Szema, K. Y.; and Lewis, C. H.: Chemical Equilibrium Laminar or Turbulent Three-Dimensional Viscous Shock Layer Flows, *Journal of Spacecraft and Rockets,* Vol. 20, No. 5, 1983, pp.454-460.

32. Maslen, S. H.: Asymmetric Hypersonic Flow, NASA CR-2123, Sept. 1972.

33. Zoby, E. V.; Sutton, K.; Olstad, W. B.; and Moss, J. N.: An Approximate Inviscid Radiating Flow-Field Analysis for Outer Planet Entry Probes, *Progress in Astronautics and Aeronautics: Outer Plant Entry Heating and Thermal Protection,* vol. 64, edited by R. Viskanta, AIAA, New York, 1979, pp. 42-64.

34. Moss, J. N.: Stagnation and Downstream Viscous Shock Layer Solutions with Radiation and Coupled Ablation Injection, AIAA Paper 74-73, June 1974.

35. Cooke, J. C.: An Axially Symmetric Analogue for General Three-Dimensional Boundary Layers, Ministry of Aviation, A.R.C. Technical Report, R&M No. 3200, June 1959.

36. Hayes, Wallace D.: The Three-Dimensional Boundary Layer, NAVORD Rep. 1313 (NOTS 384), U. S. Naval Ord. Test Station, Inyokern (China Lake, Calf.), May 9, 1951.

37. DeJarnette, Fred R.; and Hamilton, H. Harris: Inviscid Surface Streamlines and Heat Transfer on Shuttle-Type Configurations, *Journal Spacecraft and Rockets,* vol. 10, no. 6, May 1973, pp. 314-321.

38. DeJarnette, F. R.; and Hamilton, H. H. II: Aerodynamic Heating on 3-D Bodies Including the Effects of Entropy-Layer Swallowing, *Journal of Spacecraft and Rockets,* vol. 12, January 1975, pp. 5-12.

39. DeJarnette, Fred R.: Aerodynamic Heating on Complex Configurations, Technical Papers — Conference on Advanced Technology for Future Space Systems, May 1979, pp. 179-188. (Available as AIAA Paper 79-0891)

40. Thompson, R. A.; Zoby, E. V.; Wurster, K. E.; and Gnoffo, P. A.: An Aerothermodynamic Study of Slender Conical Vehicles, AIAA Paper 87-1475, June 1987.

41. Riley, C. J.; DeJarnette, F. R.; and Zoby, E. V.: Effects of Surface Pressures and Streamline Metrics on the Calculation of Laminar Heating Rates, AIAA Paper No. 88-2708, June 1988.

42. Zoby,E. V.; and Simmonds, A. L.: Engineering Flowfield Method with Angle-of-Attack Applications, *Journal of Spacecraft and Rockets,* vol. 22, no. 4, July-August 1985, pp. 214–218.

43. DeJarnette F. R.; and Davis, R. M.: A Simplified Method for Laminar and Turbulent Convective Heat Transfer Over Bodies at an Angle of Attack, NASA TN D-4720, 1968.

44. Riley C. J.; and DeJarnette, F. R.: Engineering Calculations of Three-Dimensional Inviscid Hypersonic Flow Fields, *Journal of Spacecraft and Rockets,* vol 28, November - December 1991, pp. 628–635.

45. Riley, C. J.; and DeJarnette, F. R.: Engineering Aerodynamic Heating Method for Hypersonic Flow, *Journal of Spacecraft and Rockets,* vol 29, May-June 1992, pp. 327–334.

46. Hillsamer, M. E.; and Rhudy, J. P.: Heat-Transfer and Shadowgraph Tests of Several Elliptic Lifting Bodies at Mach 10, Arnold Engineering Development Center, AEDC-TDR-64-19, Arnold AFB, TN, Feb. 1964.

47. Hamilton, H. Harris II: Calculation of Laminar Heating on Three-Dimensional Configurations Using the Axisymmetric Analogue, NASA TP 1698, September 1980.

48. Hamilton, H. H.; DeJarnette, F. R.; and Weilmuenster, K. J.: Application of Axisymmetric Analog for Calculating Heating in Three-Dimensional Flows, *Journal of Spacecraft and Rockets,* vol. 24, no. 4, July-August 1987, pp.296–302.

49. Hamilton, H. H. II; Greene, F. A.; and Weilmuenster, K. J.: Comparison of Heating Calculations with Experimental Data on a Modified Shuttle Orbiter, *Journal of Spacecraft and Rockets,* vol. 29, no. 2, March-April 1992, pp.208–215.

50. Marconi, Frank; Salas, Manuel; and Yaeger, Larry: Development of a Computer Code for Calculating the Steady Super/Hypersonic Inviscid Flow Around Real Configurations. Volume I - Computational Technique, NASA CR-2675, May 1976.

51. Weilmuenster, K. J.; and Hamilton, H. H.: Calculation of Inviscid Flow over Shuttle-Like Vehicles at High Angles of Attack and Comparisons with Experimental Data, NASA TP-2103, May 1983.

52. Hamilton, H. H.; and Greene, F. A.: An Approximate Method for Calculating Heating on Three-Dimensional Vehicles, AIAA Paper 93-2881, July, 1993.

53. Adams, J. C. Jr.; Martindale, W. R.; Mayne, A. W.; and Marchand, E. O.: Real Gas Scale Effects on Hypersonic Laminar Boundary-Layer Parameters Including Effects of Entropy-Layer Swallowing, AEDC-TR-75-2, October, 1974.

54. Murry, A. L.; Wasiewicz, J. D.; and Lewis, C. H.: Laminar Viscous Shock-Layer Flows at Angle of Attack on the Shuttle Windward Streamline, AIAA Paper 77-87, January, 1977.

55. Zoby, E. V.: Approximate Heating Analysis for the Shuttle Windward Symmetry Plane of Shuttle-Like Bodies at Large Angle of Attack, Thermophysics of

Atmospheric Entry; Progress in Astronautics and Aeronautics, edited by T. E. Horton, Vol. 82, 1982, pp. 229-247.

56. Shinn, J. C.; Moss, J. N.; and Simmonds, A. L.: Viscous Shock-Layer Heating Analysis for the Shuttle Windward Plane with Surface Finite Catalysis Recombination Rates, Entry Vehicle Heating and Thermal Protection Systems: Space Shuttle, Solar Starprobe, Jupiter Galileo Probe: Progress in Astronautics and Aeronautics, edited by P. E. Bauer and H. E. Collicott, Vol 85, 1983, pp.149-180.

57. Martindale, W. R.: Test Results from NASA Rockwell International Space Shuttle Test (OH4B) Conducted in the AEDC-VKF Tunnel B, AEDC-DR-74-8, June 1974.

58. Thompson, R. A.: Three-Dimensional Viscous Shock-Layer Application for the Space Shuttle Orbiter, Thermophysical Aspects of Reentry Flows; Progress in Astronautics and Aeronautics, edited by J. N. Moss and C. D. Scott, Vol. 103, 1986, pp.541-570.

59. Thompson, R. A.: Comparisons of Nonequilibrium Viscous Shock-Layer Solutions with Shuttle Heating Measurements, *Journal of Thermophysics and Heat Transfer*, Vol. 4, No. 2, April 1990, pp.162-169.

60. Zoby, E. V. and Thompson, R. A.: Flowfield and Vehicle Parametric Influence on Hypersonic Heat Transfer and Drag, *Journal of Spacecraft and Rockets*, Vol. 27, No. 4, July-Aug. 1990, pp. 361-368.

61. Adams, J. C, Jr.: Implicit Finite-Difference Analysis of Compressible Laminar, Transitional, and Turbulent Boundary Layers Along the Windward Streamline on a Sharp Cone at Incidence, Arnold Engineering Development Center, Arnold AFB, Tullahoma, TN, AEDC-TR-71-235, Dec. 1971.

62. Micol, J.; Aerothermodynamic Measurement and Prediction for a Modified Orbiter at Mach 6 and 10, AIAA Paper 91-1436, June 1991.

Table I. Freestream conditions.

Case	Configuration	α deg	Altitude km	p_∞ N/m^2	T_∞ K	M_∞	Re m^{-1}
1	Shuttle	30		153.26	61.9	5.83	$1.540x10^6$
2	Shuttle	34.8	46.70	100.31	260.0	9.15	$0.240x10^6$
3	Shuttle	38.3	52.97	50.92	262.0	11.90	$0.152x10^6$
4	HL-20	25		607.52	63.0	5.93	$7.540x10^6$

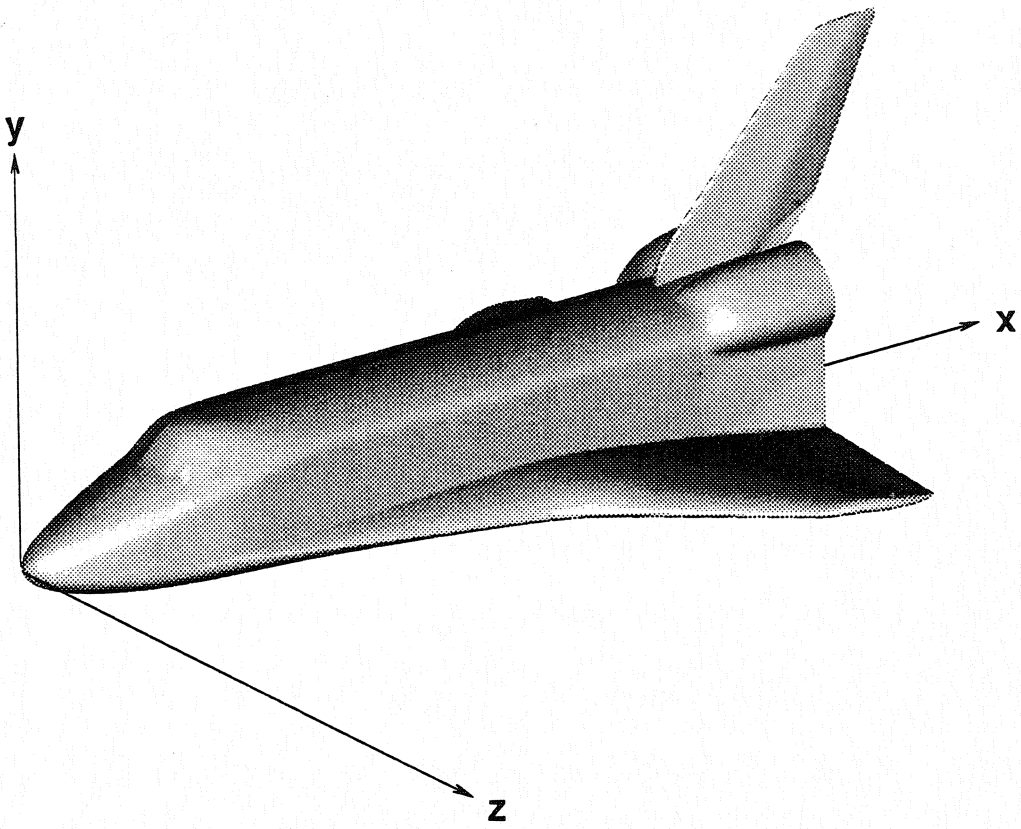

Figure 1. Shuttle Orbiter Geometry.

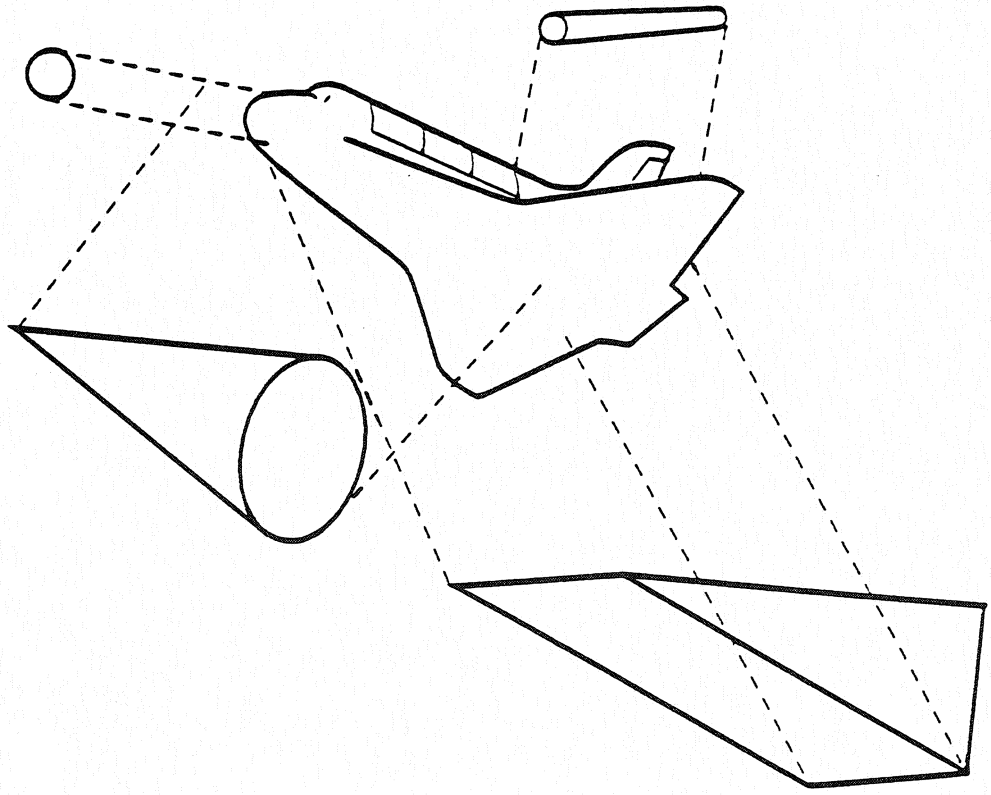

Figure 2. Simple geometry models for complex configurations.

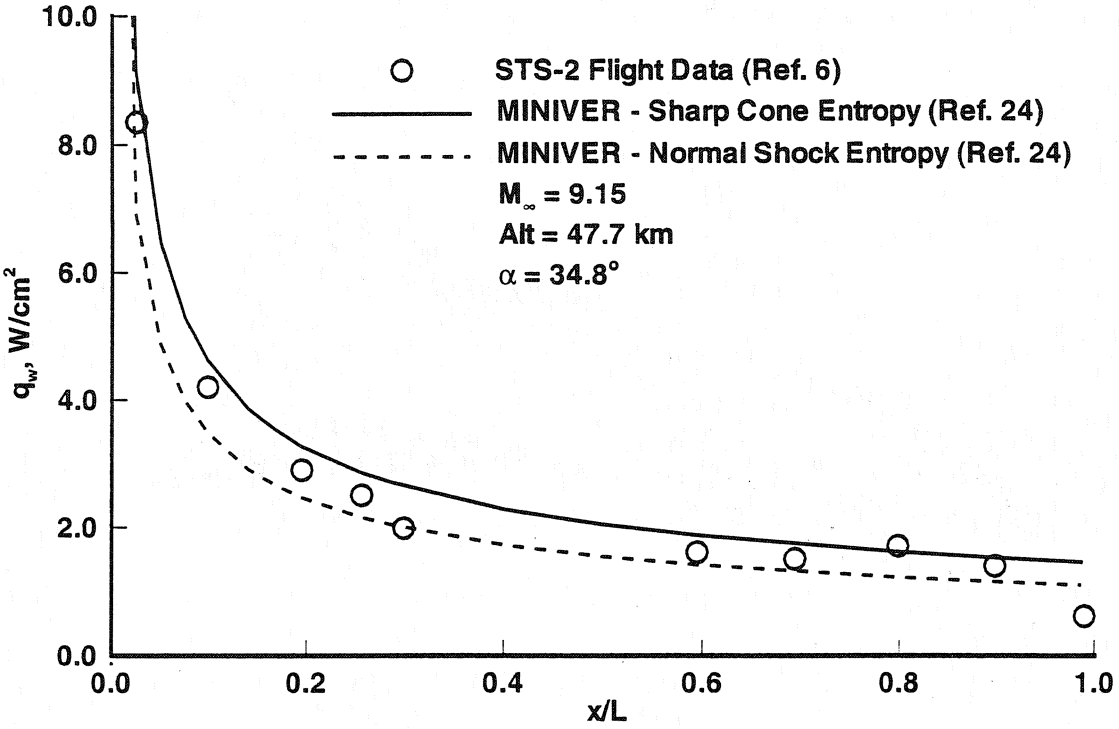

Figure 3. Windward symmetry plane heating rates predicted by engineering code options.

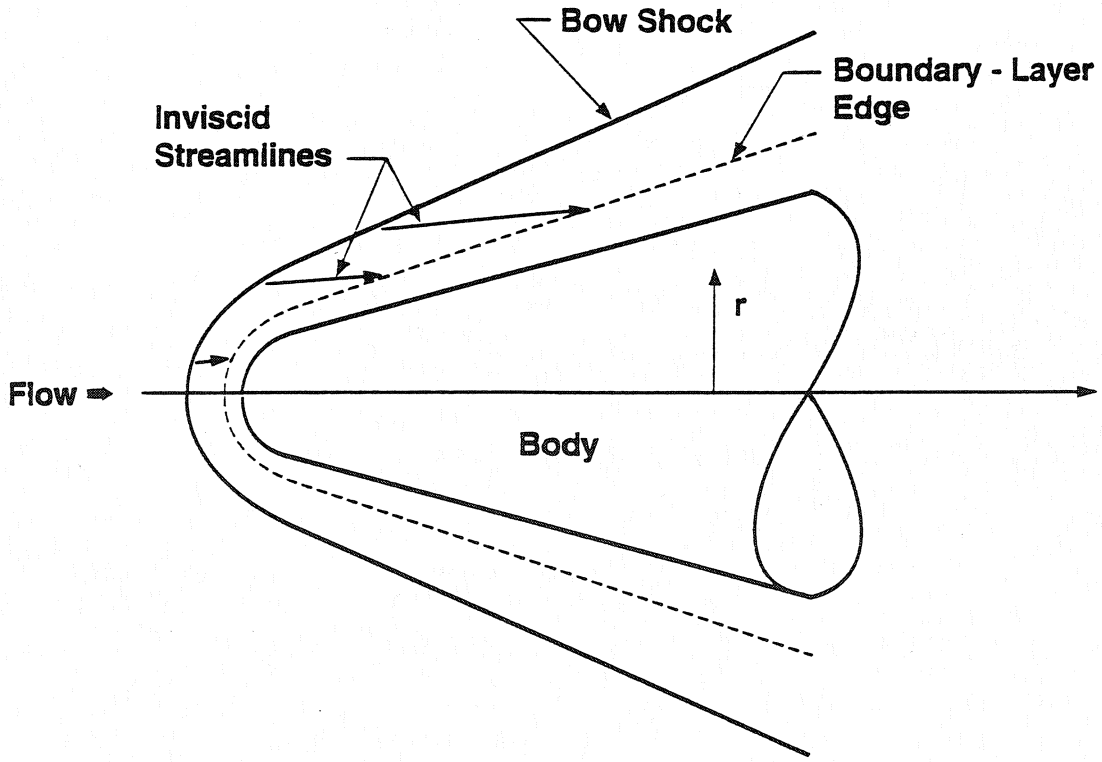

Figure 4. Inviscid streamline entrainment.

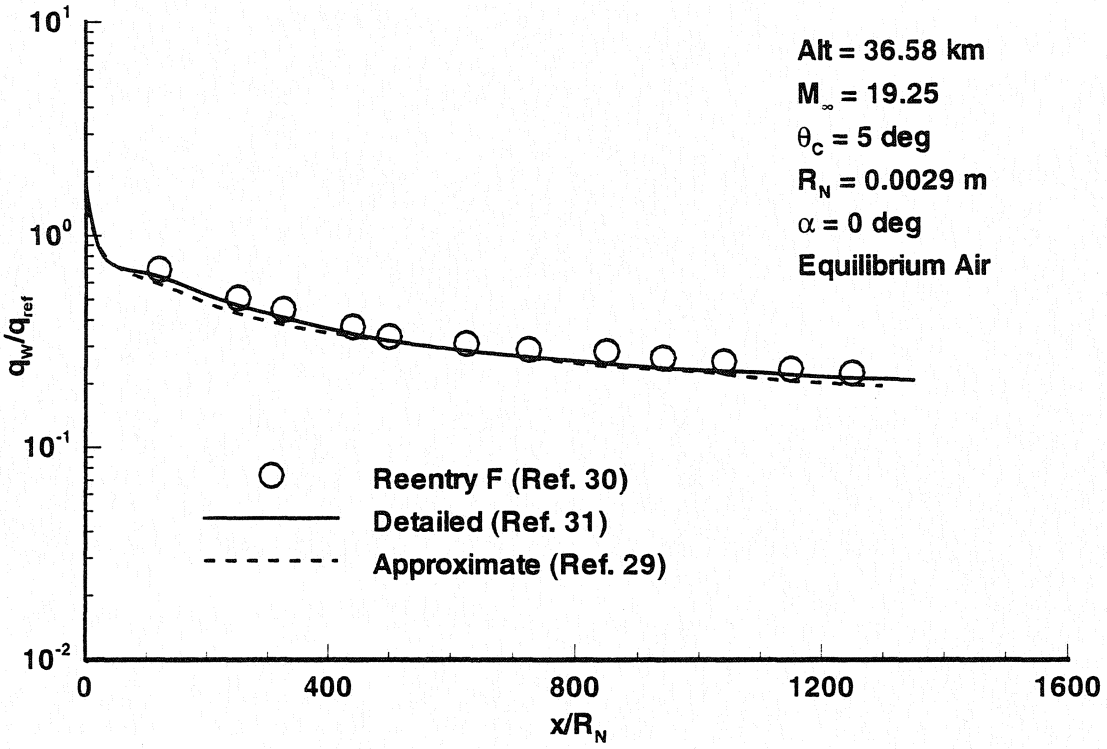

Figure 5. Heating comparisons of experimental data and predicted results from approximate and detailed flowfield codes.

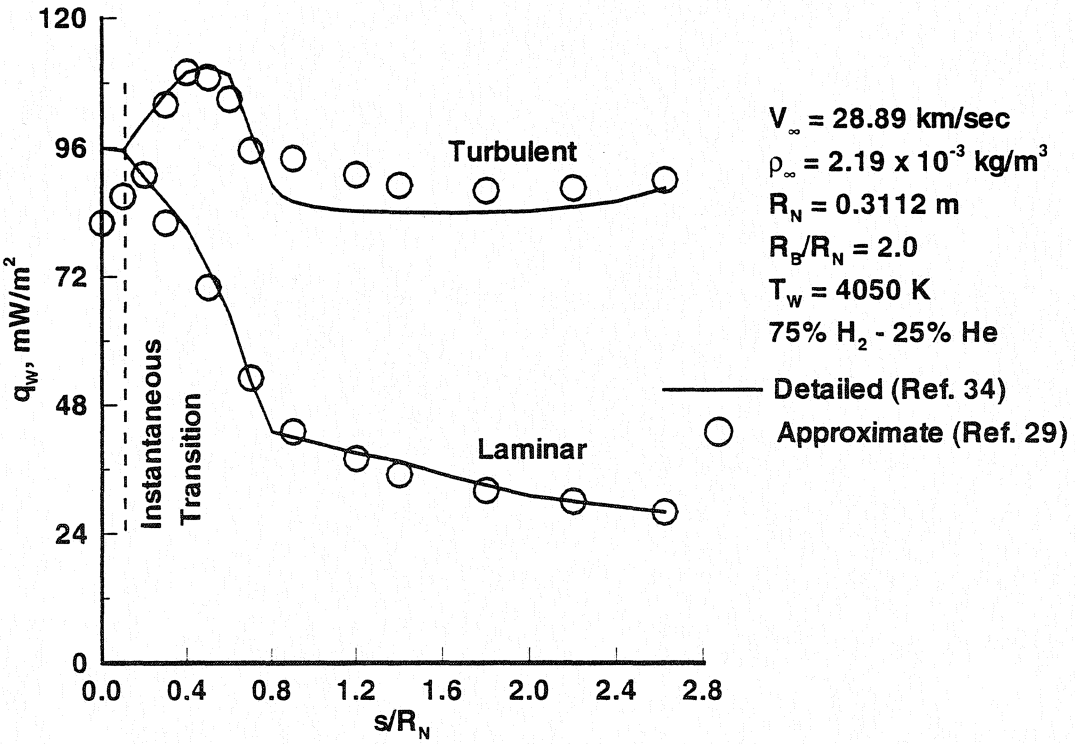

Figure 6. Heating comparisons of approximate and detailed flowfield methods at Saturn entry conditions.

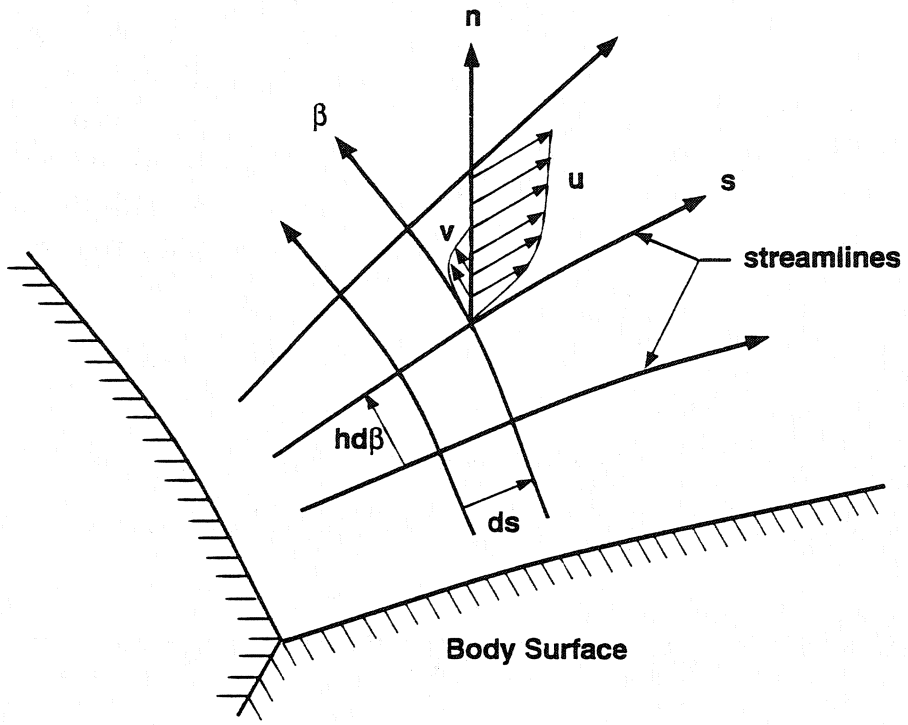

Figure 7. Typical streamlines and boundary-layer velocity profile.

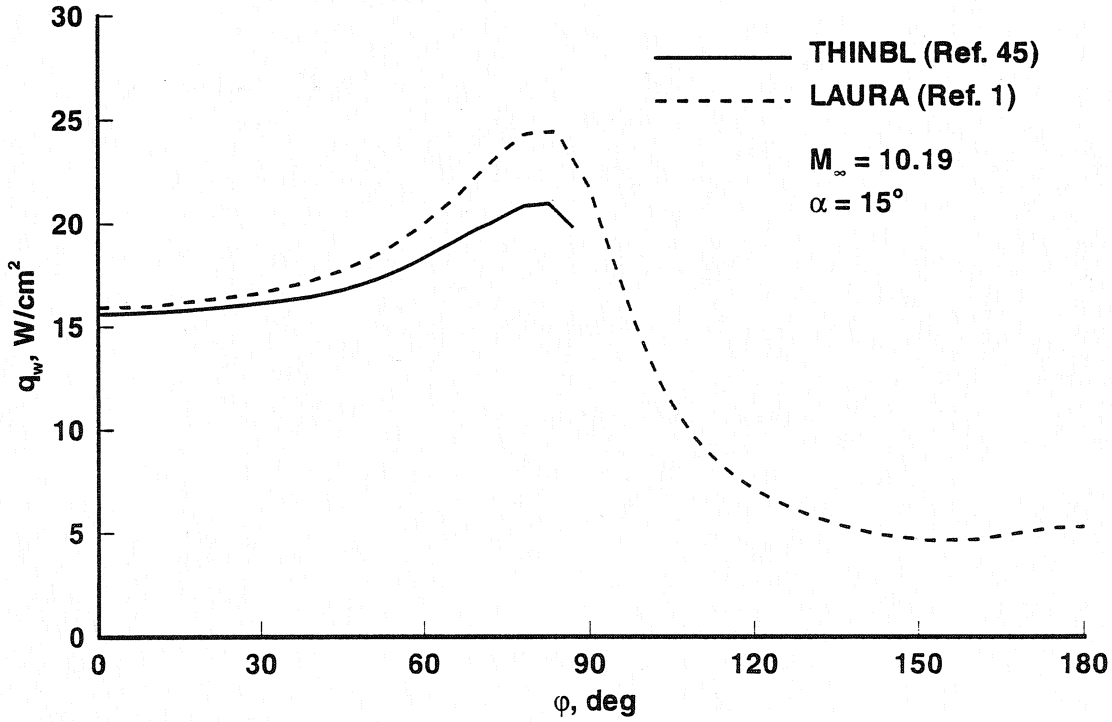

Figure 8. Comparison of predicted and experimental circumferential heating rates on a blunt 2:1 ellipsoid cone at $x/R_B = 0.4$.

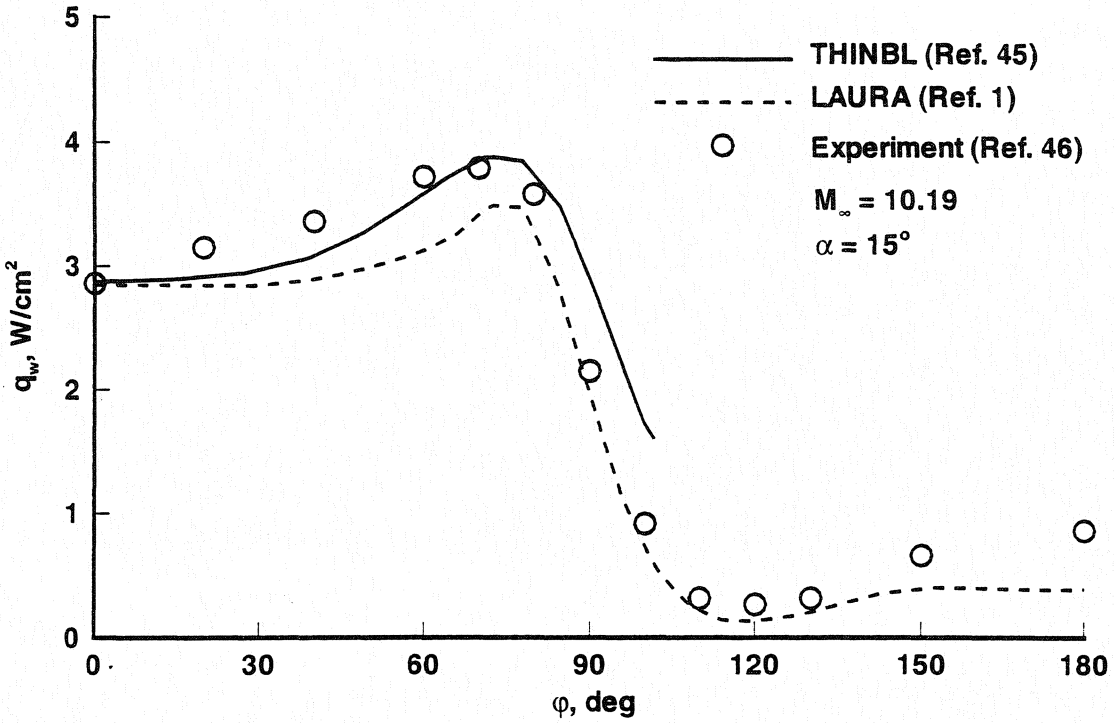

Figure 9. Comparison of predicted and experimental circumferential heating rates on a blunt 2:1 ellipsoid cone at x/R_B = 9.7.

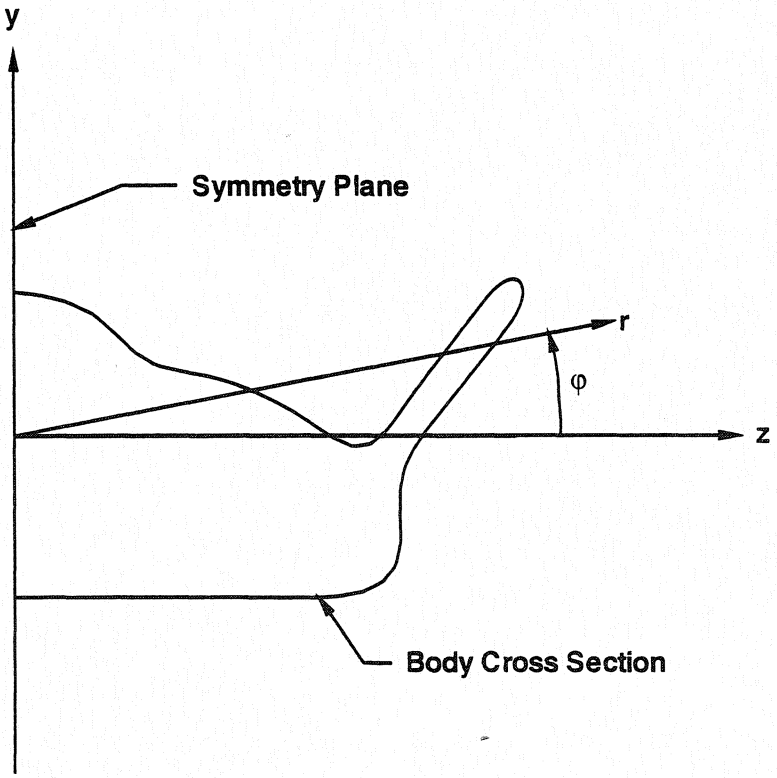

Figure 10. Cross sectional geometry of HL-20 at x/L = 0.8.

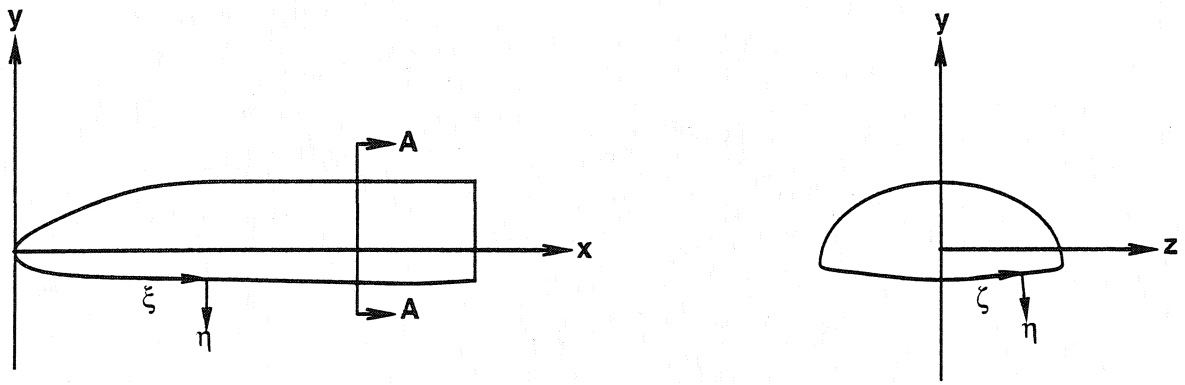

(a) Side view.

(b) Cross Section A-A.

Figure 11. Generalized coordinate system.

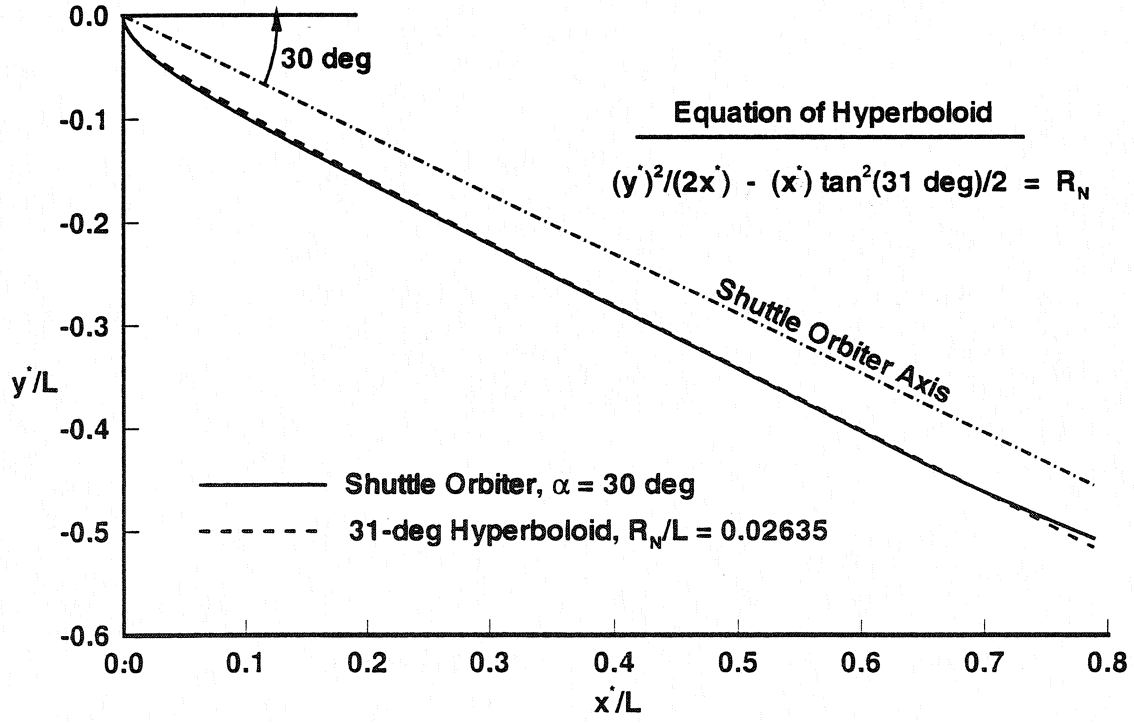

Figure 12. Orbiter windward symmetry plane surface profile at $\alpha = 30$ deg and a 31 deg asymptotic half-angle hyperboloid (Adams, Ref. 53).

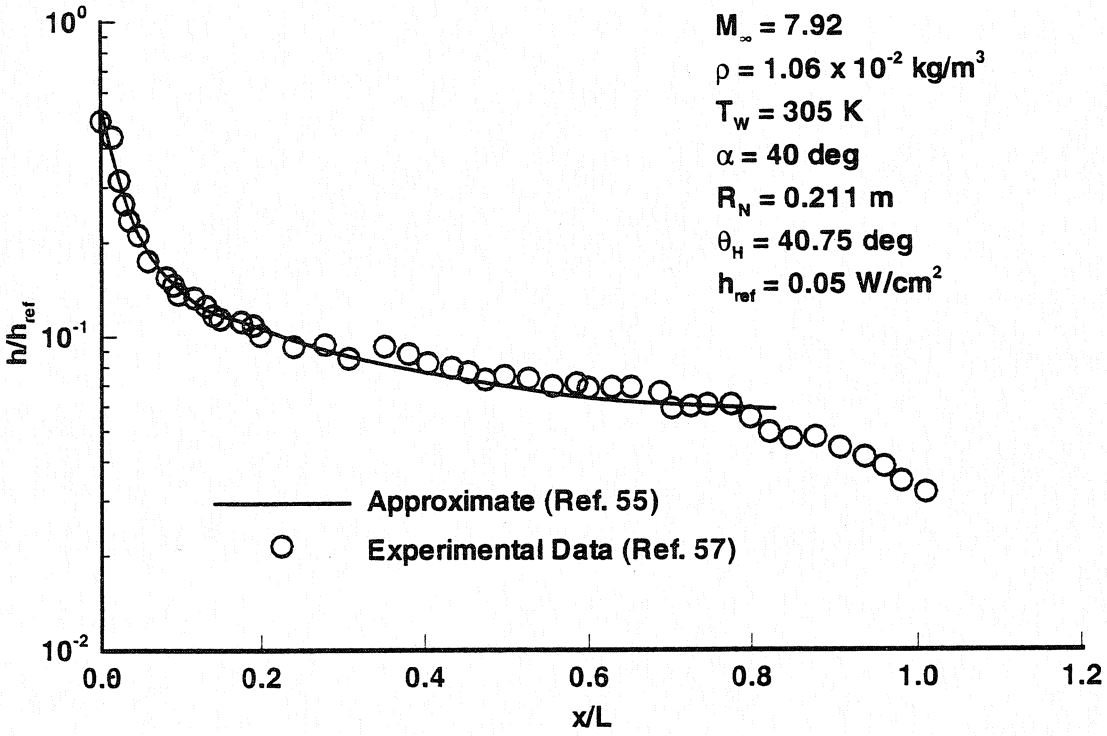

Figure 13. Comparison of predicted and experimental heating distributions along windward symmetry plane of Shuttle orbiter.

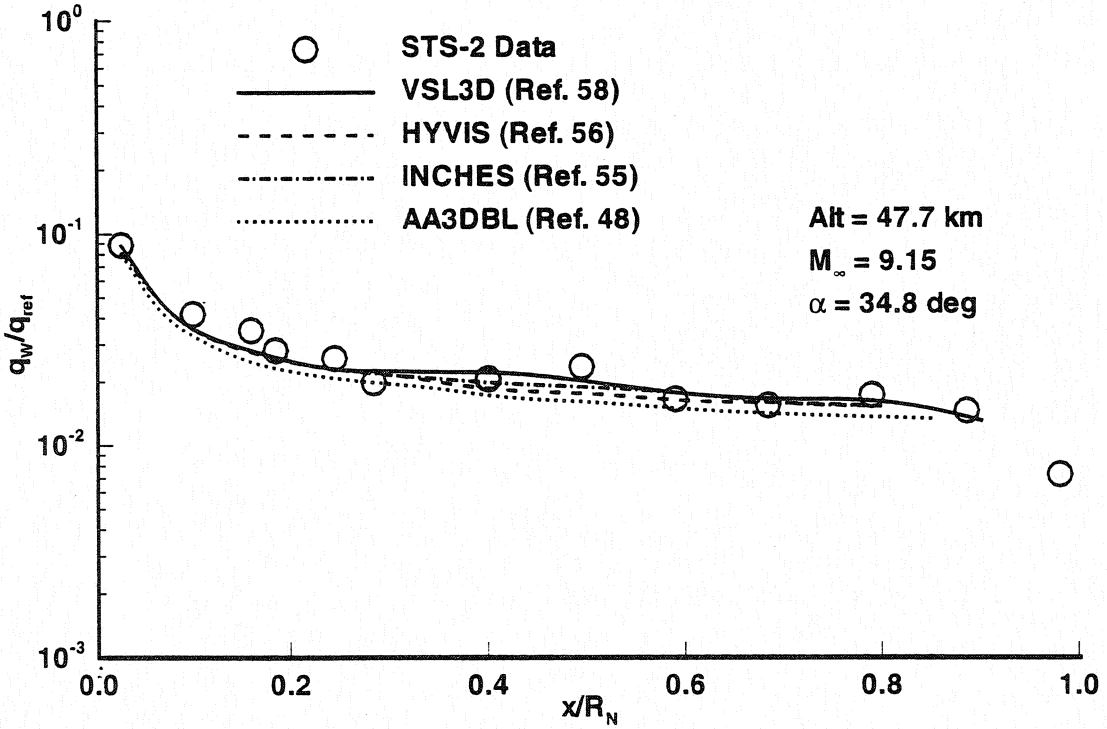

Figure 14. Comparison of heating predictions with STS-2 flight data along windward symmetry plane of Shuttle orbiter.

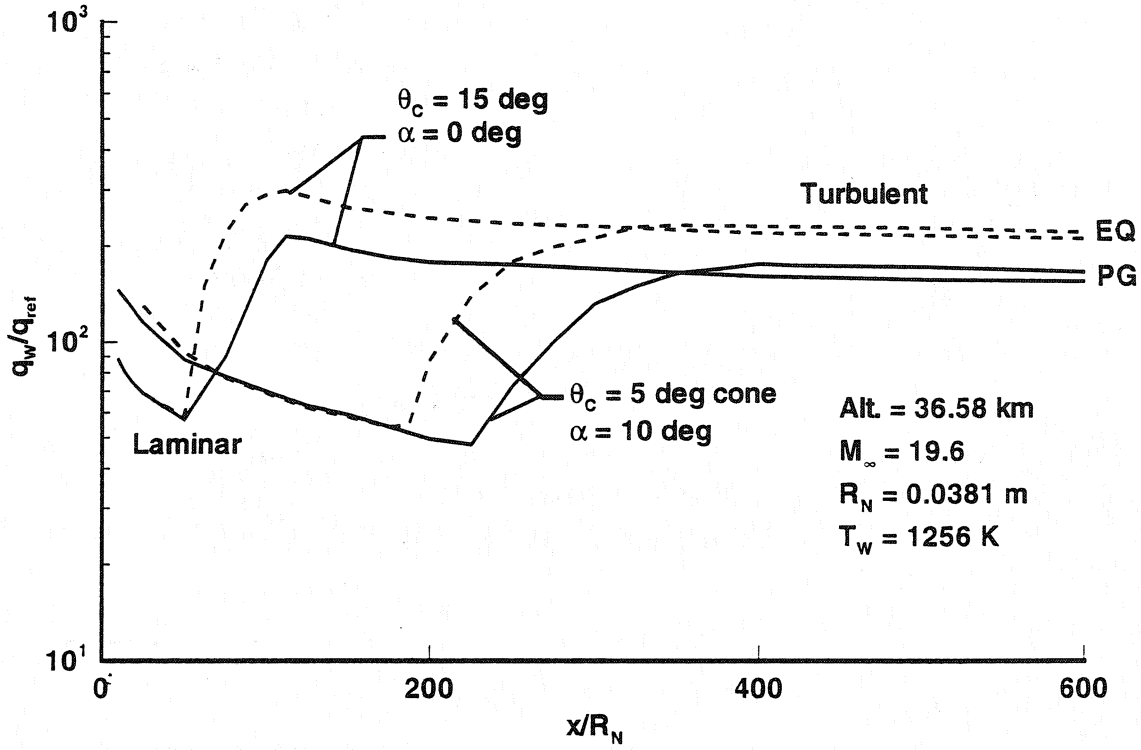

Figure 15. Effect of angle of attack on predicted conical heating rates.

(a) Shuttle Orbiter

(b) "HALIS" Orbiter

Figure 16. - Geometry descriptions.

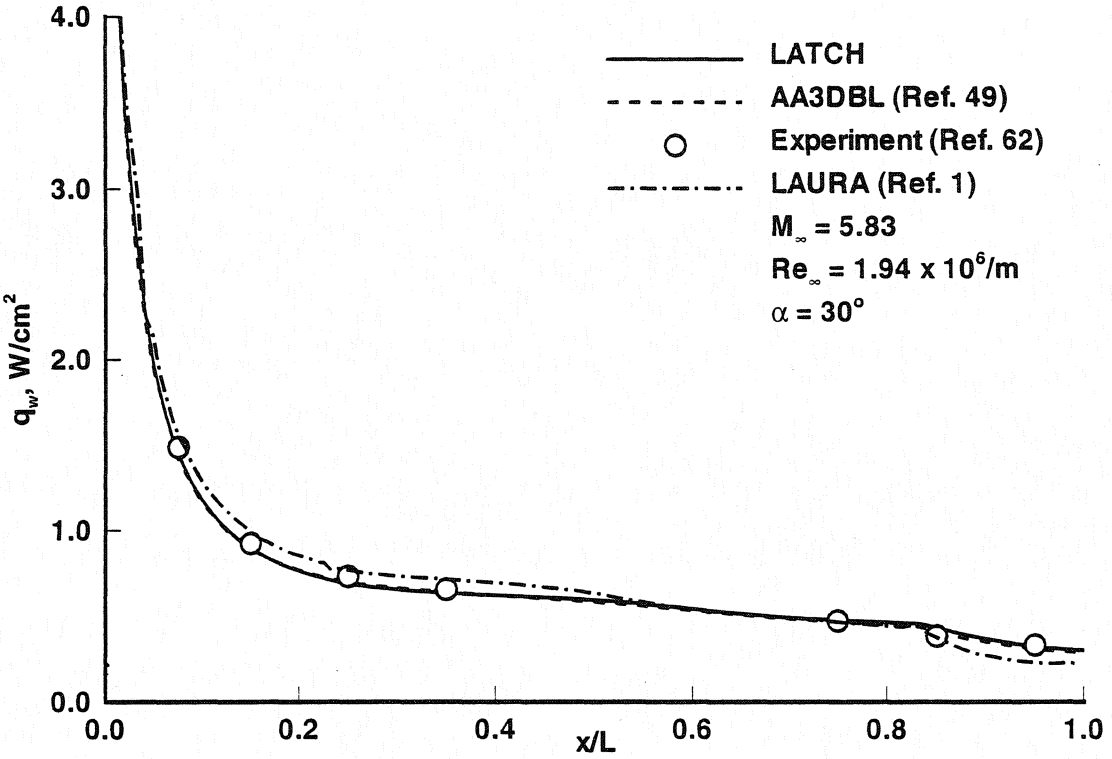

Figure 17. Windward symmetry-plane heating distribution.

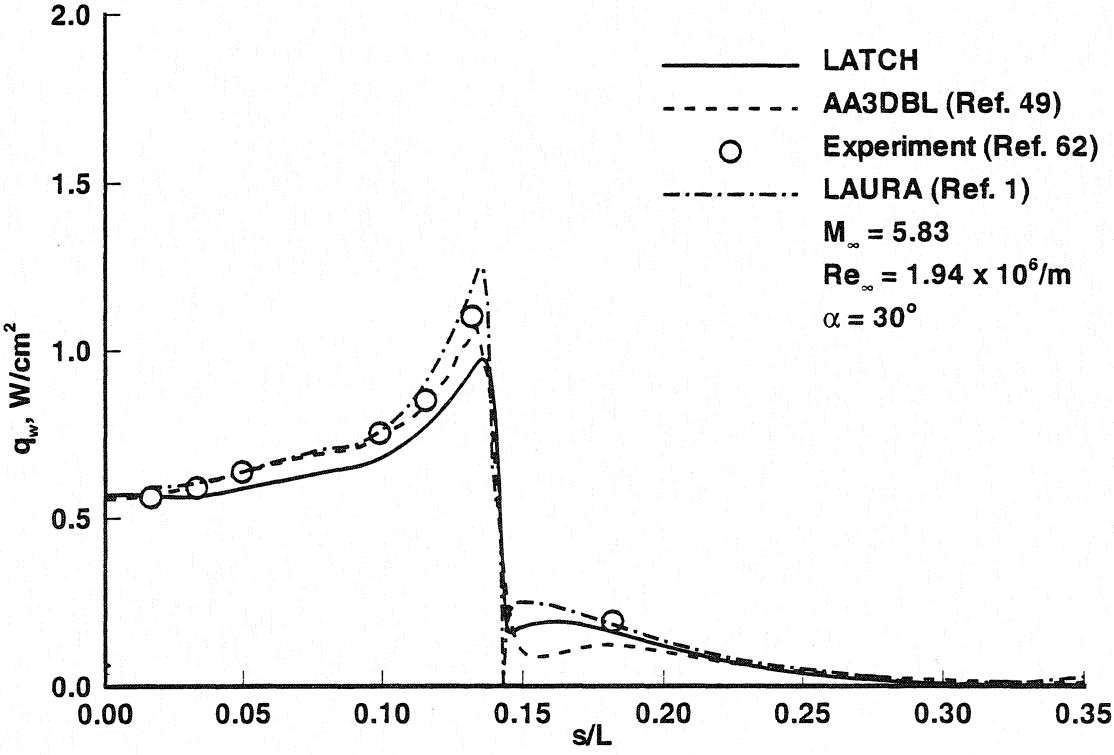

Figure 18. Circumferential heating distribution at x/L = 0.55.

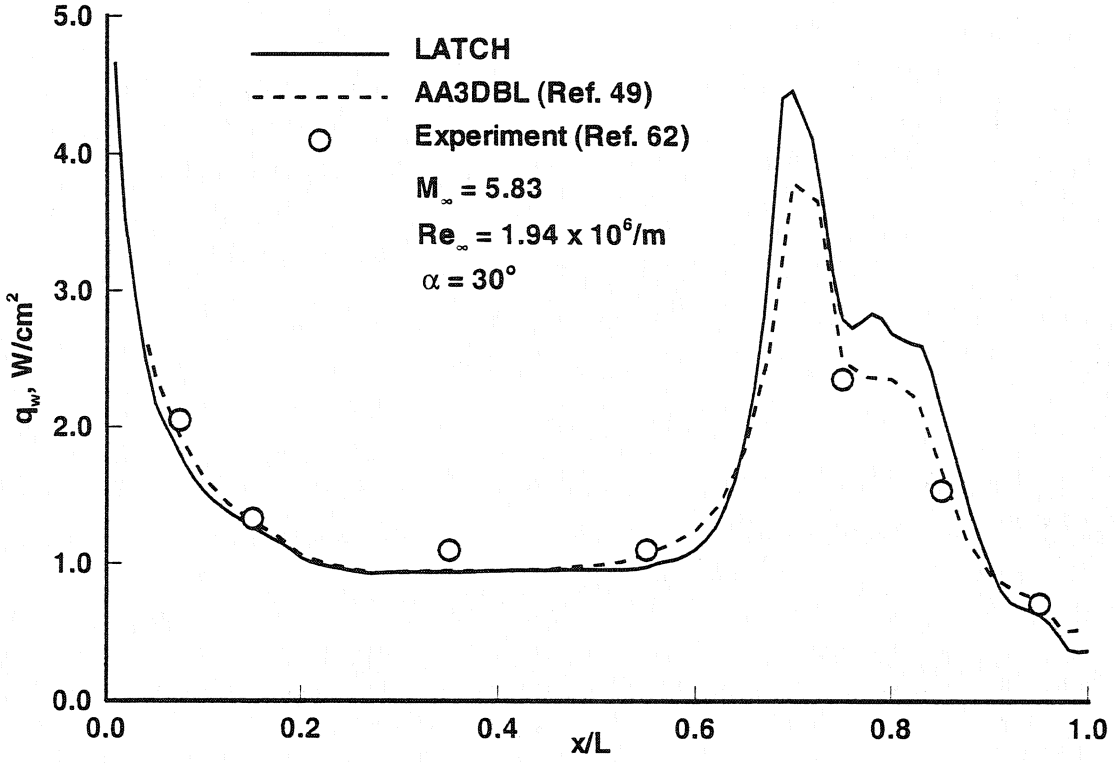

Figure 19. Maximum heating along wing leading edge.

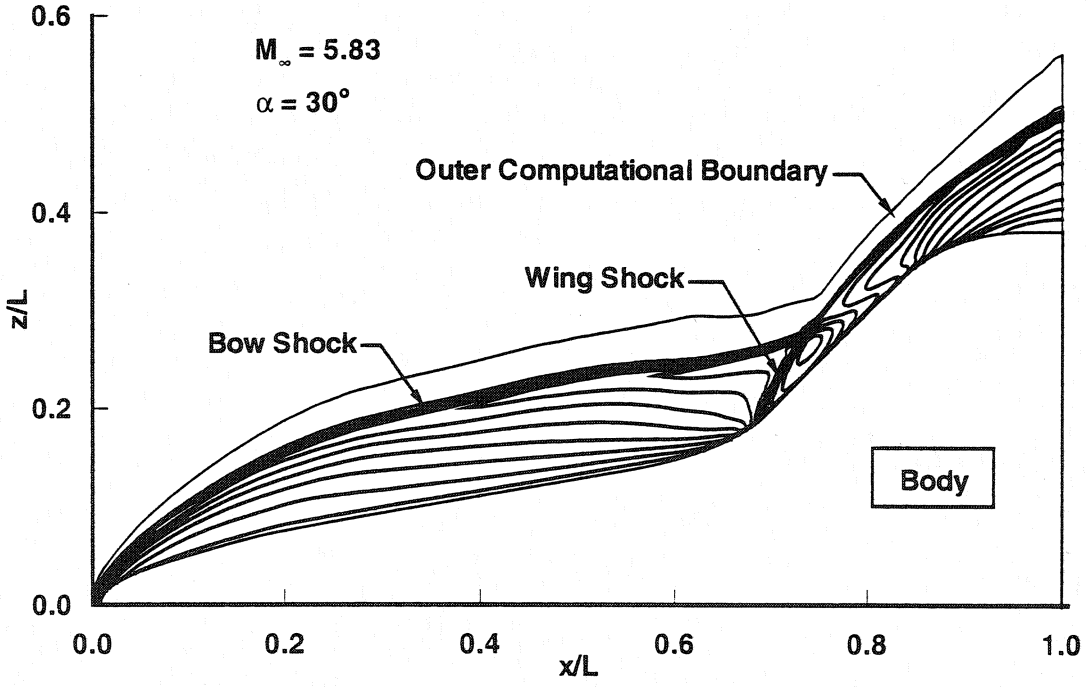

Figure 20. Density contours in plane near wing leading edge.

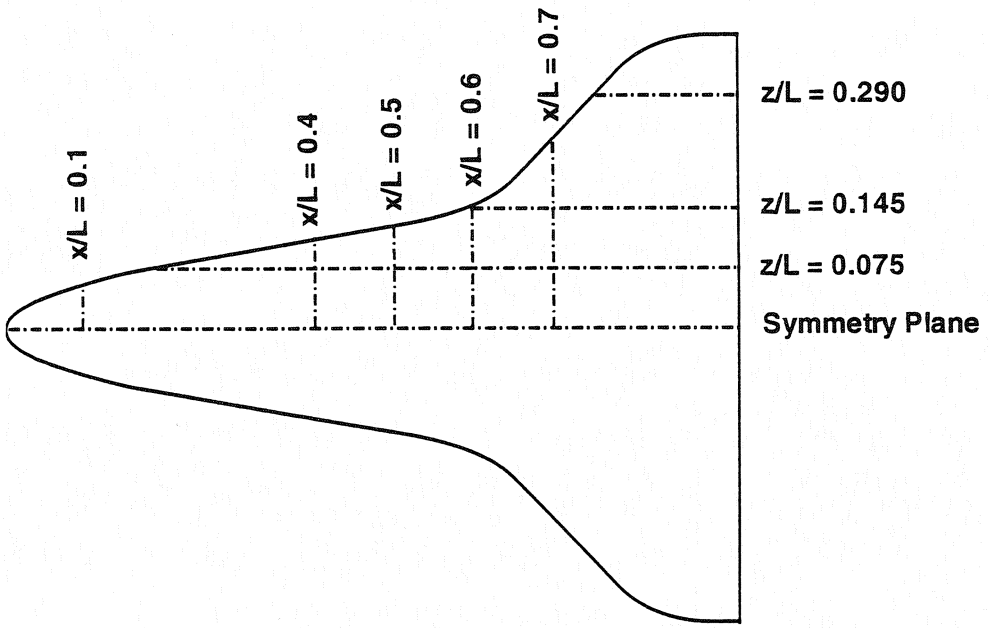

Figure 21. Locations for heating comparisons on windward side of Shuttle orbiter.

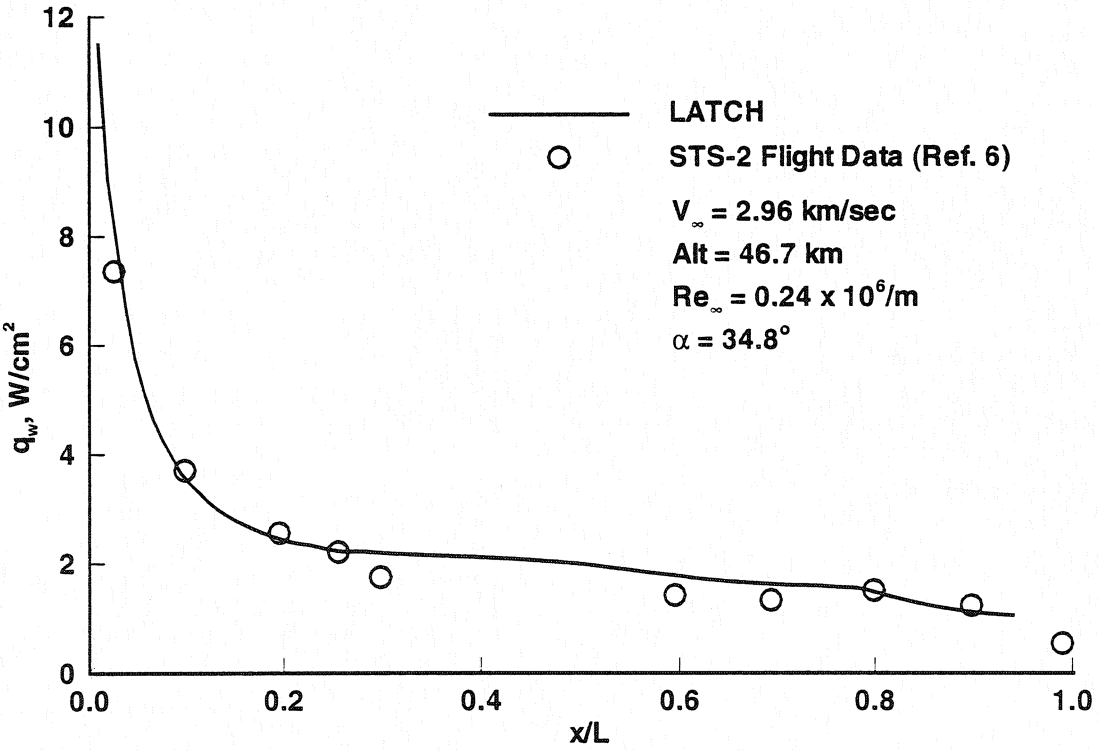

Figure 22. Windward symmetry-plane heating on Shuttle orbiter.

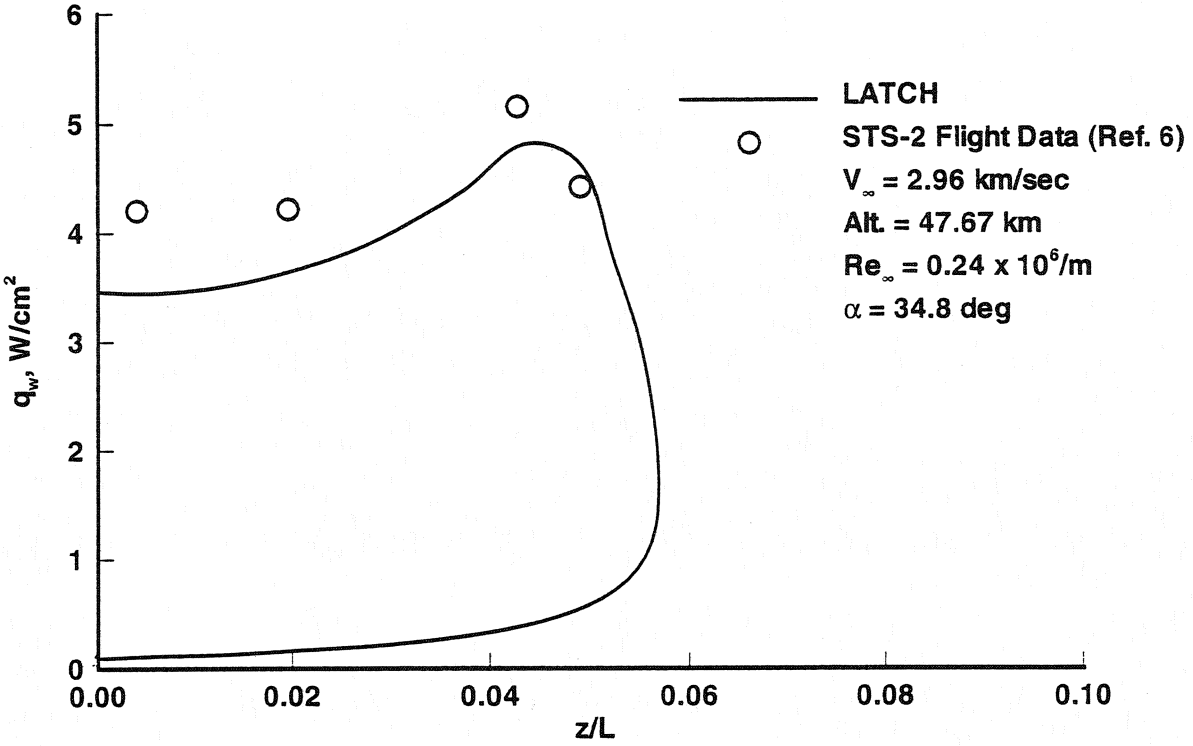

Figure 23. Lateral heating distribution on Shuttle orbiter at x/L = 0.10.

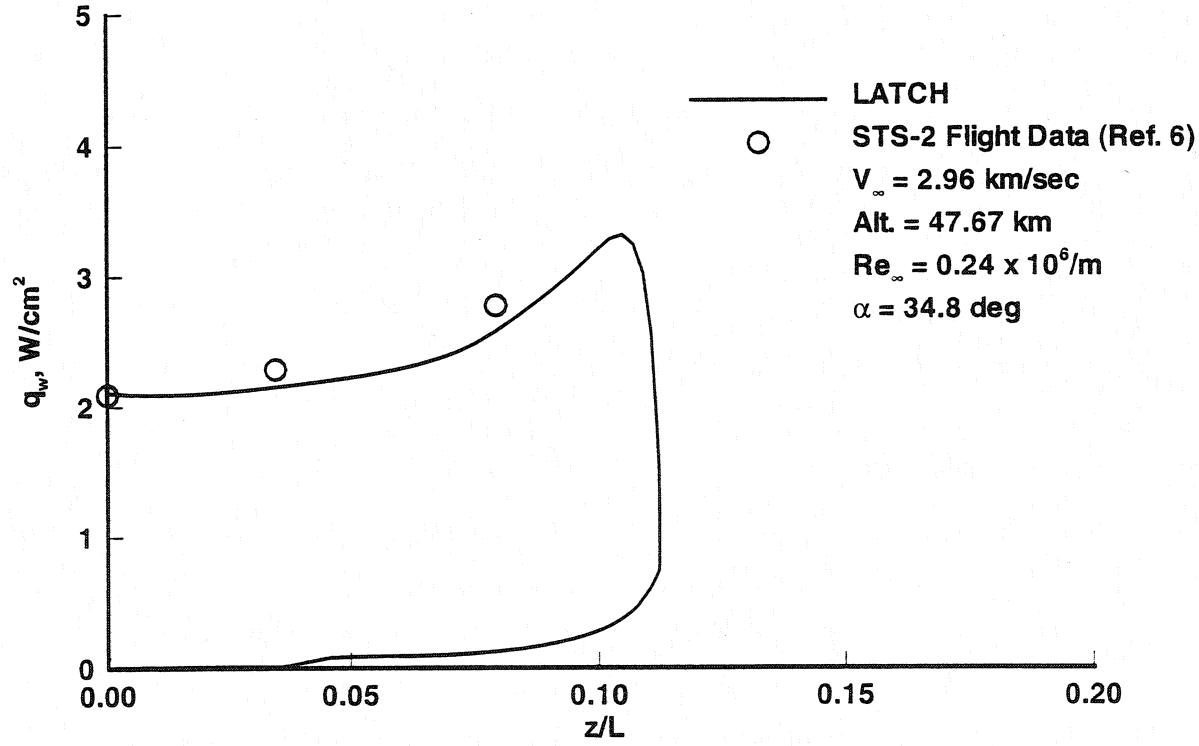

Figure 24. Lateral heating distribution on Shuttle orbiter at x/L = 0.4.

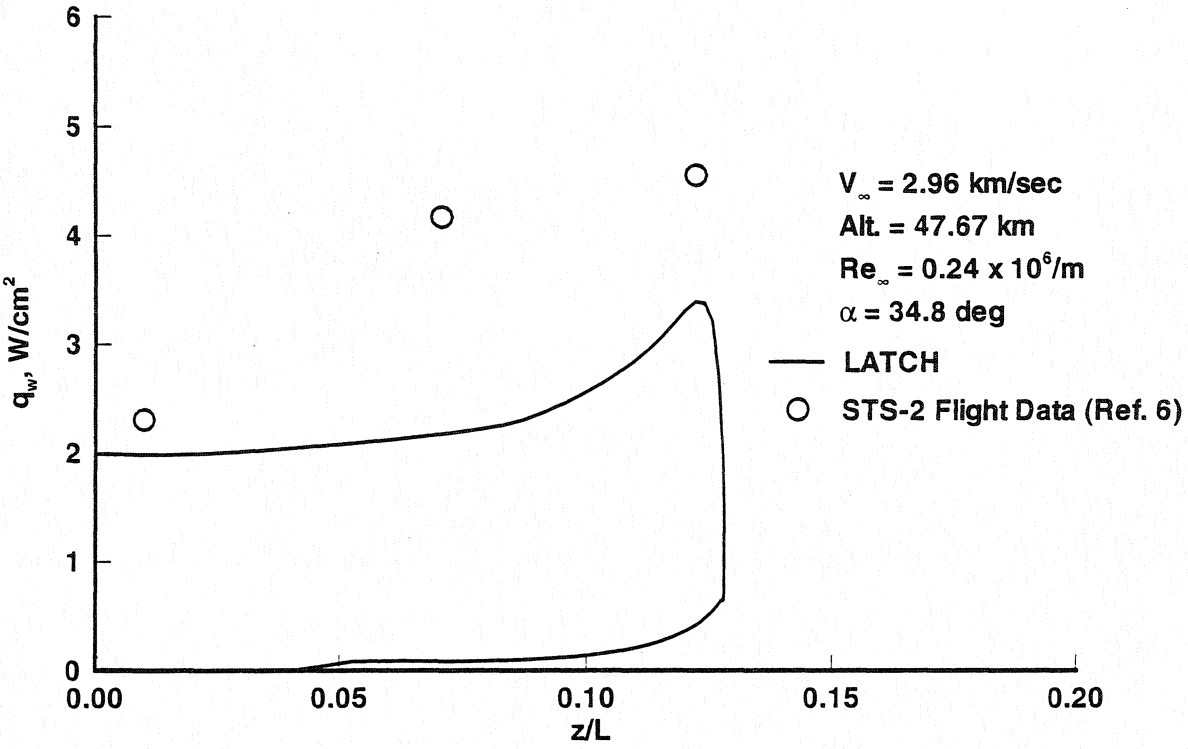

Figure 25. Lateral heating distribution on Shuttle orbiter at x/L = 0.5.

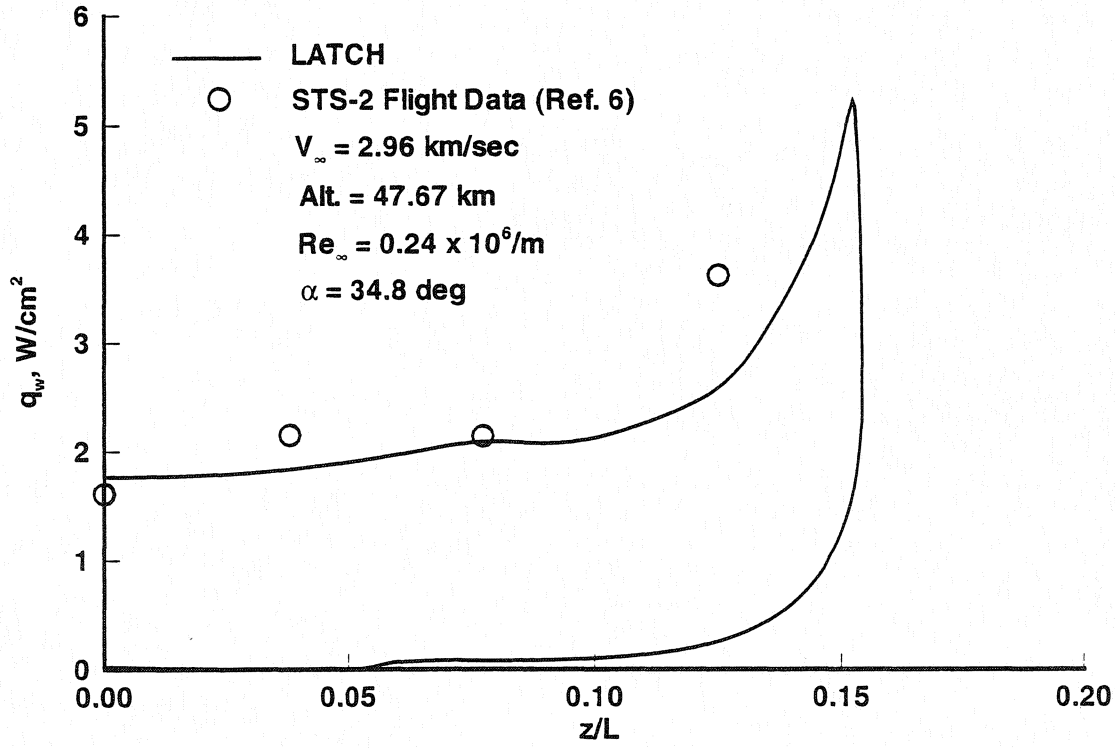

Figure 26. Lateral heating distribution on Shuttle orbiter at x/L = 0.6.

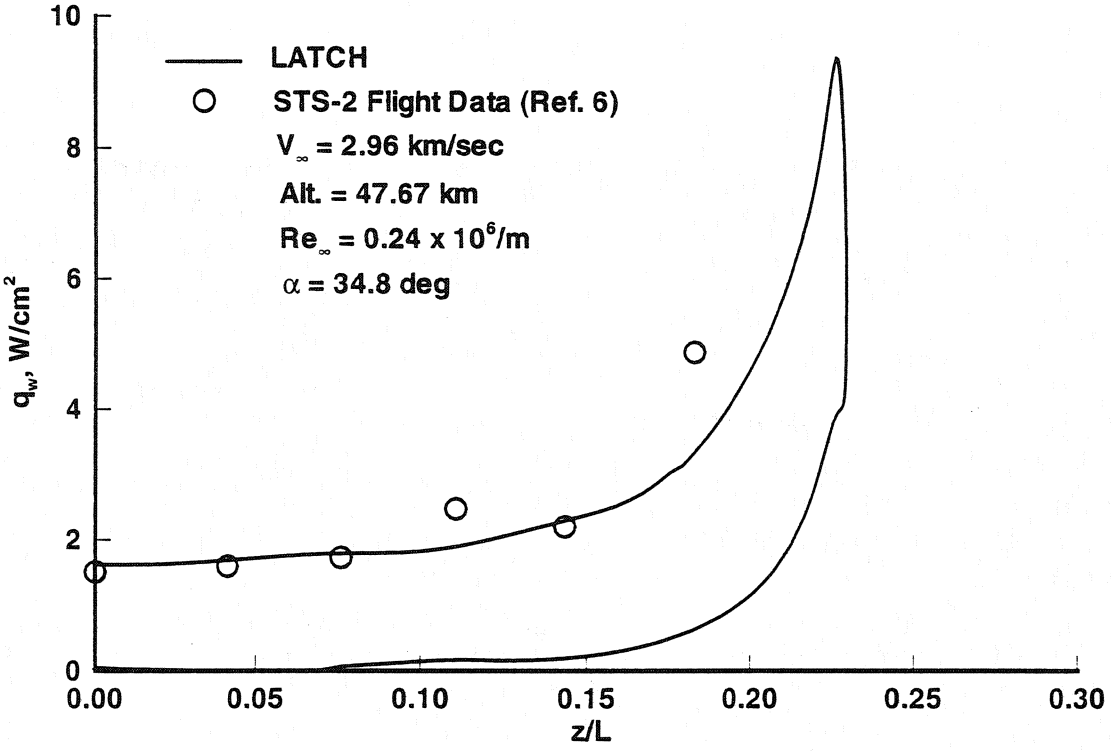

Figure 27. Lateral heating distribution on Shuttle orbiter at x/L = 0.7.

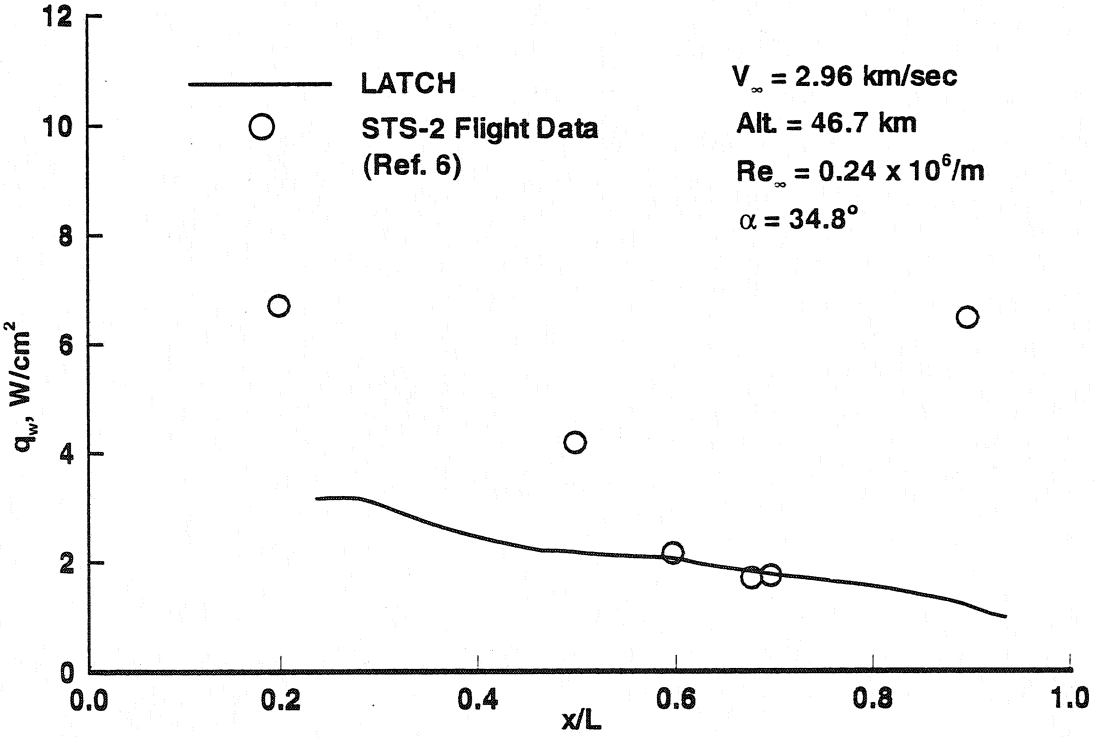

Figure 28. Heating along line parallel to windward symmetry plane of Shuttle orbiter at z/L = 0.075.

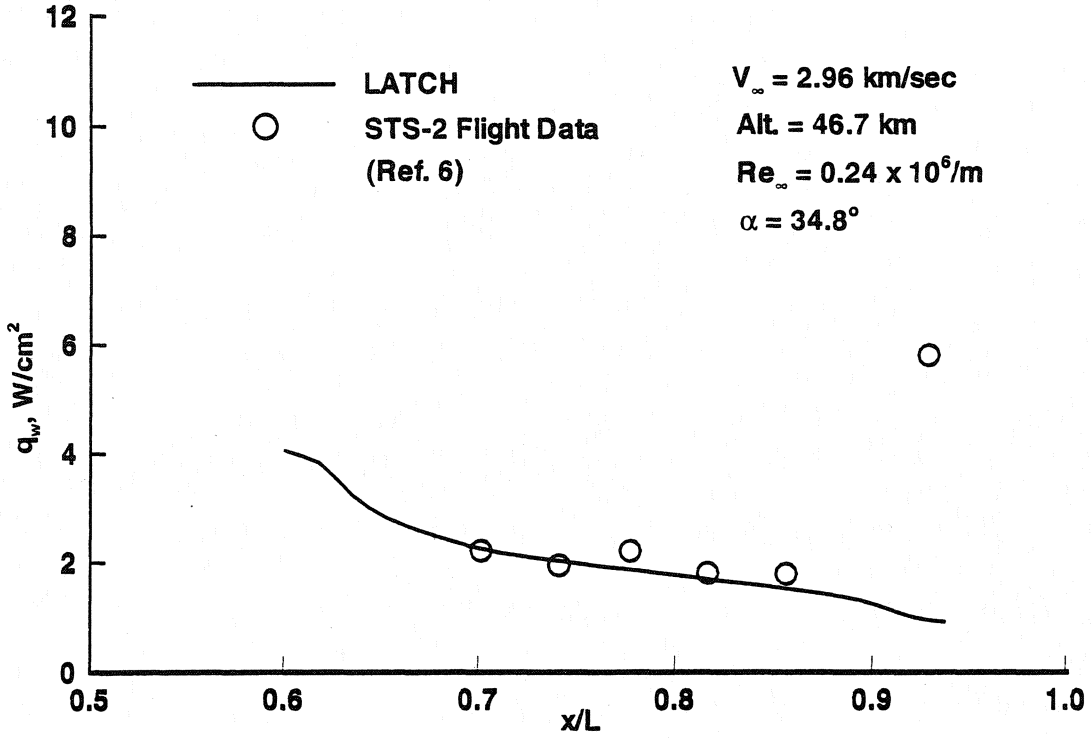

Figure 29. Heating along line parallel to windward symmetry plane of Shuttle orbiter at z/L = 0.145.

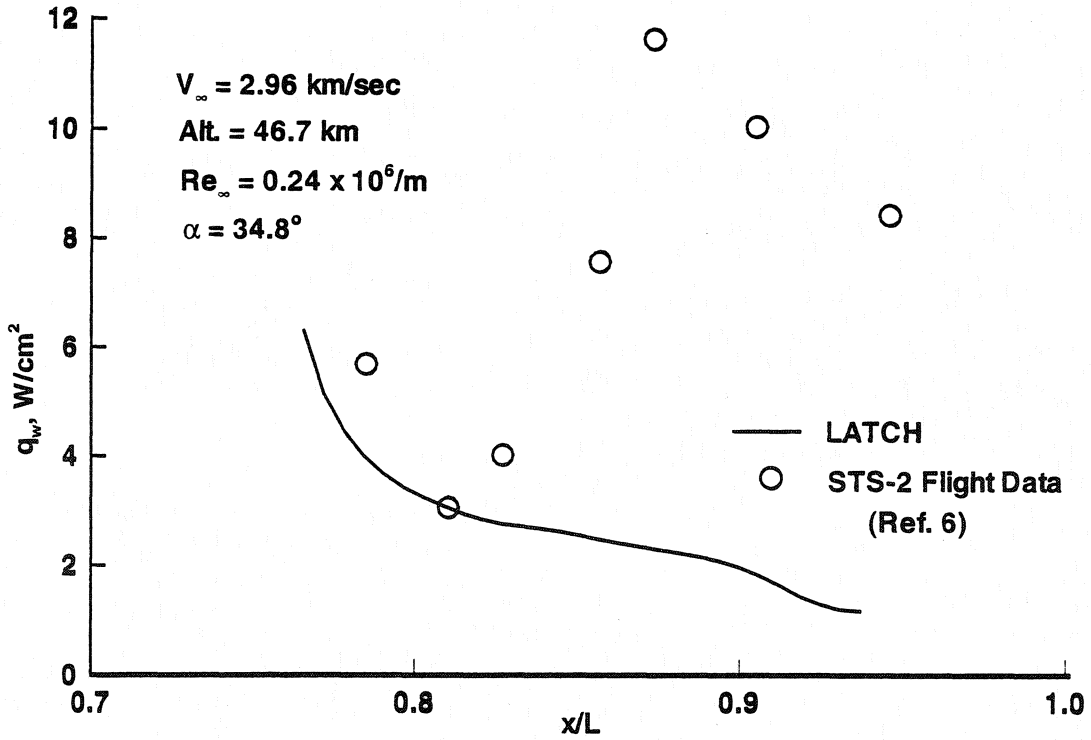

Figure 30. Heating along line parallel to windward symmetry plane of Shuttle orbiter at z/L = 0.290.

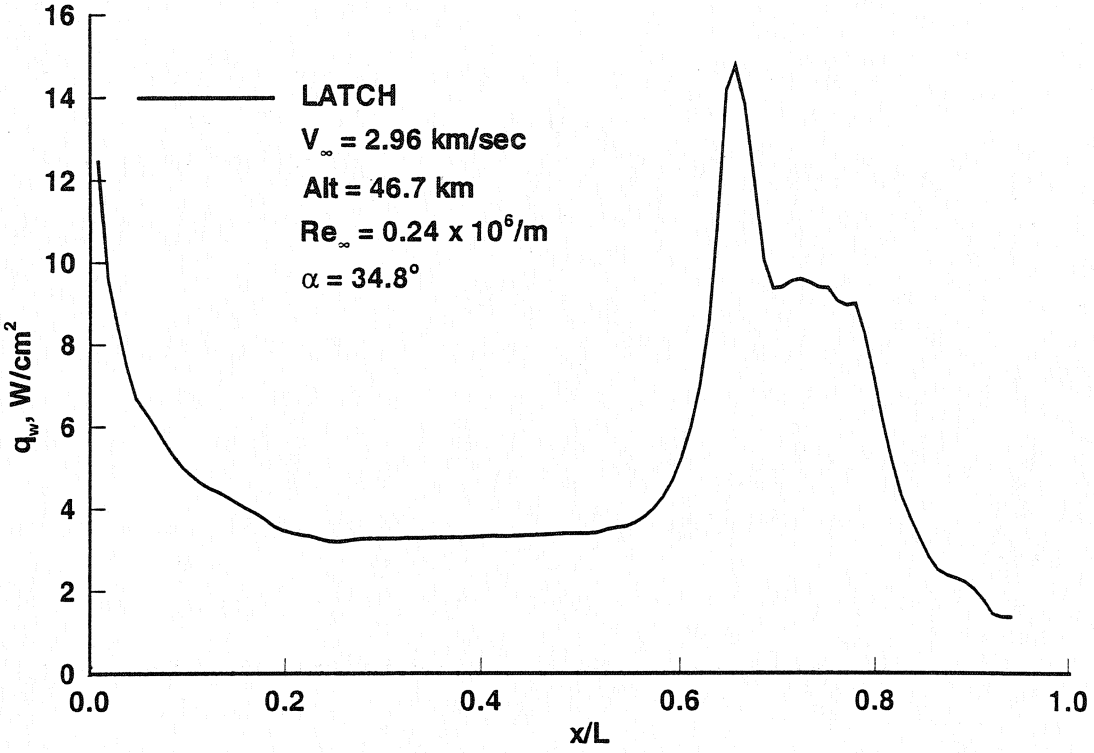

Figure 31. Maximum heating along wing leading edge on Shuttle orbiter.

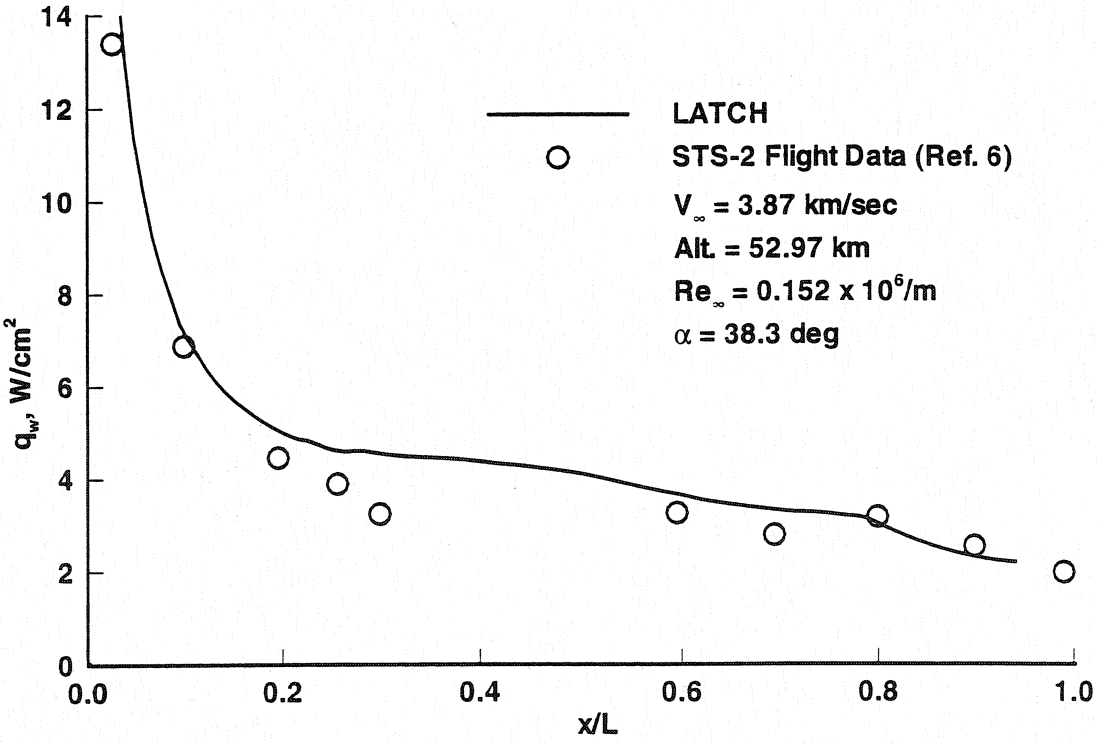

Figure 32. Windward symmetry-plane heating on Shuttle orbiter.

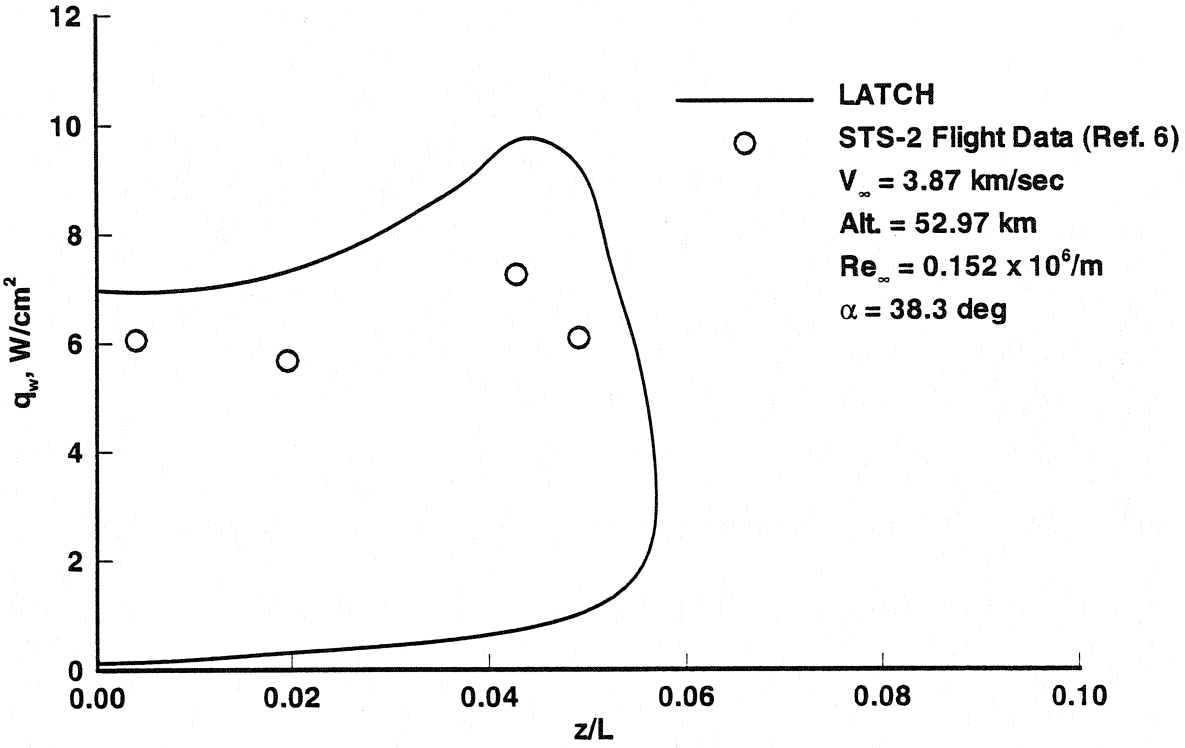

Figure 33. Lateral heating distribution on Shuttle orbiter at x/L = 0.10.

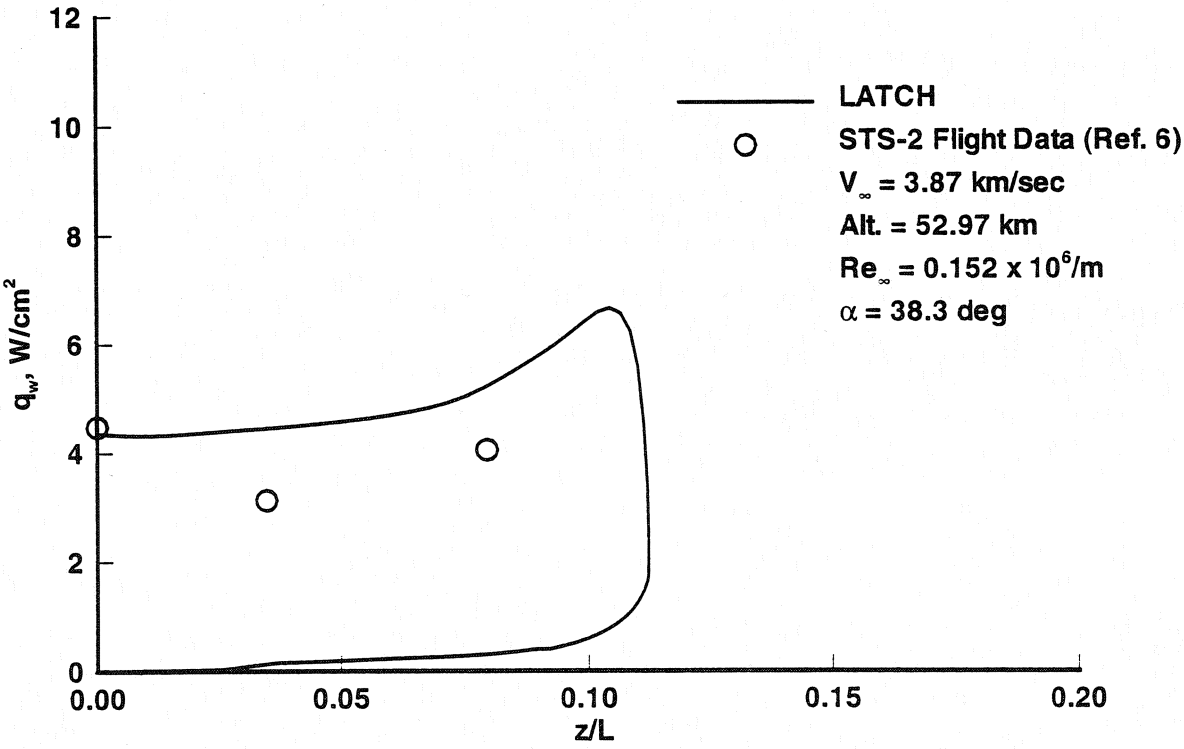

Figure 34. Lateral heating distribution on Shuttle orbiter at x/L = 0.4.

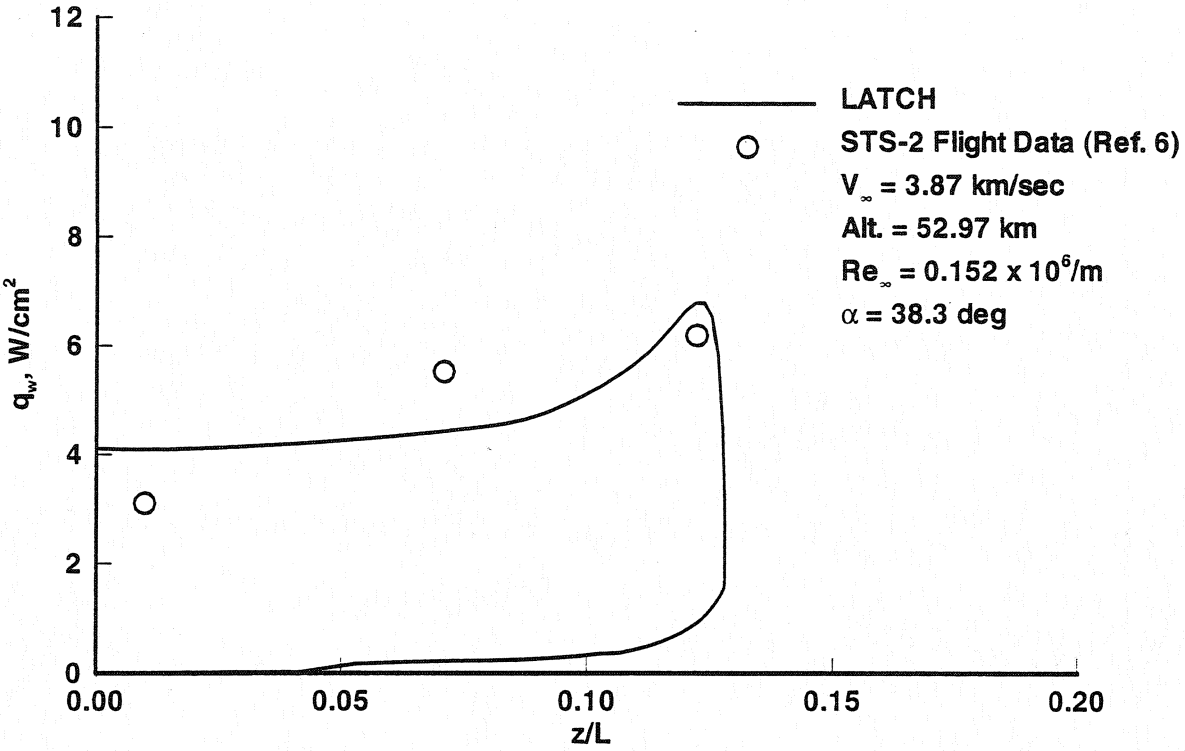

Figure 35. Lateral heating distribution on Shuttle orbiter at x/L = 0.5.

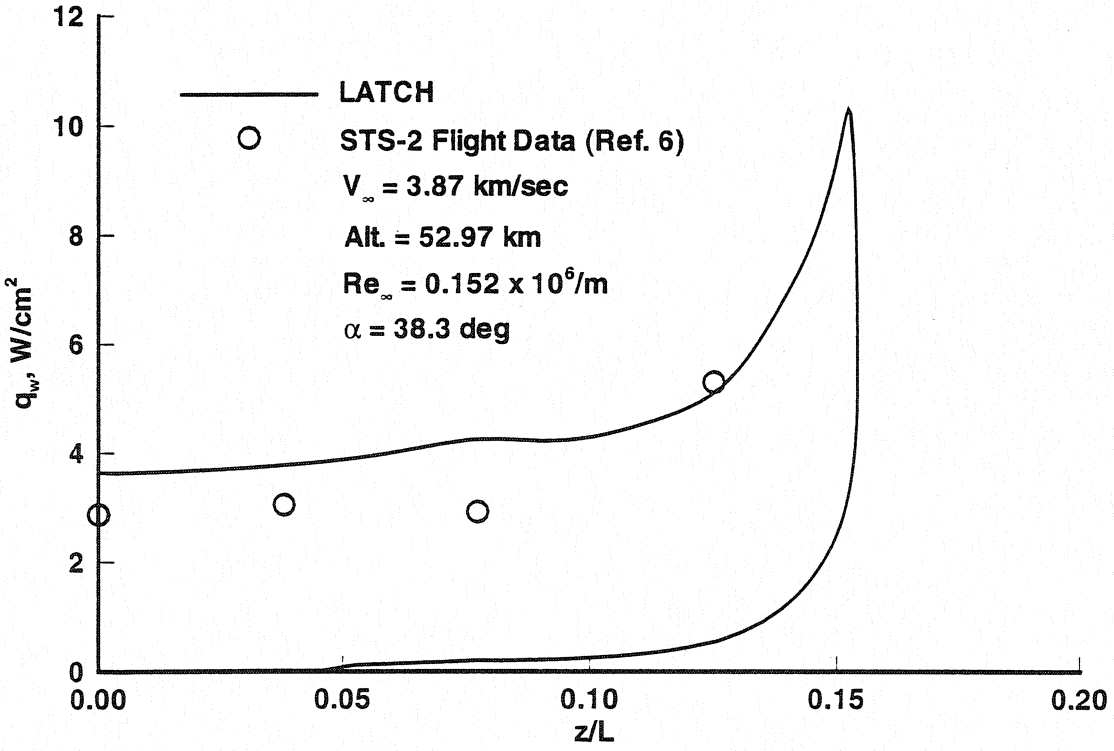

Figure 36. Lateral heating distribution on Shuttle orbiter at x/L = 0.6.

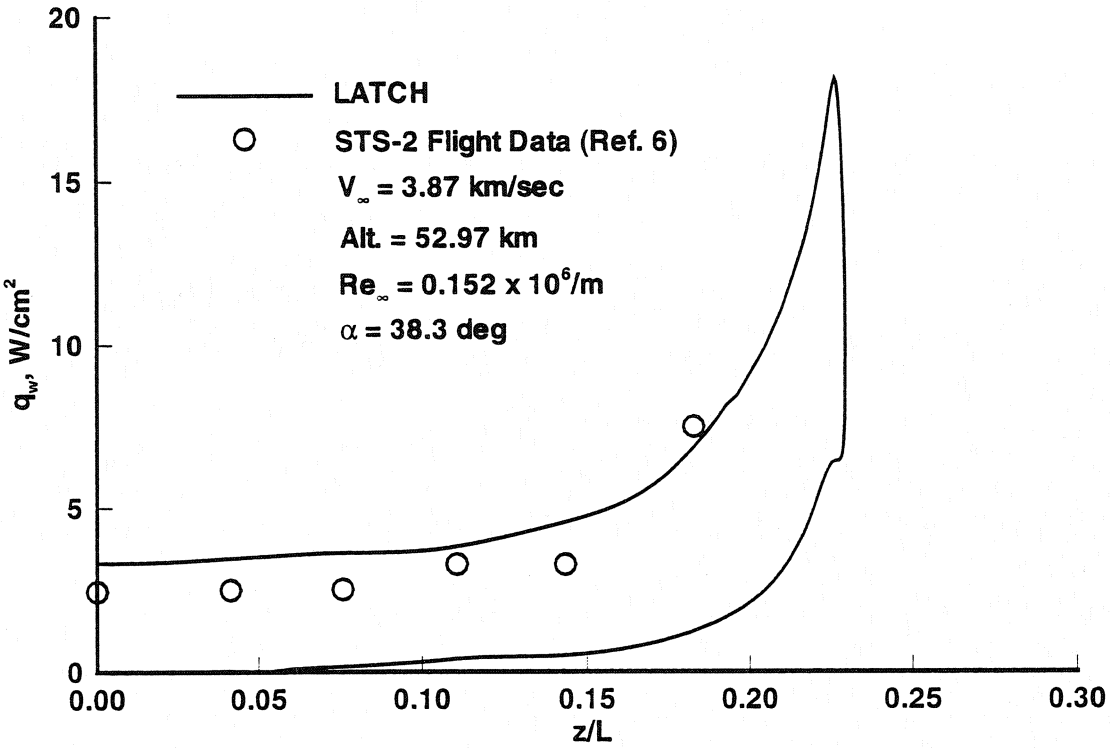

Figure 37. Lateral heating distribution on Shuttle orbiter at x/L = 0.7.

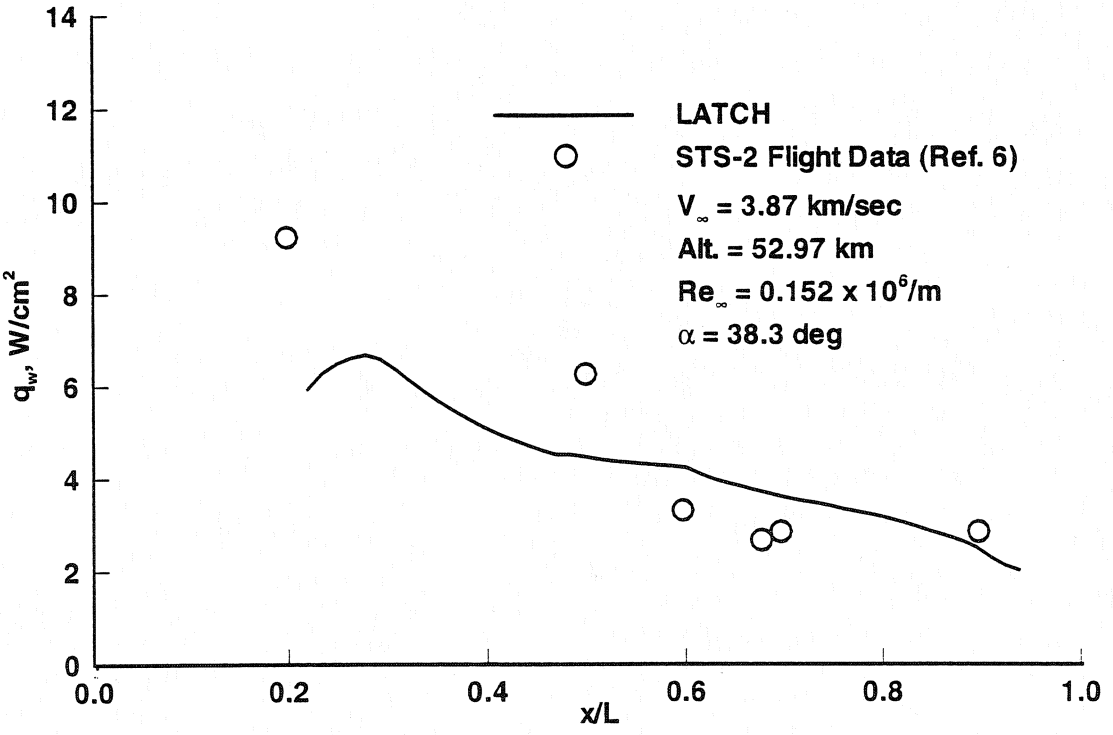

Figure 38. Heating along line parallel to windward symmetry plane of Shuttle orbiter at z/L = 0.075.

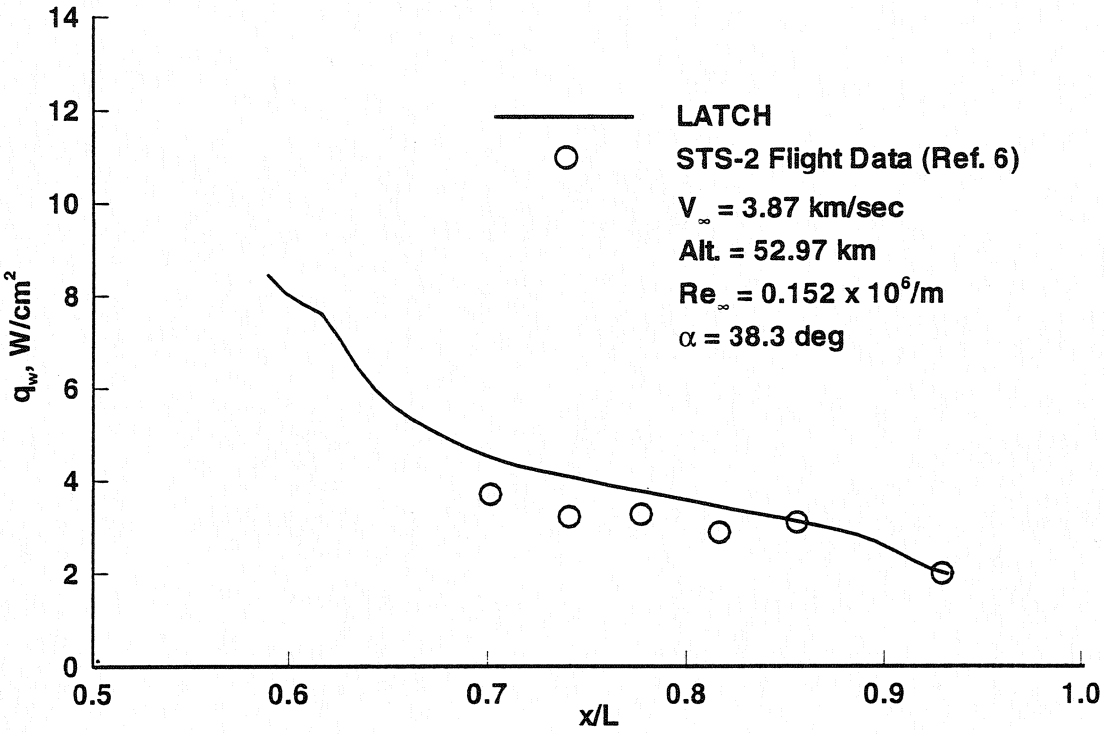

Figure 39. Heating along line parallel to windward symmetry plane of Shuttle orbiter at z/L = 0.145.

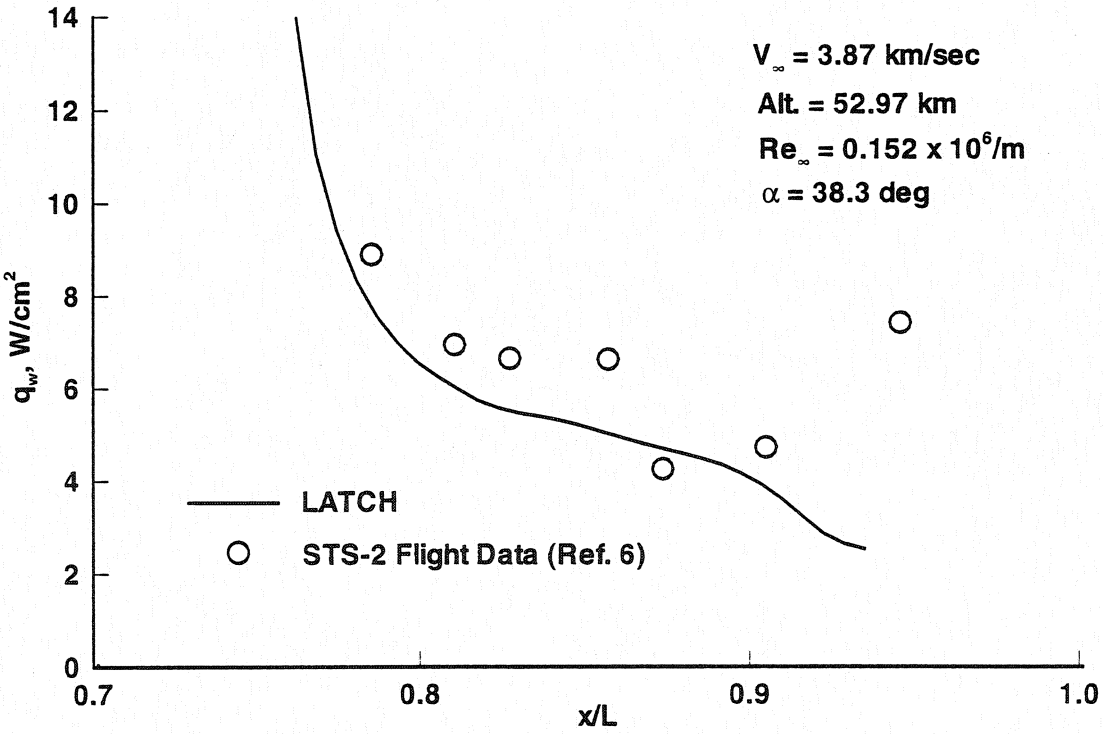

Figure 40. Heating along line parallel to windward symmetry plane of Shuttle orbiter at z/L = 0.290.

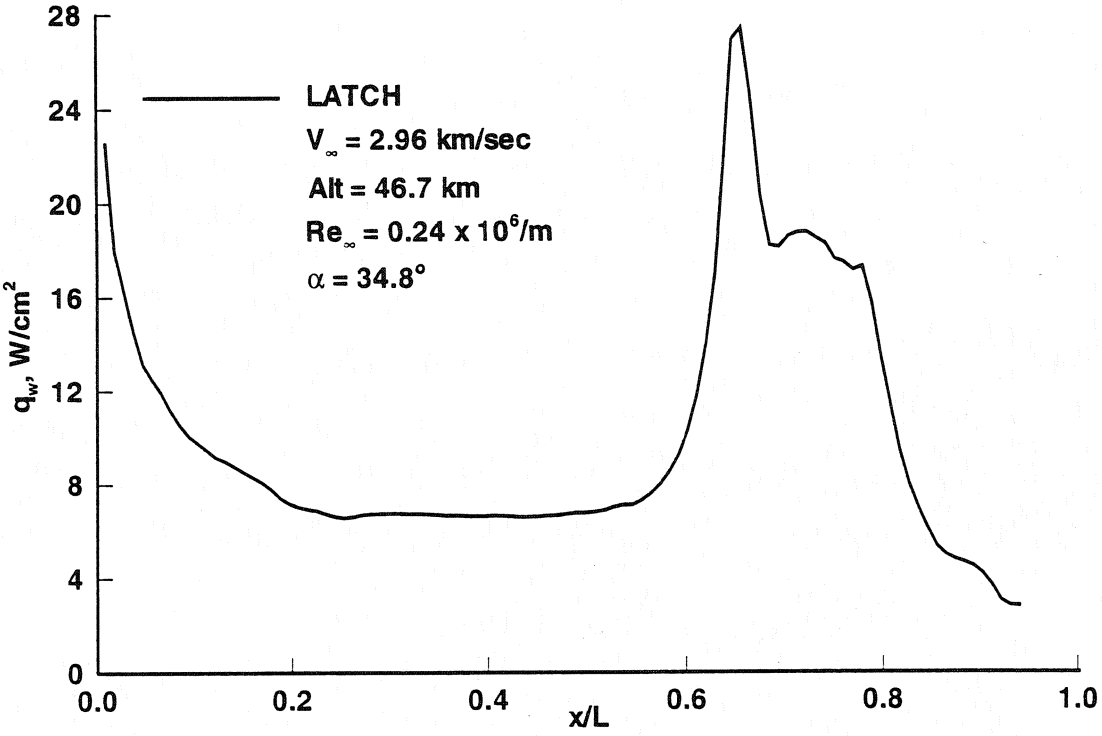

Figure 41. Maximum heating along wing leading edge on Shuttle orbiter.

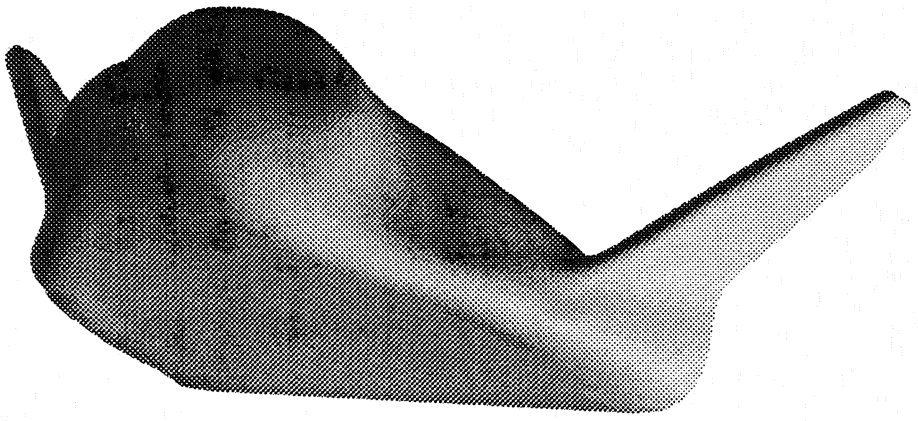

Figure 42. HL-20 geometry.

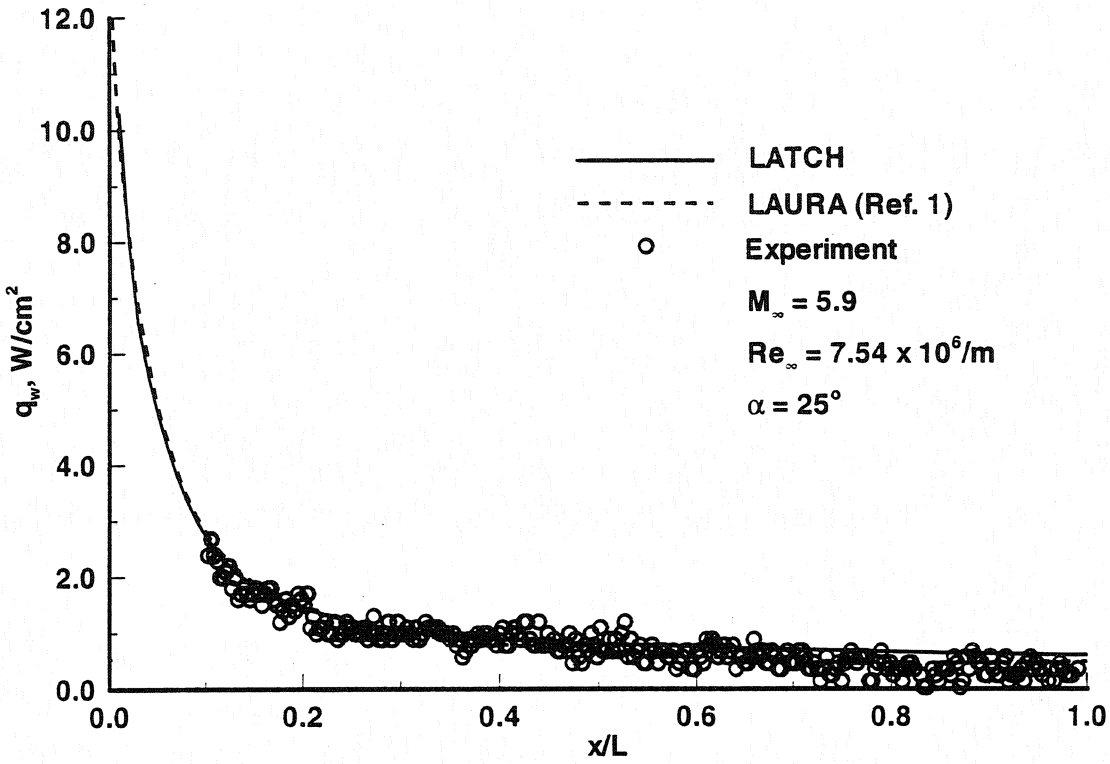

Figure 43. Windward symmetry-plane heating on HL-20.

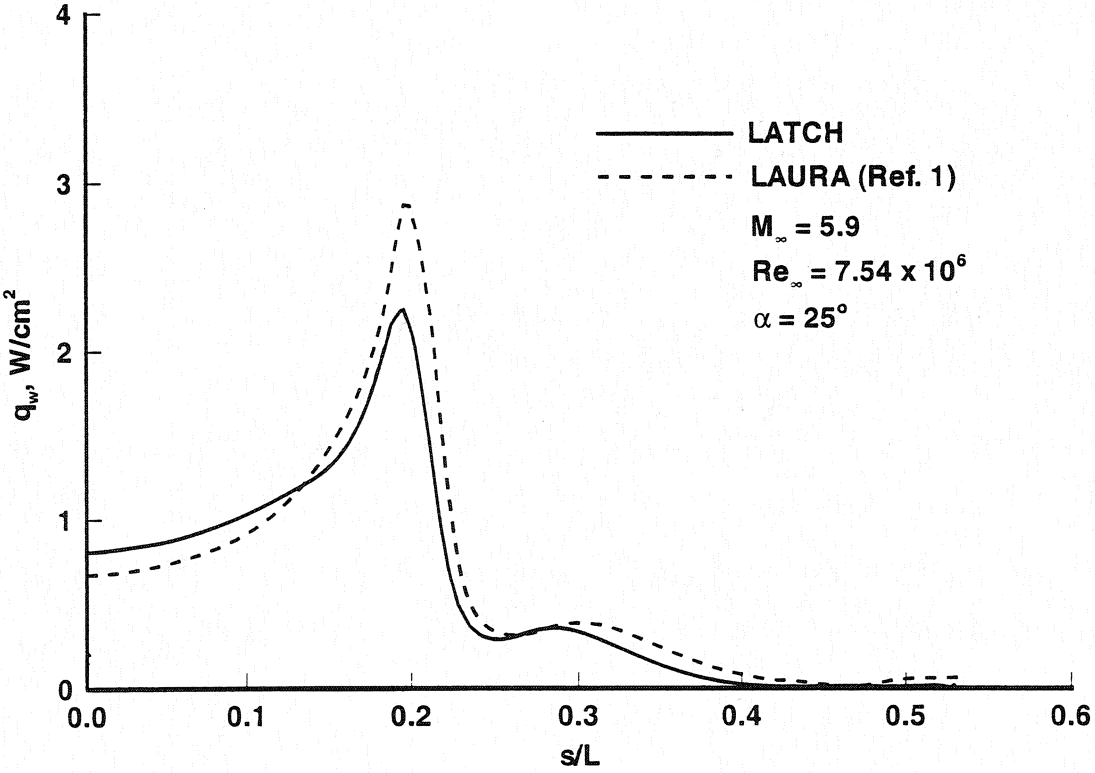

Figure 44. Circumferential heating distribution on HL-20 at x/L = 0.50.

A MULTIBLOCK ANALYSIS FOR SHUTTLE ORBITER RE-ENTRY HEATING FROM MACH 24 TO MACH 12

Peter A. Gnoffo, K. James Weilmuenster
NASA Langley Research Center
Hampton, VA 23681-0001

and
Stephen J. Alter
Lockheed Engineering & Sciences Company
Hampton, VA 23665

SUMMARY

A multiblock, laminar heating analysis for the shuttle orbiter at three trajectory points ranging from Mach 24.3 to Mach 12.86 on re-entry is described. The analysis is performed using the Langley Aerothermodynamic Upwind Relaxation Algorithm (LAURA) with both a seven species chemical nonequilibrium model and an equilibrium model. A finite-catalytic-wall model appropriate for shuttle tiles at a radiative equilibrium wall temperature is applied. Computed heating levels are generally in good agreement with the flight data though a few rather large discrepancies remain unexplained. The multiblock relaxation strategy partitions the flowfield into manageable blocks requiring a fraction of the computational resources (time and memory) required by a full domain approach. In fact, the computational cost for a solution at even a single trajectory point would be prohibitively expensive at the given resolution without the multiblock approach. Converged blocks are eventually reassembled to enable a fully coupled converged solution over the entire vehicle, starting from a nearly converged initial condition.

INTRODUCTION

The Space Transportation System (STS) was designed in an era in which large scale, computational fluid dynamic (CFD) analyses were unavailable to assist in the design process. Supercomputer technology has now progressed to the point where CFD has the resources (speed and memory) to make substantial contributions to future hypersonic vehicle design projects by providing flowfield solutions over complete, winged configurations. These solutions provide surface pressure and heating predictions at selected design points, but, more importantly, also provide insight into the very

flow structure with powerful, graphical analysis tools that show streamline traces, vorticity distributions, profile information and the like. CFD analyses are being used now, for example, in the National AeroSpace Plane (NASP) project. They are expected to play an important role in the design of future elements of our space transportation system, such as the Personnel Launch System (PLS).

The capabilities and limitations of CFD simulations for hypersonic flow over winged vehicles must be periodically reevaluated to account for advances in algorithms and computational power and to include updates to the data base for code validation. The importance of such activity is internationally recognized [1, 2]. The data base provided by the Orbiter Experiments (OEX) Program on board the Orbiters Columbia and Challenger provide a crucial benchmark for such evaluations. The objective of this paper (and companion papers [3, 4, 5]) is to perform this evaluation for the Langley Aerothermodynamic Upwind Relaxation Algorithm (LAURA) [6, 7] using the OEX benchmark. The data base emphasized herein is heat transfer from the STS-2 flight [8]. Aerodynamic coefficient data is addressed in the companion paper [5].

Details of the study follow in later sections but the general approach taken is to define three trajectory point CFD benchmarks which can efficiently utilize the compute power (processors, in-core memory, fast solid-state-device (SSD) memory) available at the inception of this study (8 processors, 128MW) in the multi-user environment on the NASA Langley Cray Y-MP and the NAS Cray Y-MP. A multiblock analysis allows different pieces of the whole to be computed separately (and in most cases, concurrently). The chemical nonequilibrium analyses include 7 species (N, O, N_2, O_2, NO, NO^+, and e^-). Finite rate wall catalysis appropriate for shuttle tiles at a radiative equilibrium wall temperature is applied. One thermal nonequilibrium case is computed which employs a two-temperature model. One equilibrium case is computed which employs thermodynamic and transport property curve fits.

COMPUTATIONAL GRID

A surface grid defined by 150 cells from the nose to the wing - fuselage - tail trailing edge and by 109 circumferential cells is employed. This grid includes the correct elevon deflections for each trajectory point as well as the OMS pods and the vertical tail. The bodyflap is defined by an additional 30 x 14 cells. The shock layer is resolved with 60 cells. Spatial grid convergence studies for a closely related test case were reported in [3]. Grid requirements defined by that study have been employed in the present work. A grid convergence study confined to the first 500 inches of the vehicle because of memory limitations is described in a later section.

Details of the baseline grid generation process are presented in Reference [5]. After the grid is generated, LAURA has the capability to redistribute mesh points across the shock layer and to align the outer boundary with the captured shock as the solution evolves. The cell Reynolds number [6, 9] at the wall is set to 3.0. The redistribution is particularly important because the volume grid generator was severely restricted in its ability to generate grids with adequate resolution near the wall. However, the one-dimensional adaption was unable to improve the grid in the vicinity of the vertical tail, including most of the OMS pods. Because the grid is insufficiently clustered in these areas heating predictions are not presented.

The grid adaption/alignment option in LAURA is based on a very simple, one-dimensional algorithm as described in Reference [9]. The option may fail when two conditions exist: (1) grid lines approaching the outer boundary converge and/or skew; and (2) the outer boundary must be pushed further away from the body to accommodate the changing position of the shock. These conditions allow negative volumes to form in the extrapolated grid. In these situations, as occurred in this study on the leeside for the Mach 12.86 case, it is best to do a global restructuring of the grid with better tools than are available in LAURA.

MULTIBLOCK ANALYSIS

The multiblock solution strategy is applied in two stages. The first stage may be regarded as a space marching solution, like the Parabolized-Navier-Stokes (PNS) methods, except that three-dimensional data blocks are employed rather than two-dimensional data planes. The second stage is a conventional, global relaxation which uses the first stage solution as an initial condition. The advantages of the three-dimensional-block marching over two-dimensional block-marching are that solution robustness is not sacrificed when employing second-order discretization in the streamwise direction and embedded subsonic pockets and shock / boundary layer interactions are easily computed - provided that the outflow boundary of the sub-domain is intelligently chosen. The sub-domain boundaries are easily tailored to the physics of a given application. The advantage of the two-dimensional-block-marching is that if the flow is sufficiently well behaved (i.e. supersonic streamwise flow above the boundary-layer and insignificant perturbations moving upstream through the boundary layer) then the stage one computation can be an order of magnitude faster than conventional, global relaxation. The tradeoffs between marching strategies are not explored in this work. It is expected that the three-dimensional-block marching strategy will provide a significantly better initial condition to the second stage computation as compared to a PNS approach.

The nose region is solved for the first stage on a (15 x 109 x 60) cell grid using extrapolation outflow boundary conditions. This domain fully contains the sonic line, except for a very narrow subsonic region in the boundary layer. Grid adaption routines are used to align the volume grid with the captured bow shock. The next windside block extends 50 cells from $i = 14$ (two planes inside the nose domain) to $i = 63$ (ahead of the wing) and from $j = 70$ (circumferential plane approximately behind the wing leading edge and fuselage corner) to $j = 109$ (the windside symmetry plane). Subsequent windside blocks extend from $i = 62$ to $i = 111$ (just past the wing tip leading edge) and from $i = 110$ to $i = 150$ (the wing / elevon trailing edge). The block boundaries on the surface for stage 1 are shown in Figure 1.

The solution in these windside blocks is initialized by injecting the k directional grid distribution function and the exit plane solution from the previous block. This injection speeds the development of a converged boundary layer profile as compared to conventional, unstaged, global relaxation techniques. Only a single plane of data is required from the upstream block to serve as an inflow boundary condition. Extrapolation is again used for the outflow boundary. The side boundary condition at $j = 70$ depends on the value of the component of Mach number normal to this plane. If this component is supersonic, the usual case for the given orientation of the side plane and the high angle of attack, then simple extrapolation provides a well posed boundary condition. If this component is subsonic, then a temporary fix is applied which forces a supersonic expansion

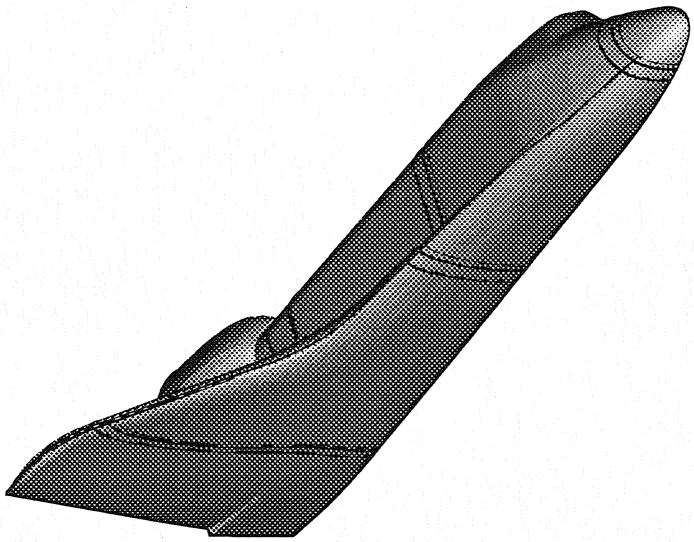

Figure 1: Block boundaries on surface for stage one computations.

by resetting the pressure in a pseudo-cell side boundary to one percent of the actual side plane pressure (i.e. $p_{i,69,k} = 0.01 p_{i,70,k}$). This fix was only required in the solution of the second windside block. It is not required at all in the second stage of the relaxation process. Some corruption of the solution is possibly introduced with this fix; however, in the present case the converged solution is not significantly different from the globally relaxed solution in the second stage. This similarity is evident in Figure 2 in which the circumferential heating in the second windside zone and second leeside zone from stage one is compared to the circumferential heating of the fully coupled domain in stage two.

Leeside blocks are marched in the same manner as the windside blocks, except that the side plane extrapolation boundary condition is replaced with an inflow boundary condition extracted from the interior of a previously converged windside domain (Figure 1). In the STS-1 cases, the leeside domains have the same range in the streamwise direction as the windside domains, though this correspondence is not generally required. The circumferential range extends from $j = 1$ to $j = 71$. Because the nth leeside block and the $n+1$th windside blocks are independent, they can be run simultaneously on the computer.

The relatively small memory requirements of these sub-domains in stage one generally expedite turnaround on multiuser supercomputers and increase relaxation cycles per CPU hour. Each sub-domain was processed using 4 to 8 CPU hours per run on a CRAY Y-MP. Furthermore, the sub-domain is divided into 8 smaller partitions (one partition per processor using an asynchronous, macrotasked relaxation strategy [7, 10]) so that elapsed time is only slightly greater than 0.5 hours for a 4 CPU hour run. Two to four runs are used to converge each sub-domain, the number depending on subjective judgements of satisfactory grid adaption and objective judgement of surface heat-transfer convergence. Surface heat transfer convergence is judged based on error norms of order 10^{-6} in the boundary layer partitions and predominant overplotting of centerline heating distributions on sequential runs.

After each sub-domain is converged the solution is saved in a master copy of the complete domain. The stage two, global relaxation process begins when all the sub-domains are filled. In this case, five streamwise zones (average length equal to 30 cells with the last zone involving a

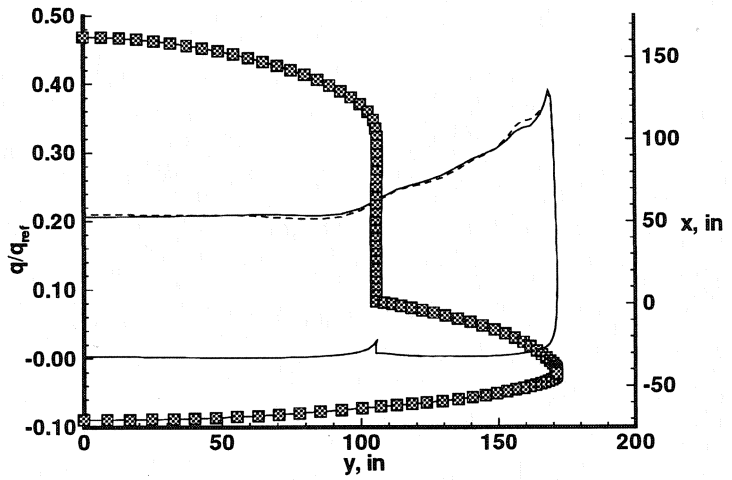

Figure 2: Circumferential heating at $i = 71$ from stage one (dashed line) and stage 2 (solid line).

special sidewall boundary condition for the vertical tail) are defined (Figure 3). This partitioning represents the best compromise between task common memory overhead and requirements for an easily vectorized tail boundary condition. On an 8 processor machine, the work of converging the five zones may be divided among 8 processors. Because of the greater memory required for the global relaxation, it is necessary to save solution Jacobians on fast, solid-state-device (SSD) memory. The global solution in stage two utilized 128 Megawords (MW) of in-core memory, 128 MW of SSD memory, and 8 processors working in a fully coupled, macrotasked mode, utilizing on average more than 7 concurrent CPUs per hour of elapsed time on a CRAY Y-MP.

The solution of the flowfield over the bodyflap must include enough of the body domain to allow for potential upstream interaction caused by the deflected bodyflap. Parts of the windside domain are extracted from the stage 2 solution over the body in order to serve as an inflow boundary for the bodyflap and allow enough area for this interaction. The block boundaries on the entire surface are presented in Figure 4 with details of the bodyflap region shown in Figure 5. Two inflow blocks and one sideflow block of one cell in width provide boundary conditions for the bodyflap well away from the interaction zone of the deflected flap. The exit plane and side plane on the actual flap have predominantly supersonic Mach number components normal to the exit surfaces; consequently, extrapolation outflow boundaries are adequate to close the problem. (Preliminary tests for a perfect gas flow wind tunnel case which include the near wake about the bodyflap indicate the extrapolation boundary condition results compare well to the full wake results. Tests at flight conditions are pending.)

Table 1 - Trajectory Points and Control Surface Parameters

flight	V_∞ m/s	ρ_∞, kg/m^3	T_∞, K	h, km	M_∞	α, deg	δ_{bf}, deg	δ_{el}, deg
STS-1	6809.	$5.294\ 10^{-5}$	205.8	73.1	23.68	39.4	15.97	-0.44
STS-2	6920.	$5.750\ 10^{-5}$	202.0	72.4	24.30	39.4	14.91	1.74
STS-2	5617.	$1.626\ 10^{-4}$	240.6	64.4	18.07	41.2	13.54	1.51
STS-2	4168.	$5.330\ 10^{-4}$	261.6	54.8	12.86	39.7	12.92	0.74

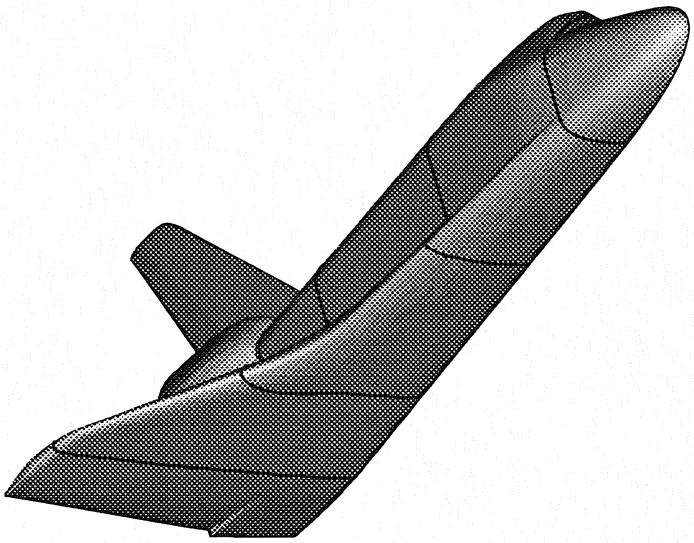

Figure 3: Block boundaries on surface for stage two computations.

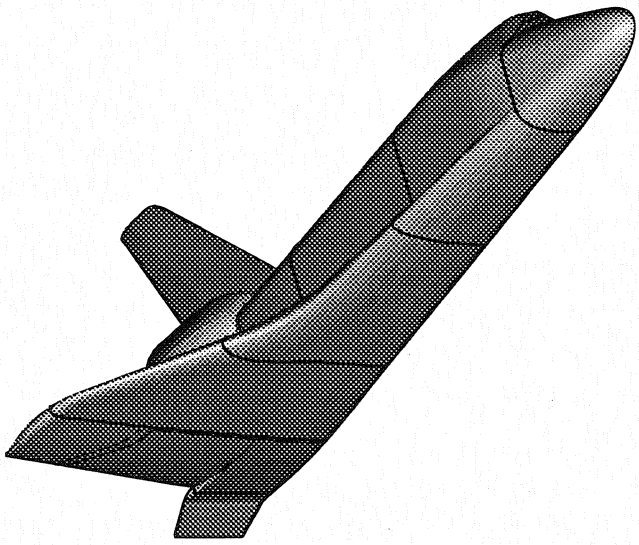

Figure 4: Block boundaries on surface for stage two computations coupled with the bodyflap.

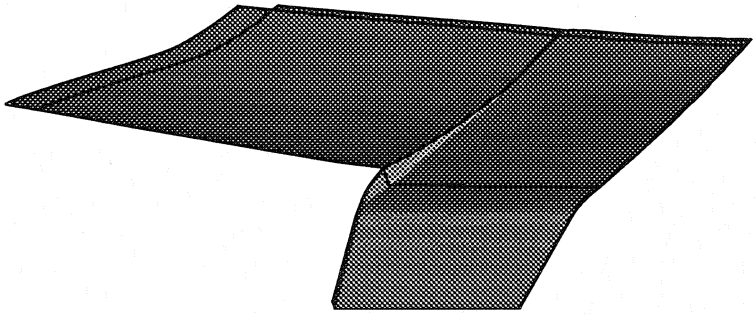

Figure 5: Detail of block boundaries over the bodyflap.

BOUNDARY CONDITIONS

Freestream conditions are given in Table 1 for each of the three selected trajectory points for STS-2. (An STS-1 trajectory point used in the companion study [5] and which served to initialize the STS-2 calculations is also presented. STS-1 results are not presented here because of space limitations and the lack of heating data in flight.) Control surface parameters for the three STS-2 trajectory points are also presented in Table 1.

No-slip conditions for velocity and temperature are applied at the wall. The normal pressure gradient at the wall is set to zero. A radiative equilibrium wall boundary condition on temperature is applied as follows in a time lagged manner for every point on the surface.

$$T_{wall}^{n+1} = \varepsilon \left[\frac{q^n}{\epsilon \sigma} \right]^{1/4} + (1 - \varepsilon) T_{wall}^{n} \tag{1}$$

where superscripts n and $n+1$ are the global iteration levels, T is temperature in degrees Kelvin, q is convective heating in W/m^2, ϵ is the surface emissivity, σ is the Stefan-Boltzmann constant, and ε is a relaxation factor for the explicit updates of the wall temperature. The surface emissivity is set equal to 0.9 for all cases. Variations about this value for the various shuttle surfaces are generally less than 10% and the associated variation of wall temperature is less than 3%, assuming that q is only weakly affected by small changes in surface temperature as compared to the difference between the adiabatic wall temperature and the actual wall temperature. The relaxation factor ε is set to 0.01.

Finite catalytic wall boundary conditions for chemical nonequilibrium flow, as defined by Zoby et. al. [11] for oxygen recombination and by Scott [12] for nitrogen recombination, are used for the entire shuttle surface. Similar relations as defined by Kolodziej and Stewart [13] for oxygen and nitrogen recombination are tested in selected cases. These relations are used outside the temperature range employed in their respective derivations.

GAS PROPERTIES

Nonequilibrium Flow

The chemical nonequilibrium analyses include 7 species (N, O, N_2, O_2, NO, NO^+, and e^-). The thermodynamic and transport properties for each of the seven species are obtained from curve fits as discussed in Reference [6]. The mixing rules for transport properties, including a molar weighted binary diffusion coefficient for each of the species, are also discussed in Reference [6]. The Lewis number is not set to a constant value. Convective heating to the surface consists of a conductive component proportional to the temperature gradient and diffusive components for each species proportional to the associated mole fraction gradient as defined within terms 3 and 4 of Equation 5 in Reference [6].

The baseline gas kinetic model is that of Park as detailed in Table 8.3 of Reference [14]. (Reaction 19 of that table is replaced with the recommended expression given on page 273 of Reference [14].) A quick check on the effects of a different gas kinetic model based on forward rates recommended by Dunn and Kang [15] and equilibrium constants of Gupta [16] for a Mach 24.3 trajectory point showed minimal effects on surface quantities. Line plots of pressure and heating in the nose region are identical for the two models. Further downstream, the same line plots would occasionally show differences of less than a few percent.

The baseline model assumes thermal equilibrium; however, one thermal nonequilibrium case for STS-1 was computed which employed a two-temperature model [6]. The effects of thermal nonequilibrium as compared to thermal equilibrium on surface heating and pressure were only evident on the wing and generally less than a few percent. The shock layer thickness over the wing leading edge is only on the order of a few inches, which allows thermal nonequilibrium effects to affect the compression to the wing leading edge and expansion to the windward surface. The related effect to normal and axial drag coefficient is less than 0.6%, but the effect on the moment coefficient is a $\Delta C_m = .00353$ (nose up), roughly corresponding to a change in bodyflap deflection of 0.7^o based on pitch curves in Reference [5]. These differences are on the order of changes which can be expected on the present grid associated with changes in numerical parameters, such as the magnitude or definition of the limiter functions in LAURA. More comprehensive tests are required to verify these effects as a general trend.

Equilibrium Flow

A Mach 12.86 trajectory point was computed using the equilibrium air curvefits of References [17] and [18] for thermodynamic and transport properties. The conductive and diffusive components of convective heating for equilibrium flow are combined in a single term involving the enthalpy gradient and reactive Prandtl number as defined by Equation 5 in Reference [19]. At this Mach number, the effects of the equilibrium model as compared to the nonequilibrium model on aerodynamic coefficients are less than 0.03% for C_N, less than 1.5% for C_A, and $\Delta C_m = .00011$. These differences, as discussed earlier, are not significant relative to other uncertainties in the simulation.

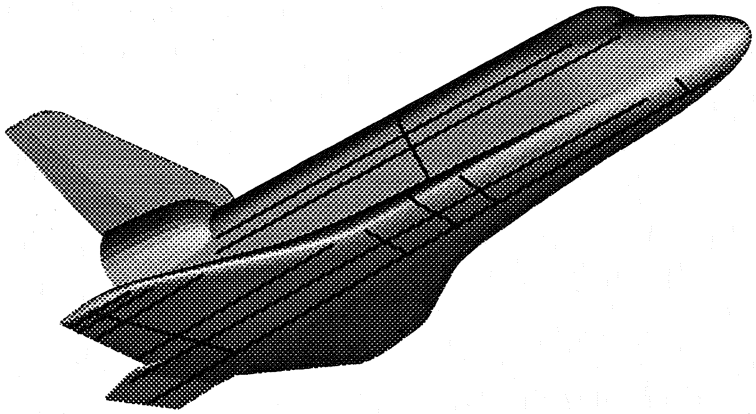

Figure 6: Traces used along the surface to compare with flight thermocouple data.

However, some significant differences in the heating in the nose region are observed for this case and will be discussed in a later section.

RESULTS AND DISCUSSION

Baseline Results

Standard, baseline settings for numerical parameters and options in LAURA are: eigenvalue limiter $\epsilon_0 = 0.30$ with aspect ratio scaling across the boundary layer, upwind limiter function as defined in Ref. [3], cell Reynolds number equal to 3 at the wall, and moderate clustering of grid at the captured shock. The baseline settings for physical model options in LAURA have already been discussed in earlier sections. Laminar flow is specified.

The STS-2 trajectory points were chosen to span a flight regime in which high temperature gas chemistry (equilibrium and nonequilibrium) significantly influence aerodynamic and aerothermal loads on the vehicle and because surface heating data are available. Furthermore, the windside flowfield to the bodyflap is laminar for this regime as deduced from thermocouple data for this flight. Transition does occur on the deflected bodyflap at Mach 18.07 and on the deflected elevons at Mach 12.86. A comprehensive series of comparisons of calculated surface heating with the flight data [8] are presented along the surface traces shown in Figure 6. Figures 7 - 21 present the Mach 24.3 trajectory point comparisons, Figures 22 - 36 present the Mach 18.07 trajectory point comparisons, and Figures 37 - 51 present the Mach 12.86 trajectory point comparisons. The figures for each trajectory point are identically organized. First, longitudinal traces on the windside are presented starting at $y = 0$ inches (centerline) progressing outward to chordwise traces near the wing tip. Lateral and circumferential traces follow starting at a plane located 126 inches behind the nose and concluding along a line situated behind the elevon hinge line. Longitudinal traces

along the leeside centerline and $y = 370$ inches outboard on the wing leeside then follow. (These traces are not visible in the view shown in Figure 6. Also, the thermocouples on the cargo bay door centerline were not operational for this flight.) Finally, longitudinal traces above and below the cargo bay door hinge line are presented. Comparisons are not presented with the thermocouple data on the OMS pods and the tail because the grid was not adequate for boundary layer resolution, as discussed in an earlier section.

The solid lines denote calculated results along the center of the data trace. Because thermocouples do not generally lie along a perfect line, dashed lines denote calculated results three to four inches to the right or left of the center of the trace and encompass the actual location of all thermocouples along the trace. An additional set of lines is presented in the figures showing heating along the elevon hinge line. These lines denote the calculated results along the identical trace extracted from the embedded bodyflap domain. The error bar associated with the flight data, taken from Ref. [8], is a root sum square of uncertainties in the measurement. All thermocouples were calibrated before the STS-1 flight and never checked again.

Rather than stepping through each individual figure, some general observations follow below.

The baseline model overpredicts heating over much of the windside centerline trace at Mach 24.3 by approximately 15%. A different model for wall catalysis, discussed in a later section, improves agreement to approximately 7%. Agreement using the baseline model along this same trace is excellent at Mach 18.07 and within 8% at Mach 12.86. The heating rise on the deflected body flap at Mach 24.3, beginning at $z = -1300$ inches, has the correct magnitude, but precedes the rise indicated by the flight data. Such behavior could be explained by underpredicting the extent of separation; however, a grid refinement study (see later section) showed no change in the onset of the heating rise. The hinge-line area is modeled without any gaps or surface discontinuities and the possible effect of real geometry on this behavior is unknown. Transitional flow is evident from the time history of the thermocouple data on the bodyflap at the other trajectory points in this study.

The other streamwise traces over the windside at Mach 24.3 are in very good agreement with the flight data, with average differences less than 10%. Streamwise traces out on the wing at Mach 18.07 show somewhat larger average differences. At Mach 12.86, these same comparisons improve again, except for thermocouples on the deflected elevons, which measure transitional flow as indicated by the time history of the thermocouple data.

The experimental data in Figures 23 and 38 at $z = -255$ inches and $z = -641$ inches diverge from the baseline prediction and the trend suggested by other experimental data points at Mach 18.07 and Mach 12.86. These same data points are in good agreement with the baseline prediction at Mach 24.3. In like manner, windside circumferential calculations at $z = -641$ inches in Figure 15 are in good agreement with the data at Mach 24.3 but differ by as much as 40% in Figures 30 and 45 for the two later trajectory points at the outboard locations. Yet the windside circumferential data immediately preceding at $z = -520$ inches and following at $z = -768$ inches are in good agreement with the baseline calculation at all three trajectory points. These inconsistencies suggest a calibration problem, but it is unlikely that this issue can be resolved until a grid refinement in all coordinate directions yielding a grid converged solution can be obtained.

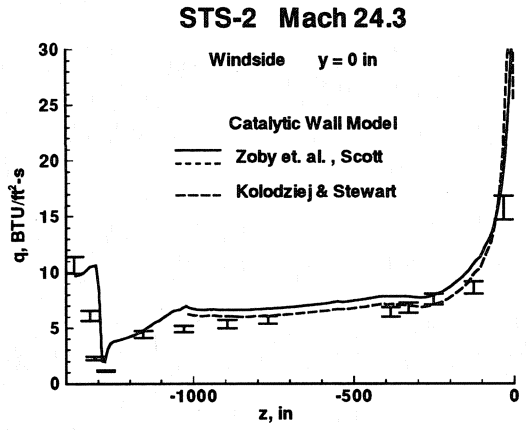

Figure 7: Heating distribution along the windside surface at y = 0 inches (centerline) for the STS-2 trajectory point at Mach 24.3.

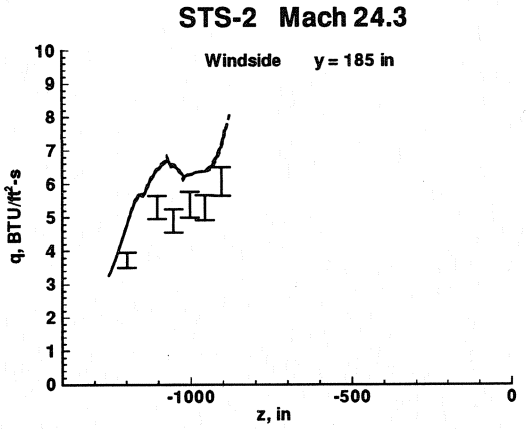

Figure 9: Heating distribution along the windside surface at y = 185 inches for the STS-2 trajectory point at Mach 24.3.

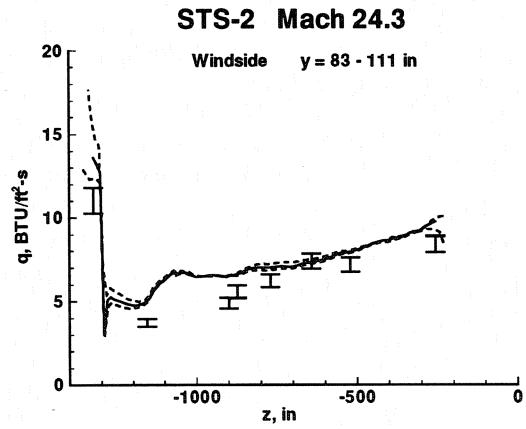

Figure 8: Heating distribution along the windside surface between y = 83 inches and y = 111 inches for the STS-2 trajectory point at Mach 24.3.

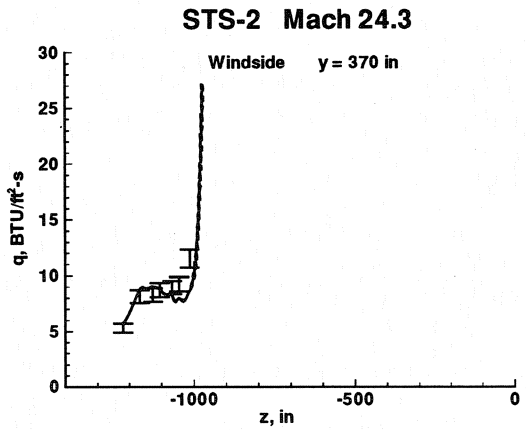

Figure 10: Heating distribution along the windside surface at y = 370 inches for the STS-2 trajectory point at Mach 24.3.

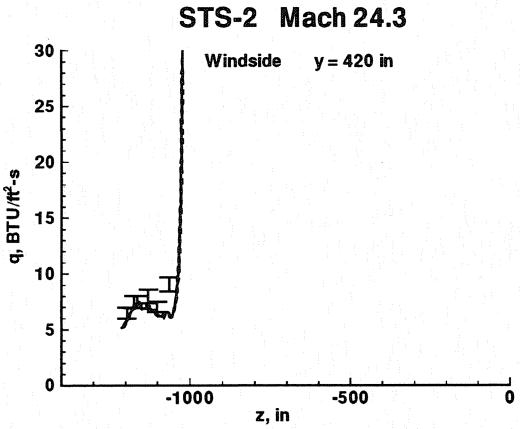

Figure 11: Heating distribution along the windside surface at y = 420 inches for the STS-2 trajectory point at Mach 24.3.

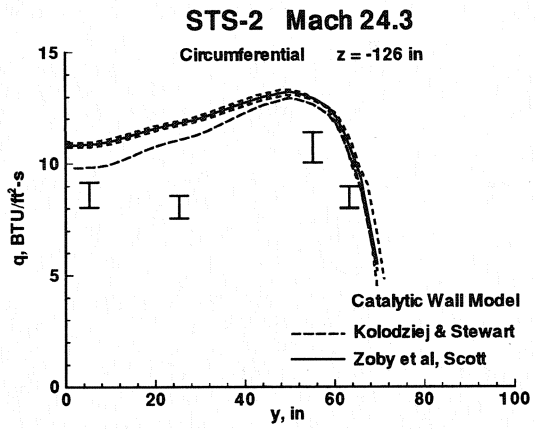

Figure 13: Circumferential heating distribution for the STS-2 trajectory point at Mach 24.3 taken 126 inches behind the nose.

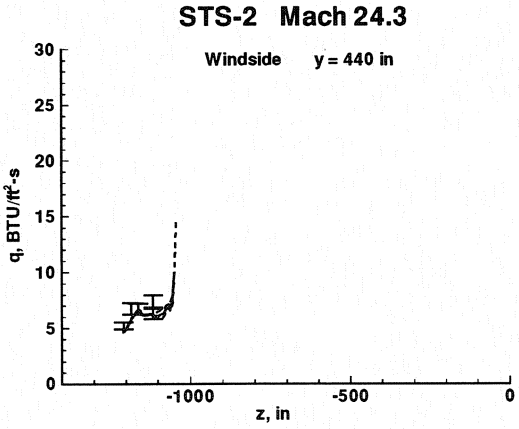

Figure 12: Heating distribution along the windside surface at y = 440 inches for the STS-2 trajectory point at Mach 24.3.

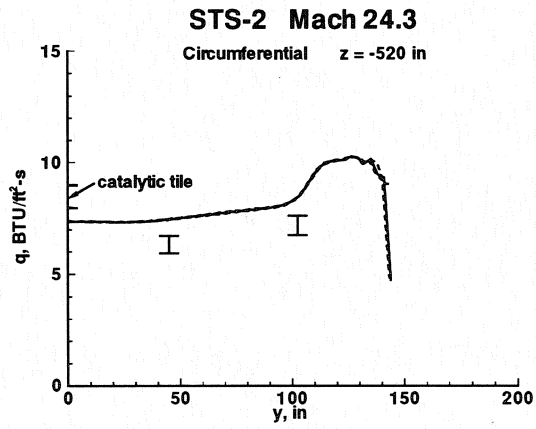

Figure 14: Circumferential heating distribution for the STS-2 trajectory point at Mach 24.3 taken 520 inches behind the nose.

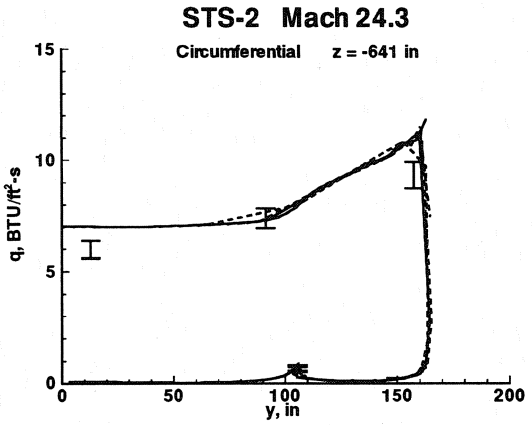

Figure 15: Circumferential heating distribution for the STS-2 trajectory point at Mach 24.3 taken 641 inches behind the nose.

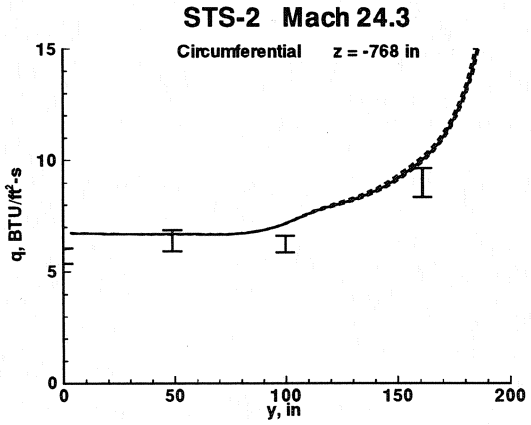

Figure 16: Circumferential heating distribution for the STS-2 trajectory point at Mach 24.3 taken 768 inches behind the nose.

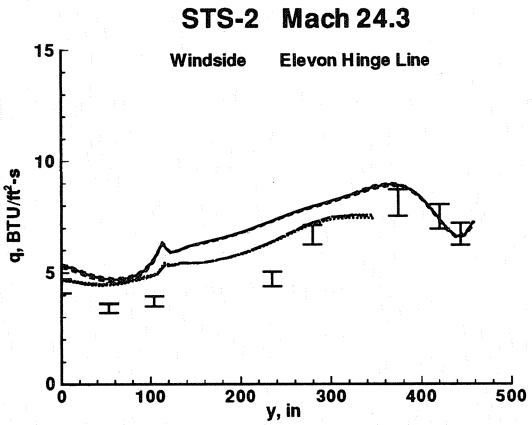

Figure 17: Heating distribution along the windside surface from the centerline to the wingtip behind the elevon hinge line for the STS-2 trajectory point at Mach 24.3. The long dash and dotted lines are extracted from the embedded bodyflap domain.

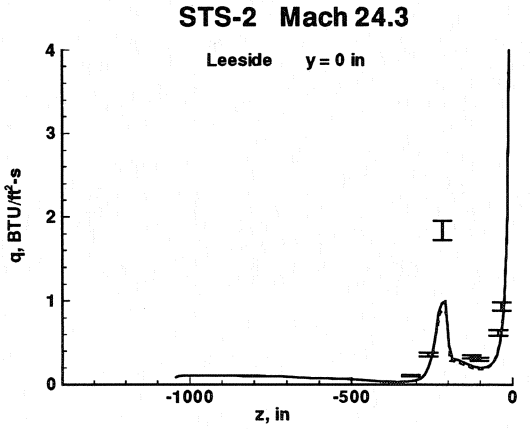

Figure 18: Heating distribution along the leeside surface at y = 0 inches (centerline)for the STS-2 trajectory point at Mach 24.3.

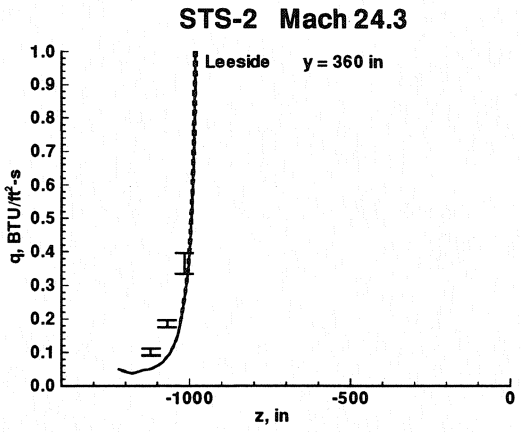

Figure 19: Heating distribution along the leeside wing surface at y = 360 inches for the STS-2 trajectory point at Mach 24.3.

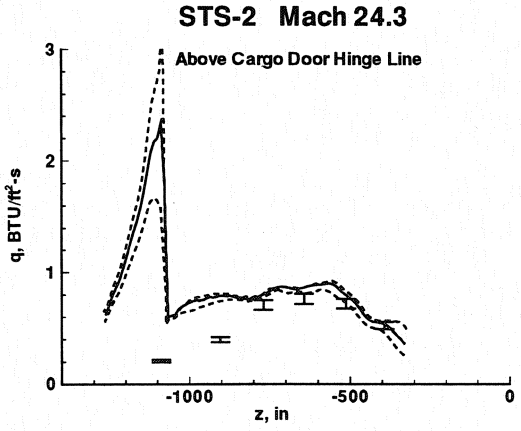

Figure 20: Heating distribution along the fuselage above the cargo door hinge line for the STS-2 trajectory point at Mach 24.3.

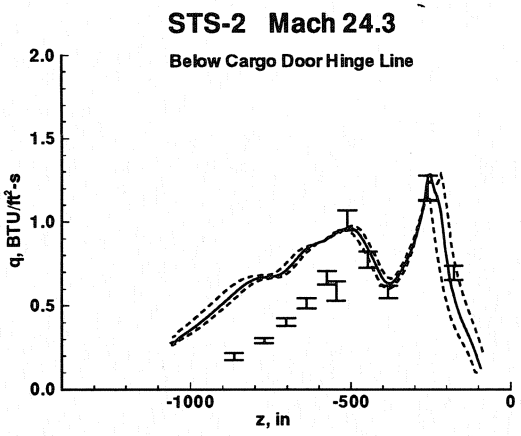

Figure 21: Heating distribution along the fuselage below the cargo door hinge line for the STS-2 trajectory point at Mach 24.3.

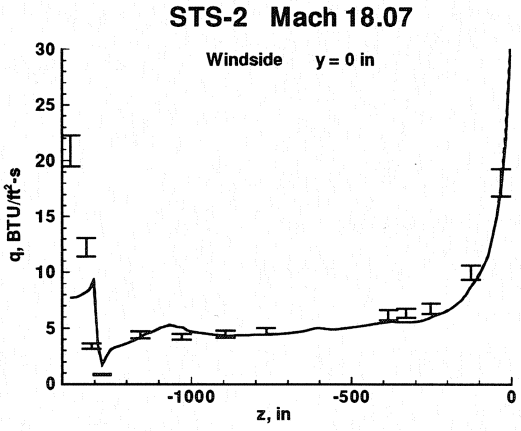

Figure 22: Heating distribution along the windside surface at y = 0 inches (centerline) for the STS-2 trajectory point at Mach 18.07.

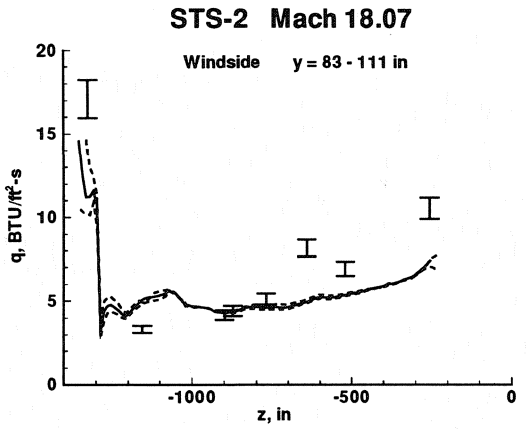

Figure 23: Heating distribution along the windside surface between y = 83 inches and y = 111 inches for the STS-2 trajectory point at Mach 18.07.

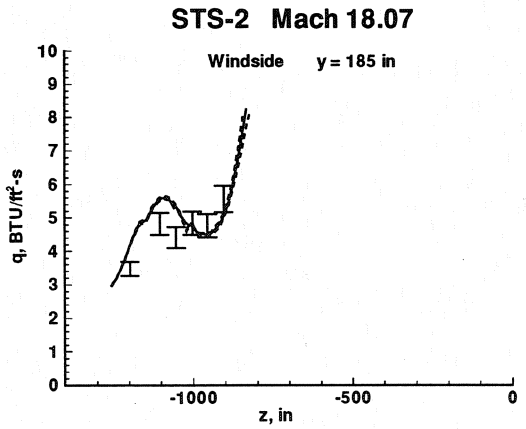

Figure 24: Heating distribution along the windside surface at y = 185 inches for the STS-2 trajectory point at Mach 18.07.

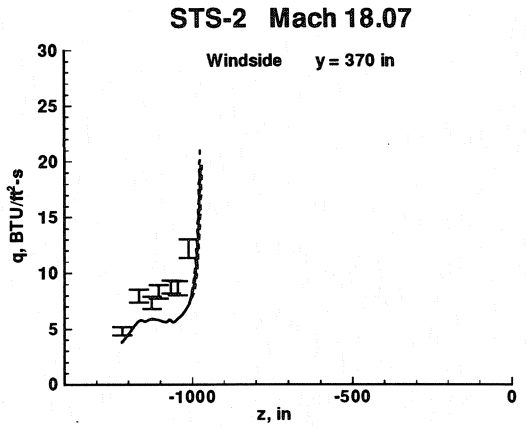

Figure 25: Heating distribution along the windside surface at y = 370 inches for the STS-2 trajectory point at Mach 18.07.

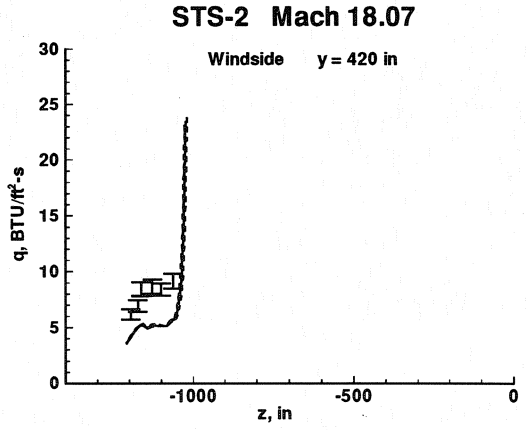

Figure 26: Heating distribution along the windside surface at y = 420 inches for the STS-2 trajectory point at Mach 18.07.

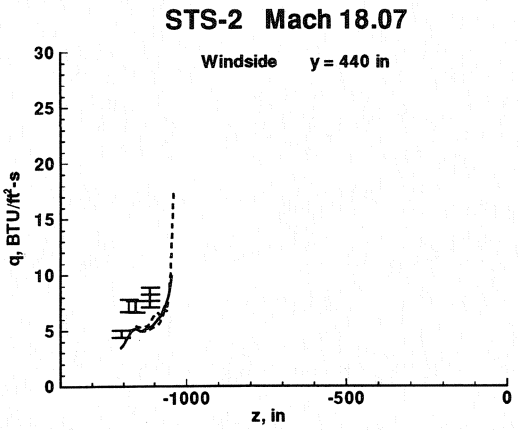

Figure 27: Heating distribution along the windside surface at y = 440 inches for the STS-2 trajectory point at Mach 18.07.

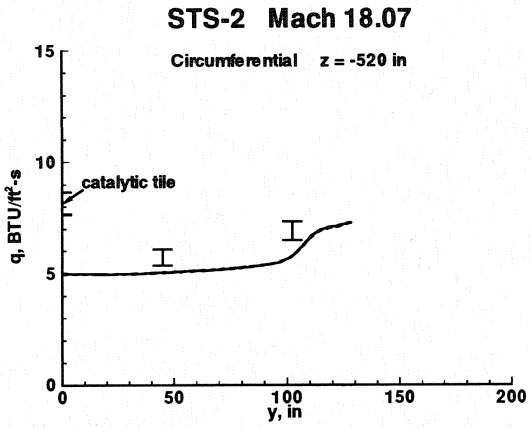

Figure 29: Circumferential heating distribution for the STS-2 trajectory point at Mach 18.07 taken 520 inches behind the nose.

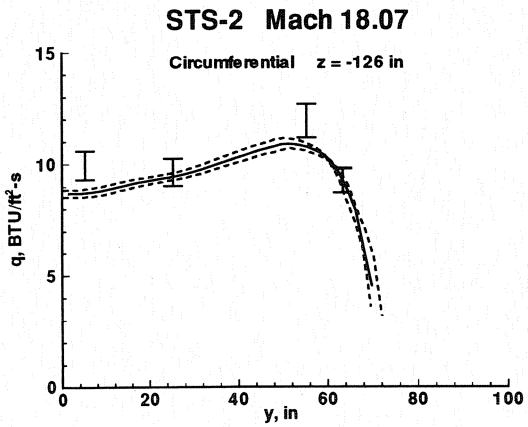

Figure 28: Circumferential heating distribution for the STS-2 trajectory point at Mach 18.07 taken 126 inches behind the nose.

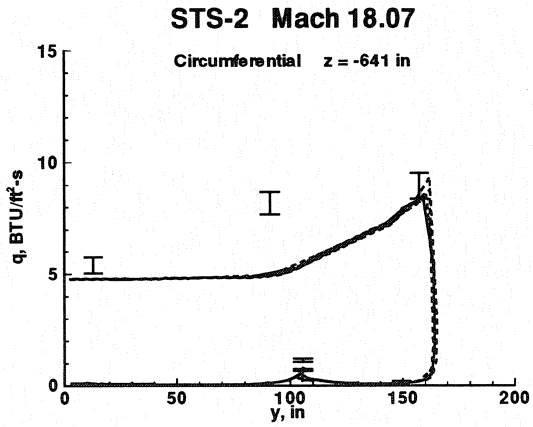

Figure 30: Circumferential heating distribution for the STS-2 trajectory point at Mach 18.07 taken 641 inches behind the nose.

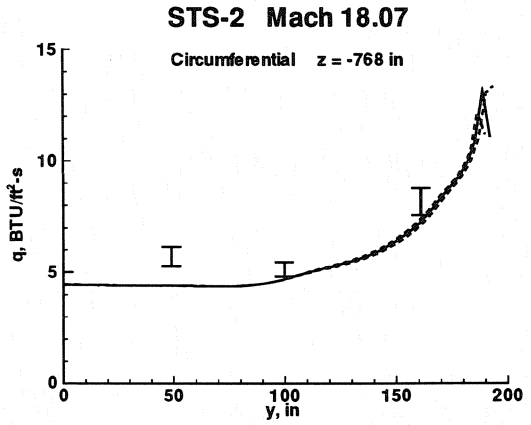

Figure 31: Circumferential heating distribution for the STS-2 trajectory point at Mach 18.07 taken 768 inches behind the nose.

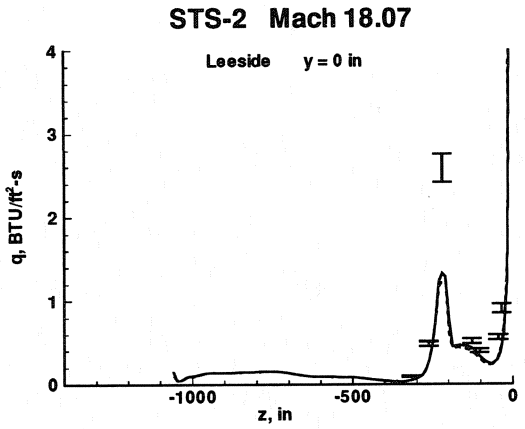

Figure 33: Heating distribution along the leeside surface at y = 0 inches (centerline)for the STS-2 trajectory point at Mach 18.07.

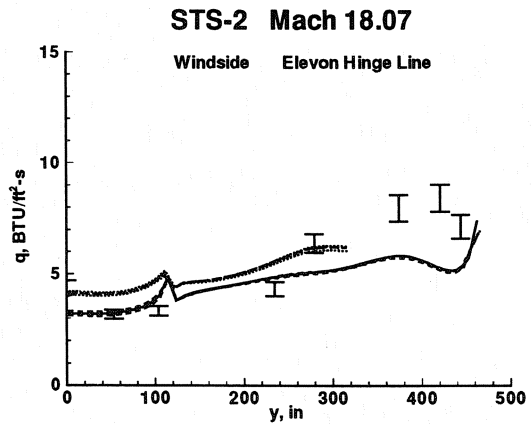

Figure 32: Heating distribution along the windside surface from the centerline to the wingtip behind the elevon hinge line for the STS-2 trajectory point at Mach 18.07. The long dash and dotted lines are extracted from the embedded bodyflap domain.

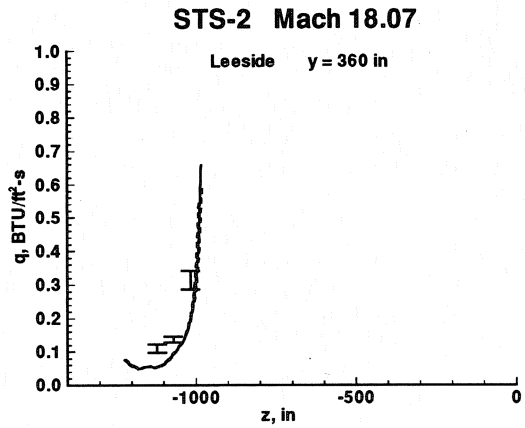

Figure 34: Heating distribution along the leeside wing surface at y = 360 inches for the STS-2 trajectory point at Mach 18.07.

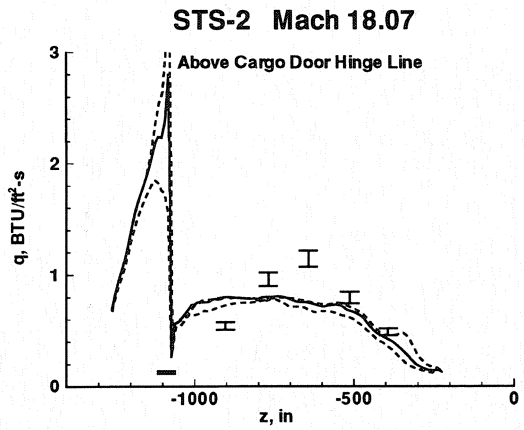

Figure 35: Heating distribution along the fuselage above the cargo door hinge line for the STS-2 trajectory point at Mach 18.07.

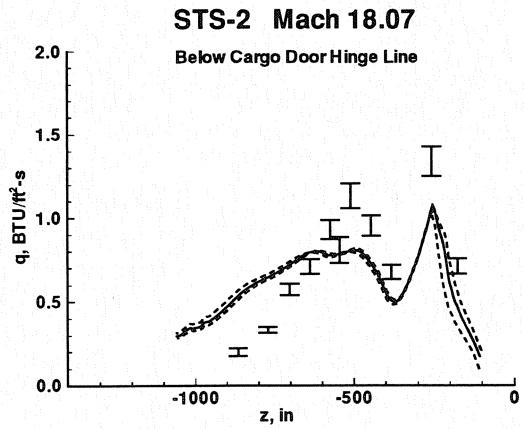

Figure 36: Heating distribution along the fuselage below the cargo door hinge line for the STS-2 trajectory point at Mach 18.07.

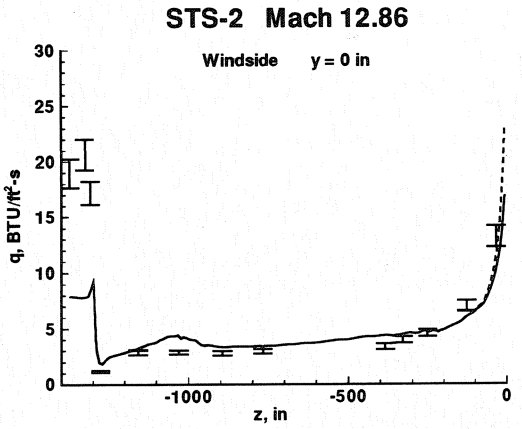

Figure 37: Heating distribution along the windside surface at y = 0 inches (centerline) for the STS-2 trajectory point at Mach 12.86.

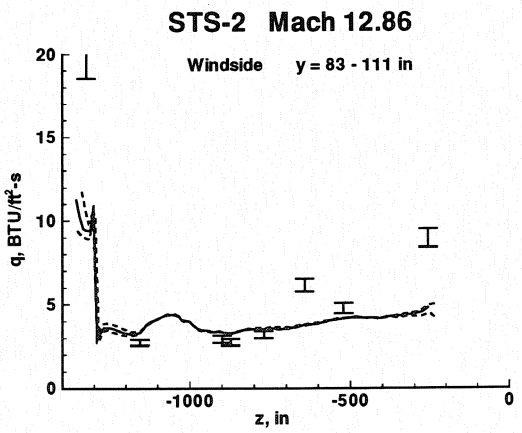

Figure 38: Heating distribution along the windside surface between y = 83 inches and y = 111 inches for the STS-2 trajectory point at Mach 12.86.

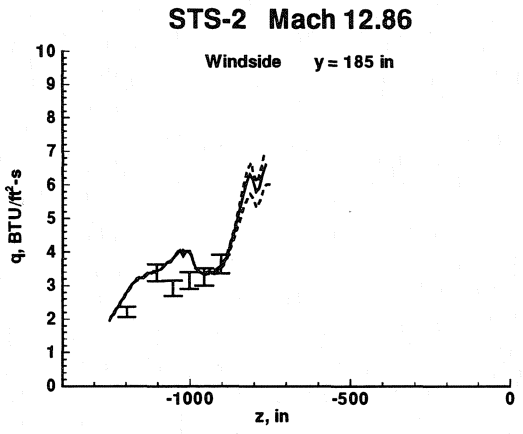

Figure 39: Heating distribution along the windside surface at y = 185 inches for the STS-2 trajectory point at Mach 12.86.

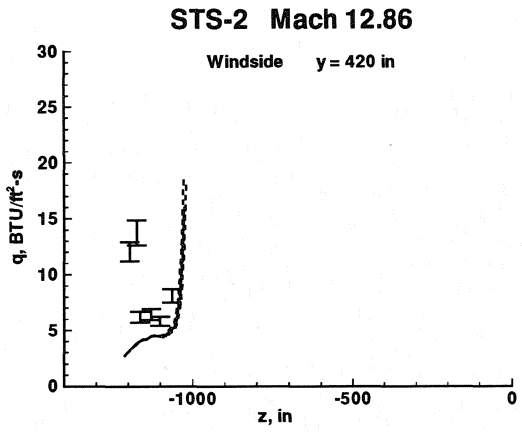

Figure 41: Heating distribution along the windside surface at y = 420 inches for the STS-2 trajectory point at Mach 12.86.

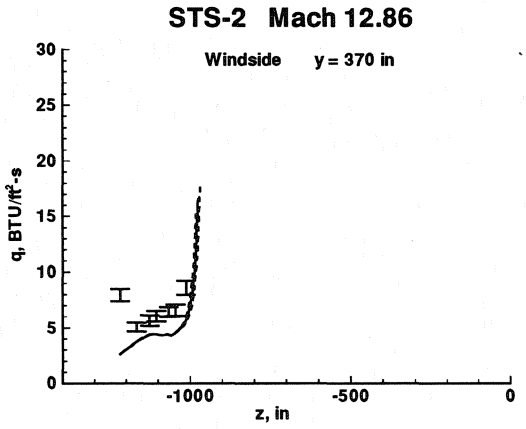

Figure 40: Heating distribution along the windside surface at y = 370 inches for the STS-2 trajectory point at Mach 12.86.

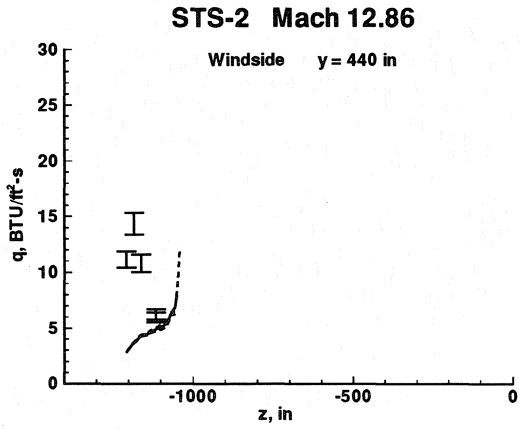

Figure 42: Heating distribution along the windside surface at y = 440 inches for the STS-2 trajectory point at Mach 12.86.

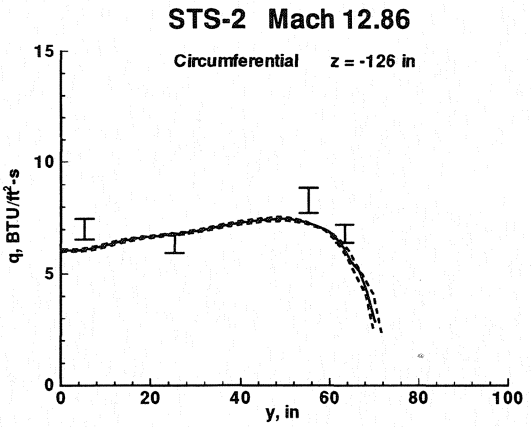

Figure 43: Circumferential heating distribution for the STS-2 trajectory point at Mach 12.86 taken 126 inches behind the nose.

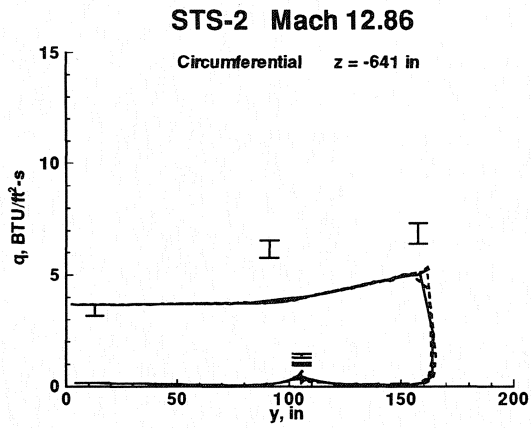

Figure 45: Circumferential heating distribution for the STS-2 trajectory point at Mach 12.86 taken 641 inches behind the nose.

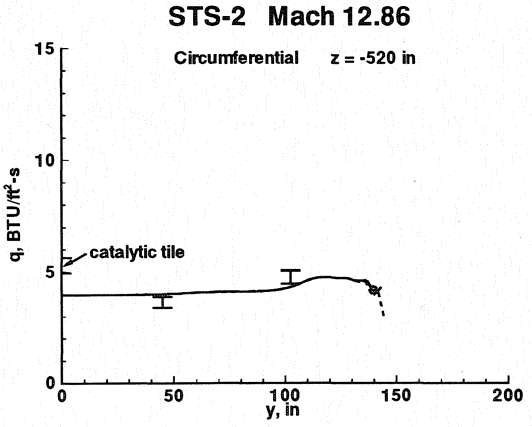

Figure 44: Circumferential heating distribution for the STS-2 trajectory point at Mach 12.86 taken 520 inches behind the nose.

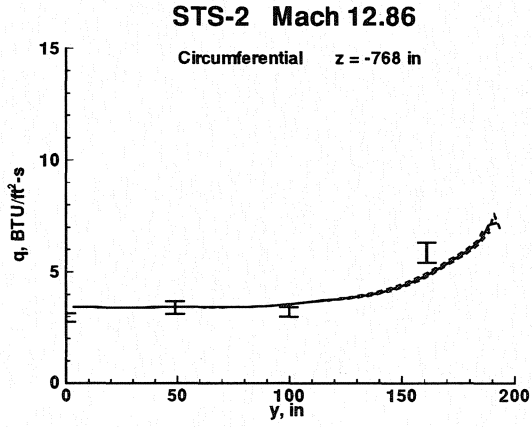

Figure 46: Circumferential heating distribution for the STS-2 trajectory point at Mach 12.86 taken 768 inches behind the nose.

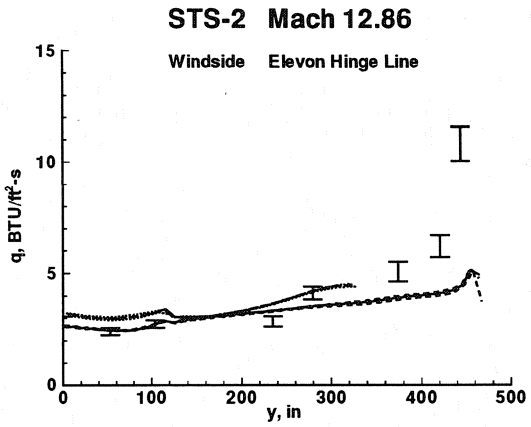

Figure 47: Heating distribution along the windside surface from the centerline to the wingtip behind the elevon hinge line for the STS-2 trajectory point at Mach 12.86. The long dash and dotted lines are extracted from the embedded bodyflap domain.

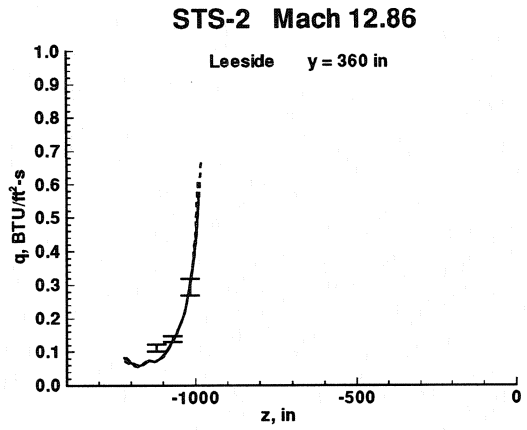

Figure 49: Heating distribution along the leeside wing surface at y = 360 inches for the STS-2 trajectory point at Mach 12.86.

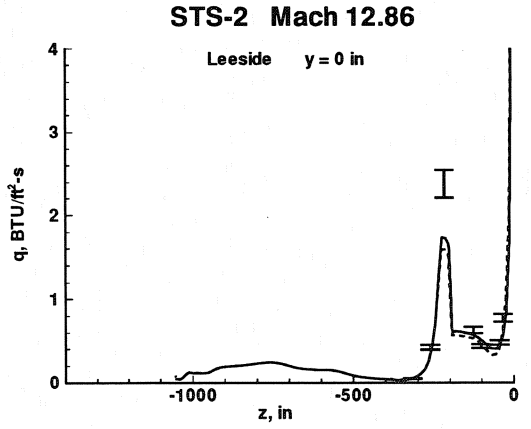

Figure 48: Heating distribution along the leeside surface at y = 0 inches (centerline)for the STS-2 trajectory point at Mach 12.86.

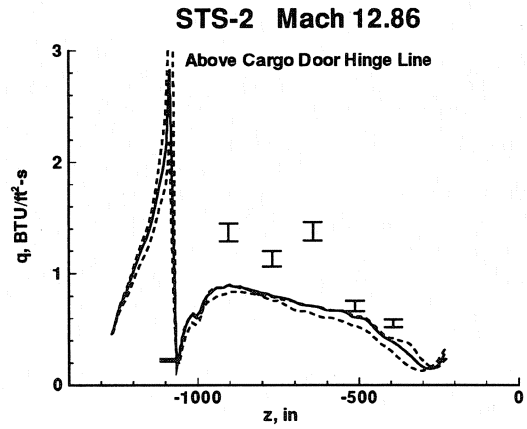

Figure 50: Heating distribution along the fuselage above the cargo door hinge line for the STS-2 trajectory point at Mach 12.86.

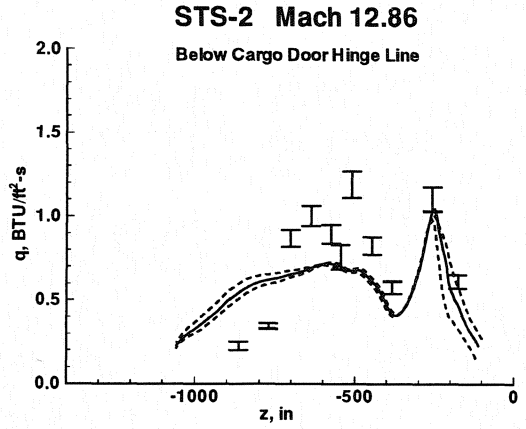

Figure 51: Heating distribution along the fuselage below the cargo door hinge line for the STS-2 trajectory point at Mach 12.86.

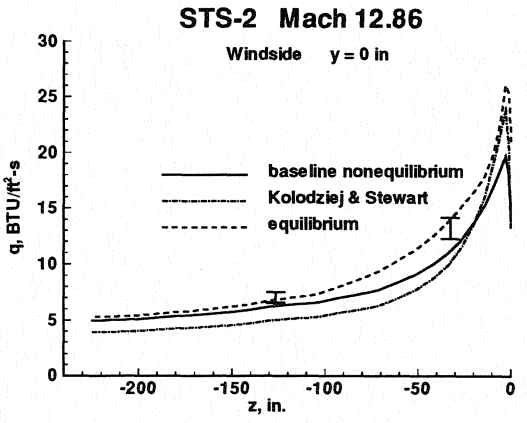

Figure 52: Heating distribution along the windside centerline near the nose at Mach 12.86 using an equilibrium and chemical nonequilibrium gas models.

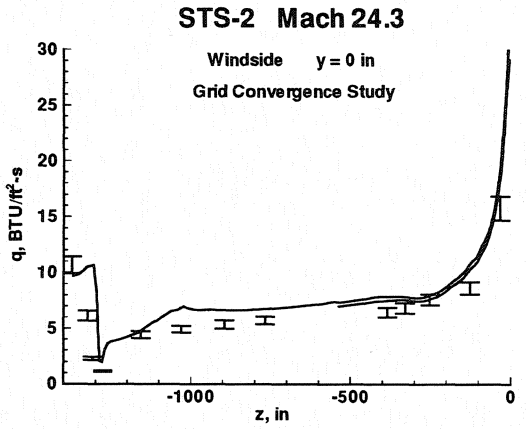

Figure 53: Heating distributions with 60 and 120 cells across the shock layer (first 500 inches) along the windside surface at y = 0 inches (centerline) at Mach 24.3.

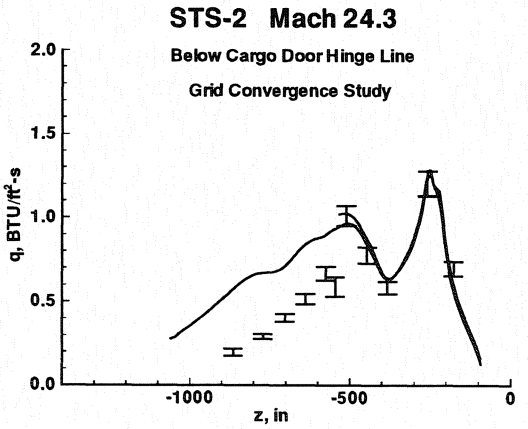

Figure 54: Heating distributions with 60 and 120 cells across the shock layer (first 500 inches) below the cargo door hinge line at Mach 24.3.

Baseline circumferential heating predictions at $z = -126$ inches at Mach 24.3 exceed the flight data by 20% to 30% as shown in Figure 13. Some improvement is noted with another wall catalytic model, to be discussed in a later section. Calculations at subsequent points in the trajectory are in excellent agreement with flight data along this same cut.

The embedded bodyflap solution, as shown Figures 17, 32, and 47, shows differences as large as 20% compared to the bodyflap free solution behind the elevon hinge line. The differences diminish at lower Mach numbers. The calculated solutions were expected to be closer together, showing little influence of the deflected bodyflap so far upstream, well beyond the boundary-layer separation point. The evaluation of the limiter function is somewhat altered at the inflow and side boundaries, which may have had a larger than expected influence on heating levels in the embedded domain. Also, the embedded domain partitions were converged to a smaller error norm (order 10^{-7}) than the full body solution because the bodyflap flowfield took longer to converge. Inboard data points are generally in good agreement with the calculations at Mach 18.07 and 12.86, with outboard locations measuring transitional effects at Mach 12.86.

Leeside centerline heating calculations are in good agreement with experimental data across the Mach number range (Figures 18, 33, 48), except for an underprediction on the center post between the windows of the canopy. A rather coarse circumferential resolution of the canopy is a suspected cause of this underprediction. The slow rise in heating levels over the cargo door is consistent with trends exhibited on later flights in which additional thermocouple data was available, and represents an improvement to some earlier calculations in a related study reported in Reference [4]. Wing leeside predictions (Figures 19, 34, 49) are in good agreement with the flight data across the Mach number range studied.

Baseline calculations are in good agreement with the flight data across the Mach number range for the first 400 inches along the data traces above and below the cargo door hinge line. Good agreement persists longer for higher Mach numbers. A second, local peak is smoothed out at the lower Mach numbers and predictions then exceed the measured data for the trace below the cargo door hinge line. A possible contributor to these differences is a grid alignment problem, discussed in a later section. Also, the validity of a radiative equilibrium wall-boundary condition is questionable at these low, leeside heating levels.

Finite-Catalytic-Wall Study

Surface heating using the finite-catalytic-wall model of Kolodziej and Stewart [13] is compared to results using the baseline model of Zoby et al [11] at Mach 24.3. Figure 7 makes the comparison along the windside centerline. Figure 13 makes the comparison in a circumferential direction on a windside plane 126 inches behind the nose. The Kolodziej and Stewart model is derived from experimental data at wall temperatures greater than actually encountered on much of the windside ($T_{wall} > 1250$ K). The baseline model is derived from viscous shock-layer computations of the windside shuttle flow, and is of questionable validity at wall temperatures greater than 1200 K. The Kolodziej and Stewart model predicts stronger catalytic effects for oxygen recombination than the baseline model at temperatures greater than ≈ 1300 K. The baseline model is more catalytic below these temperatures. The relative heating levels predicted by the two models are consistent with this crossover point. Differences between the two models, particularly in the stagnation region, are exacerbated due to the differences in the radiative equilibrium wall temperatures The present

results indicate a slight improvement of the comparison to flight data using the Kolodziej and Stewart model on the centerline and circumferential plots.

Equilibrium Flow Study

A comparison of an equilibrium prediction for windside centerline heating at Mach 12.86 with the nonequilibrium baseline model and the flight data is presented in Figure 52. Large differences are evident in the stagnation region, near $z = 0$ inches, due mostly to the finite catalytic wall boundary condition. Wall temperatures also differ here because of the radiative equilibrium wall boundary condition on temperature. The baseline nonequilibrium prediction asymptotes to the equilibrium value at approximately 400 inches behind the nose. (Only the first 220 inches are shown to highlight the region where the greatest differences exist.) At this same condition, the finite-catalytic-wall model of Kolodziej and Stewart (discussed previously) still shows nonequilibrium effects across the entire windside centerline (not shown). At these wall temperatures (approximately 1000 K), the baseline catalytic wall model calls for recombination rates a factor of 10 greater than the extrapolated model of Kolodziej and Stewart.

Grid Convergence Study and Error Estimates

As noted earlier, the grid distribution function and number of cells in the normal direction are based on grid convergence studies in References [3, 9]. These earlier studies, which focused on centerline and stagnation point heating, indicate that the present results should be within approximately 8% of a grid converged solution (based strictly on normal grid convergence studies). There is no numerical evidence to suggest this estimate is valid for the flow downstream of the bow-shock - wing-shock interaction region in the present case.

Resource limitations precluded a full, global grid convergence test. An isolated test confined to the nose region (Figures 53 and 54) for the Mach 24.3 case is well within the 8% error discussed earlier. In this case, the cell Reynolds number of the doubled grid case was equal to 3.0, as in the baseline case, but twice the number of points allowed improved resolution of the boundary layer and shock layer - resulting in a smaller maximum cell growth factor. (Large cell growth factors in LAURA tend to increase surface heating with all other factors equal as discussed in Ref. [9].)

Though not presented in the figures, streamwise doubling of the grid on the bodyflap with appropriate clustering at the hinge line was performed on selected bodyflap solutions. Some sharpening of the overpressure and heating on the deflected flap associated with the oblique shock impingement emanating from the boundary-layer separation point upstream of the flow is observed as compared to the baseline solution. The onset of separation occurred approximately 3 inches earlier, in the Mach 18.07 test case, with distance from separation to reattachment points extending approximately 21 inches. Maximum thickness of the separation bubble above the hinge line is approximately 2 inches. The effect of a gap in the hinge line is not accounted for here. Net effects on aerodynamic coefficients were trivially small.

Baseline results on the side of the fuselage (Figure 54) indicate that some aspect of the vortex scrubbing past 500 inches may have been smeared based on comparisons with the flight data. The

smearing may indicate not so much a lack of circumferential resolution as a grid which is poorly aligned with the vortical flow on the leeside. Grid adaption to local flow phenomena with a tool such as SAGE [20] is probably warranted in this instance, but has not yet been tested.

CONCLUDING REMARKS

A multiblock, laminar heating analysis using Program LAURA for the shuttle orbiter at three trajectory points for STS-2 ranging from Mach 24.3 to Mach 12.86 on re-entry is described. This approach enables the calculation of aerothermal loads across a realistic, winged body with approximately one million grid points without inordinate demands on computational resources. The correct elevon and bodyflap deflections are included for each trajectory point. The multiblock relaxation strategy partitions the flowfield into manageable blocks with appropriate boundary conditions requiring a fraction of the computational resources (time and memory) required by a full domain approach. Converged blocks are eventually reassembled to enable a fully coupled converged solution over the entire vehicle, starting from a nearly converged initial condition.

The baseline gas model for air assumes chemical nonequilibrium with seven species and thermal equilibrium. A finite-catalytic-wall model appropriate for shuttle tiles at a radiative equilibrium wall temperature is applied. Additional tests at selected points involve thermal nonequilibrium models, chemical equilibrium models, and variations on the gas kinetic model and catalytic wall model. Gas kinetic model variations made little difference on aerodynamics and heating, except in the vicinity of the wing leading edge. Average differences in calculated heating levels between the two wall catalysis models studied were approximately 10%, where differences in the wall temperatures associated with the radiative equilibrium wall boundary condition magnify this effect. At the lowest altitude studied, the Mach 12.86 nonequilibrium baseline calculation of windside centerline heating approached the equilibrium values, whereas another, less catalytic wall model remained at least 10% below the equilibrium levels. The present results are expected to be within 8% of grid converged values in the stagnation region and windside centerline. Grid related errors should be larger downstream of the bow-shock wing-shock interaction and associated with the leeside vortical flow but have not been quantified in this work.

Comprehensive comparisons to flight data along 15 linear cuts on the windside and leeside surfaces and three trajectory points are presented. Computed heating levels are generally in good agreement with the flight data and lie within the estimated experimental and numerical error bands, though a few rather large discrepancies remain unexplained. The present results have demonstrated that hypersonic, laminar flow simulations over the Space Shuttle, including appropriate physical models for gas chemistry and wall catalysis, can be achieved on available supercomputers in a multi-user environment. Furthermore, the results are achieved on grids with sufficient resolution to provide credible predictions based on both comparisons to existing flight data and on grid convergence tests of related, smaller problems. Even with the present uncertainties (which can be reduced further but never eliminated), it is believed that current CFD tools provide important benchmarking capabilities. We believe that these tools provide the most accurate ground-based predictions for aerothermal loads across this flight regime. When used in conjunction with available engineering design codes, experimental facilities, and flight tests, a system of checks becomes available that must not be ignored in the design of future elements of our space transportation system.

REFERENCES

[1] Häuser, J.; Muylaert, J.; Wong, H.; and Spel M.: "Aerothermodynamic Calculations for the Space Shuttle Orbiter,"AIAA 92-2953, July 1992.

[2] Wada, Yasuhiro; and Kubota, Hirotoshi: "Numerical Simulation of Re-Entry Flow around the Space Shuttle with Finite-Rate Chemistry," International Symposium on Space Technology and Science, Tokyo, May 20-25, 1990.

[3] Weilmuenster, K. James; and Gnoffo, Peter A.: "Solution Strategies and Heat Transfer Calculations for Three-Dimensional Configurations at Hypersonic Speeds," AIAA 92-2921, July, 1992.

[4] Kleb, W. L.; and Weilmuenster, K. James: "Characteristics of the Shuttle Orbiter Leeside Flow During a Reentry Condition," AIAA 92-2951, July, 1992.

[5] Weilmuenster, K. James; Gnoffo, Peter A.; and Greene, Francis A.: "Navier-Stokes Simulations of the Shuttle Orbiter Aerodynamic Characteristics with Emphasis on Pitch Trim and Body Flap," AIAA 93-2814, July, 1993.

[6] Gnoffo, Peter A.; Gupta, Roop N.; and Shinn, Judy: "Conservation Equations and Physical Models for Hypersonic Air Flows in Thermal and Chemical Nonequilibrium," NASA TP 2867, February 1989.

[7] Gnoffo, Peter A., "Point-Implicit Relaxation Strategies for Viscous, Hypersonic Flows," in Computational Methods in Hypersonic Aerodynamics, T.K.S. Murthy, ed., Computational Mechanics Publications, Kluwer Academic Publishers, pp 115-151, 1991.

[8] Hartung, Lin C. and Throckmorton, David A.: "Space Shuttle Entry Heating Data Book Volume I - STS-2," NASA Reference Publication 1191, Parts 1 and 2, May 1988.

[9] Gnoffo, Peter A.; Hartung, Lin C.; and Greendyke, Robert B.: "Heating Analysis for a Lunar Transfer Vehicle at Near-Equilibrium Flow Conditions," AIAA 93-0270, January 1993.

[10] Gnoffo, Peter A.: "Asynchronous, Macrotasked Relaxation Strategies for the Solution of Viscous, Hypersonic Flows," AIAA-91-1579-CP, June 1991.

[11] Zoby, E. V.; Gupta, R. N.; and Simmonds, A. L.: "Temperature-Dependent Reaction Rate Expressions for Oxygen Recombination," AIAA Progress in Astronautics and Aeronautics: Thermal Design of Aeroassisted Orbital Transfer Vehicles, Volume 96, edited by H. F. Nelson, AIAA, New York, 1985, pp 445-464.

[12] Scott, C. D.: "Catalytic Recombination of Nitrogen and Oxygen on High-Temperature Reusable Surface Insulation," AIAA Progress in Astronautics and Aeronautics: Aerothermodynamics and Planetary Entry, Volume 77, edited by A. L. Crosbie, AIAA, New York, 1981, pp 192-213.

[13] Stewart, David A.; Leiser, Daniel B.; Kolodziej, Paul; and Smith, Marnell: "Thermal Response of Integral Multicomponent Composite Thermal Protection Systems," AIAA-85-1056, June 1985.

[14] Park, Chul: "Nonequilibrium Hypersonic Aerothermodynamics," John Wiley & Sons, Inc, 1990.

[15] Dunn, Michael G.; and Kang, Sang-Wook: "Theoretical and Experimental Studies of Reentry Plasmas," NASA CR-2232, April 1973.

[16] Gupta, Roop N.; Yos, Jerrold M.; Thompson, Richard A.; and Lee, Kam-Pui: "A Review of Reaction Rates and Thermodynamic and Transport Properties for an 11-Species Air Model for Chemical and Thermal Nonequilibrium Calculations to 30 000 K,", NASA Reference Publication 1232, August 1990.

[17] Srinivasan, S.;Tannehill, J. C.; and Weilmuenster, K. J.: "Simplified Curve Fits for the Thermodynamic Properties of Equilibrium Air," NASA RP-1181, August 1987.

[18] Gupta, R. N.;Lee, K. P.; Thompson, R. A.; and Yos, J. M.: "Calculations and Curve Fits of Thermodynamic and Transport Properties for Equilibrium Air to 30 000 K," NASA RP-1260, Oct. 1991.

[19] Greene, F. A. and Gupta, R. N.: "Viscous Equilibrium Computations Using Program LAURA," Journal of Spacecraft and Rockets, Vol. 29, No. 5, Sept.-Oct. 1992, pp 627-632.

[20] Davies, C. and Venkatapathy, E.: "Application of a Solution Adaptive Grid Scheme, SAGE, to Complex Three-Dimensional Flows," AIAA Paper 91-1594, June 1991.

ASSESSMENT OF STATE-OF-THE-ART AERODYNAMIC PREDICTION METHODOLOGY IN LIGHT OF THE SHUTTLE EXPERIENCE

Charles G. Miller III
NASA Langley Research Center
Hampton, VA

A written version of this paper was not provided by the author.
Copies of presentation materials used at the Symposium are presented herein.

PREFACE

- Assessment (synonymous with estimate) subjective
- Will address future aerodynamic information sources (Triad) for design of next generation aerospace vehicle
- Will NOT address programmatic issues; e.g.:
    - Bureaucracy, in general
    - Special interests
    - Politically correct (e.g., agreements with foreign countries)
    - Schedules (time and money)
    - Acquisition challenges
    - Data management and classification (technology transfer)
    - Environmental impacts
    - Government-industry interfaces
    - so forth
- Assessment pertains only to aerodynamics
    - For ascent to orbit, descent, landing (subsonic to hypersonic)
    - Some issues may be applicable to aerothermodynamics
- Any perceived criticism of highly successful development/determination of shuttle orbiter aerodynamic characteristics unintentional
    - Success of orbiter from aerodynamic perspective testimony to validity of approach used to generate aerodynamic information
        - Successes dramatically outweigh "misses" (so-called lessons learned):
            - Hypersonic pitch-up
            - RCS interaction
            - Rocket exhaust plume interactions

SOURCES OF AERODYNAMIC INFORMATION FOR DESIGN OF AEROSPACE VEHICLES

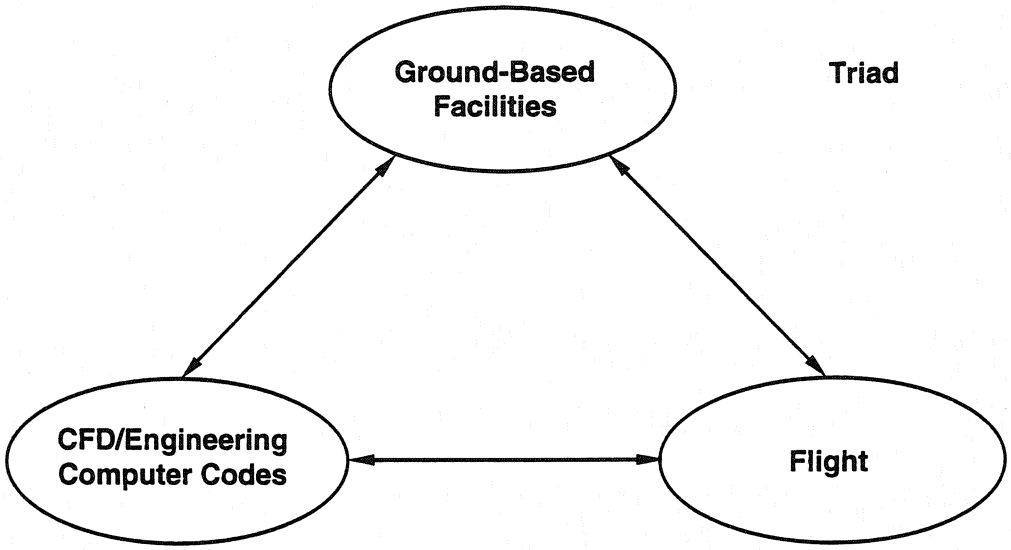

Aerodynamic information → forces and moments; pressure distributions

CONTRIBUTION TO DEVELOPMENT/ESTABLISHMENT OF SHUTTLE ORBITER AERODYNAMICS: A PERCEPTION

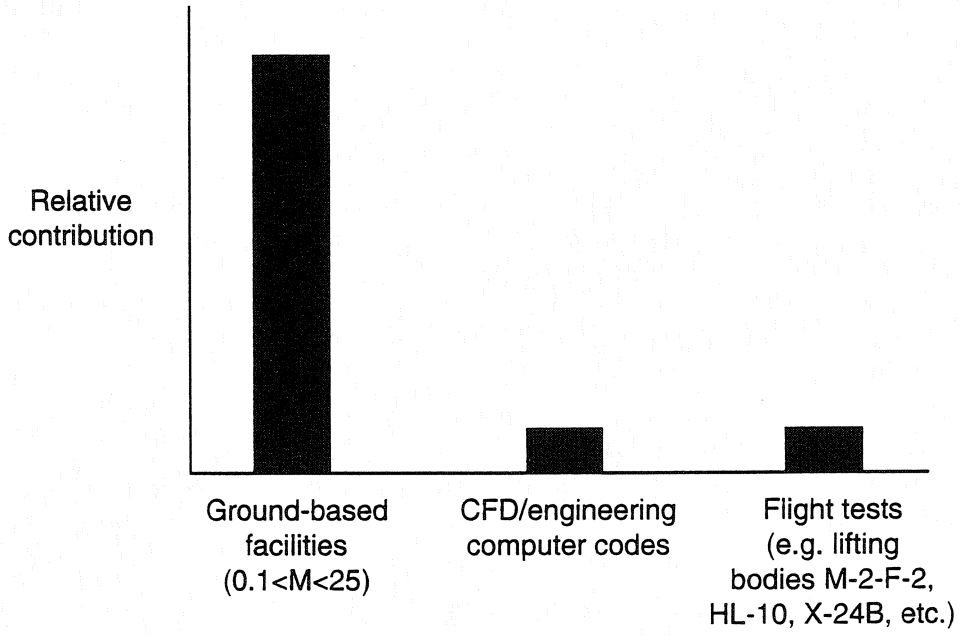

RELATIVE INTEREST IN SUBSONICS/TRANSONICS AND HYPERSONICS SINCE 1950's

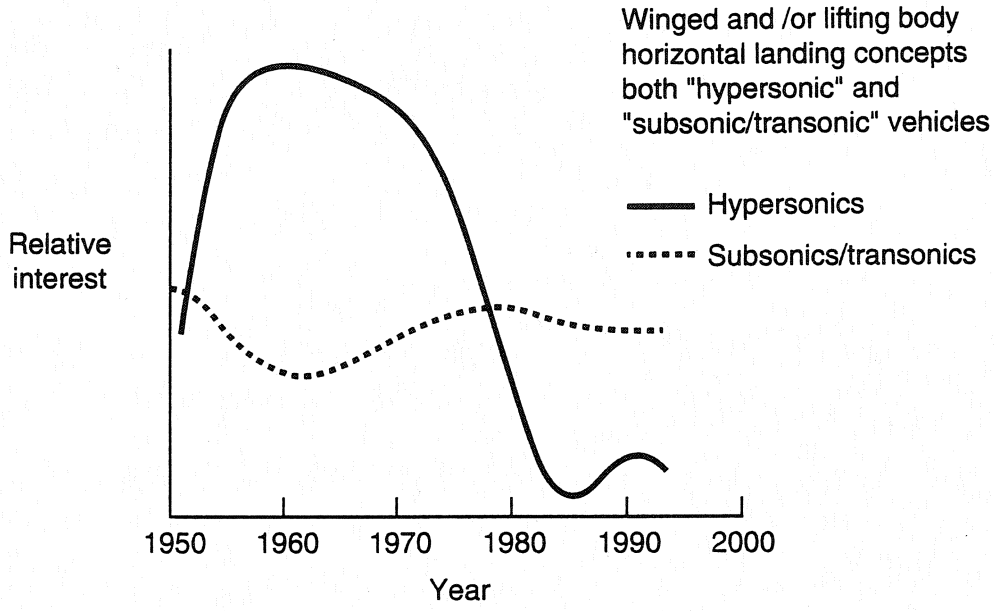

AERODYNAMIC GROUND-BASED TESTING CAPABILITY FOR NEXT GENERATION AEROSPACE VEHICLE: BETTER/WORSE THAN FOR SHUTTLE ORBITER?

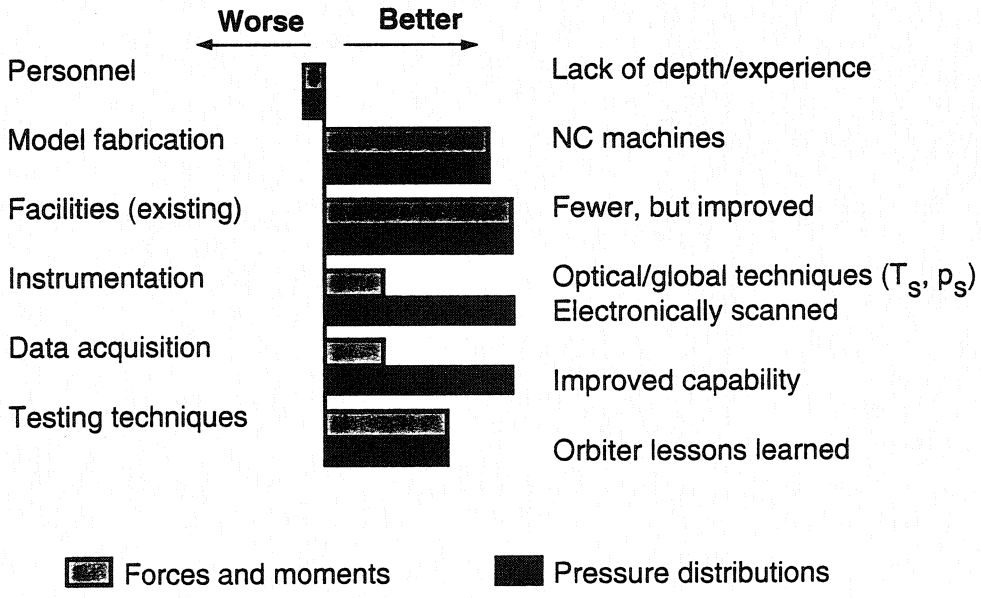

AERODYNAMIC PREDICTIVE CAPABILITY VIA CFD/ENGINEERING COMPUTER CODES FOR NEXT GENERATION AEROSPACE VEHICLE: BETTER/WORSE THAN FOR SHUTTLE ORBITER?

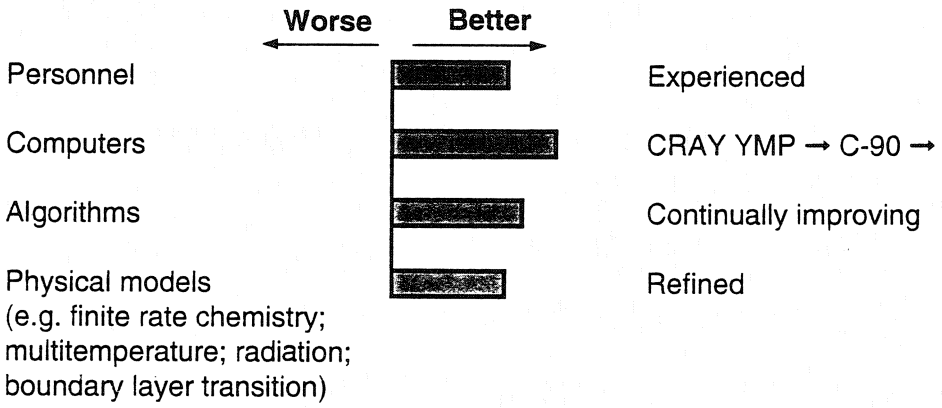

Includes codes for continuum and noncontinuum (e.g. DSMC) flows

DETERMINATION OF AERODYNAMIC CHARACTERISTICS FOR NEXT GENERATION AEROSPACE VEHICLE: A PROJECTION

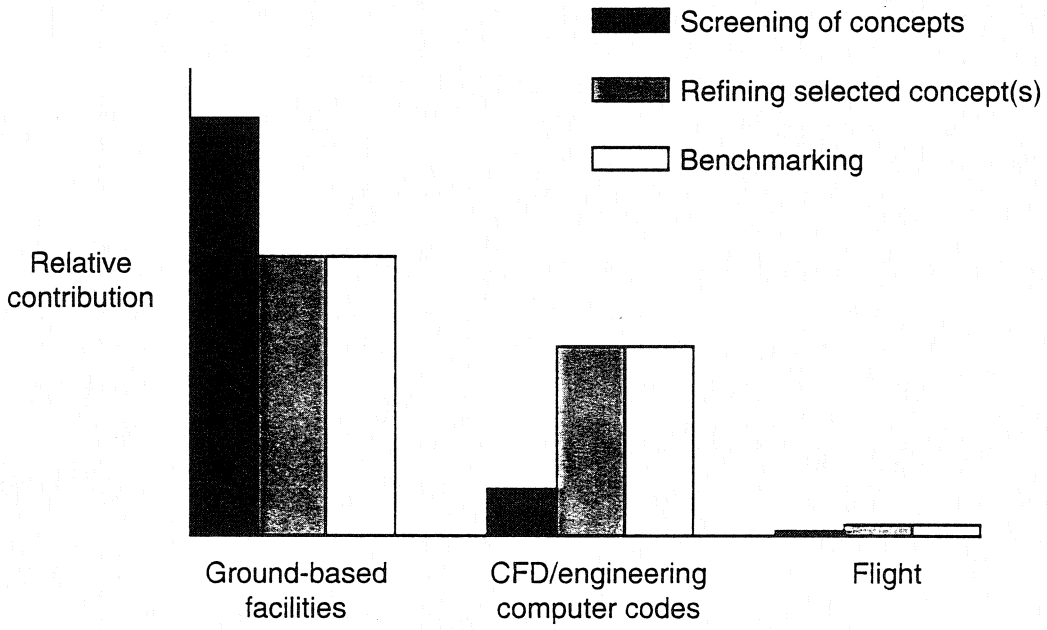

CONFIDENCE LEVEL FOR DETERMINATION OF AERODYNAMIC CHARACTERISTICS FOR NEXT GENERATION AEROSPACE VEHICLE

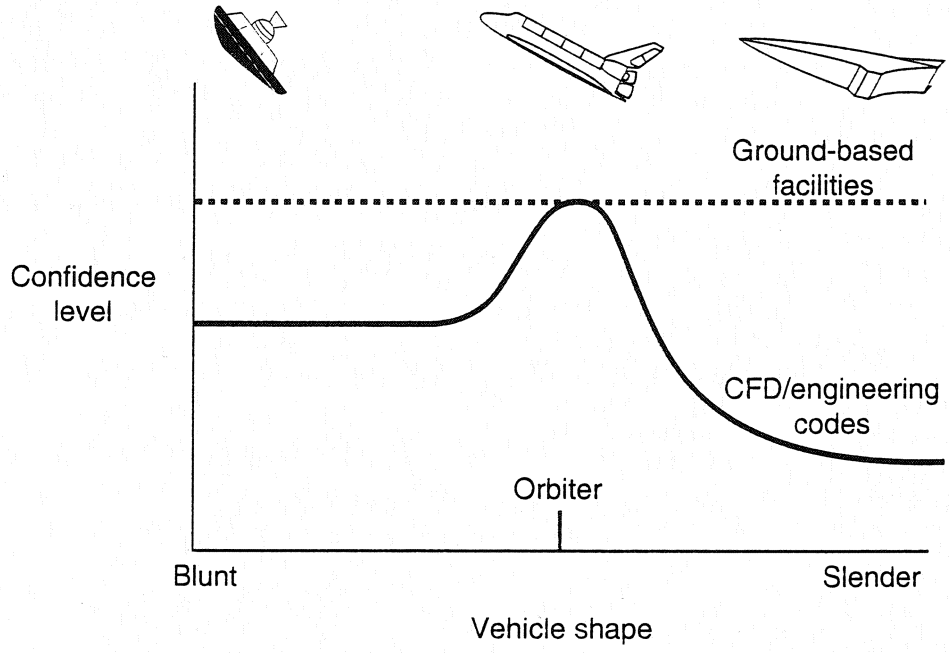

RELATIVE CONTRIBUTION OF FACILITIES AND CFD CODES TO DETERMINATION OF HYPERSONIC AERODYNAMIC CHARACTERISTICS FOR CERTAIN FLOW PHENOMENA: NEXT GENERATION AEROSPACE VEHICLE(S)

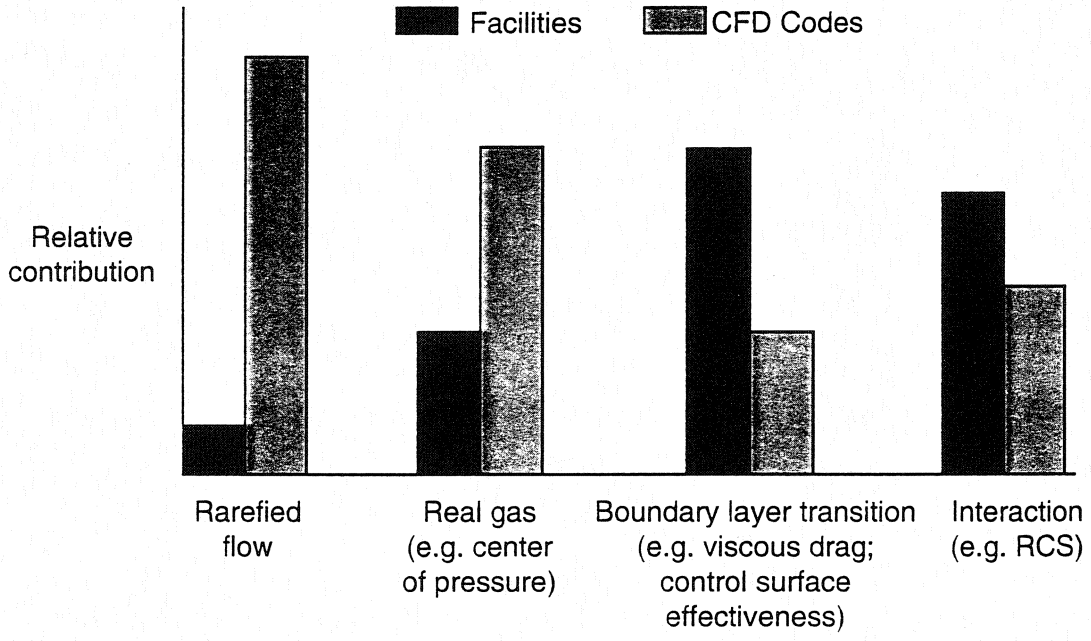

CLOSING COMMENTS

- **State-of-the-art aerodynamic prediction methodology for horizontal landing, winged and/or lifting body advanced dramatically via shuttle orbiter experience**
  - Invaluable lessons learned from orbiter flights (e.g., DFI, OEX)
    - Established confidence in approach (i.e., extensive wind tunnel testing)
    - Refined wind tunnel testing techniques and extrapolations to flight
      - e.g. use of heavy test gas to simulate real-gas effects (NASA tests in air and CF_4; Russian tests in N_2 and CO_2)
    - Provided benchmark data for calibration/validation of CFD/ engineering computer codes
- **Tools for aerodynamic design of next generation aerospace vehicle(s) improved**
  - Ground-based test capability of 1990's somewhat leaner than 1970's, but generally better
  - CFD computer codes, with capability to predict flight conditions, will be major contributor
- **Roles of ground-based facilities and CFD codes**
  - Facilities and engineering codes used to screen concepts
    - Wide range of: shapes; configuration buildup (parametrics); flow conditions; attitudes
  - Facilities and CFD roughly equal partners in initial assessment of selected concept(s) and prediction of flight performance (benchmarking)

CLOSING COMMENTS -- CONCLUDED

- Approach
  - CFD predictions and wind tunnel measurements compared to previous flight data
  - CFD predictions compared to wind tunnel measurements for next generation vehicle concept(s) (code calibration)
  - High level of confidence when:

    CFD prediction for flight = measurement extrapolation to flight

ASSESSMENT OF STATE-OF-THE-ART AEROHEATING PREDICTION METHODOLOGY IN LIGHT OF THE SHUTTLE EXPERIENCE

David A. Throckmorton
NASA Langley Research Center
Hampton, VA

A written version of this paper was not provided by the author.

Copies of presentation materials used at the Symposium are presented herein.

COMMENT CONSTRAINTS

Low-Earth Orbital Entry Velocities

Therefore, the Following are Non-Issues:

- Ionization
- Radiation
- Ablation

ORBITER-DESIGN AEROHEATING ISSUES

- Flowfield Chemistry Effects
  - Surface Catalytic Efficiency
- Separated Flows
  - Leeside
- Shock-Shock Interactions
- Boundary Layer Transition

DESIGN HEATING METHODOLOGY

Representative flow models

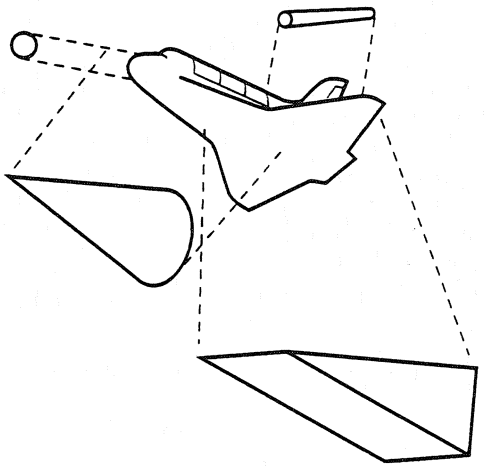

Wind tunnel calibration of heating models

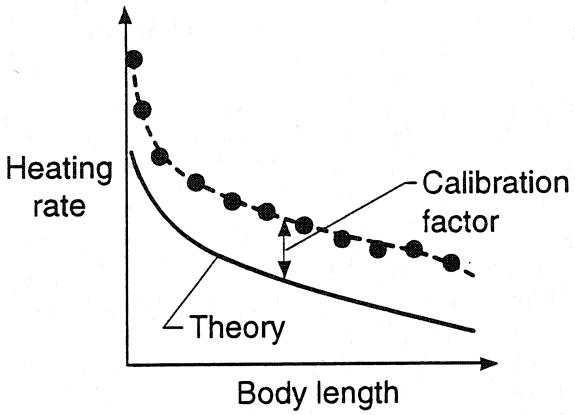

Hypersonic Boundary Layer Transition State-of-the-Art

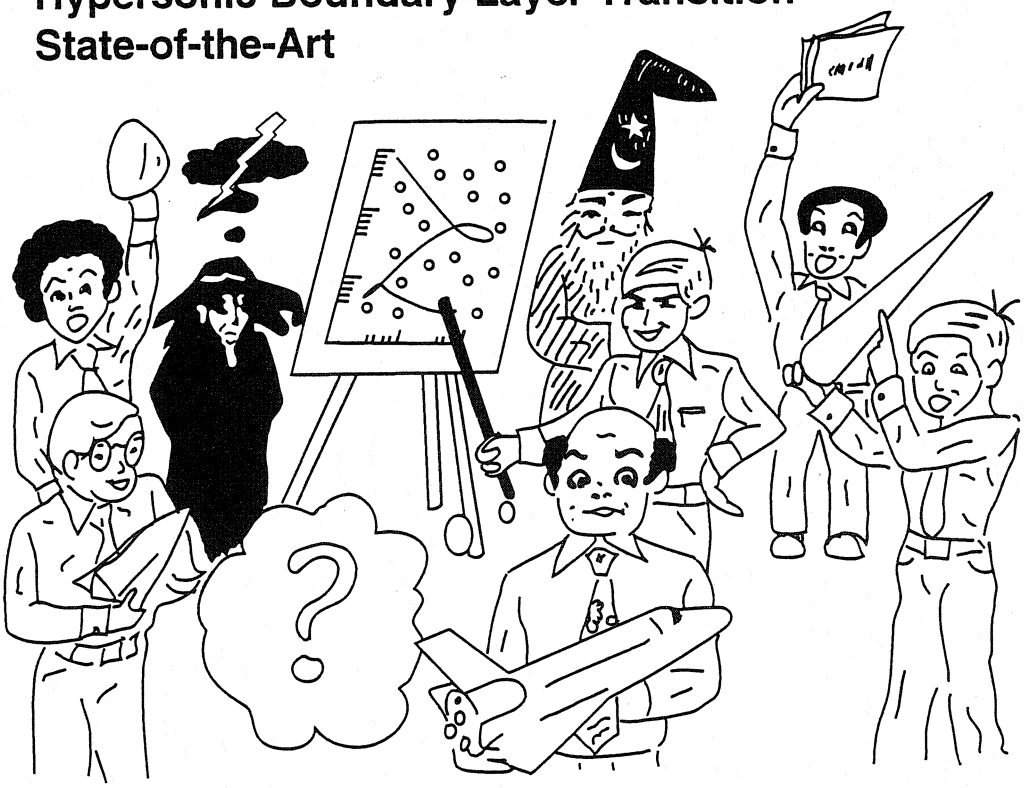

CURRENT STATE-OF-THE-ART
ROLE OF CONVENTIONAL WIND TUNNELS

- Configuration Geometry Parametrics
- Control Surface Position Parametrics
- Indicator of Configuration-Unique Flowfield Phenomena

CURRENT STATE-OF-THE-ART
ROLE OF COMPUTATIONAL FLUID DYNAMICS

- Accurate Flight Flowfield / Heating Simulation
- Flowfield Phenomena Parametrics
  - Gas Chemistry
  - Surface Catalytic Efficiency
- Multi-Point Simulations Along Trajectory

KIPP'S LAWS OF CFD

Computational Fluid Dynamic Codes:

- Are Versatile
- Provide Accurate Solutions
- Provide Inaccurate Solutions
- Require Knowledgeable, Experienced Users

CURRENT STATE-OF-THE-ART
ROLE OF "ENGINEERING" TECHNIQUES

- Conceptual Design Studies and Configuration Screening
- Physically Accurate and Consistent Interpolation Between CFD Benchmarks
- Enable Generation of Multiple Geometric-Point and Multiple Trajectory-Point Database Required for Vehicle Thermo-Structural Design

FOR NEXT-GENERATION VEHICLE DESIGN, WHAT IS STILL REQUIRED ??

- Accurate Quantitative Knowledge of Surface Catalytic Efficiency
- Transition Prediction Methodology
- Turbulence Modeling
  - Separated Flows
  - Shear Flows - Shock Interactions

Orbiter Entry Aerothermodynamic Flight Data Analysis

BIBLIOGRAPHY

Compiled by

David A. Throckmorton
NASA Langley Research Center

April 1993

GENERAL

COMPTON, H. R., Blanchard, R. C., and Walberg, G. D., "An Experiment for Shuttle Aerodynamic Force Coefficient Determination from Inflight Dynamic and Atmospheric Measurements," AIAA Paper 78-0795, April 1978.

COMPTON, H. R., Blanchard, R. C., and Findlay, J. T., "Shuttle Entry Trajectory Reconstruction Using Inflight Accelerometer and Gyro Measurements," AIAA Paper 79-0257, January 1979.

ANON., Langley Research Center OEX Task Team Report, NASA TM 80042, January 1979.

SIEMERS, P. M. and Larson, T. J., "Space Shuttle Orbiter and Aerodynamic Testing," *Journal of Spacecraft and Rockets*, Vol. 16, No. 4, July-August 1979, p.223.

SSD Intra-Division Planning Team, "Space Systems Division Orbiter Experiments Data Analysis Plan," April 1980.

COOKE, D. R., "Space Shuttle Stability and Control Flight Test Techniques," AIAA Paper 80-1608, August 1980.

STEWART, D. A., Rakich, J. V., and Lanfranco, M. J., "Catalytic Surface Effects Experiment on the Space Shuttle," AIAA Paper 81-1143, June 1981.

OFFICE of Advanced Manned Vehicles, "Evaluation of the Space Shuttle Orbiter First Orbital Flight Descent Phase," AFFTC-TR-81-21, July 1981.

HODGE, J. K., Phillips, P. W., and Audley, D. R., "Flight Testing a Manned Lifting Reentry Vehicle, Space Shuttle, for Aerothermodynamic Performance," AIAA Paper 81-2421, November 1981.

JONES, J. J., "OEX--Use of the Shuttle Orbiter as a Research Vehicle," AIAA Paper 81-2512, November 1981.

THROCKMORTON, D. A., "Research Analysis of Space Shuttle Orbiter Entry Aerothermodynamic Flight Data at the NASA Langley Research Center," AIAA Paper 81-2429, November 1981.

PRICE, J. M., "Atmospheric Modeling for Shuttle Aerothermodynamic Investigations," NOAA/SESC Workshop on Satellite Drag, March 1982.

Office of Advanced Manned Vehicles, "Evaluation of the Space Shuttle Orbiter Second Orbital Descent Phase," AFFTC-TR-82-1, February 1982.

BLANCHARD, R. C., and Duckett, R. J., "A Shuttle Upper Atmosphere Mass Spectrometer (SUMS) Experiment," AIAA Paper 82-1334, August 1982.

RICHARDSON, D. F., Phillips, P. W., and Hoey, R. G., "Optimization of the Space Shuttle Reentry for High Crossrange Based on Flight Test Results," AFFTC-TR-83-64, December 1983.

BLANCHARD, R. C., Duckett, R. J., and Hinson, E. W., "The Shuttle Upper Atmosphere Mass Spectrometer Experiment," *Journal of Spacecraft and Rockets*, Vol. 21, No. 2, March-April 1984, pp. 202-208.

THROCKMORTON, D. A., Zoby, E. V., and Kantsios, A. G., "The Shuttle Infrared Leeside Temperature Sensing (SILTS) Experiment," AIAA Paper 85-0328, January 1985.

OFFICE of Advance Manned Vehicles, "Flight Test Results from the Entry and Landing of the Space Shuttle Orbiter for the First Twelve Orbital Flights," AFFTC-TR-85-11, June 1985.

BLANCHARD, R. C., Hendrix, M. K, Fox, J. C., Thomas, D. J., and Nicholson, J. Y., "The Orbital Acceleration Research Experiment," AIAA Paper 86-1195, June 1986.

PHIILLIPS, P. W., "Aerothermodynamic Flight Test Handbook," AFFTC-TIH-86-3, November 1986.

BLANCHARD, R. C., Hendrix, M. K., Fox, J. C., Thomas, D. J., and Nicholson, J. Y., "Orbital Acceleration Research Experiment," *Journal of Spacecraft and Rockets*, Vol. 24, No. 6, November-December 1987, pp. 504-507.

ILIFF, KENNETH W., and Shafer, Mary F., "Space Shuttle Hypersonic Flight Research and the Comparison to Ground Test Results (Invited)," AIAA Paper 92-3988, July 1992.

THROCKMORTON, D.A., "Shuttle Entry Aerothermodynamic Flight Research: The Orbiter Experiments (OEX) Program (Invited)," AIAA Paper 92-3987, July 1992.

SUPPORTING ANALYSES

LARSON, T. J. , and Siemers, P. M. III, "Use of Nose Cap and Fuselage Pressure Orifices for Determination of Air Data for Space Shuttle Orbiter Below Supersonic Speeds," NASA TP 1643, July 1980.

BRADLEY, P. F., and Throckmorton, D. A., "Space Shuttle Orbiter Flight Heating Rate Measurement Sensitivity to Thermal Protection System Uncertainties," NASA TM 83138, June 1981.

GARRAHAN, J. G., "Heat-Transfer Software System Description and User's Guide," NASA CR-165780, October 1981.

OH, I. H., "Space Shuttle Wing Surface Heating-Rate Correction Program (WISHC) System Description and User's Guide," NASA CR-165785, October 1981.

PRUETT, C. D., Wolf, H., Heck, M. L., and Siemers, P. M. III, "An Innovative Air Data System for the Space Shuttle Orbiter: Data Analysis Techniques," AIAA Paper 81-2455, November 1981.

BOLAND, D. E., and Lee, T., "Langley Atmospheric Information Retrieval System (LAIRS) Description and User's Guide," NASA CR-3529, March 1982.

HECK, M. L., Findlay, J. T., Kelly, G. M., and Compton, H. R., "The Adaptation of a Strap Down Formulation for Processing Inertial Platform Data," AIAA Paper 82-1332, August 1982.

MYRICK, D. L., and Kantsios, A. G., "Incorporating Geometric and Radiative Effects Into Infrared Scanning Computer Analysis." *Thermal Infrared Sensing Diagnostics (Thermosense V), Vol. 371 of Proceedings of SPIE -- The International Society for Optical Engineering, George E. Courville*, ed., 1982, 211-215.

SCOTT, C. D., "Catalytic Recombination of Nitrogen and Oxygen on Iron-Cobalt-Chromia Spinal," AIAA Paper 83-0585, January 1983.

WELLS, W. L., and Hudgins, J. W., "Experimental Assessment of a Computer Program Used in Space Shuttle Orbiter Entry Heating Analyses," NASA TM 84572, January 1983.

PRUETT, C. D., Wolf, H., Heck, M. L., and Siemers, P. M. III, "Innovative Air-Data System for the Space Shuttle Orbiter," *Journal of Spacecraft and Rockets*, Vol. 20, No. 1, January-February 1983, pp. 61-69.

HECK, M. L., Findlay, J. T., and Compton, H. R., "Calibration of the Aerodynamic Coefficient Identification Package Measurements from the Shuttle Entry Flights Using Inertial Measurement Unit Data," AIAA Paper 83-2100, August 1983.

HECK, M. L., Findlay, J. T., and Compton, H. R., "Aerodynamic Coefficient Identification Package Dynamic Data Accuracy Determinations," *Shuttle Performance: Lessons Learned*, Part 1, NASA CP-2283, October 1983, pp. 549-571.

HECK, M. L., Findlay, J. T., Kelly, G. M., and Compton, H. R., "Adaptation of a Strapdown Formulation for Processing Inertial Platform Data," *Journal of Guidance, Control, and Dynamics*, Vol. 17, No. 1, January-February 1984, pp. 15-19.

MYRICK, D. L., and Throckmorton, D. A., "Comprehensive Analysis of Shuttle Orbiter Leeside Surface Infrared Imagery During Atmospheric Entry." *An International Conference on Thermal Infrared Sensing for Diagnostics and Control (Thermosense VIII), Vol. 581 of Proceedings of SPIE -- The International Society for Optical Engineering, Herbert Kaplan*, ed., 1985, pp. 116-121.

FLOWERS, O. L., and Stewart, D. A, "Catalytic Surface Effects on Contaminated Space Shuttle Tile in a Dissociated Nitrogen Stream," NASA TM-86770, November 1985.

THOMPSON, J. M., Russell, J. W., and Blanchard, R. C., "Methods for Extracting Aerodynamic Acceleration from Orbiter High Resolution Accelerometer Flight Data," AIAA Paper 87-2365, August 1987.

MOSS, J. N., and Bird, G. A., "Monte Carlo Simulations in Support of the Shuttle Upper Atmospheric Mass Spectrometer Experiment," *Journal of Thermophysics and Heat Transfer*, Vol. 2, No. 2, April 1988, pp. 138-144.

BLANCHARD, R. C., Larman, K. T., and Moats, C. D., "Ground and Flight Calibration Assessment of HiRAP Accelerometer Data From Missions STS-35 and STS-40." NASA TM-107602, April 1992.

MOATS, C. D., Blanchard, R. C., and Larman, K. T., "Improved HiRAP Calibration Technique." NASA TM-107656, July 1992.

BLANCHARD, R. C., Larman, K. T., and Moats, C. D., "Flight Calibration Assessment of HiRAP Accelerometer Data." AIAA Paper 93-0836, January 1993.

TRAJECTORY AND ATMOSPHERIC RECONSTRUCTION

COMPTON, H. R., Findlay, J. T., Kelly, G. M., and Heck, M. L., "Shuttle (STS-1) Entry Trajectory Reconstruction," AIAA Paper 81-2459, November 1981.

PRICE, J. M., and Blanchard, R. C., "Determination of Atmospheric Properties for STS-1 Aerothermodynamic Investigations," AIAA Paper 81-2430, November 1981.

FINDLAY, J. T., Kelly, G. M., and Heck, M. L., "Reconstruction of the 1st Space Shuttle (STS-1) Entry Trajectory," NASA CR-3561, June 1982.

FINDLAY, J. T, Kelly, G. M., Heck, M. L., and McConnell, J. G., "Entry Reconstruction of the 2nd Space Shuttle Columbia Flight: Results and Methodology," Analytical Mechanics Associates Report No. 82-8, NAS1-16087, March 1982.

KELLY, G. M., Heck, M. L., McConnell, J. G., and Findlay, J. T., "A Summary of STS3 Post-Flight Best Estimate Trajectory Results," Analytical Mechanics Associates Report No. 82-32, NAS1-16087, August 1982.

KELLY, G. M., McConnell, J. G., Heck, M. L., and Findlay, J. T., "STS4 Best Estimate Trajectory, AEROBET, and GT File Development and Results," Analytical Mechanics Associates Report No. 82-33, Contract NAS1-16087, September 1982.

KELLY, G. M., Findlay, J. T., and Compton, H. R., "Wind Estimation Using Air Data Probe Measurements to Evaluate Meteorological Measurements Made During Space Shuttle Entries," AIAA Paper 82-1333, August 1982.

KELLY, G. M., McConnell, J. G., Heck, M. L., and Findlay, J. T., "Development of and Results from the STS-5 Post-Flight Products for LaRC Aerodynamic and Aerothermodynamic Investigators," Analytical Mechanics Associates Report No. 83-2, Contract NAS1-16087, February 1983.

PRICE, J. M., "Atmospheric Definition for Shuttle Aerothermodynamic Investigations," *Journal of Spacecraft and Rockets*, Vol. 20, No. 2, March-April 1983, pp. 133-140.

PRICE, J. M., "Atmosphere Determination for Shuttle Aerodynamic Studies," AMS/AIAA/NWA Ninth Conference on Aerospace and Aeronautical Meteorology, June 1983.

FINDLAY, J. T., Kelly, G. M., Heck, M. L., and McConnell, J. G., "Results from the First Entry Flight of the NASA Space Shuttle "Challenger", STS-6," Analytical Mechanics Associates Report No. 83-9, Contract NAS1-16087, June 1983.

KELLY, G. M., Findlay, J. T., and Compton, H. R., "Shuttle Subsonic Horizontal Wind Estimation," *Journal of Spacecraft and Rockets*, Vol. 20, No. 4, July-August 1983, pp. 390-397.

FINDLAY, J. T., Kelly, G. M., Heck, M. L., and McConnell, J. G., "STS-7 Post Flight Best Estimate Trajectory Products," Analytical Mechanics Associates Report No. 83-17, Contract NAS1-16087, September 1983.

FINDLAY, J. T., Kelly, G. M., Heck, M. L., and McConnell, J. G., "STS-8 BET Results," NASA CR-172257, November 1983.

FINDLAY, J. T., Kelly, G. M., Heck, M. L., McConnell, J. G., and Henry, M. W., "STS-9 BET Products," NASA CR-172314, February 1984.

KELLY, G. M., McConnell, J. G., Findlay, J. T., Heck, M. L., and Henry, M. W., "Final STS-11 (41-B) Best Estimate Trajectory Products: Development and Results from the First Cape Landing Mission," NASA CR-172349, April 1984.

FINDLAY, J. T., Kelly, G. M., McConnell, J. G., and Heck, M. L., "STS-13 (41-C) BET Products," NASA CR-172350, July 1984.

KELLY, G. M., McConnell, J. G., Heck, M. L., Troutman, P. A., and Findlay, J. T., "Trajectory Recontruction and Aerodynamic Results from the First Discovery Flight, STS-14 (41-D)," NASA CR-172492, February 1985.

KELLY, G. M., Heck, M. L., McConnell, J. G., Waters, L. A., Troutman, P. A., and Findlay, J. T., "Challenger STS-17 (41-G) Post-Flight Best Estimate Trajectory Products - Development and Summary Results," NASA CR-172548, March 1985.

KELLY, G. M., McConnell, J. G., Heck, M. L., Troutman, P. A., Waters, L. A., and Findlay, J. T., "Post-Flight BET Products for the 2nd Discovery Entry, STS-19 (51-A)," NASA CR-172572, April 1985.

KELLY, G. M., Heck, M. L., McConnell, J. G., and Findlay, J. T., "Post-Flight Results for Shuttle Discovery Flight 51-D (STS-23)," NASA CR-177976, November 1985.

KELLY, G. M., Heck, M. L., McConnell, J. G., and Findlay, J. T., "Post-Flight Results from Challenger Mission 51-B (STS-24)," NASA CR-178039, February 1986.

FINDLAY, J. T., and Kelly, G. M., "Discovery STS-25 (51-G) Post-Flight Results," NASA CR-178203, February 1987.

FINDLAY, J. T., and Kelly, G. M., "STS-26 (51-F) Challenger Post-Flight Best Estimate Trajectory Results," NASA CR-178234, June 1987.

FINDLAY, J. T., and Kelly, G. M., "Discovery STS-27 (51-I) Post-Flight Best Estimate Trajectory Products," NASA CR-178250, June 1987.

FINDLAY, J. T., and Kelly, G. M., "Best Estimate Trajectory Results for the Challenger STS-30 (61-A) Entry Flight," NASA CR-178253, June 1987.

FINDLAY, J. T., and Kelly, G. M., "Shuttle "Atlantis" STS-31 (61-B) Post-Flight Entry Trajectory Products and Summary Results," NASA CR-178261, June 1987.

FINDLAY, J. T., and Kelly, G. M., "STS-32 (61-C) Columbia Entry BET Products and Summary Results," NASA CR-178262, June 1987.

OAKES, K. F., Findlay, J. T., Jasinski, R. A., and Wood, J. S., "Final STS-35 'Columbia' Descent BET Products and Results for LaRC OEX Investigations," NASA Contractor Report 189569, November 1991.

OAKES, K. F., Wood, J. S., and Findlay, J. T., "Final Report: STS-40 Descent BET Products-Development and Results," NASA Contractor Report 189570, November 1991.

ILIFF, K. W., Maine, R. E., and Cooke, D. R., "Selected Stability and Control Derivatives from the First Space Shuttle Entry," AIAA Paper 81-2451, November 1981.

YOUNG, J. C., Perez, L. F., Romere, P. O., and Kanipe, D. B., "Space Shuttle Entry Aerodynamic Comparisons of Flight 1 with Preflight Predictions," AIAA Paper 81-2476, November 1981.

YOUNG, J. C., "Aerodynamic Comparisons of STS-1 Space Shuttle Entry Vehicle," *Wind-Tunnel/Flight Correlation*, 1981, pp. 117-131.

ROMERE, P. O., and Young, J. C., "Space Shuttle Entry Longitudinal Aerodynamic Comparisons of Flight 2 with Preflight Predictions," AIAA Paper 82-0565, March 1982.

UNDERWOOD, J. M., and Cooke, D. R., "A Preliminary Correlation of the Orbiter Stability and Control Aerodynamics from the First Two Space Shuttle Flights, STS-1 & 2, with Preflight Predictions," AIAA Paper 82-0564, March 1982.

YOUNG, J. C., and Underwood, J. M., "The Development of Aerodynamic Uncertainties for the Space Shuttle Orbiter," AIAA Paper 82-0563, March 1982.

KANIPE, D. B., and Roberts, B. B., "Evolution of the Wind Tunnel Test Program for Space Shuttle Orbiter Jet Interaction Upon Entry and Comparison of Predictions with Flight Test Results," *JANNAF 13th Plume Technology Meeting*, Vol. 1, April 1982, pp. 83-94.

KELLY, G. M., and Findlay, J. T., "Horizontal Wind Estimates Deterministically Derived from the STS-1 Entry Flight Data -- A Comparison with Available Meteorology Data," NASA CR-165881, April 1982.

COOKE, D. R., "Space Shuttle Stability and Control Test Plan," AIAA Paper 82-1315, August 1982.

COMPTON, H. R., Scallion, W. I., Suit, W. T., and Scheiss, J. R., "Shuttle Entry Performance and Stability and Control Derivatives Extraction from Flight Measurement Data," AIAA Paper 82-1317, August 1982.

CULP, M. A., and Cooke, D. R., "Stability and Control Flight Test Results of the Space Transportation System's Orbiter," AIAA Paper 82-1316, August 1982.

GAMBLE, J. D., and Young, J. C., "The Development and Application of Aerodynamic Uncertainties in the Design of the Entry Trajectory and Flight Control System of the Space Shuttle Orbiter," AIAA Paper 82-1335, August 1982.

KANIPE, D. B., "Plume/Flowfield Jet Interaction Effects on the Space Shuttle Orbiter During Entry," AIAA Paper 82-1319, August 1982.

SIEMERS, P. M. III, Wolf, H., and Flanagan, P. F., "Shuttle Entry Air Data System Concepts Applied to Space Shuttle Orbiter Flight Pressure Data to Determine Air Data - STS 1-4," AIAA Paper 83-1003, January 1983.

FINDLAY, J. T., and Compton, H. R., "On the Flight Derived/Aerodynamic Data Base Performance Comparisons for the NASA Space Shuttle Entries During the Hypersonic Regime," AIAA Paper 83-0115, January 1983.

MAUS, J. R., Griffith, B. J., Szema, K. Y., and Best, J. T., "Hypersonic Mach Number and Real Gas Effects of Space Shuttle Orbiter Aerodynamics," AIAA Paper 83-0343, January 1983.

SCALLION, W. I., Compton, H. R., Suit, W. T., Powell, R. W., Blackstock, T. A., and Bates, B. L., "Space Shuttle Third Flight (STS-3) Entry RCS Analysis," AIAA Paper 83-0116, January 1983.

SIEMERS, P. M., III, Wolfe, H., and Flanagan, P. F., "Shuttle Entry Air Data System Concepts Applied to Space Shuttle Orbiter Flight Pressure Data to Determine Air Data - STS 1-4," AIAA Paper 83-0118, January 1983.

SUIT, W. T., Compton, H. R., Scallion, W. I., and Schiess, J. R., "Simplified Analysis Techniques to Support the Determination of Shuttle Aerodynamics," AIAA Paper 83-0117, January 1983.

ROMERE, P. O., Kanipe, D. B., and Young, J. C., "Space Shuttle Entry Aerodynamic Comparisons of Flight 1 with Preflight Predictions," *Journal of Spacecraft and Rockets*, Vol. 20, No. 1, Jan.-Feb. 1983, pp. 15-21.

SZEMA, K. Y., Griffith, B. J., Maus, J. R., and Best, J. T., "Laminar Viscous Flow-Field Prediction of Shuttle-like Vehicle Aerodynamics," AIAA Paper 83-0211, January 1983.

KIRSTEN, P. W., and Richardson, D. F., "Predicted and Flight Test Results of the Performance and Stability and Control of the Space Shuttle from Reentry to Landing," *Ground/Flight Test Technology and Correlation*, *AGARD*, February 1983.

BOURNE, C. A., and Kirsten, P. W., "Approach and Landing Characteristics of the Space Shuttle Orbiter," *Shuttle Performance: Lessons Learned*, Part 1, NASA CP-2283, October 1983, pp. 637-651.

CALLOWAY, R. L., "Lateral-Directional Stability Investigation at Mach 6," *Shuttle Performance: Lessons Learned*, Part 1, NASA CP-2283, October 1983, pp. 525-548.

COOKE, D. R., "Minimum Testing of the Space Shuttle Orbiter for Stability and Control Derivatives," *Shuttle Performance: Lessons Learned*, Part 1, NASA CP-2283, October 1983, pp. 447-472.

COMPTON, H. R., Schiess, J. R., Suit, W. T., Scallion, W. I., and Hudgins, J.W., "Stability and Control Over the Supersonic and Hypersonic Speed Range," *Shuttle Performance: Lessons Learned*, Part 1, NASA CP-2283, October 1983, pp. 473-507.

FINDLAY, J. T., Kelly, G. M., McConnell, J. G., and Compton, H. R., "Subsonic Longitudinal Performance Coefficient Extraction From Shuttle Flight Data--An Accuracy Assessment for Determination of Database Updates," *Shuttle Performance: Lessons Learned*, Part 2, NASA CP-2283, October 1983, pp. 1111-1168.

GAMBLE, J. D., "The Application of Aerodynamic Uncertainties in the Design of the Entry Trajectory and Flight Control System of the Space Shuttle Orbiter," *Shuttle Performance: Lessons Learned*, Part 1, NASA CP-2283, October 1983, pp. 595-616.

GRIFFITH, B. J., Maus, J. R., and Best, J. T., "Explanation of the Hypersonic Longitudinal Stability Problem: Lessons Learned," *Shuttle Performance: Lessons Learned*, Part 1, NASA CP-2283, October 1983, pp. 347-381.

KIRSTEN, P. W., Richardson, D. F., and Wilson, C. M., "Predicted and Flight Test Results of the Performance, Stability and Control of the Space Shuttle from Reentry to Landing," *Shuttle Performance: Lessons Learned*, Part 1, NASA CP-2283, October 1983, pp. 509-524.

ROMERE, P. O., and Whitnah, A. M., "Space Shuttle Entry Longitudinal Aerodynamic Comparisons of Flights 1-4 with Preflight Predictions," *Shuttle Performance: Lessons Learned*, Part 1, NASA CP-2283, October 1983, pp. 283-308.

SUIT, W. T., Compton, H. R., Scallion, W. I., and Gahan, L. S., "Analysis of Shuttle Oscillation in the Mach 1.7 to 1.0 Range," *Shuttle Performance: Lessons Learned*, Part 1, NASA CP-2283, October 1983, pp. 397-412.

WOODS, W. C., Arrington, J. P., and Hamilton, H. H. II, "A Review of Preflight Estimates of Real Gas Effects on Space Shuttle Aerodynamic Characteristics," *Shuttle Performance: Lessons Learned*, Part 1, NASA CP-2283, October 1983, pp. 309-346.

YOUNG, J. C., and Underwood, J. M., "The Development of Aerodynamic Uncertainties for the Space Shuttle Orbiter," *Shuttle Performance: Lessons Learned*, Part 2, NASA CP-2283, October 1983, pp. 1169-1186.

ILIFF, K. W., Maine, R. E., and Cooke, D. R., "Space Shuttle Stability and Control Derivatives Estimated from the First Entry," *Journal of Guidance, Control, and Dynamics*, Vol. 6, July-Aug. 1983, pp. 264-271.

KANIPE, D. B., "Plume/Flowfield Jet Interaction Effects on the Space Shuttle Orbiter During Entry," *Journal of Spacecraft and Rockets*, Vol. 20, No. 4, July-Aug. 1983, pp. 351-355.

MAUS, J. R., Griffith, B. J., Tolbert, D. G., and Best, J. T., "Understanding Space Shuttle Flight Data by Use of Wind Tunnel and CFD Results," AIAA Paper 83-2745, November 1983.

PHILLIPS, W. P., Findlay, J. T., and Compton, H. R., "Base Drag Determination for STS Flights 1-5," AIAA Paper 83-2719, November 1983.

ROMERE, P. O., and Young, J. C., "Space Shuttle Entry Longitudinal Aerodynamic Comparisons of Flight 2 with Preflight Predictions," *Journal of Spacecraft and Rockets*, Vol. 20, No. 1, Nov.-Dec. 1983, pp. 518-523.

YOUNG, J. C., and Underwood, J. M., "Development of Aerodynamic Uncertainties for the Space Shuttle Orbiter," *Journal of Spacecraft and Rockets*, Vol. 20, No. 6, Nov.-Dec. 1983, pp. 513-517.

BLANCHARD, R. C., and Rutherford, J. F., "The Shuttle Orbiter High Resolution Accelerometer Package (HiRAP) Experiment: Preliminary Flight Results," AIAA Paper 84-0490, January 1984.

FINDLAY, J. T., Kelly, G. M., McConnell, J. G., and Compton, H. R., "Shuttle *'Challenger'* Aerodynamic Performance from Flight Data - Comparisons With Predicted Values and *'Columbia'* Experience," AIAA Paper 84-0485, January 1984

CALLOWAY, R. L., "Real Gas Simulation for the Shuttle Orbiter and Planetary Entry Configurations Including Flight Results," AIAA Paper 84-0489, January 1984.

MAUS, J. R., Griffith, B. J., Szema, K. Y., and Best, J. T., "Hypersonic Mach Number and Real Gas Effects of Space Shuttle Orbiter Aerodynamics," *Journal of Spacecraft and Rockets*, Vol. 21, No. 2, Mar.-Apr. 1984, pp. 136-141.

FINDLAY, J. T., Kelly, G. M., Heck, M. L., and McConnell, J. G., "Final Report: Summary of Shuttle Data Processing and Aerodynamic Performance Comparisons for the First Eleven (11) Flights," NASA CR-172440, September 1984.

BLANCHARD, R. C., and Buck, G. M., "Determination of Rarefied-Flow Aerodynamics of the Shuttle Orbiter from Flight Measurements on STS-6 and STS-7," AIAA Paper 85-0347, January 1985.

GAMBLE, J. D., Cooke, D. R., Underwood, J. M., Stone, H. W., Jr., and Schlosser, D. C., "The Development and Application of Aerodynamic Uncertainties; And Flight Test Verification for the Space Shuttle Orbiter," *Space Shuttle Technical Conference*, Part 1, NASA CP-2342, January 1985, pp. 264-294.

YOUNG, J. C., Underwood, J. M., Hillje, E. R., Whitnah, A. M., Romere, P. O., Gamble, J. D., Roberts, B. B., Ware, G. M., Scallion, W. I., and Spencer, B. Jr., "The Aerodynamic Challenges of the Design and Development of the Space Shuttle Orbiter," *Space Shuttle Technology Conference*, Part 1, NASA CP-2342, January 1985, pp. 209-263.

BLANCHARD, R. C., and Rutherford, J. F., "Shuttle Orbiter High Resolution Accelerometer Package Experiment: Preliminary Flight Results," *Journal of Spacecraft and Rockets*, Vol. 22, No. 4, July-August 1985, pp. 474-480.

YOUNG, J. C., and Findlay, J. T., "An Analysis of the Space Shuttle Hypersonic Entry Trim Anomaly," AIAA Paper 85-1764, August 1985.

BLANCHARD, R. C., and Buck, G. M., "Rarefied-Flow Aerodynamics and Thermosphere Structure From Shuttle Flight Measurements," *Journal of Spacecraft and Rockets*, Vol. 23, No. 1, January-February 1986, pp. 18-24.

BUCK, G. M., and Blanchard, R. C., "Rarefied Aerodynamics and Upper Atmosphere Density from Multiple Orbiter Flight Measurements," AIAA Paper 86-0269, January 1986.

GRIFFITH, B. J., Maus, J. R., Majors, B. M., and Best, J. T., "Addressing the Hypersonic Simulation Problem," AIAA Paper 86-9775, April 1986.

BLANCHARD, R. C., "Rarefied Flow Lift-to-Drag Measurements of the Shuttle Orbiter," ICAS Paper 86-2.10.2, September 1986.

GRIFFITH, B. J., Maus, J. R., and Majors, B. M., "Analysis of the Longitudinal Stability of the Space Shuttle Orbiter Above 150 kft," AEDC-TR-86-11, February 1987.

FRITTS, D. C., Coy, L., and Blanchard, R. C., "Horizontal Gravity Wave Structure Near the Mesopause Derived from Space Shuttle Re-Entry Data," Sixth Conference on the Dynamics and Chemistry of the Middle Atmosphere, March 1987.

GRIFFITH, B. J., Maus, J. R., Majors, B. M., and Best, J. T., "Addressing the Hypersonic Simulation Problem," *Journal of Spacecraft and Rockets*, Vol. 24, No. 4, July-Aug. 1987, pp. 334-341.

BLANCHARD, R. C., and Larman, K. T., "Rarefied Aerodynamics and Upper Atmospheric Flight Results from the Orbiter High Resolution Accelerometer Package Experiment," AIAA Paper 87-2366, August 1987.

KOPPENWALLNER, G., "Low Reynolds Number Influence on Aerodynamic Performance of Hypersonic Lifting Vehicles," *Aerodynamics of Hypersonic Lifting Vehicles, AGARD*, November 1987.

BLANCHARD, R. C., Hinson, E. W., and Nicholson, J. Y., "Shuttle High Resolution Accelerometer Package Experiment Results: Atmospheric Density Measurements Between 60-160 km," AIAA Paper 88-0492, January 1988.

BLANCHARD, R. C., "Density from Shuttle Accelerometer Flight Data -- Comparisons with Atmospheric Models." Fourth National Aero-Space Plane Technology Symposium, Paper No. 104-B, February 1988.

HENRY, M. W., Siemers, P. M. III, and Wolf, H., "An Evaluation of Shuttle Entry Air Data System (SEADS) Flight Pressure: Comparison With Wind Tunnel and Theoretical Predictions," AIAA Paper 88-2052, May 1988.

SIEMERS, P. M. III, Wolf, H., and Henry, M. W., "Shuttle Entry Air Data System (SEADS) - Flight Verification of an Advanced Air Data System Concept," AIAA Paper 88-2104, May 1988.

WOLF, H., Henry, M. W., and Siemers, P. M. III, "Shuttle Entry Air Data System (SEADS): Optimization of Preflight Algorithms Based on Flight Results," AIAA Paper 88-2053, May 1988.

BLANCHARD, R. C., and Hinson, E. W., "Rarefied Flow Pitching Moment Coefficient Measurements of the Shuttle Orbiter," ICAS Paper 88-1.5RI, August 1988.

FRITTS, D. C., Blanchard, R. C., and Coy, L., "Gravity Wave Structure Between 60 and 90 km Inferred from Space Shuttle Re-Entry Data," *Journal of Atmospheric Sciences*, Vol. 46, No. 3, February 1989, pp. 423-434.

BLANCHARD, R. C., and Hinson, E. W., "Flight Measurements of Shuttle Orbiter Pitching Moment Coefficient and Elevon Effectiveness in the Rarefied-Flow Regime," NASA TP 2889, March 1989.

BLANCHARD, R. C., Hinson, E. W., and Nicholson, J. Y., "Shuttle High Resolution Accelerometer Package Experiment Results: Atmospheric Density Measurements Between 60-160 km," *Journal of Spacecraft and Rockets*, Vol. 26, No. 3, May-June 1989, pp. 173-180.

BLANCHARD, R. C., and Hinson, E. W., "Hypersonic Rarefied-Flow Aerodynamics Inferred from Shuttle Orbiter Acceleration Measurements." Paper No. 7 presented at the International Conference on Hypersonic Aerodynamics, Manchester, England, September 1989.

BLANCHARD, R. C., "Shuttle Entry Density Measurements (Between 60 and 160 km)." Proceedings of Workshop held at AFGL, October 20-21, 1987, Environmental Research Papers, No. 1053, GL-TR-90-0033 I & II, Editor, Frank A. Marcos, February 1990.

HINSON, E. W., Nicholson, J. Y., and Blanchard, R. C., "Determination of Shuttle Orbiter Center of Gravity from Flight Measurements," NASA TM-102627, November 1990.

BLANCHARD, R. C., Barrett, M., Larmen, K. T., "The High Resolution Accelerometer Package (HiRAP) Flight Experiment Summary for the First Ten Flights," NASA RP 1267, April 1992.

BLANCHARD, R. C., Nicholson, J. Y., and Ritter, J. R., "STS-40 Orbital Acceleration Research Experiment Flight Results During a Typical Sleep Period," NASA TM-104209, Januaary 1992.

BLANCHARD, R. C., Nicholson, J. Y., and Ritter, J., "STS-40 Orbital Acceleration Research Experiment Flight Results During a Typical Sleep Period." *International Journal of Microgravity Research and Application*, Vol. 2, 1992, pp. 86-93.

BLANCHARD, R. C., Larman, K. T., and Moats, C. D., "Rarefied Flow Shuttle Aerodynamics Flight Model." NASA TM-107698, October 1992.

BLANCHARD, R. C., Nicholson, J. Y., and Ritter, J. R., "Preliminary OARE Absolute Acceleration Measurements on STS-50." NASA TM-107724, February 1993.

BLANCHARD, R. C., Ozoroski, T. A., and Nicholson, J. Y., "SUMS Experiment Flight Results on STS-35." NASA TM-107738, February 1993.

AEROHEATING AND FLOWFIELD CHARACTERISITCS

BRADLEY, P. F., Siemers, P. M. III, and Pruett, C. D., "Comparison of Forward Fuselage Space Shuttle Orbiter Flight Pressure Data to Wind-Tunnel and Analytical Results in the Hypersonic Mach Number Range," AIAA Paper 81-2477, November 1981.

THROCKMORTON, D. A., "Benchmark Aerodynamic Heat Transfer Data From the First Flight of the Space Shuttle Orbiter," AIAA Paper 82-0003, January 1982.

ZOBY, E. V., "Comparison of Free-Flight Experimental and Predicted Heating Rates for the Space Shuttle Orbiter," AIAA Paper 82-0002, January 1982.

THROCKMORTON, D. A., "Space Shuttle Orbiter Entry Heating and Thermal Protection," University of Kansas Aerospace Colloquium, April 1982.

HAMILTON, H. H. II, "Approximate Method for Predicting Heating on the Windward Side of Space Shuttle Orbiter and Comparisons With Flight Data," AIAA Paper 82-0823, June 1982.

LEE, D. B., and Harthun, M. H., "Aerothermodynamic Entry Environment of the Space Shuttle Orbiter," AIAA Paper 82-0821, June 1982.

RAKICH, J. V., Stewart, D. A., and Lanfranco, M. J., "Results of a Flight Experiment on the Catalytic Efficiency of the Space Shuttle Heat Shield," AIAA Paper 82-0944, June 1982.

SCOTT, C. D., and Derry, S. M., "Catalytic Recombination and Space Shuttle Heating," AIAA Paper 82-0841, June 1982.

SHINN, J. L., Moss, J. N., and Simmonds, A. L., "Viscous-Shock-Layer Heating Analysis for the Shuttle Windward Symmetry Plane With Surface Finite Catalytic Recombination Rates," AIAA Paper 82-0842, June 1982.

THROCKMORTON, D. A., "Influence of Radiant Energy Exchange on the Determination of Convective Heat Transfer Rates to Orbiter Leeside Surfaces During Entry," AIAA Paper 82-0824, June 1982.

WEILMUENSTER, K. J., and Hamilton, H. H. II, "A Comparison of Computed Space Shuttle Orbiter Surface Pressures with Flight Measurements," AIAA Paper 82-0937, June 1982.

ZOBY, E. V., "Analysis of STS-2 Experimental Heating Rates and Transition Data," AIAA Paper 82-0822, June 1982.

THROCKMORTON, D. A., Hamilton, H. H. II, and Zoby, E. V., "Preliminary Analysis of STS-3 Entry Heat-Transfer Data for the Orbiter Windward Centerline," NASA TM-84500, June 1982.

RIED, R. C., Goodrich, W. D., Li, C. P., Scott, C. D., Derry, S. M., and Maraia, R. J., "Space Shuttle Orbiter Entry Heating and TPS Response: STS-1 Predictions and Flight Data," *Computational Aspects of Heat Transfer in Structure*, 1982, pp. 327-347.

BRADLEY, P. F., Siemers, P. M. III, and Weilmuenster, K. J., "An Evaluation of Space Shuttle Orbiter Forward Fuselage Surface Pressures: Comparison with Wind Tunnel and Theoretical Predictions," AIAA Paper 83-0119, January 1983.

GOODRICH, W. D., Derry, S. M., and Bertin, J. J., "Shuttle Orbiter Boundary-Layer Transition - A Comparison of Flight and Wind Tunnel Data," AIAA Paper 83-0485, January 1983.

GUPTA, R. N., Moss, J. N., Simmonds, A. L., Shinn, J. L., and Zoby, E. V., "Space Shuttle Heating Analysis with Variation in Angle of Attack and Surface Condition," AIAA Paper 83-0486, January 1983.

HODGE, J. K., and Audley, D. R., "Aerothermodynamic Parameter Estimation from Space Shuttle Thermocouple Data During Transient Flight Test Maneuvers," AIAA Paper 83-0482, January 1983.

THROCKMORTON, D. A., and Zoby, E. V., "Orbiter Entry Leeside Heat-Transfer Data Analysis," AIAA Paper 83-0484, January 1983.

HODGE, J. K., Audley, D. R., Phillips, P. W., and Hertzler, E. K., "Aerothermodynamic Flight Envelope Expansion for a Manned Lifting Reentry Vehicle (Space Shuttle)," *Ground/Flight Test Technology and Correlation*, February 1983.

CUNNINGHAM, J. A., and Haney, J. W., Jr., "Space Shuttle Wing Leading Edge Heating Environment Prediction Derived from Development Flight Data," *Shuttle Performance: Lessons Learned*, Part 2, NASA CP-2283, October 1983, pp. 1083-1109.

GOODRICH, W. D., Derry, S. M., and Bertin, J. J., "Shuttle Orbiter Boundary Layer Transition at Flight and Wind Tunnel Conditions," *Shuttle Performance: Lessons Learned*, Part 2, NASA CP-2283, October 1983, pp. 753-780.

HANEY, J. W., Jr. "Orbiter Entry Heating Lessons Learned from Development Flight Test Program," *Shuttle Performance: Lessons Learned*, Part 2, NASA CP-2283, October 1983, pp. 719-753.

HARTHUN, M. H., Blumer, C. B., and Miller, B. A., "Orbiter Windward Surface Entry Heating: Post-Orbital Flight Test Program Update," *Shuttle Performance: Lessons Learned*, Part 2, NASA CP-2283, October 1983, pp. 781-804.

HELMS, V. T., "Leeward Centerline Heating Predictions for the Space Shuttle Orbiter," *Shuttle Performance: Lessons Learned*, Part 2, NASA CP-2283, October 1983, pp. 913-947.

HERTZLER, E. K., and Phillips, P. W., "Flight Test Derived Heating Math Models for Critical Locations on the Orbiter During Reentry," *Shuttle Performance: Lessons Learned*, Part 2, NASA CP-2283, October 1983, pp. 703-718.

HODGE, J. K., "Trends in Shuttle Entry Heating from the Correction of Flight Test Maneuvers," *Shuttle Performance: Lessons Learned*, Part 2, NASA CP-2283, October 1983, pp. 687-702.

SCOTT, C. D., "A Review of Nonequilibrium Effects and Surface Catalysis on Shuttle Heating," *Shuttle Performance: Lessons Learned*, Part 2, NASA CP-2283, October 1983, pp. 865-890.

SIEMERS, P. M. III, Bradley, P. F., Wolfe, H., Flanagan, P. F., Weilmuenster, K. J., and Kern, F., "Shuttle Flight Pressure Instrumentation: Experience and Lessons for the Future," *Shuttle Performance: Lessons Learned*, Part 2, NASA CP-2283, October 1983, pp. 1255-1275.

STEWART, D. A, Rakich, J. V., and Lanfranco, M. J., "Catalytic Surface Effects on Space Shuttle Thermal Protection System During Earth Entry of Flights STS-2 through STS-5," *Shuttle Performance: Lessons Learned*, Part 2, NASA CP-2283, October 1983, pp. 827-845.

THROCKMORTON, D. A., Zoby, E. V., and Hamilton, H. H. II, "Orbiter Catalytic/Non-Catalytic Heat Transfer as Evidenced by Heating to Contaminated Surfaces on STS-2 and STS-3," *Shuttle Performance: Lessons Learned*, Part 2, NASA CP-2283, October 1983, pp. 847-864.

THROCKMORTON, D. A., "Benchmark Determination of Shuttle Orbiter Entry Aerodynamic Heat-Transfer Data," *Journal of Spacecraft and Rockets*, Vol. 20, No. 3, May-June 1983, pp. 219-224.

ZOBY, E. V., "Comparisons of STS-1 Experimental and Predicted Heating Rates," *Journal of Spacecraft and Rockets*, Vol. 20, No. 3, May-June 1983, pp. 214-218.

ZOBY, E. V., "Analyses of STS-2 Experimental Heating Rates and Transition Data," *Journal of Spacecraft and Rockets*, Vol. 20, No. 3, May-June 1983, pp. 232-237.

SCOTT, C. D., "Effects of Nonequilibrium and Surface Catalysis on Shuttle Heat Transfer - A Review," AIAA Paper 83-1485, June 1983.

WILLIAMS, S. D., and Curry, D. M., "An Assessment of the Space Shuttle Orbiter Thermal Environment Using Flight Data," AIAA Paper 83-1488, June 1983.

WEILMUENSTER, K. J., "High Angle of Attack Inviscid Flow Calculations Over a Shuttle-like Vehicle with Comparisons to Flight Data," AIAA Paper 83-1798, July 1983.

HAMILTON, H. H. II, "Approximate Method for Predicting Heating on the Windward Side of Space Shuttle Orbiter and Comparisons with Flight Data," *Progress in Astronautics and Aeronautics*, Vol. 85, 1983, pp. 21-53.

THROCKMORTON, D. A., "Influence of Radiant Energy Exchange on the Determination of Convective Heat-Transfer Rates to Orbiter Leeside Surfaces During Entry," *Progress in Astronautics and Aeronautics*, Vol. 85, 1983, pp. 78-96.

AUDLEY, D. R., and Hodge, J. K., "Identifying the Aerothermodynamic Environment of the Space Shuttle Orbiter, Columbia," *Identification and System Parameter Estimation 1982, Proceedings of the Sixth Symposium*, Vol. 2, Pergamon Press, 1983, pp. 1347-1352.

THROCKMORTON, D. A., and Zoby, E. V., "Orbiter Entry Leeside Heat-Transfer Data Analysis," *Journal of Spacecraft and Rockets*, Vol. 20, No. 6, November-December 1983, pp. 524-530.

WILLIAMS, S. D., "Columbia: The First Five Flights Entry Heating Data Series, Vol. 1, An Overview," NASA CR-171820, Nov. 1984.

WILLIAMS, S. D., "Columbia: The First Five Flights Entry Heating Data Series, Vol. 2, The OMS Pod," NASA CR-171657, May 1983.

WILLIAMS, S. D., "Columbia: The First Five Flights Entry Heating Data Series, Vol. 3, The Lower Windward Surface Centerline," NASA CR-171665, May 1983.

WILLIAMS, S. D., "Columbia: The First Five Flights Entry Heating Data Series, Vol. 4, The Lower Windward Wing 50% and 80% Semi-Spans," NASA CR-171666, May 1983.

WILLIAMS, S. D., "Columbia: The First Five Flights Entry Heating Data Series, Vol. 5, The Side Fuselage and Payload Bay Door," NASA CR-171732, January 1984.

WILLIAMS, S. D., "Columbia: The First Five Flights Entry Heating Data Series, Vol. 6, The Upper Lee Side Surface Centerline," NASA CR-171795, July 1984.

HARTUNG, L. C., and Throckmorton, D. A., "Computer Graphic Visualization of Orbiter Lower-Surface Boundary-Layer Transition," AIAA Paper 84-0228, January 1984.

SHINN, J. L., and Simmonds, A. L., "Comparison of Viscous-Shock-Layer Heating Analysis with Shuttle Flight Data in Slip Flow Regime," AIAA Paper 84-0226, January 1984.

THROCKMORTON, D. A., and Hartung, L. C., "Analysis of Entry Aerodynamic Heat Transfer Data for the Orbiter Wing Lower Surface," AIAA Paper 84-0227, January 1984.

ZOBY, E. V., Gupta, R. N., and Simmonds, A. L., "Temperature-Dependent Reaction-Rate Expression for Oxygen Recombination at Shuttle Entry Conditions," AIAA Paper 84-0224, January 1984.

PETLEY, D. H., Smith, D. M., Edwards, C. L. W., Carlson, A. B., and Hamilton, H. H. II, "Surface Step Induced Gap Heating in the Shuttle Thermal Protection System," *Journal of Spacecraft and Rockets*, Vol. 21, No. 2, March-April, 1984, pp. 156-161.

GUPTA, R. N., Moss, J. N., Simmonds, A. L., Shinn, J. L., and Zoby, E. V., "Space Shuttle Heating Analysis with Variation in Angle of Attack and Catalycity," *Journal of Spacecraft and Rockets*, Vol. 21, No. 2, March-April 1984, pp. 217-219.

LUTES, C. D., and Hodge, J. K., "Nonlinear Modeling and Initial Condition Estimation for Identifying the Aerothermodynamic Environment of the Space Shuttle Orbiter," AIAA Paper 84-1749, June 1984.

THOMPSON, R. A., "Three-Dimensional Viscous-Shock-Layer Applications for the Space Shuttle Orbiter," AIAA Paper 85-0246, January 1985.

WILLIAMS, S. D., Curry, D. M., and Goodrich, W. D., "A Sensitivity Analysis of the Shuttle Orbiter Heating," AIAA Paper 85-0901, June 1985.

ZOBY, E. V., Gupta, R. N., and Simmonds, A. L., "Temperature-Dependent Reaction Rate Expressions for Oxygen Recombination," *Progress in Astronautics and Aeronautics*, Vol. 96, 1985, pp. 445-464.

SHINN, J. L., and Simmonds, A. L., "Comparison of Viscous-Shock-Layer Heating Analysis with Shuttle Flight Data in Slip Flow Regime," *Progress in Astronautics and Aeronautics*, Vol. 96, 1985, pp. 491-510.

SCOTT, C. D., "Effects of Nonequilibrium and Wall Catalysis on Shuttle Heat Transfer," *Journal of Spacecraft and Rockets*, Vol. 22, No. 5, Sept.-Oct. 1985, pp. 489-499.

THROCKMORTON, D. A., and Hartung, L. C., "Shock-Interaction-Induced Heat Transfer to the Orbiter Wing Lower Surface," *Journal of Spacecraft and Rockets*, Vol. 22, No. 5, September-October 1985, pp. 516-522.

THOMPSON, R. A., "Three-Dimensional Viscous Shock Layer Applications for the Space Shuttle Orbiter," *Progress in Astronautics and Aeronautics*, Vol. 103, 1986, pp. 541-570.

BLACKWELL, H. E., Scott, C. D., Hoffman, J. A., Mende, S. B., and Swenson, G. R., "Spectral Measurement of the Space Shuttle Leeside Shock Layer and Wake," AIAA Paper 86-1262, June 1986.

HODGE, J. K., and Audley, D. R., "Aerothermodynamic Parameter Estimation from Shuttle Thermocouple Data During Transient Flight Test Maneuvers," *Journal of Spacecraft and Rockets*, Vol. 23, No. 5, Sept.-Oct. 1986, pp. 453-460.

HARTUNG, L. C., and Throckmorton, D. A., "Computer Graphic Visualization of Orbiter Lower Surface Boundary Layer Transition," *Journal of Spacecraft and Rockets*, Vol. 24, No. 2, March-April 1987, pp. 109-114.

THOMPSON, R. A., "Comparison of Nonequilibrium Viscous-Shock-Layer Solutions with Windward Surface Shuttle Heating Data," AIAA Paper 87-1473, June 1987.

SUTTON, K., Zoby, E. V., and Hamilton, H. H. II, "Overview of CFD Methods and Comparisons with Flight Aerothermal Data. AGARD Symposium on Validation of Computational Fluid Dynamics, May 1988.

HARTUNG, L. C., and Throckmorton, D. A., "Space Shuttle Entry Heating Data Book, Volume 1 - STS-2, Parts 1 and 2," NASA RP-1191, May 1988.

HARTUNG, L. C., and Throckmorton, D. A., "Space Shuttle Entry Heating Data Book, Volume 2 - STS-3, Parts 1 and 2," NASA RP-1192, May 1988.

HARTUNG, L. C., and Throckmorton, D. A., "Space Shuttle Entry Heating Data Book, Volume 3 - STS-5, Parts 1 and 2," NASA RP-1193, May 1988.

THROCKMORTON, D, A., Dunavant, J. C., and Myrick, D. L., "Shuttle Infrared Leeside Temperature Sensing (SILTS) Experiment -- STS 61-C Results," AIAA Paper 88-2668, June 1988.

DUNAVANT, J. C., Myrick, D. L., Zoby, E. V., and Throckmorton, D. A., "Shuttle Infrared Leeside Temperature Sensing (SILTS) Experiment STS 61-C Final Results," NASA TP-2958, December 1989.

THOMPSON, R. A., "Comparison of Nonequilibrium Viscous-Shock-Layer Solutions with Windward Surface Shuttle Heating Data," *Journal of Thermophysics and Heat Transfer*, Vol. 4, No. 2, April 1990.

THROCKMORTON, D. A., Zoby, E. V., Dunavant, J. C., and Myrick, D. L., "Shuttle Infrared Leeside Temperature Sensing (SILTS) Experiment-STS-28 Preliminary Results," AIAA Paper 90-1741, June 1990.

BOUSLOG, S. A, An, M. Y., Hartmann, L. N., and Derry, S. M., "Review of Boundary Layer Transition Flight Data on the Space Shuttle Orbiter," AIAA Paper 91-0741, January 1991.

THROCKMORTON, D. A., Zoby, E. V., Dunavant, J. C., and Myrick, D. L., "Shuttle Infrared Leeside Temperature Sensing (SILTS) Experiment-STS-35 and STS-40 Preliminary Results," AIAA Paper 92-0126, January 1992.

KLEB, W. L., and Weilmuenster, James K., "Characteristics of The Shuttle Orbiter Leeside Flow During A Reentry Condition," AIAA Paper 92-2951, July 1992.

WEILMUENSTER, J. K., and Gnoffo, P. A., "Solution Strategies And Heat Transfer Calculations For Three-Dimensional Configurations At Hypersonic Speeds," AIAA Paper 92-2921, July 6-8, 1992.

☆U.S. GOVERNMENT PRINTING OFFICE: 1995—841-253-13

COLOR FIGURES

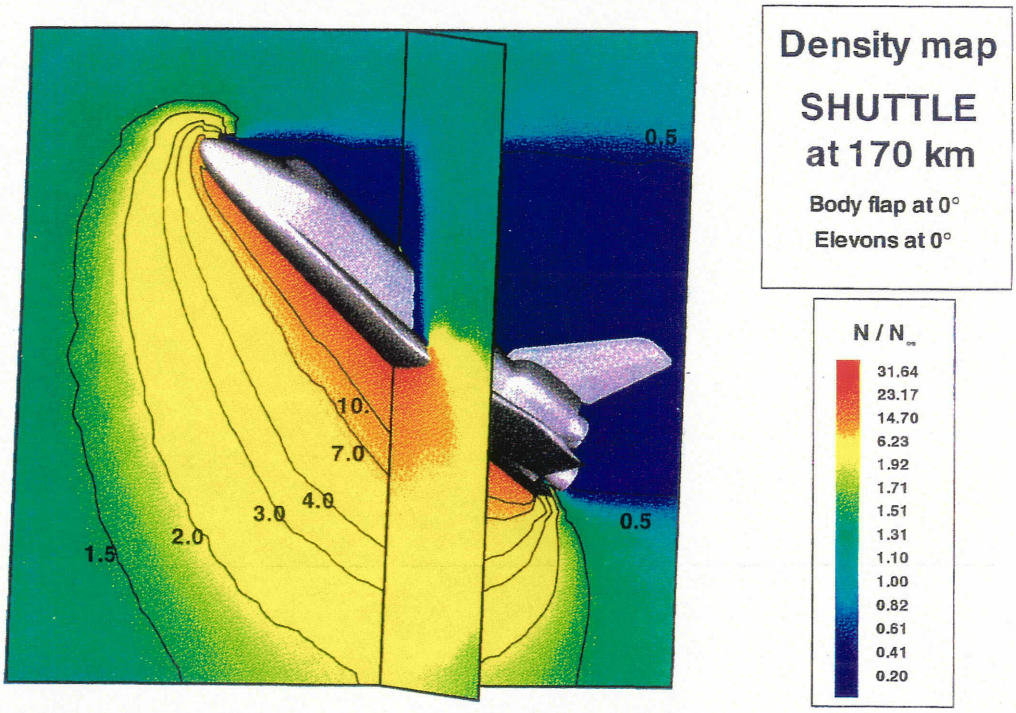

Figure 2. Total density map around Shuttle Orbiter at 170 km altitude.

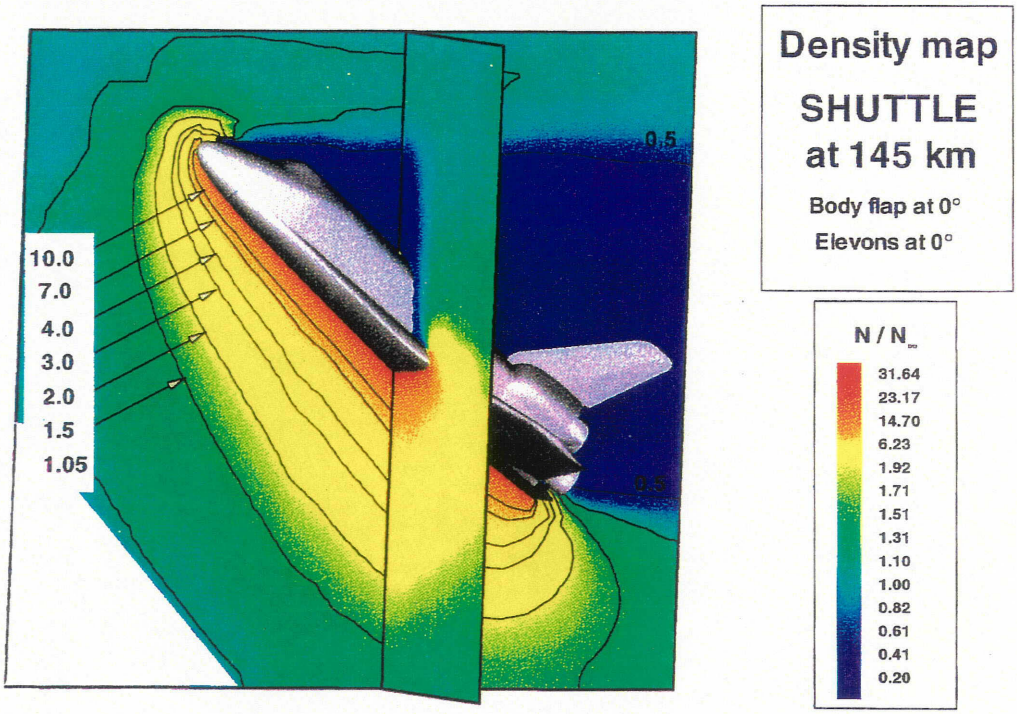

Figure 3. Total density map around Shuttle Orbiter at 145 km altitude.

(Color versions of black and white photographs shown on page 588.)

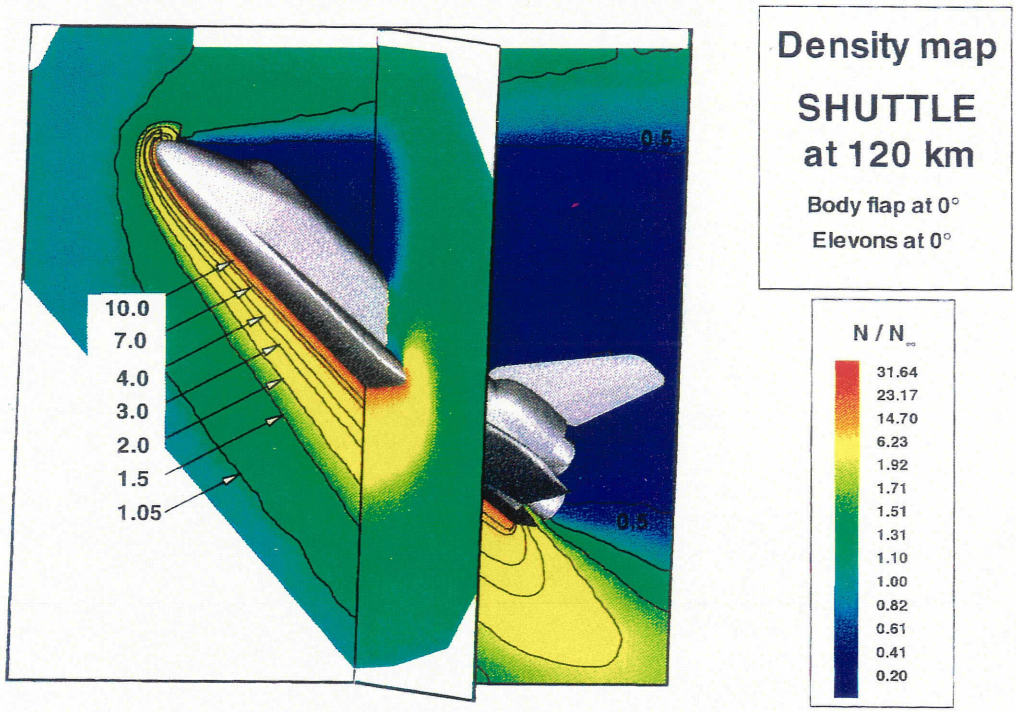

Figure 4. Total density map around Shuttle Orbiter at 120 km altitude.

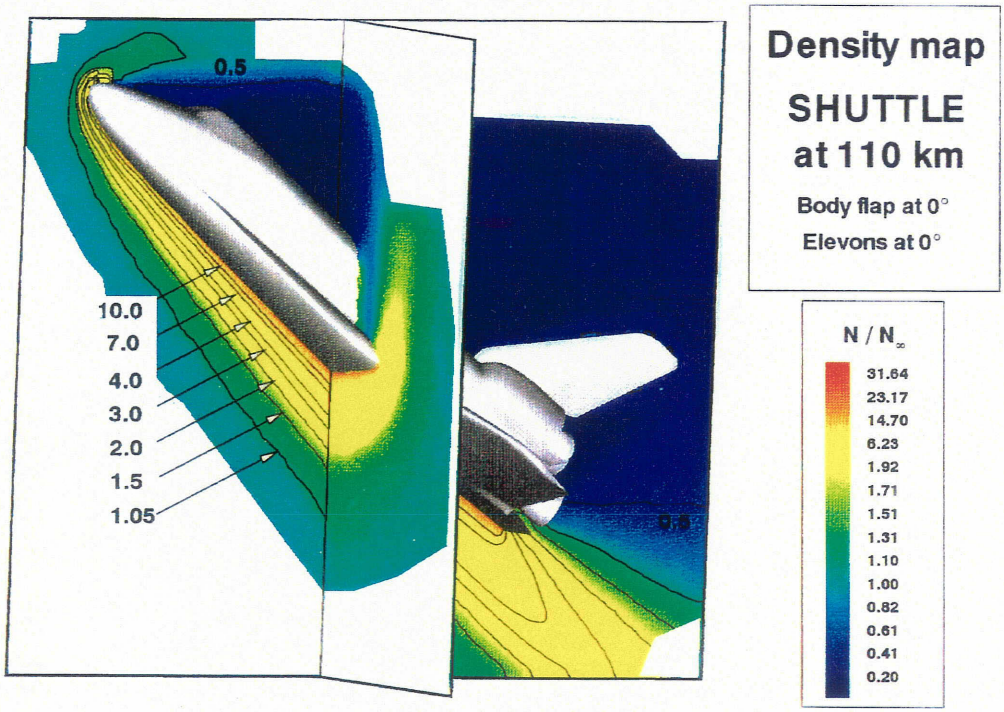

Figure 5. Total density map around Shuttle Orbiter at 110 km altitude.

(Color versions of black and white photographs shown on page 589.)

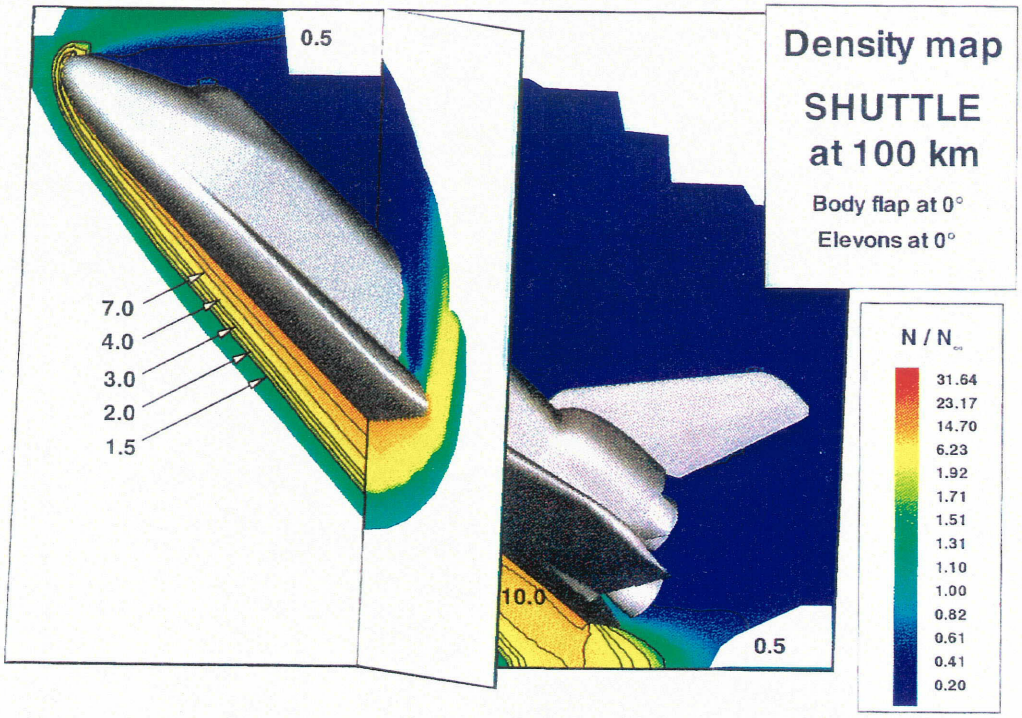

Figure 6. Total density map around Shuttle Orbiter at 100 km altitude

(Color version of black and white photograph shown on page 590.)

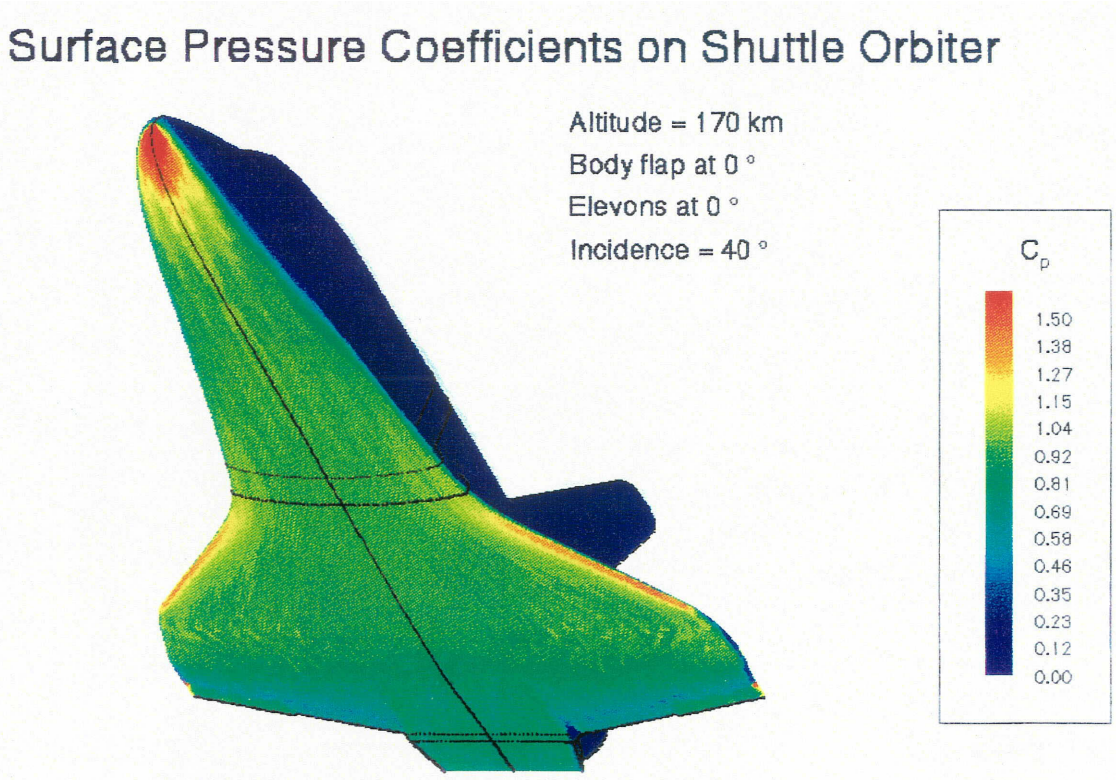

Figure 22. Pressure force distribution on Shuttle Orbiter at 170 km.

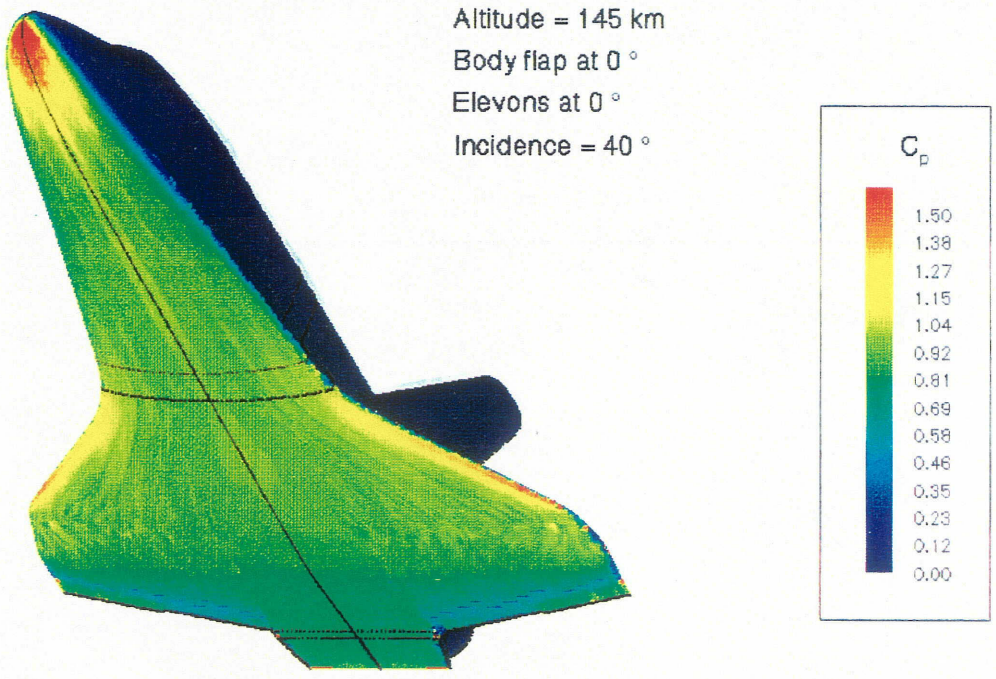

Figure 23. Pressure force distribution on Shuttle Orbiter at 145 km.

(Color version of black and white figures shown on page 599.)

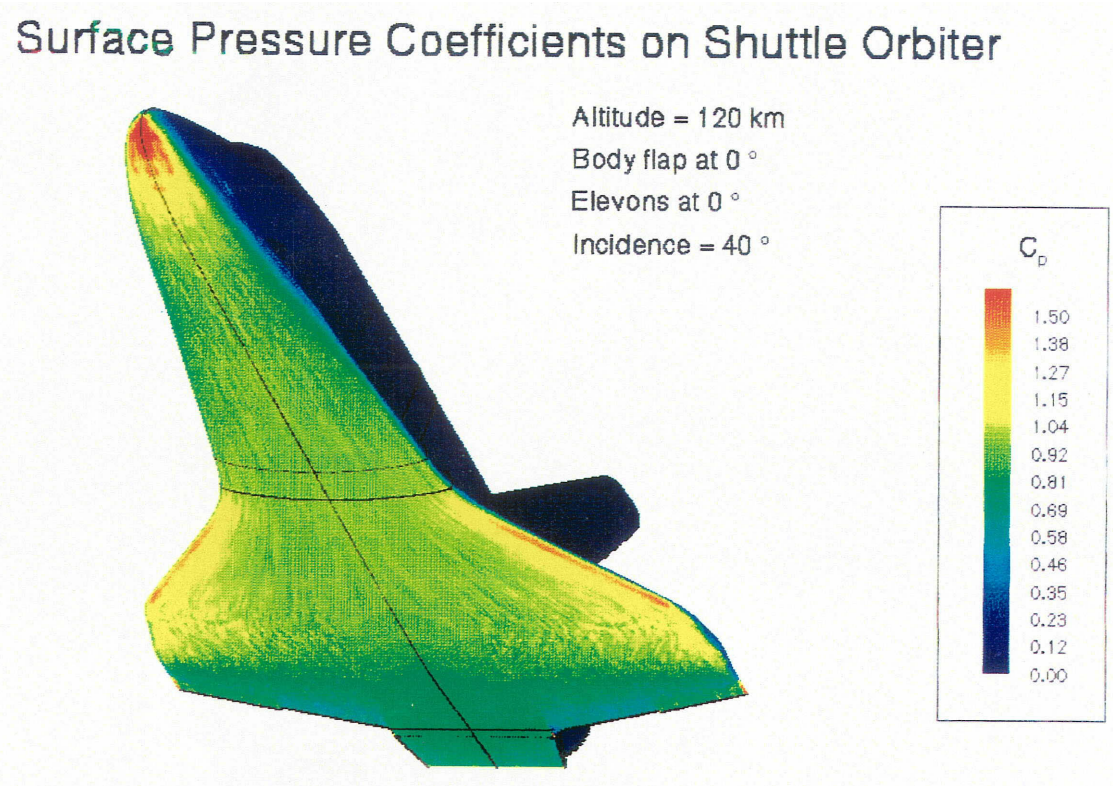

Figure 24. Pressure force distribution on Shuttle Orbiter at 120 km.

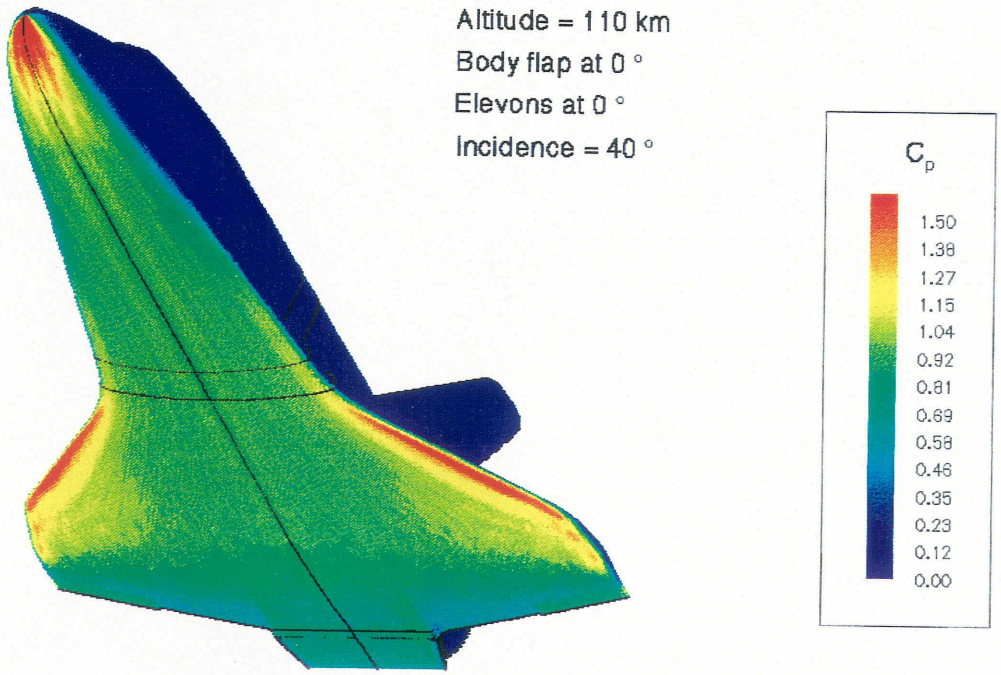

Figure 25. Pressure force distribution on Shuttle Orbiter at 110 km.
(Color version of black and white figures shown on page 600.)

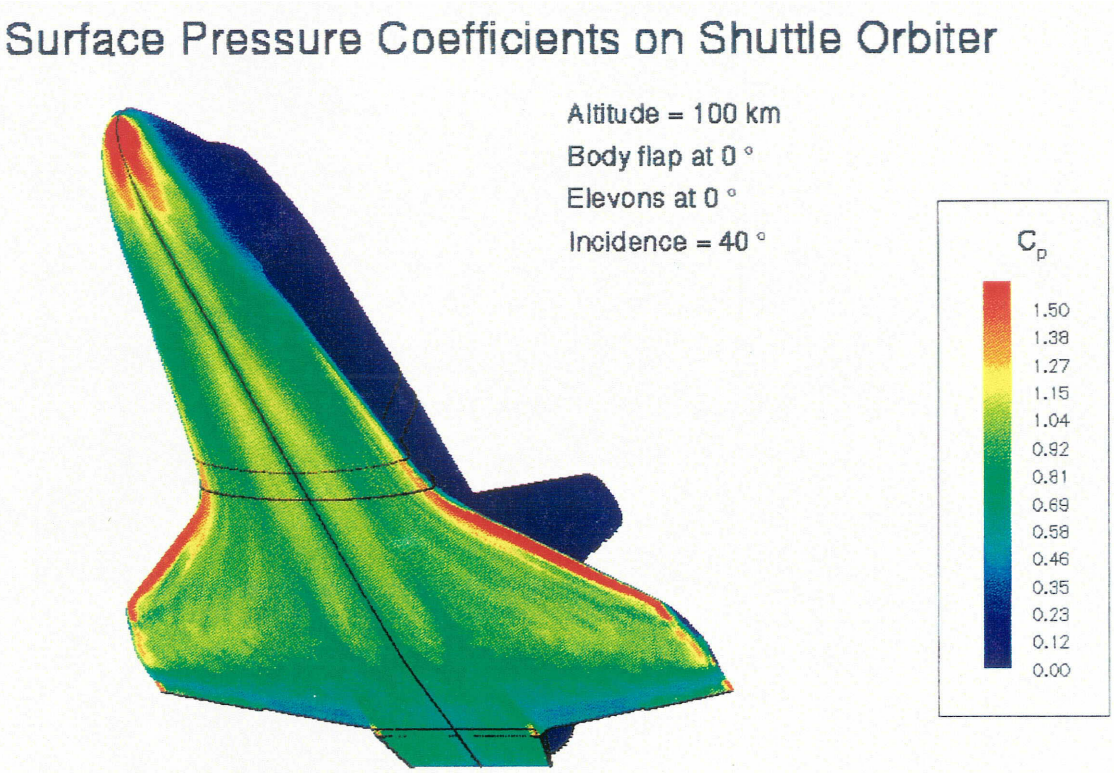

Figure 26. Pressure force distribution on Shuttle Orbiter at 100 km.

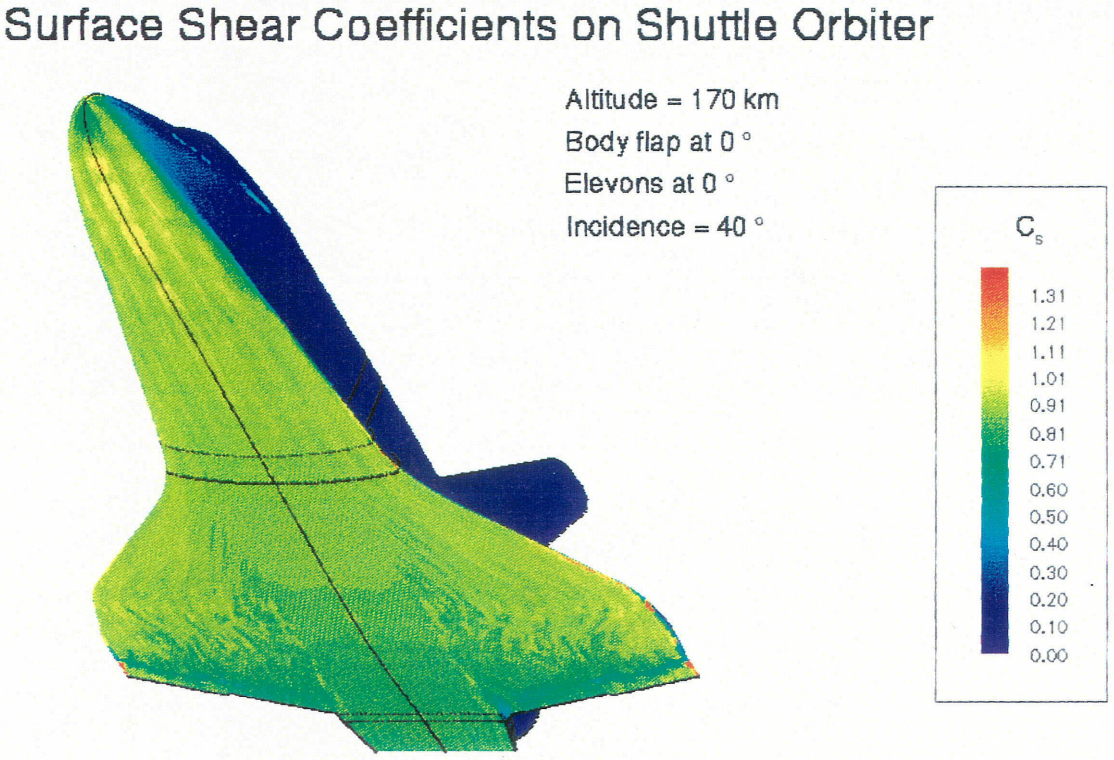

Figure 27. Shear force distribution on Shuttle Orbiter at 170 km.
(Color versions of black and white figures shown on page 601.)

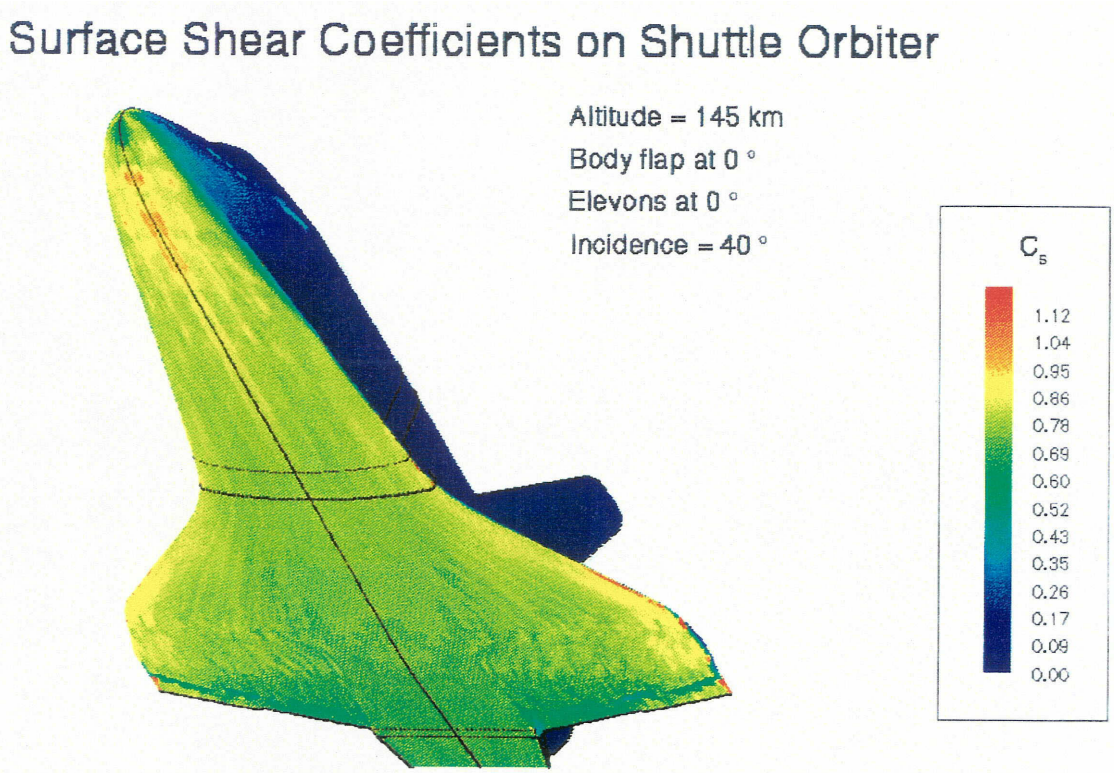

Figure 28. Shear force distribution on Shuttle Orbiter at 145 km.

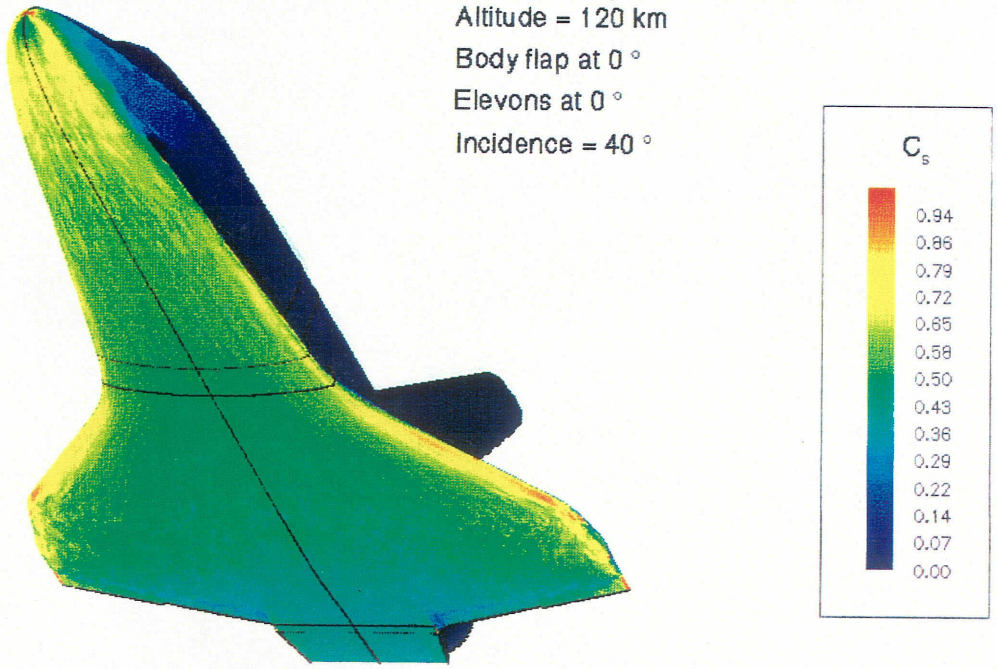

Figure 29. Shear force distribution on Shuttle Orbiter at 120 km.
(Color versions of black and white figures shown on page 602.)

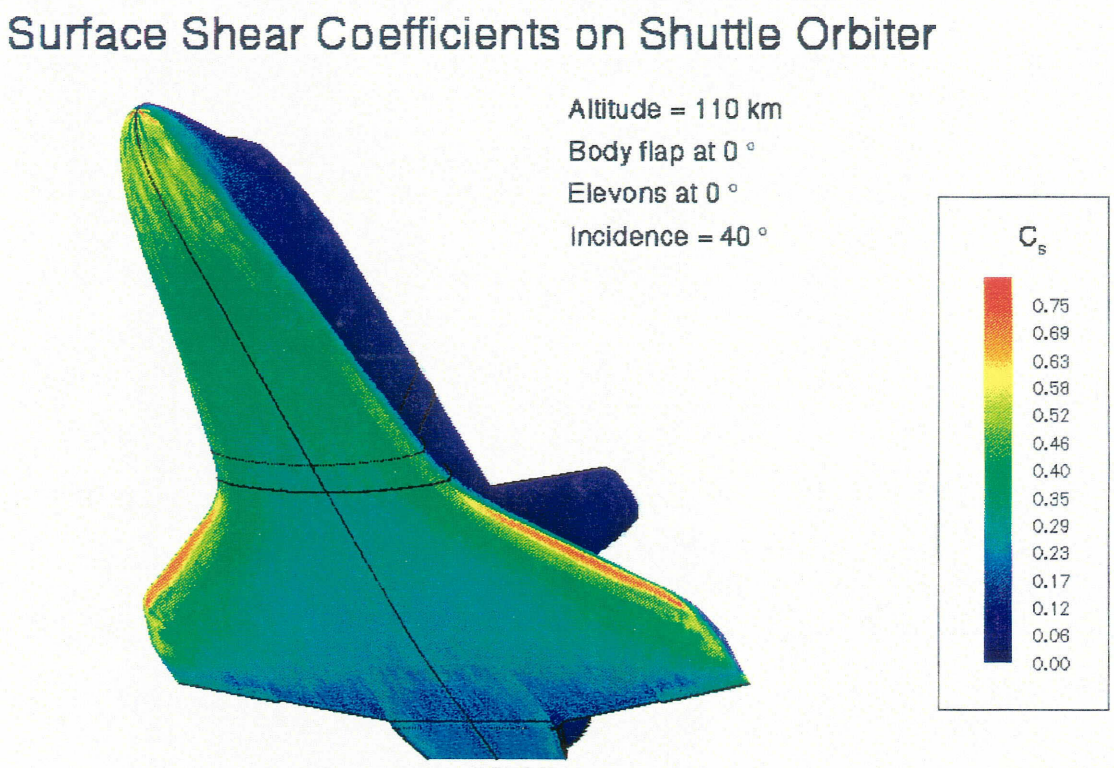

Figure 30. Shear force distribution on Shuttle Orbiter at 110 km.

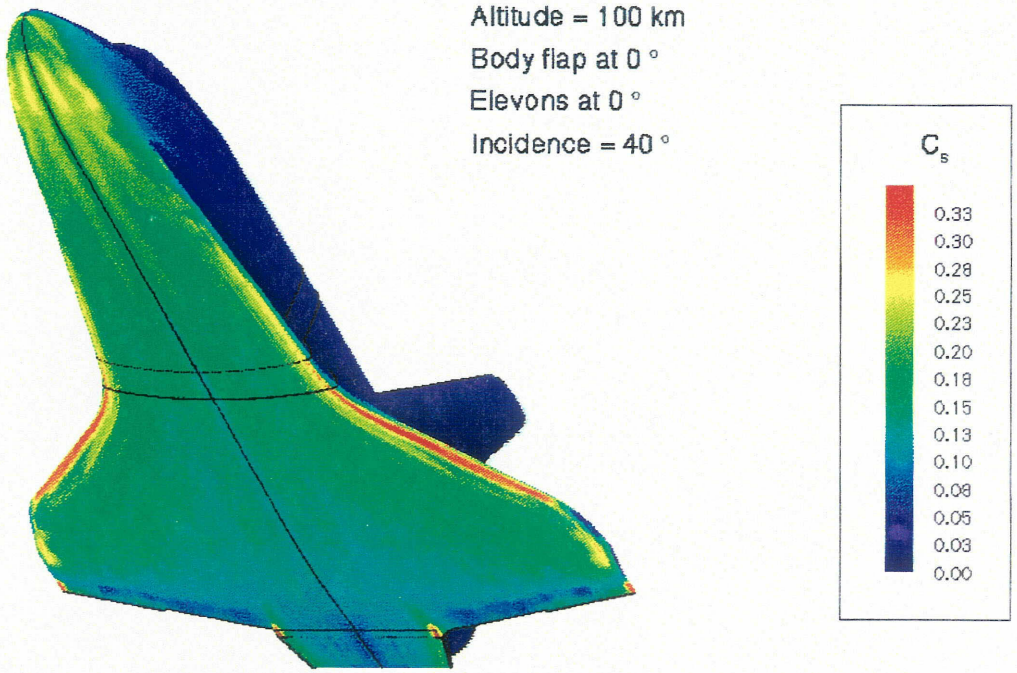

Figure 31. Shear force distribution on Shuttle Orbiter at 100 km.
(Color versions of black and white figures shown on page 603.)

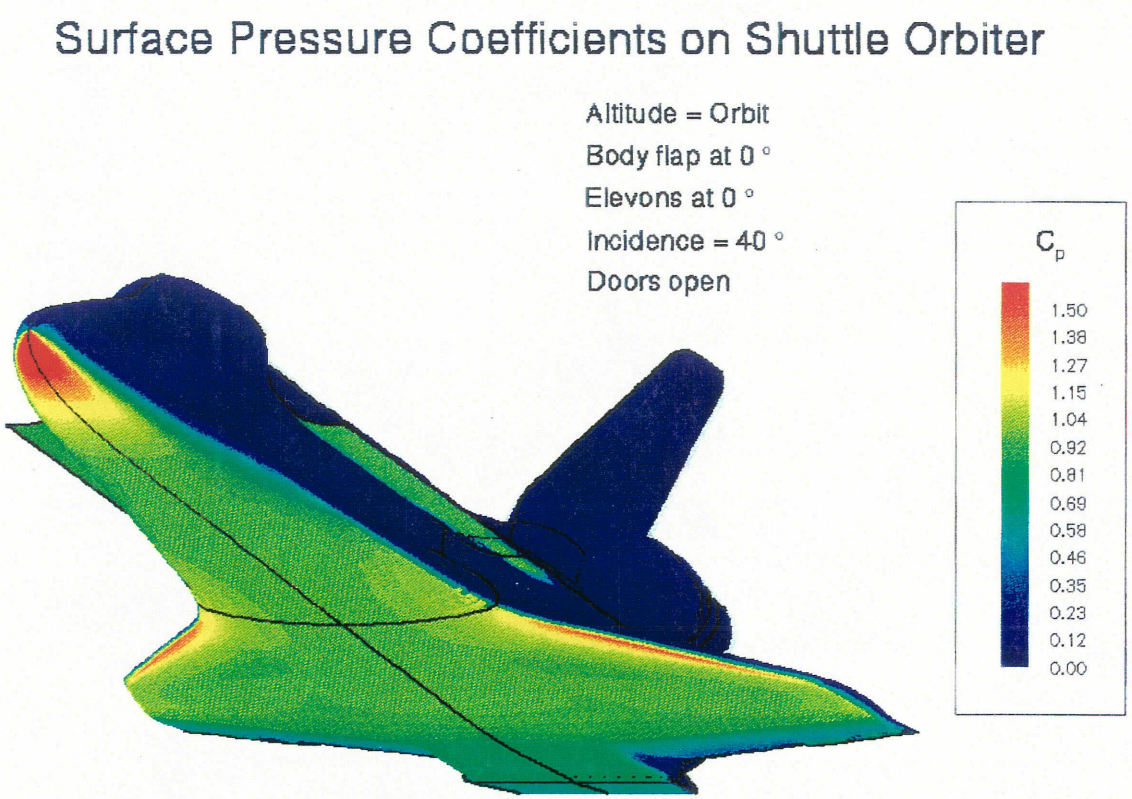

Figure 33. Pressure force distribution on Shuttle Orbiter in orbit at 40 degrees incidence.

(Color version of black and white figure shown on page 604.)

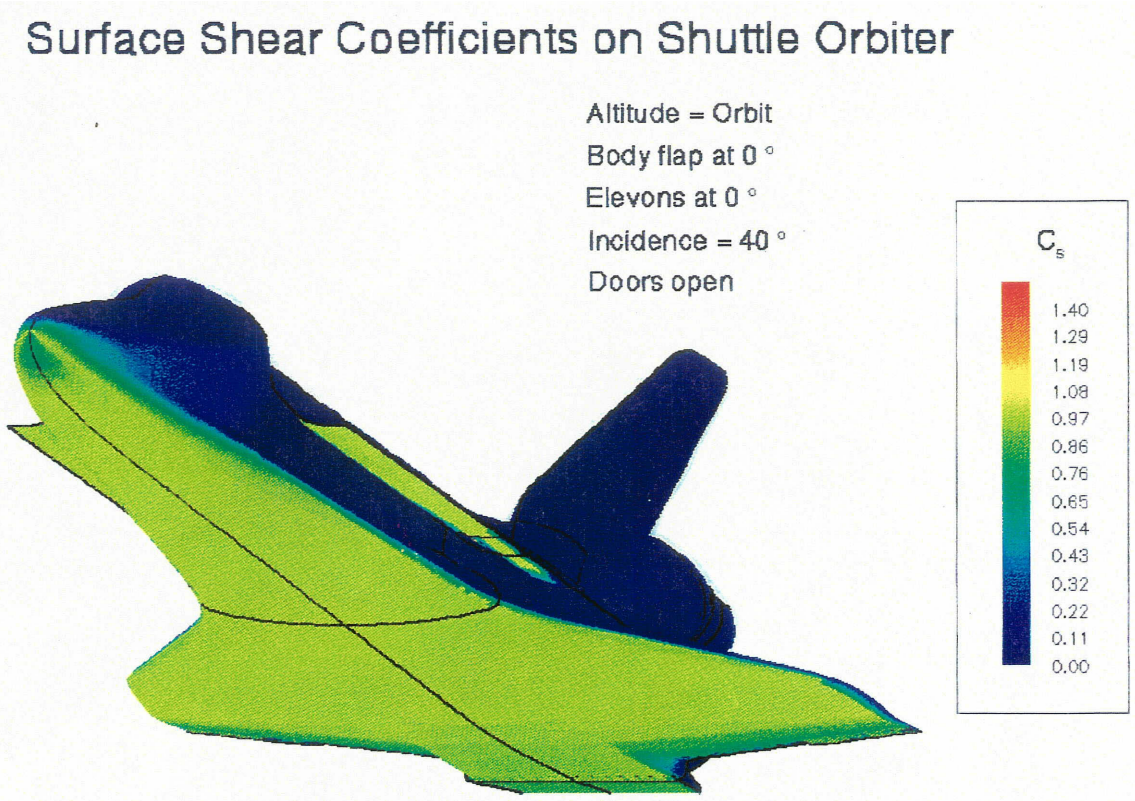

Figure 34. Shear force distribution on Shuttle Orbiter in orbit at 40 degrees incidence.

(Color version of black and white figure shown on page 605.)

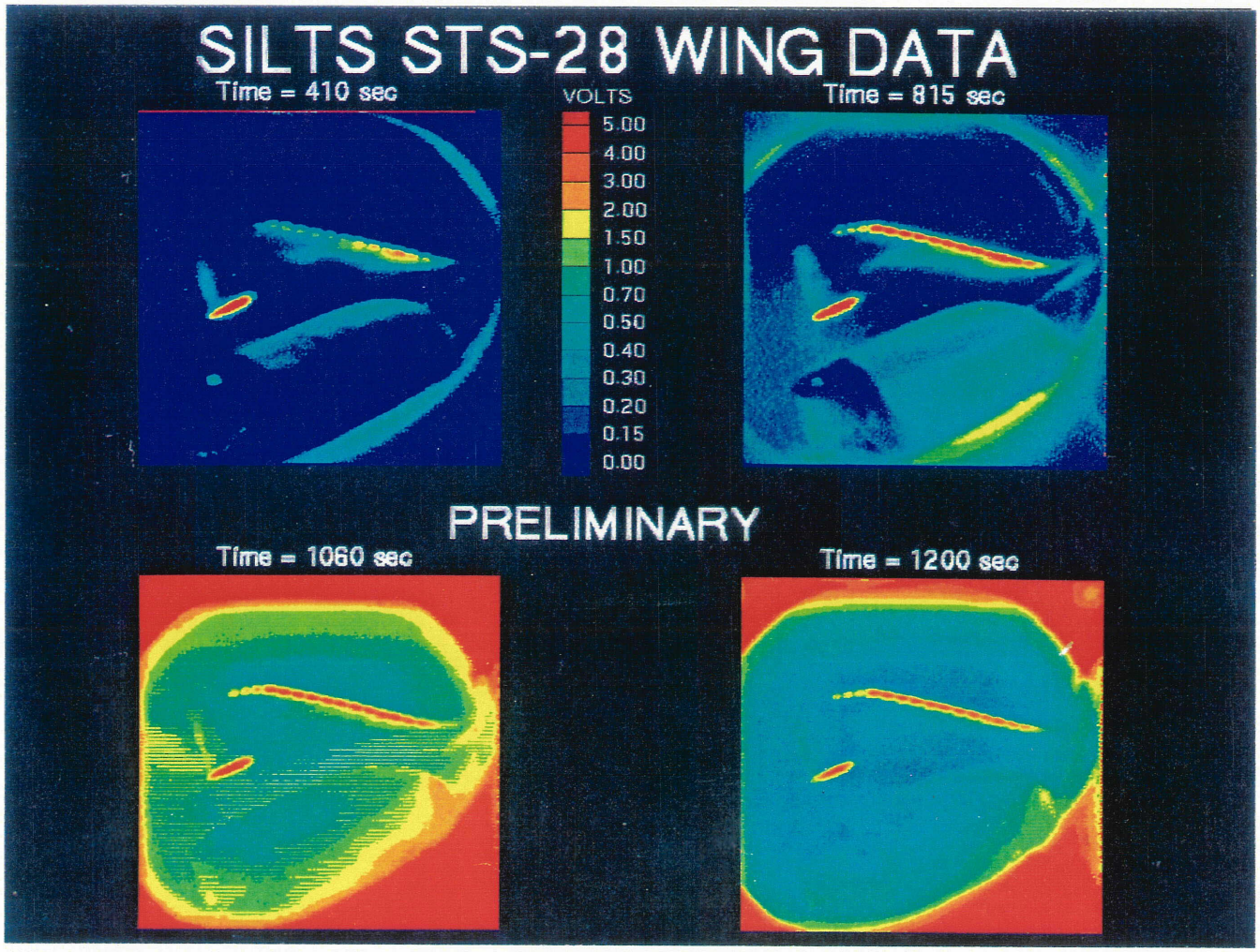

Figure 9
(Shown in black and white on page 816.)

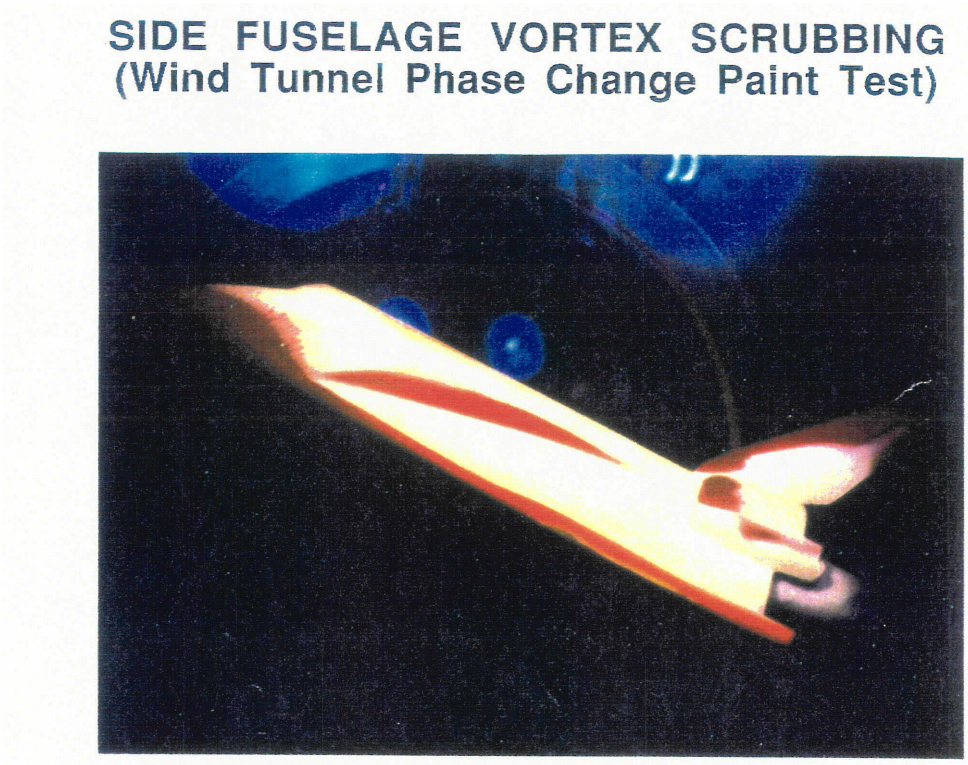

Figure 13

(Shown in black and white on page 818.)

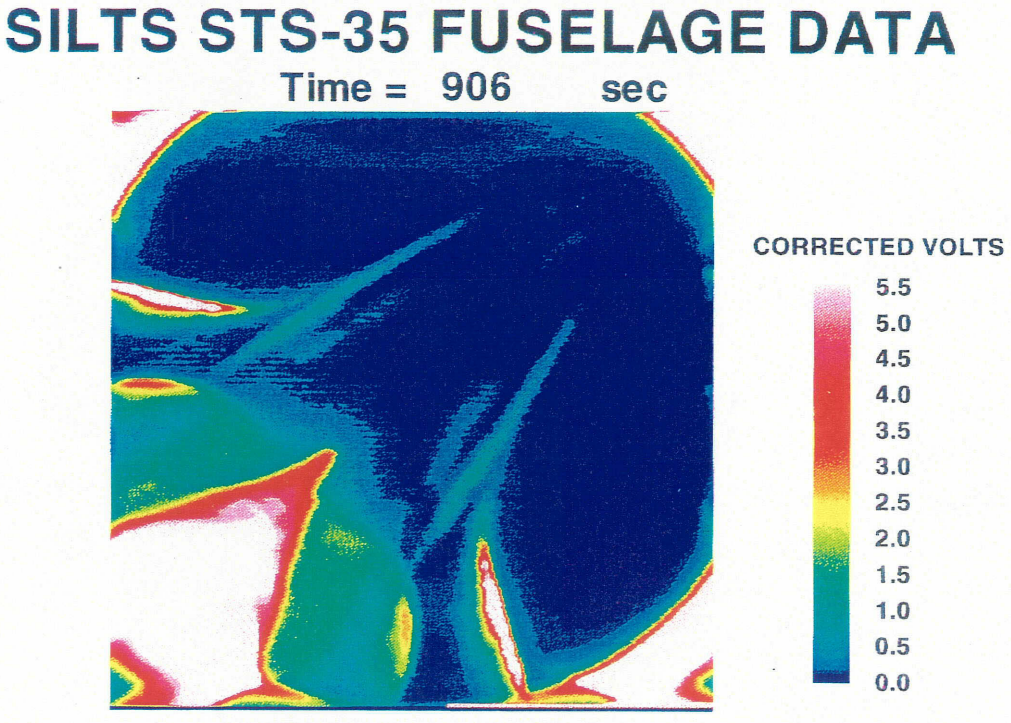

Figure 16

(Shown in black and white on page 819.)

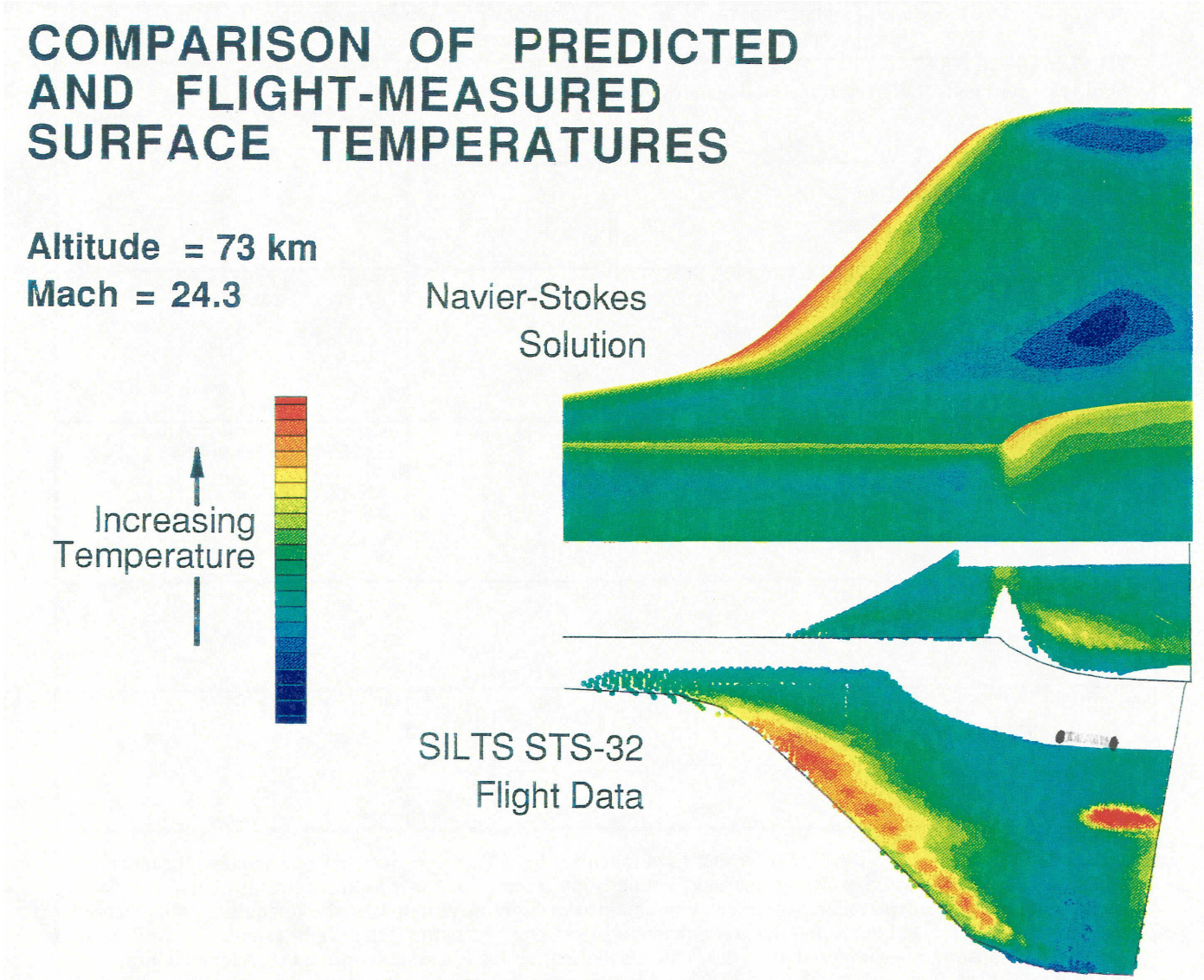

Figure 20

(Shown in black and white on page 821.)

REPORT DOCUMENTATION PAGE

Form Approved
OMB No. 0704-0188

1. AGENCY USE ONLY *(Leave blank)*	2. REPORT DATE	3. REPORT TYPE AND DATES COVERED
	April 1995	Conference Publication

4. TITLE AND SUBTITLE
Orbiter Experiments (OEX) Aerothermodynamics Symposium

5. FUNDING NUMBERS
WU 506-40-91-01

6. AUTHOR(S)
David A. Throckmorton, Editor

7. PERFORMING ORGANZATION NAME(S) AND ADDRESS(ES)
NASA Langley Research Center
Hampton, VA 23681-0001

8. PERFORMING ORGANIZATION REPORT NUMBER
L-17373B

9. SPONSORIING/MONITORING AGENCY NAME(S) AND ADDRESS(ES)
National Aeronautics and Space Administration
Washington, DC 20546-0001

10. SPONSORING/MONITORING AGENCY REPORT NUMBER
NASA CP-3248, Part 2

11. SUPPLEMENTARY NOTES

12a. DISTRIBUTION/AVAILABILITY STATEMENT
[redacted] Publicly Available
Subject Categories 34 and 16

12b. DISTRIBUTION CODE

13. ABSTRACT *(Maximum 200 words)*

Initiated in the mid-1970's, the NASA Orbiter Experiments (OEX) Program provided a mechanism for utilization of the Shuttle Orbiter as an entry aerothermodynamic flight-research vehicle, as an adjunct to its normal operational missions. OEX experiment instrumentation obtained in-flight measurements of the requisite parameters for determination of the Orbiter's aerodynamic characteristics over the entire entry flight regime, as well as the aerodynamic-heating rates imposed upon the vehicle's thermal protection system during the hypersonic portion of atmospheric entry. Data derived from the OEX complement of experiments comprise benchmark hypersonic flight data. These data are being used in a continual process of validation of state-of-the-art methods, both experimental and computational, for simulating/predicting the aerothermodynamics characteristics of advanced space transportation vehicles. This Orbiter Experiments Aerothermodynamics Symposium provided a forum for the dissemination of OEX experiment results, and for demonstration of the manner in which OEX data are being used for validation of advanced vehicle aerothermodynamics design tools.

14. SUBJECT TERMS	15. NUMBER OF PAGES
Space shuttle; Flight data; Aerodynamics; Aerothermodynamics	462
	16. PRICE CODE A20

17. SECURITY CLASSIFICATION OF REPORT	18. SECURITY CLASSIFICATION OF THIS PAGE	19. SECURITY CLASSIFICATION OF ABSTRACT	20. LIMITATION OF ABSTRACT
Unclassified	Unclassified	Unclassified	